Dynamic NMR Microscopy

動態核磁顯微成像

VOLUME I

A thesis presented in partial fulfilment of
the requirements for the degree of
Doctor of Philosophy in Physics
at
Massey University

by

Yang Xia

夏 陽

1992

Abstract

The theory and practice of Dynamic NMR Microscopy are described in detail. The description consists of a brief presentation of **k**-space imaging which includes the 2-D filtered back-projection (PR) reconstruction algorithm as well as the influence of various image contrast factors, a detailed discussion of **q**-space imaging which employs the Pulsed-Gradient Spin-Echo (PGSE) sequence and a thorough description of Dynamic NMR Microscopy which combines both **k**-space and **q**-space mapping. The velocity and self-diffusion image artifacts and errors associated with Dynamic NMR Microscopy have also been investigated extensively.

As part of this work, various modifications to and developments of the existing imaging system have been made. These include the probe design for 'non-trivial' flow imaging experiments and software programming using assembly, BASIC, FORTRAN and PASCAL languages. Several instrument-related issues in NMR microscopy have also been investigated. They include the attempt to improve spatial resolution by scaling down the receiver coil, the zero-frequency 'glitch' artifact in images and the effect of induced eddy current in imaging experiments.

The results of the comprehensive water capillary flow experiments have shown that simultaneous measurement of velocity and self-diffusion coefficient can be made both accurately and precisely using Dynamic NMR Microscopy. Imaging experiments which investigate molecular motion of relevance to plant physiology, fluid dynamics and polymer physics have been carried out. In the *in vivo* botanical studies, velocities of approximately 10 μm/s in the castor bean experiment and 45 μm/s in the *Stachys* experiment have been measured. In the rheological studies, induced secondary flow (eddy) around the abrupt junction in a tube was observed, which has agreed well with numerical simulation of the Navier-Stokes equation. In the studies of unusual rheological properties of high molar mass polymer solutions, velocity profiles for WSR301 polyethylene oxide (PEO)/H_2O in capillary flow were measured and fitted using the power law model. The measurement of self-diffusion profiles for monodisperse PEO standards in D_2O has shown clear evidence for the breakdown of molecular entanglements in semi-dilute solutions once the shear rate exceeds the equilibrium tube renewal rate, τ_d^{-1}.

Acknowledgments

First of all, I wish to express my sincere gratitude to my parents for their constant encouragement from the early years of my education by creating an environment conducive to study and thinking, also for their great sacrifices during the years of my study abroad.

I would like to thank my chief supervisor, Professor Paul T. Callaghan, for providing continuing guidance and careful instruction throughout the project and for his great patience while this manuscript has been written. I would also like to thank my co-supervisors, Professor David A.D. Parry and Associate Professor Rod K. Lambert, for their support especially during Paul's six-month leave to Europe.

I wish to express my sincere thanks to the following people:

Professor Ken R. Jeffrey of the Physics Department, University of Guelph, Ontario, Canada for his help in the manufacturing of the plant-imaging probe, for his computer simulation of the induced eddies in the stepped tube using Navier-Stokes equation and for his advice during his six-month visit at Massey University;

Associate Professor Rod K. Lambert of the Physics and Biophysics Department, Massey University for his advice on PEO rheology measurements and other rheological issues;

Dr Ella Campbell of the Plant Biology Department, Massey University for her various advice regarding botanical samples, and for identifying the species, *Stachys sylvatica* L. ;

Walter Köckenberger of University of Bayreuth, Bayreuth, Germany for his advice on the castor bean imaging experiments;

Vasil Sarafis of University of Western Sydney, Sydney, Australia for his advice on the *Equisetum* and moss velocity imaging experiments;

Dr Al Rowland of the Plant Biology Department, Massey University for photographing several plant samples using an optical microscope;

Associate Professor Graeme Midwinter of the Chemistry and Biochemistry Department, Massey University for supplying the HPLC tubing in the polymer flow experiment;

Dr Colin Jenner of the Waite Agricultural Research Institute, The University of Adelaide, Australia for his advice on the preparation of wheat grain samples;

Ian R. Brooking of the Fruit and Trees Division of DSIR, Palmerston North for supplying the wheat samples used in the wheat grain experiments;

Dr Rosie Wang of Brisbane, Queensland, Australia for carrying out the GPS analysis for the WSR 301 PEO sample;

My father, Professor Chen-Au Hsia of Shanghai Institute of Plant Physiology, Academia Sinica, Shanghai, China, for his advice on various botanical issues during his recent visit to New Zealand while this manuscript was being written;

Other overseas visitors to the department and the NMR research group for their advice and friendship during their visits: Dr Milo Shott, Open University, UK; Dr M. Iko Burgar of BHP Melbourne Research & New Technology, Australia; Associate Professor Jim Pope of University of New South Wales, Kensington, Australia; Dr Ted M. Garver of Lakehead University, Ontario, Canada; Professor Wilmer G. Miller of Department of Chemistry, University of Minnesota, Minneapolis, USA; Sharon L. Umbach, Department of Food Technology, University of Minnesota, St Paul, USA;

Fellow colleagues and post-graduate students in the NMR research group: Dr Phil Back, Andrew Coy, Craig Rofe and Lucy Forde for their friendship;

The staff of the mechanical workshop and electronic workshop at Massey University for providing technical assistance on a number of occasions.

The staff of the Physics and Biophysics Department, Massey University for their support and friendship;

Massey University for providing financial support in the form of a Graduate Assistantship.

Finally I would like to express my deep appreciation and special thanks for the unfailing encouragement and support given to me by my wife, Ping.

Contents

VOLUME TWO Appendices: Software development

List of Figures

List of Tables

List of Symbols

a	RF coil radius	34
a_m	Complex admixture amplitudes of a spin system	6
B	Magnetic field	5
B_0	Amplitude of the main magnetic field	5
B_1	Amplitude of the transverse rf field $\mathbf{B_1}(t)$	10
$\mathbf{B_1}(t)$	RF field (in the transverse plane)	10
c	Concentration	282
c_p	Specific heat at the constant pressure	88
c^*	Critical concentration	282
D	Self-diffusion coefficient	40
D_s	Centre-of-mass self-diffusion coefficient	282
D_0	Zero concentration self-diffusion coefficient	289
D	Self-diffusion tensor	54
E(m)	Energy eigenvalues of a spin system	6
$E_c(\mathbf{r})$	Normalized contrast factor	36
$E(\mathbf{g},\delta,\Delta)$	Echo signal amplitude	54
f_0	Resonant frequency	34
F	Noise figure of an instrument	16
F[ ]	Fourier transform of the function in [ ]	60
g	Field gradient in **q** space	53
g_m	Maximum gradient employed in dynamic imaging	63
G	Field gradient	23
$\mathcal{H}$	Hamiltonian operator	5
I	Spin quantum number	5
I	The dimensionless spin angular momentum operator	5
I_e	Induced eddy currents	175
I_z	The z component of **I**	5
j	90° shift of the phase	102
k	Thermal conductivity of the fluid	88
k	Static reciprocal space vector	27
k_B	Boltzmann constant	9
k_{FWHM}	Digital self-diffusion coefficient value	64
k_V	Digital velocity value	64
l	Length of the capillary tube	89
L	Length of the conductor	16

Chapter 1 Introduction

1.1 An introduction

Nuclear Magnetic Resonance (NMR) has proved to be unique in obtaining details of local molecular environments. In conventional NMR experiments, a sample is placed in a *very* uniform magnetic field, so that the resonant frequency of the nuclei depends upon the external magnetic field strength modified slightly but solely by the local molecular structure.

NMR imaging, by contrast, relies upon a deliberately non-uniform magnetic field to non-invasively derive and display the hetero-structure of the sample. The first experimental demonstrations of the feasibility of NMR imaging were published in 1973. Since then, NMR imaging, or MRI, has become a novel tool in scientific research and hospital diagnosis. Although the proton (^{1}H) is still the most commonly used nucleus because of its sensitivity, imaging using other nuclei (^{17}O, ^{19}F and ^{31}P) has become possible in practice. Where the voxel resolution of the image is less than $(100\ \mu m)^3$, NMR imaging can be termed NMR microscopy.

In practice, it is difficult to *quantitatively* relate the NMR image intensity with the nuclear spin density, because there are other factors which complicate a proportional interpretation. These factors include magnetic susceptibility variation due to the hetero-structure of the sample and the relaxation of the nuclei. However, molecular information can be quantitatively and accurately extracted in imaging experiments by incorporating appropriate image contrast schemes. (An image contrast scheme is a method to emphasize the contribution of a certain molecular information through the intensity of the image.) Such information includes the chemical shift, the nuclear spin relaxation rates and the magnetization phase shift associated with motion. It is these quantitative measurements which make NMR imaging a unique tool in scientific research and practical applications. This thesis will demonstrate some of the applications which are possible using the contrast which derives from motion-induced phase-shifts.

In NMR imaging, the measurement is carried out in a reciprocal space (**k** space) which is conjugate to the static displacement space **r**. Thus a Fourier relationship relates the signal in **k** and the nuclear spin density in **r**, and NMR imaging can be referred to as

k-space imaging. In an analogue manner the Pulsed-Gradient-Spin-Echo (PGSE) method involves measurement of the signal in a reciprocal space (**q** space) which is conjugate to the dynamic displacement space **R**. In that sense the PGSE experiment may be regarded in a form of imaging in its own right. The "image" obtained from a Fourier transformation in **q** space is the averaged propagator of the motion. From this propagator, velocity and self-diffusion coefficient of molecules may be derived. Combined **k**-space and **q**-space imaging is termed **Dynamic NMR Microscopy**, and is capable of obtaining velocity and self-diffusion maps simultaneously. The theoretical discussion and the quantitative application of this technique are the principal subject of this thesis.

Because of the phase-encoding inherent in the PGSE method, Dynamic NMR Microscopy requires complex signal detection, *i.e.*, both the in-phase and quadrature-phase signals must be obtained simultaneously. The phase modulation due to motion also implies that the usual symmetry relationship, $S^*(\mathbf{k})=S(-\mathbf{k})$, is no longer available in **k**-space imaging experiments and a full four-quadrant sampling must be used in image reconstruction.

The images described in this thesis are reconstructed using the filtered back-projection reconstruction (PR) algorithm and carried out on a micro-imaging system with an electromagnet. The PR algorithm is chosen because it is straightforward and easy to implement, and also because its pulse sequence has the smallest signal loss in the 'dead' time between the slice formation and the sampling. Therefore it is one of the most sensitive imaging techniques. The demand for good signal-to-noise ratio in the image becomes so critical in NMR microscopy that every stage of the experiment has to be optimized. This includes the optimization of the gradient coil and rf coil, which often suggests the need to design a new imaging probe for each specific experiment.

In terms of sensitivity of imaging experiments, the electromagnet is unfavourable because of its low magnetic field strength and poor field stability. However, the electromagnet environment does provide three distinct advantages over high-field superconducting magnets. First, an electromagnet provides a convenient geometry for applications which are of interest in this work, namely fluid flow and vascular motion in plants. The ample space above and below the electromagnet gives easy access for these two very different kinds of translational motion measurements. Second, vertical flow measurements in an electromagnet permit the use of a solenoidal receiver coil while such experiments in the vertical-bore superconducting magnets require a saddle-shape receiver coil having only a third of the sensitivity. Of course a

horizontal-bore superconducting magnet does share the electromagnet advantage, but at a cost greatly in excess of the vertical-bore superconducting magnet of the same frequency strength and over an order of magnitude higher than the electromagnet. The final advantage of an electromagnet is that there is less need to provide gradient shielding in order to avoid disturbances due to the induced eddy currents. This advantage becomes particularly important in our experiments using Dynamic NMR Microscopy because pulsed magnetic field gradients of up to 10 T m^{-1} amplitude are used to measure the delicate velocity and slow self-diffusion.

The purpose of this thesis is to demonstrate that Dynamic NMR Microscopy can be used to obtain unique information about molecular dynamics of relevance to plant physiology, fluid dynamics and polymer physics; to demonstrate that molecular information can be measured in imaging experiments both accurately and precisely; to demonstrate that the experimental results can be presented as microscopic-spatial-resolution images with a velocity resolution up to several microns per second and a self-diffusion sensitivity as low as several orders of magnitudes smaller than that for free water; and to demonstrate that these measurements can be performed using a standard electromagnet.

In this work, much effort has been devoted to discussing image artifacts in Dynamic NMR Microscopy, to examining the accuracy and precision of the measurement, to verifying every possible error source and its influence on the final velocity and self-diffusion results, and to carrying out various experiments in order to test Dynamic NMR Microscopy and its variants. Based on this part of the work, the results of other 'non-trivial' experiments, such as the polymer flow experiment and *in vivo* biological studies, can be quoted with confidence.

1.2 Organisation of the thesis

This thesis is divided into 10 chapters.

Chapter 2 provides a theoretical description of NMR and NMR imaging. The imaging reconstruction technique employed in this work, the filtered back-projection reconstruction (PR) algorithm, is described in detail together with a discussion of the influences of various image contrast factors.

Following a review of imaging dynamic processes using NMR, Chapter 3 provides a detailed theoretical description of Dynamic NMR Microscopy. The discussion of the precision and accuracy of the velocity and self-diffusion maps obtained in Dynamic NMR Microscopy is included. This chapter also presents a special variant of the technique, termed 'one-shot' velocity microscopy.

In Chapter 4 a brief description of the existing NMR microscopic imaging system is given first, followed by some developments and modifications to this system which form part of the present work. These include both probe designing and software programming.

Experimental results are presented in five separate chapters. Chapter 5 provides an 'experimental introduction' which includes several instrument-related problems in NMR microscopy and some 'static' microscopic images which serve as the calibration results for the instrument. Chapter 6 describes the dynamic imaging results using water flow in capillaries, which provides experimental tests for the two dynamic imaging techniques used in this work. Chapter 7 presents the results of several *in vivo* botanical applications. In Chapter 8 and Chapter 9, the results of two rheological experiments are presented. One experiment studied water flow through two complex geometries in comparison with that of numerical simulations and the other studied a non-Newtonian fluid, poly-ethylene oxide (PEO), through a teflon capillary at high shear.

A summary and future work is given in Chapter 10.

Appendices, in the separate volume, give the software listings (in assembly, FORTRAN, BASIC and PASCAL) which form part of this work.

Chapter 2 Nuclear Magnetic Resonance Imaging

In conventional NMR a sample, which is usually homogeneous, is placed in a uniform magnetic field, so that the local molecular environment can be revealed via the resonant frequency spectrum of the nuclear spins. In NMR imaging, by contrast, a heterogeneous sample is placed in a non-uniform magnetic field, so that the hetero-structure of the sample can be revealed via the spatial dependence of the resonant frequencies. The basic physics of NMR and NMR imaging is well understood and described elsewhere[1-5]. A brief review is given in this chapter as a theoretical basis for the understanding of dynamic NMR imaging.

2.1 Nuclear magnetic resonance

After the discovery of NMR phenomenon in 1946 by two independent groups[6, 7], NMR spectroscopy has been mostly used to distinguish the chemical structure of different molecules.

2.1.1 Nuclear magnetism

A **single** nucleus in an external magnetic field oriented along the z axis ($\mathbf{B}=B_0\mathbf{k}$) experiences the Zeeman interaction with the magnetic field, for which a quantum mechanical description is given by the Hamiltonian operator

$$\mathcal{H} = -\gamma B_0 \hbar I_z \qquad [2.1]$$

where the constant γ is termed the gyromagnetic ratio (the ratio of magnetic dipole moment (μ) and angular momentum ($\hbar\mathbf{I}$) of a specific nucleus), $\hbar$ is Planck's constant divided by 2π, and I_z is the z component of the dimensionless spin angular momentum operator **I**. $\mathbf{I}^2$ has an eigenvalue of I(I+1) where I is either integer or half-integer and termed the spin quantum number (or simply, the spin).

A general state, $|\psi\rangle$, of a nuclear spin system is described by a linear combination of its spin eigenstates

$$|\psi\rangle = \sum_m a_m |I\ m\rangle \qquad [2.2]$$

where { $|I\ m\rangle$ } is the set of basis eigenkets, m are the azimuthal quantum numbers with values of integer or half-integer between I and -I, and a_m are the complex admixture amplitudes. From the energy eigenvalue equation

$$\mathcal{H}|\psi\rangle = E(m)\,|\psi\rangle \qquad [2.3]$$

one obtains the energy eigenvalues

$$E(m) = -m\gamma\hbar B_0 \qquad [2.4]$$

Therefore the energy difference between any two adjacent eigenstates of a spin system, known as the Zeeman splitting, is

$$\Delta E = \gamma\hbar B_0 \qquad [2.5]$$

The time evolution of a spin system is described by the time-dependent Schrödinger equation

$$i\hbar\frac{\partial}{\partial t}|\psi(t)\rangle = \mathcal{H}|\psi(t)\rangle \qquad [2.6]$$

where $i^2 = -1$. If the Hamiltonian, $\mathcal{H}$, is time-independent, the evolution of the spin system can be derived from the above equation as

$$|\psi(t)\rangle = U(t)\,|\psi(t_0)\rangle \qquad [2.7]$$

where U(t) is the evolution operator, given by

$$U(t) = \exp\left[-\frac{i}{\hbar}\mathcal{H}t\right] \qquad [2.8]$$

U(t) corresponds to a rotation of the state, $\psi(t)$, about the z axis with an angular frequency

$$\omega = -\gamma B \qquad [2.9]$$

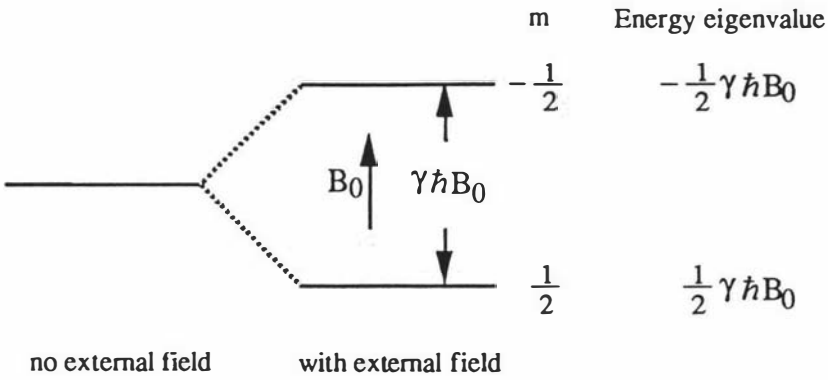

Figure 2.1 A spin half system

known as the Larmor precession frequency. The negative sign indicates the clockwise precession for the positive γ. For nuclear spins in laboratory magnetic fields, this frequency has a magnitude in the radio frequency (rf) region of the electromagnetic spectrum.

As indicated in Eq[2.4], a spin system with $I=\frac{1}{2}$ has only two eigenstates (Figure 2.1), corresponding to $m=\frac{1}{2}$ (spin up) and $m=-\frac{1}{2}$ (spin down) states, given by

$$E(\pm\tfrac{1}{2}) = \mp\tfrac{1}{2}\gamma\hbar B_0 \qquad [2.10]$$

Since the nucleus of interest in this work, the proton, has $I=\frac{1}{2}$, the following discussion is restricted to spin half particles.

2.1.2 Macroscopic magnetization

Any practical sample, no matter how small, contains an enormous number of nuclei. It is the macroscopic ensemble average of the observable quantities in which we are interested. For such an ensemble average, it is convenient to employ the density matrix operator ρ. The elements of the density matrix may be defined by any convenient but complete set of basis states, as

$$\rho_{mn} = \langle m | \rho | n \rangle$$

$$= \overline{a_m a_n^*} \qquad [2.11]$$

where $\overline{\quad}$ refers to the ensemble average. In particular the diagonal elements are given by

$$\rho_{mm} = \langle m | \rho | m \rangle$$

$$= \overline{|a_m|^2} \qquad [2.12]$$

Hence ρ, in the chosen representation for non-interacting spin half particles, is given by

$$\rho = \begin{bmatrix} \overline{|a_{1/2}|^2} & \overline{a_{1/2}^* a_{-1/2}} \\ \overline{a_{1/2} a_{-1/2}^*} & \overline{|a_{-1/2}|^2} \end{bmatrix} \qquad [2.13]$$

where the diagonal elements represent the population (or probability) in the corresponding eigenstates, and the off-diagonal elements are related to the coherence between the states.

For an observable quantity, A, its ensemble averaged expectation value, $\langle \overline{A} \rangle$, can be conveniently expressed using the density matrix formalism, as

$$\langle \overline{A} \rangle = \mathrm{Tr}(\rho A) \qquad [2.14]$$

In the current context, the observable quantity $\overline{A}$ is just the (macroscopic) magnetization **M**, given by

$$\mathbf{M} = \overline{\langle N\gamma\hbar\mathbf{I} \rangle} \qquad [2.15a]$$

or $$\mathbf{M} = N\gamma\hbar[\, \overline{\langle I_x \rangle}\mathbf{i} + \overline{\langle I_y \rangle}\mathbf{j} + \overline{\langle I_z \rangle}\mathbf{k}\,] \qquad [2.15b]$$

where N is the number of spins per unit volume, **i**, **j** and **k** are the unit vectors along x axis, y axis and z axis respectively.

Eq[2.15] is important because it may be shown that any state of the density matrix for an ensemble of non-interacting spin half particles may be described using the macroscopic magnetization defined in this manner, thus permitting a semiclassical description of the spin system. In this thesis, we shall be dealing with Hydrogen nuclei

(protons) attached to molecules in liquid state for which internuclear dipolar terms in $\mathcal{H}$ can be ignored. Furthermore, we shall not be concerned with the delicate scaling coupling between spins. In consequence the semiclassical description will be appropriate to describe the spin dynamics in the liquid state.

In the absence of an external magnetic field, the ensemble average of the magnetization vector should be zero due to the random directions of the magnetic dipoles of the nuclei.

If, however, a sample is immersed in an external field and in thermal equilibrium, the density operator associated with this magnetization vector is given by

$$\rho = \frac{\exp(-\mathcal{H} / k_B T)}{Tr[\exp(-\mathcal{H} / k_B T)]} \qquad [2.16]$$

where k_B is the Boltzmann constant, T the absolute temperature of the spin system and $\mathcal{H}$ given by Eq[2.1]. The transverse component of **M** is obviously zero due to the even distribution of the azimuthal phase angles of the precessing nuclei in the transverse plane. This corresponds to phase incoherence leading to zero value of the off-diagonal elements of ρ,

$$\overline{a_{1/2}^{*}\, a_{-1/2}} = \overline{a_{1/2}\, a_{-1/2}^{*}} = 0 \qquad [2.17]$$

The z component of the magnetization **M** arises from the difference in populations between the upper and lower energy states. At room temperature, the magnitude of this magnetization in the equilibrium state, M_0, can be derived as

$$\begin{aligned} M_0 &= \langle M_z \rangle \\ &= N\gamma\hbar\langle I_z \rangle \\ &= N\gamma\hbar\, Tr(\rho I_z) \\ &= \frac{N(\gamma\hbar)^2 B_0}{4k_B T} \end{aligned} \qquad [2.18]$$

For a spin half system at room temperature, the population difference between the $m=-\frac{1}{2}$ and the $m=+\frac{1}{2}$ states can be calculated from the diagonal elements of ρ, as

$$\overline{|a_{-1/2}|^2} - \overline{|a_{1/2}|^2} = \frac{\exp(\gamma\hbar B_0/2k_BT) - \exp(-\gamma\hbar B_0/2k_BT)}{\exp(\gamma\hbar B_0/2k_BT) + \exp(-\gamma\hbar B_0/2k_BT)}$$

$$= \frac{\gamma\hbar B_0}{2k_BT} \qquad [2.19]$$

For protons at $B_0 = 1.4$ T (60 MHz), it is equal to about 5×10^{-6}, a small value resulting from the small value of $\gamma\hbar B_0$ (Zeeman splitting) compared to k_BT (Boltzmann energy). It is worth noting that the resulting small magnetization of nuclei at room temperature limits detection sensitivity and leads to resolution limitation in NMR imaging.

2.1.3 Excitation of a spin system

Many NMR experiments consist of three 'stages'. First, the sample is placed in an external magnetic field, **B**, and allowed to reach the equilibrium state (**preparation**). Second, a perturbation is applied to the sample in order to force the spins in the sample into a non-equilibrium state so that the off-diagonal elements of ρ are no longer zero (**excitation**). Last, the response of the sample's spin system to this perturbation is recorded via the detector (**detection**). Therefore the time evolution of magnetization has now to be considered. In the semiclassical description, the time evolution of the macroscopic magnetization in the presence of a magnetic field can be conveniently described by equating the torque to the rate of change of the angular momentum, as

$$\frac{d\mathbf{M}}{dt} = \gamma(\mathbf{M} \times \mathbf{B}) \qquad [2.20]$$

When $\mathbf{B}=B_0\mathbf{k}$, the above equation has a solution which corresponds to a precessional motion about **k** at the rate ω_0 given by Eq[2.9].

The usual perturbation to the spin system is achieved by the application of a small linearly polarized rf field $\mathbf{B}_1(t)$ oscillating in the transverse plane. This field is actually a superposition of two counter-rotating fields in the transverse plane (Figure 2.2a)

$$\mathbf{B}_1(t) = \mathbf{i}2B_1\cos\omega t$$

$$= (\mathbf{i}B_1\cos\omega t - \mathbf{j}B_1\sin\omega t) + (\mathbf{i}B_1\cos\omega t + \mathbf{j}B_1\sin\omega t) \qquad [2.21]$$

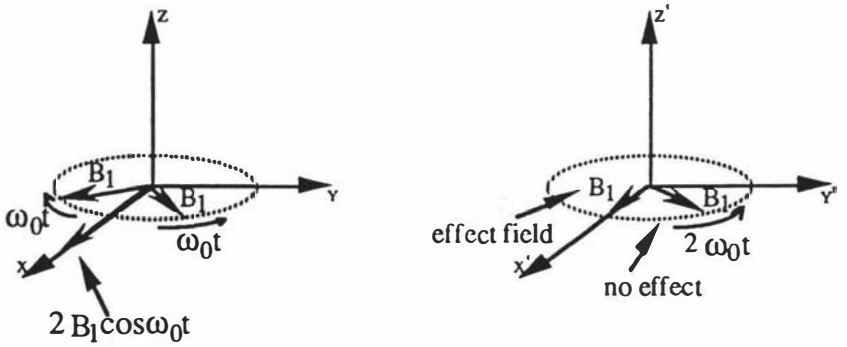

(a) Laboratory frame (b) Rotating frame (on resonance)

Figure 2.2 B_1 field in laboratory frame and rotating frame

Provided $B_1 << B_0$, a frame of reference can be introduced in which one component of $\mathbf{B}_1(t)$ is stationary (Figure 2.2b). In this rotating frame (on resonance), the precession frequency of the magnetization will be proportional to an effective field, given by B_1.

Since **M** is rotating at the Larmor frequency ω_0 about z axis in the laboratory frame, it will appear to be stationary in this rotating frame if ω is equal to ω_0. In this case $\mathbf{B}_1(t)$ provides the only non-zero field, and one of the two components will have 'dramatic' influence on the nuclei despite its small magnitude compared with $\mathbf{B}_0$ while the other component which rotates at 2ω in the opposite direction will have negligible effect (provided $B_1 << B_0$). This is the nuclear magnetic resonance phenomenon.

Combining Eq[2.20] and the first term of Eq[2.21] yields the equation for motion of the magnetization. In the rotating frame and given the initial condition, $\mathbf{M}(0)=M_0\mathbf{k}$, the solution to this equation is

$$M_{x'} = 0 \qquad [2.22a]$$

$$M_{y'} = M_0 \sin\omega_1 t \qquad [2.22b]$$

$$M_{z'} = M_0 \cos\omega_1 t \qquad [2.22c]$$

where ω_1 equals γB_1. The direction of the rf field in the rotating frame defines the x' axis.

Eq[2.22] implies that on the application of an rf field which is rotating right at the Larmor frequency, the magnetization precesses about the perturbation field B_1 at ω_1 in the rotating frame (Figure 2.3).

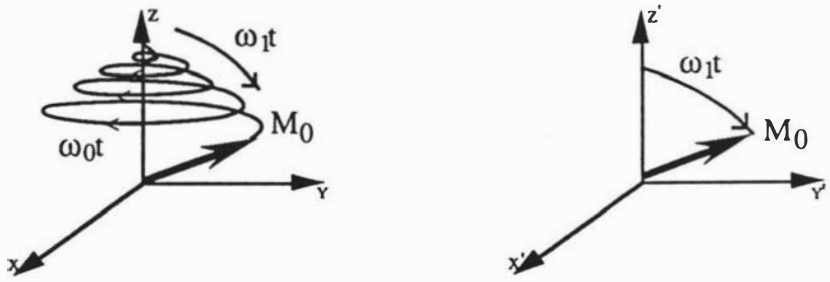

(a) Laboratory frame (b) Rotating frame

Figure 2.3 Macroscopic magnetization vector in laboratory frame and rotating frame

The amount of rotation, ϕ, is given by a time integral of the amplitude of the rf field, as

$$\phi = \gamma \int_0^{t_p} B_1(t)dt \qquad [2.23]$$

with t_p is the duration of the pulse. The integral in Eq[2.23] is required because $B_1(t)$ is not necessarily constant during the interval t_p. A rotating field with the amplitude and duration appropriate to tip **M** by ϕ degrees is called a $\phi|_x$ rf pulse. By appropriately phase shifting the rf field other axes in the rotating frame may be defined.

2.1.4 Spin relaxation processes

Following the disturbance from the equilibrium, the magnetization **M** suffers relaxation processes which may be described by

$$\frac{dM_z}{dt} = -\frac{M_z - M_0}{T_1} \qquad [2.24a]$$

and $$\frac{dM_\perp}{dt} = -\frac{M_\perp}{T_2} \qquad [2.24b]$$

where $M_\perp$ is referred to the transverse component.

T_1 is known as the **spin-lattice** (or **longitudinal**) relaxation time because the process involves an energy exchange between the spin system and its surrounding thermal reservoir. T_2 is called the **spin-spin** (or **transverse**) relaxation time because it describes the decay in phase coherence between the individual spins. T_2 processes

arise from both the fluctuations of local magnetic fields and the influence of static magnetic fields while T_1 processes are only from the influence of fluctuating magnetic fields. Consequently $T_1 \geq T_2$ for any spin system.

It is known that the decay of the signal in the time domain leads to a spectral broadening in the frequency domain. In practice, the signal normally decays faster than the 'natural' rate due to the relaxation alone. Other contributions include, for example non-uniformity of $\mathbf{B}_0$ across the sample. Broadening due to relaxation processes is named **homogeneous** and is inherently irreversible while broadening due to non-uniformity of $\mathbf{B}_0$ is named **inhomogeneous** and can be removed using an appropriate rf pulse sequence.

2.1.5 Bloch equation

If it is assumed that the change of the magnetization following excitation is *independently* caused by external magnetic fields and relaxation processes, then the equation of motion of **M** can be written by combining Eq[2.20] and Eq[2.24] as

$$\frac{d\mathbf{M}}{dt} = \gamma (\mathbf{M} \times \mathbf{B}) + [-\frac{M_x\mathbf{i} + M_y\mathbf{j}}{T_2} - \frac{(M_z - M_0)\mathbf{k}}{T_1}] \qquad [2.25]$$

This is the well-known **Bloch equation**[8]. The first term is due to the precessional motion and the second term is due to the relaxation. While a precise evaluation of the spin system requires quantum mechanical treatment, the Bloch equation does provide a phenomenological description for liquids and 'liquid-like' systems where the Hamiltonian is always of a simple magnetic (vector) form.

2.1.6 Signal detection

In nuclear magnetic resonance, signal detection is achieved by means of a transverse receiver coil. A resonant rf pulse induces non-zero transverse components whose precession in the transverse plane will induce a weak but detectable oscillating emf. The signal following an rf pulse is termed the **Free Induction Decay** (FID). Immediately following a $90°|_x$ pulse, the magnetization is given by

$$M_x(0) = M_z(0) = 0 \qquad [2.26a]$$

and $$M_y(0) = M_0 \qquad [2.26b]$$

Subsequently, assuming a uniform field B_0, the evolution of magnetization can be obtained by solving the Bloch equation, as

$$M_x(t) = M_0 \exp(-t/T_2)\sin\omega_0 t \qquad [2.27a]$$

$$M_y(t) = M_0 \exp(-t/T_2)\cos\omega_0 t \qquad [2.27b]$$

and $$M_z(t) = M_0[\ 1 - \exp(-t/T_1)\ ] \qquad [2.27c]$$

as illustrated in Figure 2.4.

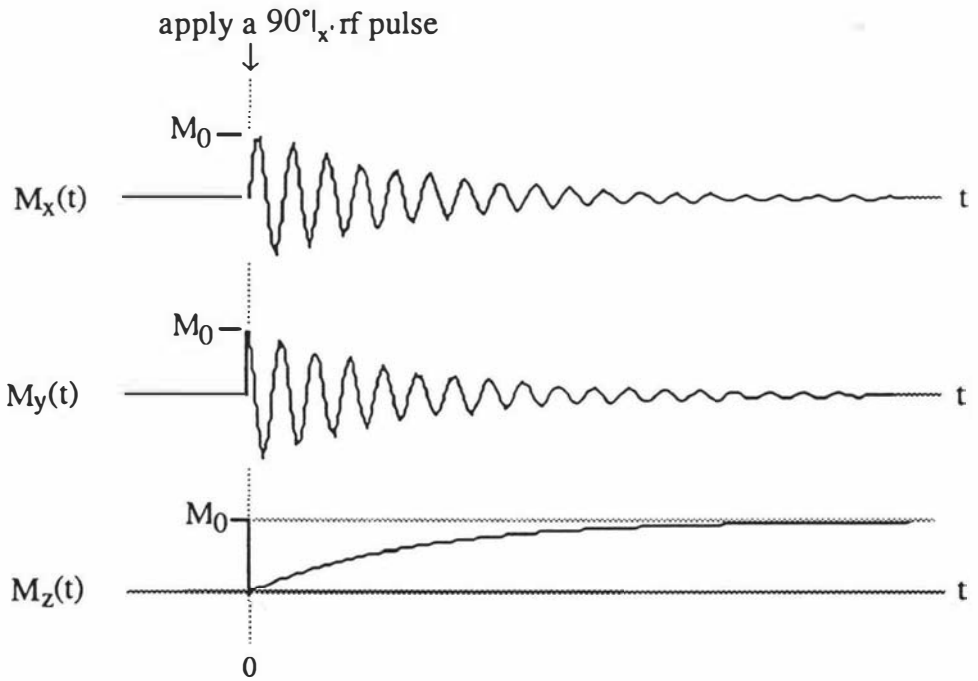

Figure 2.4 The response of a spin system to the application of a 90°l_x· rf pulse in the case of $T_1=T_2$

$M_y(t)$ is the real (or in-phase) signal and $M_x(t)$ is the imaginary (or quadrature-phase) signal. Both signals may be acquired as audio-frequency (af) oscillation by the usual phase-sensitive heterodyne detection method. The Fourier transformation (FT) of the FID signal is a Lorenztian in the frequency domain (Figure 2.5) with a line-width of $(\pi T_2)^{-1}$.

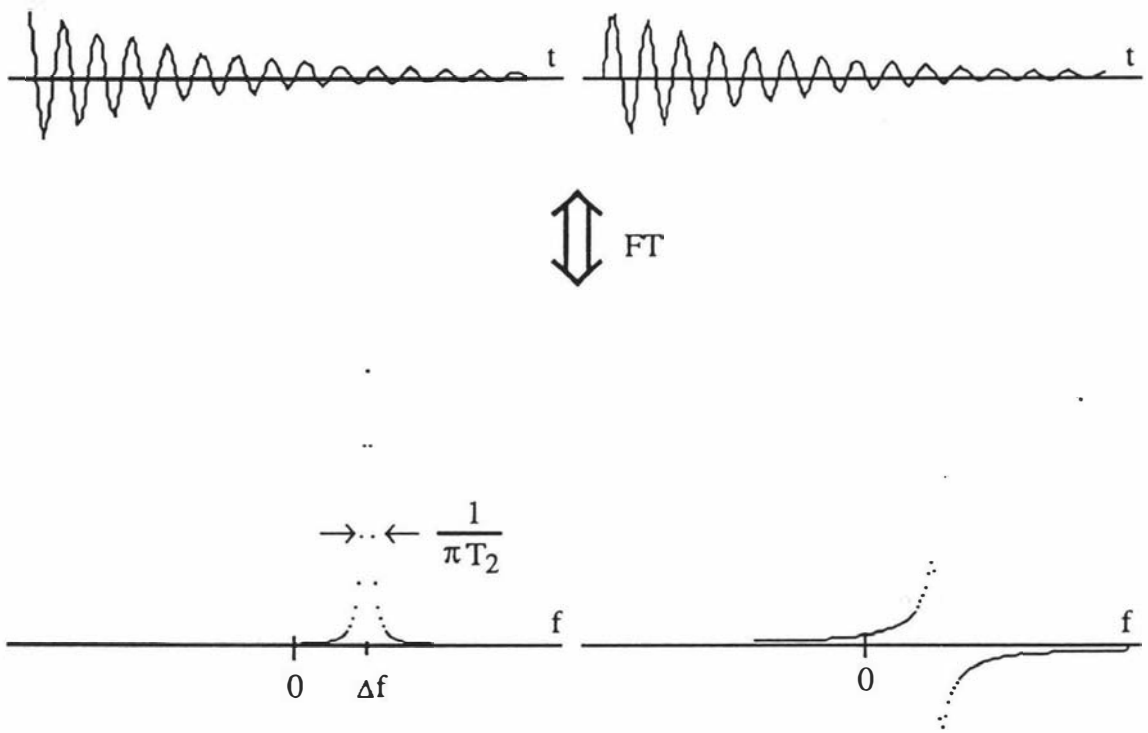

Figure 2.5 Fourier transform of the FID signal

2.1.7 The signal-to-noise ratio

NMR is an insensitive technique, the emf induced by the transverse magnetization in the receiver coil being on the order of several microvolts. This rather weak signal is superposed on the noise emf arising from random thermal motion of electrons in the wire of the receiver coil, the so-called Johnson noise. It is the ratio of the available signal to noise (S/N) which is important in any NMR experiment and this ratio is a limiting factor in high resolution imaging.

The signal amplitude is proportional to sample volume. From Eq[2.18], it is clear that the signal for a given volume at a given temperature can be maximized by using a large magnetic field and by using the nucleus with the largest possible gyromagnetic ratio, the proton.

Sources of noise may be numerous. In a well-designed instrument the probe and the rf pre-amplifier obviously determine the overall noise and hence the sensitivity. The fundamental thermal noise power for an rf coil is given by

$$\sigma_t = (4\, k_B\, T_c\, \Delta f\, R)^{1/2} \qquad [2.28]$$

where T_c is the coil temperature in Kelvin, Δf is the bandwidth (in Hertz) of the receiver's band-pass filter (which should be set equal to the sampling bandwidth to prevent the aliasing of signal and noise from outside the observation spectrum), R is the resistance of the coil. At radio frequencies, the rf current is confined to a thin layer of the wire at its surface due to the skin effect (the distance through which the magnitude of a travelling plane wave decreases by a factor of e^{-1}).

By invoking the principle of reciprocity, Hoult and Richards[9] have derived the equation for the proton signal-to-noise ratio (expressed in terms of the peak signal over the rms noise) as

$$S/N = \frac{KV_s(B_1)_{xy}N_s\gamma\hbar^2\omega_0^{7/4}}{6.73k_BT_s}\left(\frac{p}{k_BT_cLF\sigma\Delta f}\right)^{1/2}\left(\frac{1}{\mu_0\mu_r\rho_T}\right)^{1/4} \qquad [2.29]$$

where K is a numerical factor dependent upon the receiver coil's geometry, V_s is the sample volume, $(B_1)_{xy}$ is the component of $\mathbf{B}_1$ perpendicular to the main field $\mathbf{B}_0$ in the volume element due to unit current flowing at the centre of the receiver coil, N_s is the number of spins per unit volume, T_s is the sample temperature in Kelvin, p is the perimeter of the conductor, L is the length of the conductor, F is the noise figure of the pre-amplifier, σ is a factor taking account of the reduction in skin depth which arises from the proximity of turns in the coil, and ρ_T is the resistivity of the conductor.

It is of interest to note that the signal-to-noise ratio depends on $(\omega_0)^{7/4}$ whereas the analysis considering the signal alone (using Eq[2.18]) implies only ω_0^2. This discrepancy arises because Eq[2.29] allows for the reduction in skin depth (with consequent attenuation of Q) as ω_0 increases.

Due to the $(B_1)_{xy}$ term in the above equation, it is clear that the choice of receiver coil's geometry is important in the optimization of the signal-to-noise ratio. Two common coil configurations are the solenoid coil and the saddle coil, given in Figure 2.6. Both the saddle coil in vertical-bore superconducting magnets and the

(a) solenoid coil (b) saddle coil

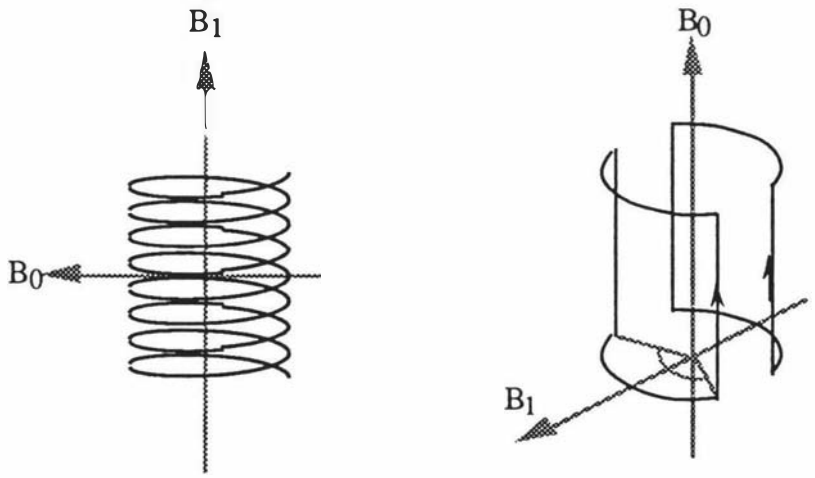

Figure 2.6 Two common configurations for the transverse rf receiver coil

solenoid coil in electromagnets provide an easy access to the centre of the probe, while the employment of a solenoid coil in vertical-bore superconducting magnets requires a side-entry for the sample. In terms of sensitivity, however, a solenoid coil is about three times better than that of a saddle coil[9, 10]!

2.1.8 Spin-echo, stimulated-echo and phase cycling

A pulse sequence is a series of pulsed fields linked up in a certain order of time. The application of a pulse sequence manipulates the spin system and its response to the sequence provides an opportunity to observe specific features of the spin Hamiltonian. There are numerous sequences for spin manipulation. The following text describes three important pulse sequences which will be extensively used in this work.

Spin-echo sequence

The first sequence considered is the spin-echo (or Hahn echo)[11]. This sequence is important because it has the effect of removing all the dephasing due to inhomogeneous broadening. For example, immediately following a 90° pulse, all spin magnetizations precess coherently in the transverse plane. If the steady magnetic field $B_0\mathbf{k}$ is not perfectly uniform but varies slightly across the sample space, the Larmor frequency at different parts of the sample will vary, each frequency corresponding to a small region where the variation of B_0 is negligible. Each of these regions is called an 'isochromatic group'. Viewed from the rotating frame at the resonance frequency ω_0,

some isochromatic groups will therefore precess faster than ω_0 while others will be slower than ω_0. Consequently the bulk magnetization vector will soon be dephased at a rate faster than that due to the transverse relaxation alone.

If at a time τ after the application of the 90° pulse a 180° pulse is applied, the direction of the dephasing magnetization will be reversed but their positions associated with local fields will remain. Then at time 2τ an echo signal will appear as the refocused transverse magnetization vector with the signal amplitude (Eq[2.26b]) in the rotating frame as

$$M_y(2\tau) = M_0 \exp(-2\tau/T_2) \qquad [2.30]$$

Eq[2.30] states that any reduction in the amplitude of M_y will only be due to T_2 and the loss due to the field inhomogeneity is recovered. It is worth noting that a requirement for the spin-echo sequence is that the spins have not moved from one isochromatic group site to another during the time 2τ. In other words, there is no translational motion of molecules.

There are two basic forms of the spin-echo sequence, namely $90°|_{x'}$-τ-$180°|_{y'}$ and $90°|_{x'}$-τ-$180°|_{x'}$, which are shown in Figure 2.7a and Figure 2.7b respectively.

Stimulated-echo sequence

The second pulse sequence which is important in this work is the stimulated-echo sequence. It is known from the previous discussions that T_2 defines the longest time one can measure the induced signal in the transverse plane and T_1 determines how long one has to wait to repeat the measurement. For many materials especially biological samples, T_2 values are typically tens of milliseconds but T_1 values are much longer, often on the order of a second. However, it is T_1 which limits the time for the measurement, because T_1 is the time for the spins returning to the thermal equilibrium while T_2 is just a time for the spin phases from coherence to disorder. Therefore an experiment could be very inefficient in these situations.

To maximize the echo time, one can use the 'stimulated-echo' sequence[11], shown in Figure 2.8, which, in effect, splits the 180° pulse into two 90° pulses (the second and the third pulses in this diagram). Following the initial $90°|_x$ pulse, the transverse magnetization has been established. The second $90°|_x$ pulse will tip the y-component of the transverse magnetization to the longitudinal axis so that it only suffers T_1 relaxation. Of course the x-component of the transverse magnetization is unaffected

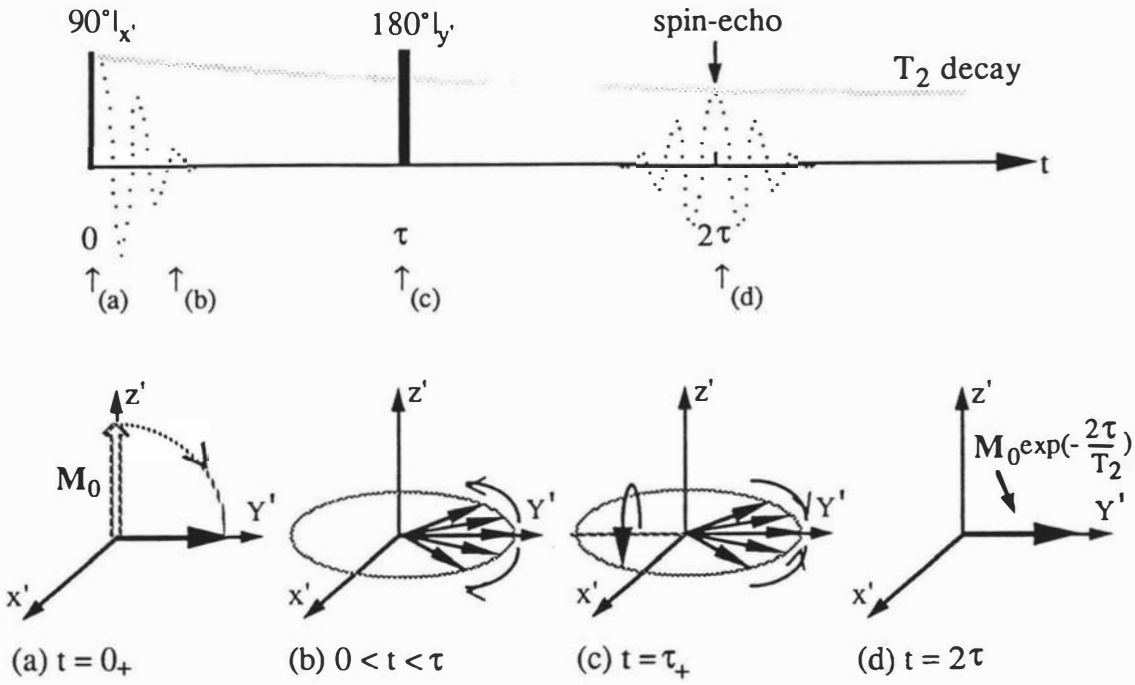

Figure 2.7a $90°I_{x'}$ - τ - $180°I_{y'}$ pulse sequence and spin-echo

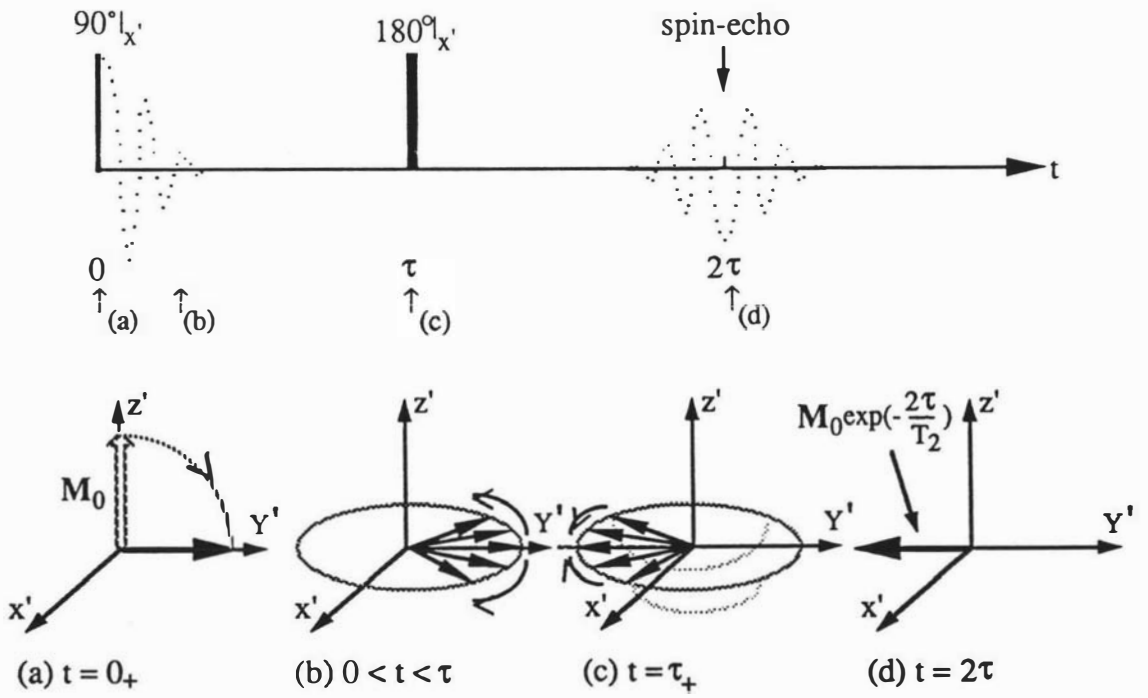

Figure 2.7b $90°I_{x'}$ - τ - $180°I_{x'}$ pulse sequence and spin-echo

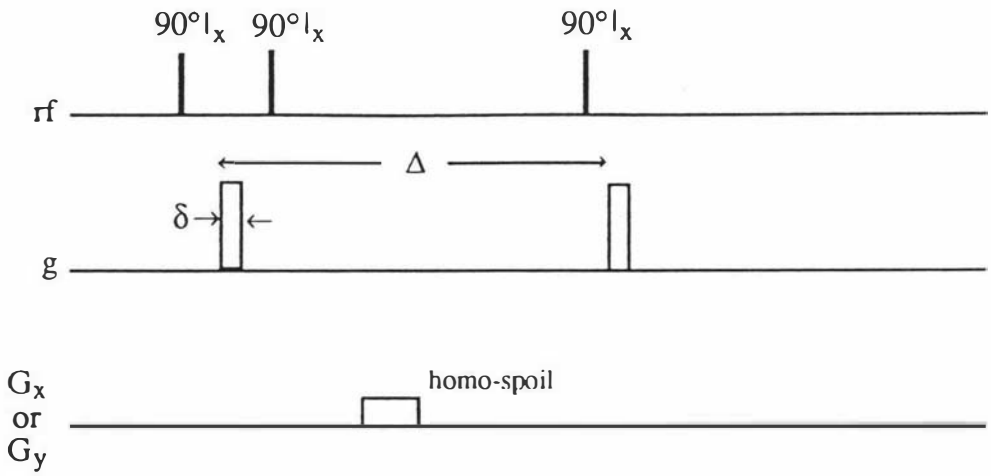

Figure 2.8 Stimulated-echo pulse sequence

by this $90°I_x$ pulse and so remains in the transverse plane to suffer T_2 decay. After a time delay, the last $90°I_x$ pulse will bring the longitudinal spin vector back to the transverse plane for detection. Therefore the maximum delay time can be stretched to the order of T_1.

Two points are worthy of mention. First, only half the signal could possibly be recovered because only the y-component is stored along the longitudinal axis, a price paid for the long echo time. Second, more than one final signal can arise from the transverse magnetization established by the initial $90°I_x$ pulse because each following $90°I_x$ pulse will produce a spin echo. Therefore some sort of 'cleaning' pulse is commonly used to destroy these unwanted transverse magnetizations (the homo-spoil gradient pulse).

Rf phase cycling

In NMR, not only the magnitude but also the orientation, or phase, of the resultant transverse magnetization ($\mathbf{M}_\perp$) are important in signal detection. The phase of the signal is determined by the phases of the rf transmitter and receiver. In most NMR spectrometers the rf phase can be adjusted in steps of 90° by a simple digital selection process. In consequence the orientation of the transmitter pulse field ($\mathbf{B_1}(t)$) in the rotating frame can be set to x', y', -x', or -y'. Similarly, by adjusting the phase of the mixing signal used in heterodyne detection, the NMR signal can be measured in-phase (0°) and in quadrature (90°).

Practical system are never perfect and it is important to distinguish the NMR signal from any non-NMR interference. This can be done using an rf phase cycling

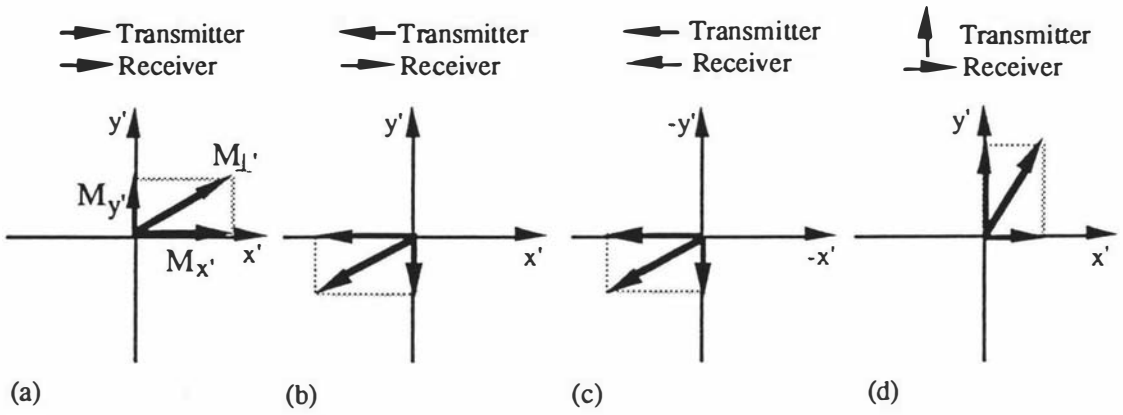

Figure 2.9 RF phase cycling. (a) Definition of vector directions in the transverse plane. (b) Inverting the excitation phase by 180°. (c) Inverting the receiver phase synchronously with the excitation phase. (d) Changing the excitation phase by 90°.

sequence. There are three basic relationships in rf phase cycling. First, inverting the excitation phase by 180° will result in the inversion of signal while any non-NMR interference signal will be unaffected (Figure 2.9b). Second, inverting the receiver phase synchronously with the excitation phase leads to NMR signal addition and interference cancellation (Figure 2.9c). Third, changing the excitation phase by 90° will interchange the signals in the in-phase and quadrature-phase receiver channels (Figure 2.9d).

Based on these three relationships, the most famous and useful rf phase cycling sequence is the CYCLOPS pulse[12]. It is a four-phase cycle which sweeps the four quadrants in a 90° step and is commonly used in modern dual-channel spectrometers. In our spectrometer, because the signal is processed through one common channel on the time sharing basis, no rf phase cycling is needed. However, a simplified two-step phase cycling sequence will be incorporated into the 'one-shot' velocity microscopy, discussed later in Ch 3.7.

2.2 Theory of NMR imaging

'Conventional' NMR imaging is used to determine the spatial distribution of stationary nuclear spin density. Numerous imaging sequences have been developed in the last two decades to produce such 'static' NMR images. In the following text, the general theory of spatially encoding nuclear spins is introduced first which includes the slice selection and **k**-space mapping. The image reconstruction technique used in this

work, the filtered back-projection reconstruction (PR) algorithm, is discussed in detail. The relationship between the spatial resolution and the signal-to-noise ratio in NMR imaging, and hence NMR microscopy, is also discussed.

2.2.1 Spatially encoding nuclear spin magnetization

It is known that the Larmor frequency of nuclear spins is a measure of the external magnetic field experienced (Eq[2.9]), hence any variation in the external field leads to a change of the Larmor frequency. In high resolution NMR spectroscopy, specific efforts are made to improve the uniformity of the field over the sample space so that each chemically identical nucleus resonates at the same frequency.

NMR imaging, by contrast, relies on the usage of a non-uniform external field purposefully adjusted to disperse the NMR resonance frequencies of the various volume elements (voxels) of a sample. A one-dimensional example is shown in Figure 2.10 where the field is varied linearly across the sample space. All the nuclei in the

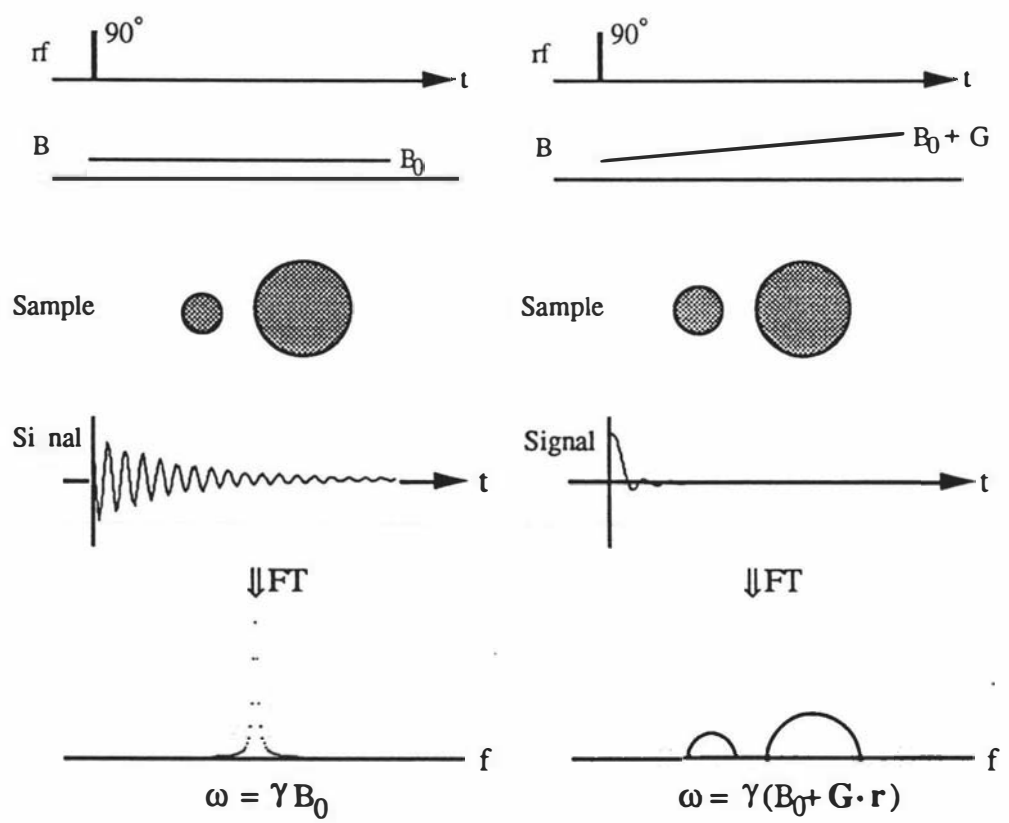

(a) Without the field gradient (b) With the field gradient

Figure 2.10 The effect of the magnetic field gradient in NMR

plane perpendicular to the field gradient will experience the same field strength and contribute to the signal amplitude at the same frequency. In other words, spatial displacements are turned into frequency displacements. The frequency spectrum therefore takes a form which represents the shape of the sample, known as the '1-D image' or 'projection profile'.

In practice, this linear field gradient arises from a superposition of a uniform polarizing field $\mathbf{B}_0$ and an additional gradient field $\mathbf{G}$. To distinguish any spatial location in real space, three orthogonal gradients in the component of $\mathbf{G}$ parallel to $\mathbf{B}_0$ are sufficient, namely G_x, G_y, G_z. Conventionally the direction of the main polarizing field is defined as the z axis, hence the gradient field is denoted as the variation of the polarizing field along three orthogonal axes (Figure 2.11), i.e.,

$$\mathbf{G} = \nabla B_0 \qquad [2.31]$$

or $$G_x = \frac{\partial B_z}{\partial x}, G_y = \frac{\partial B_z}{\partial y} \text{ and } G_z = \frac{\partial B_z}{\partial z} \qquad [2.32]$$

Hence the expression of the precession frequency in a NMR imaging experiment can be written as

$$\omega(\mathbf{r}) = -\gamma(B_0 + \mathbf{G}\cdot\mathbf{r})\mathbf{k} \qquad [2.33]$$

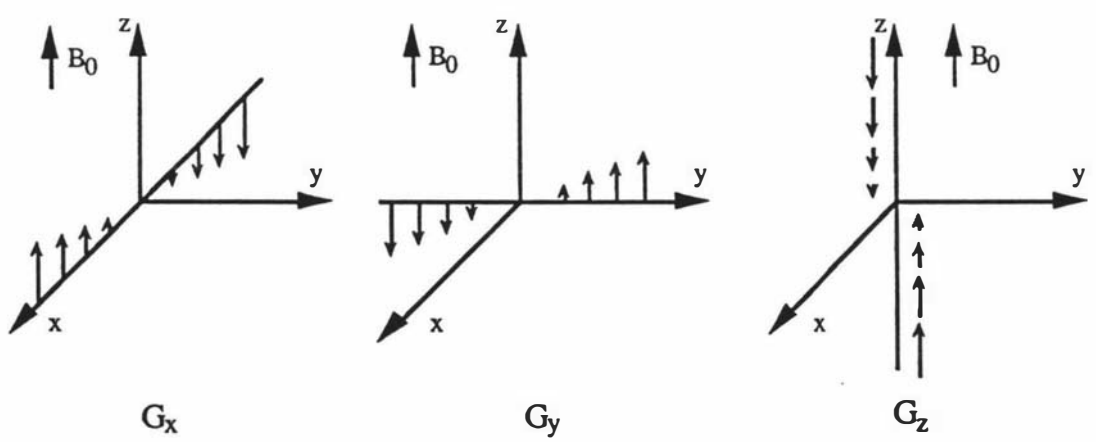

Figure 2.11 Magnetic field gradient (along the axes)

2.2.2 Selective excitation

NMR imaging is inherently a three-dimensional experiment. Although it is possible to perform an imaging experiment in three dimensions, it is common to image only two dimensions by generating a two-dimensional slice through the sample. This strategy reduces the size of data array from N^3 to N^2 where N is the number of discrete points to be sampled, and the result is consistent with the final two-dimensional visual display.

The means to selectively and non-invasively excite the nuclear spins within a thin slice is achieved by using simultaneously (Figure 2.12) a narrow-band rf pulse and a gradient field in the direction orthogonal to the slice plane (imaging plane)[13]. In other words, the bandwidth of the excitation pulse is made small in comparison with the spectral width which has been broadened by the application of the gradient. Using linear response theory, in order to excite a rectangular slice in frequency domain, the time dependence of the rf pulse requires a sinc, ($\frac{\sin(at)}{at}$), amplitude modulation. However, the response of the nuclei spin system for large turn angles is highly non-linear and can only be described exactly by solving the equation of motion of **M** numerically[14].

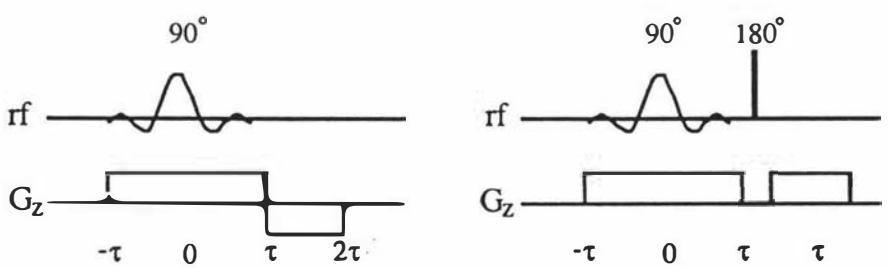

(a) A pulse sequence used to select a slice along the z axis

(b) An alternative pulse sequence when G_z must remain positive

Figure 2.12 Pulse sequences for selective excitation

Despite this, the linear response model gives qualitatively similar results for large turn angles and is a useful aid in understanding the selective excitation process. A mathematical description of this approach has been given[15] by considering the evolution of **M** in the presence of an rf field and an additional gradient field in two rotating frames, x'y'z' and x"y"z", as shown in Figure 2.13.

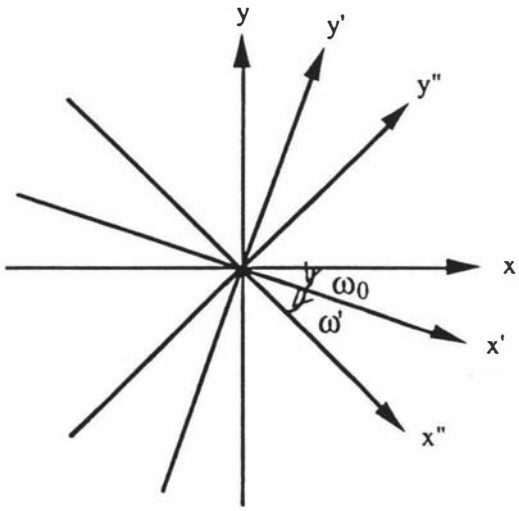

Figure 2.13

The laboratory frame and two rotating frames used in the analysis

In the usual x'y'z' rotating frame, B_1 is stationary and lies along the x' axis. This rotating frame is useful in the analysis because it simplifies the motion of **M** by eliminating the effect of B_0. In the second x"y"z" rotating frame, **M** does not precess at ω' and $B_1(t)$ is no longer stationary. This rotating frame is useful in the analysis because it makes the evolution equations of M_x and M_y more symmetrical so that they can be treated as the real and imaginary parts of a transverse magnetization, $M_{\perp"}$, in the complex plane, as

$$\frac{dM_{\perp"}}{dt} = \gamma M_0 B_1(t) \exp[\, -i\omega'(t + \tau)\,] \qquad [2.34]$$

The solution of Eq[2.34] contains an integral corresponding to a Fourier transformation of $B_1(t)$ from $-\tau$ to τ, namely, $F\{B_1(t)\}$, as

$$M_{\perp"} = \gamma M_0 \exp(-i\omega'\tau)F\{B_1(t)\} \qquad [2.35]$$

Since the x"y"z" frame has rotated $\omega' 2\tau$ clockwise with respect to the x'y'z' frame during the rf pulse time, one obtains

$$M_{\perp'} = M_{\perp"} \exp(i\omega' 2\tau)$$

$$= \gamma M_0 F\{B_1(t)\} \exp(i\omega'\tau) \qquad [2.36]$$

The extra phase shift term, $\exp(i\omega'\tau)$, is a function of position in the sample space and so leads to a dephasing of the signal. It can be removed by using a 'rephasing' gradient which is applied in the opposite direction (Figure 2.12a) or a spin echo sequence (Figure 2.12b). Therefore

$$M_{\perp'} = \gamma M_0 F\{B_1(t)\} \quad [2.37]$$

or $$M_{y'} = \gamma M_0 Re[F\{B_1(t)\}] \quad [2.38]$$

The variation of $M_{y'}$ with respect to ω' is termed the slice profile. At 2τ, $M_{y'}$ is proportional to the real part of the Fourier transform of the applied rf pulse. It means that to obtain a rectangular slice of spins, a sinc modulated rf pulse is required in the time domain since the rectangular function and the sinc function are a FT pair[16].

In the above analysis, the precession frequency of $B_1(t)$, ω, is identical with ω_0 (i.e., $\mathbf{B}_1$ is stationary in the x'y'z' frame) therefore the slice selected is at the centre of the field. By changing the precession frequency of $B_1(t)$, the position of the plane where $\mathbf{M}$ and $B_1(t)$ precess at the same frequency can be adjusted, that means the position of the slice can be shifted along the gradient axis, as

$$z = (\omega - \gamma B_0)/\gamma G_z \quad [2.39]$$

The width of the selected slice is determined by the bandwidth of B_1 field, Δf, and the magnitude of the gradient, as

$$\Delta z = \Delta\omega/\gamma G_z \quad [2.40]$$

where $\Delta\omega$ is equal to $2\pi\Delta f$. The relationship between the ω, z and Δz is shown in Figure 2.14.

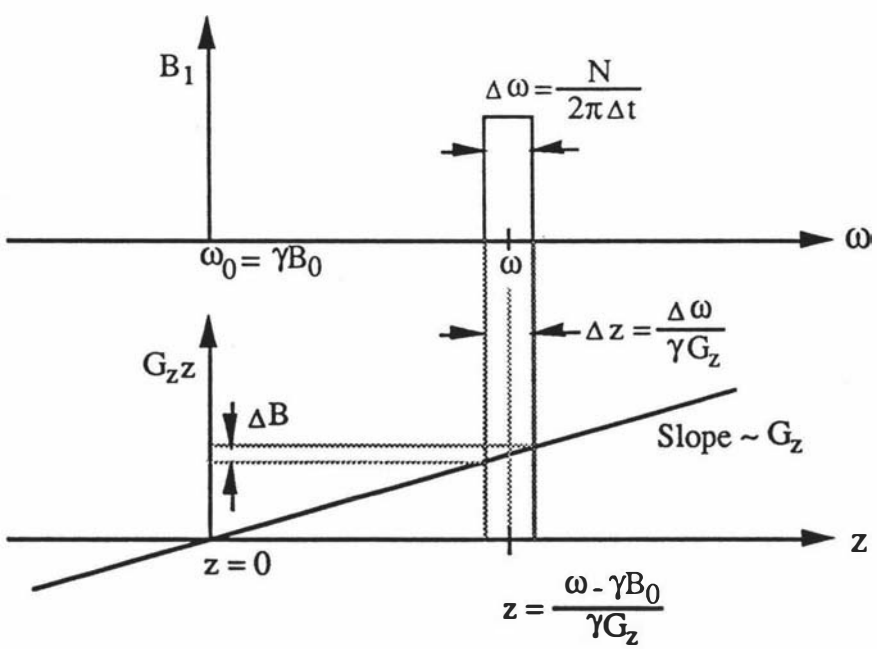

Figure 2.14 Basic relationships in the slice excitation

It is worth noting that the signal in Figure 2.12a is refocussed using a phase inversion caused by an inverted gradient pulse and is termed the gradient echo, while the echo in Figure 2.12b is refocussed using a phase inversion caused by an rf pulse. This echo is termed the spin-echo. The advantage of the spin-echo is that it minimizes the effect of magnetic field and chemical shift inhomogeneities, but it suffers from signal loss if T_2 relaxation occurs during the echo formation time. By contrast, the gradient echo is very sensitive to magnetic field and chemical shift inhomogeneities because only those inhomogeneities caused by the gradients are refocussed, but the relaxation signal loss in the gradient echo could be less since less time is required for the echo formation.

2.2.3 k-space imaging

Since the selective excitation has defined a 'thin' slice, the sample can now be considered as two-dimensional rather than three-dimensional. The nuclear spin density, $\rho(\mathbf{r})$, is defined as the contribution of each image voxel in the transverse plane towards the detected signal S(t). For an ideal system, $\rho(\mathbf{r})$ is equal to $M_{y'}$, and consequently, equal to M_0 if a $90°|_x$ pulse has been applied. In practice $\rho(\mathbf{r})$ is proportional to $M_{\perp}$, precessing in the transverse plane, where the constant of proportionality will depend upon the sensitivity of the receiver.

The acquisition of the NMR signal occurs in the absence of the rf field but in the presence of the applied mapping gradients which are oriented in the plane of the slice. This signal is given by

$$S(t) = \int \rho(\mathbf{r}) \exp[\, -i\omega(\mathbf{r})t \,] d\mathbf{r} \qquad [2.41]$$

where $\omega(\mathbf{r})$ is given by Eq[2.33] and the integral is over the defined three dimensional space. In the heterodyne detection frame where the reference frequency is γB_0, the above equation becomes

$$S(t) = \int \rho(\mathbf{r}) \exp[\, -i\gamma \mathbf{G} \cdot \mathbf{r} t \,] d\mathbf{r} \qquad [2.42]$$

Utilizing the slice selection strategy, image reconstruction requires sampling the entire two-dimensional space. This spatial mapping procedure is more clear if a reciprocal space, **k** space[17], is introduced by defining

$$\mathbf{k} = (2\pi)^{-1} \int_0^t \gamma \mathbf{G}(t')dt' \qquad [2.43]$$

with a unit of m^{-1}. Normally the gradient pulse is constant over the time period t, thus Eq[2.43] becomes

$$\mathbf{k} = (2\pi)^{-1}\gamma \mathbf{G}t \qquad [2.44]$$

The direction of **k** space is determined by the direction of the gradient but the magnitude of traverse in **k** space can be determined by changing either the application time or the gradient magnitude. After a selective 90° pulse, the initial sampling point defines the origin of **k** space. From then on, its position is determined by the time effect of the imaging gradients. There are a number of ways in which the entire **k** space can be sampled. It is the method of **k** space traverse which results in different NMR imaging techniques. Two common examples are given in Figure 2.15, the polar raster sampling, and Figure 2.16, the Cartesian raster sampling.

The signal expressed in the formalism of **k** space is then

$$S(\mathbf{k}) = \int \rho(\mathbf{r}) \exp[\, -i2\pi \mathbf{k}\cdot\mathbf{r} \,] d\mathbf{r} \qquad [2.45]$$

Eq[2.45] states that the spin density can be obtained by a Fourier transform of the detected signal, as

$$\rho(\mathbf{r}) = \int S(\mathbf{k}) \exp[\, i2\pi \mathbf{k}\cdot\mathbf{r} \,] d\mathbf{k} \qquad [2.46]$$

Eq[2.45] and Eq[2.46] claim that the signal can be acquired in **k** space during an experiment and the image of the nuclear spin density can be reconstructed in the conjugate **r** space via a two-dimensional Fourier transform.

In the image reconstruction procedure, if $\rho(\mathbf{r})$ is a real function, then there is a symmetry relationship, as

$$S^*(\mathbf{k}) = S(-\mathbf{k}) \qquad [2.47]$$

(a) Polar raster sampling

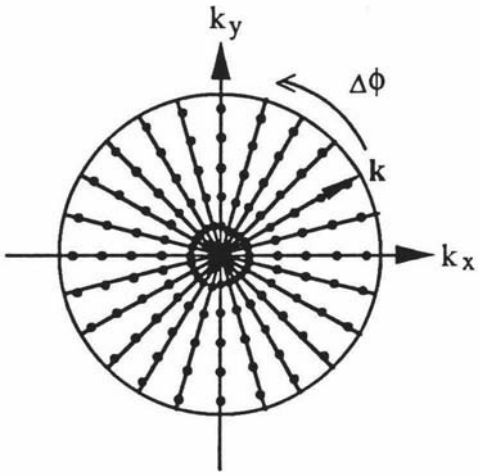

(b) Pulse sequence to traverse in polar raster for the first quadrant

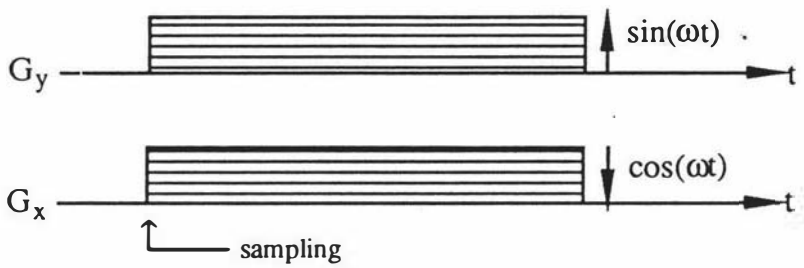

Figure 2.15 Polar raster sampling in **k** space

(a) Cartesian raster sampling

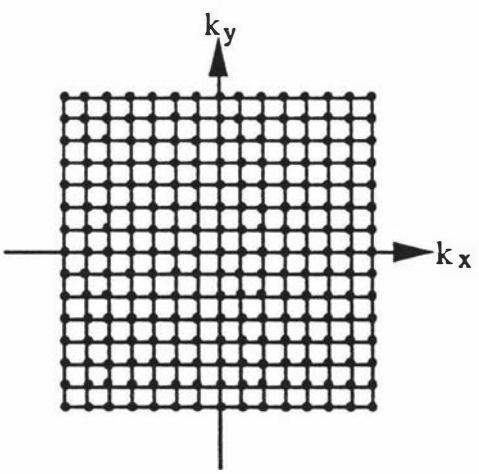

(b) Pulse sequence to traverse in Cartesian raster for the first quadrant

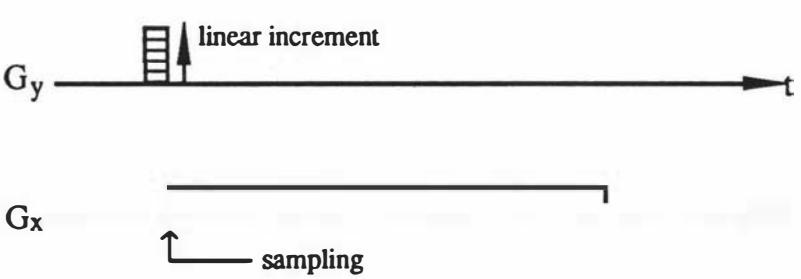

Figure 2.16 Cartesian raster sampling in **k** space

where S* is the complex conjugate of S. Since the real spectrum is identical in the opposite **k** direction and the imaginary spectrum has the opposite sign in the opposite **k** direction, this symmetry implies that to reconstruct an image, the signal sampling is needed only in two quadrants. This relationship has been widely used in NMR imaging. However, it is found that some image artifact will be introduced via the imperfections of instrument when this symmetry relationship is employed. Ch 5.3 gives some detailed simulation and imaging results.

2.2.4 Filtered back-projection reconstruction

The pulse sequence for the filtered back-projection reconstruction (PR) method is shown in Figure 2.17. It employs a polar sampling raster (Figure 2.15) and is based on the well-established algorithms used in X-ray tomography. In the spatial mapping period, the G_x and G_y gradients are applied simultaneously following the cosine and sine relationships respectively. The sampling point in **k** space is therefore defined by

$$\phi = \tan^{-1}(G_y/G_x) \qquad [2.48a]$$

and

$$|G| = (G_x^2 + G_y^2)^{1/2} \qquad [2.48b]$$

Therefore the signal and the spin density given by Eq[2.45] and Eq[2.46] can now be rewritten in polar coordinates as

$$S(k,\phi) = \int_0^{\pi} \int_{-\infty}^{+\infty} \rho(x,y)\exp[\, -i2\pi \mathbf{k}\cdot\mathbf{r} \,]\, r\, dr\, d\phi \qquad [2.49]$$

and

$$\rho(x,y) = \int_0^{\pi} \{ \int_{-\infty}^{+\infty} S(k,\phi)\exp[\, i2\pi \mathbf{k}\cdot\mathbf{r} \,]\, |k|\, dk \}\, d\phi \qquad [2.50]$$

It is worth noting that the inner integral in Eq[2.50] represents a one-dimensional Fourier transform (Figure 2.18) where the signal has been multiplied by a ramp |k|. This step is termed 'filtering' which removes the 'star artifacts' or 'blurring' produced by the simple back-projection reconstruction process[18]. The result of this one-dimensional transform is termed the 'filtered profile'

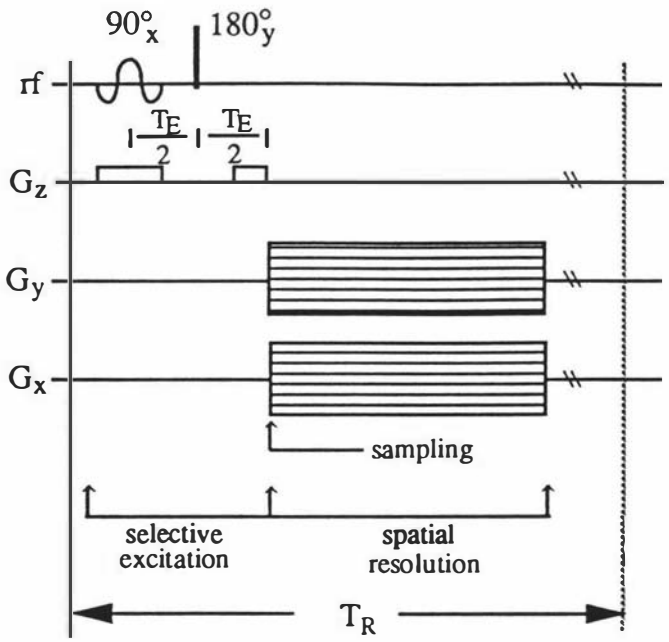

Figure 2.17

Pulse sequence employed in the filtered back-projection resonstruction

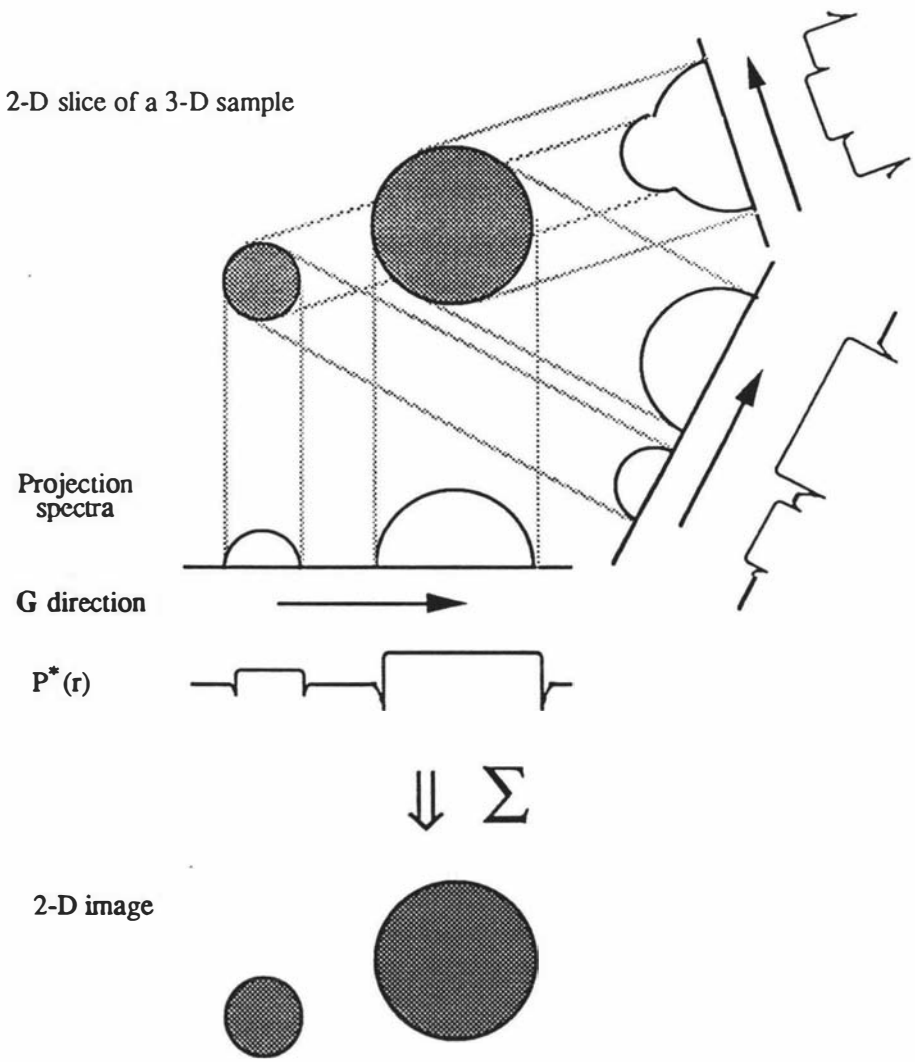

Figure 2.18 The filtered back-projection reconstruction

$$P^*(r) = \int_{-\infty}^{+\infty} S(k,\phi)\exp[\, i2\pi kr \,]\, |k|\, dk \qquad [2.51]$$

which contains information of all points, along the gradient direction, satisfying

$$r = x\cos\phi + y\sin\phi \qquad [2.52]$$

Eq[2.52] states that the result of a 1-D FT of the projection data at a given angle ϕ represents the value of the 2-D FT of the object function $\rho(x,y)$ in **k** space along the radial direction, r, with the given angle ϕ. This filtered profile is then projected into the image plane by summing through **k** space

$$\rho(x,y) = \sum_{j=1}^{m} P^*(x_j,y_j,\phi_j)\Delta\phi \qquad [2.53]$$

where $\Delta\phi = \pi/m$, the step increment size where the symmetry relationship given by Eq[2.47] is employed. The back-projected image is then interpolated into a Cartesian matrix to form the final 2-D image (Figure 2.19).

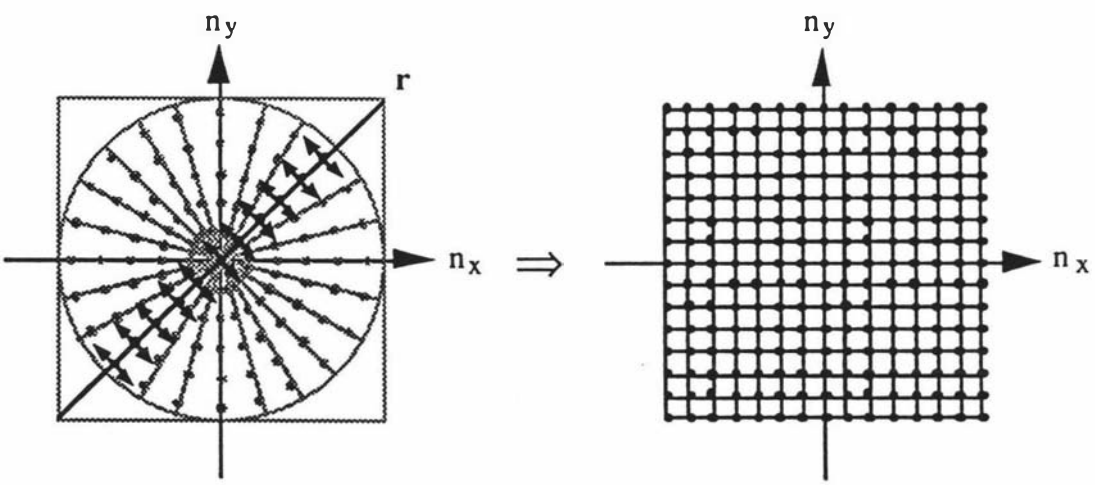

Figure 2.19 The interpolation process in PR method

Projection reconstruction was the method Lauterbur used to produce the first ever NMR image in 1972. It was chosen in this work because this method is very straightforward and easy to implement in imaging instrument. It also has the shortest 'dead' time before sampling and therefore it is one of the most sensitive imaging

methods[5]. There are, of course, some disadvantages of this method. One of them is due to the polar raster sampling, where the inner part (which corresponds to lower frequency components) are sampled more densely than the outer region (which corresponds to higher frequency components). This implies that the fine details are worse represented than the coarse features in the images. By comparison, the commonly used Fourier imaging[19] and the 'spin-warp'[20, 21] sequences offer the same resolution for both high and low frequencies but suffer signal loss and unwanted T_2 contrast during the phase-encoding period.

2.2.5 S/N, resolution and its limits - NMR microscopy

For a given instrument, the signal-to-noise ratio (S/N) obtainable from a volume element of the sample, in principle, will be proportional to the number of spins in this volume. As the decrease of the voxel size, the number of spins contributing to the signal in voxel is also decreased so as the S/N. Thus a minimum acceptable S/N corresponds to a minimum voxel resolution.

Since the publication of the first NMR image in 1973[22], its potential for hospital diagnosis was noticed immediately and MRI whole-body scanners are now routinely used as a unique medical diagnosis tool. The current resolution for medical applications is of order (1 mm)^3. By contrast with the 'scaling-up' in medical applications, the 'scaling-down' of the imaging technique came somewhat later, in 1986[23-26]. For a resolution less than (100 μm)^3, NMR imaging technique is termed **NMR microscopy** simply because it is the smallest volume element which can be resolved by an human eye. Between these two extremes, small scale applications of imaging have proven useful in various scientific and industrial applications (Figure 2.20).

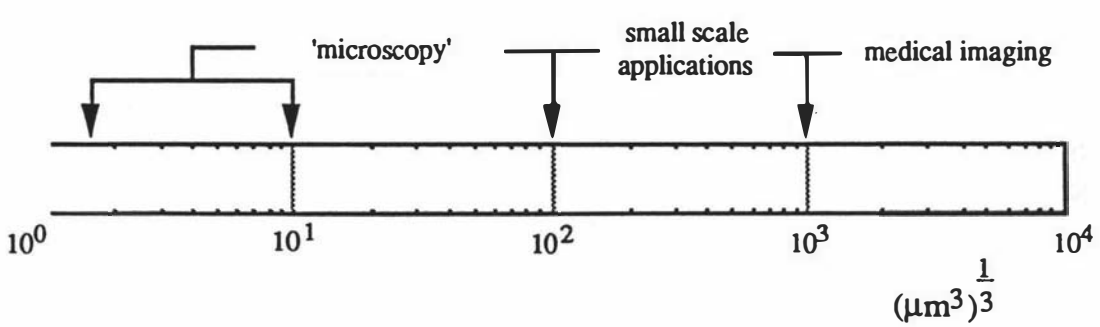

Figure 2.20 Resolution scale in NMR imaging

In imaging experiments, S/N can be derived by considering the reference time domain S/N which has been given in Ch 2.1.7, while resolution may be defined in terms of the Rayleigh criterion. For an ideal solenoidal copper-wire coil and a proton sample, the time-domain peak signal to rms noise ratio can be derived[9, 27] as

$$\frac{S_0}{\sigma_t} = 2.72\times10^{-3}a^{-1}F^{-1/2}\sigma^{-1/2}V_s f_0^{7/4}\Delta f^{-1/2}N_{acc}^{1/2} \qquad [2.54]$$

where a is the rf coil radius, F the noise figure of the spectrometer, σ the rf coil proximity factor, V_s the volume of the sample, f_0 the resonant frequency, Δf the bandwidth of the spectrometer and N_{acc} the number of time-domain accumulations per projection.

In two-dimensional imaging experiments, an optimal band-width is given by setting the pixel spacing equal to the fundamental line-width ($1/\pi T_2$) so that

$$\Delta f = N/\pi T_2 \qquad [2.55]$$

Thus the spatial resolution at an optimal broadening and a circular sample can be derived as[27]

$$\Delta x = 16a^{1/2}(S/N)^{1/2}F^{1/4}\sigma^{1/4}\Delta z^{-1/2}(N_{acc}N_p T_2)^{-1/4}f^{-7/8} \qquad [2.56]$$

where N_p is the number of projections, Δz the thickness of the slice and S/N the final image signal amplitude to rms noise ratio.

For an optimal detection system where F=1, σ=5 and a=NΔx/4 where N is the number of the discrete sampling points, Eq[2.56] can be simplified as

$$\Delta x = 144(S/N)\Delta z^{-1}N(N_{acc}N_p T_2)^{-1/2}f^{-7/4} \qquad [2.57]$$

which sets an upper limit to the S/N and resolution.

The sensitivity provides the first order limitation to the S/N and resolution. There are other factors which also limit the S/N and resolution. For examples, T_2 relaxation which gives a natural NMR line-width in any sample, self-diffusion of mobile molecules which sets an intrinsic limit in an experiment, susceptibility of a heterogeneous sample which degrades the linearity of the imaging gradient, and chemical shift of a sample which perturbs the natural line-width.

Because of the limitations which arise from the S/N and resolution, it is important to optimize the information obtained within a given experimental time. Using the fact that the slice selection disturbs only one slice in the sample and spins in other longitudinal locations are available for immediate excitation, the imaging waiting time (T_R - T_2^*) can be used to obtain images by the multi-slicing method at no increase of the experimental time. This multi-slicing method requires a shift of the main resonant frequency (Eq[2.39]) and was not used in this work because of the spectrometer limitations.

It is worth noting that the fast imaging sequences widely used in medical NMR imaging have little use in NMR microscopy. This is because to reduce the imaging time, there are two basic approaches. One is to reduce the time required for each repetition (short T_R) and the other is to cover more 'area' in **k** space during the 'transverse coherence time' within one repetition. Both FLASH[28] and SSFP[29] are fast imaging sequences utilizing the first approach, and offer about 50-100 fold reduction in imaging time by using a small turn angle, say 15°. However, the intensity of the transverse signal using a flip angle of 15° is only about 26% (sin15°) of that excited by a 90° pulse. EPI[30, 31] utilizes the second approach to the fast imaging, and can actually cover the entire **k** space within one scan! The key to the technique is to use fast gradient switching to traverse the entire **k** space within the time scale of T_2 and fast sampling to collect enough points from the 'gradient echoes' between every two switchings. However, fast sampling in EPI requires a broad band receiver (for example, to sample 128 points within 1 ms, the bandwidth of the receiver channel needs to be 128/0.001=128kHz.). Fast gradient switching in EPI requires firstly smaller coil inductance which is contrary to the consequence of bigger or more powerful gradient coils. It also induces bigger eddy currents in the surrounding metals which degrade more severely the linearity of the gradient. Therefore while a trade-off in S/N using fast imaging sequences is feasible in medical NMR imaging where the main pressure is the experimental time, such signal loss is undesired in NMR microscopy because the signal is so valuable that every part of the imaging procedure has to be optimized.

2.3 The influence of contrast factors in NMR imaging

An image contrast can be defined as the intensity change (or modulation) of the image due to the contribution of certain molecular information other than the nuclear

spin density. In the previous discussions of imaging processes, the influences of contrast factors on the image intensity have been ignored purposefully for simplicity. Generally speaking, any imaging experiment consists of two phases, the preconditioning period and the imaging period[32]. The preconditioning period provides the desired image contrast and the imaging period is responsible for the spatial resolution and differentiation of the local structure. If no specific contrast scheme is employed, a 'normal' spin density map will be obtained although, strictly speaking, all images are more or less weighted by a contrast which combines the influences of several intrinsic contrast factors (simultaneously) such as the relaxation contrasts. Therefore the actual relationship between the signal and the nuclear spin density is given by

$$S(\mathbf{k}) = \int \rho(\mathbf{r}) E_c(\mathbf{r}) \exp[\, -i2\pi \mathbf{k}\cdot\mathbf{r} \,]\, d\mathbf{r} \qquad [2.58]$$

and

$$\rho(\mathbf{r}) E_c(\mathbf{r}) = \int S(\mathbf{k}) \exp[\, i2\pi \mathbf{k}\cdot\mathbf{r} \,]\, d\mathbf{k} \qquad [2.59]$$

The image reconstruction returns not simply $\rho(\mathbf{r})$ but $\rho(\mathbf{r})E_c(\mathbf{r})$, where $E_c(\mathbf{r})$ is the (normalized) contrast factor. The interest in these image contrast factors is two-fold: the first is the possible reduction of image artifact due to these contrasts; the second is the potential information obtainable via these contrasts. In the following, the influences of several common image contrast factors in NMR imaging are discussed.

2.3.1 Relaxation processes, T_1 and T_2

T_1 and T_2 relaxation are the most common contrasts which influence the image intensity. In the discussion of NMR imaging in Ch 2.2, the influence of relaxation has been deliberately ignored for simplicity and convenience. However, the relaxation contrasts are present intrinsically in all experiments and they are the primary factors which influence the image intensity. While such contrasts are undesirable in the interpretation of nuclear spin density, they are useful in their own right. For example, T_1 varies[33] greatly between different biological tissues or normal and abnormal tissues, so that a knowledge of T_1 distribution is extremely useful in the differentiation of biological soft tissue.

$T_1(\mathbf{r})$ contrast can be incorporated into the PR imaging sequence simply by repeating experiments at different repetition time, T_R. The image contrast function is then given approximately by

$$E_c(\mathbf{r}) = 1 - \exp(-T_R/T_1(\mathbf{r})) \qquad [2.60]$$

An alternative method to apply T_1 contrast is to incorporate the inversion-recovery sequence prior to the slice excitation (Figure 2.21). There is a zero cross-over point in the inversion-recovery sequence at $0.693T_1$, therefore it can be used to suppress the component with a characteristic T_1 value (an example is given later in Ch 5.6). For this pulse sequence, the image contrast function becomes

$$E_c(\mathbf{r}) = 1 - 2\exp(-\tau/T_1(\mathbf{r})) + \exp[-(T_R - \tau)/T_1(\mathbf{r})] \qquad [2.61]$$

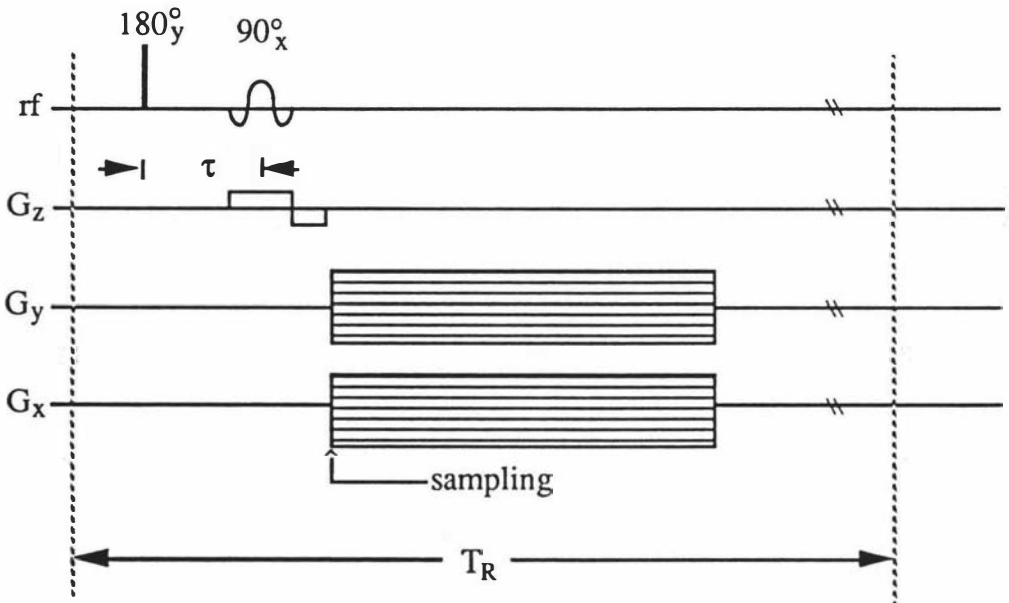

Figure 2.21 The application of the inversion-recovery sequence in NMR imaging

Comparing with other common imaging pulse sequences such as the Fourier Imaging, the standard PR sequence has very little $T_2(\mathbf{r})$ contrast because the signal acquisition in PR can be started right after the 90° slice excitation pulse. However, a $T_2(\mathbf{r})$ contrast can be incorporated into the imaging sequence by using a longer T_E. By repeating the imaging experiment at a fixed T_R but with different T_E, a $T_2(\mathbf{r})$ relaxation map can be obtained with an image contrast function as

$$E_c(\mathbf{r}) = \exp(-T_E/T_2(\mathbf{r})) \qquad [2.62]$$

provided that T_R is considerable larger than T_E to ensure that the T_2 contrast is dominant.

2.3.2 Chemical shift

Chemical shift is the most common parameter which chemists use to identify the structure of molecules. It arises from the orbital shielding effect of the electrons which perturbs the magnetic field at the spin site and is defined as the fractional resonant frequency shift of the spins caused by their chemical environments. Chemical shift is expressed in units as parts per million (ppm), the positive or negative sign of which indicates a shift to higher or lower field which means to lower or higher frequency. For ^{1}H NMR, the reference is commonly TMS, $(CH_3)_4Si$, and the proton in free water has a chemical shift around 4.5 ppm[3]! In imaging experiments using homogeneous water samples, however, this proton chemical shift is simply ignored because it represents zero displacement of the image object if the resonant frequency is right at the water frequency.

If a sample contains more than one chemical species, however, the situation will be different. This is because in the analysis so far, it has assumed that whenever there is no field gradient, the frequency domain signal of the sample is a single peak with a natural width $1/(\pi T_2)$. This assumption is precisely valid if all the spins in the sample are in one chemical environment. In the case of two chemical environments, however, the direct relationship between the resonant frequency and the spatial position, given by Eq[2.33], becomes

$$\omega(\mathbf{r}) = -\gamma(B_0 + \mathbf{G}\cdot\mathbf{r} + \delta_i B_0 \times 10^{-6})\mathbf{k}, \ (i = 1,2) \qquad [2.63]$$

where δ_i represent two different chemical shifts in this case. Therefore, any standard imaging method will reconstruct two position-shifted images simultaneously (provided the spectrometer has high enough resolution). Thus the final image is a superposition of these two images.

To overcome the image artifact due to chemical shift, a large mapping gradient is important. This is because an achievable resolution in imaging can be quoted

approximately, by setting the frequency width of the image pixel dimension equal to the line-width broadening due to chemical shift, as

$$\gamma G_x x = \Delta\delta\gamma B_0 \times 10^{-6} \qquad [2.64]$$

where x is the image pixel size and $\Delta\delta$ is the range of chemical shifts in ppm for a heterogeneous sample. Ideally one requires the left-hand side of Eq[2.64] bigger than the right-hand side. The worst image artifact due to chemical shift happens when the spectral broadening due to the mapping gradient is small in comparison with the frequency separation due to chemical shift differences. In other words, the broadening due to chemical shift is more than one pixel size. It is also worth noting that the artifact due to chemical shift is field dependent so that it is worse in high field imaging.

On the other hand, this chemical shift information is useful in differentiation different chemical species and a chemical shift contrast can be incorporated into NMR imaging, such as the CSI[34, 35] and CHESS[36, 37] pulse sequences.

2.3.3 Susceptibility

While the external origin of the magnetization **M** is the applied magnetic field, the intrinsic origin of it is due to the magnetic susceptibility, χ_m, because

$$\mathbf{M} = \frac{\chi_m}{\mu_0(1+\chi_m)}\mathbf{B} \qquad [2.65]$$

where μ_0 is the absolute permeability ($4\pi\times10^{-7}$ H m^{-1}). χ_m is a dimensionless number, positive for the paramagnetic materials and negative for diamagnetic materials (the biological and organic materials studied in this work).

Because the sample being imaged is heterogeneous, χ_m will depend upon spatial position. At the boundaries of local internal structures between themselves or with air, a difference of two neighbouring χ_m, even just a few ppm, will induce a local magnetic field gradient across the boundary. These induced internal magnetic field gradients will degrade the homogeneity of the applied field, not only at the boundaries but also in the space near these boundaries. This means that the susceptibility differences are 'local' at the boundaries, their effects are 'distant' into the nearby media.

As a consequence, additional T_2 relaxations are induced in these regions. Hence it results in image distortions.

However, because of χ_m being in an order of -10^{-5} for most of the diamagnetic materials, it has a very small effect. Nonetheless the effect due to the magnetic susceptibility is field-dependent. The higher the field, the bigger the effect. Simulations have shown that dramatic image distortions could be induced even the susceptibility difference is only 3 ppm at 20 kHz receiver band-width[38]. Clearly the image distortion is worst at microscopic resolution[39]. On the other hand, the image distortion due to the local susceptibility differences may be used to reveal the internal boundary structure of a sample. It is not the subject of this work and requires further study.

2.3.4 Flow and diffusion

This work deals with liquid or liquid-like samples containing moving molecules, such as water solution, polymer solutions and biological samples. Hence the random Brownian motion, self-diffusion, of molecules is important. It is known that the self-diffusion of molecules set an intrinsic limit to the resolution, because the one-dimensional rms distance of which molecules move under the Brownian motion is $(2Dt)^{1/2}$ where D is the self-diffusion coefficient of the molecules and t is the observation time. Hence Brownian motion leads to an irreversible loss of the echo signal[11]. Another type of motion of interest concerns fluid flow. A molecule with a velocity v will move to a new position over a specific time interval in the image pulse sequence. Hence it also leads to signal loss. More important, because magnetic field gradients are used in imaging experiments, motion will lead to image artifacts. For example, motion during the signal acquisition will lead to phase anomalies while motion between repetitions will lead to the 'fresh spin' effect.

However, with carefully designed experiments, the effect of motion can be used as a contrast which can be interpreted to produce a map of motion. Motions in concern in this work fall into two main categories, ordered and disordered, i.e., laminar flow and Brownian motion. Both can provide unique information about the sample because velocity is associated with mass flow of the fluid and self-diffusion coefficient reflects the microscopic structures of molecules and their surroundings. Maps of velocity and self-diffusion coefficient of the sample could be very useful in any *in vivo* studies of biological samples, fluid dynamics and rheology. The detection of velocity and self-

diffusion using NMR imaging is the theme of this work. Chapter 3 will deal with them in detail.

2.4 Summary

This chapter has reviewed the theory of NMR and NMR imaging.

The review of NMR has been restricted to spin-half particles since the nucleus of interest in this work is proton. After a brief introduction of nuclear magnetism of a single nucleus using the quantum mechanical approach, the so-called 'semiclassical' approach has been used in discussions to describe the spin dynamics. This is because the protons of concern in this work are non-scalar coupled and are attached to molecules in liquid or liquid-like state, for which internuclear dipolar terms in $\mathcal{H}$ can be ignored. Three basic pulse sequences, namely spin-echo, stimulated-echo and phase cycling, have also been discussed since they were used extensively in this work.

The discussion of NMR imaging has included the role of magnetic field gradient, selective excitation, two-dimensional **k**-space mapping and filtered back-projection (PR) reconstruction, the image reconstruction method used in this work. The concept of **k**-space mapping is particularly important because it not only provides a powerful approach in the understanding of other complicated pulse sequences but it also serves as an analogy in the discussion of Dynamic NMR Microscopy.

It is known that the NMR image intensity cannot be simply interpreted as the nuclear spin density of the sample. The image intensity is 'modulated' by relaxation, chemical shift, susceptibility, flow and self-diffusion. The influences of these molecular parameters, both as the causes of image artifacts and in providing potential information about the sample, have been discussed. It is these quantitative measurements of the molecular information which make NMR imaging a powerful and unique tool in scientific research and practical applications.

Chapter 3 Dynamic NMR Imaging

The previous chapter dealt with the theory of NMR imaging, by which the spatial distribution of the proton density, $\rho(\mathbf{r})$, can be reconstructed. This type of imaging can be termed **static NMR imaging**.

Among several contrast factors discussed briefly in the last chapter, velocity and self-diffusion contrasts are of particular interest in this work and the technique discussed in this chapter is designed specifically to reveal the spatial distribution of these two functions. This type of imaging is termed **dynamic NMR imaging** in this thesis, since the information in the final images relates to molecular dynamics. In particular this thesis will deal specifically with the measurement of velocity and self-diffusion coefficient via the nuclear spin phase shifts arising from the use of Pulsed-Gradient Spin-Echo method, and demonstrate how they can be measured precisely and accurately using NMR microscopy.

This chapter starts with a review of various techniques available in imaging motion. The second section discusses the Pulsed-Gradient Spin-Echo (PGSE) method, which plays a central role as the technique of preference in this work. The next four sections present **Dynamic NMR Microscopy** in detail. In Ch 3.7, a 'one-shot' velocity imaging method is discussed as a simplified version of Dynamic NMR Microscopy. The last section summarizes and compares the techniques employed in this work.

3.1 A review of imaging dynamic processes using NMR

The measurement of velocity and self-diffusion coefficients using NMR has been of interest[11, 40, 41] since the discovery of the NMR phenomenon in 1946. The main advantage of NMR over other conventional methods of motion detection is the non-invasive nature of the measurement process. In NMR experiments[42-44], translational motion can be detected by measuring the signal amplitude changes due to translation of unpolarized 'fresh' spins[45], by measuring the echo signal attenuation under the influence of rf gradient pulses[46-48], by measuring the phase shifts which are induced by a magnetic field gradient[49, 50], or by measuring a resonant frequency shift related to velocity[51, 52]. Among these the phase shift method is of special importance

because it can be designed to be highly accurate, very sensitive to motion and be used to measure velocity and self-diffusion simultaneously[50, 53].

3.1.1 Contrast and spatial mapping

As discussed in the previous chapter, imaging pulse sequences can be divided into two segments, a contrast segment and a spatial mapping segment. In the current context, a velocity and/or diffusion contrast scheme is employed. The choice of spatial mapping method is not very important since the dynamic contrast scheme can be incorporated with more than one mapping methods. If slice selection is used in imaging, the spatial mapping segment can be subdivided into two parts, namely the slice selection part and the mapping part. Depending on the order of segments, the two approaches to perform an imaging experiment are

slice-selection + contrast + mapping

and contrast + slice-selection + mapping.

During an imaging experiment involving flow, the signal in the first approach is always influenced by the so called 'time of flight' effect which arises because of the finite time existing between the slice selection and signal acquisition. This effect is proportional to the local flow rate at each pixel and represents an artifact. Unless 'time of flight' is the contrast scheme of interest, the best way to remove this effect is to use the second approach, namely, to apply a desired contrast for all the spins inside the rf receiver coil and leave the slice selection as later as possible before the signal acquisition. Provided that the active region of the rf coil is larger than the slice thickness, the signal would then contain the desired contrast effect in the desired slice. However the slice selection method available for this second approach generally involves a 180° soft refocused pulse which occupies a longer time in the critical pre-sampling period and is inherently less efficient than the 90° soft excitation pulse which is used in the first approach.

Sometimes the division between the slice selection and the contrast is not obvious. For example, the 90° slice selection gradient itself can be used to impose flow contrast simultaneous with the slice excitation[54]. This is because the slice selection gradient disturbs the spins in a similar manner to the phase encoding gradient. Because this effect is generally much weaker it can be used to detect (high) velocity flow[55-58]. The influence of this slice selection gradient is discussed in Ch 3.4.

3.1.2 Classification and comparison of velocity imaging techniques

The measurement of flow using NMR can be classified using the following table:

Table 3.1: Classification of velocity imaging

	ρ(r) independent of time			ρ(r) dependent on time	
motion	steady-state			regular	irregular
methods	spin 'freshness'	phase encoding	q-space mapping	gating	fast imaging
examples	laminar flow, turbulent flow			small animal imaging, medical blood flow	

The time-dependent spin density experiment deals mainly with imaging small animals and medical blood flow[59-67], which is not the topic of this work although it is a rapidly developing field with many useful and unique applications especially in hospital diagnoses and medical research. It is briefly discussed later in this section.

The time-independent spin density experiment relates to homogeneous fluids in steady state flow. The imaging experiments in this category can be divided into three subcategories according to the specific contrast schemes employed.

First subcategory of velocity imaging: spin 'freshness'

In the first subcategory termed spin 'freshness', a velocity image is constructed by obtaining either single or multiple spin density maps. The single-experiment technique results in an image in which pixel intensity is proportional to local velocity. The multiple-experiment technique usually involves a subtraction or division of two or more images constructed under different *static* imaging conditions so that the resultant signal amplitude or ratio represents a local velocity.

There are two basic contrast schemes in this subcategory, one is the 'time of flight' method and the other is the steady-state method. The 'time of flight' method[68-75] involves tagging spins first and detecting them at a later time. This method can be incorporated very nicely in 2-D imaging experiments by applying the slice excitation twice. Two slices could be, either at the same or different positions, and either in parallel or orthogonal planes[71]. The first slice excitation establishes an initial transverse plane, the second slice excitation detects magnetization in the new plane after

a time delay (just before the spatial mapping). If the flow is normal to the initial slice plane, then each voxel element will contain different percentages of 'fresh' undisturbed spins and those which have already been in the transverse plane during the first excitation. Therefore the signal after the second slice excitation will reveal this ratio of 'once-sliced' spins to 'twice-sliced' spins and in principle, by varying the delay time or other parameters between the two slices, a velocity image can be reconstructed. Clearly the maximum flow rate is limited by the slice thickness. In order to detect a wide range of velocities, a thick slice is desirable but a thick slice reduces the voxel resolution and increases the requirement for the longitudinal uniformity of the sample.

The steady-state contrast method uses a continuous train of rf pulses in which spins never return to thermal equilibrium. This means that the pulse repetition time is much shorter than the T_1 of the sample. Images are constructed with normal imaging sequences, however, the turn-angle trajectories of the moving spins will inevitably be different from those of the stationary spins. Most steady-state methods require two imaging experiments with different values of delay time[29, 76-82], thus each has a different sensitivity to velocity. Some examples are the steady-state free-precession method and the even-echo method.

The velocity images obtained in this spin 'freshness' subcategory are usually not very accurate. Nonetheless velocity profiles have been obtained successfully using this type of imaging[70, 79]. However, such methods have the advantage of hardware and software simplicity, and also offer the possibility of fast imaging. Most applications have been in MRI for the purpose of a quick and direct visualization of blood vessels, commonly known as MR angiography[83].

Second subcategory of velocity imaging: phase encoding

In the second subcategory termed phase encoding, phase shift contrast is employed before the signal acquisition. Usually this involves the application of a field gradient which induces a phase shift of transverse magnetization across the imaging plane. There are three different ways to apply a field gradient, namely by steady gradients[49], bipolar gradients[84] and a narrow pulsed-gradient pair[53]. In order to calculate a velocity image, both in-phase and quadrature-phase signals are recorded. The phase of the signal at each pixel location is analyzed to yield the local velocity. Although most of the methods in this subcategory still rely on acquisition of two or more 'data' images to produce a velocity image, the original data images are no longer amplitude modulated as in the first subcategory, but phase modulated. In the following analysis, the term 'data images' are used to refer to those images reconstructed directly

using FIDs. The terms of velocity or diffusion images are reserved to those subsequently constructed via appropriate image operations.

There are numerous ways to incorporate the phase shift contrast scheme with imaging sequences. The resultant velocity imaging techniques can be accurate[85], sensitive to flow[86, 87] and fast[88-93]. These techniques are expected to have wider applications both in MRI and non-medical applications such as in material science and rheology studies. Some MRI applications have demonstrated great potential in medical diagnosis, for example, by producing a clear map of blood vessels in human head[94]. The 'one-shot' velocity imaging method which will be discussed in Ch 3.7 falls into this subcategory.

Third subcategory of velocity imaging: q-space mapping

In the third subcategory termed q-space mapping, velocity and self-diffusion images are obtained by first acquiring a series of data images in a space which is conjugate to the space of motion. Subsequent Fourier analysis produces both velocity and self-diffusion images. Although the dynamic contrast scheme in this third subcategory could be the same as that used in the second subcategory (phase encoding), the final velocity and diffusion images in the third subcategory are computed from a set of multiple data images. This means that a multi-dimensional space is explicitly employed in imaging involving more than the three spatial dimensions. Only the experiments in this latter subcategory can be used to accurately and simultaneously construct velocity and self-diffusion images.

The velocity contrast scheme in which a Fourier analysis is employed was first suggested by Moran[84]. By using a bipolar gradient to impose phase contrast in a series of images each obtained using a different degree of phase encoding, a joint spin density, $\Delta(\mathbf{r},\mathbf{v})$, as a function of the six components of $\mathbf{r}$ and $\mathbf{v}$ is obtained. This original Moran proposal is a useful approach only in the ideal situation of simple velocity fields. However it is too simplistic to treat the spin displacements in terms of $\mathbf{r}$ and $\mathbf{v}$ alone. For more complex motions, self-diffusion of molecules is present. The appropriate function to describe the motion of molecular ensembles is the conditional probability, $P_s(\mathbf{r}|\mathbf{r}', \Delta)$, for a spin originating at $\mathbf{r}$ to move to $\mathbf{r}'$ in a well defined time Δ. (It should be noted that even at microscopic resolution, NMR microscopy still deals with sufficient number of nuclei in each pixel that the ensemble view point still holds.) The contrast function sensitive to this conditional probability is the narrow PGSE sequence. The combination of the PGSE contrast scheme and the static NMR imaging, known as Dynamic NMR Microscopy[95], is the theme of this work. This powerful

technique is able to determine local molecular ensemble behaviours in heterogeneous systems, providing in principle a resolution of order 10 μm for the static dimension and 10 μm/s for the velocity dimension. It is worth noting that the phase shift contrast scheme employed in the second subcategory, the phase encoding, is similar to that employed in this **q**-space mapping subcategory, and in a sense can be regarded as 'simplified version' of the **q**-space technique. The factor which fundamentally distinguishes the techniques in the two subcategories is the use of Fourier analysis in the **q**-space mapping.

While a few groups[56, 57, 96] have used multiple phase-encoding scheme, the Fourier methodology was not employed in their work. Redpath *et al* [97] first utilized the Fourier analysis in their work although no velocity image was shown. The first experimental results of combined **k**-space and **q**-space mapping were demonstrated in 1988, in which simultaneous measurements of velocity and self-diffusion coefficient were obtained at a microscopic resolution[95].

3.1.3 Classification and comparison of self-diffusion imaging techniques

Imaging self-diffusion using NMR has until recently been of less interest than imaging velocity. The schemes sensitive to the self-diffusion can be classified using the following table:

Table 3.2: Classification of self-diffusion imaging

	$\rho(\mathbf{r})$ independent of time			$\rho(\mathbf{r})$ dependent on time
examples	stationary samples, constant motions			regular motion, irregular motion
methods	steady state	phase encoding	**q**-space mapping	generally not available

In the case of $\rho(\mathbf{r})$ being time-dependent, there is no reliable method to measure self-diffusion of molecules. This is because the basic principle behind the diffusion measurement relies on a signal attenuation due to the unrecoverable loss of phase coherence caused by the Brownian motion[98-100]. Where regular or irregular motions exist in a sample with $\rho(\mathbf{r})$ being time-dependent, the phase incoherence caused by such translational motion is often more severe than that caused by the Brownian motion thus masking the effect of the latter.

In the case of $\rho(\mathbf{r})$ being time-independent, the basic contrast schemes of self-diffusion imaging can be classified in a manner similar to the velocity imaging. Compared with the varieties available in velocity contrast schemes, all the self-diffusion measurements are based on signal attenuation due to incoherent random motion[41]. Self-diffusion imaging falling into the first and second subcategories can be modified directly from the standard static imaging pulses by adding appropriate contrasts, for example, the steady-state method[101, 102] and the pulsed gradient method[103-105]. Most velocity sensitive methods are equally applicable for imaging self-diffusion with the exception of the 'time of flight' contrast. While some experiments aim to obtain a diffusion-weighted proton map in a single shot[106, 107], construction of self-diffusion images requires several diffusion-weighted data images, each obtained under a different contrast condition[108-110]. Dynamic NMR Microscopy, which falls into the third subcategory, can be used to construct a self-diffusion image simultaneously with a velocity image.

Another type of 'diffusion imaging' involves the measurement of solvents diffusing into submerged solid or polymer samples[111] using standard NMR imaging methods in which the solvent front is observed over successively periods of time. Such applications do not measure self-diffusion but mutual diffusion and are not of interest in this thesis.

Regarding the measurement of self-diffusion using NMR imaging, there are at least four points worthy of note. First, apart from the Brownian motion, there are other factors which may cause signal amplitude attenuation in the pulse sequence designed to detect self-diffusion. These include perfusion or micro-circulation of molecules in the sample[112] and the existence of velocity shear such as in laminar flows[113]. These influences can become dominant in a self-diffusion measurement and should be carefully addressed during experiments. Second, the measurement of self-diffusion in a heterogeneous sample where the structure of the sample results in restricted geometry may result in restricted diffusion[114-116]. This will lead to apparent diffusion values being attenuated. The reduction of apparent self-diffusion is highly geometry- and size-dependent thus it could provide a useful tool to probe these complicated structures. A third concern is the existence of internal magnetic field gradients induced by the different susceptibilities at and around the boundaries of a hetero-structured sample. These internal gradients will degrade the quality of an image severely and thus lead to image artifacts[117, 118]. Finally, the measurement of self-diffusion much slower than that of free water (10^{-9} m^2/s) should be handled carefully because the tiny movement/vibrations of the sample or probe due to the induced eddy current in the

surrounding metals will ruin the chance of accurate self-diffusion measurement, a well known fact in conventional pulsed-gradient NMR experiments.

3.1.4 Static signal suppression in dynamic imaging

In some imaging experiments, especially using biological samples, both stationary and moving spins are present, and the number of stationary spins is often dominant. In this situation, small residual phase shifts in stationary spin signals can lead to apparent spin motion, thus resulting in a velocity error. These shifts might arise from eddy currents due to the switching of gradients, or rf pulse defects. It is appropriate to derive a method which suppresses the stationary spin signal and produces an image of the moving spins only. To produce a null image from stationary spins either the excitation must be motion sensitive or some form of stationary signal suppression must be employed. There are various methods available, such as the Steady-State Selective-Saturation(SSSS)[89], the even-echo method[70, 78], a subtraction of images obtained with different flow contrasts[58, 80, 82, 83, 119], a final 90° 'storage' pulse which returns any in-phase magnetization to the z-axis but which leaves quadrature magnetization in the transverse plane for detection[87, 120].

These stationary signal suppression methods generally result in first order cancellation of stationary signals, but still leave some small residual signals uncompensated[119]. Where a field gradient is used to encode velocity, a higher order cancellation can be achieved by successively alternating the encoding gradient in sign synchronously with the acquisition rf phase[87, 94, 121]. An application of this high order suppression will be discussed in Ch 3.7.

It is worth noting that the imaging technique in the third subcategory, Dynamic NMR Microscopy, is intrinsically much better in the *differentiation* of the stationary spin signal, although it doesn't employ any specific method to suppress the stationary spin signal. This is because Dynamic NMR Microscopy constructs the conditional probability P_s for each pixel so that the spectrum of motion is observed. In other words, the velocity is no longer directly related to a simple ratio of image pixel amplitudes, but is viewed in a conjugate space.

3.1.5 Limitations of measurements

The range of measurable velocities using NMR imaging is limited by the sensitivity of the particular contrast scheme employed. The techniques employing phase shift contrast are most sensitive and accurate. For all techniques, the largest velocity which can be measured is limited in practice by the uniformity length of receiver coil, while the smallest measurable velocity is limited intrinsically by the superposed random motion of the sample's molecules. In the ideal case where the self-diffusion is the only random motion, the degree to which diffusion masks the average flow would dependent on the observational time. This is because velocity displacements are linear with time, t, whereas rms diffusional displacements vary as $t^{1/2}$.

By using a stimulated-echo sequence, the longest observational time can be set to around T_1, therefore the best resolution of velocity measurements by NMR is of order $(D/T_1)^{1/2}$ while the maximum spin displacement sensed during the observational time is given by vT_1. Thus for free water the smallest velocity which can be measured is of order 50 μm/s, but for macromolecules with substantially smaller self-diffusion coefficients, even allowing for shorter T_1 values, this lower limit may be as small as 1 μm/s[122].

3.1.6 Imaging biological samples

In the flow and/or diffusion imaging experiments, imaging using non-biological samples is usually easier than that using biological samples because a non-biological sample can often be modified to suit the requirements of the imaging instrument. The difficulties in imaging biological samples arise from the requirement to maintain a steady state sample condition during the total signal acquisition time. In this regards, imaging using small animals, to obtain a map of blood flow, is more difficult than that of using plants because of the periodic and pulsatile period associated with the animal cardiac cycle. In such animal studies the signal acquisition has to be gated to this cycle[57, 75, 79].

On the other hand, these difficulties in small animal flow imaging are rewarded by their relatively high flow rates compared with those inside vascular tubes of plants. Water translocation rate inside the vascular bundles of plants is much more delicate, often in an order of 30 to 200 μm/s[123]. This small flow rate is very close to the limit of measurement. For irregular motions, however, some high-speed imaging technique

has to be used so that the signal acquisition can be completed in a short time. But these fast imaging techniques could only have extremely limited applications in NMR microscopy because of the low sensitivity.

When working with biological samples, the detectable velocity limit discussed in Ch 3.1.5 is sometime difficult to achieve. This is because a steady state condition of biological samples is not always easy to maintain. The most obvious problem is the physical movement of the sample. Secondly, the probe environment is often not suitable for living samples such as plants. These biological samples can also be partially damaged in the process of fitting them into the probe. All these effects will result in unstable dynamic processes inside biological samples. Reduction of the experimental time is therefore not just a matter of efficiency. In our experiments considerable efforts have been spent to maintain biological samples in a viable state (Ch 4 and Ch 7), and to optimize the time efficiency of the velocity mapping methods (Ch 3.7).

3.2 q-space imaging

Detecting motion using phase shifts is of special importance because of the direct relationship which exists between the nuclear spin displacements and the associated phase displacements. For example it is possible to distinguish between the phase shift due to net motion and the phase spreading due to self-diffusion. Furthermore, higher order motions, such as acceleration, can be selectively measured[54]. In this section, the influence of this phase-shift contrast scheme on the signal amplitude in the presence of self-diffusion and velocity is discussed in detail first, then it is recast into the imaging context.

3.2.1 PGSE technique

The suggestion that it is possible to measure microscopic random flow (self-diffusion) using the spin-echo technique was made long before the invention of NMR imaging[11, 41, 124]. In the absence of diffusion and flow and using a common $90°|_{x'}$-τ-$180°|_{y'}$ pulse sequence, a spin-echo appears in the rotating frame at 2τ (Figure 3.1a). This is because small inhomogeneities of the polarizing magnetic field cause nuclear spins to dephase more rapidly than the effect of T_2 relaxation. However, this dephasing due to the field inhomogeneity can be removed by inverting all spin phases using a

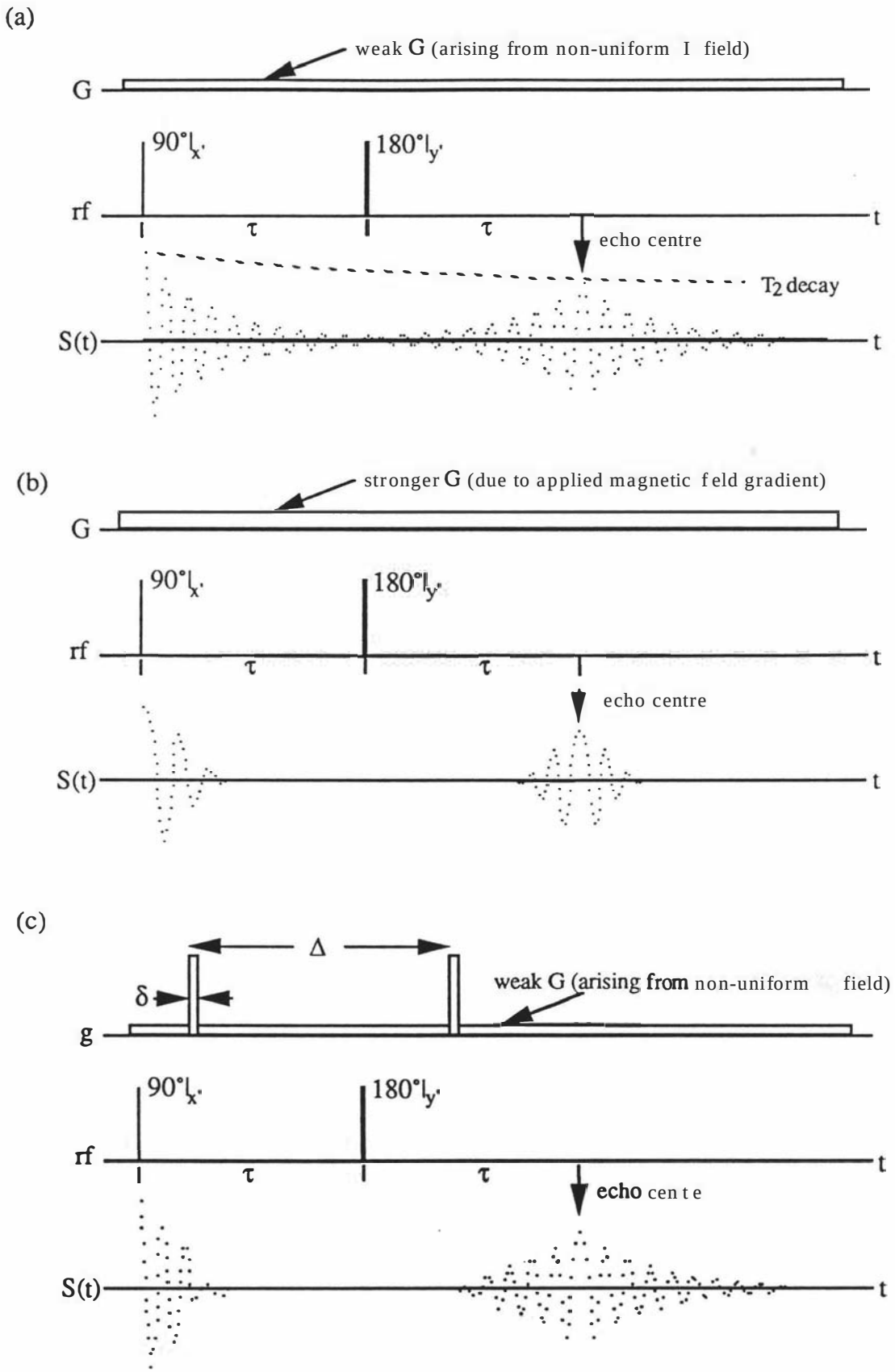

Figure 3.1 Effect of magnetic field gradient in NMR experiments

$180°|_{y'}$ rf pulse. The amplitude of the signal maximum (echo) will therefore reflect the effect of T_2 relaxation alone and is given by

$$M(2\tau) = M_0 \exp(-2\tau/T_2) \qquad [3.1]$$

If the existence of self-diffusion of molecules is considered, the signal amplitude will suffer a further attenuation, provided an additional magnetic field gradient is applied. This is because the self-diffusion of molecules causes nuclei to migrate to a region with different magnetic field during the observation time Δ. Therefore the transverse magnetization cannot be refocussed perfectly following the 180° pulse. Due to the random nature of the Brownian motion, the dephasing of the magnetization due to self-diffusion is irreversible. It is this additional signal decay that enables the measurement of self-diffusion using NMR. For a steady gradient experiment (Figure 3.1b), it can be shown that

$$M(2\tau) = M_0 \exp(-2\tau/T_2) \exp(-\frac{2}{3}\gamma^2 G^2 \tau^3 D) \qquad [3.2]$$

where D is the self-diffusion coefficient and G is the amplitude of the field gradient.

The major disadvantage of the steady gradient experiment is its requirement for a large band-width for excitation and detection, due to the presence of the gradient in the periods of the excitation and detection. McCall, Douglass and Anderson[125] first suggested that the gradient can be applied in the form of pulses so that they can be switched off during excitation and detection. The first experiment and theoretical analysis using this pulsed-gradient spin-echo (PGSE) sequence were given by Stejskal and Tanner[50, 53] based on the Bloch-Torrey equation[126]. The basic form of PGSE sequence is shown in Figure 3.1c, where the dephasing and refocussing of the nuclear spins occur in two strong and identical field gradient pulses of magnitude g, duration δ and separation Δ. In order to distinguish the PGSE gradient pulse amplitude for the steady gradient amplitude used for the static imaging, the lower case symbol is used.

The position of each nucleus following the initial 90° rf pulse is recorded in the presence of the first gradient pulse in the form of phase shift. Between the two gradient pulses the molecules containing the nuclei keep changing their positions due to self-diffusion and/or translational flow. All prior phase shifts are inverted following the 180° rf pulse. After the second gradient pulse, any nucleus which has not moved between the two gradient pulses will be refocused perfectly, while any motion of the nucleus will result in an incomplete refocussing.

Following a similar approach used for the steady state gradient case, the echo amplitude for this pulsed gradient case is given by

$$M(g,\delta,\Delta) = M_0 \exp(-\gamma^2\delta^2 g^2 D\Delta) \qquad [3.3]$$

where it has been assumed that $\delta << \Delta$ (the narrow pulse approximation) and the dephasing due to T_2 is negligible in comparison with that due to the field gradient.

An alternative theoretical description[53, 125] involves the use of a self-correlation function[127-129] of the nuclear spin, $P_s(\mathbf{r}|\mathbf{r}',\Delta)$, which is defined as the spatial probability distribution function that a nucleus initially at position $\mathbf{r}$ will have moved to position $\mathbf{r}'$ at the later time Δ. The evolution of $P_s(\mathbf{r}|\mathbf{r}',\Delta)$ can be derived as

$$\partial P_s/\partial t = -\nabla'\cdot\mathbf{v}\, P_s + \nabla'\cdot\mathbf{D}\cdot\nabla' P_s \qquad [3.4]$$

where $\mathbf{D}$ is the so-called diffusion tensor, a more general symbol allowing for an orientational dependence of the molecular mobility. For a constant flow of velocity $\mathbf{v}$, Eq[3.4] has the solution[53] as

$$P_s(\mathbf{r}|\mathbf{r}',\Delta) = (4\pi D\Delta)^{-3/2} \exp\{ -[(\mathbf{r}'-\mathbf{r}) + \mathbf{v}\Delta]^2/4D\Delta \} \qquad [3.5]$$

where $\mathbf{D}$ is replaced by a scalar, D, because the molecules of interest in this work are all in the isotropic state.

The influence of this self-correlation function on the signal amplitude can be evaluated by considering the echo signal amplitude[38], $E(\mathbf{g},\delta,\Delta)$, at the instant of the sampling origin. In the narrow gradient pulse approximation this echo amplitude is given by

$$E(\mathbf{g},\delta,\Delta) = \int\rho(\mathbf{r}) \int P_s(\mathbf{r}|\mathbf{r}',\Delta) \exp[i\gamma\delta\mathbf{g}.(\mathbf{r}'-\mathbf{r})]\, d\mathbf{r}'d\mathbf{r} \qquad [3.6]$$

where $\rho(\mathbf{r})$ is the local nuclear spin density. By substituting Eq[3.5] into Eq[3.6] and normalizing the echo amplitude, the above equation has a form as

$$E(\mathbf{g},\delta,\Delta) = \exp(-\gamma^2\delta^2 g^2 D\Delta + i\gamma\delta\mathbf{g}\cdot\mathbf{v}\Delta)$$

$$= \exp(-\gamma^2\delta^2 g^2 D\Delta)\exp(i\gamma\delta\mathbf{g}\cdot\mathbf{v}\Delta) \qquad [3.7]$$

It can be seen that the signal amplitude depends upon the self-diffusion (the first exponential decay term) and the signal phase depends upon the translational flow (the second complex oscillatory term).

The narrow gradient pulse condition is particularly useful since it allows us to probe P_S directly. In the case of finite width of pulses the expression for $E(\mathbf{g},\delta,\Delta)$ is more complex although for self-diffusion superposed on flow, a simple interpretation is possible which retains the essential features of the above equation. An exact analysis for the special case of Brownian motion shows that Δ may be replaced by $(\Delta - \delta/3)$ in Eq[3.7] as well as in Eq[3.3]. However, it is easy to show that the phase shift arising from velocity v is given exactly by Eq[3.7] irrespective of the pulse width. No such simple interpretation is available where P_S is non-Gaussian.

3.2.2 q-space imaging

The PGSE technique has been established as a tool to probe motions of molecules governed by the conditional probability, $P_S(\mathbf{r}|\mathbf{r}',\Delta)$. In imaging experiments, however, because of the fundamental resolution limitations, the microscopic inhomogeneity at the molecular level cannot be resolved and signal arises from a very large region on a scale of a few tens of microns. In other words macroscopic molecular ensembles are probed. Furthermore, it should be noted that $P_S(\mathbf{r}|\mathbf{r}',\Delta)$ is a function of the 'static' displacement **r**.

If $P_S(\mathbf{r}|\mathbf{r}',\Delta)$ is spatially averaged within pixels, an 'averaged propagator'[130], $\overline{P_S}(\mathbf{r}'-\mathbf{r},\Delta)$, can be defined as

$$\overline{P_S}(\mathbf{R},\Delta) = \int_{\text{pixel}} \rho(\mathbf{r}) P_S(\mathbf{r}|\mathbf{r}+\mathbf{R},\Delta)\,d\mathbf{r} \qquad [3.8]$$

which gives the *averaged* probability that any molecule in the pixel will move a displacement $\mathbf{r}'-\mathbf{r}$ over the time Δ. **R** is the dynamic displacement, given by

$$\mathbf{R} = \mathbf{r}'-\mathbf{r} \qquad [3.9]$$

It is worth noting that for non-imaging applications of PGSE, Eq[3.8] holds but the 'pixel' in this case corresponds to the entire sample.

Using this concept, the echo signal amplitude given by Eq[3.6] can be recast in an intensity-normalized form as

$$E(\mathbf{g},\delta,\Delta) = \int \overline{P_S}(\mathbf{R},\Delta) \exp[i\gamma\delta\mathbf{g}.\mathbf{R}]d\mathbf{R} \qquad [3.10]$$

$E(\mathbf{g},\delta,\Delta)$ in Eq[3.10] differs from pixel to pixel and is therefore a spatially dependent quantity. Eq[3.10] is instantly recognisable as a Fourier relation in which $E(\mathbf{g},\delta,\Delta)$ and $\overline{P_S}(\mathbf{R},\Delta)$ are conjugate. As discussed previously in Ch 2.2, the standard NMR imaging in the presence of imaging gradients is referred to as **k**-space imaging[33] by defining a reciprocal vector space, $\mathbf{k}=(1/2\pi)\gamma\mathbf{G}t$, in which the **k** space signal is conjugate to the spin density, $\rho(\mathbf{r})$, in the real space via a Fourier relationship. In a similar analogue manner the space reciprocal to the dynamic displacement, **R**, may be defined as[95, 38]

$$\mathbf{q} = (1/2\pi)\gamma\mathbf{g}\delta \qquad [3.11]$$

Consequently Eq[3.10] can be written as

$$E(\mathbf{q},\Delta) = \int \overline{P_S}(\mathbf{R},\Delta) \exp[i2\pi\mathbf{q}.\mathbf{R}]\, d\mathbf{R} \qquad [3.12]$$

The PGSE experiment can therefore be viewed as an imaging process in its own right, for which the sampling occurs in the conjugate **q** space and, upon Fourier transformation, yields the image of $\overline{P_S}(\mathbf{R},\Delta)$ in **R** space[95, 38].

Traditionally in the conventional PGSE experiment, the analysis is not performed in this way, but rather, the data is plotted in the manner of Stejskal and Tanner[50] as $\log(E(\mathbf{g}))$ vs g^2, in anticipation of the Gaussian dependence expected from Brownian motion. This traditional approach will be discussed later in Ch 3.6 as an alternative data analysis method. Nonetheless the direct computation of $\overline{P_S}$ is possible, and $\overline{P_S}(\mathbf{R},\Delta)$ is labelled as the dynamic image, in a manner analogous to the static image, $\rho(\mathbf{r})$.

It is useful to consider the nature of $\overline{P_S}$ in the conventional PGSE experiment which measures unrestricted self-diffusion in liquids. Here the sample is homogeneous and $P_S(\mathbf{r}|\mathbf{r}',\Delta)$ is independent of starting position, **r**. Therefore there is no need to speak of an 'averaged propagator' and $P_S(\mathbf{r}|\mathbf{r}',\Delta)$ is identically the dynamic image, $\overline{P_S}(\mathbf{R},\Delta)$. For Brownian motion $P_S(\mathbf{R},\Delta)$ is a Gaussian curve centred at **R**=0, the square root of

the self-diffusion coefficient is equal to the Full-Width-Half-Maximum (FWHM) of this Gaussian curve, given by

$$\text{FWHM} = \frac{2}{\pi}(\gamma\delta g)[(\ln 2)D\Delta]^{1/2} \qquad [3.13]$$

Where flow is also present the diffusive motion is superposed on a local frame of velocity, **v**, and $P_S(\mathbf{R},\Delta)$ will retain the same Gaussian shape but will be centred at $\mathbf{R}=\mathbf{v}\Delta$. However, many PGSE experiments are performed on samples which are macroscopically uniform but microscopically inhomogeneous. Examples include studies of restricted diffusion in porous materials. Such experiments can be used to obtain information about the geometry of barriers to self-diffusion. Clearly the case of restricted diffusion involves severe inhomogeneity of $P_S(\mathbf{r}|\mathbf{r}',\Delta)$ at the molecular level. The averaged propagator defined in this section becomes a powerful tool to reveal the barrier geometry by the Δ dependence of $P_S(\mathbf{r}|\mathbf{r}',\Delta)$[131]. This particular topic is not dealt with in this work but is reviewed elsewhere[38, 100].

3.3 Theory of Dynamic NMR Microscopy

Based on the previous discussions, the theory of Dynamic NMR Microscopy is now presented systematically.

3.3.1 Combined k-space and q-space imaging

A typical dynamic imaging experiment involves a sample with molecules undergoing both Brownian motion (D) and translational motion (**v**), and acquisition of the time domain signal evolved under the influence of both the PGSE gradient **g** and the resolution gradient **G**. These evolutions involve spin precessions only about the z-axis which therefore commute. This leads to a signal modulation in both **k**- and **q**-space described by separable, linear operators as[38, 113]

$$S(\mathbf{k},\mathbf{q}) = \int \rho(\mathbf{r}) \exp[i2\pi\mathbf{k}.\mathbf{r}] \int \overline{P_S}(\mathbf{R},\Delta) \exp[i2\pi\mathbf{q}.\mathbf{R}]\, d\mathbf{R}\, d\mathbf{r} \qquad [3.14]$$

Despite the fact that both $\overline{P_S}(\mathbf{R},\Delta)$ and $\rho(\mathbf{r})$ may depend on **r**, the effect of the PGSE sequence is simply to impart an image contrast, $E(\mathbf{q},\mathbf{r},\Delta)$, to each pixel in the static image. This contrast is defined by

$$E(\mathbf{q},\mathbf{r},\Delta) = \int \overline{P_S}\,(\mathbf{R},\Delta)\,\exp[i2\pi\mathbf{q}.\mathbf{R}]\,d\mathbf{R} \qquad [3.15]$$

The above equation can be evaluated[50, 53] for the finite pulse width case and it gives

$$E(\mathbf{q},\mathbf{r},\Delta) = \exp[-\gamma^2\delta^2 g^2 D(\Delta-\delta/3) + i\gamma\delta\mathbf{g}.\mathbf{v}\Delta] \qquad [3.16a]$$

or $$E(\mathbf{q},\mathbf{r},\Delta) = \exp[-4\pi^2 q^2 D(\Delta-\delta/3) + i2\pi\mathbf{q}.\mathbf{v}\Delta] \qquad [3.16b]$$

Therefore Eq[3.14] can be rewritten in terms of static imaging, as

$$S(\mathbf{k},\mathbf{q}) = \int \rho(\mathbf{r})E(\mathbf{q},\mathbf{r},\Delta)\exp[i2\pi\mathbf{k}.\mathbf{r}]\,d\mathbf{r} \qquad [3.17]$$

Eq[3.17] states that image reconstruction in **k** space will now yield $\rho(\mathbf{r})E(\mathbf{q},\mathbf{r},\Delta)$. There are three points which could be noted immediately. First, since $E(\mathbf{q},\mathbf{r},\Delta)$ may reflect the effects of phase shifts as well as phase spreading, it is inherently complex. This implies that the usual $S^*(\mathbf{k})=S(-\mathbf{k})$ symmetry in **k**-space mapping is no longer available and reconstruction must employ full four-quadrant sampling. This leads consequently to the computation of both real and imaginary images, $\rho(\mathbf{r})E(\mathbf{q},\mathbf{r},\Delta)$.

Second, the local conditional probability and its Fourier transform in Eq[3.17] represents a finite imaging voxel, although ideally this volume, $d\mathbf{r}$, should be infinitesimal. Thus $\overline{P_S}\,(\mathbf{R},\Delta)$ is implicitly a function of the pixel coordinate, **r**, and $E(\mathbf{q},\mathbf{r},\Delta)$ refers to the normalised echo contribution from the pixel at **r**.

Finally, because $\overline{P_S}\,(\mathbf{R},\Delta)$ represents a normalized probability, $E(0,\mathbf{r},\Delta)$ is unity. This obvious but important result is consistent with the reproduction of the conventional spin density map when the PGSE gradient is zero, which implies that $E(\mathbf{q},\mathbf{r},\Delta)$ may be obtained independently of $\rho(\mathbf{r})$ by normalizing to the zero **q** image. One consequence of $E(0,\mathbf{r},\Delta)$ being unity is that when $\mathbf{q}=\mathbf{0}$, the construction returns

$$\rho_R(\mathbf{r},0) = \rho(\mathbf{r}) \qquad [3.18a]$$

and $$\rho_I(\mathbf{r},0) = 0 \qquad [3.18b]$$

This means that the real part $\rho_R(\mathbf{r},0)$ is just the 'static' spin density $\rho(\mathbf{r})$ (along with any additional contrast factor) defined previously in Eq[2.59], while the imaginary part $\rho_I(\mathbf{r},0)$ should be zero. However, it is worth noting that any additional contrast factor, $E_c(\mathbf{r})$ in Eq[2.59], will have no effect in the final velocity and self-diffusion images constructed in Dynamic NMR Microscopy, because the normalization of $E(\mathbf{q},\mathbf{r},\Delta)$ to the zero $\mathbf{q}$ image 'divides out' the effect of $E_c(\mathbf{r})$.

Figure 3.2 shows a basic pulse sequence which represents the Dynamic NMR Microscopy experiment. This pulse sequence can be divided into three segments, the slice excitation, the dynamic contrast and the spatial mapping. The first and the last segments are identical to these used in the static imaging. Due to the extra time required for the dynamic contrast, there will be some additional transverse relaxation contrast during **k**-space image construction. However this relaxation contrast will have no effect on the final velocity and self-diffusion images due to the normalization procedure.

In the dynamic contrast period, a single dimension in **q** space is chosen so that the over-all imaging process is four dimensional. The method can be easily generalized to two or three dimensions in **q** space although this leads to excessively long experiments because of the low sensitivity associated with the NMR method and the consequent need for signal averaging. The direction in which self-diffusion and flow is measured is, of course, determined by the direction in which **g** is applied. The

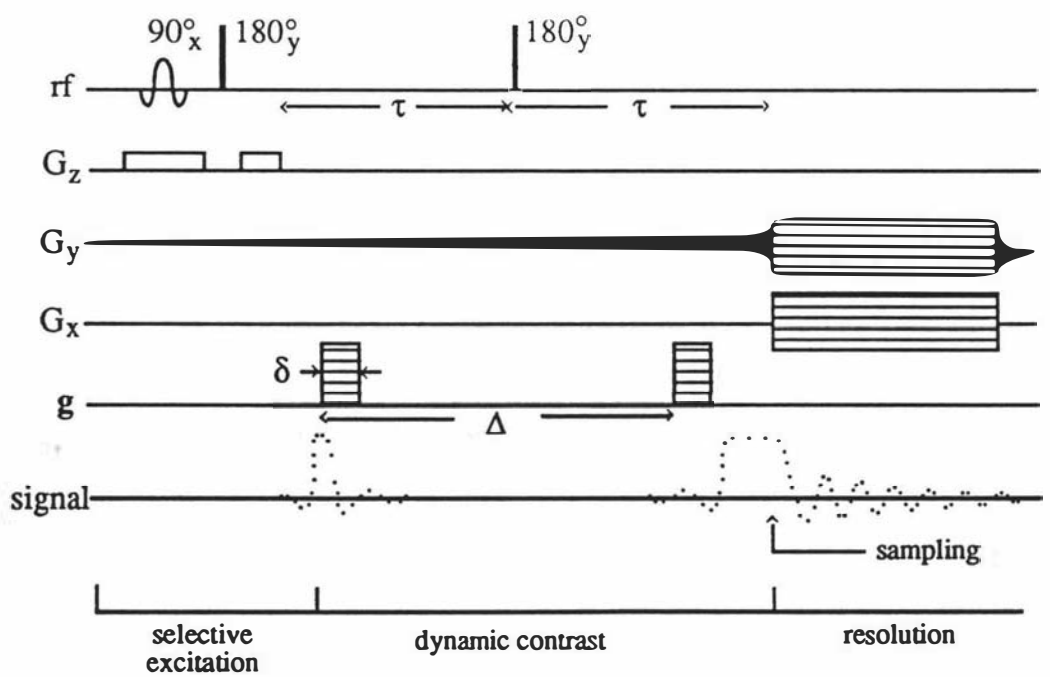

Figure 3.2 A pulse sequence used in Dynamic NMR Microscopy

amplitude of **g** determines the **q**-vector amplitude, q. If the dynamic dimension conjugate to q is defined as Z where Z=z'-z and the relevant components of the diffusion tensor and the velocity in the Z direction are D and v, $E(q,\mathbf{r},\Delta)$ has the form of an oscillatory function of q modulated by a Gaussian decay, namely

$$E(q,\mathbf{r},\Delta) = \exp[-4\pi^2q^2D(\Delta-\delta/3) + i2\pi qv\Delta] \qquad [3.19]$$

The (complex) q-space Fourier transform of this function corresponds to the dynamic image of $E(q,\mathbf{r},\Delta)$ and is given by the convolution

$$F[E(q,\mathbf{r},\Delta)] = [4\pi D(\Delta-\delta/3)]^{-1/2} \exp[-\frac{Z^2}{4D(\Delta-\delta/3)}] \otimes \delta(Z-v\Delta) \qquad [3.20]$$

where δ is the delta function. $F[E(q,\mathbf{r},\Delta)]$ corresponds to a Gaussian of width $2(\ln 2)^{1/2}[D(\Delta-\delta/3)]^{1/2}$ centred at $v\Delta$. This one-dimensional image of P_s will be referred to as the dynamic displacement profile. The conjugate pair represented by Eq[3.19] and Eq[3.20] is shown in Figure 3.3. Clearly $F[E(q,\mathbf{r},\Delta)]$ is more amenable to direct interpretation than $E(q,\mathbf{r},\Delta)$ since the velocity and self-diffusion coefficient are simply related to two clearly defined features of the Gaussian profile, namely the profile peak centre and profile width. However, the possibility to determine the velocity and diffusion via $E(q,\mathbf{r},\Delta)$ directly will be discussed later in Ch 3.6. To simplify equations

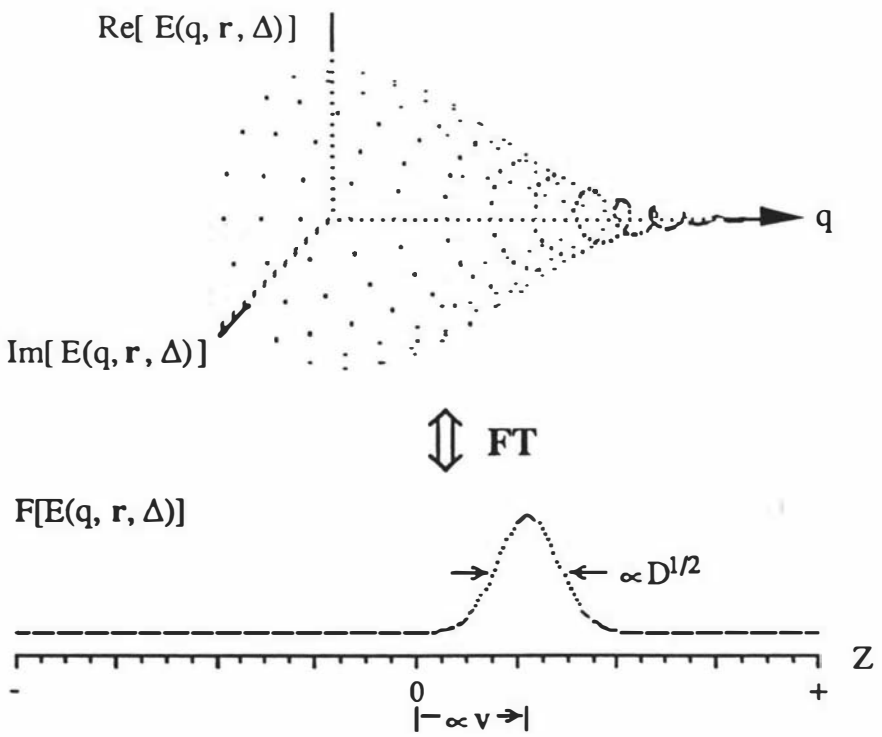

Figure 3.3 The Fourier relationship in Dynamic NMR Microscopy

in the following analysis, the distinction between Δ and $(\Delta-\delta/3)$ will be ignored with the understanding that this replacement is always implied.

In summary, the Fourier relationships for (normal) static imaging and dynamic imaging are shown in Table 3.3.

Static Imaging ($\mathbf{g} = 0$)	
FT[**k**] $S(\mathbf{k}) <==> \rho(\mathbf{r})$	
Dynamic Imaging ($\mathbf{g} \neq 0$)	
FT[**k**] $S(\mathbf{k},q) <==> \rho(\mathbf{r})E(\mathbf{q},\mathbf{r},\Delta)$	FT[**q**] $E(\mathbf{q},\mathbf{r},\Delta) <==> \overline{P_S}(\mathbf{R},\Delta)$

Table 3.3 Fourier relationships for static and dynamic imagings.

3.3.2 Digital Fourier transform and interpretation

In practice, the operations in Dynamic NMR Microscopy are required to recast to a manner consistent with digital sampling, as the following. Imaging experiments are carried out with the q-contrast gradient being successively stepped in n_D steps to some maximum value g_m. Each step corresponds to a 'slice' in **q** space, where one pair of complex images (one in-phase and one quadrature-phase) is reconstructed using the normal **k**-space reconstruction algorithm. The real image in the first slice ($\mathbf{q}=0$) should produce the 'static' $\rho(\mathbf{r})$ image while the first imaginary image should be zero (within the accuracy of the noise). n_D is the number of slices in addition to the $\mathbf{q}=0$ slice. The total number of **q**-slices, n_D+1, is usually small, typically 10 to 18 in our experiments, because of the restraints of total imaging time. After the completion of the n_D+1 **q**-slices, the **q**-space Fourier transformations are performed successively at each pixel location along the **q** direction, which returns the dynamic displacement profile in **R** space. The peak offset and the FWHM of the peak are stored at the corresponding pixel location of the velocity and diffusion images separately.

The complete operations in a Dynamic NMR Microscopy experiment are illustrated in Figure 3.4 [132, 133]. It is worth noting that this method is akin to multiple-

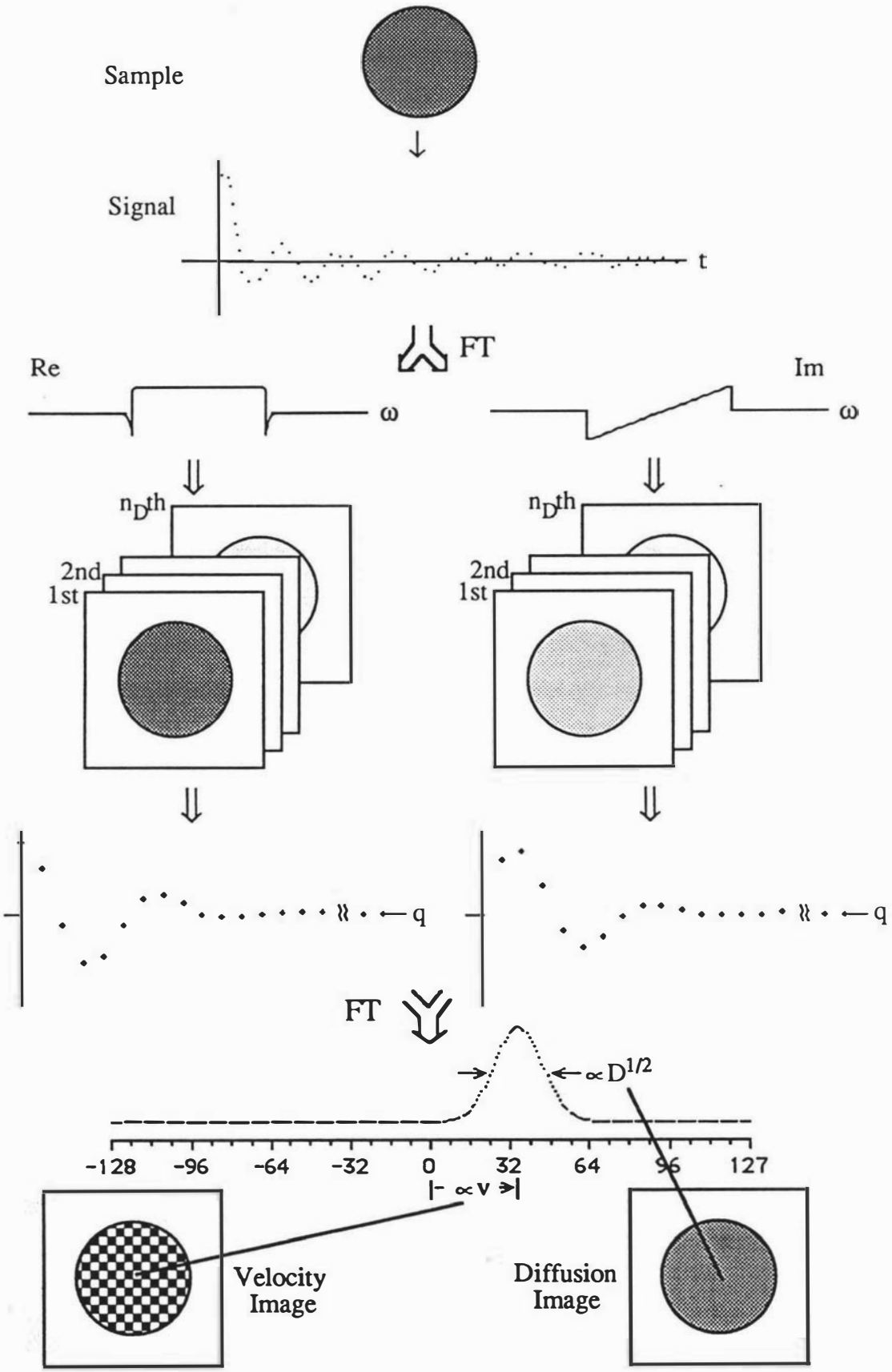

Figure 3.4 Experimental procedures in Dynamic NMR Microscopy

slicing methods except that here the slices represent n_D+1 different discrete layers in q space rather than real space. A zero-filling of the q data from n_D+1 to N is incorporated before Fourier transformation in q space where N is a large number (typically 256). This procedure improves the accuracy of the FFT process and results in a much larger number of data points defining the displacement profile, a necessary feature equivalent to the data interpolation so that the peak centre and width can be calculated more accurately.

The last step of dynamic imaging is to interpret the digital values obtained from the discrete FT into SI units. In the following discussion the 'time' and 'frequency' domain pictures are retained for the conjugate spaces relating to dynamic imaging simply for convenience. The initial time domain data is sampled in the positive, real and imaginary domains, in N steps from 0 to N-1 while the complex transforms represent signed frequencies of N steps between -N/2 to N/2 -1.

Two functions, h(nT) and H(k/NT) are termed a Fourier transform pair[16] if they are related with each other via the discrete Fourier transformation, as the following two equations

$$h(nT) \text{ where } n = 0..N-1 \qquad [3.21a]$$

and $$H(k/NT) \text{ where } k=-N/2\ ..N/2-1 \qquad [3.21b]$$

$$H(k/NT) = \sum_{n=0}^{N-1} h(nT)\exp(-i2\pi kn/N) \qquad k = 0,1,2,...,N-1 \qquad [3.22a]$$

and $$h(nT) = (1/N)\sum_{k=0}^{N-1} H(k/NT)\exp(i2\pi kn/N) \qquad n = 0,1,2,...,N-1 \qquad [3.22b]$$

where 1/NT gives the frequency domain sampling interval and n and k are the variables in the time and frequency domains respectively.

In Dynamic NMR Microscopy experiments, the sampling interval T is equivalent to $(1/2\pi)\gamma\delta(g_m/n_D)$ since q has been defined in Eq[3.11]. In this manner the separate oscillatory and damping terms of Eq[3.16] may be written as

$$E(n,\mathbf{r},\Delta) = \exp[\, i\,(\gamma\delta v\Delta)\,(\frac{g_m}{n_D})\,n]\,\exp[-\gamma^2\delta^2\,(\frac{g_m}{n_D})^2\,Dn^2\Delta] \qquad [3.23]$$

where **r** is determined by the pixel location in which $E(n,\mathbf{r},\Delta)$ is computed, v and D depend on the chosen pixel and are therefore functions of **r**. The ratio $(\frac{g_m}{n_D})$ represents the step size in **q** space.

The dynamic displacement profile (Eq[3.20]) arising from the Fourier transform is the convolution

$$P_S(\frac{k}{N},\,\Delta) = (\frac{\pi(\frac{n_D}{g_m})^2}{\gamma^2\delta^2D\Delta})^{1/2}\exp[-\frac{\pi^2k^2(\frac{n_D}{g_m})^2}{\gamma^2\delta^2N^2D\Delta}] \otimes \delta\,(\frac{k}{N} - \frac{\gamma\delta v\Delta(\frac{g_m}{n_D})}{2\pi}) \qquad [3.24]$$

Therefore peak centre of the dynamic displacement profile occurs at the digital value

$$k_v = \frac{N\gamma v g_m \delta\Delta}{2\pi n_D} \qquad [3.25]$$

and so the value of the mean molecular velocity in the pixel position **r** is given, in SI units, by

$$v = \frac{2\pi n_D k_v}{N\gamma g_m \delta\Delta} \qquad [3.26]$$

The use of a complex transformation (and hence the acquisition of both in-phase and quadrature-phase images) permits positive and negative velocities to be distinguished.

The Full-Width-Half-Maximum (FWHM) of $\overline{P_S}\,(\mathbf{R},\Delta)$ in digital units is given by

$$k_{FWHM} = (\frac{2}{\pi})(\ln 2)^{1/2}\,N\gamma\delta\,(\frac{g_m}{n_D})\,(D\Delta)^{1/2} \qquad [3.27]$$

and so the value of the mean molecular self-diffusion coefficient in the pixel corresponding to this profile can be derived in SI units as

$$D = \frac{(n_D k_{FWHM})^2}{(4\ln 2/\pi^2)\gamma^2 N^2 g_m{}^2 \delta^2 \Delta} \qquad [3.28a]$$

or $$D = \frac{3.56(n_D k_{FWHM})^2}{\gamma^2 N^2 g_m{}^2 \delta^2 \Delta} \qquad [3.28b]$$

3.3.3 Velocity-compensated Dynamic NMR Microscopy

The application of Dynamic NMR Microscopy to liquids in high shear is of interest in this work since there exists the potential to study rheological properties at the molecular level. For example, in the case of high polymer solutions the molecular relaxation times can be of order 10^{-1} s or greater. In capillary flow it is possible to achieve a velocity shear, $\partial v/\partial r$, in excess of the polymer relaxation rate so that significant conformational changes may result at molecular level. These conformational changes can be investigated via the measurement of molecular self-diffusion coefficients.

The accurate measurement of self-diffusion by Dynamic NMR Microscopy in the presence of a velocity shear is complicated by the additional line broadening due to this velocity shear, an effect which will be discussed in detail later in Ch 3.5. The magnitude of this effect is proportional to the velocity spread in the pixel, Δv[132], and it is an artifact in the image. This velocity shear artifact becomes much worse for high polymers, because the values of self-diffusion coefficients may be exceedingly small so that the effect of the velocity spread may prove devastating. For example, suppose that it is to measure a typical high polymer diffusion coefficient of order 10^{-13} m^2 s^{-1}. For this experiment Δ will be required to be of order 20 ms given possible gradient strengths. If the shear rate in a 1 mm diameter capillary is of order 10 s^{-1}, as required to produce conformational changes, then the velocity spread across a typical 20 μm pixel is 2×10^{-4} m s^{-1} and $\Delta D^{1/2}$ is of order 10^{-5} m s$^{-1/2}$. Such an enormous value makes the experiment impossible.

Provided that the flow is laminar, the longitudinal constancy of the velocity could be used to cancel the coherent phase shifts due to the velocity shear via a compensating PGSE pulse train. Because of the stochastic nature of Brownian motion, the phase spreading associated with self-diffusion will continue relentlessly so that the remaining line-width of the pixel dynamic displacement profile should be due to these random motions alone. This form of "flow compensation" was originally noted for

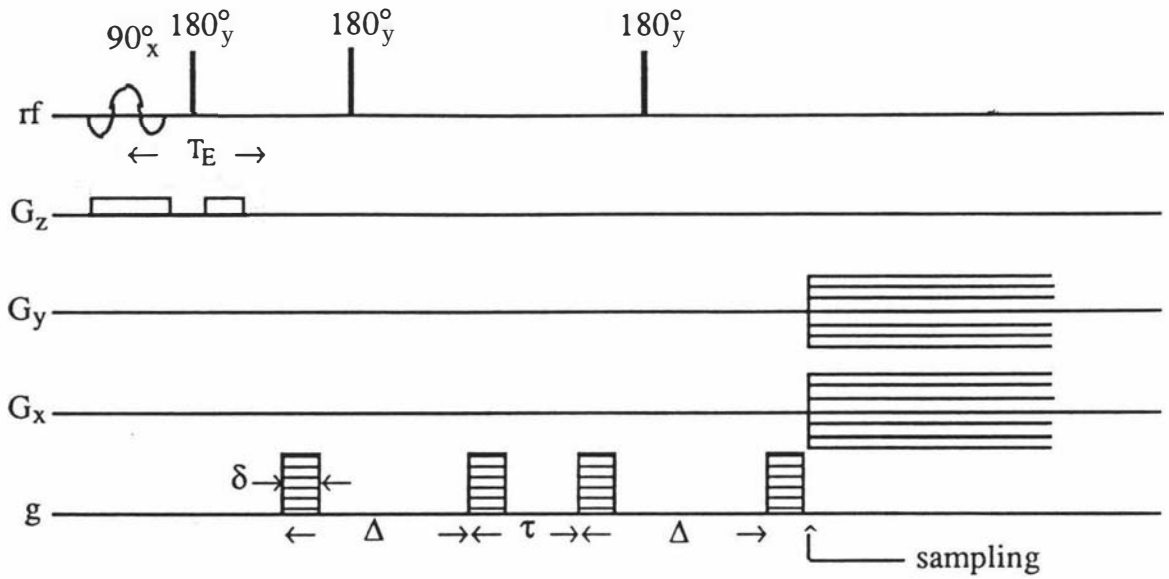

Figure 3.5 A pulse sequence used in the velocity-compensated Dynamic NMR-Mic r scopy

even-echoes in a multiple echo train[41] and has been used for flow suppression in medical MRI[78, 79, 83, 88]. It is worth noting that for such an approach, any effects due to turbulence or other chaotic motion will still be apparent due to their 'random' nature. For the steady state polymer experiment where high viscosities are involved, the Reynolds' number will be very low and the flow should be highly laminar.

The pulse sequence used in the velocity-compensated Dynamic NMR Microscopy is shown in Figure 3.5. Compared with the standard dynamic imaging pulse sequence (Figure 3.2), there are, in effect, two identical PGSE sequences applied in succession in the dynamic contrast segment. The 180° rf pulse of the second PGSE sequence inverts all the phase shifts left over after the first PGSE pair which are associated with the coherent motions, thus the effect due to the velocity are cancelled out completely. The diffusive effects in this double PGSE sequence produce exactly twice the attenuation of a single spin echo experiment given by Eq[3.28].

3.4 Precision and accuracy of the velocity map obtained in Dynamic NMR Microscopy

In obtaining velocity maps it is essential to transform the q-space data to the conjugate real or **R** space domain in order to locate the dynamic displacement profile centre. In our software, the velocity is determined simply by searching the maximum

peak height in the profile. This section discusses the precision and accuracy of the velocity map obtained in Dynamic NMR Microscopy experiments and some potential artifacts associated with it. In general, the digital velocity value obtained from the displacement profile, k_v, can be 'decomposed' using the following expression

$$k_v = k_{true} + k_i + k_{ss} + k_{GDP} + k_{ho} \qquad [3.29]$$

where k_{true} represents the true velocity, k_i the influence due to the instrument and software artifacts, k_{ss} the artifact due to the slice selection gradient, k_{GDP} the artifact due to the instrumental phase shift caused by the PGSE gradient (not arising from molecular motion) and k_{ho} the artifact due to the 'dynamic' inhomogeneity of the sample.

3.4.1 The influence of the instrument

In velocity computations, errors could be introduced by the instabilities of the instrument and the sample, such as small changes of the flow rate during the hour-long experiment and the drift of the phase sensitive detector. All these hardware-related drifts in experiments could affect the detection phase of the complex signal, which in turn results in errors in the velocity image. These small but troublesome problems have to be addressed by the experimenter for each individual case.

One possible systematic error which could affect the accuracy of velocity measurement is the imperfect phase setting of the spectrometer's phase sensitive detector. Before an experiment this phase has to be set so that the real signal in frequency domain is a perfect 'absorption' spectrum and the imaginary signal is a perfect 'dispersion' spectrum, otherwise there would be some initial phase shift which will result in a 'velocity' error. To illustrate this effect, some computer simulations have been carried out to produce several sets of 18 pair complex data images which suffer Brownian motion alone. In these simulations the image pixel intensities in the 18 imaginary data images are 50%, 10%, 0%, -10% of those in the respective real data images, which are equivalent to phase offset errors of 26.6°, 5.7°, 0° and -5.7° respectively. Figure 3.6 shows two dynamic displacement profiles for the 26.6° case and the 0° perfect case, where the 26.6° case is clearly distorted. Figure 3.7 shows the velocity profiles through the centres of the four velocity images, the velocity artifacts are 4, 1, 0, -1 digits respectively in the usual -128 to 127 digital scale. It is interesting to note that this phase offset has little effect on the diffusion maps, the corresponding profiles through the diffusion maps are shown in the next section.

(a) The per f ct case, 0° phase shift

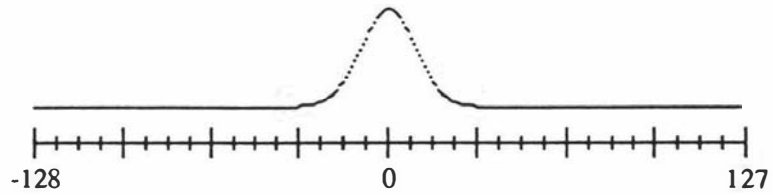

(b) 26.6° phase shift (imaginary intensity is 50% of real)

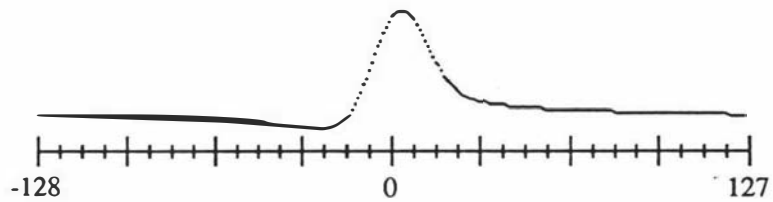

Figure 3.6 Phase shift in dynamic displacement pro f les

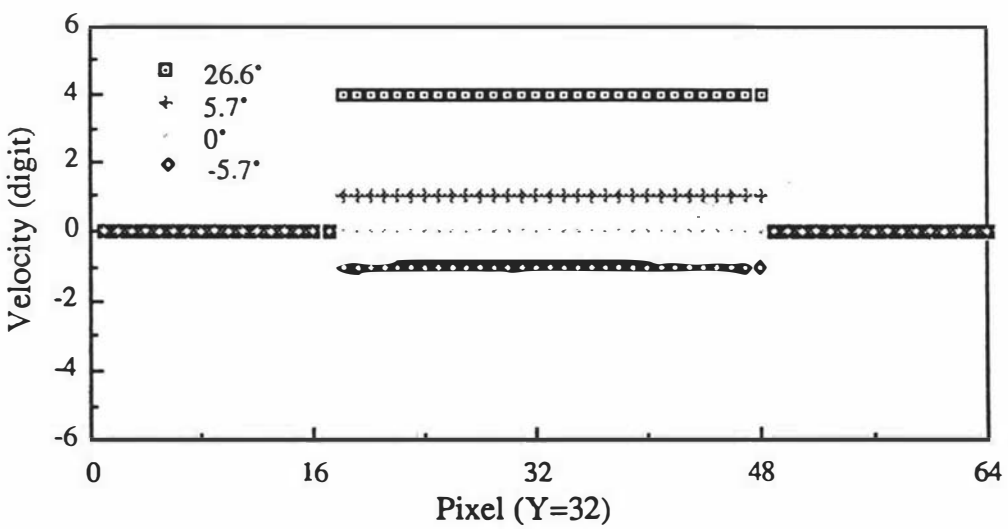

Figure 3.7 Cross sectional profiles through simulated velocity images showing the artifact due to the initial phase offsets

The phase of the projection profiles could also be affected (slightly) by the strength of the mapping gradients and the directions in which they are applied. This change of the phase settings is probably due to the induced eddy currents in the surrounding metal pieces, which will produce a velocity artifact in a way similar to the one which has just been discussed. In our experiments these instrument-related phase offsets can be compensated for in the software (refer to Ch 4.4 for more details).

Given the fact that a rather simple algorithm is employed in the calculation of the velocity, the velocity map is remarkably accurate. However, experimental noise is unavoidable and does influence the accuracy of the velocity by slightly and randomly distorting the phase of the profile. Figure 3.8a shows a velocity profile for the simulated Brownian motion and with a perfect phase setting, but in the presence of a ±10% random noise in the data image set (this ±10% noise level is typical in our experiments). From this graph, it is clear that the velocity map in any real experiment is always perturbed by these small random errors which are between ±2 digits. Figure 3.8b shows the histogram of this velocity image, which is centred near the zero. The histogram of the velocity image from the noise-free simulated data set is shown in Figure 3.8c and is of course centred at zero. Using a routine in ImageShow™ software (see Ch 4.5), an arithmetic average over all the pixels of this velocity map is 0.30 digit. However, for each individual pixel this noise influence will be between ±2 digits and will be critical in the lower end of the detection range. In our imaging analysis procedure, this random noise influence can be examined by performing an on-line FFT to display the P_S spectrum using a routine in ImageShow™ software. In Ch 3.6 an alternative data analysis method is discussed which is equally useful in theory but is much more sensitive to the presence of the experimental noise.

In summary, provided care has been taken into account during an experiment the influence of the instrument hardware and software on the velocity image only affects the precision of the measurement but produces no systematic errors.

3.4.2 The influence of the slice selection gradient

As discussed in Ch 2.2 and Ch 3.1, the slice selection is normally employed in an imaging pulse sequence before the spatial mapping to select a thin slice for detection. This slice selection sequence forms a spin echo over a short but finite timescale, Δ_S. Where the detection direction of the spin motion is normal to this slice plane, this echo will suffer a phase shift which will depend on the 'separation' Δ_S, duration δ_S and the

(a) A cross sectional profile through the noise-affected vel o ity image

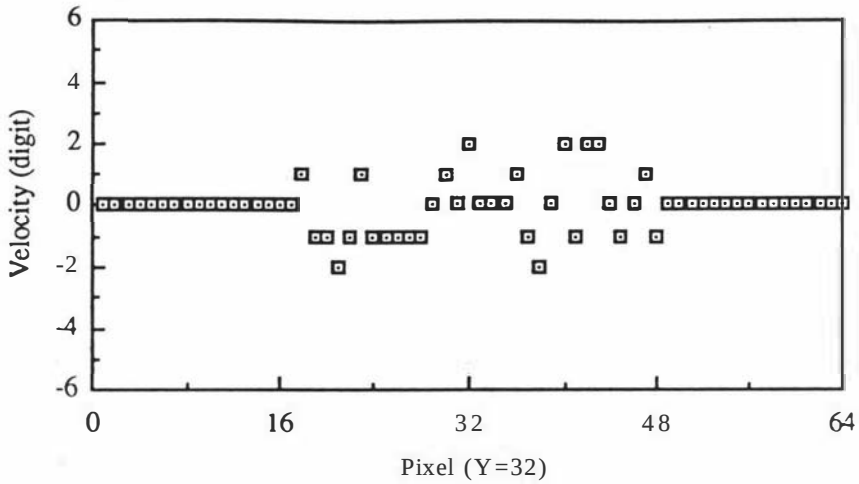

(b) The histogram of the noise-affected vel o ity image

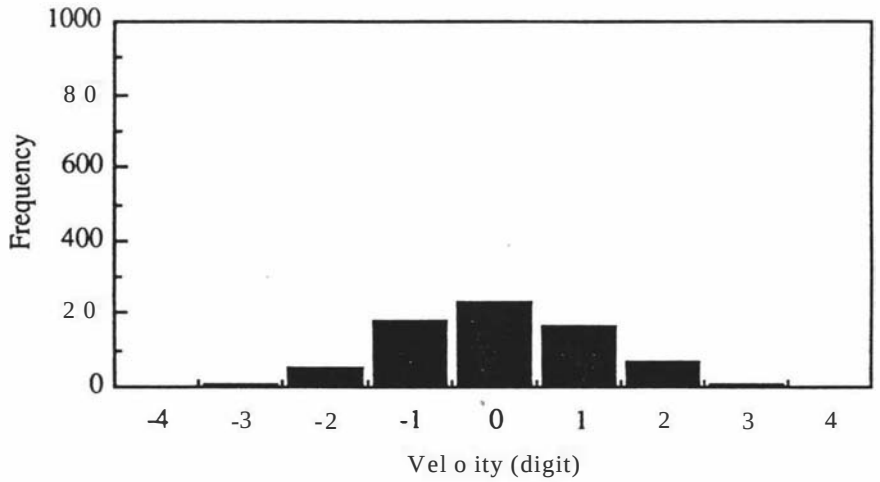

(c) The histogram of the noise-free vel o ity image

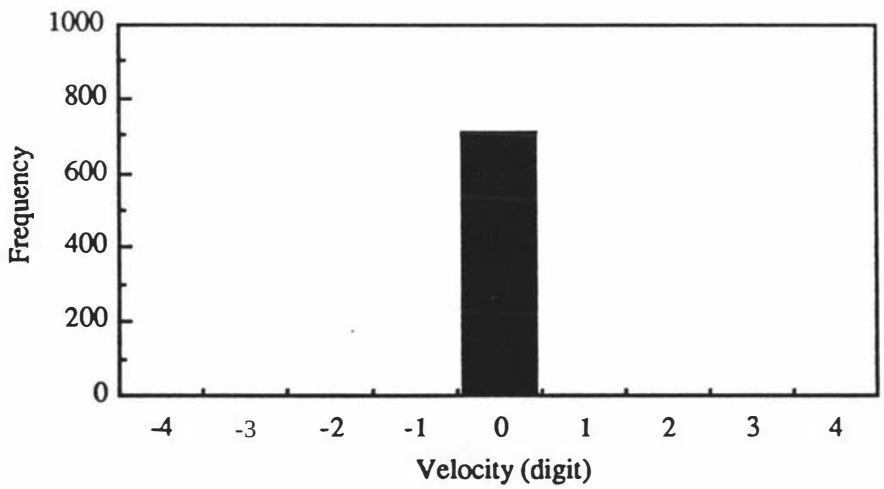

Figure 3.8 **The influence of experimental noise on velocity images**

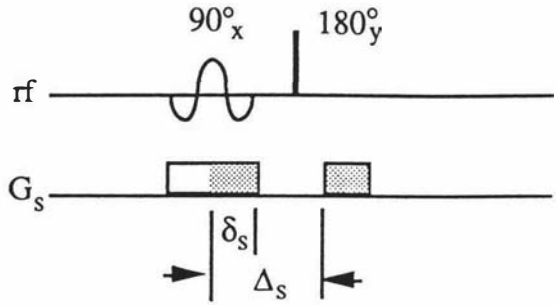

Figure 3.9

The "PGSE-like" effect of the slice selection gradient

magnitude of the slice selection gradient G_S. In other words, some velocity artifacts will be introduced by this 'PGSE-like' sequence, shown in Figure 3.9.

Using Eq[3.19], the phase shift artifact due to the slice selection gradient, ϕ_S, is

$$\phi_S = \gamma \delta_S G_S v \Delta_S \qquad [3.30]$$

If Δ, δ and g represent the duration, separation and magnitude of the PGSE gradient in the pulse sequence, then the percentage of this artifact comparing with the desired phase shift associated with the flow, ϕ_{PGSE}, is given by

$$\phi_S/\phi_{PGSE} = \delta_S G_S \Delta_S/\delta g \Delta \qquad [3.31]$$

From the above two equations, it is clear that ϕ_S is velocity-dependent and common to each q-space slice (Eq[3.30]). Its velocity-dependency will lead to spatial dependency, and could lead to artifacts in capillary flow experiments where v varies strongly across the image. But the percentage influence of this artifact is velocity-independent (Eq[3.31]), which means that it has the same impact everywhere on the image. Given a typical set of experimental parameters (for a 0.5 mm slice) as δ_S=2ms, G_S=0.0936T/m, Δ_S=4ms, δ=2ms, g=0.936T/m, Δ=5ms and v=6mm/s, ϕ_S is equal to 1.2rad, ϕ_{PGSE} equal to 15rad and ϕ_S/ϕ_{PGSE} equal to 8%. However, by reducing Δ_S and ϕ_S, this artifact can be minimized as illustrated by an example later in Ch 8.

In practice, if velocities in a flow field are all in one direction and of similar magnitude, the slice selection artifact can be compensated to some extend by examining the phase of the zero q-slice and applying this fixed phase correction to all q-space data in the spectrometer. In Ch 6.2.3 an interesting result is given for two oppositely signed velocities in the same flow field where such simple compensation method no longer works.

3.4.3 Gradient-dependent phase shifts

In many spectrometers the phase of the signal arising from stationary spins depends upon the magnitude and/or direction of the applied PGSE gradient, g. This may be caused by some induced eddy currents in the nearby metals or imperfections of the gradient coil. The switching of the gradient pulses can also cause some field shift due to the flux-stabilizer response in the case of electromagnet-based spectrometers. Thus some velocity errors are introduced by these additional hardware-related phase shifts.

This type of artifact can be compensated provided that these additional phase shifts are consistently reproducible. In our instrument the gradient-dependent phase shift is compensated by first measuring it at each g value for a stationary sample and then storing these values in a table for later automatic compensation during "phasing" the spectra under software control. A complete dynamic imaging experiment is then performed on a stationary sample and the velocity map is inspected to ensure that the mean velocity is everywhere 0±2 on the usual -128 to 127 digital scale, i.e., no velocity error due to the gradient-dependent phase shift. It is worth noting that this "phasing" method should not be confused with the autophasing routine used in normal NMR experiments because here the desired phase shifts arising from flow are to be quantified. Consequently autophasing is clearly forbidden in dynamic imaging experiments.

3.4.4 The influence and artifact due to the 'dynamic' inhomogeneity of the sample

The velocity measurement can also be influenced by the 'dynamic' inhomogeneity of the sample. This 'dynamic' inhomogeneity refers to the velocity variation within one pixel as well as within the entire flow field. The velocity variation within one pixel will result in an error in velocity measurement, while the 'pixel-averaged' velocity variation within the entire flow field will result in an uneven signal-to-noise ratio improvement across the velocity image.

In imaging experiments all nuclear spins within one voxel are treated as 'isochromats' and the differences among these spins are not detectable. This assumption is generally valid in static imaging experiments, but its validity could become much less for a sample in which the molecules are moving at different flow

rates. In this sample, for a given pixel with a finite size, the signal contributed to that pixel arises from spins with different flow rates or even stationary. Consider a situation where the moving spins occupy A_v area of a pixel and the rest of the pixel area, A_s, is occupied by the stationary spins. The sum of A_v and A_s gives the total pixel size. Using Eq[3.19], the signal for that pixel is given by

$$S(q,\mathbf{r},\Delta) = A_s\exp(-4\pi^2q^2D_s\Delta) + A_v\exp(-4\pi^2q^2D_v\Delta)\exp(i2\pi qv\Delta) \qquad [3.32]$$

where D_s and D_v are the diffusions for the stationary and moving spins respectively. The Fourier transform of the above equation is therefore

$$F[S(q,\mathbf{r},\Delta)] = A_s[4\pi D_s\Delta]^{-1/2}\exp[-\frac{Z^2}{4D_s\Delta}] \otimes \delta(0) + A_v[4\pi D_v\Delta]^{-1/2}\exp[-\frac{Z^2}{4D_v\Delta}] \otimes \delta(Z - v\Delta) \qquad [3.33]$$

Eq[3.33] states that in the situation where both stationary spins and moving spins are present, the resultant dynamic displacement profile, P_s, is just a superposition of two Gaussians, one representing the stationary spins and which is centred at zero and the other representing the moving spins and which is centred at $v\Delta$. The final velocity is between the zero and $v\Delta$ depending upon A_s, A_v, D_s and D_v.

Computer simulations have been carried out for the case where D_s and D_v are assigned to be equal. The result is shown in Figure 3.10. The linear relationship implies that one can obtain the true velocity by simply scaling the apparent velocity using the knowledge of $A_v/(A_v+A_s)$, where (A_v+A_s) is just the total pixel size. It can also be shown that if there is a velocity distribution among spins within a pixel, the experimental velocity for that pixel is just an average.

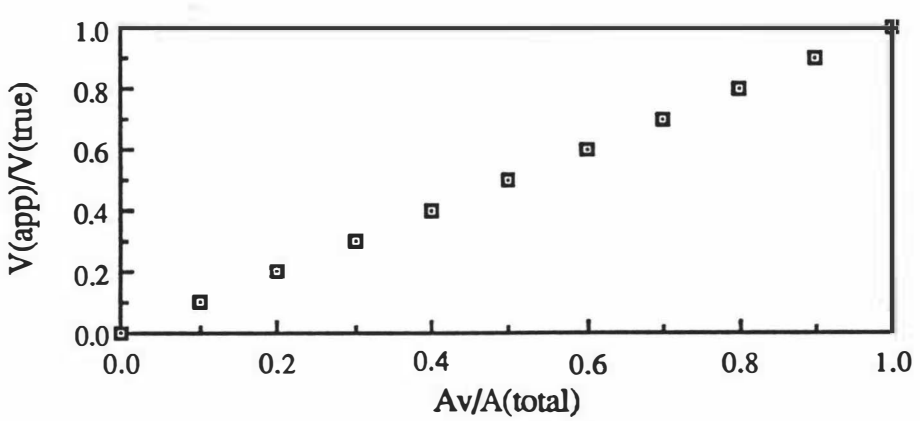

Figure 3.10 Simulation of the artifact due to the 'dynamic' inhomogeneity of the sample

However, the real situation may be more complicated than this linear relationship, because D_S and D_V could be different for different structures of the sample due to the restricted geometries. This has to be addressed for each individual case where Eq[3.33] can be used to simulate the relationship.

Apart from averaging velocities within one pixel, the sample containing moving molecules would have an interesting impact on the S/N as well. This is because although the selected slice could move only a short distance within the rf coil during the period of the spin echo, it could move a great deal further during the repetition time, T_R, which is normally allowed for spin-lattice recovery. This means that successive acquisitions are replenished with fresh fluid whose spins have the full equilibrium magnetization, an effect which permits T_R to be considerably shorter than T_1 (the 'time of flight' effect). The impact of this effect is directly proportional to 'pixel-averaged' local velocities. In the capillary flow case, the signal gain due to this replenishment is the greatest at the centre of the tube and nothing for the slowly moving fluid elements close to the wall. This would lead to a S/N improvement proportional to this effect.

3.5 Precision and accuracy of the diffusion map obtained in Dynamic NMR Microscopy

The computation of self-diffusion coefficients using the FWHM of the dynamic displacement profile depends on the assumption of the profile being an ideal Gaussian. Compared with the precision and accuracy of the velocity measurement in Dynamic NMR Microscopy, the diffusion measurement, which relies on phase spreading, is inherently much more susceptible to various artifacts. There are standard problems in conventional PGSE NMR which enhance the apparent diffusion rate by inducing phase incoherence. These include sample container movement, spectrometer rf or polarizing field instabilities and imperfect gradient pulse matching due to induced eddy current and/or to noise and ripple in the gradient power supply. In this section only those additional effects peculiar to dynamic imaging are considered.

Generally the digital width of the dynamic displacement profile, k_{FWHM}, can be considered as arising from a combination of the true diffusion width, k_{true}, and other errors and artifacts as

$$k_{FWHM} = k_{true} + k_S + k_Z + k_{V_S} + k_{tr} + k_{non} + k_T \qquad [3.34]$$

where k_S is the artifact due to the instrumental system and software, k_Z the artifact due to the zero-filling and signal truncation, k_{V_S} the artifact due to the velocity shear, k_{tr} the artifact due to the transverse diffusion and velocity, k_{non} the artifact due to the non-uniformity of the PGSE gradient and k_T the artifact due to the temperature gradient in the sample.

3.5.1 The influence of instrumental system errors in calculations

There are several possible sources which lead to extra broadening in Fourier domain. The first is due to the method of calculating the FWHM used in the software. There are different cases (refer to the procedure 'searching' in Appendix A3 for details) where one side or both sides of pixel amplitudes are not exactly equal to the half peak value (which would be true most of the time) and the FWHM given by the computer could be larger than the real FWHM by between zero and one digit in our software. No simple method can remove this error source completely, but by increasing the Fourier transform digit array size (say from 256 to 1024), one can reduce the percentage effect of this error at a price of longer computation time.

The second possible error which could affect the accuracy of the measurement is the presence of a finite base line in the dynamic displacement profile in the Fourier domain. This base value could be caused by noise and/or spikes in the time domain due to external interference during an experiment. A finite base line can also be introduced[132] by not halving the pixel amplitude at the time origin before Fourier transformation of the asymmetrical q-space data. In our experiments a correction procedure has been incorporated in the computer program to compensate this finite base line problem.

The precision of the diffusion measurement can be affected by the 'quantization' of the finite digital values in calculation. For example, for a given set of experimental parameters (g=0.936T/m, δ=2ms and Δ=5ms), diffusion values in the range of free water are listed in the following table.

Table 3.4 Digital 'quantization' effect of diffusion calculation

256 array		1024 array	
k_{FWHM}	D (10^{-9} m^2s^{-1})	k_{FWHM}	D (10^{-9} m^2s^{-1})
...		...	
12	1.80	...	
		49	1.88
		50	1.96
		51	2.04
13	2.12	52	2.12
		53	2.20
		54	2.28
		55	2.37
14	2.45	56	2.46
		57	2.54
		58	2.63
		59	2.73
15	2.82	60	2.82
...			

It can be seen that the diffusion values have been 'quantized', an effect which is enhanced by the squaring operation on finite digits. In our -128 to 127 scale, the 'step' size for such quantization is about $(0.3\sim0.4)\times10^{-9}$ m^2s^{-1}! It is obvious that this diffusion 'resolution' can be improved by using a bigger digital array during the transformation.

As discussed for the velocity imaging case, the precise measurement of the diffusion is also influenced by the initial phase offset and the presence of experimental noise. Compared with its influence on the velocity imaging, the initial phase offset has much smaller impact on the diffusion map. Figure 3.11 has shown the central slices through four diffusion maps constructed from the simulated Brownian motion data sets in which the phase offsets in the 18 imaginary data images are 26.6°, 5.7°, 0° and -5.7° respectively. The ±5.7° phase offsets have no effect on the final diffusion maps. The influence of 10% experimental noise on images is simulated in a similar manner as before, a slice through the centre of the diffusion map is shown in Figure 3.12a while Figure 3.12b shows the histogram of this diffusion image together with that of the noise-free case in Figure 3.12c. The arithmetic average of all the pixels over this diffusion image is 22.54 digit, the average of 95% of the most frequent values is 22.72 digit and these digits are distributed between 21 to 25 digits (23 is the noise-free case).

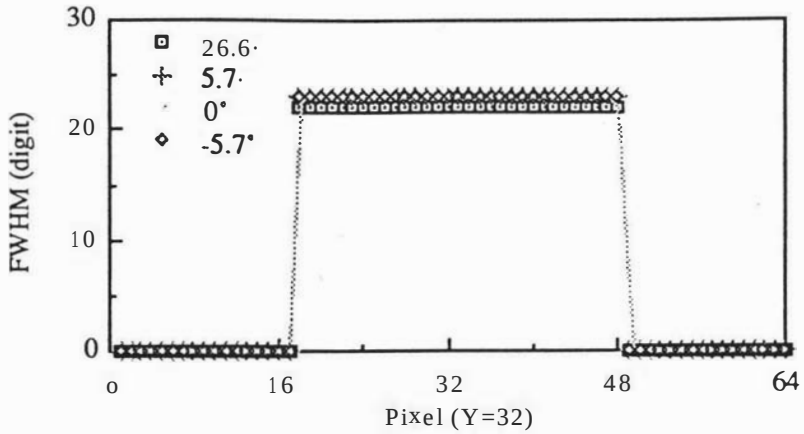

Figure 3.11 Cross s e tonal pro fles through the noise-affected diffusion images

(a) A slice through the noise-affected diffusion image

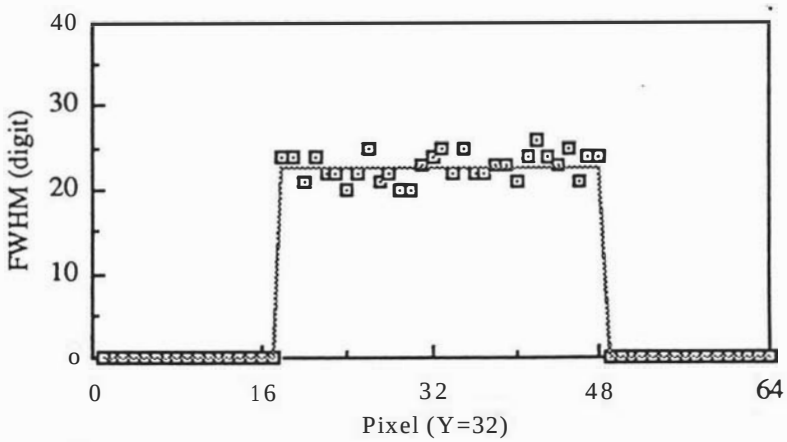

(b) Histogram of the noise-affected diffusion image

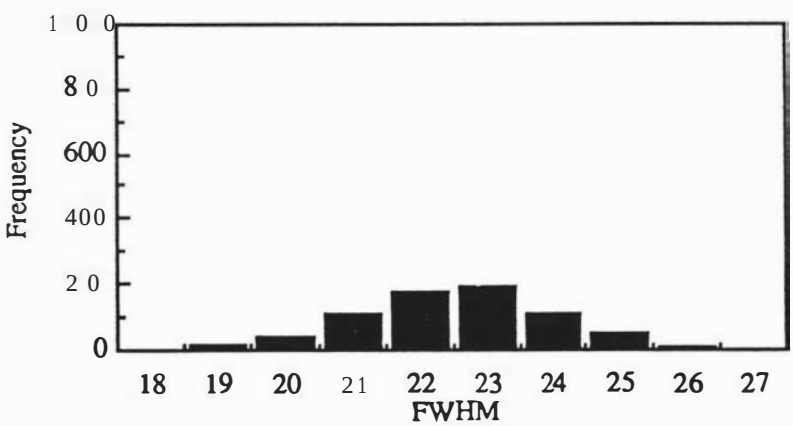

(c) Histogram of the noise-free di fusion image

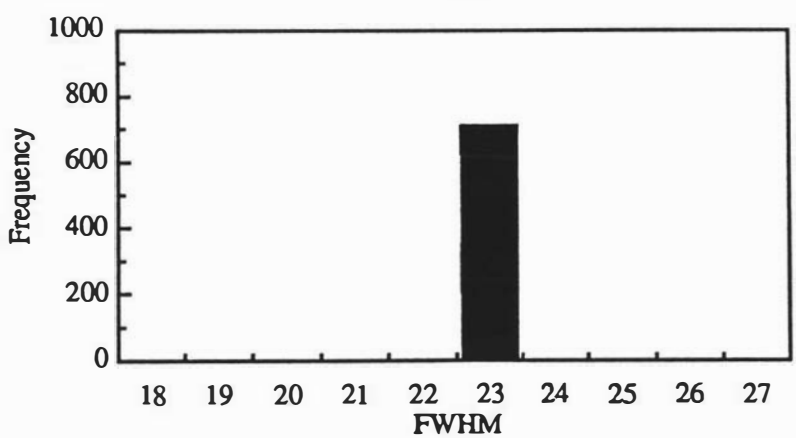

Figure 3.12 The influence of experimental noise on diffusion images

In summary, for a well designed experiment, the maximum system error, k_S, which affects the accuracy of the diffusion measurement is about +1 digit. The uncertainty of this measurement, however, is dependent upon the digital array size in transformation and the presence of actual experimental noise. The uncertainty due to the digital array size is about $\pm 0.2\times10^{-9}$ m^2s^{-1} for free water if a 256 array is used.

3.5.2 Digital broadening due to zero-filling and signal truncation

In dynamic imaging experiments, zero-filling is used to improve the accuracy of the final results (the use of zero-filling in q space is equivalent to data interpolation in Z space). Because zero-filling corresponds to the multiplication of the q-domain signal by a step function, sinc convolution is unavoidably introduced in Z space and extra broadening will result as illustrated in Figure 3.13a.

This effect is not important if P_S is sufficiently broader than the sinc function, a condition equivalent to requiring that the signal amplitude has significantly decayed at the maximum gradient value g_m corresponding to the last data point n_D before the onset of zero-filling. In our experiments, the parameters g, δ and Δ are chosen so that the signal is completely attenuated at the last q slice. Figure 3.13b shows the results obtained in a simulation of this effect for zero-filling from an n_D value of 18 to N=256. It is clear that the artifact due to zero-filling, k_Z, is small for k_{FWHM} values above 10 and therefore it could be neglected comparing with other errors in the measurement.

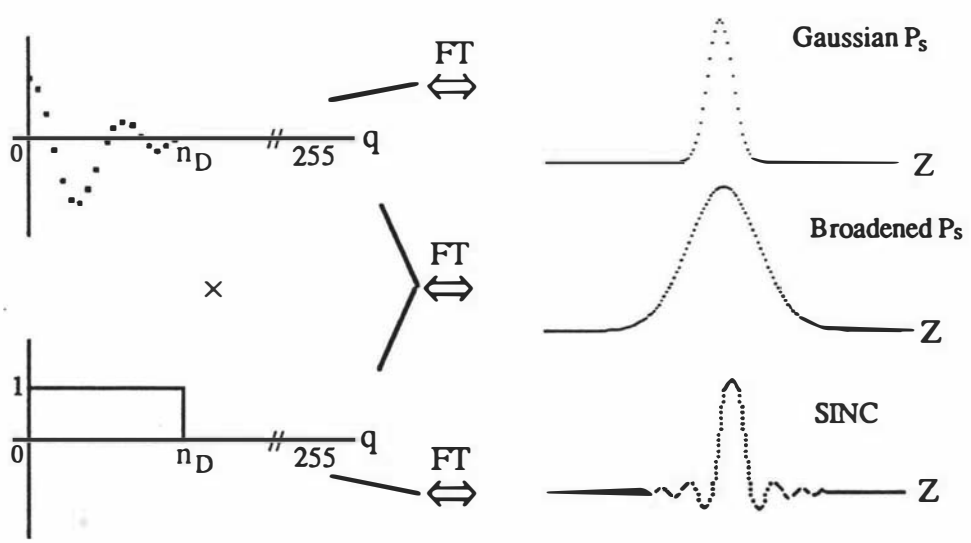

Figure 3.13a Zero-filling in q space results in a broadened P_S due to the SINC modulation

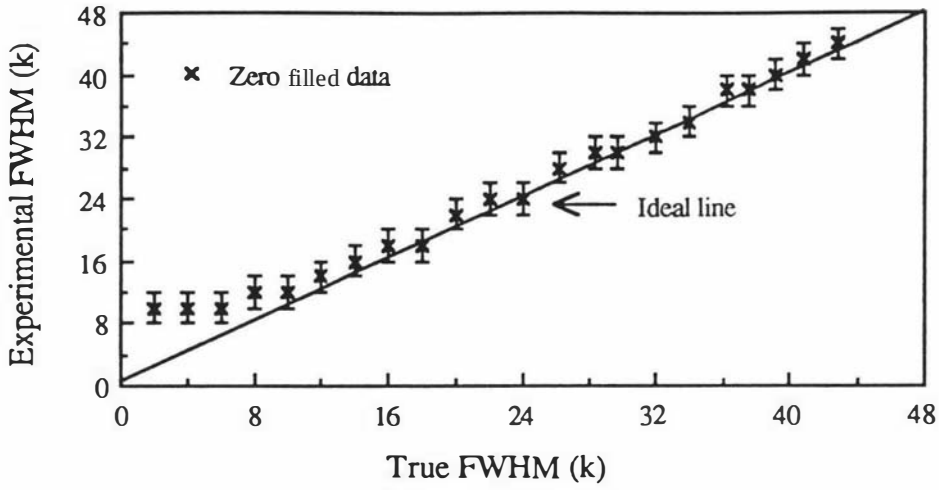

Figure 3.13b Simulation of the extra broadening due to the zero-filling of P_s

3.5.3 Systematic errors in diffusion coefficients measured in the presence of a velocity shear

In the calculation of self-diffusion coefficients, it is assumed that the broadening arises only from Brownian motion. In many experiments however, such as the capillary flow examples, a local velocity shear exists. Thus a range of velocities is represented within a single pixel, thereby additionally broadening the dynamic displacement profile. Figure 3.14 shows three possible cases. In Figure 3.14a there is no translational motion of the molecules so that the spread in distances moved (i.e., the broadening) during the detection time Δ is simply due to the self diffusion and given by $(2D\Delta)^{1/2}$. In Figure 3.14b there is a translational motion of the molecules but no velocity shear, so the broadening is still $(2D\Delta)^{1/2}$. In Figure 3.14c, however, a velocity shear exists within a single pixel therefore the broadening becomes of order $(2D\Delta)^{1/2} + \Delta v_s\Delta$, where Δv_s is the maximum velocity spread within that pixel. It is obvious that the criteria for the precise measurement of self-diffusion is given by

$$\Delta v_s\Delta/(2D\Delta)^{1/2} << 1 \qquad [3.35a]$$

or

$$\Delta v_s << (D/\Delta)^{1/2} \qquad [3.35b]$$

For free water with a Δ equal to 5 ms, the right hand side of the Eq[3.35b] is about 0.7 mm/s. This inequality is usually valid in our experiments of water flow in the capillaries. However, experiments where very slow self-diffusion is to be measured in

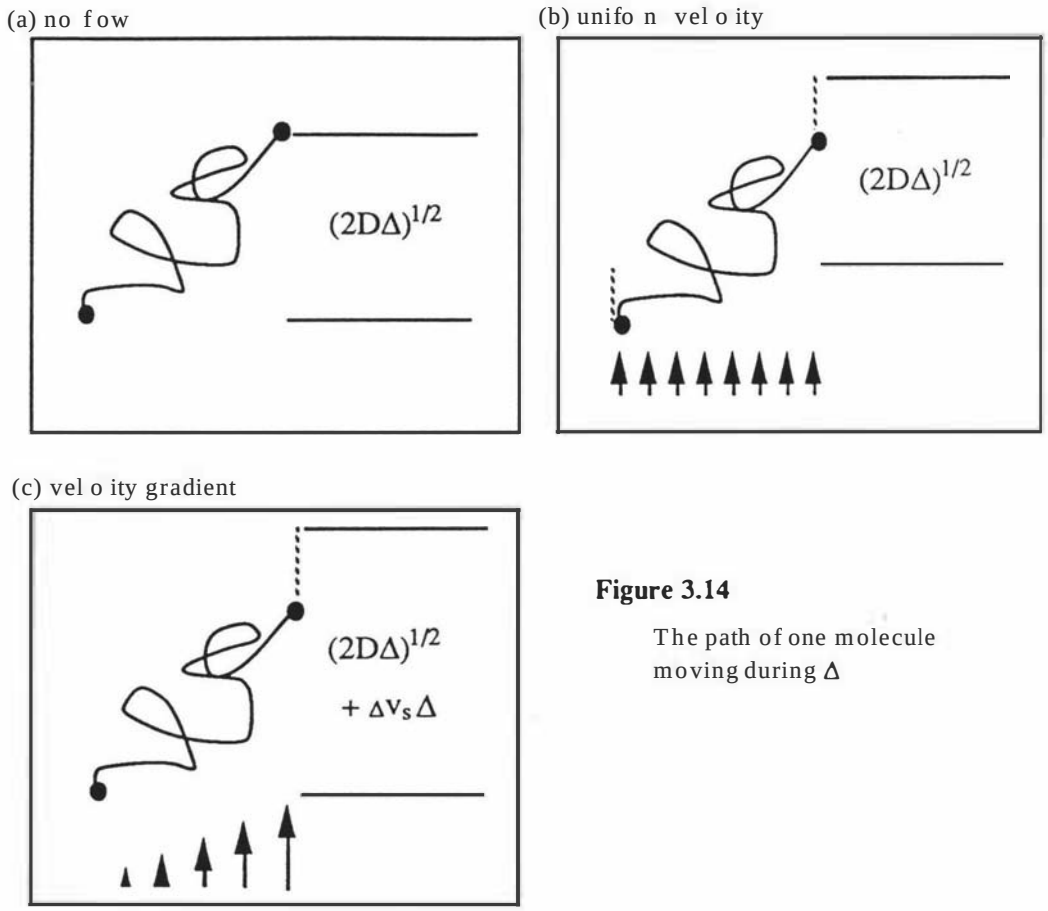

Figure 3.14

The path of one molecule moving during Δ

high shear will also be concerned with in this thesis, where this inequality does not apply (Ch 9). This corresponds to the case shown in Figure 3.14c which involves a spatial conformational change of macromolecules.

Strictly speaking, a finite-width pixel in the image is represented by an infinitesimally wide region of the frequency space, provided any fundamental line broadening in the frequency domain is neglected. In precisely the same manner the initial sampling points are infinitesimally wide in **q**. Ideally therefore there can be no shear within a pixel. In practice however a number of effects may broaden the dynamic displacement profile. These include apodization and relaxation broadening, and the effect of interpolation when the PR reconstruction is the choice of imaging algorithm. In the flow experiments where the Z direction coincides with the shear axis, such broadening effects would lead to a distribution in phases within the pixel, which will emulate the effect of diffusion in the direction of the velocity and so lead to a systematic error in the measurement of D.

An alternative approach to analyze the influence of the velocity shear can be carried out using Eq[3.25], where a velocity spread, Δv_S, in adjacent pixels in a flow field can be calculated numerically as

$$k_{Vs} = \frac{Ng\gamma\delta\Delta}{2\pi n_D} \Delta v_S \qquad [3.36]$$

Substituting the above equation into Eq[3.28], the extra self-diffusion due to this velocity spread can be calculated as

$$\Delta D = 0.09(\Delta v_S)^2\Delta \qquad [3.37]$$

It is worth noting that the phase spreads associated with steady state velocity shear and Brownian motion are fundamentally different in the sense that the former is coherent and hence intrinsically reversible. A method for compensating these phase shifts has been discussed in Ch 3.3.3, the velocity-compensated Dynamic NMR Microscopy.

3.5.4 The influence of transverse velocity and diffusion

The usual assumption of the steady state condition in imaging becomes much more critical in the dynamic NMR imaging. Echo refocusing requires phase coherence at molecular level, therefore the velocity distribution in each pixel element of the image is required to remain constant over the time scale of an imaging experiment, as well as the mean velocity of each molecule to remain constant over the time of the detection. Where transverse self-diffusion occurs in the presence of a velocity shear, some lateral migration, and hence velocity variation, is inevitable. This incoherent phase loss will cause a slight enhancement of the apparent self-diffusion coefficient in experiments.

For simplicity the time-scale for migration can be set as Δ. The rms phase shift due to lateral migration between the first and second PGSE pulses may be simply obtained by noting that the rms distance moved laterally is $(2D\Delta)^{1/2}$. In consequence the rms phase shift in the longitudinal direction due to the transverse diffusion under a velocity shear, $\frac{\partial v}{\partial r}$, is given by

$$\langle\phi_{tr}^2\rangle^{1/2} \sim 2\pi q\Delta\frac{\partial v}{\partial r}(2D_\perp\Delta)^{1/2} \qquad [3.38]$$

By comparison the rms phase shift associated with the longitudinal diffusion is given by

$$\langle\phi_{true}^2\rangle^{1/2} \sim 2\pi q(D_{\parallel}\Delta)^{1/2} \qquad [3.39]$$

The apparent phase shift can therefore be derived as

$$\langle\phi^2\rangle^{1/2} \sim [\,\langle\phi_{true}^2\rangle + \langle\phi_{tr}^2\rangle\,]^{1/2}$$

$$\sim \langle\phi_{true}^2\rangle^{1/2}[1+\frac{\langle\phi_{tr}^2\rangle}{\langle\phi_{true}^2\rangle}]^{1/2}$$

$$\sim \langle\phi_{true}^2\rangle^{1/2}[1+\Delta^2(\frac{\partial v}{\partial r})^2\frac{D_{\perp}}{D_{\parallel}}]^{1/2} \qquad [3.40]$$

Eq[3.40] shows that under the normal isotropic case, where $D_{\perp} \sim D_{\parallel}$, and with a typical value of Δ in the range 5 ms to 100 ms, accurate measurement of self-diffusion can be achieved if the shear rate is restricted to below 200 s^{-1}.

The above analysis has assumed that there is no transverse velocity component in the flow field. The existence of the transverse velocity could greatly enhance the apparent self-diffusion by causing the imperfectly refocused echo. In our capillary flow experiments, the flow of the sample is driven by a small gravitational pressure head difference. If the sample tube is not positioned perfectly vertically, some transverse velocities do occur. This small transverse velocity component could have some impact on the accurate diffusion measurement at the microscopic resolution. For example, at 20 μm pixel resolution, a 5° misalignment could give a transverse component of 0.5 mm/s if the vertical velocity is 6 mm/s. For a detection time of 5 ms, the lateral spin migration is about 2.5 μm, which means that 13% of the spins exchange their positions between the adjacent pixels.

Another source of transverse motion arises from the effect of tiny air bubbles, formed by the dissolved air in water. These bubbles tend to adhere with the wall of the capillary thus causing some local turbulence near the wall. The transverse velocity due to these tube position and air bubbles will enhance the self-diffusion. In Ch 8 the influence of the transverse velocity on the diffusion map due to a sample tube which exhibits a sudden change in diameters is demonstrated.

3.5.5 The Influence of PGSE gradient non-uniformity

In measurements of dynamic displacements using PGSE sequences, it is required that the migration distance should be small compared with the dimensions of the gradient uniformity region. In most microscopy applications the gradient uniformity boundary is defined by the ±0.4% contour since this corresponds to a 1 pixel distortion for a 256^2 image. Generally the 0.4% gradient contour along the sample axis will be located inside the rf coil. For example, the 2.1 mm diameter solenoidal rf coil used in our capillary flow experiments has a length of 6 mm while the distance between the 0.4% contours is 2.5 mm. Therefore the effects of migration outside the sensitive region of the rf coil could be neglected and the attention can be focussed on the effects of first order variations in the gradient.

It is the variation in magnetic field gradient along the direction of the steady-state velocity which will concern us. In most situations this will correspond to the solenoidal rf coil axis and also the axis normal to the slice plane. Here z is reserved for this direction although it is important to note that this need not necessarily correspond with the direction of the polarizing field. It is convenient to describe the field variation along the z axis in terms of a Taylor expansion,

$$B_0(z) = B_0(0) + z\frac{\partial B_0}{\partial z} + \frac{1}{2}z^2\frac{\partial^2 B_0}{\partial z^2} + \ldots \qquad [3.41]$$

For an ideal PGSE gradient coil system, $B_0(0)$ and all the high order terms are zero while the first order derivative is the desired gradient, g. In this analysis, however, the effect of $\partial^2 B_0/\partial z^2$ being non-zero is allowed for while the constant term is irrelevant in the present context.

Consider the behaviour of a slice of finite thickness along the z axis. Even though one may be concerned only with a single pixel of the image, the effect of the second order term in z may be significant because this pixel may be extended along the z axis. The situation is further complicated when net motion along the z axis is included. Thus it is necessary to quantify these effects and set limits on the allowed gradient non-linearity.

In our analysis[113] the attention is focussed on a pixel at (static) position r (=[x,y,z]) in the image with slice thickness $2z_0$ in which the local velocity in the z-direction is v and the local self-diffusion coefficient is D. As defined in Ch 3.2, the

vector **R** with components [X,Y,Z] is used as the dynamic displacement. It is assumed that the sample density along the pixel slice is uniform and given by $1/2z_0$. Consider an element of the slice between z and z+dz. At the first gradient pulse Z = z'-z is zero while at the second Z = z'-z is non zero. The phase shift following the second gradient pulse is therefore given by

$$\phi = i\gamma\delta g[(z+Z) - z] + i\gamma\delta(\frac{1}{2}\frac{\partial^2 B_0}{\partial z^2})[(z+Z)^2 - z^2] \qquad [3.42]$$

Consequently the pixel contrast factor may be rewritten as

$$E(q,\mathbf{r},\Delta) = \int_{-z_0}^{z_0} [\frac{1}{2z_0} dE(q,\mathbf{r},\Delta)]\, dz \qquad [3.43]$$

where $dE(q,\mathbf{r},\Delta)$ is the contrast factor for an element of the slice between z and z+dz and is given by

$$dE(q,\mathbf{r},\Delta) = \int_{-\infty}^{\infty} \exp[i2\pi qZ + i2\pi q\chi(Z^2+2zZ)/2z_0]\, P_s(Z,\Delta)\, dZ \qquad [3.44]$$

where $\chi = (\partial^2 B_0/\partial z^2)(z_0/g)$ [3.45]

In the above derivation it has been assumed that the superposed diffusion and flow are governed by the function $P_s(Z,\Delta)$, as given by Eq[3.8] previously. The ratio χ is a useful measure of the deviation from linearity of the PGSE gradient over the slice thickness. In general $\chi << 1$.

The conditional probability for the spin to move to z' is $P(Z,\Delta)$, a Gaussian in Z, convoluted with a delta function centred at $Z=v\Delta$. It is convenient to make the substitution $\zeta = Z - v\Delta$, where ζ represents the distance moved due to diffusion alone and in most experiments is very much smaller than the slice thickness. In changing coordinate frames $P(Z,\Delta)$ becomes $P(\zeta + v\Delta,\Delta)$, a Gaussian in ζ centred at $\zeta=0$. Making this substitution, Eq[3.44] becomes

$$dE(q,\mathbf{r},\Delta) = \exp[i2\pi qv\Delta(1+\chi(v\Delta+2z)/2z_0)] \times \int_{-\infty}^{\infty} \exp[i2\pi q\zeta(1+\chi(v\Delta+z)/z_0)]\exp[i2\pi q\chi\zeta^2/2z_0]P(\zeta+v\Delta,\Delta)\, d\zeta \qquad [3.46]$$

This expression can be further simplified by noting that $P(\zeta+v\Delta,\Delta)$ is small for $\zeta^2>2D\Delta$. This means in effect that, except for a small part of the slice with thickness of order $(2D\Delta)^{1/2}$, $\zeta << 2(v\Delta + z)$ in Eq[3.46], and one can neglect the non-linear phase shift represented by the last oscillatory term in the integrand. Since this thickness is a small fraction of the slice the simplification is reasonable. Upon integration over the slice, this approximation yields

$$E(q,\mathbf{r},\Delta) = \exp[i2\pi q_1 v\Delta]\exp[-4\pi^2 q_2^2 D\Delta]\times \int_{-z_0}^{z_{01}} \frac{}{z_0} \exp[i2\pi q\chi\, v\Delta\, z/z_0 - 4\pi^2 q^2 2\chi D\Delta\, z/z_0]\, dz$$

$$= \exp[i2\pi q_1 v\Delta]\exp[-4\pi^2 q_2^2 D\Delta]\,[e^{\alpha} - e^{-\alpha}]/2\alpha \qquad [3.47]$$

where $q_1 = q(1+\frac{1}{2}\chi v\Delta/z_0)$ [3.48a]

$$q_2^2 = q^2(1 + 2\,\chi v\Delta/z_0) \qquad [3.48b]$$

$$\alpha = -2\lambda\chi + i\phi\chi \qquad [3.48c]$$

and ϕ and λ are the usual phase shift and attenuation factors, given by

$$\phi = 2\pi q v\Delta \qquad [3.49a]$$

and $$\lambda = 4\pi^2 q^2 D\Delta \qquad [3.49b]$$

Eq[3.47] states that, apart from the last term involving α, the effective velocity and diffusion values are perturbed only by a shift of order $\chi v\Delta/z_0$. Since $v\Delta/z_0$ is less than or of order unity, this shift can be neglected provided $\chi << 1$. Under the same condition, the phase and amplitude effects associated with α are small compared with the leading terms $\exp[i2\pi q v\Delta]$ and $\exp[-4\pi^2 q^2 D\Delta]$.

In contrast with the shift, $\chi v\Delta/z_0$, the coefficients of χ in α are larger than unity. In a typical experiment for the maximum gradient employed at $n_D = 20$, $\lambda \leq 3$ while $\phi \leq 30$ if the Nyquist sampling condition is to be obeyed. Clearly both the real and imaginary terms in α are less than unity provided $\chi < 0.01$. Given this reasonable constraint, the effect of the last term in Eq[3.47] can be assessed by expanding it to the fourth order in a power series. Hence one obtains

$$E(q,\mathbf{r},\Delta) = \exp[i\phi(1+\tfrac{1}{2}\chi v\Delta/z_0)]\exp[-\lambda(1 + 2\,\chi v\Delta/z_0)]\times [\,1 + \tfrac{1}{6}(4\lambda^2 - \phi^2)\chi^2 - i\tfrac{4}{3}\lambda\phi\chi^2] \qquad [3.50]$$

Under normal conditions, the last amplitude term represents a small additional attenuation, except in the case that the velocity is very small and $(4\lambda^2 - \phi^2) > 0$. For v=0, the condition for the neglect of gradient non-uniformity is given by $\lambda\chi << 1$. For high velocity experiments the additional phase shift is of order $\lambda\phi\chi^2$ while the attenuation is of order 1- $\phi^2\chi^2$. This additional attenuation of the signal arising from gradient non-uniformity will lead to an increase in the apparent diffusion coefficient. Unlike the systematic error which depends on shear rate, this shift will depend on the squared magnitude of the velocity through the ϕ^2 term. The effective exponent $(1/6)\phi^2\chi^2$ leads to an increase in the diffusion coefficient by a factor

$$D_{eff}/D = (1+ 0.7\chi^2v^2\Delta/D) \qquad [3.51]$$

It is clear however that both the amplitude and phase factors can, in effect, be neglected in practice provided $\chi << 0.01$. This condition is precisely satisfied provided that the initial slice is stimulated well within the ±0.4% gradient contours.

The above analysis shows that there are no special problems associated with gradient non-uniformity in diffusion/flow experiments provided that reasonable precautions are taken regarding the slice thickness.

The Influence of PGSE gradient non-uniformity in the velocity-compensated Dynamic NMR Microscopy

In Ch 3.3.3, the velocity-compensated Dynamic NMR Microscopy has been introduced as a variant of the technique which is able to measure self-diffusion accurately at the presence of high velocity shear. In this velocity-compensated variant, very large phase excursions, $i2\pi\mathbf{q}.\mathbf{R}$, may be possible in each PGSE sequence although the final result is a velocity null. This means that the conditions of the Nyquist theorem no longer provide a restriction on ϕ and it is possible to generate phase shifts greatly in excess of χ^{-1}. Therefore the effect of gradient non-uniformity must be reconsidered.

Following the same analysis as used in considering the single-pair PGSE sequence, one obtains the echo signal as[113]

$$E(q,\mathbf{r},\Delta) = \exp[i2\pi qv\Delta\chi(v\Delta+v\tau)/z_0] \exp[-4\pi^2q_3^2D(2\Delta)] [e^{\alpha} - e^{-\alpha}]/2\alpha \qquad [3.52]$$

where $q_3^2 = q^2(1+2\chi(v\Delta+v\tau)/z_0)$ [3.53a]

and $\alpha = 4\pi^2 q^2 D(2\Delta)\ 2\chi$ [3.53b]

or $\alpha = 4\lambda\chi$ [3.53c]

where λ has been defined as $4\pi^2 q^2 D\Delta$ in Eq[3.49].

The first term in Eq[3.52] represents a residual phase shift of order $(\chi v\Delta/z_0)\phi$, where it has assumed that $\tau << \Delta$ and ϕ is the 'normal' phase shift associated with each pair of gradient, equal to $2\pi qv\Delta$. The second term indicates that the apparent diffusion coefficient is enhanced by a factor $[1+2\chi(v\Delta+v\tau)/z_0]$. It is worth noting that the attenuation exponent in the double PGSE sequence experiment is now doubled in comparison with that defined by Eq[3.48]. The factor $[e^{\alpha} - e^{-\alpha}]/2\alpha$ represents the dominant artifact and, to the fourth order, is equivalent to a multiplicative factor $(1 + \frac{1}{6}(2\lambda)^2\chi^2)$. This is similar to the artifact in the single PGSE sequence experiment but without the terms involving the phase shift ϕ. Again the effect may be neglected provided $\chi < 0.01$.

It is clear that in the measurement of self-diffusion, the double PGSE imaging experiment is no more sensitive to artifacts associated with gradient non-uniformity than the single PGSE imaging sequence. However such non-uniformity can cause a residual phase shift following the double PGSE sequence with a size given in Eq[3.52]. Since $v\Delta$ is typically an order of magnitude less than the slice thickness, $\chi v\Delta/z_0$ will be of order 10^{-3} or less provided that the excited slice lies between the ±0.4 % gradient contours. Thus the use of this velocity compensation sequence allows one to measure diffusion coefficients in the presence of large steady-state velocity fields. The artifacts associated with the high velocity and large velocity shear would be reduced by a factor of $\chi v\Delta/z_0$ in the velocity-compensated Dynamic NMR Microscopy. The remaining perturbation to the accurate measurement of self-diffusion would be due to the influence of the transverse diffusion.

3.5.6 The Influence of temperature variation in the sample

Due to its temperature dependency, the precise measurement of the self-diffusion coefficient is closely related with the knowledge of a sample's temperature. In the situation where the molecules in the sample are moving, it would be difficult to keep a constant temperature for both the sample and the probe, thus a temperature variation exists within the sample. For example, in our Poiseuille flow experiments, the probe is

situated between the magnet pole pieces which are controlled to around 30 °C while the water sample (before flowing into the probe) is at the room temperature, around 25 °C. The following text evaluates the temperature distribution inside the sample and its influence on diffusion measurement for water capillary flow experiments.

To simplify the analysis of the temperature distribution within the sample, several assumptions have to be made. The first assumption is that all the physical properties of the sample apart from D (for example, c_p, ρ, η, k) are temperature-independent. Strictly speaking, this assumption is questionable, because all these properties and especially the viscosity and the density, are temperature-dependent! However it is a useful simplification in attempting to find how the temperature varies across the capillary tube. There are two immediate consequences of this assumption regarding the fluid properties. First, the velocity profile will remain unaltered along the capillary at the fully developed region, which reaffirms the critical requirement for a steady state condition in our experiments and analysis. The second benefit is that the energy equation can be decoupled from the momentum equation, which will therefore greatly simplify the analysis.

The second assumption is that the flow in the region of interest is hydrodynamicaly fully developed, which means that the velocities are constant longitudinally. Given the fact that a long thin capillary is used in experiments, this second assumption is valid in practice.

The last assumption is that the region which is of interest is also thermally fully developed. It is assumed that the inside wall of the capillary tube has a uniform temperature in the region of the receiver coil and is transmitting a constant heat flux to the liquid. Actually the temperature of the capillary wall during the water flow is difficult to determine precisely. This is because any thermal description of the probe together with the capillary tube is very complicated due to the complex arrangement of various materials such as teflon, air, copper and pc board. Taking the worst case for analysis, it could be assumed that the capillary wall is at the same temperature as that of the magnet, namely 30 °C. Given the fact that the complete probe is situated closely within the large thermal mass of the constant temperature magnet pole pieces, this assumption is reasonable.

Using the above assumptions, the momentum equation (the Navier-Stokes equation) for a laminar tube flow in cylindrical coordinates can be written as

$$\frac{\eta}{r}\frac{d}{dr}\left(r\frac{dv}{dr}\right) = \frac{dp}{dx} \qquad [3.54]$$

where η is the dynamic viscosity of the fluid and dp/dx is the pressure drop longitudinally.

Given the boundary conditions (no-slip at the wall, $v|_{r=r_0} = 0$, and radial symmetry at the centre line, $\frac{\partial v}{\partial r}|_{r=0} = 0$), the solution for the above equation yields the classical Poiseuille velocity profile as

$$v(r) = v_{max}\left(1 - \frac{r^2}{r_0^2}\right) \qquad [3.55]$$

where r_0 is the radius of the tube and v_{max} is the maximum velocity, given by

$$v_{max} = \Delta P r_0^2/4\eta l \qquad [3.56]$$

in which ΔP is the pressure decrement over the length l of the tube, defined by the height difference Δh as

$$\Delta P = \rho g \Delta h \qquad [3.57]$$

where ρ is the density of the fluid and g is the gravitational acceleration, equals 9.8 m/s^2.

The energy equation[134, 135] for the above sample system under the same assumptions can be written as

$$\frac{\partial T}{\partial x} = \frac{k}{v\rho c_p r}\frac{\partial}{\partial r}\left(r\frac{\partial T}{\partial r}\right) \qquad [3.58]$$

where v is given by Eq[3.55], k is the thermal conductivity of the fluid, c_p is the specific heat at the constant pressure.

By noting the boundary conditions (no-temperature-jump at the wall, $T|_{r=r_0} = T_w$, and radial symmetry at the centre line, $\frac{\partial T}{\partial r}|_{r=0} = 0$) and the constant heat flux assumption ($\frac{\partial T}{\partial x}$ = constant), the solution of the above equation can be derived by twice integrating with respect to r. Hence

$$T(x,r) = T_w - \frac{v_{max} r_0^2 \rho c_p}{8k} \frac{\partial T}{\partial x} [3 - 4(\frac{r}{r_0})^2 + (\frac{r}{r_0})^4] \qquad [3.59]$$

In our example, the longitudinal temperature gradient is approximately

$$\frac{\partial T}{\partial x} \sim \frac{T_w - T_e}{x} \qquad [3.60]$$

where T_e is the entrance temperature of the fluid.

Using the above two equations and the relevant data (T_w = 303 °K, T_e = 298 °K, x = 0.03 m, ρ = 998 kg/m^3, c_p = 4190 J/kgK, k = 0.591 W/mK, v_{max} = 3×10^{-3} m/s, r_0 = 0.35×10^{-3} m), at the centre of the rf coil, the water temperature at the wall of the capillary is equal to 30 °C and the water temperature at the centre of the capillary is equal to 29.8 °C. This corresponds to an insignificant difference in the self-diffusion values.

It is worth noting that in the above analysis, the weakest assumption is the constant heat flux condition, Eq[3.60], for such a complicated thermal system. Nevertheless, comparing with other errors in the diffusion measurement, the above analysis shows that the influence of the temperature variation on the self-diffusion imaging experiments for the water sample can be ignored in our system.

3.6 Alternative data analysis methods available for Dynamic NMR Microscopy

This section discusses two alternative methods which could be used, in principle, to analyze the data obtained in Dynamic NMR Microscopy experiments.

3.6.1 Analysis of velocity and diffusion using the moment method

In the measurement of velocity and self-diffusion using Dynamic NMR Microscopy, it has been anticipated that a centre-shifted Gaussian curve would be returned by the FT of q-space data, and therefore the peak centre and peak width are

used to calculate the velocity and the self-diffusion coefficient respectively. In imaging experiments, however, background noise is inevitable and will influence the shape of the dynamic displacement profile. Thus it will introduce errors into the velocity measurement. In the conventional NMR studies it is known that the peak position and width of a spectral peak can be determined using the moment method[1]. The following text discusses how the moment method might be used as an alternative data analysis method in dynamic imaging.

A Gaussian function, A(x), is given by

$$A(x) = k \exp[-\alpha^2(x-x_0)^2] \qquad [3.61]$$

Its peak is centred at x_0, k and α are two constants representing the amplitude and the attenuation respectively. The width of this Gaussian curve is given by

$$FWHM = \frac{2(\ln 2)^{1/2}}{\alpha} \qquad [3.62]$$

The zeroth, first and second moments of A(x) are given respectively by

$$M_0 = \int_{-\infty}^{+\infty} A(x)dx \qquad [3.63]$$

$$M_1 = \int_{-\infty}^{+\infty} xA(x)dx \qquad [3.64]$$

and

$$M_2 = \int_{-\infty}^{+\infty} x^2A(x)dx \qquad [3.65]$$

By substituting Eq[3.61] into the above three equations, these three moments can be easily derived, as

$$M_0 = \frac{k}{\alpha}(\pi)^{1/2} \qquad [3.66]$$

$$M_1 = \frac{kx_0}{\alpha}(\pi)^{1/2} \qquad [3.67]$$

and $$M_2 = \frac{k}{\alpha}(\pi)^{1/2}(x_0^2 + \frac{1}{2\alpha^2}) \qquad [3.68]$$

The first and second moments can be normalized to the zeroth moment, as

$$M_1^* = M_1/M_0 = x_0 \qquad [3.69]$$

and $$M_2^* = M_2/M_0 = x_0^2 + \frac{1}{2\alpha^2} \qquad [3.70]$$

Eq[3.69] can be instantly recognized as the peak centre of the Gaussian curve. The width of the curve can be derived using the above results, as

$$FWHM = [8\ln 2(M_2^* - M_1^{*2})]^{1/2} \qquad [3.71]$$

Therefore the velocity and self-diffusion are well defined by Eq[3.69] and Eq[3.71]. It seems that the moment method should give more accurate results than the rather simple 'peak offset' algorithm currently employed in Dynamic NMR Microscopy, because the moment method considers the influence of all pixels in the profile and should be able to remove the velocity error due to the random phase distortion.

However, the application of this method in the computer has shown a contrary result: the moment method is far more sensitive to the presence of experimental noise, and is therefore almost useless in practical situations. To test this algorithm, two sets of 18 complex pairs of data images have been generated to simulate the Poiseuille flow experiment using Eq[3.19]. One set data is generated 'noise-free' and the other set is generated using the identical signal but in the presence of random noise with maximum amplitude about 10% of the maximum signal amplitude (this ratio is similar to the practical experimental situation of 'good' signal-to-noise ratio!). Figure 3.15a and 15b show the cross sectional profiles through the centres of velocity and diffusion images reconstructed using both methods on the 'noise-free' data set. It is clear that both methods are equally capable of reconstructing the velocity and diffusion images. In fact the moment method is slightly better than the 'peak-offset' method in the diffusion calculation because it returns a uniform diffusion digit. However, when used the noisy data, the situation changes as shown in Figure 3.15c and Figure 3.15d. The profiles using the simple 'peak offset' method are still remarkably accurate (subject only to small random fluctuations due to the noise) but those using the moment method are severely perturbed.

(a) Velocity profiles through the noise-free images

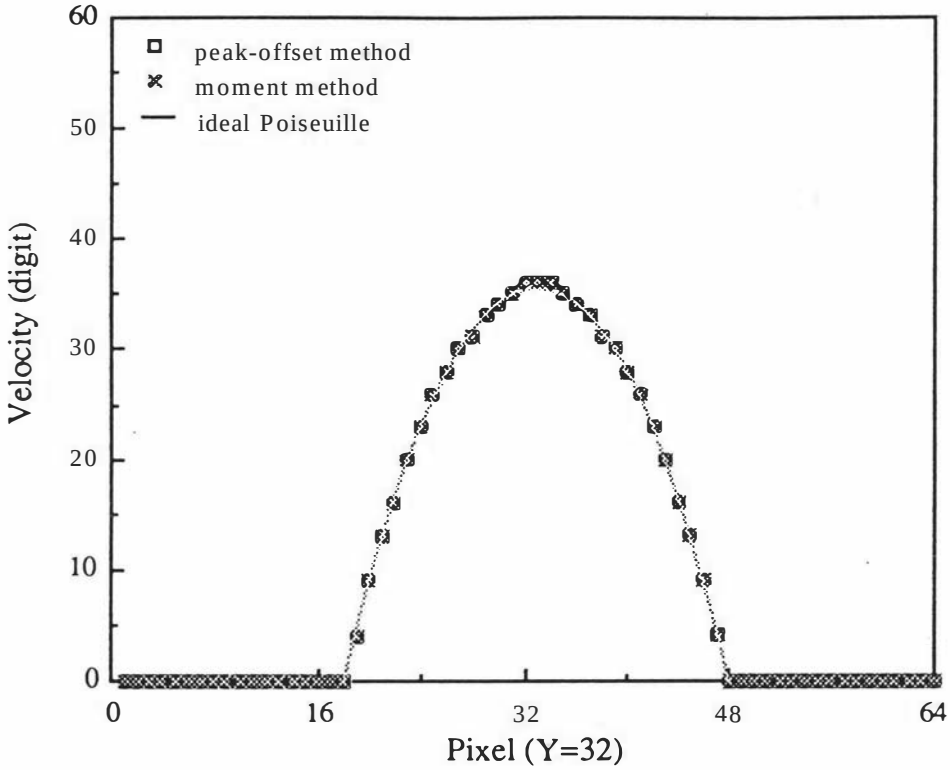

(b) Diffusion profiles through the noise-free images

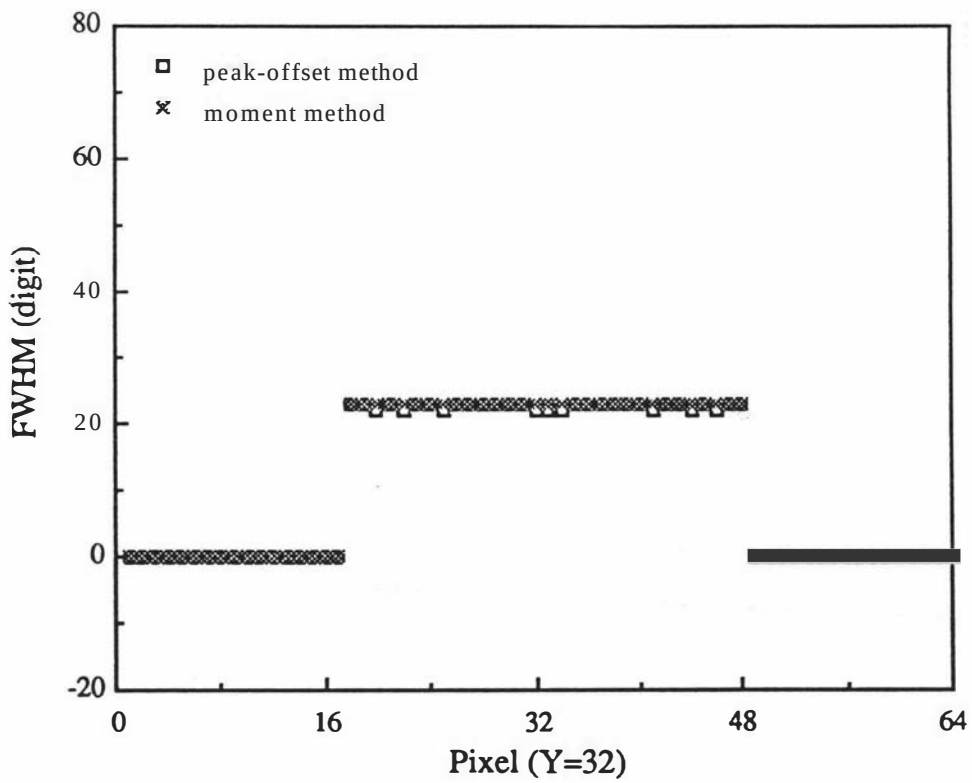

Figure 3.15 Simulation results comparing the peak-offset method and the moment method

(c) Vel o ity profiles through the noi s -affected images

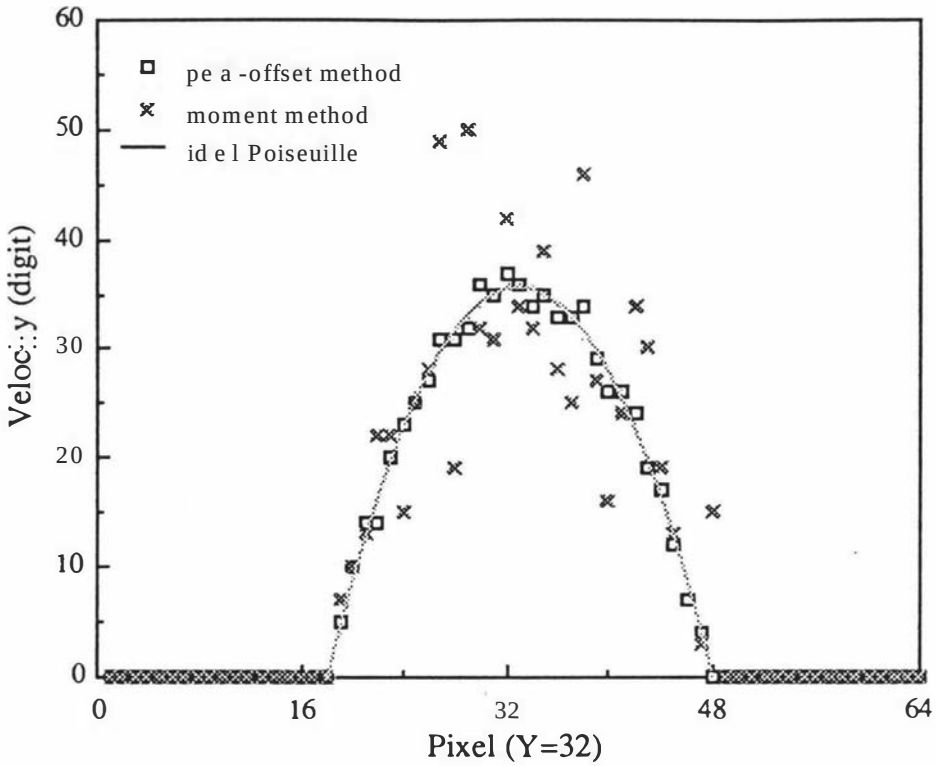

(d) Diffusion profiles through the noise-affected images

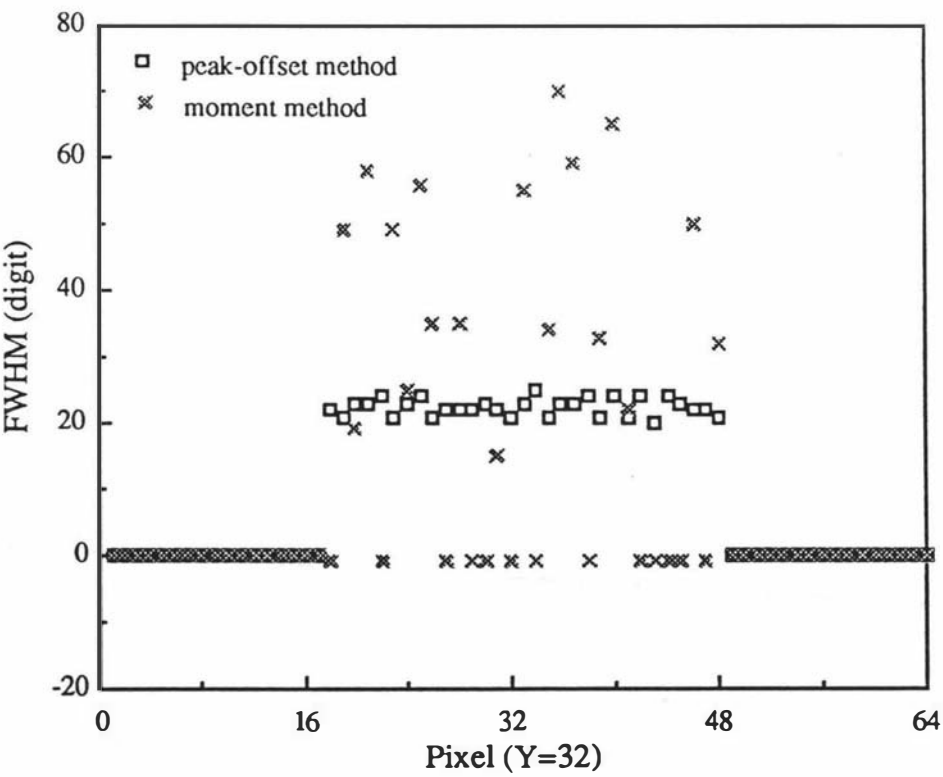

Figure 3.15 Continues

The reason for the failure of the moment method in practice is that it takes into account all the pixels in the displacement profile spectrum (including those far from the peak centre) and is therefore unavoidably more sensitive to the presence of noise. Therefore it is useful only if the signal-to-noise ratio of the data is excellent. On the other hand, the 'peak offset' method checks the maximum peak position in the profile and ignores all the remaining pixels. This is equivalent to applying a very severe band pass filter to the profile. Thus it retains its capability even when the signal-to-noise ratio of the data becomes quite bad. Of course the price paid for this high 'noise resistance' is the possibility of small random errors when the profile is phase distorted.

3.6.2 Least squares fit analysis method

In Ch 3.3 two equations, Eq[3.19] and Eq[3.20], have been derived as the central core of Dynamic NMR Microscopy. Although these two equations are a Fourier transform pair, the use of F[E(q,**r**,Δ)] has been preferred in the analysis of the 'raw' E(q,**r**,Δ) data in order to calculate the velocity and self-diffusion coefficient. In the following analysis, direct computation using E(q,**r**,Δ) is discussed.

The direct computation method employs a least squares fit. It is useful to rewrite Eq[3.19] in terms of its real and imaginary parts, as

$$S_R(g,\mathbf{r},\Delta) = A \exp[-\gamma^2\delta^2 g^2 D(\Delta-\delta/3)] \cos(\gamma\delta g v\Delta) \qquad [3.72a]$$

and

$$S_I(g,\mathbf{r},\Delta) = A \exp[-\gamma^2\delta^2 g^2 D(\Delta-\delta/3)] \sin(\gamma\delta g v\Delta) \qquad [3.72b]$$

Clearly, a division of $S_I(g_i,\mathbf{r},\Delta)$ by $S_R(g_i,\mathbf{r},\Delta)$ will remove the diffusion term and leave the ratio

$$\text{ratio}_{vi} = \frac{S_I(g_i,\mathbf{r},\Delta)}{S_R(g_i,\mathbf{r},\Delta)}$$

$$= \tan(\gamma\delta g_i v\Delta) \qquad [3.73]$$

Taking the inverse of tangent function from both sides, the velocity can be revealed as

$$v = \frac{1}{\gamma\delta g_i\Delta} \tan^{-1}(\text{ratio}_{vi}) \qquad [3.74]$$

By plotting $\tan^{-1}(\text{ratio}_{vi})$ vs $(\gamma\delta g_i\Delta)$ for each q slice in which g_i is the variable, the velocity can be obtained from the slope of the straight line fitted through these points.

There are two obvious disadvantages in the line fitting of Eq[3.74]. First, due to the discontinuity property of the tangent curve at $\pm n\pi/2$, (n=1,2,..), the velocity values at and near these regions would be lost or contain large errors. This would be a problem if the sample has a wide flow field. The second disadvantage is, due to the periodic property of the tangent curve, there is a possibility of one velocity digital value representing two or more different velocities with phase angles $n\pi$ apart.

The self-diffusion coefficient can also be calculated through a similar least squares fit method, named Stejskal-Tanner method[50]. It is the classical method used widely in conventional NMR to measure the self-diffusion coefficient for liquid samples. This approach firstly takes the modulus of the complex data so that the phase information contained in the oscillatory term are lost while the decay information remains unaltered, as

$$\text{modulus}_{Di} = (S_{Ri}^2 + S_{Ii}^2)^{1/2}$$

$$= |A| \exp[-\gamma^2\delta^2 g_i^2 D(\Delta-\delta/3)] \qquad [3.75]$$

Then all the pixels are normalized to the first pixel (q=0) so that the amplitude terms disappear. By taking the natural logarithm from both sides of Eq[3.75], the self-diffusion can be revealed as

$$D = -\frac{1}{\gamma^2\delta^2 g_i^2(\Delta-\delta/3)} \ln(\text{modulus}_i) \qquad [3.76]$$

By plotting the normalized intensity against $[\gamma^2\delta^2 g_i^2(\Delta-\delta/3)]$ in which g_i^2 is the variable, the diffusion coefficient can be calculated from the slope of the fitted line.

In the calculation of the pixel modulus using Eq[3.75], the influence of the noise power has to be taken into account. By denoting Re and Im as the true signals and N_R and N_I as the real and imaginary part of the noise, the apparent image pixel amplitudes can be written as

$$Re' = Re + N_R \qquad [3.77a]$$

$$Im' = Im + N_I \qquad [3.77b]$$

Therefore the modulus of the image pixels are

$$Re'^2 + Im'^2 = (Re + N_R)^2 + (Im + N_I)^2$$

$$= (Re^2 + Im^2) + (N_R^2 + N_I^2) + 2(ReN_R + ImN_I) \qquad [3.78]$$

The first term in Eq[3.78] is the true modulus of the signal, the second term is the contribution from the noise power which has to be subtracted, the last term is the random noise term. Therefore in our software, instead of using Eq[3.75] directly, the noise power for each pair of q images is calculated first using the first 128 pixels at the edge of the images (for which Re and Im will be zero) as

$$Noise(q)^2 = \frac{1}{128}\sum_i (Re'(q)_i^2 + Im'(q)_i^2)$$

$$= \frac{1}{128}\sum_i (N_R(q)_i^2 + N_I(q)_i^2) \qquad [3.79]$$

where the sum is over the i=1 to 128 pixels. Then the modulus becomes

$$modulus(q) = (Re(q)^2 + Im(q)^2 - Noise(q)^2)^{1/2} \qquad [3.80]$$

In the implementation of the least squares fit method, the scatter of the data makes the weighting important. For a set of q data, the first pixel is always the most reliable one because the signal is the highest. The data becomes much less reliable with the increase of the gradient g. There are many ways of weighting a set of discrete data in literatures. A double least squares fit approach is used in our software. That is, in the first time an unweighted least squares fit is performed, the slope b and the intercept a are calculated. Then a weighted fit is performed for the second time using the weighting factor of $1/\sigma_i^2$, in which the standard deviation σ is calculated from the relationship $y_i=a+bx_i$.

These two least squares fit methods have been used in our experimental data analysis, some results will be presented in Ch 6 to Ch 9. A short conclusion is given here first. The least squares fit methods can be used to analyze the data in Dynamic NMR Microscopy experiments. If the signal-to-noise ratio of the data images are good, these two methods should give more accurate results than the FFT method, especially in the case of the self-diffusion calculations where the least squares fit method avoids some artifacts associated with the conjugate domain. But if the signal-to-noise ratio of

the data images is not very good, the FFT method is far better than these least squares fit methods. This is due to the 'noise-resistant' algorithms used in the FFT method and the procedure of zero filling in the conjugate space.

3.7 'One-shot' velocity microscopy

The ability to simultaneously construct velocity and self-diffusion images in Dynamic NMR Microscopy requires comprehensive information about the spin system everywhere in both **k** space and **q** space. Experiments are carried out by stepping through a sequence of PGSE gradients and repeating the **k**-space imaging at each q value. Dynamic NMR Microscopy, in its simplest form, is essentially a four-dimensional approach and is therefore time consuming. In situations where a velocity image is of principal interest, one can reconstruct velocity map from a single value of PGSE gradient[87, 94]. This reduces the experimental time significantly.

The 'one-shot' velocity micro-imaging method used in this thesis utilizes the gradient phase cycling[94] which nulls the signals from stationary spins and produces the sinusoidal dependency of the image intensity on the velocity of the moving spins. A higher order suppression of stationary spin signal can be achieved by combining gradient phase alternation with the use of a final rf 'z-storage' pulse[87] which rotates the transverse magnetization of the stationary spins to the z-axis. A four-quadrant interpreting routine is also developed in our method to calculate the velocity from the phase shift between 0 and 2π.

3.7.1 Gradient phase cycling and 'z-storage' rf pulse

The stepping of PGSE gradient in Dynamic NMR Microscopy imposes a contrast given by Eq[3.16], which is a decaying function modulated by a complex oscillatory term. To obtain a velocity image alone, one can acquire a single q-slice along with a normalised image, using a pulse sequence shown in Figure 3.16. The first part of the pulse sequence is the dynamic contrast segment, the second part is the slice selection and the final is the standard **k**-space mapping. The stimulated-echo sequence discussed previously in Ch 2.1.8 is utilized in this pulse sequence.

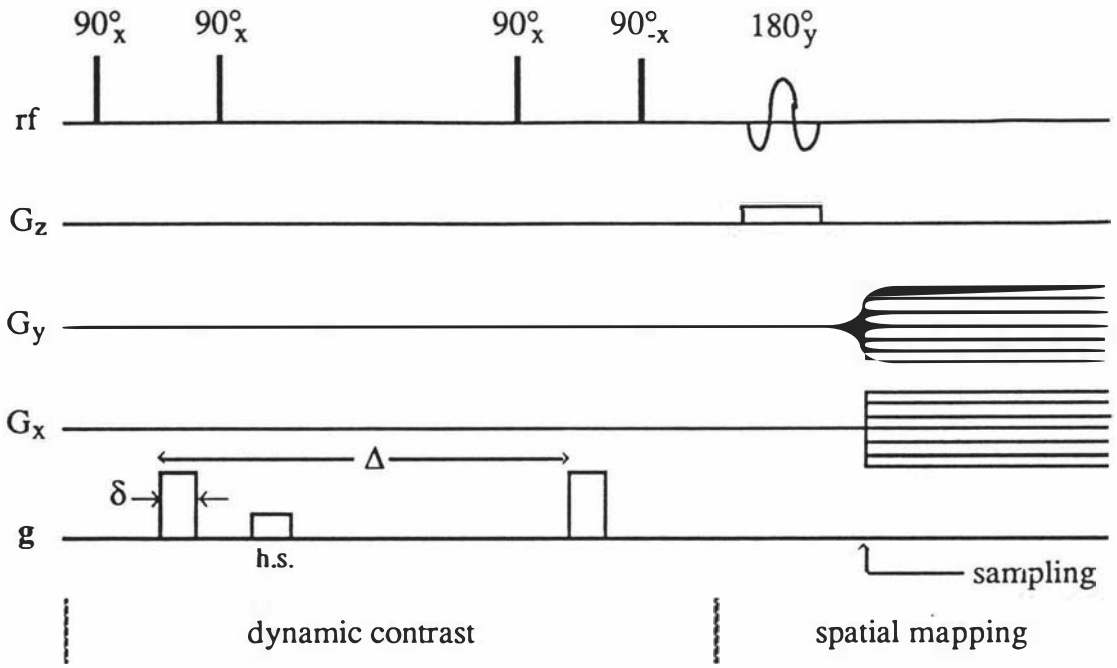

Figure 3.16 A pulse sequence used in the 'one-shot' velocity microscopy

To ensure precise nulling of signal from all but the moving spins, this method uses a final 90° z-storage rf pulse followed by a spin-echo formed by a slice-selective $180°|_y$ sinc pulse together with the employment of gradient phase cycling. Leaving the 180° slice selection pulse until just before the spatial mapping is a necessary precaution to ensure that all the signals arise from the slice of interest. The alternative approach, which begins with slice-selection and uses hard pulses for the remaining spin manipulation, will inevitably lead to some contamination of the image from out of slice magnetization induced by the subsequent hard pulses.

Previously in Ch 2.1.8 the role of rf phase cycling in reducing the detection error has been discussed. In our instrument with a single detection channel, a full rf cycle (CYCLOPS) is not necessary and only 0° and 180° rf phase cycling is used. With the implementation of the 'one-shot' velocity-encoding method in our instrument, the effect of additional gradient phase cycling is considered.

Gradient phase cycling provides a high degree of stationary spin signal suppression. It utilises the fact that the signal phase shift due to PGSE pulses depends upon the sign of the PGSE gradient, g, so that -g induces $-\phi$ where ϕ is given by Eq[3.19]. Consequently the net phase of the transverse magnetization not only depends on the excitation and the detection phases but also the sign of g. A gradient phase cycling routine used in the 'one-shot' velocity imaging method is shown in the following table:

Table 3.5: Phase cycling table for the 'one-shot' velocity imaging

rf phase	Gradient phase	Even co-addition (no 90°I_{-x} pulse)			Odd co-addition (90°I_{-x} pulse included)		
		Acquis. phase	Re signal	Im signal	Acquis. phase	Re signal	Im signal
0	+g	0	cos(ϕ)	0	0	0	sin(ϕ)
180	+g	180	-cos(ϕ)	0	180	0	-sin(ϕ)
0	-g	0	cos(ϕ)	0	180	0	-sin(ϕ)
180	-g	180	-cos(ϕ)	0	0	0	sin(ϕ)
resultant $M_{\perp}$ resultant image		$\cos(\gamma\delta g v\Delta)$ $\rho_{even}(\mathbf{r})$			$-j\sin(\gamma\delta g v\Delta)$ $\rho_{odd}(\mathbf{r})$		

(ote: where M . refers to the magneti z tion in t e t ansver s plane, q is equal to lyogv l l, Re and 1m signals refers to the in-phase and quadrature-phase signals res p tively.)

In the above table there are two sequences of detection phases, 'even' and 'odd'. In the 'even' sequence, no final 90°I_{-x} z-storage pulse is used and the sign of the signal acquisition is independent of the gradient sign. This sequence is thus not sensitive to signal phase change. The image is therefore given by

$$\rho_{even}(\mathbf{q},\mathbf{k}) = \rho(\mathbf{r})\exp[-(\gamma\delta g)^2 D\Delta]\cos(\gamma\delta g v(\mathbf{r})\Delta) \qquad [3.81]$$

By contrast in the 'odd' sequence, the final 90°I_{-x} z-storage pulse is included and the sign of the signal acquisition is dependent on the gradient sign. This sequence is therefore sensitive to the signal phase change in quadrature channel (and hence velocity). The signal thus leads to an image $\rho_{odd}(\mathbf{q},\mathbf{k})$, given by

$$\rho_{odd}(\mathbf{q},\mathbf{k}) = \rho(\mathbf{r})\exp[-(\gamma\delta g)^2 D\Delta]\sin(\gamma\delta g v(\mathbf{r})\Delta) \qquad [3.82]$$

As a consequence of the odd co-addition, the stationary spins make no contribution to the image and the resulting image is proportional to the flow rate when $\gamma\delta g v(\mathbf{r})\Delta$ is small. The relationships between the final transverse magnetization in each voxel and the alternative phase cycling methods can be seen clearly in Figure 3.17.

The first PGSE pulse dephases the spin vector. Two 90° pulses behave like a 180° pulse, inverting the phase of the spins. The following PGSE pulse refocuses the dephased spins. The refocusing process can be sub-divided into four different cases. In the even-coadding case, the final 90° z-storage pulse is not included. For stationary spins, the second PGSE pulse will refocus the spin vector into the in-phase direction

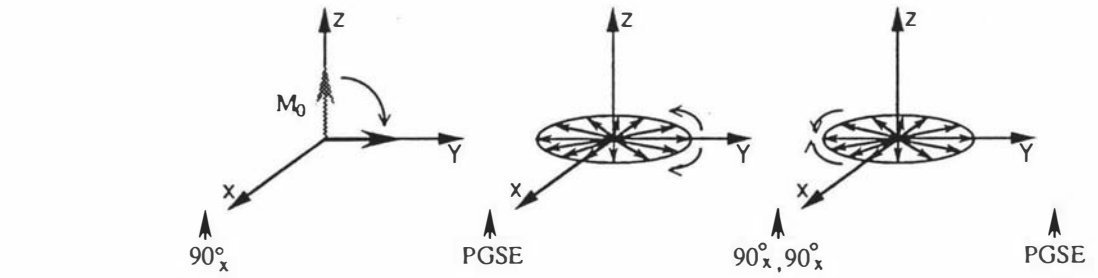

Case (i): Even coadding with stationary spins

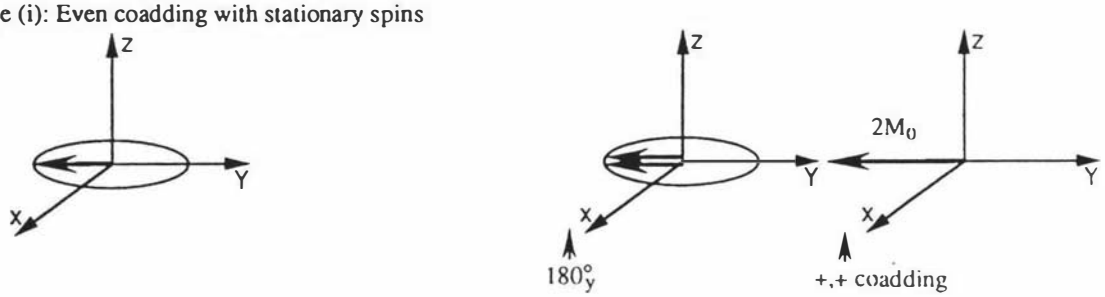

Case (ii): Even coadding with moving spins

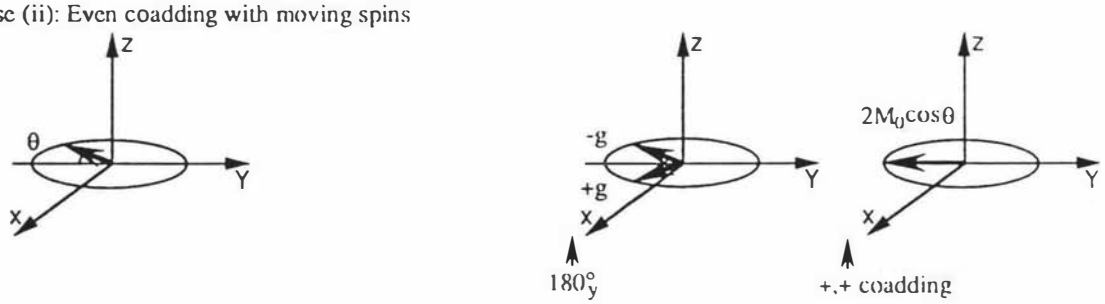

Case (iii): 90°_{-x} z-storage and odd coadding with stationary spins

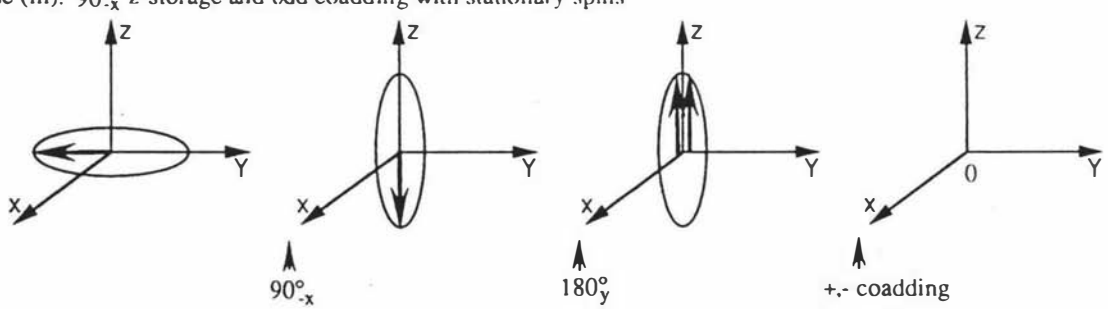

Case (iv): 90°_{-x} z-storage and odd coadding with moving spins

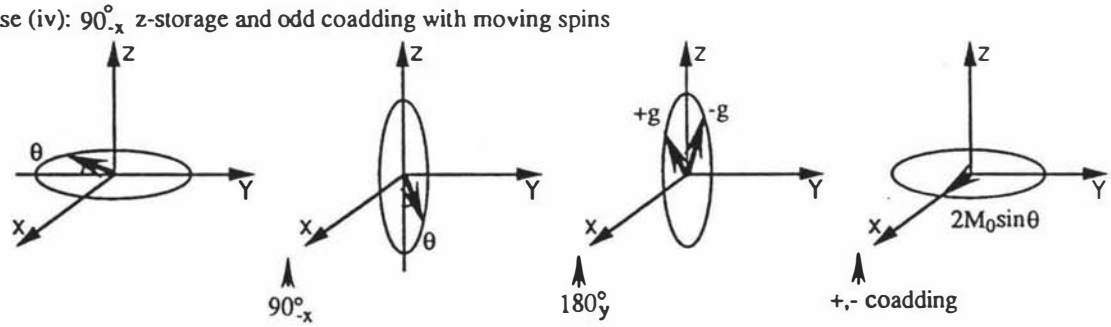

Figure 3.17 The evolution of the magnetization vector during the experiment

perfectly (S_0). For moving spins, however, this vector will have a net phase shift. The gradient phase cycling will produce a negative phase shift, and the even-coadding will cancel the quadrature component, leaving the vector along the in-phase direction (S_1). In the odd-coadding case, the final z-storage pulse will tip the vector away the transverse plane to the z axis. Therefore the signals from stationary spins will be cancelled out completely (S_2), leaving no transverse component. By contrast, the x component of the moving spins won't be affected by this $90°|_{-x}$ pulse and will remain in the transverse plane. The gradient phase cycling and the odd-coadding will add the opposite signed signals together, give a quadrature signal (S_3).

In summary, the final signal remaining in the transverse plane in each of the four cases is given respectively by

$$S_0(q,r,\Delta) = 2M_0e^{-\alpha} \qquad [3.83a]$$

$$S_1(q,r,\Delta) = 2M_0e^{-\alpha}\cos(2\pi qv\Delta) \qquad [3.83b]$$

$$S_2(q,r,\Delta) = 0 \qquad [3.83c]$$

$$S_3(q,r,\Delta) = -j[2M_0e^{-\alpha}\sin(2\pi qv\Delta)] \qquad [3.83d]$$

where α is the diffusive term representing $(\gamma\delta g)^2D\Delta$ and j indicates a 90 degree shift of the image phase.

Although the experiment is depicted as being performed in a two parts, i.e., obtaining P_{odd} and P_{even} separately, these images can be independently calculated from the same data set, as shown in Table 3.6. This approach would not only be more efficient but also more accurate because any errors due to either the sample and/or system drifts would have the same effect on both images so that the ratio used to calculate $\mathbf{v}(\mathbf{r})$ would be much less affected.

Table 3.6: Alternative phase cycling table for the 'one-shot' velocity imaging

rf phase	Gradient phase	Acquisition phase	Addition Memory
0	+g	0	M1 and M2
180	+g	180	M1 and M2
0	-g	0	M1
0	-g	180	M2
180	-g	0	M2
180	-g	180	M1

Note: M1 refers to the memory address where the even co-addition is taken place and M2 where the odd co-addition taken place.

3.7.2 High order stationary signal suppression

The success of this 'one-shot' technique relies upon excellent suppression of the stationary signal. For an ideal system, either a final 90° z-storage pulse or gradient phase cycling would be sufficient to construct a velocity image for the moving spins only. In practice, however, an inevitable inhomogeneity of rf field will give imprecise rotations of the spin signal. Also the ripple of the gradient power supplies will lead to an imperfect matching of the area under the two oppositely directed gradient pulses. If the phase cycling and the z-storage pulse are combined together, the stationary spin signals can be suppressed to a higher order.

To account for the effect of an imperfect $90°|_{-x}$ rf pulse and an imperfect matching of the area under the two oppositely directed gradient pulses, let the final turn angle be $\frac{1}{2}\pi$-$\delta\theta_1$ and the area difference cause a phase difference $\delta\theta_2$, where θ_2 is the phase shift due to flow, $\gamma\delta g v(\mathbf{r})\Delta$. For the odd-coaddition, the transverse magnetization following the final θ_{-x} pulse will be

$$\begin{aligned}\rho_{odd}(\mathbf{r}) &= -\tfrac{1}{2}\rho(\mathbf{r})[\cos(\tfrac{1}{2}\pi-\delta\theta_1)(\cos\theta_2 - \cos(\theta_2+\delta\theta_2))+j(\sin\theta_2 + \sin(\theta_2+\delta\theta_2))] \\ &\approx -\rho(\mathbf{r})\sin\delta\theta_1\sin\delta\theta_2\sin\theta_2 - j\rho(\mathbf{r})\sin\theta_2\cos\delta\theta_2 \\ &\approx -\rho(\mathbf{r})\delta\theta_1\delta\theta_2 - j\rho(\mathbf{r})\sin(\gamma\delta g v(\mathbf{r})\Delta)(1-\tfrac{1}{2}\delta\theta_2{}^2) \end{aligned} \quad [3.84]$$

To simplify the expression the $e^{-\alpha}$ diffusive attenuation factor has been deliberately neglected. The odd-phase cycling method therefore results in the image, $-j\rho(\mathbf{r})\sin(\gamma\delta g v(\mathbf{r})\Delta)$, with all deviations reduced to second order. The equivalent result for the even co-addition in which no final $90°|_{-x}$ rf pulse is used is given by

$$\begin{aligned}\rho_{even}(\mathbf{r}) &= -\tfrac{1}{2}\rho(\mathbf{r})[\cos\theta_2 + \cos(\theta_2+\delta\theta_2) + j(\sin\theta_2 - \sin(\theta_2+\delta\theta_2)] \\ &\approx -\rho(\mathbf{r})\cos\theta_2\cos\delta\theta_2 - j\rho(\mathbf{r})\cos\theta_2\sin\delta\theta_2 \\ &\approx -\rho(\mathbf{r})\cos(\gamma\delta g v(\mathbf{r})\Delta)(1- j\delta\theta_2+\tfrac{1}{2}\delta\theta_2{}^2) \end{aligned} \quad [3.85]$$

$\rho_{even}(\mathbf{r})$ is phase shifted to first order in $\delta\theta_2$ and attenuated to second order in $\delta\theta_2$. Consequently the real part of $\rho_{even}(\mathbf{r})$ is $-\rho(\mathbf{r})\cos(\gamma\delta g v(\mathbf{r})\Delta)$ with all deviations reduced to second order.

It should also be noted that the gradient mismatch angle $\delta\theta_2$ can be minimized by using an external switching to change the direction of (constant) current flow rather than using a bipolar power supply. This is the method used in our apparatus.

3.7.3 Velocity computation

A direct and quantitative measurement of $v(\mathbf{r})$ is possible by taking the ratio of the even co-addition and odd co-addition images so that diffusive attenuation effects cancelled. Experiments reported on here are concerned both with a slow flow regime and with higher velocities where $\gamma\delta g v(\mathbf{r})\Delta$ can take values anywhere between 0 and 2π. Assuming that the image phase difference represented by -j has been adjusted, one obtains

$$v(\mathbf{r}) = \frac{1}{\gamma g \Delta \delta} \tan^{-1}\left(\frac{\rho_{odd}(\mathbf{r})}{\rho_{even}(\mathbf{r})}\right) \qquad [3.86]$$

It is interesting to note that this expression is almost identical with Eq[3.74] where velocity is calculated from the slope of a straight line least-squares-fitted through a series of data points plotted against the variable g. The difference between these two methods is, this 'one-shot' method seeks a *direct* calculation using the image pixel intensities so that an accurate relationship between the quadrature signal amplitudes and spin phase shift is required. In Dynamic NMR Microscopy, because of the least squares fit method and the multiple slices, any error due to the imperfections of the system won't be too much a problem provided that these imperfections do not result in drifts in one direction only. In other words, either random fluctuation or constant offset is acceptable in Dynamic NMR Microscopy.

In order to uniquely determine the quadrant in which the solution to $\tan^{-1}(\rho_{odd}(\mathbf{r})/\rho_{even}(\mathbf{r}))$ may be found, the independent signs of amplitude in each pixel of the odd and even images must be known. Clearly it is not permissible to use a reconstruction method which returns the image modulus and the image must be reconstructed in the phase sensitive mode.

For low velocities the linearity of $\tan(\phi)$ for ϕ small implies that the image will be directly proportional to $v(\mathbf{r})$. The detection of high velocities are possible for samples of which the zero flow condition can be obtained so that the velocity map can be computed using the sine and cosine dependences of the odd and even images within 2π upon the unperturbed zero flow image $\rho(\mathbf{r})$. The advantage of this approach is that one may use the sine dependence within $\pm\frac{1}{4}\pi$ of 0 and π and the cosine dependence within $\pm\frac{1}{4}\pi$ of $\frac{1}{2}\pi$ and $\frac{3}{2}\pi$ phase shifts. This 'octant' approach has been used in analyzing our capillary flow data. Figure 3.18 shows schematically the experimental procedures involved in the 'one-shot' velocity microscopy.

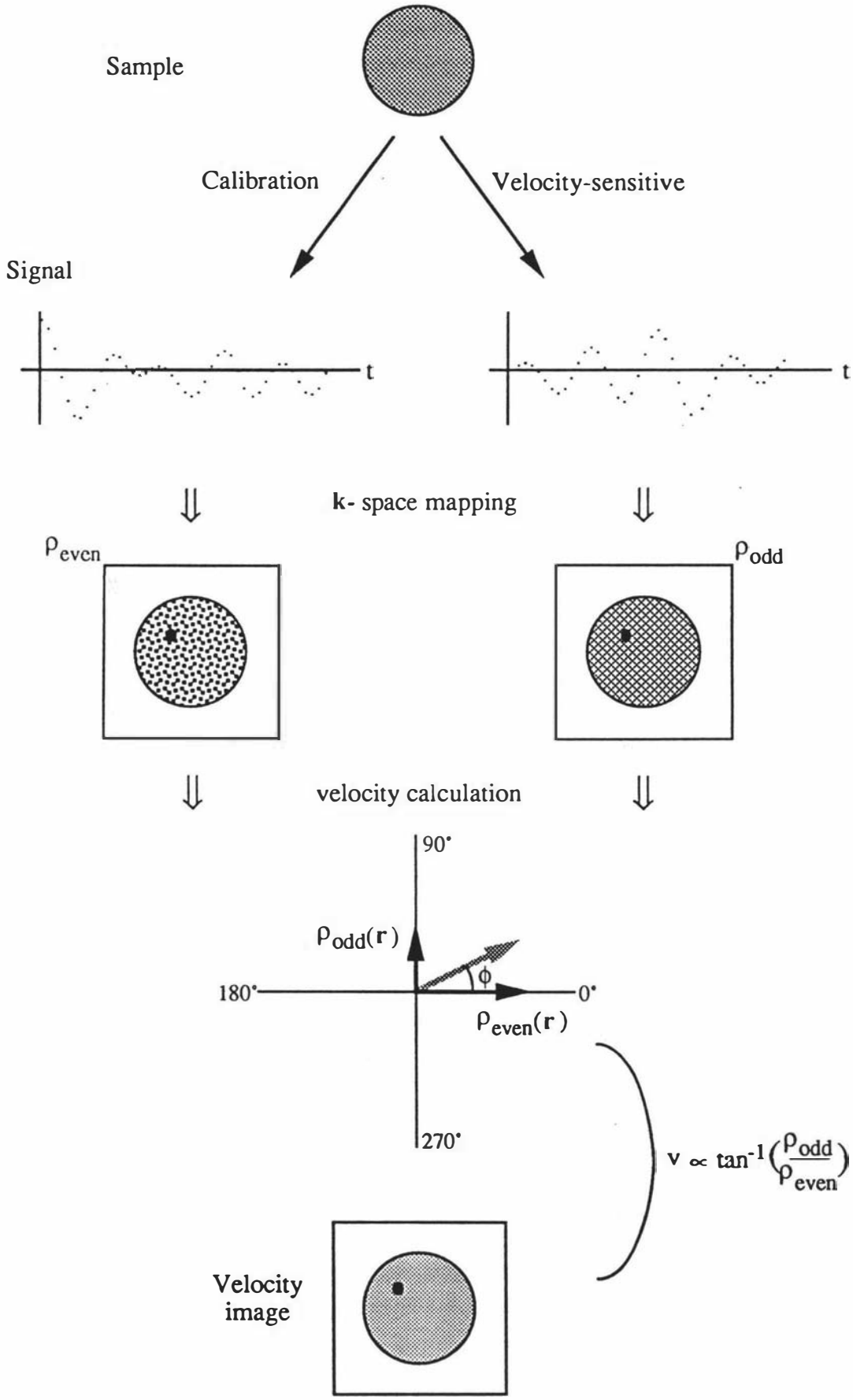

Figure 3.18 Experimental procedures in the 'one-shot' velocity microscopy

3.7.4 Precision and accuracy of the measurements

Many effects which affect the precision and accuracy of the velocity measurement discussed previously for Dynamic NMR Microscopy no longer exist for the 'one-shot' velocity imaging method. For example, the gradient-dependent phase shift can be adjusted easily because only one q-slice is acquired; the 'time of flight' effect is much less for the slice gradient used in the 180° self-focusing selective excitation pulse. But the precision and accuracy of velocity measurement using this 'one-shot' method is not better than that of Dynamic NMR Microscopy, simply because the 'one-shot' method relies upon the direct intensity calculation for each individual pixel position. Any noise and system imperfections contribute directly to this velocity computation. Such random errors are by far the most serious error sources in this 'one-shot' method. For example, in our experiments, the noise level at the final image is often around 10% of the maximum signal amplitude. Therefore the velocity calculated from Eq[3.86] exhibits a 20% random error before taking the inverse of the tangent function!

3.8 Conclusion

Following a review of velocity and self-diffusion imaging techniques, this chapter has discussed in detail the theories of Dynamic NMR Microscopy and a more efficient 'one-shot' velocity micro-imaging method. Two alternative data analysis methods available for Dynamic NMR Microscopy have also been discussed.

To detect the translational motion of nuclear spins, both the multiple q-slicing and the 'one-shot' method utilize the direct relationship which exists between the nuclear spin displacements and the associated phase shifts. Of course the ability of constructing simultaneously velocity and self-diffusion maps makes Dynamic NMR Microscopy a more sophisticated technique. However, there are some situations where the 'one-shot' method could be a preferable choice provided the sacrifice of the diffusion information is acceptable. In particular the 'one-shot' method will provide a velocity map in a much short experimental time than Dynamic NMR Microscopy.

In terms of sensitivity to velocity, both methods are able to obtain velocity maps at a spatial resolution of a few tens of microns and with a velocity resolution of a few tens of microns per second.

In terms of accuracy and precision of the velocity measurement, Dynamic NMR Microscopy is better than the 'one-shot' method because the latter relies on the direct interpretation of image pixel intensities and hence is more sensitive to the presence of noise and system imperfections. There is no systematic error for both methods. The precision of the measurements for both methods is subject only to the presence of experimental noise. For the self-diffusion measurement, however, extra care has to be taken during the experiment to ensure an accurate measurement.

In terms of computer memory requirement, the 'one-shot' method obviously requires much less memory than the multi q-slicing method, and is therefore more convenient when working with a larger image matrix, for example, either 128^2 or 256^2.

Chapter 4 Development of the FX-60 NMR Micro-Imaging System

This chapter describes the NMR micro-imaging system on which the experiments forms part of this thesis were carried out. A general description of the existing imaging system is given first. More detailed descriptions of the developments undertaken as part of this work are then given in Section 4.2 to 4.5.

4.1 The FX-60 NMR micro-imaging system

The FX-60 NMR micro-imaging system at Massey University is based on a JEOL FX-60 multi-nuclear NMR spectrometer. This rather old rf spectrometer has an electromagnet which generates a static 1.4 T polarizing magnetic field ($\mathbf{B}_0$), corresponding to a proton NMR frequency of 60 MHz (or more accurately, 59.75 MHz). The geometry of the electromagnet dictates the main field direction (Figure 4.1), and hence the choice of the gradient and rf coil configurations.

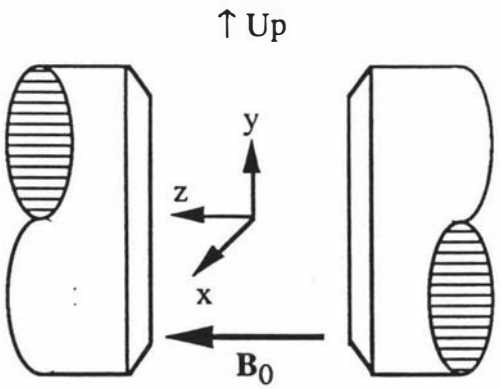

Figure 4.1 The geometry of the magnet system

Beside the original spectrometer, several major items such as the rf modulator, a pulse programmer, three gradient units and the image processing and display computers were added. A block diagram of the system is shown in Figure 4.2.

The pulsed $B_1(t)$ field, orthogonal to the direction of the main magnetic field ($\mathbf{B}_0$), is used to tip the magnetization vector prior to detection. The master clock of the

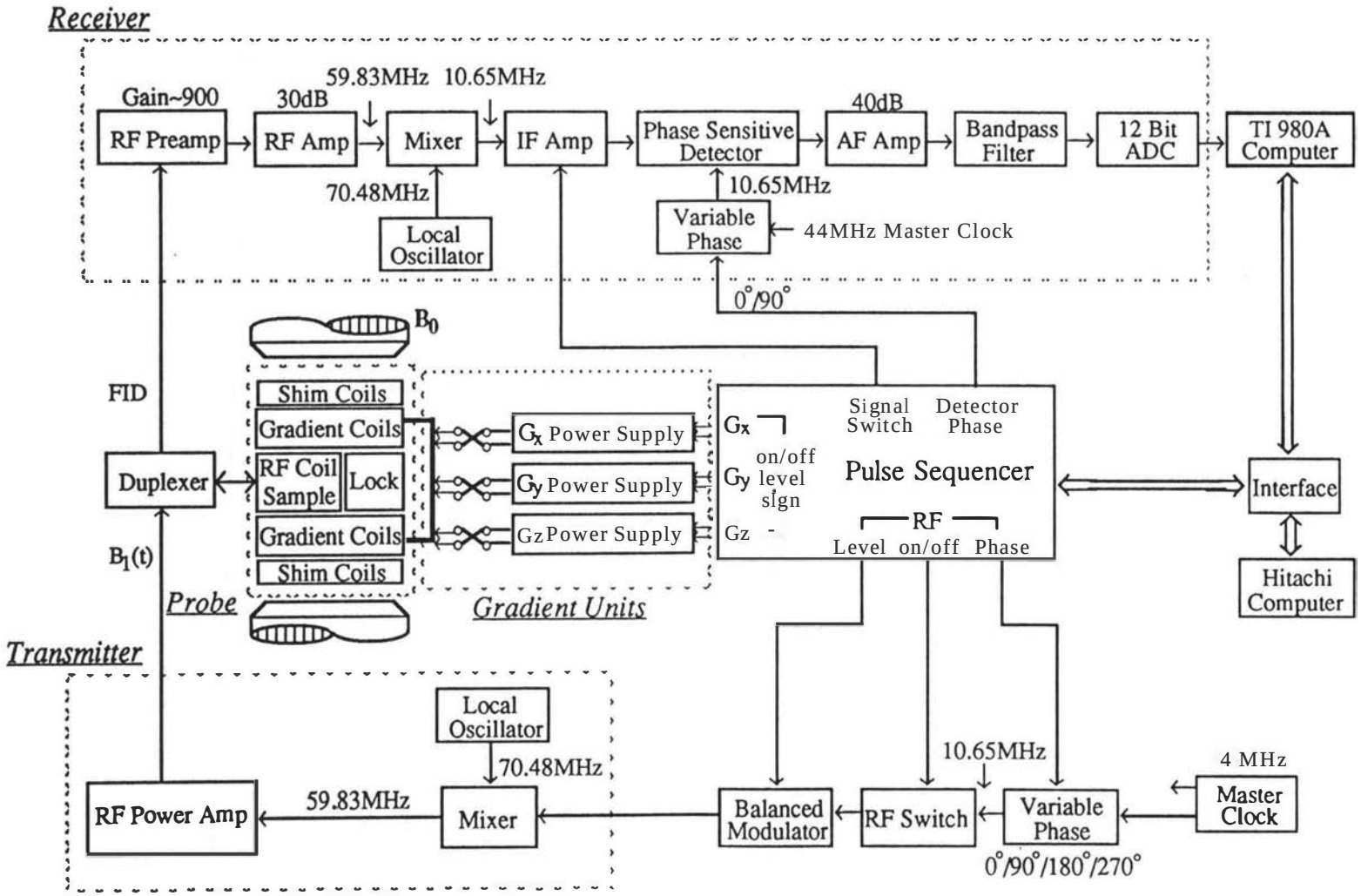

Figure 4.2 Massey FX-60 NMR micro-imaging system

imaging system operates at 44 MHz. This signal is fed into the frequency divider and the four-phase generator, yielding signals at 10.65 MHz with four different phases of 90° apart. The radio frequency pulses are then selected by a specially designed pulse programmer[25] which controls an rf switch (to chop the continuous rf wave into the pulse form). The pulses are envelope-modulated by a double balanced modulator[25] to the desired pulse form (such as the sinc pulse used for the slice selection), mixed with the appropriate frequency to produce the 59.75 MHz rf signal, and finally amplified by a broadband rf power amplifier (rf transmitter). The output pulses are supplied via a duplexer (because a single transmitter/receiver coil configuration is used in this system) to the rf coil surrounding the sample.

The induced μV-level NMR signal (FID) is routed via the duplexer into a low-noise pre-amplifier. Further amplification is made through a single stage rf amplifier, followed by a mixer which produces an 10.65 MHz intermediate frequency (if) signal. The mixer is used to convert the high frequency (rf) signal to the low frequency (if) signal but maintains the phase information. This if signal is then fed into a two-stage if amplifier, followed by a second mixer, which acts as a phase sensitive detector (PSD), producing an audio frequency (af) signal. A common channel is used for both the in-phase and quadrature signals which are collected successively by alternating the phase of the if reference input. The absolute phase of the signal may be set by continuously adjusting the phase of the if reference. These in-phase and quadrature signals are respectively proportional to M_x and M_y and represent the real and imaginary parts of the complex time domain data. A band-pass filter which has a band-width equal to the observation spectrum width is used to reduce the aliasing of the noise, and a 12 bit analog-to-digital converter (ADC) is used to convert the signal to the digitized form, which is stored in the TI-980A computer memory temporarily, and finally transferred to the Hitachi computer for the image reconstruction.

In the data acquisition and image reconstruction, two computers are employed, a Texas Instruments 980A computer and a Hitachi MB16000 personal computer. As an original part of JEOL FX-60 spectrometer, the TI-980A is a 16 bit computer with 32 kwords of memory and is supported by an extensive assembly language software package[136], which provides various routines to carry out such functions as control pulse timing and phase, the collection and averaging of data, analysis of data including apodization filtering, integration and fast Fourier Transformation (FFT). A light pen is provided for interacting with the computer system, and an oscilloscope is used to display data in real time, or to analyze them subsequently. During imaging experiments, the TI-980A computer stores the parameter settings loaded from the Hitachi computer,

and in addition enables other local parameters to be set. It also allows real time experimental control, the collection of the **k** space data, the application of filters and Fourier transformation. The filtered profile $P^*(x,y,\phi)$, given by Eq[2.51], is then transferred to the Hitachi, via a parallel interface, for the image reconstruction, display and analysis.

Before starting an imaging experiment, a pulse sequence (a multi-component function of time) is generated by a versatile pulse programmer, which can be divided into two parts, a software code generator and a hardware sequencer[25]. The code generator is based on the Hitachi computer which generates binary pulse sequence codes for a particular experiment. Each command in a pulse sequence contains the destination (1 byte), the command (1 byte) and the time (3 bytes). The complete pulse codes are then transferred to a 4 kbytes RAM in the pulse sequencer. At the beginning of an experiment, the TI-980A computer starts the pulse sequencer which subsequently controls the timing of the events by sending out the commands step by step according to the pulse sequence codes stored in the RAM.

The image processing and display function is performed using the Hitachi computer, which is based on an Intel 8088 microprocessor and supported by the MS-DOS operating system. It is configured with 256 kbytes of main memory and 192 kbytes of graphics memory, and has two 320 kbytes floppy disk drivers (DOS 1.1). A 640×400 pixel image in 8 colours or a 320×200 pixel image in 16 colours can be displayed on the screen. After receiving the data from the TI-980A, the Hitachi performs the back projection reconstruction of the image. The image is stored in the upper memory as an array of maximum 256×256 pixels with 16 bits per data point (pixel), so that the dynamic range of a pixel is ±32767. The final image can be stored on a floppy disk.

The data management in a Dynamic NMR Microscopy experiment is more complicated and is completed in the following way. A pixel array size of 64×64 is chosen for the q images. This reduced size helps to alleviate the data storage problem. During an experiment, each pair of q images are successively stored on a disk, one 320 kbyte floppy holding up to 18 real/imaginary pairs. After the data acquisitions, each corresponding set of 18 data pixels is zero-filled to a domain of 256 pixels and a complex discrete FT analysis follows. In analyzing the q data, because the Hitachi memory is insufficient to hold the entire data set, the data analysis requires a series of disk readings. In order to avoid the 2×18×64×64 (=147456) disk reading operations which would be required if successively q-modulated pixels were read via DOS,

assembly language routines had been written which rapidly read from and write to individual disk sectors directly. This enables 2×18×1024 corresponding bytes from the 18 real and imaginary q images to be processed simultaneously[132].

Several programs had been written in FORTRAN to fully automate the imaging experiments and subsequent analysis[132, 137] on the Hitachi. In order to speed up the processes of image reconstruction, display and analysis, various assembly language subroutines had been written as function routines to support the FORTRAN programs.

An important part of the imaging system is the rf probe (effectively a solid copper box which is situated between the magnet pole faces). The probe hosts the deuterium NMR lock system for the static field, the shim coils, the gradient coils and the rf coil as well as its turning circuit. The lock system, which is actually a small continuous wave (cw) NMR spectrometer with a drift-detector and feed-back loop, is used to provide long term stability for the main field. Short term (transient) stability of the main field is provided by a standard flux stabiliser. The nine shim coils, mounted on the exterior of the side-panels (silver plated fibre-glass pc board) of the probe, are used to generate small field gradients which can compensate the non-uniformity due to the main magnet or probe environment.

Any discussion of the field gradients requires descriptions of the gradient power supply. In the FX-60 micro-imaging system, there are three gradient units. Each of the three gradient units consists of a gradient coil, a gradient coil power supply and a current switch. Dynamic NMR Microscopy requires much larger gradients than those used in conventional (static) imaging. Sub-100μm resolution implies the need for gradients of order 0.2 T m^{-1} while PGSE experiments imply the need for gradients in excess of 1 T m^{-1}.

In the existing imaging system, the imaging gradients are produced by two quadrupolar coils while the slice selection and q gradient is produced by a planar coil. The choice of gradient coil configuration is mostly dictated by the geometry of the magnet and available space inside the probe. These gradient coils are driven by three KEPCO model ATE power supplies operating in a constant current mode. A programmable KEPCO ATE 75V/15A power supply which drives the q gradient coil had been specially modified[132] to reduce the rms ripple and noise to 0.006% I_{0max} in order to provide accurate matching of the PGSE pulse areas.

To achieve a constant output level, each gradient power supply is set to the desired level at least 100 ms before the gradient pulse is required. Darlington transistor switches controlled by the pulse sequencer ON/OFF gates are used to direct the currents between the gradient coils or a dummy load, which in our case is a resistor with resistance equal to the resistance of the gradient coil. Protection from overheating is provided by a thermistor sensor which triggers the KEPCO crowbars.

The following two tables summarize the performance of the power supplies and gradient units.

Table 4.1 Characteristics of the KEPCO Power Supplies

	X Gradient	Y Gradient	Z Gradient
Model	ATE 25/4	ATE 75/15	ATE 25/10
Max Output (V)	25	75	25
Max Output (A)	4	15	10
Ripple (mA_{pp})	0.87	0.9	0.73
Ripple (% I_{0max})	0.22	0.0060	0.0073

Note: These measurements were made with the output current equal to 2 A.

Table 4.2 Characteristics of the gradient systems

	G_x	G_y	G_z
Coil configuration	quadrupolar	planar	quadrupolar
Coil resistance (Ω)	2.25	2.18	1.62
Coil inductance (μH)	85	54	45
Inductance* (μH)	86	58	46
$Gradient_u$ ($G\ cm^{-1}\ A^{-1}$)	23.74±0.06	9.36±0.01	14.89±0.09
$Gradient_{max}$ ($G\ cm^{-1}$)	95	140	149

Notes:
1. Resistances and inductances are measured by using HP4192A LF Impedance Analyzer. Frequency has been set to 1 kHz when measuring inductances.
2. Inductances* including the lead wires after the coils and the probe has been assembled.
3. The values of the unit gradient, $Gradient_u$, are the calibrated ones.
4. Non-SI units of $G\ cm^{-1}$ are used but the conversion is 100 $G\ cm^{-1}$ = 1 $T\ m^{-1}$.

The rf coil (in a solenoidal form due to the geometry of the electromagnet) is used both for irradiating the sample and detecting the NMR signal. The reception mode is critical for signal sensitivity which will be the highest when the coil has the smallest possible size for a given sample. It is therefore necessary to have a few different

diameter coils to optimize the sensitivity according to the sample examined. In transmission, the smaller the coil diameter, the more intense the rf field produced, and the shorter the 90° pulse time. Optimizing sensitivity also requires that the Q of the rf circuit be optimized. It is worth noting that in practice, the value of Q is not only dependent on the factor $\omega L/R$ for the coil, but also on capacitive loss to the surrounding conductors (such as the gradient coils), the dielectric loss in the matching capacitors, the manner in which the coil is made, the way in which the coil and its tuning circuit is mounted, and finally, the sample inside the rf coil. Therefore a perfect match can only be achieved by a last-minute tuning after the particular sample is inside the rf coil. In the existing system three rf coils were available with diameters: 13 mm, 5.8 mm, and 2.1 mm. Each can be plugged into the probe. The following table lists the parameters of these three rf coils.

Table 4.3 Characteristics of rf coils

	Large coil	Medium coil	Small coil
Diameter (mm)	13	5.8	2.1
Wire Dimension (mm)	0.8×3	0.76	0.376
No. of Turns	3	6	12
Inductance (μH)	0.141	0.179	0.181
Quality Factor Q	54	61	40
Sensitivity (S/N)	108	520	2030
90° Pulse Time (μs)	11.5	3.5	1.5

Notes:
1. The inductances were measured using a H 4192A LF Impedance Analyzer at 1 MHz frequency.
2. The quality factor Q is for the whole rf circuit, and is measured when the coil has been plugged into the probe but the probe is outside the magnet and there is no sample inside the coils.
3. The sensitivity is measured using 1 mg Ethanol sample. The values have been normalised in terms of 10 mg H_2O.

4.2 'Super-G_y' gradient imaging probe

As part of this work, a new imaging probe which can produce a maximum G_y gradient up to 7.3 T/m was designed and manufactured. This new probe enables the study of macromolecular deformation in very viscous polymer flows at high shear rate.

4.2.1 Design considerations

As it will be shown in Ch 9, polymer deformation can be investigated by the measurement of self-diffusion of the molecules. For viscous flow, the diffusion coefficient could be very low (compared with that of water) and therefore a much stronger gradient is required than in conventional imaging experiments. For example at Δ=5ms and δ=1ms, a gradient of 1.4 T/m would give a signal attenuation of 73% if the self-diffusion coefficient of the sample is 2×10^{-9} m^2s^{-1}, but the same gradient strength could only cause about 0.01% attenuation if the diffusion of the molecules drops to 2×10^{-13} m^2s^{-1}.

A stronger field gradient can be achieved by using a more powerful gradient power supply to deliver more current to the coil. However this approach is expensive and leads to problems of coil heating. It was therefore decided to design a new gradient coil specifically for the polymer flow experiments. Due to the geometry of the electromagnet and the experiment planned, a stronger gradient in the y direction is required.

The existing imaging probe and the magnet is shown schematically in Figure 4.3. The 32 mm gap between the magnet pole faces defines the maximum available space. Inside the probe, most of the space was occupied by a 80 mm long solid cylindrical 'tube' which hosts the quadrupolar G_x and G_z coils. The quadrupolar configuration was chosen because it gives a larger uniform region and a stronger gradient per unit inductance. Some initial simulation was carried out to investigate the possibility of constructing a gradient coil inside the quadrupolar coil cylinder, but this approach was given up as unsatisfactory because of the restricted coil dimensions. Therefore, the solution was to specially design a new set of gradient coils and hence a new imaging probe for the polymer flow experiments.

Provided the same current is used, a stronger gradient can be achieved if one scales the size of the gradient coil down. This approach offers the advantage that the torque acting on the coil assembly is lower. The disadvantage of a smaller gradient coil arises from the resulting sacrifice in the size of the gradient uniform region (a 0.4% distortion corresponds to one pixel in a 256 pixel array, or 1.6% distortion in a 64 pixel array). In the polymer flow experiments, a smaller uniform region is actually acceptable because a small (< 1 mm i.d.) diameter sample tube is employed in these experiments. Thus the design aim for the new imaging probe was to achieve the highest possible G_y gradient by exchanging the positions of the G_x and G_z coils with the G_y coil therefore

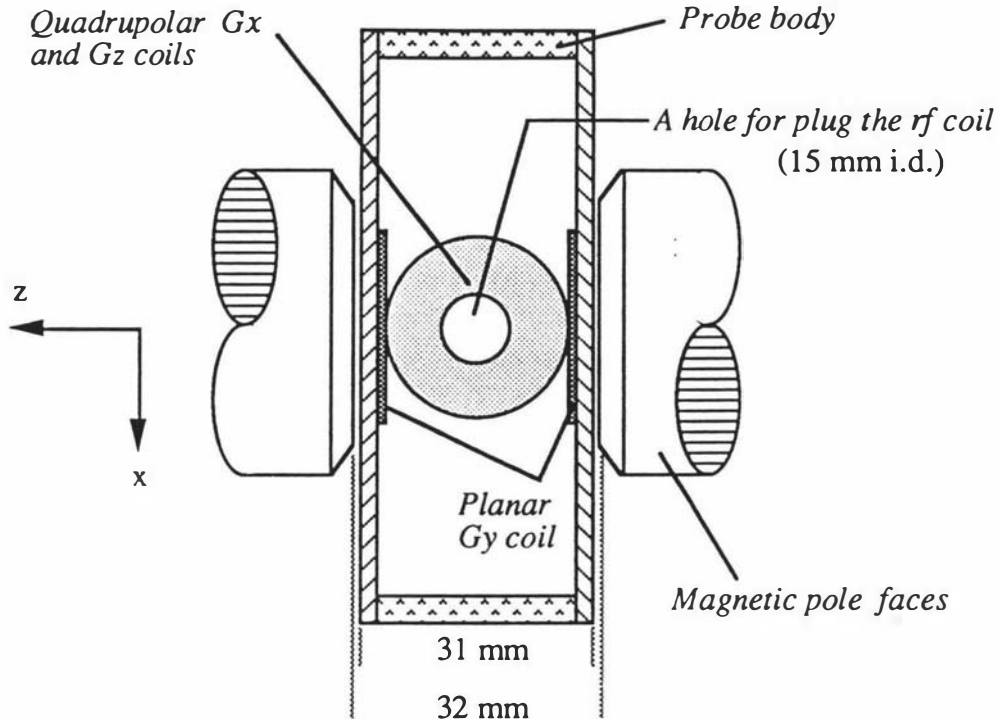

Figure 4.3 A schematc cross sectional top view of the existing imaging probe

minimizing the space occupied by the mapping gradient coils. To achieve microscopic resolution at 60 MHz, the mapping gradient required to spread a 1 mm diameter sample to a 10 kHz profile width is about $(2\pi\times10\text{kHz})/(\gamma\times1\text{mm})$ = 23 G/cm, therefore an upper limit of mapping gradient of around 50 G/cm at 10 A is satisfactory. In the new imaging probe, a planar G_x and a flat Helmholtz coil for G_z were chosen. The G_y coil could now be placed closer to the sample at the centre of the probe. One obvious choice for the G_y gradient coil configuration is to use the planar coil design of Anderson[138].

The theories of the opposed Helmholtz coils (Maxwell pair) and the planar coil have been well established and optimum values for ideal coils have been given by Anderson and Tanner[138, 139]. Therefore computer simulations for a gradient coil usually involve the use of a combination of the coil separation and the number of turns to achieve the required strength of the gradient. Other choices, such as the diameter of the wire, have to be compromised to meet the other gradient requirements, such as the maximum coil inductance, resistance and the tolerable gradient uniformity.

4.2.2 Calculation of the gradients

A gradient in the z direction can be generated by an opposed Helmholtz coils, which can be in the form of either a circular or square shape (Figure 4.4), the square design was our choice (due to the availability of the existing simulation software[25, 132]). The gradient field strength for such an opposed Helmholtz coils can be calculated as follows.

The field at a field point (x_1,y_1,z_1) due to the current I flowing through a wire element dl at the source point (x,y,z) is given by the Biot-Savart Law as (Figure 4.5)

(a) circular shape

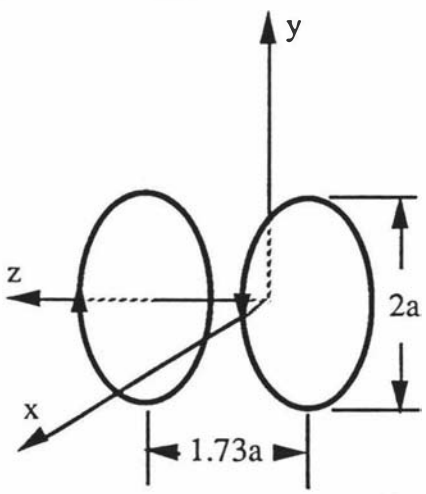

(b) square shape

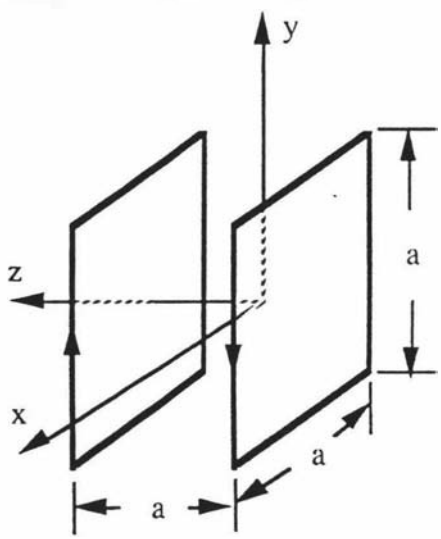

Figure 4.4 Opposed Helmholtz coil geometry

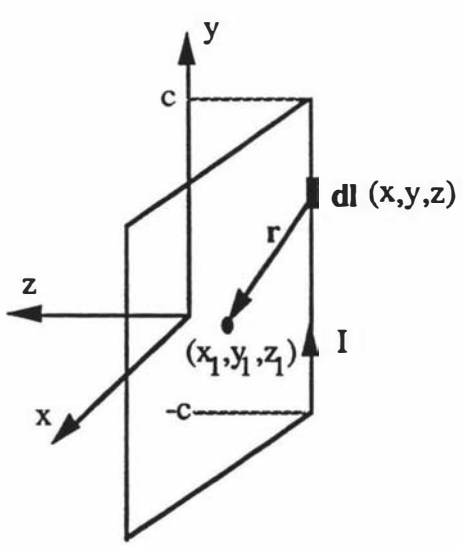

Figure 4.5

Magnetic field strength

$$\mathbf{B} = (\mu_0/4\pi)(Id\mathbf{l}\times\mathbf{r})/r3 \qquad [4.1]$$

where $d\mathbf{l} = dx\mathbf{i} + dy\mathbf{j}$ [4.2]

and $\mathbf{r} = (x_1-x)\mathbf{i} + (y_1-y)\mathbf{j} + (z_1-z)\mathbf{k}$ [4.3]

In Eq[4.2], the **i** term is the wire segment parallel with the x axis and the **j** term the y axis. Let us consider the **j** term first. Since $d\mathbf{l} = dy\mathbf{j}$ one has

$$dB_z = d(\mathbf{B}\cdot\mathbf{k})$$

$$= -\frac{\mu_0}{4\pi}\frac{Idy(x_1-x)}{[(x_1-x)2+(y_1-y)2+(z_1-z)2]3/2} \qquad [4.4]$$

Thus the field gradient at the field point (x_1,y_1,z_1) due to the current at the source point (x,y,z) is

$$G_{z|point} = \frac{\partial(dB_z)}{\partial z_1}$$

$$= \frac{3\mu_0 I}{4\pi}\frac{(x_1-x)(z_1-z)dy}{[(x_1-x)2+(y_1-y)2+(z_1-z)2]5/2} \qquad [4.5]$$

Integrating the above equation gives the field gradient at (x_1,y_1,z_1) due to an entire wire segment running from (-c, c) as

$$G_{z|line} = \int_{-c}^{c} G_{z|point}$$

$$= \frac{3\mu_0 I}{4\pi}(x_1-x)(z_1-z)\int_{-c}^{c}\frac{dy}{[(x_1-x)2+(y_1-y)2+(z_1-z)2]5/2} \qquad [4.6]$$

The result of the above integration can be shown to be

$$G_{z|line} = \frac{3\mu_0 I}{4\pi}\frac{(x_1-x)(z_1-z)}{[(x_1-x)2+(z_1-z)2]2}\left\{\frac{(y_1-c)}{[(x_1-x)2+(z_1-z)2+(y_1-c)2]1/2}\right.$$

$$-\frac{(y_1-c)^3}{3[(x_1-x)2+(z_1-z)2+(y_1-c)2]3/2} - \frac{(y_1+c)}{[(x_1-x)2+(z_1-z)2+(y_1+c)2]1/2}$$

$$\left.+\frac{(y_1+c)^3}{3[(x_1-x)2+(z_1-z)2+(y_1+c)2]3/2}\right\} \qquad [4.7]$$

The field gradient due to a wire segment parallel with the x axis can be calculated in a similar manner where $d\mathbf{l} = dx\mathbf{i}$, and the final result can be derived as:

$$G_{z\parallel line} = -\frac{3\mu_0 I}{4\pi}\frac{(y_1-y)(z_1-z)}{[(y_1-y)^2+(z_1-z)^2]^2}\left\{\frac{(x_1-c)}{[(y_1-y)^2+(z_1-z)^2+(x_1-c)^2]^{1/2}}\right.$$

$$-\frac{(x_1-c)^3}{3[(y_1-y)^2+(z_1-z)^2+(x_1-c)^2]^{3/2}}-\frac{(x_1+c)}{[(y_1-y)^2+(z_1-z)^2+(x_1+c)^2]^{1/2}}$$

$$\left.+\frac{(x_1+c)^3}{3[(y_1-y)^2+(z_1-z)^2+(x_1+c)^2]^{3/2}}\right\} \qquad [4.8]$$

Eq[4.7] and Eq[4.8] were used to simulate the field gradient strength and the orthogonal gradients for the Gz coil. A 10 turns square Helmholtz coil with a length of 23 mm per side with a separation of 23 mm and using Gauge 33 wire was built.

The optimum parameters for the planar coil have been given by Anderson[138]. He has pointed out that, once the separation between the two plans of the coil, $2Z_0$, is determined, $w=1.55Z_0$ and $Y_c=1.19Z_0$ give the optimum gradient uniformity. There is, however, some choice in the length of the coil, l, which is governed by a set of factors. Taking the G_y gradient coil for example. The wire segment parallel to the x axis is the main wire with a length of l, it is responsible for the generation of the desired field gradient, $G_y=\partial B_z/\partial y$. The wire segment parallel to the y axis is the return wire, with a length of w, which can actually produce a field gradient along the x direction, $G_x=\partial B_z/\partial x$. This G_x gradient generated by G_y coil is an error term and a longer l can reduce this undesired orthogonal gradient at the centre of the probe. A longer l also improves the uniformity of the field gradient but has little influence on the strength of the gradient. However, making l longer also increases the resistance and inductance of the coil, which are often limited by the available gradient power supply. The diameter of the wire could also be varied to make the resistance of the coil suitable for the power supply, but the small size of the gradient coil in this case, together with the desire for more turns, is a limiting factor in the choice of wire thickness. The following table lists some simulation results related to the choice of the coil length for a G_y planar coil.

Table 4.4 Choice of the coil length for a G_y planar coil

	l = 20 mm	l = 40 mm	l = 60 mm
G_y (T m^{-1} A^{-1})	7.55×10^{-2}	8.79×10^{-2}	8.84×10^{-2}
G_y % error	8.5	3.1	2.5
G_x (T m^{-1} A^{-1})	7.6×10^{-4}	1.2×10^{-4}	9.2×10^{-5}

Notes: 1: G_x and G_y are calculated at the centre of the probe.
2: The percentage error of G_y is at z=4mm.

(a) Gx coil (b) Gy coil

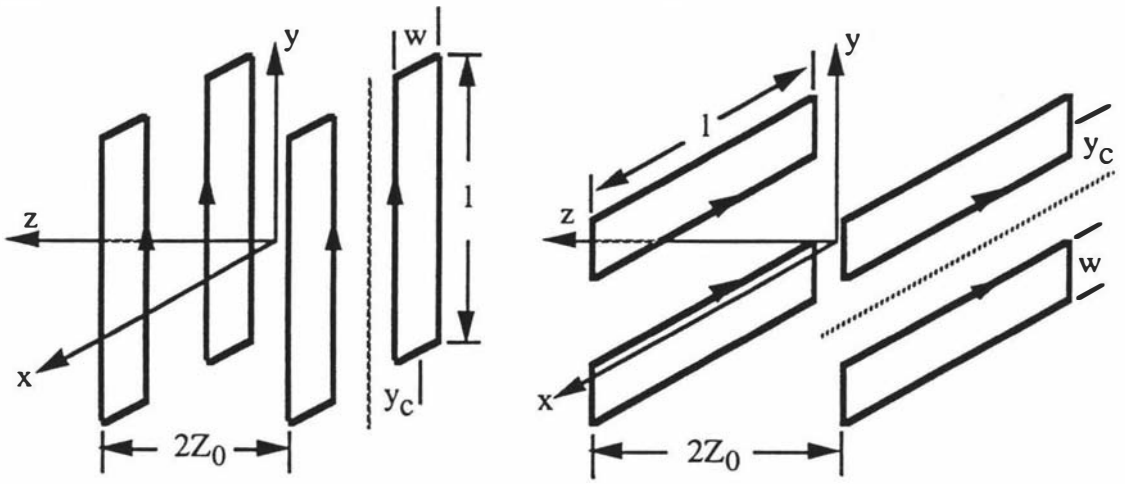

Figure 4.6 Planar coil geometry

The planar coils are shown schematically in Figure 4.6. The coils used to produce G_x and G_y are identical in terms of configuration with the only difference being a rotation of 90 degree in the x-y plan. Therefore the calculations is similar for both. The equations used to simulate the planar coil has been given in detail before[132], thus only the final results are given here.

For the G_y coil,

$$G_{yline} = \int_{-c}^{c} G_{ylpoint}$$

$$= \frac{\mu_0 I}{4\pi} \{ \frac{(y_1-y)2}{[(y_1-y)2+(z_1-z)2]2} [\frac{-(x_1-c)3}{[(x_1-c)2+(y_1-y)2+(z_1-z)2]3/2}$$

$$+ \frac{(x_1+c)3}{[(x_1+c)2+(y_1-y)2+(z_1-z)2]3/2}] + \frac{[(z_1-z)2-2(y_1-y)2]}{[(y_1-y)2+(z_1-z)2]2} [$$

$$\frac{-(x_1-c)}{[(x_1-c)2+(y_1-y)2+(z_1-z)2]1/2} + \frac{(x_1+c)}{[(x_1+c)2+(y_1-y)2+(z_1-z)2]1/2}] \}$$

[4.9]

for the field gradient at (x_1,y_1,z_1) due to an entire wire segment (-c,c), and for a return wire

$$G_{ylline} = \int_{-e_i}^{c_i} G_{ylpoint}$$

$$= \frac{\mu_0 I}{4\pi}(x_1-x)\{ \frac{1}{[(x_1-x)2+(y_1-c_i)2+(z_1-z)2]3/2} -$$

$$\frac{1}{[(x_1-x)2+(y_1-e_i)2+(z_1-z)2]3/2} \} \qquad [4.10]$$

where $c_i = y_c+w/2$ and $e_i=y_c-w/2$ (as in Figure 4.6).

Eq[4.9] and Eq[4.10] were used to calculate the field gradient strength and the orthogonal gradients for different choices of the G_x and G_y coils. For the G_x coil, a 12 turns planar coil with a length of 40 mm using Gauge 30 wire was finally chosen (y_c=14mm, w=18.3mm, z_0=11.8mm).

The design of the G_y coil was difficult because of the desired gradient strength and the coil dimensions. To obtain a stronger gradient, one has to reduce the size, i.e., scale down uniformly. This in turn limits the maximum number of turns one can have. It is found that this limitation can be compensated by the use of multi-layers instead of one layer (Figure 4.7) while keeping the same sized uniform region. Multi-layers however lead to much greater difficulties in winding the coil. A final choice for the G_y coil was to use three layers of planar coils, each on top of the other. Each coil layer has 7 turns so that the total number of turns is 21 with a separation of 10 mm and a length of 24 mm.

The uniform regions of these three gradient coils were simulated using the computer programs which can be found in Appendix A2. The results were checked to ensure that the uniform regions of each coil satisfies the non-distortion requirement in the dynamic imaging experiment.

4.2.3 Construction and calibration

The construction of the new imaging probe was fairly straightforward with the only real difficulty being in making the multi-layer G_y coil. The G_y coil is constructed on a solid perspex block and covered with a thin layer of Araldite. Attention was given to fixing the G_y coil block onto the copper probe body rigidly in order to eliminate any movement of the coil caused by the torque induced by the pulsed current. G_x and G_z

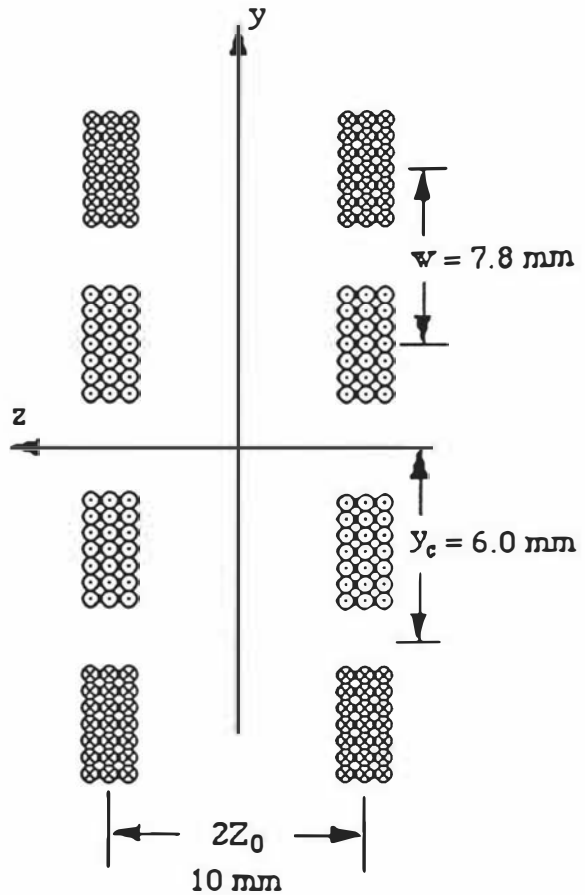

Figure 4.7

Three-layer Gy gradient coil for the new imaging probe

coils are wound directly on the interior-side of the probe side-panels (silver-coated pc board) and also covered with a layer of Araldite. Miniature sockets and plugs have been made, so that the probe side-panels can be separated from the probe body.

A 12 turn 2.1 mm i.d. rf coil was constructed using #28 Gauge copper wire within a perspex tube which was fitted into the G_y coil block and also fixed on the probe body. The rf and its turning circuit is similar to that used previously[132] and a Q factor of 40 was found for this circuit. Figure 4.8 shows the finished probe and its gradient coils.

The gradients were calibrated using the standard PGSE sequence to measure the diffusion coefficient for water. For a sample of known diffusion coefficient, if the supplied current is known, then the gradient strength of the coil can be calculated using the following equation (based on Eq[3.76])

$$G_2 = G_1 \sqrt{\frac{D_1}{D_2}} \qquad [4.11]$$

(a) the probe

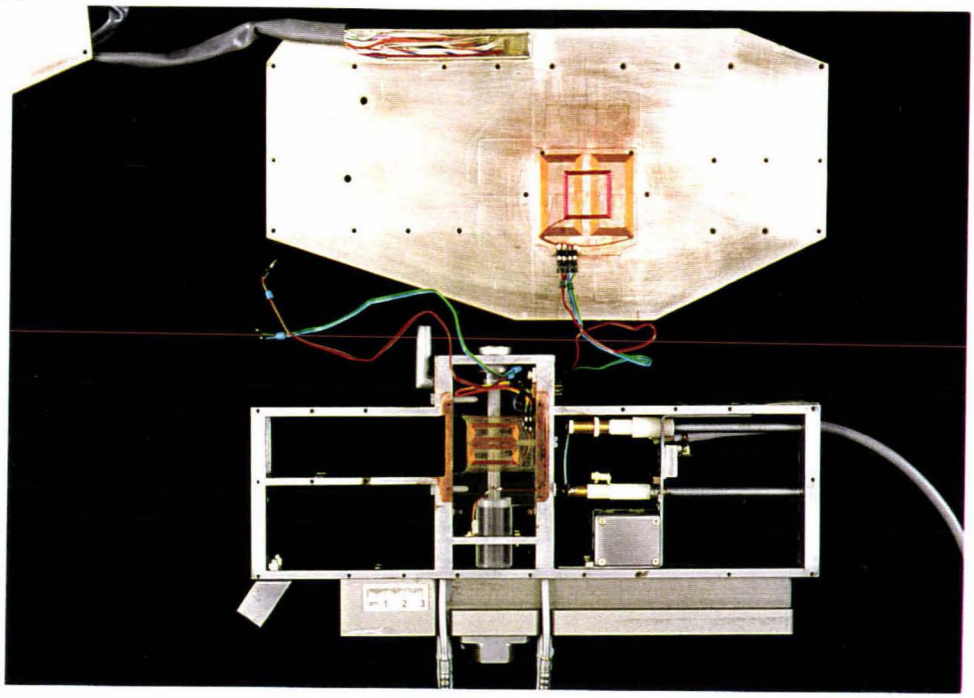

(b) the G_y coil

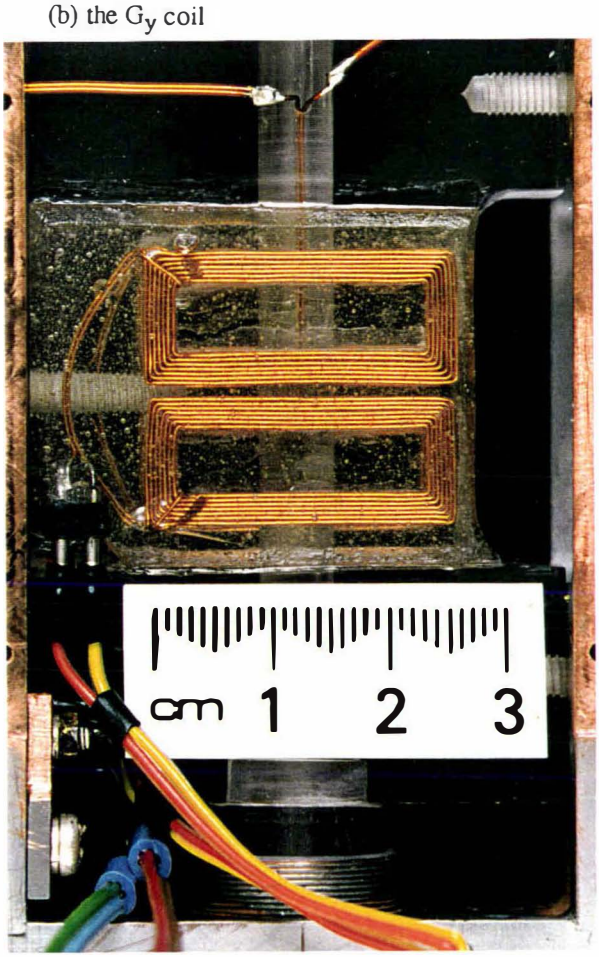

(c) the G_x and G_z coils

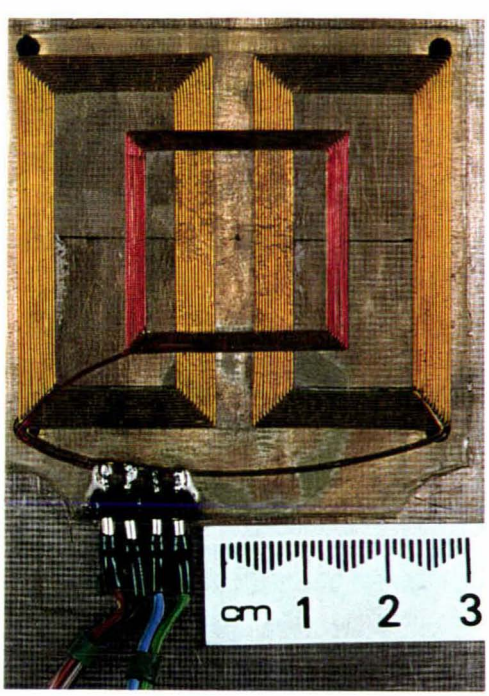

Figure 4.8 Photos showing the new 'super-G_y' imaging probe

where G_2 is the calibrated gradient and G_1 is the assumed gradient and D_1 is the measured self-diffusion coefficient and D_2 is the theoretical self-diffusion coefficient. D_2 was taken as 2.4×10^{-9} m^2s^{-1} which corresponds to a probe temperature around 27 °C. The following table gives some characteristics of the coils and field gradients for this new imaging probe.

Table 4.5 Characteristics of the Gradients

	G_x	G_y	G_z
Coil configuration	Planar	Planar	Helmholtz
Gauge of wire	30	30	33
Number of turns	12	3×7	10
Coil resistance (Ω)	1.48	1.31	0.71
Coil inductance (μH)	36.1	51.7	8.0
Resistance* (Ω)	1.8	1.6	1.0
Gradient$_{us}$ (G cm^{-1} A^{-1})	6.5	48.7	4.0
Gradient$_{uc}$ (G cm^{-1} A^{-1})	7.75	48.73	4.74
Gradient$_{max}$ (G cm^{-1})	31	731	47.4

Note 1, The gradients were determined at the centre of the coils.
2, Resistances and inductances were measured using a HP4192A LF Impedance Analyzer. The frequency was set to 1 kHz when measuring the inductances.
3, Resistance* were measured from the connecting plugs after the coils and the probe had been assembled.
4, Gradient$_{us}$ were the simulated unit gradients and Gradient$_{uc}$ were the calibrated unit gradients.
5, Gradient$_{max}$ were calculated using the power supplies listed in Table 4.1.

Some standard static micro-imaging experiments and dynamic imaging experiments using polymer samples were carried out using this new imaging probe. They have shown that the design of this special probe was successful. Details of results can be found in Ch 5, Ch 6 and Ch 9.

4.3 Imaging probe for plants

The electromagnet in the FX-60 micro-imaging system provides a geometry which is ideal for imaging some botanical samples, because of the easy longitudinal access and the ability to use solenoidal transverse rf coil. However, as discussed

previously (Ch 3.1), there are at least two difficulties which arise when measuring velocity and diffusion for plants. These are the delicate signal and the requirements to maintain a viable environment inside the probe. The viability condition requires a supply of fresh water, suitable light and the maintenance of constant temperature and humidity during the hour-long experiments.

This section describes the design and construction of a new imaging probe which was designed purposely to give the maximum available space inside the probe taking into consideration the requirements of imaging living botanical samples.

4.3.1 Design considerations

Imaging botanical samples *in vivo* is difficult! This difficulty arises from two requirements. First, NMR is a very insensitive technique and the highest sensitivity can be achieved only when the receiver coil is closely wound around the sample at the imaging position (higher filling factor), therefore the smallest possible rf coil is desirable. The second requirement of imaging botanical samples comes from the need to maintain a viable environment for the living (moving and growing) sample, which normally requires us to maintain a certain light level, temperature, humidity and to supply constantly some sort of 'liquid nutrient'. In Dynamic NMR Microscopy experiments, the situation generally becomes worse because a much larger gradient is required to measure the flow and/or diffusion. Therefore inside the probe, the gradient coils usually occupy most of the space surrounding the sample, leaving only a narrow pathway for loading the sample. This structure requires that one end of the sample has to be small enough to be able to pass through this narrow pathway (usually a hole).

In the experimental preparation of the Castor bean experiment (refer to Ch 7), the above two requirements became very demanding. The existing 'general purpose' imaging probe obviously didn't satisfy the above requirements, the space in the central part of the probe has been occupied by a 80 mm long solid cylindrical 'tube' which hosts the quadrupolar G_x and G_z coils (refer to Figure 4.3 in Ch 4.2). A similar problem occurs for the newly developed 'super G_y' imaging probe described in Ch 4.2 in which, again, the central space is occupied by the powerful G_y gradient coil. Because of the geometry of the electromagnet, the most efficient way of constructing a gradient coil is of the planar coil or the flat Maxwell pair configurations. Therefore the solution was to design a new imaging probe which maximizes useful space in the central part of the probe and provides a suitable loading pathway of botanical samples.

4.3.2 Construction and calibration

The construction of this new imaging probe utilized an original JEOL high resolution proton probe. All original components inside that high resolution probe were removed and extensive modifications were made on the probe copper body so as to give the access to the plants. Because there are no special requirements for the gradient coils, the mapping gradient coils, G_x and G_z, in this imaging probe were based on the same planar coil designs used in the 'super G_y' imaging probe. The G_y gradient coil has used the same planar coil design in the existing imaging probe[132]. The rf system also used the same circuit as in the 'super G_y' imaging probe but its position was relocated so that a larger central volume is available to accommodate the life-support system for plants. Three gradient coils were wound, by Professor Ken R. Jeffrey of the Physics Department, Guelph University, Ontario, Canada (a visitor to our research group), directly on the interior of the probe side-panels (silver-coated pc board) with the respective positions of G_y, G_z, G_x from the pc boards towards the inside. Some 0.5 mm thick copper sheets were used to gain the extra 1 mm space required. The connecting wires of the gradient coils were made deliberately long so that the miniature sockets and plugs of the coils didn't occupy the useful central space. Figure 4.9 shows the finished probe and gradient coils. The following table summarizes some of its characteristics.

Table 4.6 Characteristics of the Gradients

	G_x	G_y	G_z
Coil configuration	Planar	Planar	Helmholtz
Gauge of wire	30	32	33
Number of turns	12	15	10
Coil resistance (Ω)	1.6	2.0	1.2
Inductance* (μH)	40.5	51.9	14.2
Resistance* (Ω)	2.0	2.4	1.3
$Gradient_{us}$ (G cm^{-1} A^{-1})	6.5	9.3	4.0
$Gradient_{uc}$ (G cm^{-1} A^{-1})	7.75	9.36	4.74
$Gradient_{max}$ (G cm^{-1})	31	140	47.4

Note 1, The gradients were determined at the centre of the coils.

2, Resistance* and Inductance* were measured from the connecting plugs after the coils and the probe had been assembled.

3, $Gradient_{us}$ were the simulated unit gradients and $Gradient_{uc}$ were the calibrated unit gradients.

4, $Gradient_{max}$ is calculated using the power supplies listed in Table 4.1.

(a) the probe

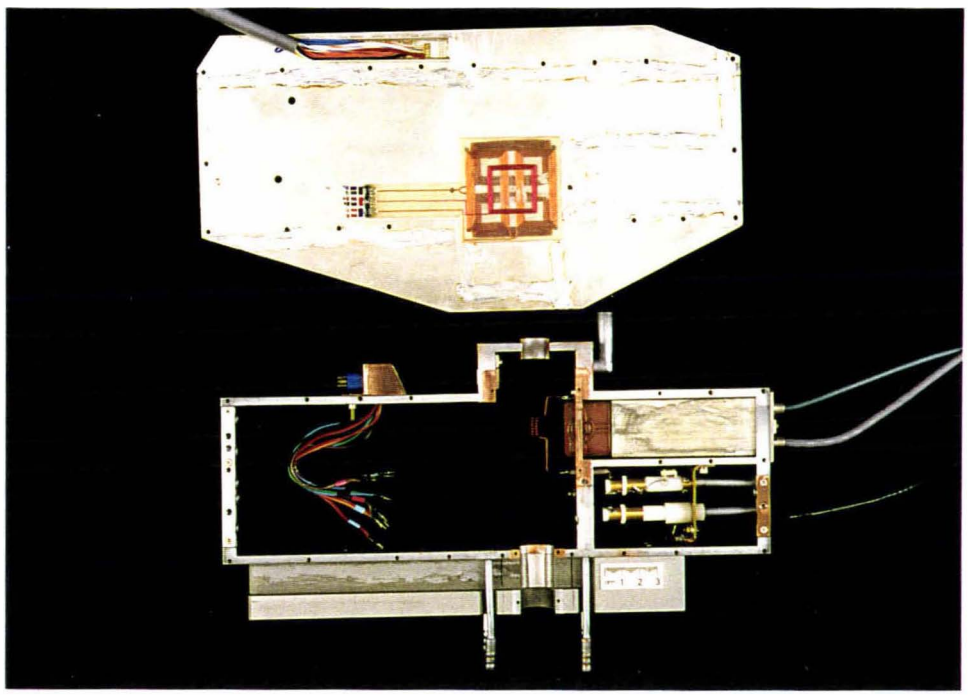

(b) the G_x, G_y and G_z coils

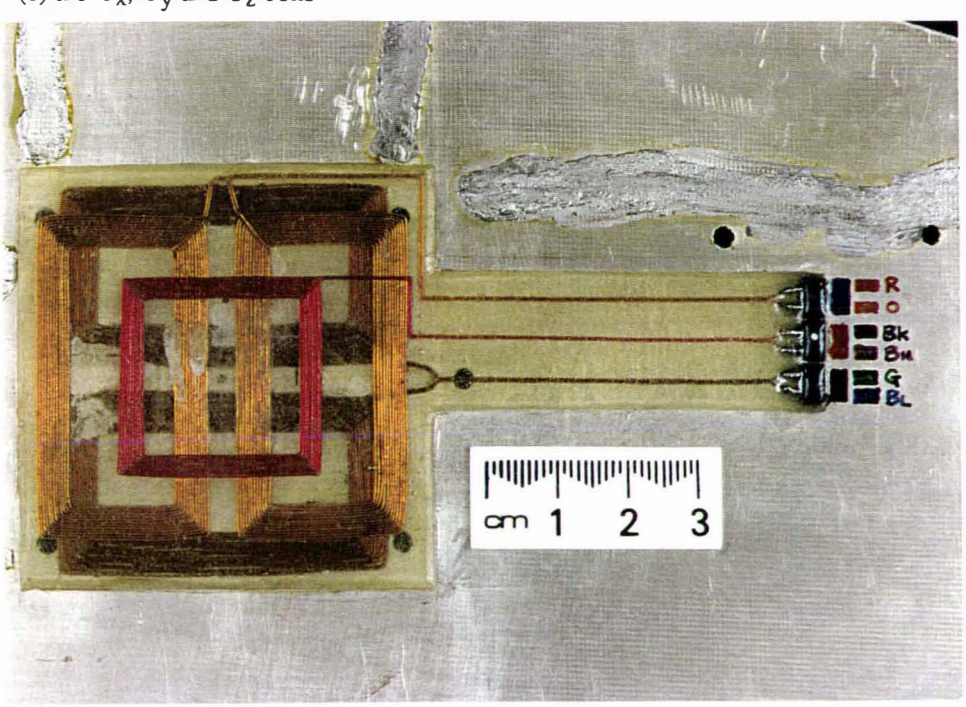

Figure 4.9 Photos showing the new plant-imaging probe

To carry out the Castor bean experiment, several sealed containers were designed and manufactured for this probe using 0.5 mm thick perspex sheet. Each container has a filling tube, an overflow tube and a drainage tube so that the fluid inside these containers can be changed easily during the experiment. An air bubbling system is also designed for this probe so to maintain the dissolved air level inside the fluid in these containers. Figure 4.10 shows schematically the cross sectional views of this new imaging probe for three possible experiments.

Both static and dynamic imaging experiments were carried out using this new imaging probe. They have shown that the design of this special probe is successful. Details of results can be found in Ch 5 and Ch 7.

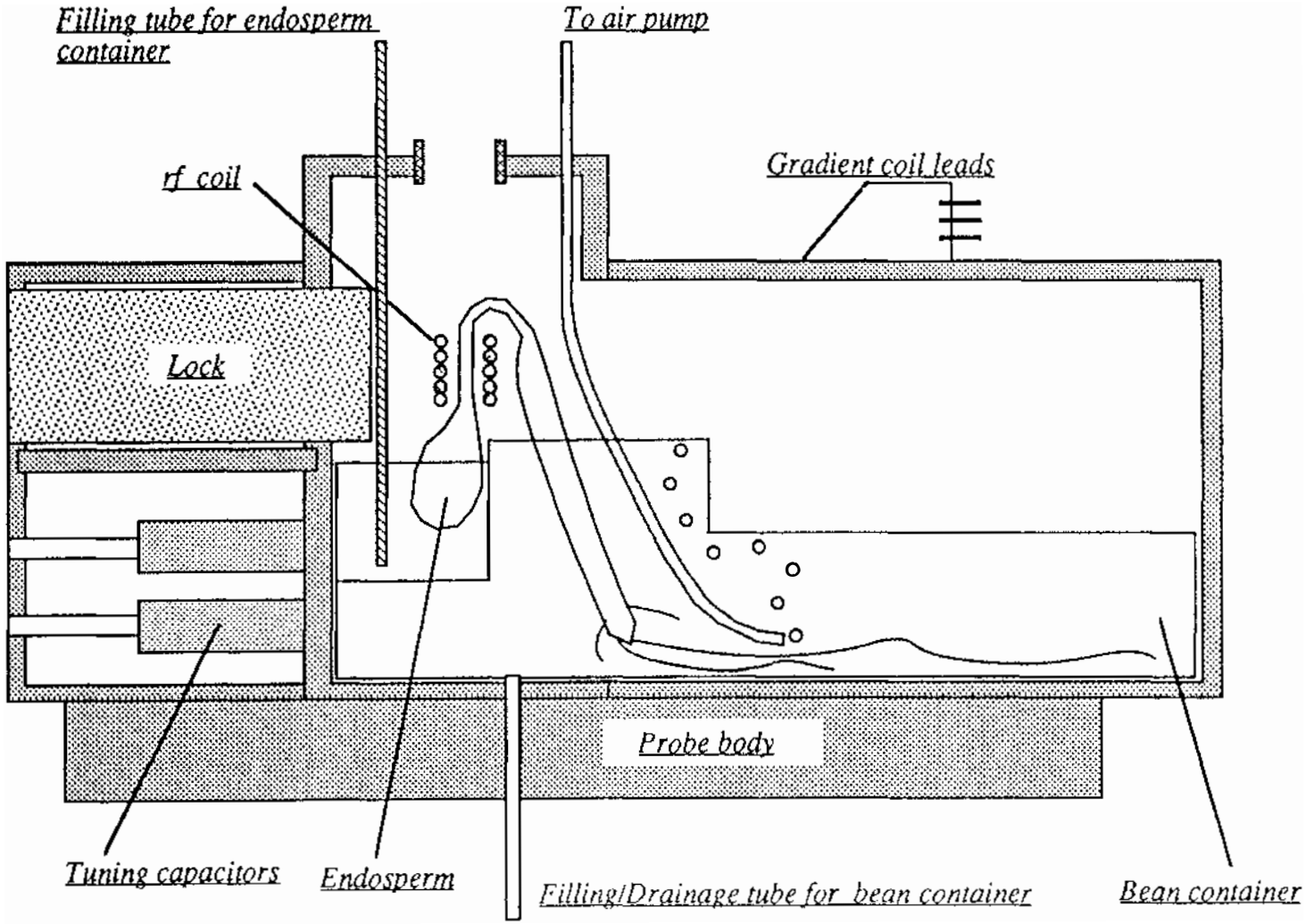

Figure 4.10a A schematic diagram showing imaging the 'hook' of a castor bean

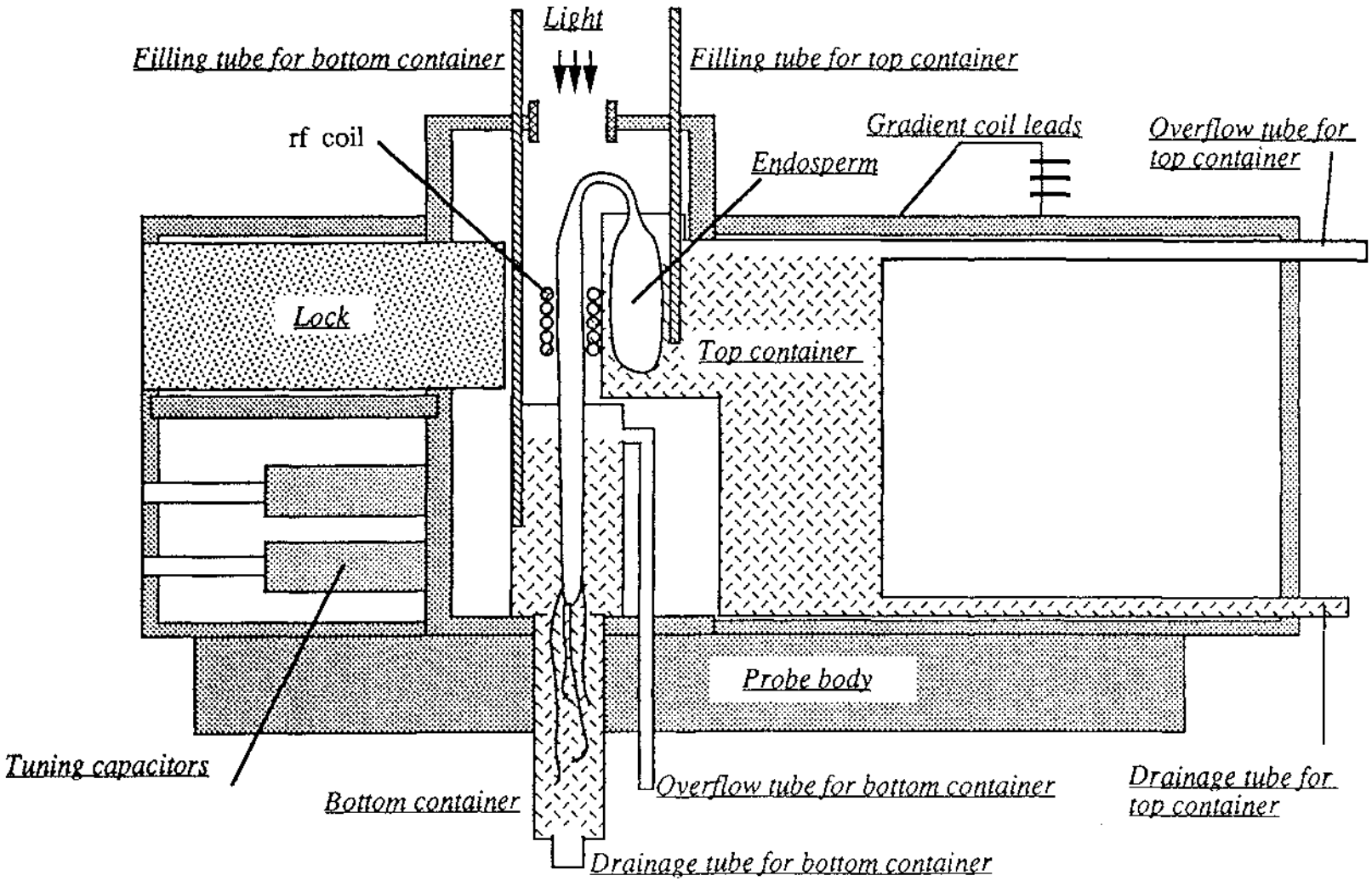

Figure 4.10b A schematic diagram showing imaging the hypocotyl of a castor bean

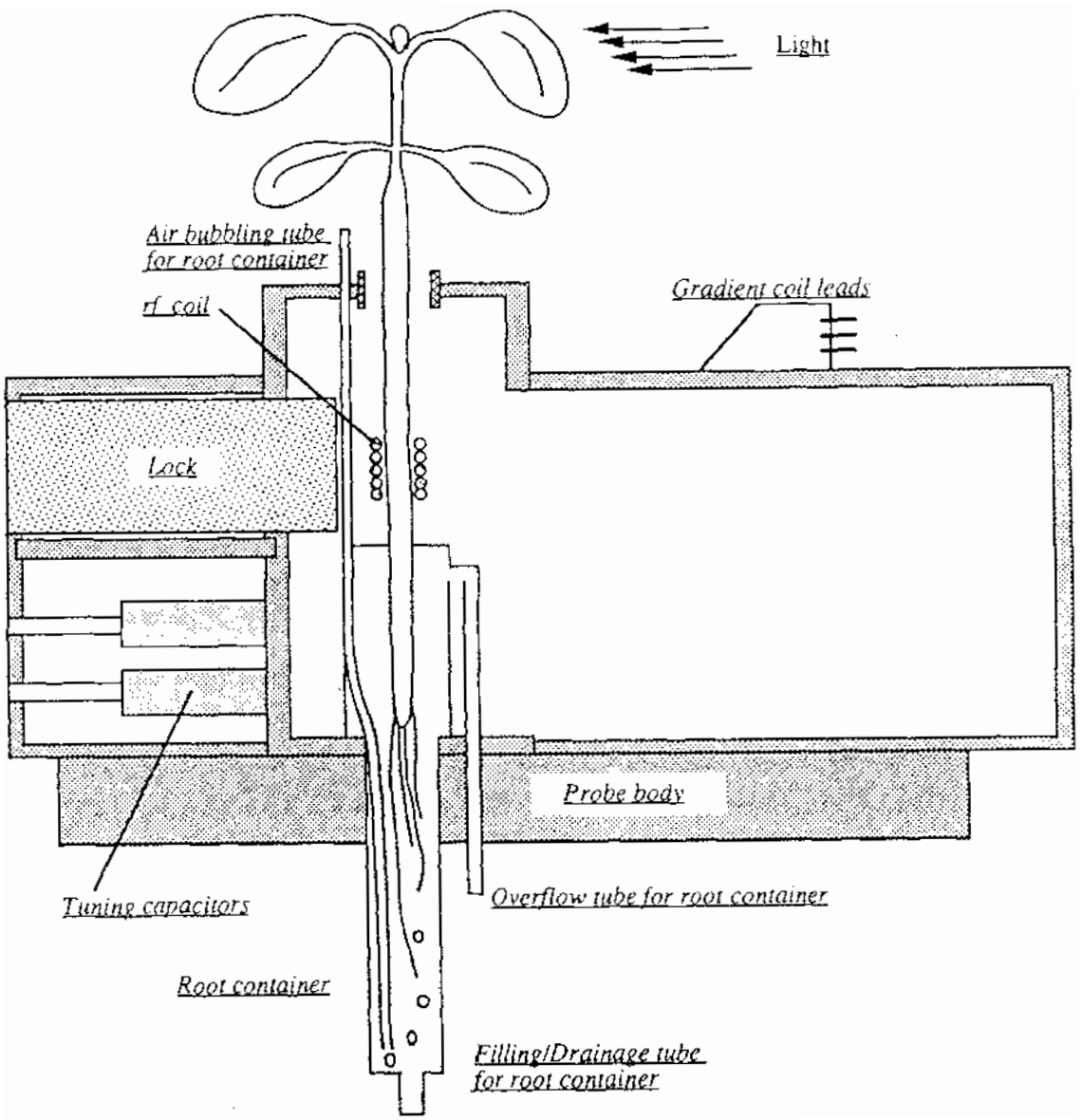

Figure 4.10c A schematic diagram showing imaging a mature castor bean

4.4 Software development for the TI-980A and Hitachi computers

Various software developments on the TI-980A and Hitachi computers have been undertaken either to improve the performance of the existing software or to carry out new experiments. In the FX-60 micro-imaging system, the signal acquisition and processing, including the FFT, are performed on the TI-980A computer and the image reconstruction and display are performed on the Hitachi computer. Some descriptions are given here for these software developments and the full listings of the associated code can be found in Appendix A1 and A2.

4.4.1 Software developments on the TI-980A computer

The TI-980A computer is an original part of the JEOL FX-60 spectrometer. This 16 bit computer is supported by an extensive assembly language software package, which provides various functions such as controlling pulse timing and phase, collecting and averaging data, analyzing data including apodization filtering, integration and Fourier transformation. A complete listing of the assembly language source code has been generously supplied by JEOL Ltd, but without detailed documentation. This fact, together with previous extensive modifications made by other people in this laboratory, has made a 'quick' and clear understanding of the software very difficult. One more difficulty in understanding the TI-980A software arises from the fact that this computer has no disassembler package and therefore any modification has to be done at the machine code level. Figure 4.11 gives a brief flow chart of the imaging software on the TI-980A computer. The procedures inside the dash-line box are required by one static imaging experiment while these together with all other procedures are required in a Dynamic NMR Microscopy experiment. A manual restart is required, following the dash-line arrows, for repeating the dynamic imaging experiment.

Quadrant phase compensation

In an imaging experiment, the mapping gradients, **k**, are required to cover at least two quadrants so that the direction of the gradient has to be switched during an experiment as well as the strength of gradient to be varied. The phase of the signal can be set correctly in one direction of the gradient but it may be (slightly) out of phase in the opposite direction of the gradient. This type of distortion is due to the imperfections of the field gradient, and could be worse in a flow imaging experiment where a full four quadrant sampling is required.

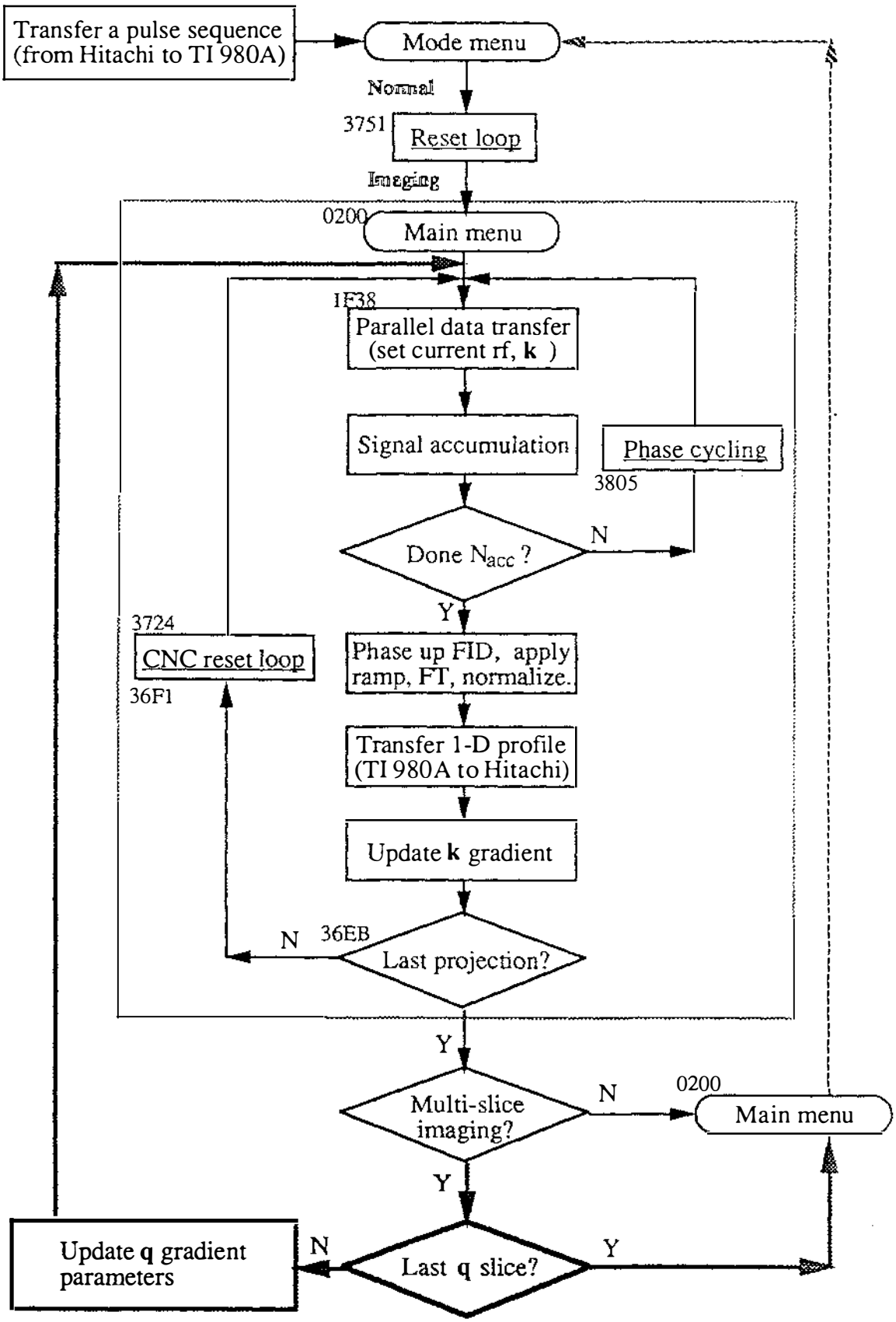

Fig 4.11 A brief flow ch a for the imaging software in TI-980A computer

There seems no simple way to eliminate the origin of this distortion except to compensate it in the software. Ideally, to compensate this type of distortion, one should examine the phase shift at each projection angle throughout the four quadrants and record them in a table so that they can be used to phase-adjust the echo during an experiment. But this ideal solution would be not only very time consuming but also impractical because this phase shift is dependent on the strength of the mapping gradient for a particular experiment.

Considering the fact that the difference of these phase shifts are normally fairly small, the compensation procedure in a flow imaging experiment was simplified as follows. First the phase is set correctly for the **k** vector at zero degrees. Then three different (and compromised) phase values for the mapping vector in the remaining three quadrants were recorded. During the updating of the **k** vector in an experiment, the software will check the current quadrant and override the spectrometer phase setting by using an appropriate phase value recorded beforehand. This method has proven very successful. A list of the routine can be found in Appendix A1.

One-shot velocity imaging

RF and gradient phase cycling are required in the 'one-shot' velocity imaging experiment proposed in Ch 3.7. Using the Table 3.5 in Ch 3.7, this cycling is performed in four steps and various modifications have been made to the existing static imaging software (within the underlined procedures in Figure 4.11). At the moment, to perform one experiment, two versions of software are required with the difference in the phase cycling procedure. Figure 4.12 shows the steps involved in the phase cycling procedure of the velocity-encoding version of the software, while the complete list of the various modifications can be found in Appendix A1. The gradient phase cycling is carried out by setting a spare bit of the '04' register. The ON/OFF state of this TTL output is used to trigger a simple relay circuit (see Figure 6.3).

Other modifications

There are other small modifications to the TI-980A software. For example, to switch an rf pulse ON/OFF during an imaging experiment measuring the transverse velocity and to reconstruct the complex image pair simultaneously at the 128×128 array size *etc.* These modifications are also listed in Appendix A1.

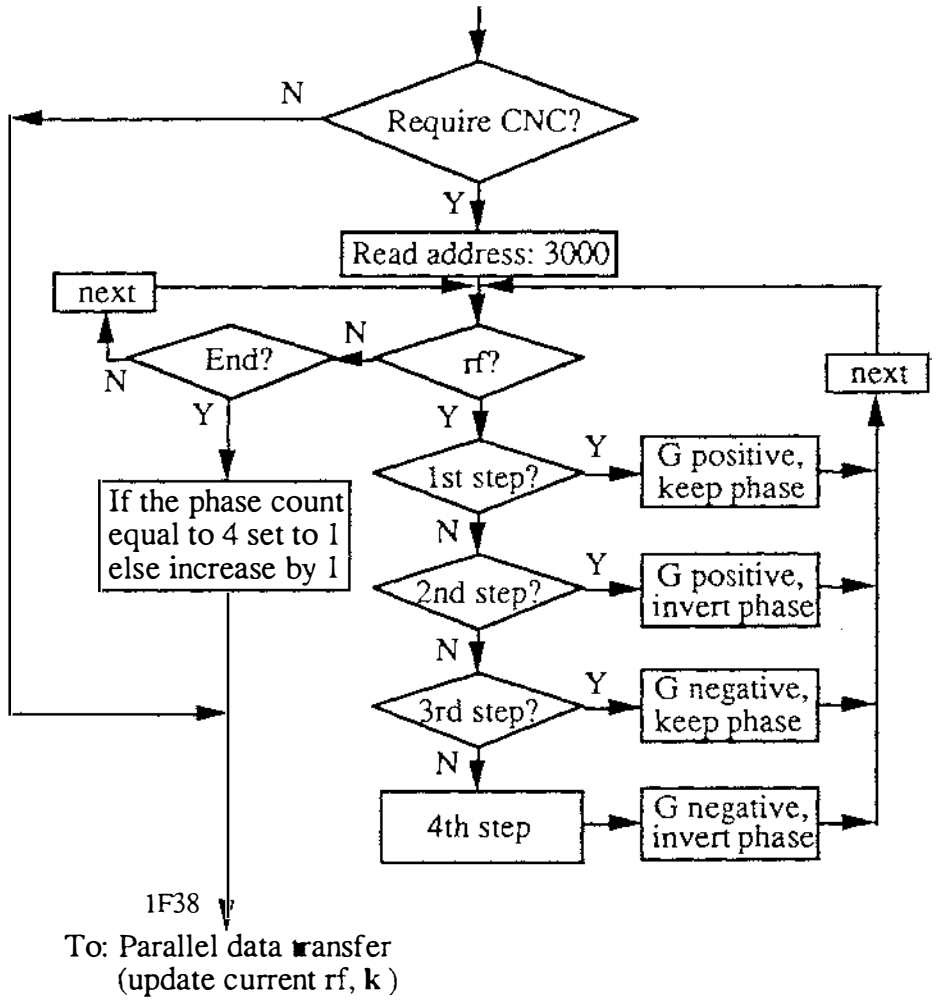

Figure 4.12 Flow chart for the phase cycling loop in the velocity-sensitive version

4.4.2 Software developments on the Hitachi computer

Various modifications have also been carried out on the Hitachi computer based on programs used previously[132, 137]. For example, to image the complex image pair for a 128×128 array, various subroutines were written using the Intel 8088 assembly and FORTRAN languages. There are also modifications for the image display and analysis software (PICTURE.FOR), for the pulse generating software (PULSE.BAS) and for the image reconstruction software (FBP.FOR). Some image transfer software has also been written on the Hitachi computer to send the data out through the RS232C port to the modem port of the Macintosh computer. Appendix A2 lists some of the software written.

4.5 Software development for the Macintosh computer: ImageShow™

A major part of the imaging system development was the introduction of Macintosh computers and consequently, the software developments for the Macintosh. In the following text, an 'historical' review of this development is given first and then detailed descriptions of the full program and various function routines are given in terms of the human-computer interface. A listing of the complete source code for the software can be found in Appendix A3.

4.5.1 An introduction to the development of ImageShow™

The original FX-60 imaging system used an Hitachi MB16000 personal computer for image reconstruction, display and analysis, and several major pieces of software(for example, FBP and PICTURE[137], FLOW, FLOWA and FLOWD[132]) were written to perform these tasks. Although the graphics capability of the Hitachi monitor (64 d.p.i., 640×400 pixels and 3×1-bit depth per pixel, 8 out of 16 colours simultaneously; or 320×200 and 16 out of 16 colours simultaneously) is still acceptable to complete these tasks, the computer itself limits further developments because it is based on Intel 8088 CPU, running at 4.77 MHz clock frequency and equipped with only 256 kbytes of RAM. To speed up operations, numerous assembly routines were written to perform various graphics tasks, including such simple procedures as drawing a line on the screen. Obviously, it has been essential to upgrade the Hitachi system.

One logical choice would have been to remain in the IBM family so that most of the software could have been utilised in the new computer (although it should be noted that Hitachi has stopped manufacturing and the graphics arrangement of other IBM systems are different from that of the Hitachi). Instead of that 'natural' choice, it was decided to choose the Macintosh computer, because it is a fast, menu-driven graphics-orientated computer with a high resolution 13 inch colour monitor (72 d.p.i., 640×480 pixels and 3×8-bit depth per pixel with 256 colours out of 16 millions simultaneously on the screen). More importantly, it has a 256 kbytes ROM chip which hosts all of the necessary graphics routines and functions. It is interesting to note that the VGA monitor for the IBM computer has similar specifications to the Macintosh colour monitor and one can buy an IBM compatible computer for less than half the price paid for a Macintosh. However the IBM computer doesn't have all the graphics routines and functions built-in.

Software development on the Macintosh started with Yang Xia using Language Systems™ FORTRAN since FORTRAN had been used on the Hitachi computer. It was discovered however that this FORTRAN wasn't suitable for our tasks on the Macintosh because it requires special prefixes whenever one wishes to pass variables, making the program very awkward!

There is a programming package called MPW™ Shell (Macintosh Programming Workshop) available for the Macintosh. It is an application package which provides an integrated, window-based environment for program editing, compiling, linking and execution. Many programming languages are available to be run within the MPW™ environment. After some investigation, MPW™ PASCAL was chosen because the original operation system and function calls in the Macintosh's ROM are written in PASCAL (this has changed recently since Apple company has rewritten its operation system using C++ for System 7!). It is never trivial to write software for the Macintosh, or more accurately, to write software for the Macintosh using the Macintosh philosophy[140]! This is because ideal Macintosh applications are supposed to be self-explanatory, menu-driven and with input in a dialogue-box. Software complexity is the price paid for user friendliness! The initial work on ImageShow™ was carried out by Yang Xia who explored methods needed to work with a colour window, set up menus, define various colour scales and so on. Then Andrew Coy joined the research group, and explored how to program in the Macintosh way (i.e. to use the bit-map graphics, the colour palette, and deal with dialogue boxes, ...). During Andrew's one year absence in Africa, Yang Xia continued the development of the current version of ImageShow™ which now has more than 8000 lines of source code. At the same time, Paul Callaghan also wrote a few routines for image processing. The software is still continuing to expand. Therefore ImageShow™ is really a result of a team effort!

For complete documentation, a full description of the software code is given. The author(s) responsible for each particular routine is clearly stated. It should be noted that ImageShow™ was designed to process images reconstructed using the Hitachi computer. Due to the non-square pixel size on the original Hitachi graphics screen, one has to display less pixels on the longer side of the pixel dimension so that a square image can be displayed on the screen as square. But pixels on a Macintosh screen are indeed square. To be compatible with the old non-square images and the new square images, there are two versions of ImageShow™ (with a bit of extra effort, one can easily combine the two versions into one, but it hasn't been done yet). The following description is based on the better-written square version.

Some conventions used in the following descriptions

The outlined word (for example, Image) indicates the title of each menu as its appearance in the menu bar while the underlined and bold word (for example, **Open**) means an individual menu item (actually an operation command). The high-lighted radio controls (circular) or buttons (squared or rectangular) indicate the default responses which occur upon pressing the return key. The default parameter settings are chosen so that a default response will be either the most convenient or least 'harmful' one. The name 'slice' refers to a row of image pixels (a cross sectional profile) across the image horizontally. The italic words with arrows in the following diagrams provide additional explanations.

4.5.2 A broad description of ImageShow™

ImageShow™ can be started by double clicking on the icon (shown to the right). After confronting a copyright statement, one can get into the program by means of the menu bar shown below:

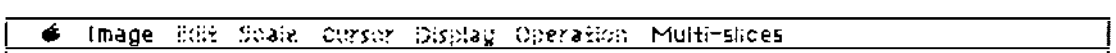

Apart from the usual apple symbol, , which gives access to various desk accessories, there are only two menus enabled initially, Image and Multi-slices (the disabled menu items indicated in a greyed style). By selecting **Open** from Image menu, one opens one image at a time. After having opened one image, all the other menus are enabled so that further analysis can be carried out. The other entry is by selecting one of the menu items from Multi-slices menu, this operation opens a series of images in some required sequence. For example, velocity and self-diffusion images can be constructed and analyzed using the Multi-slices menu. The methods used to get correct sequences of the images can be found in the relevant sections.

An image

The image data format required by ImageShow™ is of the "IMGE" type, which has an icon as shown at the right. This file format is a long queue of data points with the beginning of the (n+1)th 'slice' directly following the end of the nth 'slice' (n=1,2,...). For example, in a 64×64 image data set, the first pixel (on the top left corner) is labelled #0 (offset equals zero), the top right corner pixel is #63, the first pixel on the next line down is #64, ..., the last pixel on the bottom right corner is therefore #8191. Each pixel on an image has a dynamic range of

-32767 to +32767 in digits. This version of ImageShow™ supports 64×64, 128×128 and 256×256 images.

Each image, opened on the screen in a window, has both a raw data and a bit map in the memory. Any operation is based on the values of the raw data but presented in the bit map and drawn on the screen in a window. Therefore the original raw data is never altered (except in one special operation). Each image is also associated with a colour scale and there are some default settings of the colour scales. Apart from the data images opened from Multi-slices, the colour scale is always displayed next to the image in a separate window. The size of the image window and the colour scale window can be changed by dragging the bottom right-hand corner of the windows. ImageShow™ supports multi windows, so one can open as many windows as one like. For this version of ImageShow™ there is a maximum limit of 40 windows one can open at one time although the only limitation is the computer RAM size.

The following are the various pull-down menus available in ImageShow™(version 4.0). The menu Edit is required by the Macintosh computer but not available in ImageShow™ so that it is greyed.


About ImageShow...

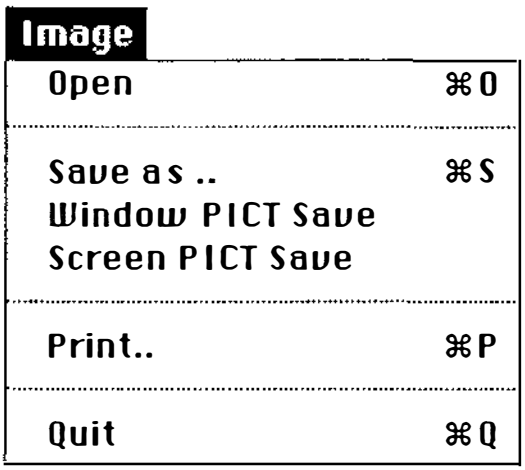
Image
Open ⌘O
Save as .. ⌘S
Window PICT Save
Screen PICT Save
Print.. ⌘P
Quit ⌘Q

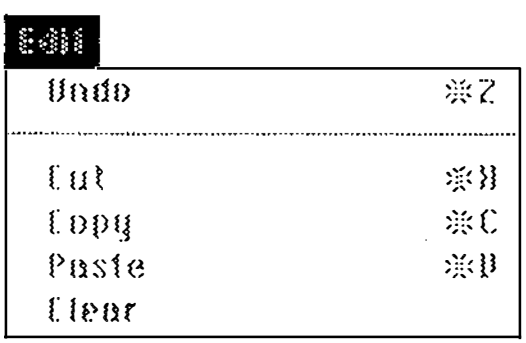
Edit
Undo ⌘Z
Cut ⌘X
Copy ⌘C
Paste ⌘V
Clear

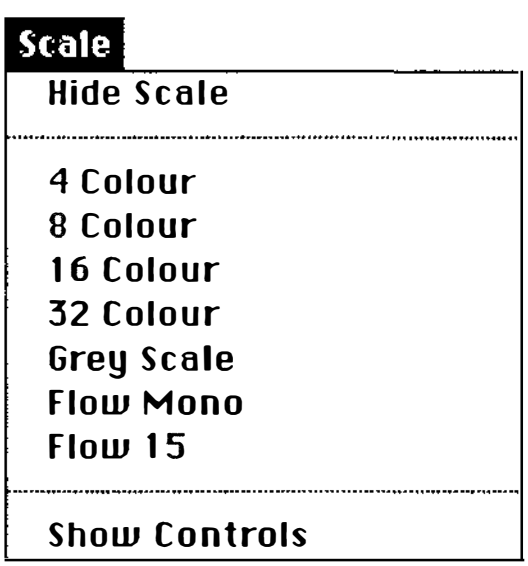
Scale
Hide Scale
4 Colour
8 Colour
16 Colour
32 Colour
Grey Scale
Flow Mono
Flow 15
Show Controls

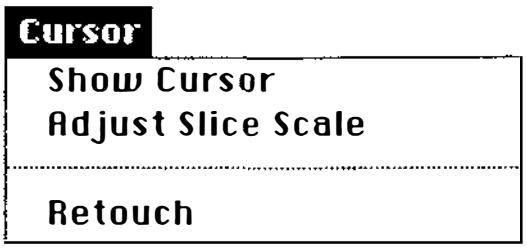
Cursor
Show Cursor
Adjust Slice Scale
Retouch

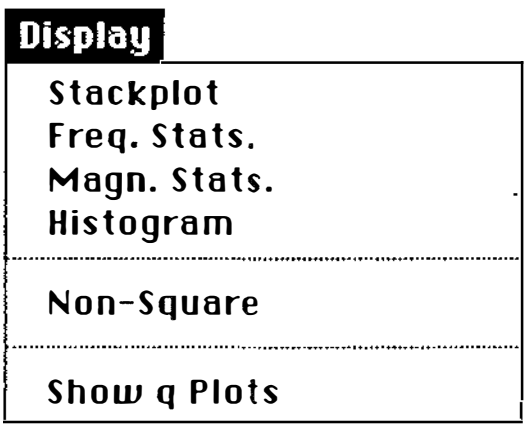
Display
Stackplot
Freq. Stats.
Magn. Stats.
Histogram
Non-Square
Show q Plots

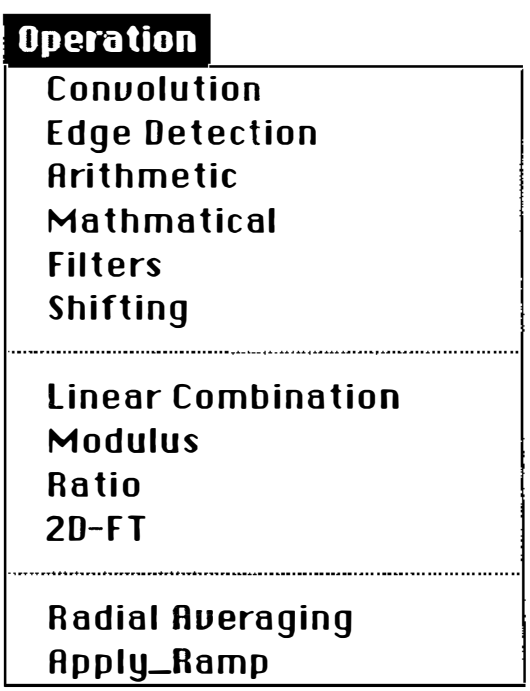
Operation
Convolution
Edge Detection
Arithmetic
Mathmatical
Filters
Shifting
Linear Combination
Modulus
Ratio
2D-FT
Radial Averaging
Apply_Ramp

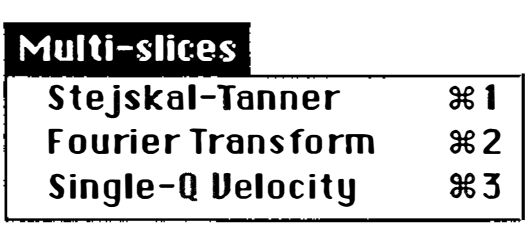
Multi-slices
Stejskal-Tanner ⌘1
Fourier Transform ⌘2
Single-Q Velocity ⌘3

4.5.3 Description of image presentation and display routines

Open in Image (written by Andrew Coy and Yang Xia)

This routine opens image files with the type "IMGE". A standard dialogue box appears (shown at the right) which displays all the available files (the type IMGE) in that particular folder (directory). The selected image file is highlighted.

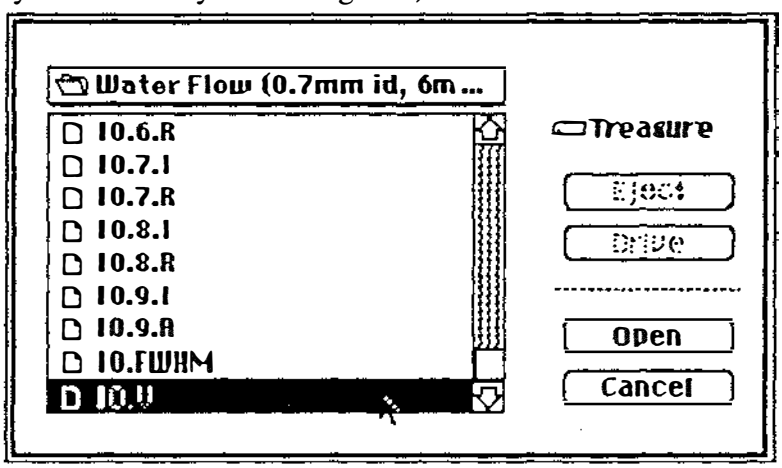

By clicking the 'Open' button or double clicking the highlighted file name, one can open that image. If the image array size is not 64×64, 128×128 or 256×256, a dialogue box will appear to indicate that an 'unconventional' size has been encountered.

Save as in Image (written by Andrew Coy and Yang Xia)

This routine operates in two modes: firstly a dialogue box appears which is asking for the name of the image to be saved, if no slice is plotted on the screen, it will save the image in the current window using the type "IMGE" ; but if there is a slice drawn on the bottom of the screen, it will save a CricketGraph™ data file of multiple slices around the current cursor position (see Show Cursor below for details of this mode). The statement above the name box indicates which mode it is.

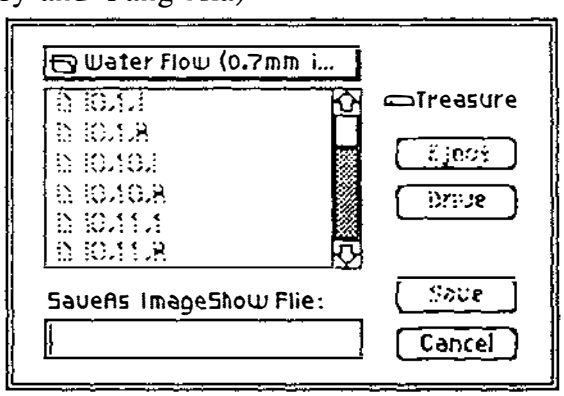

Window PICT Save in Image (written by Andrew Coy)

This routine saves the current image using the PICT format so that it can be opened by other commercial graphics software such as PixelPaint™, Studio/8™ or Canvas™.

Screen PICT Save in **Image** (written by Andrew Coy)

This routine saves the complete screen as a PICT file. It can be used to prepare a page showing several images for visual presentations and publications.

Print in **Image** (written by Yang Xia and Andrew Coy)

This routine opens a standard Macintosh printing dialogue box, but operates in several modes. It will (1) print a cross-sectional slice of an image if it is in **Show Cursor** and there is a slice window on the bottom of the screen, (2) print a multi-slice linear regression and FFT plots if it is in **Show q-Space Plots**, (3) print the statistical information if it is in **Freq. Stats.** or **Magn. Stats.**, (4) print a histogram if it is in **Histogram**, or (5) print an image in the current window. The quality of the hard copy of the image is dependent upon the type of printer available. A better quality copy can be obtained by first saving the image into a PICT format and then using a high d.p.i. printers such as colour laser printer. In Mode (1) printing a cross-sectional slice of an image, there is an option of either NORMAL (print each pixel as a single dot) or VECTOR (print a profile which joins all the pixels together).

Quit in **Image** (written by Yang Xia and Andrew Coy)

Return to finder.

Hide Scale in **Scale** (written by Andrew Coy)

Hide the colour scale of the current window (**Show Scale** will bring it back).

4 Colour ~ **Flow 15** in **Scale** (written by Yang Xia and Andrew Coy)

The colour scales that are available for selection are shown. Normally the default is set at **32 colour**, but it is set at **Flow 15** for the data images opened from the **Stejskal-Tanner** or **Fourier Transform** menu items.

Show Controls in **Scale** (written by Andrew Coy)

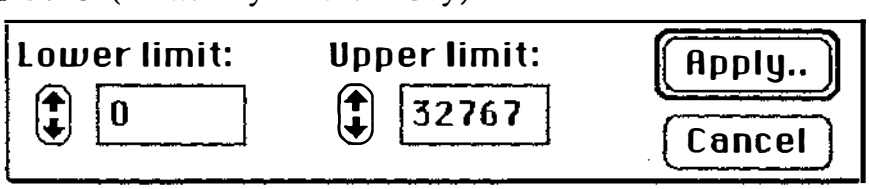

This routine is used for adjusting the upper limit and base value for the current image. The initial default settings are dependent upon the maximum and minimum values founded in an image file. The **Flow Mono** or **Flow 15** scales are designed specifically for displaying both positive and negative values so that the lower limit should be equal to the upper limit. To change a value, one can either type the number required into the appropriate boxes or click the up or down arrow. The

number is changed in steps of 1000 each time the up or down arrow has been clicked. Clicking the "Cancel' button to exit.

Show Cursor in Cursor (written by Yang Xia)

When Show Cursor is selected from the menu, a separate slice window appears at the bottom of the screen. When the cursor (now a cross cursor) is placed in any position inside the image, the bottom window will show the current cursor coordinates and the pixel value, a slice horizontally cross the image will also be drawn. The red dot on the slice indicates the cursor position. The plot of the current slice can be printed using the Print menu item, or values of the current slice plus another nine neighbouring slices (total five horizontal and five vertical ones) can be saved as a CricketGraph™ file for further analysis by selecting Save as in the Image menu. Select Hide Cursor to finish.

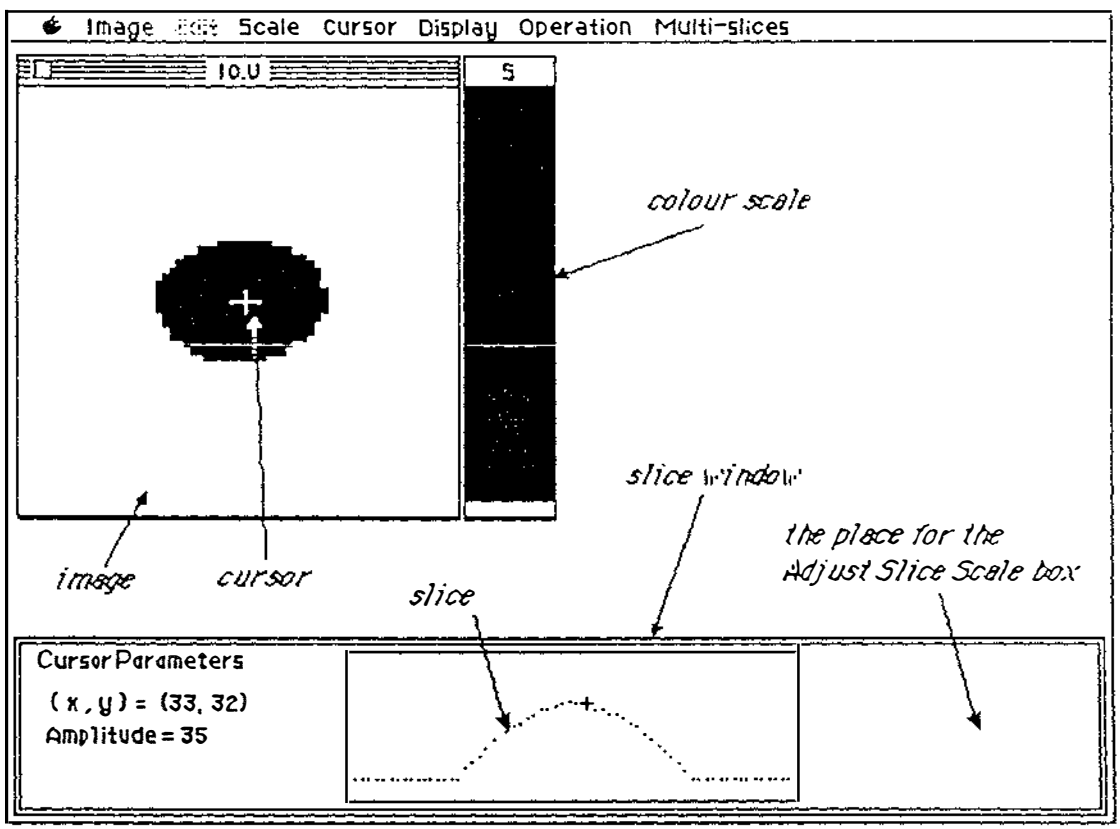

Adjust Slice Scale in Cursor (written by Yang Xia)

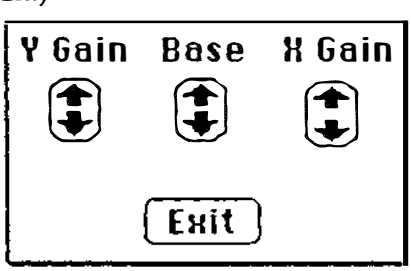

This is used to adjust the default settings used to draw slice. After selecting this menu item, a small dialogue box will appear at the right hand side of the slice window (as shown in the above). By clicking up or down arrows, the slice can be expanded in both vertical and horizontal directions. The baseline of the

slice can also be adjusted. The expansion along the horizontal direction is centred at the cursor position. Click the 'Exit' button to quit the adjust mode.

Stackplot in Display (written by Yang Xia and Paul Callaghan)

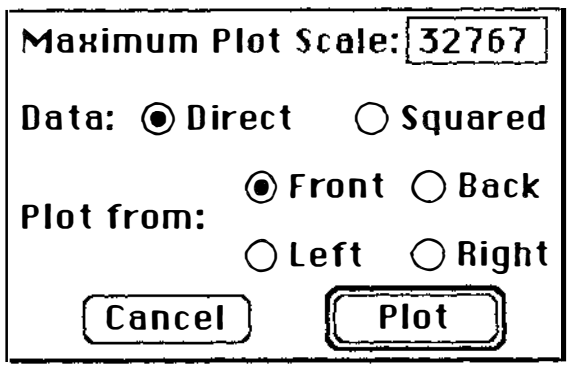

This routine makes a stacked plot of the current image. The maximum plot scale should be adjusted according to the maximum pixel value in the current image. During plotting, the pixels can be plotted either directly or squared the value beforehand (the use of squared data is fairly rare). The image can be plotted from one of four different directions. The stacked plot can also be saved as a PICT format file using Window PICT Save in the Image menu.

Non-Square in Display (written by Andrew Coy)

A square format is the initial setting of the display window. To change to a non-square format, select Non-Square and then drag the bottom right corner of the image window to resize it. Select Square to change a non-square window to a square format.

4.5.4 Description of image processing routines

Convolution in Operation (written by Paul Callaghan and Yang Xia)

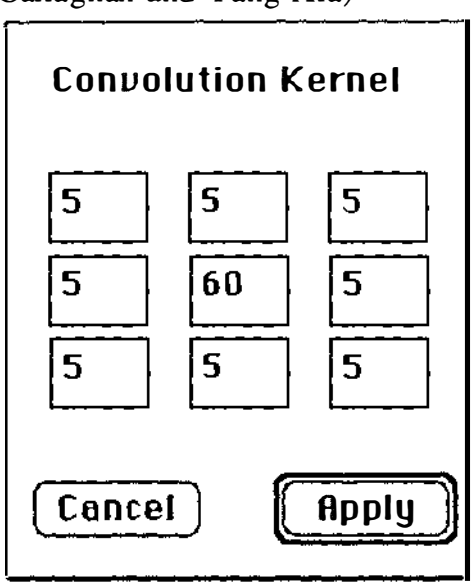

This routine performs a convolution of the current image with a filter function. Applying a convolution in the frequency domain (on an image) is equivalent to multiplying by a filter function in the time domain (while acquiring FIDs in the spectrometer). There are various algorithms available in the image processing literature. A very basic one is chosen here which is formed by a 3 by 3 matrix. For a default setting (as shown in the right), each pixel is assigned with 60% of its original value and 5% from each of eight neighbouring pixels. The

default setting can be adjusted as desired but the sum of the numbers in all nine pixels should equal to 100. The larger the central value becomes, the less the convolution effects the original image.

Edge Detection in **Operation** (written by Paul Callaghan and Yang Xia)

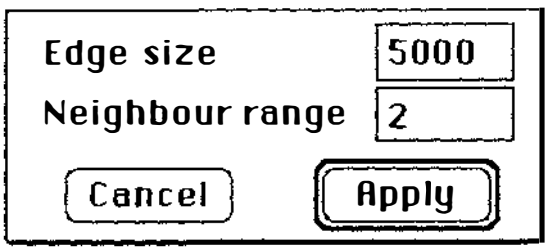

This routine detects the edge of the current image. The algorithm employed in this routine uses the specified edge size and neighbour range while checking through the entire image. If any two pixels within the neighbour range have a magnitude difference over the specified size, it is treated as an edge of the image and assigned a maximum (32767), otherwise it is assigned a value of zero.

Filters in **Operation** (written by Yang Xia)

This routine can apply a high-pass, low-pass or band-pass filter to the current image. The unit of these numbers is simply the amplitude of pixel intensity.

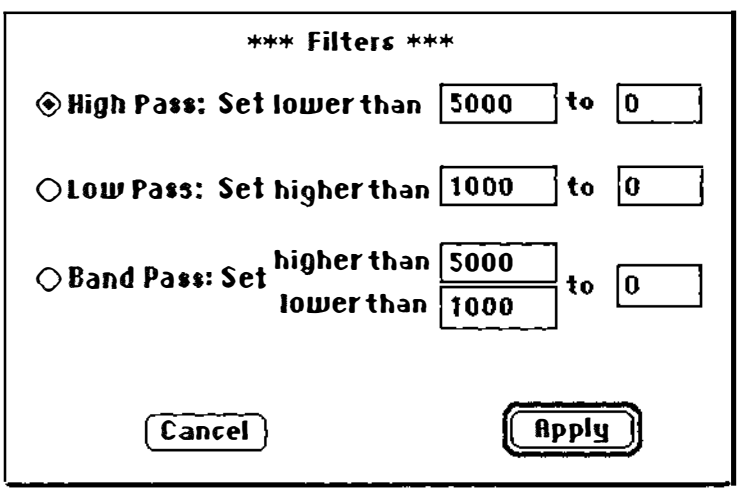

Shifting in **Operation** (written by Yang Xia)

This routine moves the image up, down, towards the left or towards the right within the current window. The number entered is the number of pixels to be shifted.

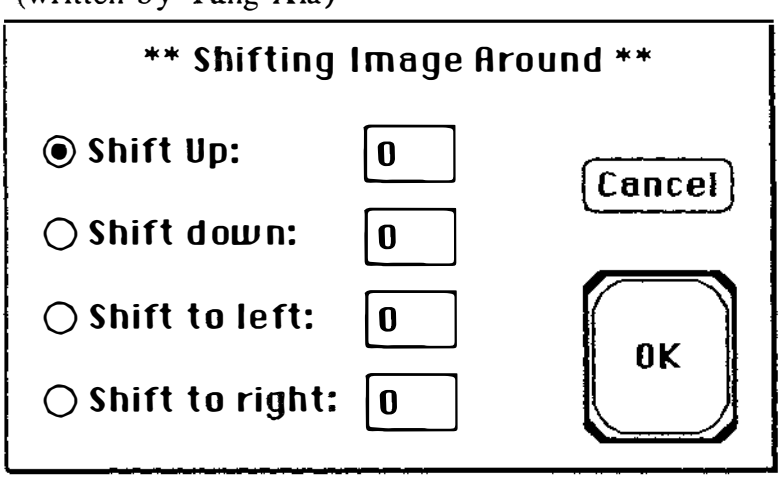

Linear Combination in Operation (written by Yang Xia)

This routine makes a linear combination image of two images, the current image and the immediately previous image. One can specify the percentage of each image involved. It should be note that when adding or subtracting two images, the dynamic range of any pixel in the new image should be within ±32767.

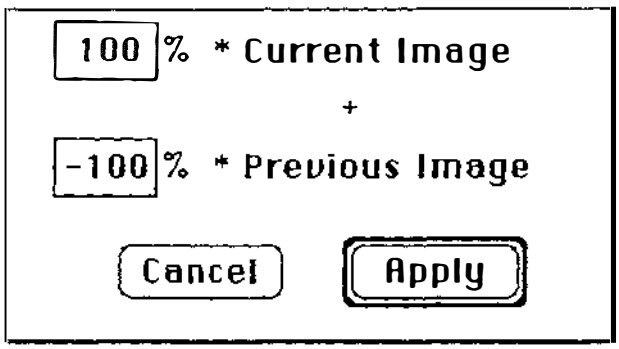

Modulus in Operation (written by Yang Xia)

This routine makes a modulus image of two images, the current image and the immediately previous image. Modulus is the operation such as $m_i = \sqrt{a_i^2+b_i^2}$, where the m_i is the pixel value in the new image while a_i and b_i are the pixel values from the appropriate coordinate of the two original images.

Ratio in Operation (written by Yang Xia)

This routine makes a ratio image by dividing two images, the current image and the immediately previous image. The threshold can be set from the dialogue box.

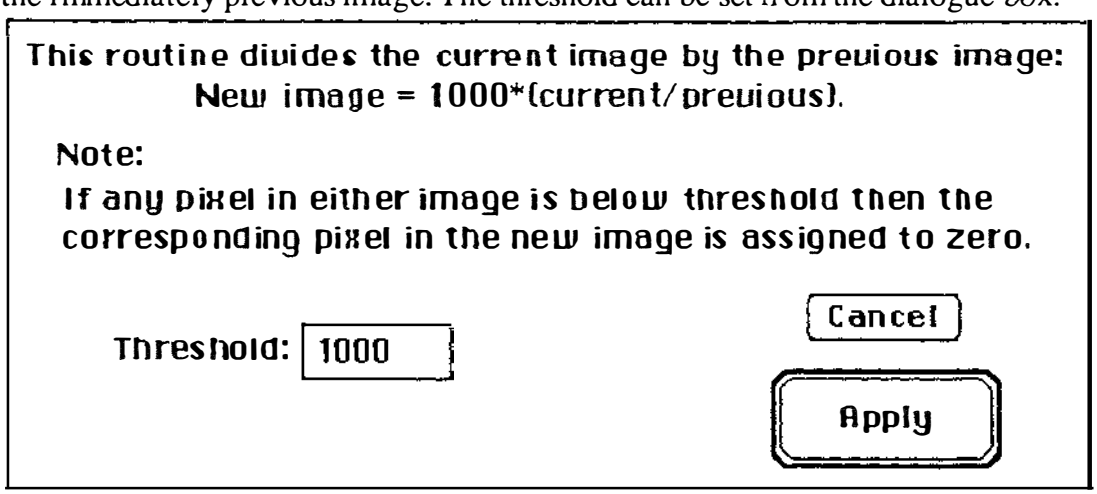

Radial_Averaging in Operation (written by Yang Xia)

This routine is specifically designed for smoothing centrally-symmetrical circular objects. By knowing the boundaries of the object, this routine will calculate the radius of the object, then generate a new image by azimuthal averaging from the defined centre. If the object defined by the entered boundaries is not circular, the radius is calculated by the average of its longer and shorter diameters.

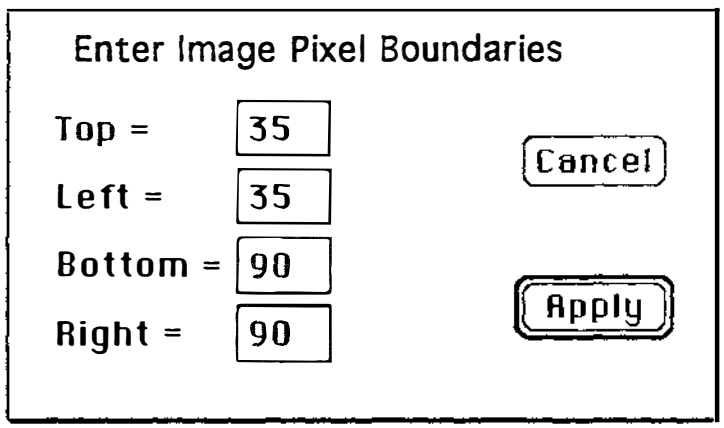

Apply_Ramp in Operation (written by Yang Xia)

This routine makes a new image by adjusting the baseline 'slope' of the current image from the defined balance point along a chosen direction. It is a useful routine when the initial phase setting of the spectrometer is offseted.

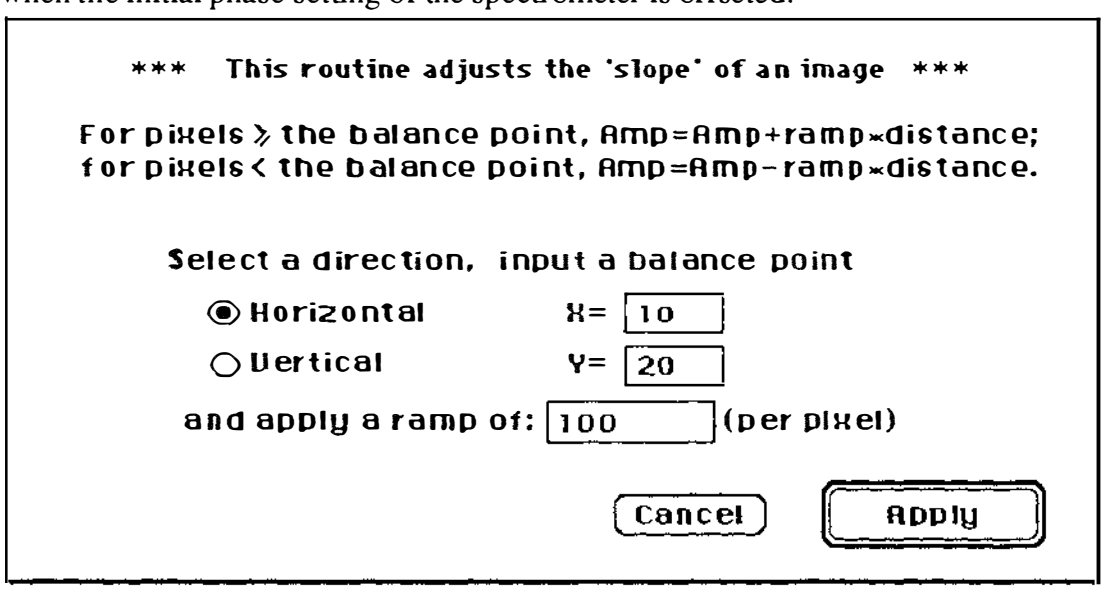

Retouch in Cursor (written by Yang Xia)

This routine can modify the raw data of individual pixels of the current image in the memory. By specifying the coordinates of the pixel, one can check

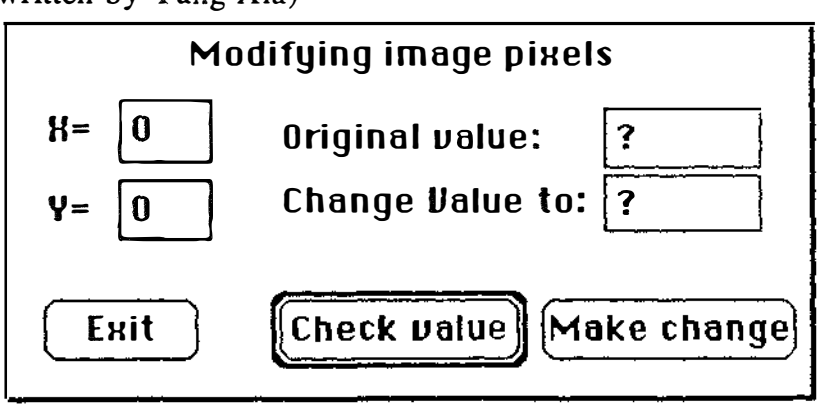

the value of the pixel and make a change if there is a need. (the author is not responsible for the mis-use of this routine.)

4.5.5 Description of arithmetic and mathematic routines

Arithmetic in **Operation** (written by Yang Xia)

This routine can make a new image by performing various arithmetic operations on the current image pixel by pixel. If a pixel value is negative, the algorithm employed in the Square Root operation returns -1.

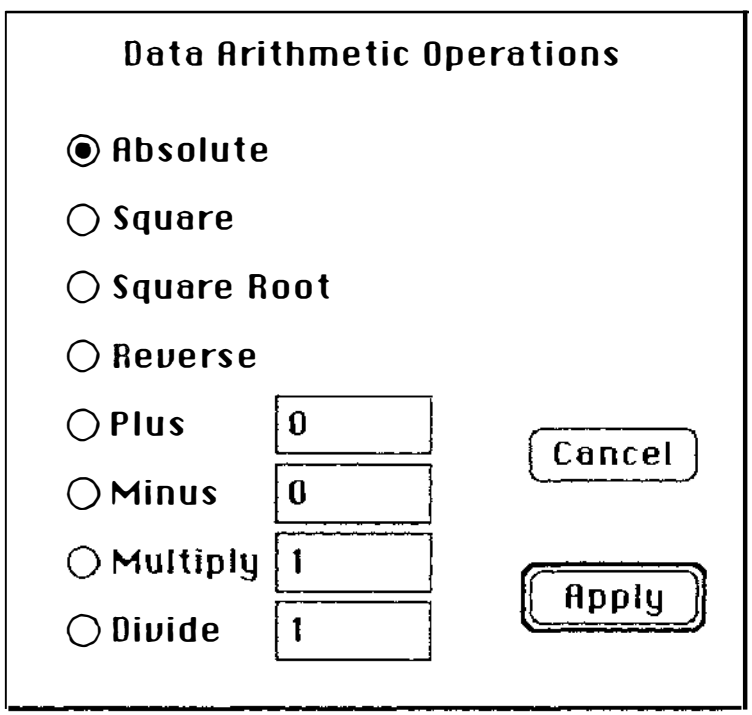

Mathematic in **Operation** (written by Yang Xia)

This routine makes a new image by performing ArcSin, ArcCos or ArcTan operations pixel by pixel on the current image. It is designed for an alternative method of the **Single-Q Velocity** in **Multi-slices** menu in case of the corresponding Cos image is not available (see the relevant sections for details). Each operation on an individual pixel returns a principal value, in radians, of the pixel value. In the ArcSin and ArcCos operations, any pixel value bigger than 1000 (corresponding to an argument bigger than 1 in our algorithm) will be set to 1000 which returns $\pi/2$ in ArcSin or zero in ArcCos, any pixel value smaller than -1000 (corresponding to an argument smaller than -1) will be set to -1000 which returns $-\pi/2$ in ArcSin or π in ArcCos. The precision on the new image can be adjusted by changing the factor inputted.

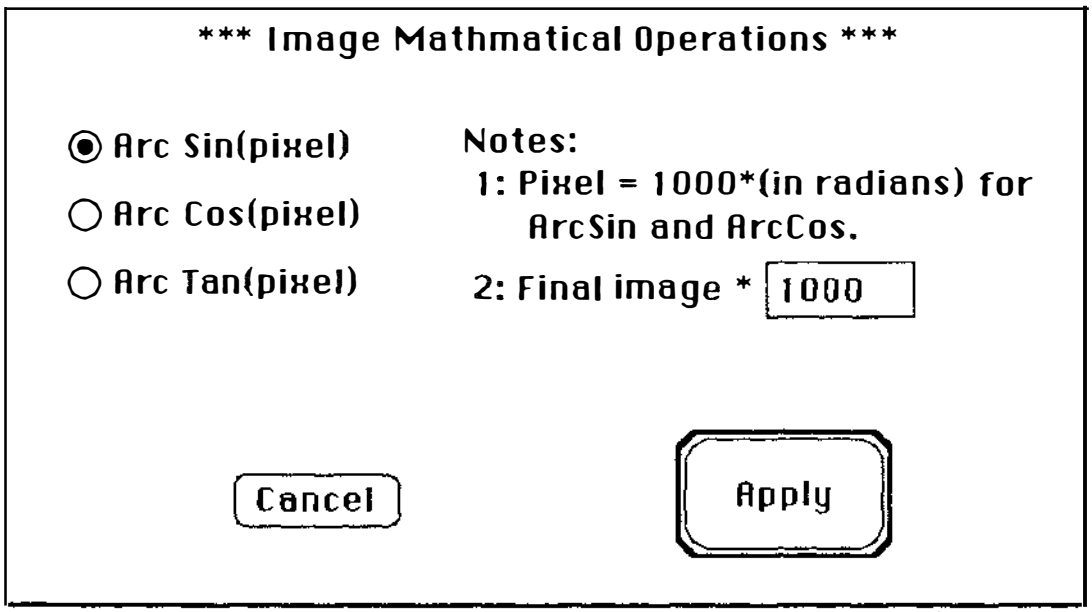

2 D FT in Operation (written by Yang Xia)

This routine performs a two-dimensional Fourier transformation using two images, the current image and the immediately previous image. The output of this operation is presented as a pair of complex images, real and imaginary. If the two input images are acquired using Fourier Imaging sequence and opened in a way that the real first and the imaginary second, then this routine can be used to construct images using Fourier imaging method. The exponential apodization filters can be applied in two orthogonal directions. The centres are equal to half the total sampling points, and the exponents can be entered as desired. The default values are the optimum numbers.

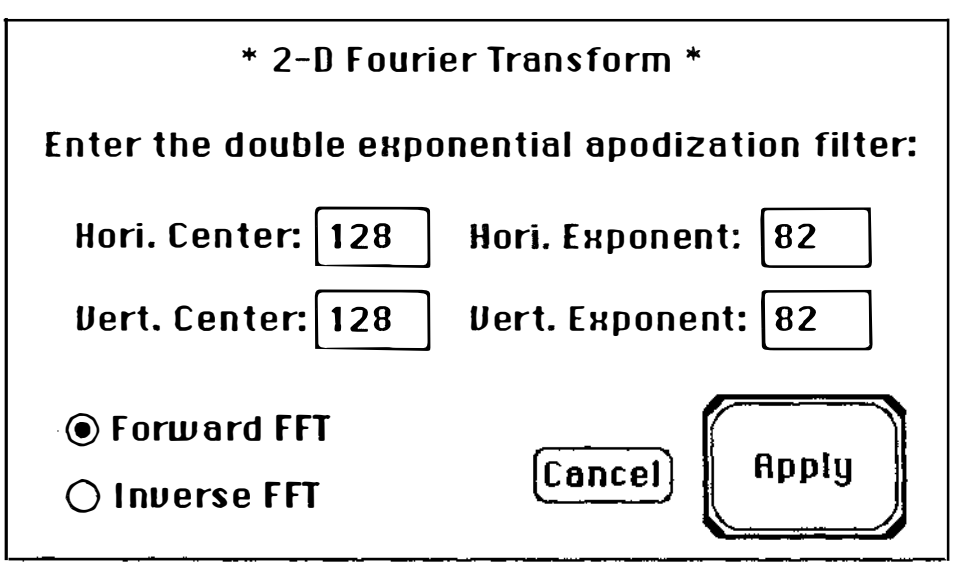

After the Fourier transformation, the program will search through the entire images to prevent the overflow of image pixel values. In the situation of there is an

overflow in the images, another dialogues box will appear, as shown below, listing the maximum number and suggested scale factor. One can either do the scaling, which gives both real and imaginary images correctly scaled, or let the images overflowed which would be useful if a detailed examination of the low-intensity image structures is required.

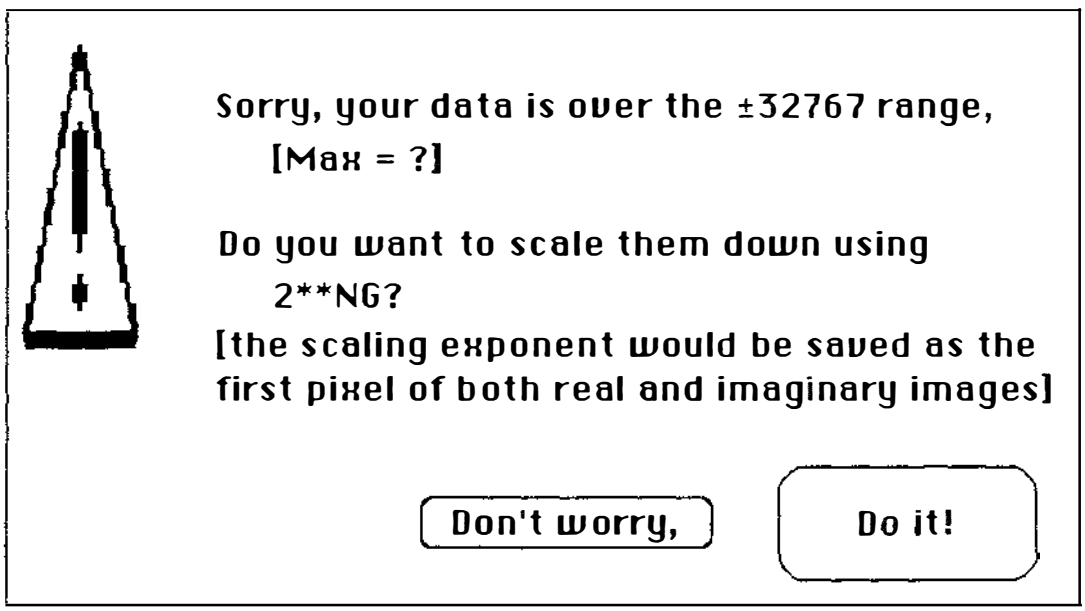

4.5.6 Description of statistical routines

Freq. Stats. in Display (written by Yang Xia)

This routine can scan through the current image, count all the different pixel values in the entire image array and the frequency with which each value occurs. A list is given of each value in order from the greatest to least frequent. The result is shown in a separate window on the screen as the 95% most frequent values (on the left of the list screen) and 5% least frequent values (on the right of the screen). This list can also be printed by using **Print** menu. The algorithm employed in this routine is written by Yang Xia, there may be some other algorithm available in literature which is more efficient than this rather simple 'one-afternoon' algorithm. The modification of this routine to employ a more efficient algorithm is left for future work. The maximum number of different frequencies in this version of ImageShow™ is limited to 1000. In case of over this limit in an operation, there would be a dialogue box appeared indicating that.

Magn. Stats. in **Display** (written by Yang Xia)

This routine can also scan through the current image, count all the different pixel values in the entire image array and the frequency with which each value occurs. But the two lists it is given on the screen (95% most frequent and 5% least frequent ones) are in the order of pixel magnitudes instead of frequencies. Other features of this routine are similar with those in **Freq. Stats.**.

Histogram in **Display** (written by Yang Xia)

This routine scans through all the pixels in the current image and sorts the values according to the frequency with which a particular value appears. The results are displayed as a histogram. A plot is drawn on the bottom part of the screen, in which the bars in red indicate these values which are within the 95% of the most frequent in occurring numbers and the bars in blue indicate those below 5%. This routine is also limited to a maximum of 1000 different pixel values. The histogram may be printed by using **Print** menu.

4.5.7 Description of flow/diffusion analysing routines

Stejskal-Tanner in **Multi-slices** (written by Yang Xia)

This routine performs a linear least squares fit to the multi-slice data images obtained using Stejskal-Tanner method[50], and constructs a new image which is proportional to the slope of the fitted line. One can only enter this routine after just having opened ImageShow™, because this operation normally involves quite a large number of images so that a 'clean' start is appropriate. Before the operation is carried out, a dialogue box (see below) will be displayed on the screen, and if the required parameters are entered correctly, the new image is a map of the self-diffusion of the sample.

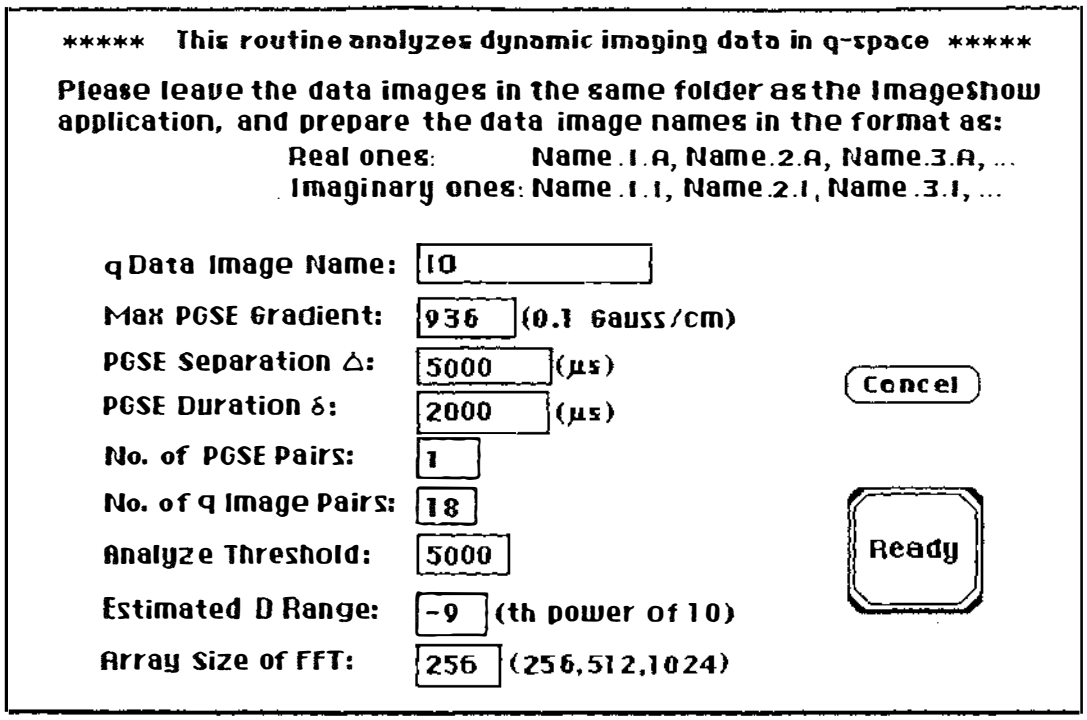

An explanation of the parameters used in this routine:

1. q Data Image Name: The name given to the images without the suffix.

2. Max PGSE Gradient: The maximum magnitude of the q gradient applied during the data acquisition, in 0.1 G/cm. The default value is 93.6G/cm.

3. PGSE Separation Δ: The separation of the two PGSE pulses, in μs.

4. PGSE Duration δ: The width of each PGSE pulse, in μs.

5. No. of PGSE pairs: For normal Dynamic NMR Microscopy, the number is 1; but enter 2 for the velocity-compensated Dynamic NMR Microscopy because there are two pairs of PGSE pulses in the sequence (see Ch 3.3.3 for more details).

6. No. of q Image Pairs: The total number of data images pairs in one experiment (n_D+1). The maximum setting in this version of ImageShow™ is 18. The minimum requirement is 3 pairs.

7. Analyze Threshold: A threshold used for the analysis. Any coordinate where the pixel value in the first real data image (the in-phase image) is less than this threshold will not be analyzed and a zero will be placed in this coordinate in the corresponding velocity and diffusion images. This is a very useful parameter to reduce the time used for analysis.

8. Estimated D Range: An estimation of the order of the diffusion coefficient to be computed is preferred if a range of precise diffusion value is to be presented in one image (which may always be true in any practical experiments). This is because the numerical values for diffusion coefficients in SI units is very small so that pixel values are given by multiplying them with a big number in order to keep the pixel values between 0 and 32767. For example, the normal default setting is -9 (corresponding to 10^{-9} m^2s^{-1}) so that the diffusion map is given by a multiplying factor of 10^{+12}.

Therefore the image is able to present a range of diffusion values within 3.2×10^{-8} to 1×10^{-11} m^2s^{-1}.

9. Array Size of FFT: This is the array size used in the FFT routine. A larger array size gives better precision but requires longer computing time. Fourier transform an array of the size of 1024 roughly takes four times longer than that of an array of the size of 256.

Individual pixel values at any particular coordinates of the image can be examined by using Show q-Space Plots succeedingly. (for this version of the ImageShow™, this routine is only available to 64×64 and 128×128 images)

Fourier Transform in Multi-Slices (written by Yang Xia)

This is the main routine used to construct velocity and diffusion images in Dynamic NMR Microscopy experiments. It performs a fast Fourier transform on the multi-slice data images, and constructs two new images. One image is a map of the peak offset of the dynamic displacement profile, and the other is a map of the FWHM of the peak. If the data images are acquired using Dynamic NMR Microscopy, then the peak offset map is the velocity image and the FWHM map is the self-diffusion image. Individual pixel values at any particular position of the images can be examined by using Show q-Space Plots successively.

As the above Stejskal-Tanner routine, one can only enter this routine after just having opened the ImageShow™ and the same dialogue box is displayed as in the above. Actually most of these parameters are not necessary for the construction of velocity and diffusion images along, because the pixel values given in these two images are simply the dimensionless digits. The values in SI units can be calculated by using the formulas given in Ch 3.3 (and incorporating Ch 3.4 and Ch 3.5). But these parameters are necessary if one wants to perform 'on-line' display of FFT and ST plots using Show q-Space Plots successively. (for the current version of the ImageShow™, this routine is also only available for 64×64 and 128×128 images)

Show q-Space Plots in Multi-Slices (written by Yang Xia)

This routine can perform 'on-line' linear least squares fit on the multi-slice data images. It can display a linear regression plot (using the Stejskal-Tanner method) and a fast Fourier transform plot of the multi-slice data at any point indicated by the cross cursor which is place inside an image. This routine is only available after an entry from either the Stejskal-Tanner or Fourier Transform routines. The linear least squares

plot gives the slope of the fitted line, while the FFT plot gives the peak offset and the peak's FWHM. Both plots can be printed using Print.

Single-Q Velocity in Multi-slices (written by Yang Xia)

This routine performs a series of calculations using the single-q 'one-shot' velocity imaging method (refer to Ch 3.7) and constructs a velocity image. The parameters in the following dialogue box have the same meanings as those used in the Stejskal-Tanner and Fourier Transform routines.

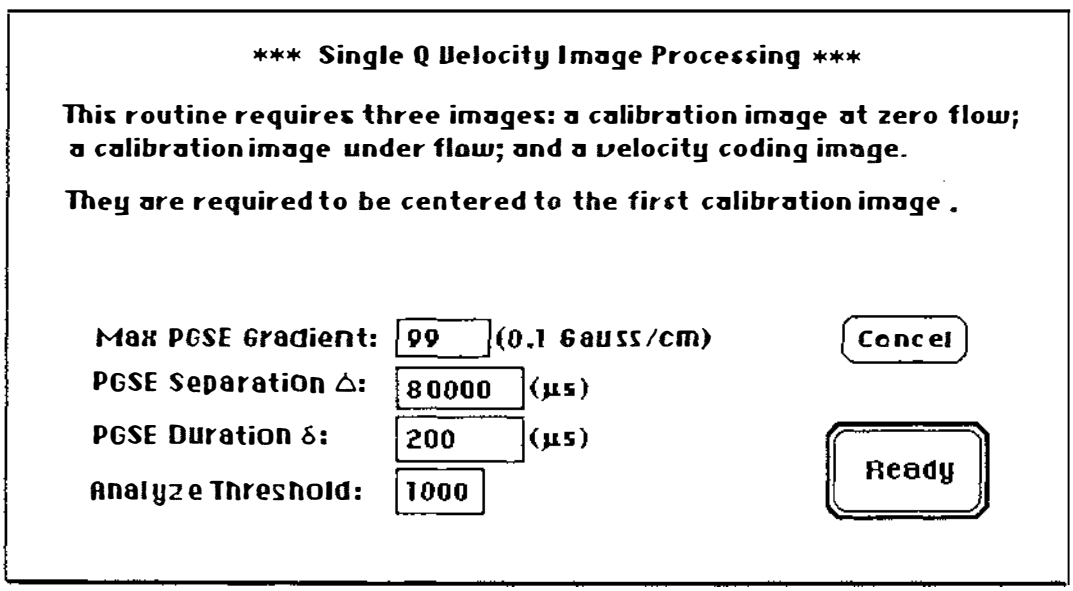

4.6 Summary

This chapter has first described the existing micro-imaging system based on a FX-60 spectrometer with an electromagnet. As an important part of the imaging system, the specification of the existing imaging probe has been described in detail, including those of the gradient coils and rf coils. The power supplies for the gradient coils have also been described.

Ch 4.2 to Ch 4.5 have described and discussed the hardware and software development which had been undertaken as part of this work. It may be worth noting here that a significant amount of time has been spent fixing various basic spectrometer instabilities and breakdowns, which is an 'integral but unstated' part of this work.

The design of the two new imaging probes reflects one aim in this work, using the usually unfavourable low-field electromagnet to carry out 'non-trivial' imaging

experiments which are normally carried out using more expensive superconducting magnets. The design consideration and manufacture of these two new imaging probes represents two extreme requirements in experiments, a very powerful gradient and an easy access to a big central space inside the imaging probe. These two new imaging probes together with the previously-existing probe (named the 'standard' imaging probe in the later text) form a complete instrumental environment which is suitable for different samples.

The software development for the TI-980A and Hitachi computers has involved various modifications to the existing software packages. As a major part of the software development in this work, a comprehensive image analysis software, ImageShow™, has been written for the Macintosh computer. This software has enabled the construction of final velocity and self-diffusion images in the Macintosh computer using the data images generated by the Hitachi computer, and the analysis and image process of both static and dynamic images.

Chapter 5 Static NMR Microscopy: Experimental Results

The first section in this chapter dealt with experimental considerations for carrying out microscopic imaging experiments in an electromagnet-based spectrometer. The next three sections are devoted to discussing work carried out in order to achieve higher spatial resolution, to reduce an image artifact (the zero-frequency 'glitch') and to quantitatively assess the induced eddy current effect in imaging experiments. Ch 5.5 presents some static microscopic images which serve as tests of the imaging probes and the instrument while Ch 5.6 demonstrates the use of T_1 contrast in imaging experiments.

5.1 Designing experiments in the FX-60 micro-imaging system

The electromagnet in the FX-60 has a horizontal B_0 (z) axis. This means that sample access is in the vertical (y) direction and is customary to select an imaging slice plane transverse to this y axis (i.e., in the x-z plane). The experiments in this work were carried out using the filtered back-projection reconstruction (PR) method with a typical (static) imaging pulse sequence as shown in Figure 5.1. This pulse sequence can be divided conceptually into two parts. The first part is used for the slice excitation with the usual 90°-180° pulse pair and the gradient along the vertical direction, G_y in this case. The G_y magnitude determines the slice thickness of the sample using Eq[2.40]. The larger the gradient, the thinner the slice which leads to better resolution but poorer S/N.

The second part of the pulse sequence comprises planar imaging where the G_x and G_z gradients are adjusted during the reconstruction according to cosine and sine relationships respectively. These two mapping gradients define a net gradient vector at some angle to the G_x axis. The gradient stepping angle ($\Delta\phi$ in Eq[2.53]) during an imaging experiment can be as small as desired. Clearly a finer turning angle improves the spatial resolution. In our system, the maximum number of level changes is limited to 120 steps in software, therefore the minimum turning angle increment is 2° for 0°-180° projection imaging or 4° for 0°-360° imaging. The 1 ms pre-pulses of the mapping gradients are used to delay the formation of the spin echo so that the origin of the **k**

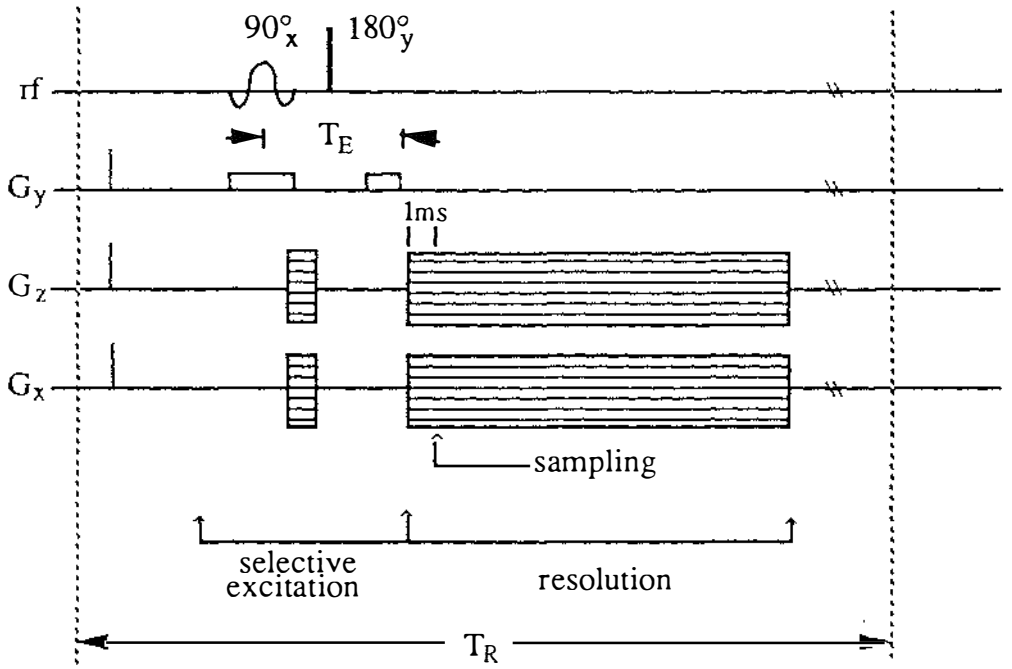

Figure 5.1 A static imaging pulse sequence used in experiments

space does not coincide with gradient switching. This can improve the quality of the image (slightly) because there is always some time required for the gradient power supply to settle and for the gradient induced by the eddy current to decay. A 2 μs pre-pulse is also employed for each gradient before the slice excitation. These short pulses have the effect of establishing the current supply level well before the instant when the current is re-directed from the dummy load to the gradient coil, so reducing the gradient rise time.

The sampling time starts at the centre of the echo using the positive half of the echo only. Sampling lasts a time $N/\Delta f$ where N is the number of the data points sampled by the spectrometer and Δf is the band-width of the spectrometer. An alternative approach in data acquisition is to sample the entire echo from the negative time, which increases the signal-to-noise ratio in principle but, in practice, where the T_2 of the sample is short in comparison with T_E (typically 4ms), the result may not be much better than that obtaining from the half-echo sampling.

For a particular projection angle, the real and imaginary time domain signals are obtained by detecting the quadrature signals. The signal is accumulated in N_{acc} repetitive co-additions to improve S/N (S/N is improved as the square root of the number of the accumulations). The choices of N_{acc} together with that of the slice thickness usually represents a compromise determined by requirements for the image

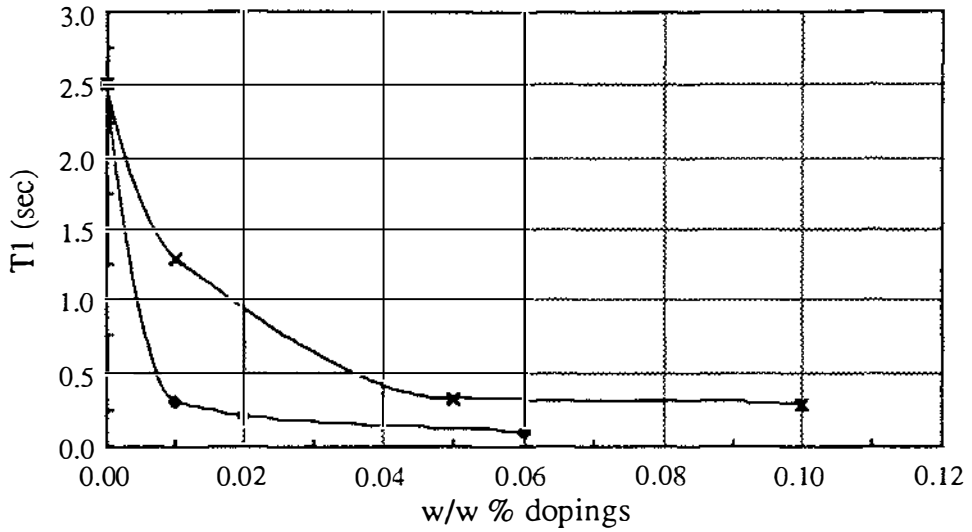

Figure 5.2 T_1 vs doping (the cross is $CuSO_4$ and the diamond is $MnCl_2$)

quality. FFT is then performed to obtain the frequency domain signal (1-D profile). This signal can be exponentially filtered to improve S/N at the price of poorer resolution. The optimum filter is determined by the criterion that adjacent pixels should be resolved with a magnitude difference of greater than 80%. Multiplying the signal by a ramp before Fourier transformation, the filtered profile, $P^*(x,y,\phi)$ given by Eq[2.51], can be obtained. After the current $P^*(x,y,\phi)$ has been transferred to the Hitachi computer, the values of G_x and G_z gradients are updated according to the pulse sequence codes stored in the TI-980A memory until the required quadrants have been sampled.

Although FID signal lasts of order T_2 seconds, the repetition time, T_R, between the accumulations is determined by T_1. In imaging experiments using water phantoms the T_1 of water can be reduced by doping $CuSO_4$ or $MnCl_2$. The approximate relationship of T_1 of water and the percentages of the doping are shown in Figure 5.2.

5.2 An attempt to improve spatial resolution: 0.9 mm id rf coil

Any attempt to resolve finer structure in NMR imaging always stimulates the development of NMR microscopy. Higher spatial resolution can be achieved by scaling down the receiver system since the signal-to-noise ratio of an image varies as the rf coil radius. In practice it will be necessary to use small samples in order to achieve high

spatial resolution at a given finite digital array size. For example to achieve a 10 μm spatial (pixel) resolution for a 256×256 digital array, the diameter of the sample has to be smaller than 10μm×256 = 2.5 mm.

The smallest rf coil in the existing imaging system is 2.1 mm in diameter. In an attempt to achieve higher spatial resolution, a 24 turn rf coil with an internal diameter of 0.9 mm was designed and built using #28 Gauge copper wire. This was an adaptation of a previous design[132] using a perspex coil holder for mounting. The 24 turns of this rf coil were not necessary but were chosen so that the inductance for this rf coil could be similar to the existing rf coils in order to keep the rf tuning circuit unaltered. In the construction of this rf coil, special attention was required to precisely locate the rf coil's geometric centre to the centre of the probe.

The quality factor of this ultra-small rf coil has been measured as 36 (when connected in the rf tuning circuit), which is close to that of the existing 2.1 mm rf coil. The calibration of the ultra-small rf coil in the imaging system had produced some unexpected results. It was found that the 180° pulse time for this new rf coil was almost identical with that of the 2.1 mm rf coil, and the S/N was very close to that using the 2.1 mm rf coil as well!

This suggests that the size of the receiver coil may have an optimum lower limit, and that beyond this limit, one cannot gain higher sensitivity by simply scaling down the dimension of the receiver coil. The causes of this lower limit are probably two-fold and relate to the quality factor, Q, of the coil and the inevitable noise power (Johnson noise) in the system. For the solenoid coil, the highest Q is achieved when the separation of the wires is about three to four times their radius and the length of the coil is a little less than its diameter[10]. This optimum condition is obviously unpractical for this 0.9 mm i.d. rf coil which is reflected in the lower Q factor.

The consequence of achieving higher spatial resolution is to cause a reduction in the sample voxel size. This leads to proportional reduction of the spin signal. However, the background noise power is more or less constant for a given coil (for a given length of wire and at a given temperature). Therefore the resolution limit occurs where the noise power dominates the signal. The Johnson noise of the receiver coil cannot be avoided. However noise due to the pre-amplifier and other electronically induced noise can be reduced. One method is to use an ultra-low-noise amplifier, such as dc SQUID (Superconducting Quantum Interference Devices)[141] or Charge Sensitive Pre-amplifier[142], in the receiver channel. Other method is to cool the pre-amplifiers to a

lower temperature. The noise figure can be halved if the operating temperature is reduced from the room temperature to liquid nitrogen temperature (77 K) for some GaAs MOSFETs amplifiers[143].

5.3 The zero-frequency 'glitch' in image reconstruction

An image is constructed through Fourier transformation of original FIDs acquired in the time domain. If the convention used in NMR is retained, an image is a map of spatial frequency distributions of nuclear spins. The centre of the frequency space is usually the centre of the image, provided one is working 'on-resonance'. In practice there is often an artifact visible in NMR images, named the zero-frequency artifact. The appearance of the zero-frequency artifact in images is different, depending upon the particular image reconstruction method employed. For example, in the filtered back-projection reconstruction (PR) method a 'glitch' will appear as a point of several pixels right at the centre of the image, while in Fourier Imaging (FI) method a line with a width of several pixels will run across the image through the middle. Working slightly off-resonance can shift this artifact away from the centre of the image but doesn't necessarily remove the problem. The degree to which the artifact affects an image is different in different imaging systems, and may differ at different times for the same instrument.

To investigate the origin of the zero-frequency artifact, it is necessary to consider how an image is constructed. In the signal acquisition, one can either sample the full echo or half the echo, and the Fourier transformation in these two cases are shown in Figure 5.3. In the full echo case, one gets a symmetrical profile in the real part and nothing in the imaginary part (Figure 5.3a), while in the half echo case, one still gets a symmetrical profile with half the magnitude in the real part but an asymmetric profile in the imaginary part (Figure 5.3b). The non-zero character of the imaginary profile is not a problem, because once the spectrum has been phased correctly, the image reconstruction can be completed by using the real profiles only.

In 'standard' image reconstruction, the symmetry relationship, $S^*(\mathbf{k})=S(-\mathbf{k})$ given by Eq[2.47], is commonly employed, where S^* is the complex conjugate of the sample signal S and $\mathbf{k}$ is the reciprocal space in which the time domain signal is sampled. A two-dimensional Fourier transformation of $S(\mathbf{k})$ will yield the desired spin density distribution $\rho(\mathbf{r})$. This relationship implies that to construct an image in

(a) Symmetrical time domain profile

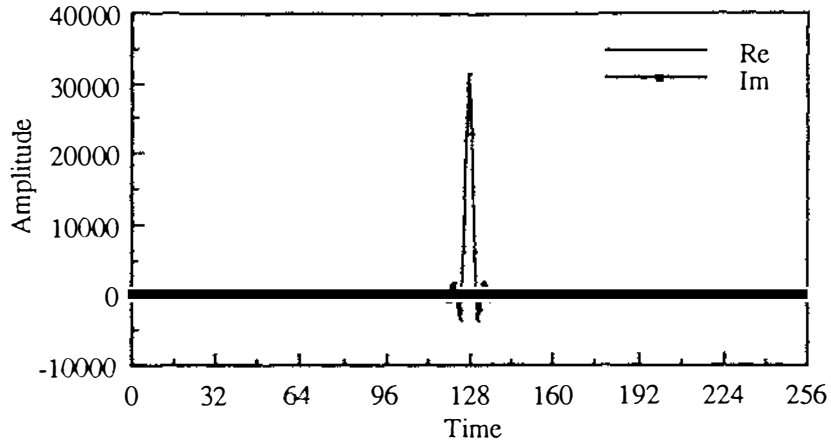

FT of symmetrical time domain profile

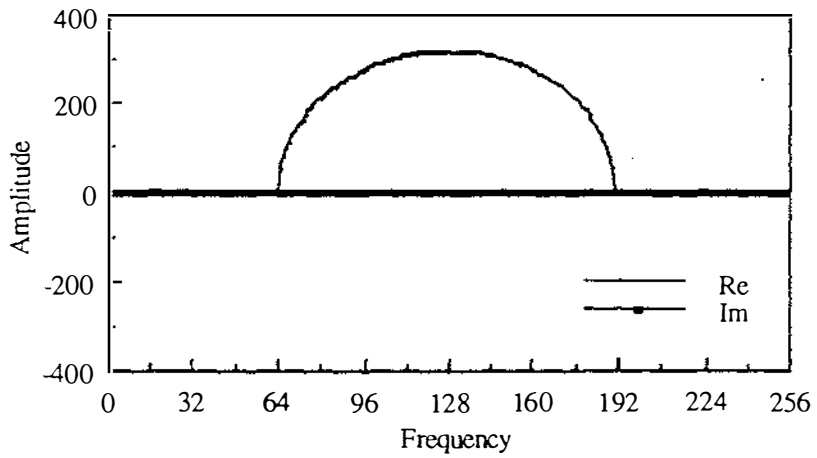

(b) Asymmetrical time domain profile

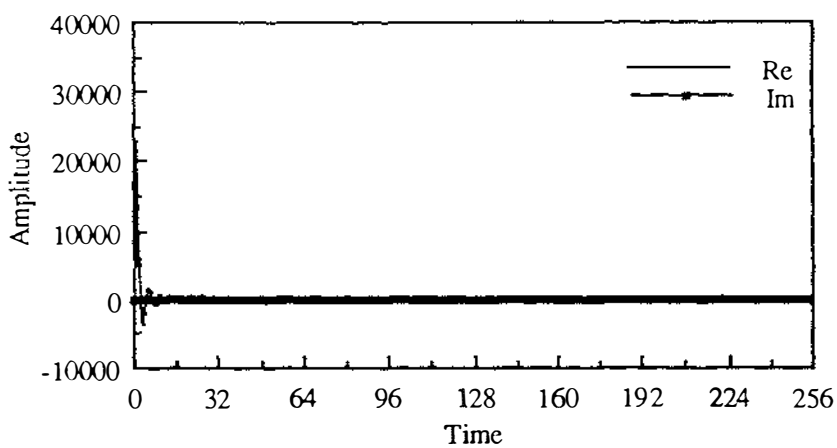

FT of asymmetrical time domain profile

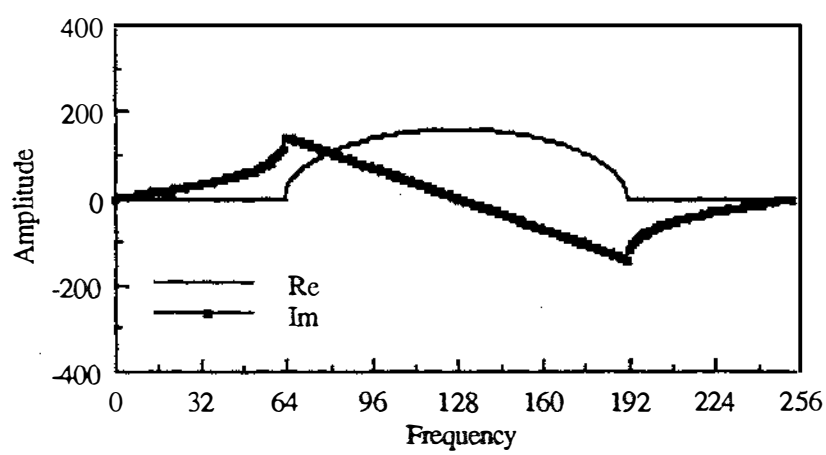

Figure 5.3 Symmetrical and asymmetrical profiles in time and frequency domains

practice, one needs to sample only two quadrants. Apart from some special cases which require reconstruction of complex images (as in Dynamic NMR Microscopy), this relationship is usually valid with the advantage of simplifying required hardware and software.

Now assume that there is a small nearly constant or slowly varying offset, S_{offset}, existing in the receiver. This could be caused by any dc-like drifts, or charging and discharging of coupling capacitors in the receiver's amplifiers due to sudden changes of the time domain sample signals, S(k). The Fourier transformation of this small offset signal is a narrow offset spectrum centred at the zero frequency. Therefore the final profile used for the image reconstruction is a linear superposition of the one-dimensional profile of the sample signal, S, and this offset spike. The wave-form of this offset spike will lie somewhere between a perfectly phased absorption or dispersion spectrum, depending on the proportions of S_{offset} in the time domain in-phase and quadrature channels.

The offsets in the in-phase and quadrature channels correspond to the real and imaginary parts of the offset signal. Figure 5.4 shows several simulated FT profiles of example offsets and the sample signal shown in Figure 5.3b. From these results it can be seen that if one channel of the receiver is offset-free and the other channel has a slow decaying offset signal, then the offset spikes at the in-phase and quadrature-phase channels would take the forms of correctly phased dispersion or absorption spectrums respectively. The positions of the dispersion and absorption in the real and imaginary parts depend upon which channel is offset-free, and the 'width' of this spike is dependent upon the decay rate of the offset signal. If both channels are subject to offsets with different decay rates, then the offset spike would be intermediate between pure absorption and dispersion. It is interesting to note that the effect of this offset signal is quite dramatic, in the simulations shown in the above figure, the maximum offset signal in the time domain is only 2% of the maximum sample signal.

The presence of this offset spectrum in the receiver of the spectrometer implies that the useful relationship, $S^*(\mathbf{k}) = S(-\mathbf{k})$, is no longer valid because the key assumption used in the above symmetry relationship is that $\rho(\mathbf{r})$ is a real function, implying that the real spectrum is symmetrical in $\mathbf{k}$, while the imaginary spectrum symmetrical in $\mathbf{k}$. This suggests a means by which the artifact may be partially or wholly removed.

(a) Offset at the real channel only

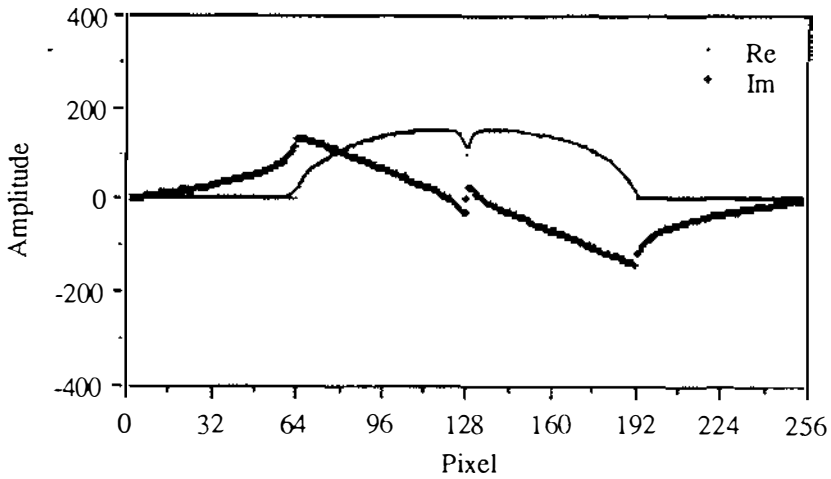

(b) Offset at the imaginary channel only

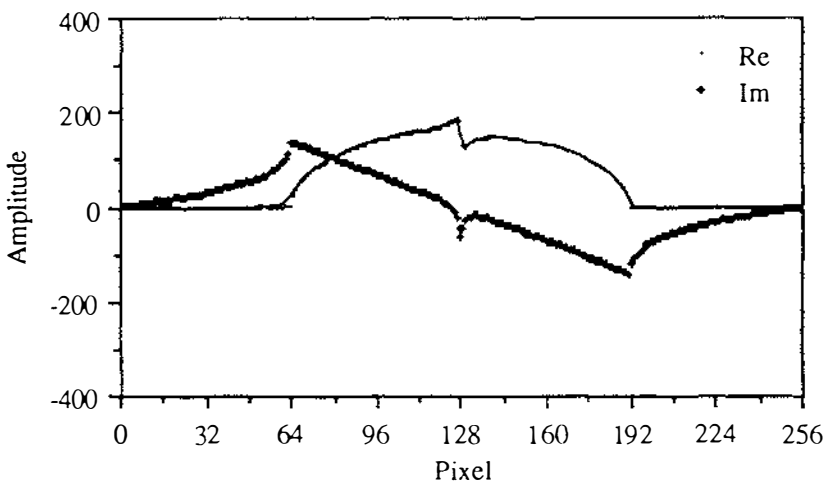

(c) Offset at both the real and imaginary channels

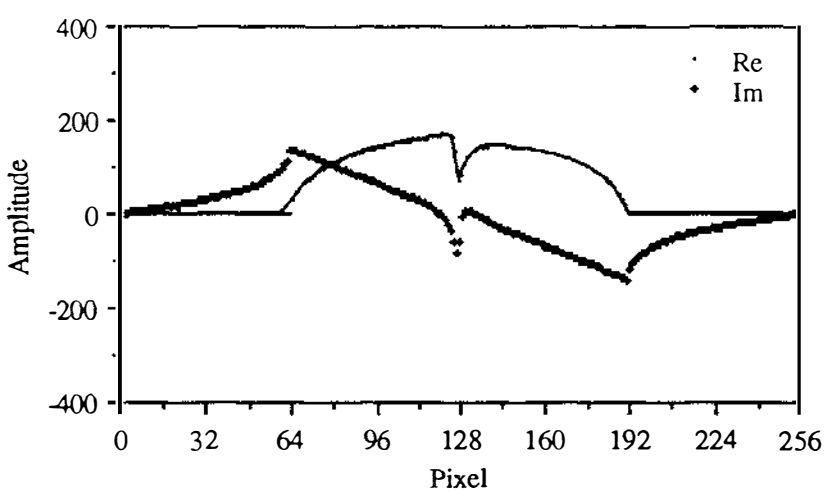

Figure 5.4 Simulation of the zero-frequency 'glitch' artifact in NMR imaging

By using a full four-quadrant sampling, the image over 0°-180° would be subjected to a possible zero frequency artifact, but continuing construction from 180°-360° should remove this artifact to some extent. The effect of the artifact cancellation is dependent upon what sort of the offset spectrum is present during a particular imaging experiment. In the situation of a dispersion spike, the full quadrant reconstruction will cancel the artifact completely, whereas for a pure absorption spike, there would be no cancellation. In most cases, there would be some degree of the artifact cancellation dependent upon the degree of asymmetry of the offset spike. Figure 5.5 shows an experimental example comparing the 0°-360° four-quadrant construction with the usual 0°-180° construction using the same sample where the artifact was close to a dispersion spectrum, the effect of the artifact cancellation is excellent. By adjusting the phase-sensitive detector reference phase so that the artifact spike is dispersion-like, one can take effective advantage of this cancellation effect.

To complete the full four-quadrant sampling, some system modifications were required in both hardware and software. In the hardware, both mapping gradients have to be reversed during the image reconstruction, while the modification in software enables construction of images over 360°. However, to get the same signal-to-noise ratio in this four-quadrant sampling method, the signal acquisition number for each direction in **k** space can be halved so that the total experimental time is the same as that used in the two-quadrant sampling method. This is what has been done to obtain the results shown in the above Figure 5.5.

(a) A slice through the centre of a water phantom image using 180° PR

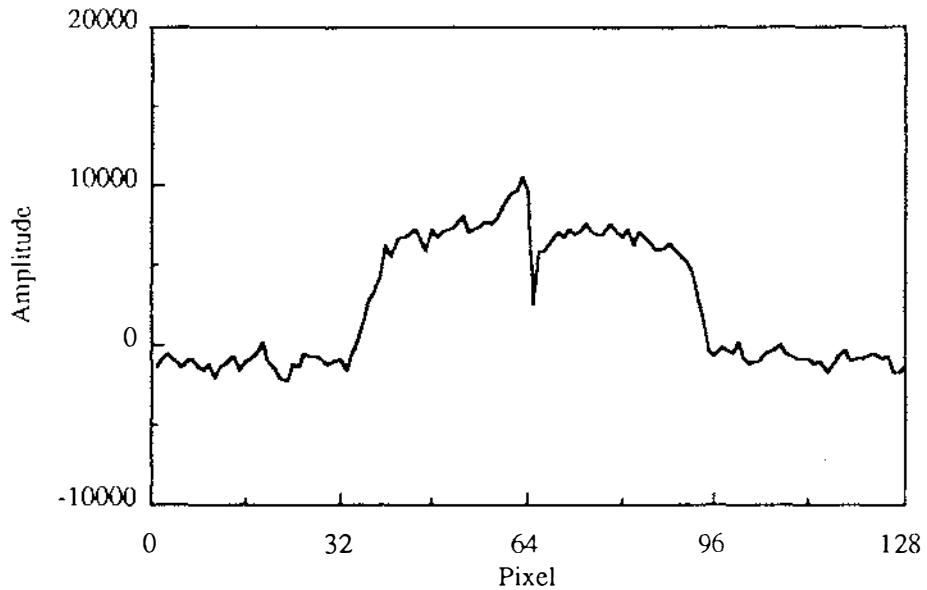

(b) A slice through the centre of a water phantom image using 360° PR

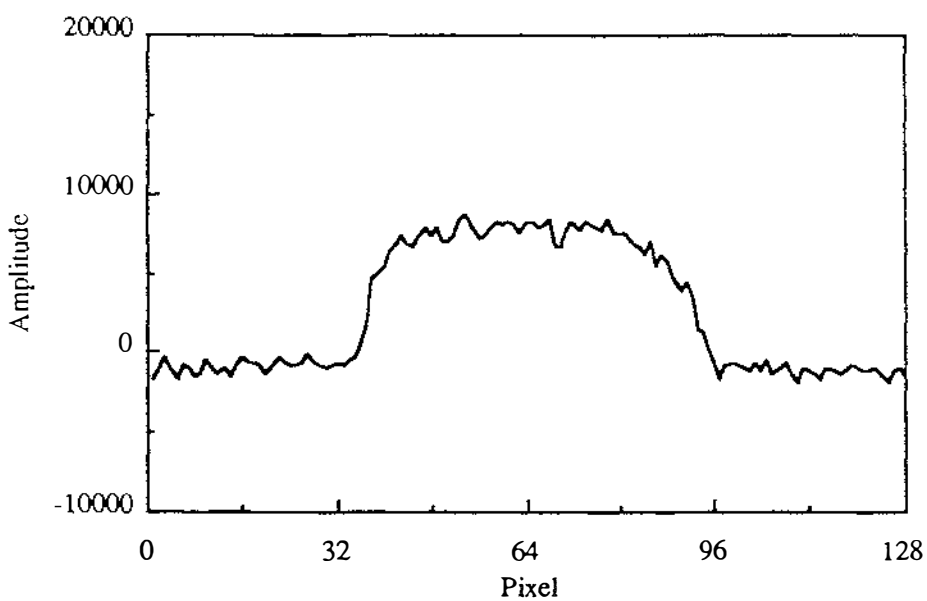

Figure 5.5 Experimental results comparing imaging using 180° PR and 360° PR

5.4 Induced eddy current effect in imaging

Eddy current phenomena appear when conducting media are subjected to time varying magnetic fields. Because of the presence of metallic surfaces in the vicinity of the magnetic field gradient coils, the fields generated by induced eddy currents are a major problem associated with switching magnetic field gradients in NMR imaging applications. It is well-known that artifacts due to eddy currents are much more severe in superconducting magnets than in electromagnets. The effect of eddy currents in our electromagnet is investigated as follows.

5.4.1 Induced eddy current problem

The induced eddy current is usually a complicated function, consisting of a zero order (B_0-like) component which can shift the resonant frequency, a first order spatial-derivative (G-like) component which can distort the desired gradient profile and other high order components which can produce further artifacts.

The time evolution of eddy currents in metal during and after formation depends upon structure, shape and electrical conductivity of the surrounding metal. The initial response of the eddy current is associated with the interaction of gradient pulses with the metal and is proportional to the current switching rate, di/dt. The field produced by the eddy current opposes the change in field which the metal experienced, a requirement of Lenz's law. Thus the purposefully shaped gradient pulse is distorted (Figure 5.6). The after-switching evolution of the eddy current is also governed by Lenz's law and is usually a relatively slow decay.

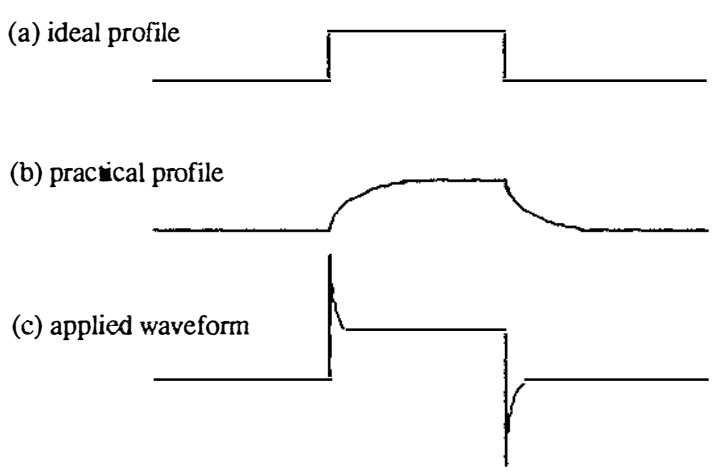

Figure 5.6
The pulse distortion due to induced eddy currents

There are two different approaches to the removal of eddy current artifacts. One approach uses 'pre-emphasis' on the leading edge and 'de-emphasis' on the falling edge of the gradient coil current using electronic devices to multi-exponentially overshoot and undershoot the applied gradient current during the switch on and off processes (Figure 5.6c). This is an empirical solution which is commonly used in commercial instruments. For each gradient, this approach involves the shaping of the pulsed gradient current using three or more decaying exponentials, each being adjusted by an iterative and time-consuming trial-and-error procedure. The advantage of this 'pre-emphasis' approach is that it does not require additional space inside the bore of the magnet. However, the results of this approach are usually not very satisfactory in practice. This is because the induced eddy current is a complicated multi-component function with not only the zero and first order terms but also other high order terms, therefore there is no way that any gradient current shaping in three orthogonal first order coils (gradient coils) can compensate the effect due to the eddy current with completely satisfactory.

A different approach is to cancel the stray magnetic field outside the gradient coil assembly by adding another set of gradient coils at the outside of the primary gradient coils[144-148]. This screening strategy is by far the most thorough approach to solving the eddy current problem, but it has some disadvantages. For example, coil design and manufacture becomes quite complicated, the gradient coil assembly occupies more bore space due to the additional coils, the desired gradient strength at the centre of the probe is reduced and eddy currents in the metal inside the gradient coil assembly are not compensated.

5.4.2 Measurement of induced eddy currents

The effect of eddy currents in our electromagnet was investigated using the pulse sequence shown in Figure 5.7. The signal was acquired over a wide range of τ for every gradient coil of the three imaging probes. The time domain signals were then Fourier transformed and plotted. Of the nine series of experimental plots, there are basically three types of behaviour, as shown in Figure 5.8 to Figure 5.10.

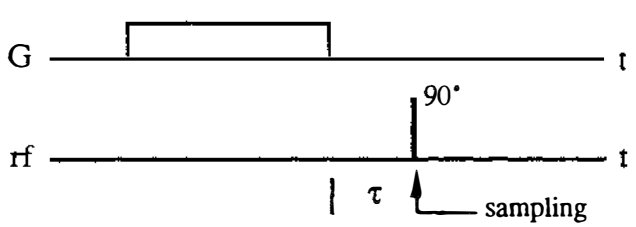

Figure 5.7

A pulse sequence used in the measurement of eddy current effect

(a) τ = 10.07 ms

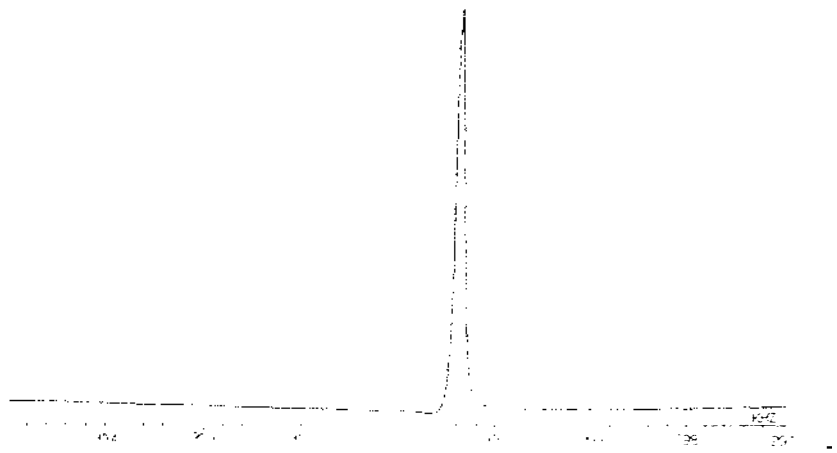

(b) τ = 0.87 ms

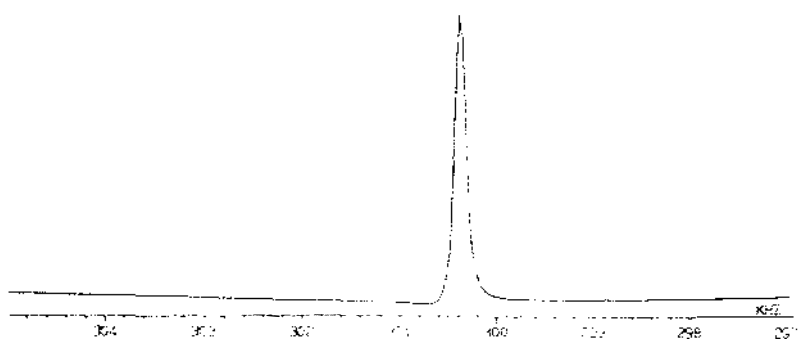

(c) τ = 0.27 ms

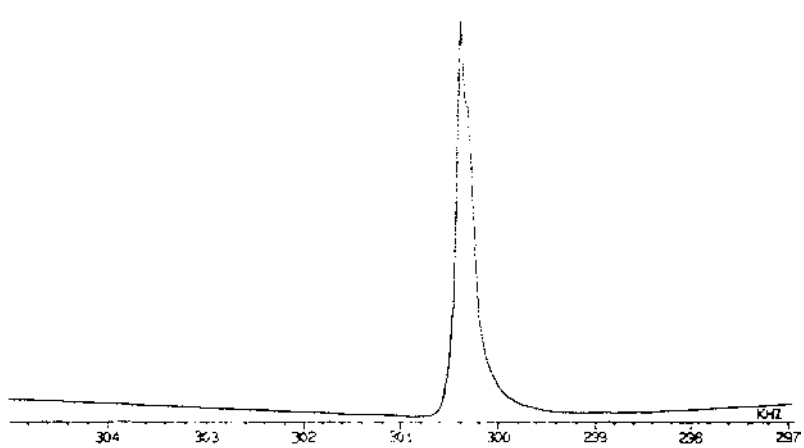

Figure 5.8 FT plots from FIDs for the G_z of the plant-imaging probe

(a) τ = 10.07 ms

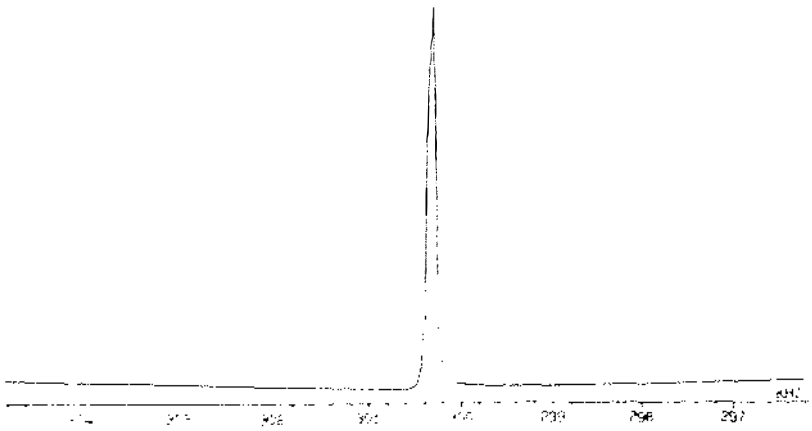

(b) τ = 0.87 ms

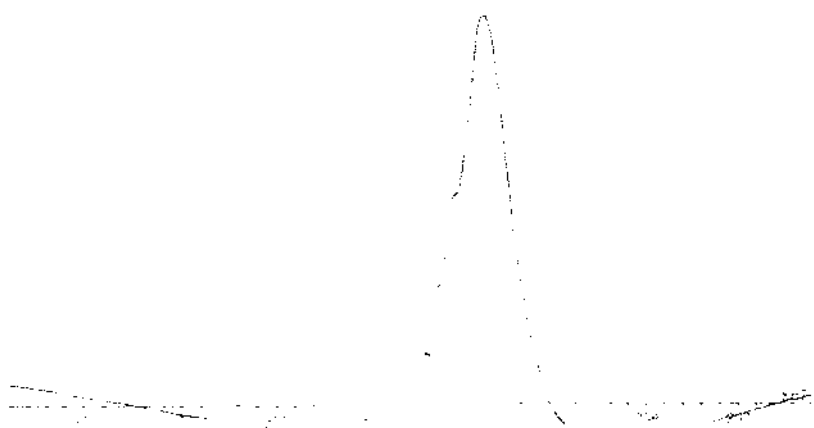

(c) τ = 0.27 ms

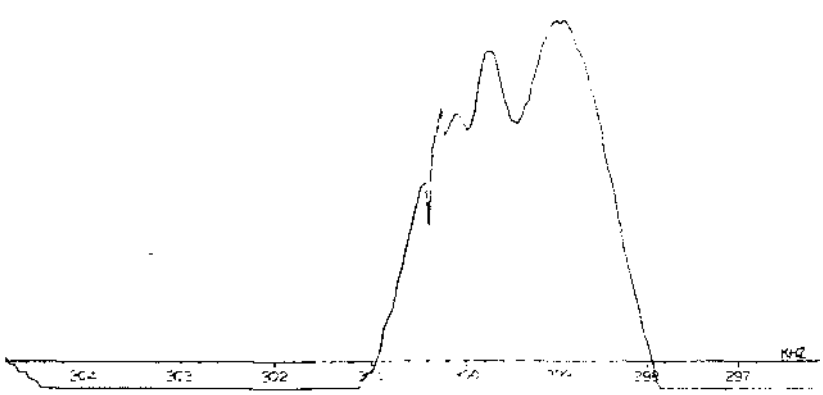

Figure 5.9 FT plots from FIDs for the G_y of the standard imaging probe

(a) τ = 10.07 ms

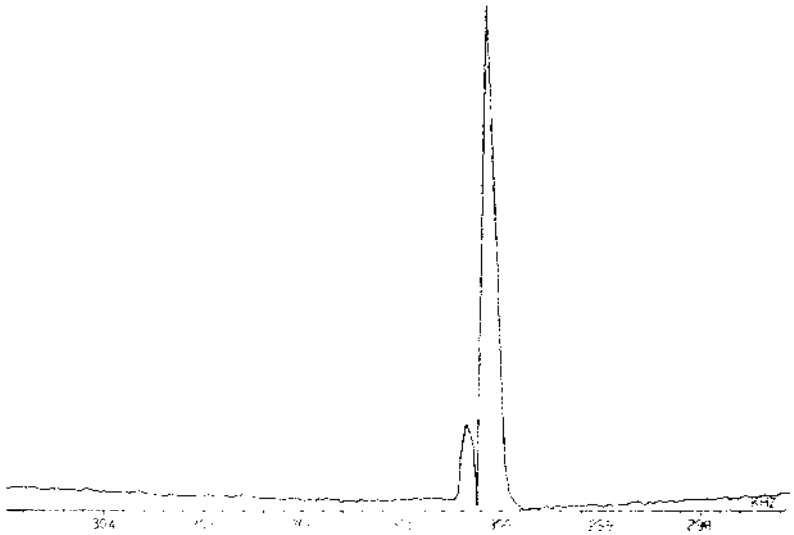

(b) τ = 0.27 ms

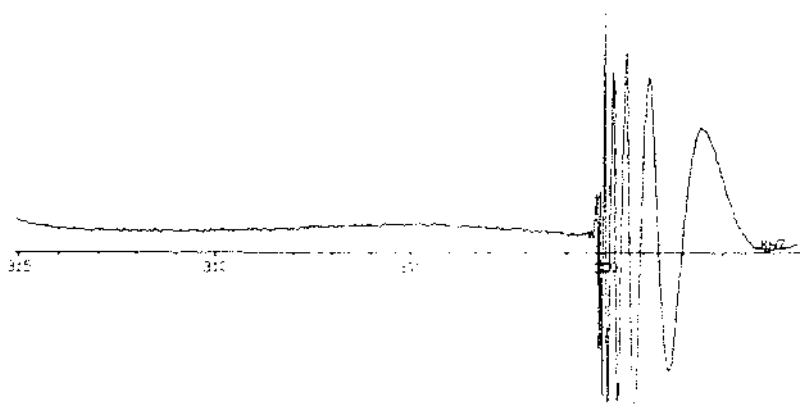

(c) Modulus of (b)

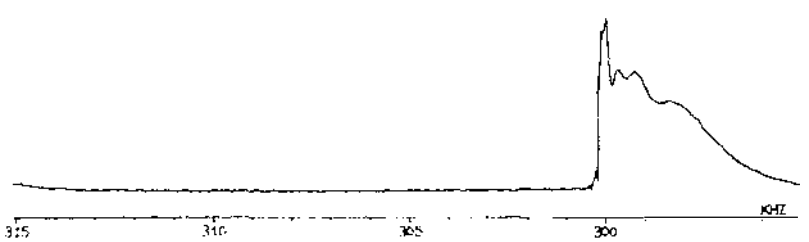

Figure 5.10 FT plots from FIDs for the G_x of the 'super-G_y' probe

Figure 5.8 (G_z of the plant-imaging probe) shows that there is no change of the signal wave-form and very little shift of the signal peak for different τ (only slight phase distortions of the peak can be seen at the shortest τ). This implies that there is little eddy current left 0.27 ms after the gradient pulse has been switched off.

Figure 5.9 (G_y of the standard imaging probe) shows that the spectral peak is broadened and position-shifted considerably for small τ. This means that there is a strong eddy current which has, at least, both the B_0-like and G-like components. The B_0-like component causes the position-shift of the peak and the G-like component causes the broadening of the peak.

Figure 5.10 (G_x of the 'super-G_y' probe) is of interest. At short delay times, the spectra show wave-forms which have an appearance similar to the 'wiggles' signal, known in the early NMR literature from the fast passage effect[149], which is caused by a linear and rapid swept of the angular frequency ω through the resonance frequency, ω_0[150]. It thus suggests that there is a decaying B_0-like component in eddy currents.

The magnitude of the induced B_0-like component for each gradient coil was measured from the shift of the spectral peak and shown in Figure 5.11. Among the nine gradient coils, five coils have significant induced B_0-like field. They are the three planar coils, G_y coils of the standard imaging probe and the plant-imaging probe and G_x coil of the 'super-G_y' probe, and two quadrapolar coils, G_x and G_z of the standard imaging probe.

All three planar coils are in each probe the closest to the magnet pole pieces and are wound directly on the inner metal surfaces of the side panels of the probes. On the other hand, the smallest induced B_0-like field is produced by the planar G_z coils which use the Maxwell pair geometry (the 'super-G_y' probe and the plant-imaging probe). They are also the most inner layers on the probes. Therefore it is clear that there are at least two causes which lead to a significant B_0-like field, the distance from metal surfaces and the geometry of the gradient coil. The Maxwell pair geometry results in the least amount of B_0-like component in eddy currents, almost none in these two cases.

As for the two quadrapolar coils of the standard imaging probe, more data is needed to be conclusive. One possible cause for the significant B_0-like eddy current in the standard imaging probe may be due to the fact that both quadrapolar coils are wound on a cylindrical coil holder. If the holder is not oriented perfectly, then the angle misalignment could result in error in both coils.

(a) The standard imaging probe

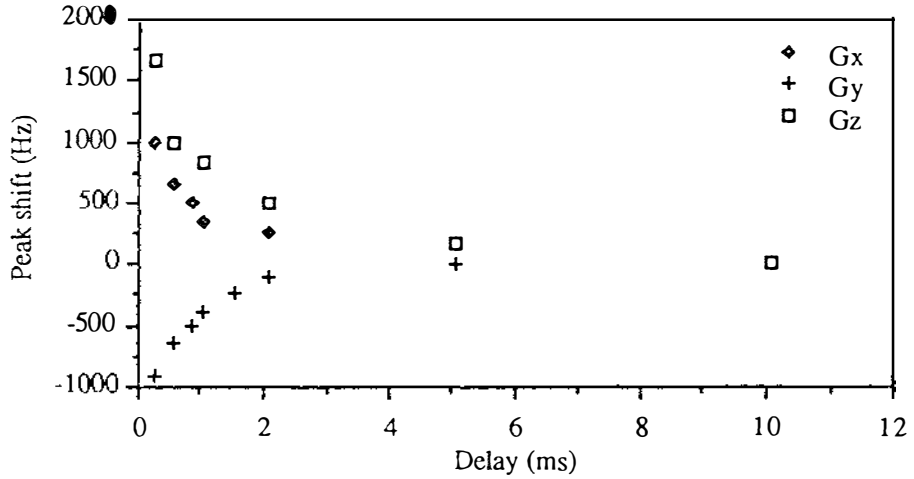

(b) The 'super-Gy' imaging probe

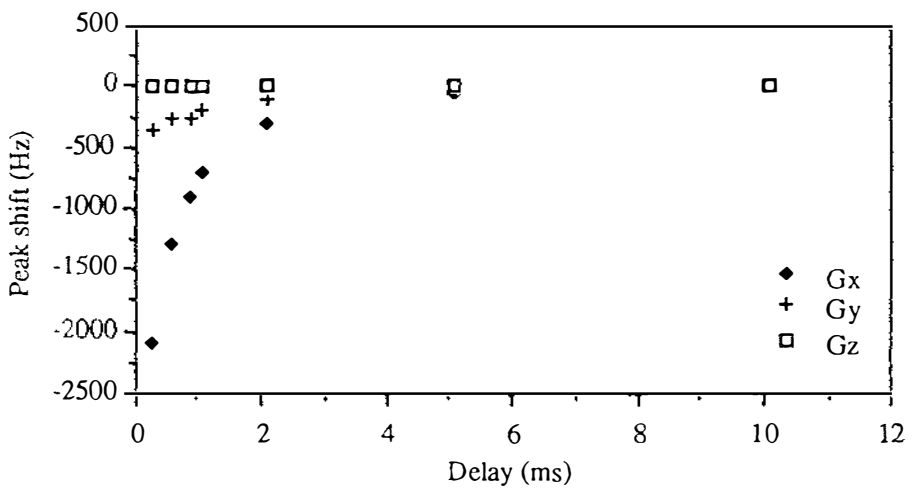

(c) The plant-imaging probe

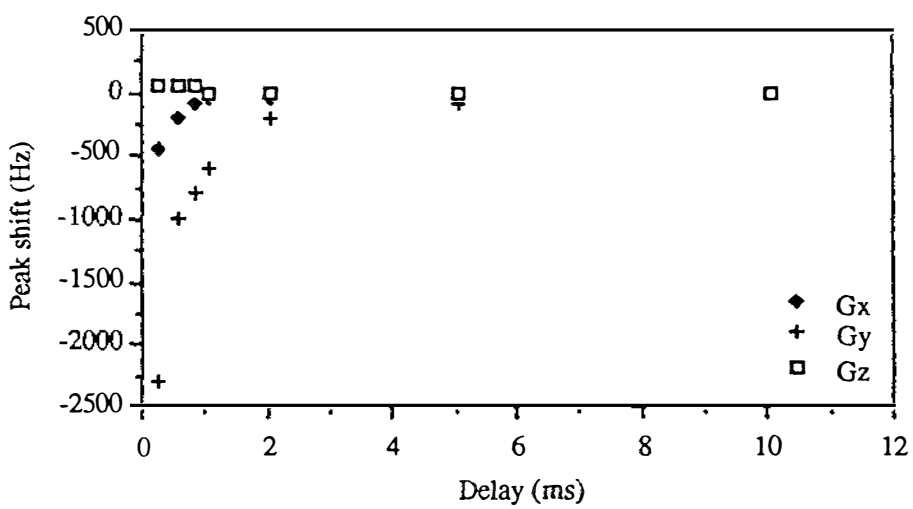

Figure 5.11 Measurements of B_0 shift due to induced eddy currents

To estimate the time constant of eddy currents, the total 'width' of the broadened peak or 'wiggled' signal was measured from each plot. After subtracting the 'natural' line-width of the spectrum, the broadened width was interpreted as the effect of a linear gradient. (It should be noted that such interpretation is an approximation to account for the effect of both the B_0-like and G-like components.) The natural logarithm of the percentage change of this 'eddy gradient' over the desired gradient (refer to Ch 4) was plotted against the delay time, τ, shown in Figure 5.12. The data were fitted using a simple straight line, where the 1/slope of the fitted line was interpreted as the time constant. The results are summarized together with the maximum ω_0 shift due to the B_0-like component for each coil in the following table. (the intercept of the fitted line, ($e^{int.}$), was also given.)

Table 5.1 Measurement of time constant of eddy current

	G_x			G_y			G_z		
Probe	$\Delta\omega_0$(Hz)	τ (ms)	$e^{int.}$	$\Delta\omega_0$(Hz)	τ (ms)	$e^{int.}$	$\Delta\omega_0$(Hz)	τ (ms)	$e^{int.}$
Standard	1000	0.51	0.54	-900	0.64	1.3	1600	0.61	0.31
Super-G_y	-2100	0.66	9.5	-350	0.72	0.037	0	0.66	0.76
Plant	-450	0.64	1.7	-2300	1.2	1.2	50	1.1	0.97

Note: $\Delta\omega_0$(Hz) was measured at τ=0.27 ms and the maximum pulse current of 10A.

It can be seen that the time constant of the residual eddy current in our electromagnet is less than 1 ms for most coils. If a time delay of 1 ms is used after the gradient pulse is switched off, the eddy current problem can be avoided. This is the method used in our experiments. By comparison, the eddy current in superconducting magnet lasts much longer, often for tens to hundreds of milliseconds[151-154]. Artifacts due to the eddy current induced fields in a superconducting magnet can therefore be much more severe than in an electromagnet.

The reason for a longer time constant for eddy currents in superconducting magnets may due to their metal structure. Superconducting magnets usually consist of several concentric cylinders, each at a different temperature such as the room temperature stainless steel outer shell, the 80 K and 40 K aluminium cryogenic radiation shields and the 4.2 K stainless-steel spool. It is known[155] that the long-

(a) The standard imaging probe

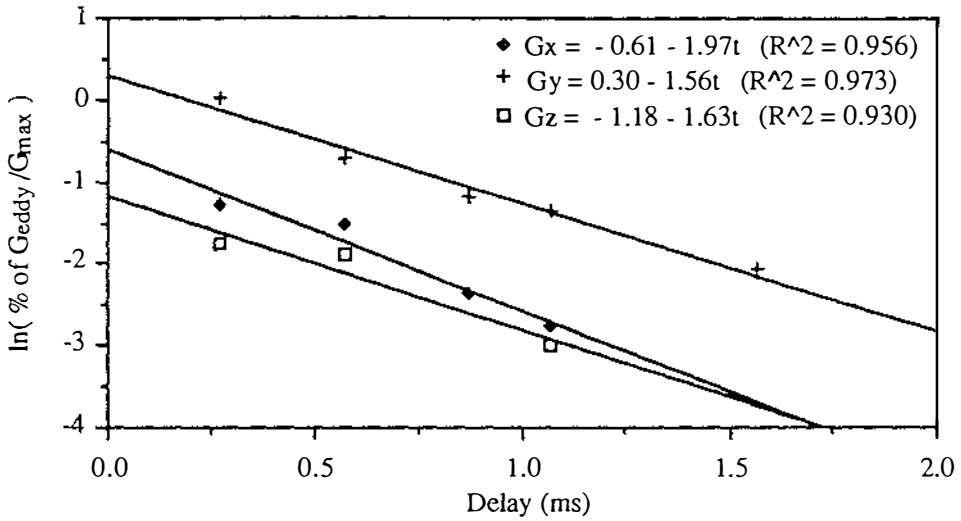

(b) The 'super-Gy' imaging probe

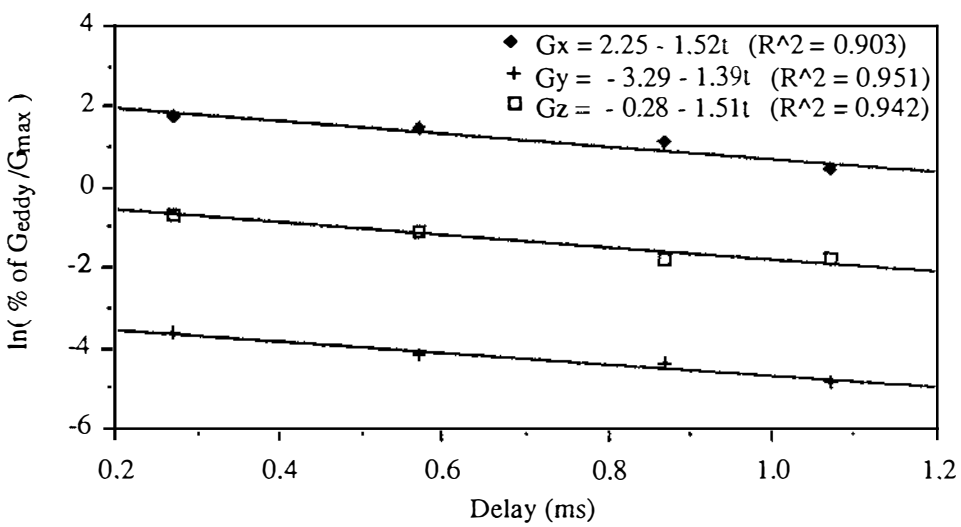

(c) The plant-imaging probe

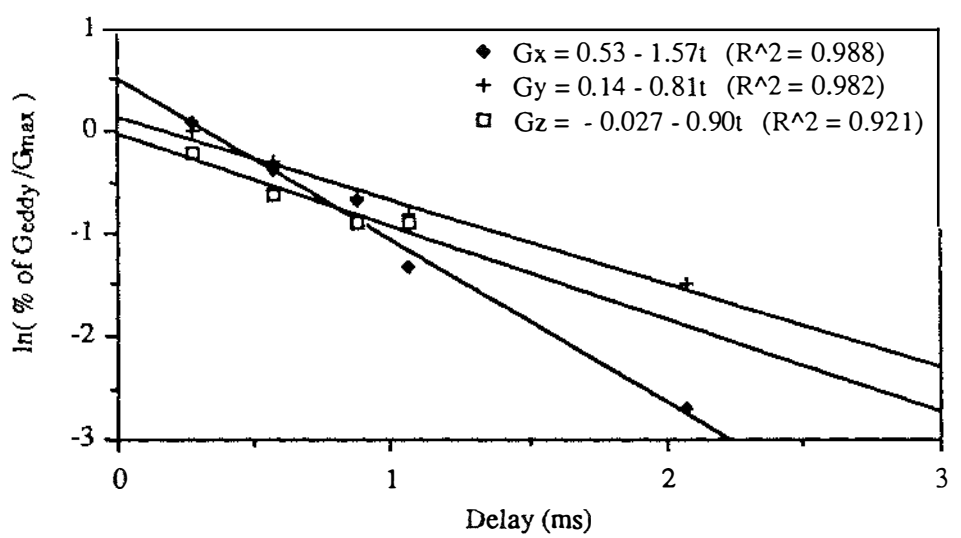

Figure 5.12 Logarithm of 'eddy gradients' as a percentage of the desired gradients

lasting tail of eddy currents in a superconducting magnet arises mainly from the 80 K shield. The fact that the closer room-temperature outer shell has less eddy currents is consistent with the eddy current behaviour in an electromagnet. Both the room temperature outer shell of a superconducting magnet and the metal of an electromagnet are at high (room) temperature and made of steel (high resistivity).

5.4.3 Simulation and discussion

In order to interpret the results shown in Figure 5.8 to Figure 5.10, computer simulations were carried out based on a Bloch-like expression, because the spectral peak should be a Lorentzian at the long τ limit, as

$$I_e(t) = A \exp(-t/T_a) \exp(\pm i\, \omega(t)\, t) \qquad [5.1]$$

where A is the maximum magnitude of the eddy-influenced signal, the first exponential term determines the decay of the signal with a time constant T_a and the second complex oscillation term represents a phase twist associated with the eddy-influenced signal.

If $\omega(t)$ in Eq[5.1] is independent of time, say

$$\omega(t) = c \qquad [5.2]$$

then $I_e(t)$ is just a normal FID which is a Lorenztian in the frequency domain with a width being $1/(\pi T_a)$ and the constant c being γB_0.

If, however, $\omega(t)$ is a function of time and takes the following form

$$\omega(t) = ct \qquad [5.3]$$

Then the Fourier transform of Eq[5.1] is the so-called 'wiggles' signal, shown in Figure 5.13. The positive or negative sign in the second complex oscillation term determines a direction where the 'wiggles' begin.

Now let us consider an induced eddy current which consists of a decaying B_0-like component and a G-like component. For the simplest case where only one time constant is associated with the B_0-like component, Eq[5.1] can be written, for the eddy current, as

$$I_e(t) = A \exp(-t/T_{a'}) \exp[\, i\, (b \exp(-n/T_b) + c)\, t\,] \qquad [5.4]$$

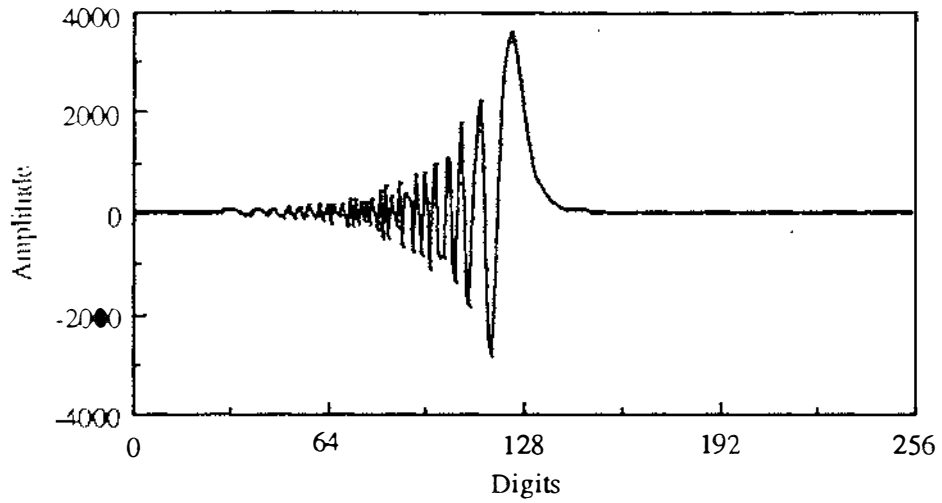

Figure 5.13 The wiggles signal

In the above equation, $T_{a'}$ determines the width of the eddy-influenced peak which counts both the natural line-width arising from spin relaxation and the effect due to the G-like component, b determines the amplitude of the decaying B_0-like component influencing the applied B_0. The decay of the B_0-like component has been assumed as a single exponential decay with T_b being the time constant and c has been defined in Eq[5.2].

By setting b=0 and c=constant, Figure 5.14 compares the Fourier transform of Eq[5.4] at two different values of $T_{a'}$. It is clear that a change in $T_{a'}$ results in a change in the width of the peak.

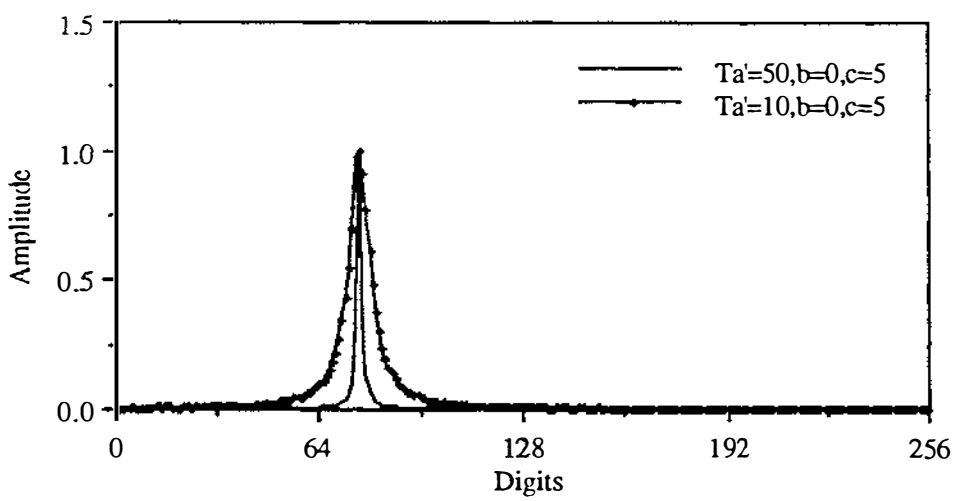

Figure 5.14 The change of the peak width due to different Ta'

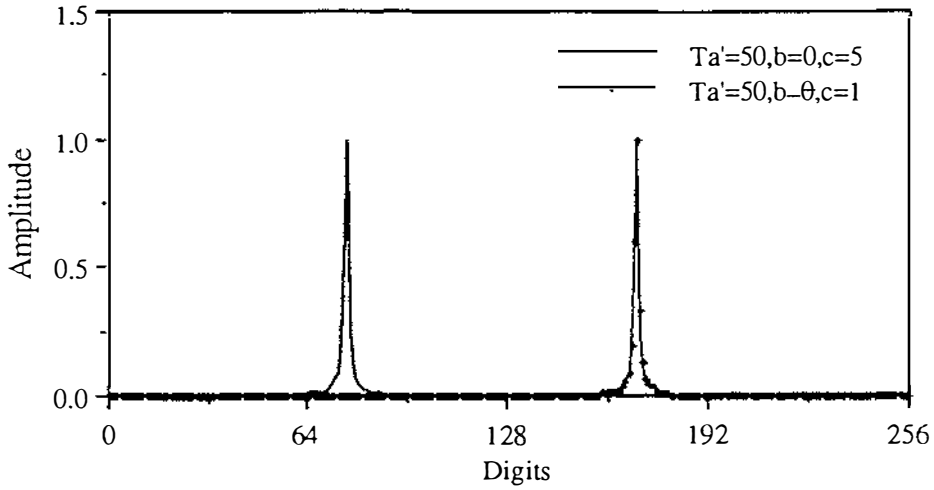

Figure 5.15 The change of the peak position due to different c

By setting b=0 and $T_{a'}$=constant, Figure 5.15 compares the Fourier transform of Eq[5.4] at two different values of c. It is obvious that a change in c results in a shift of the peak.

By setting b≠0 and $T_{a'}=T_b$, Figure 5.16 shows the Fourier transform of Eq[5.4] as well as the modulus of the complex signal. These plots have indeed exhibited the basic features of the experimental eddy-influenced plots shown in Figure 5.10. It is worth noting that the value of $T_{a'}$ in this simulation has been set to be equal to the value which corresponds to the narrow peak in Figure 5.14 but the apparent width of the wiggled signal in Figure 5.16 appears much wider than in Figure 5.14. It can therefore be concluded that the G-like component in the G_x-induced eddy fields of the 'super-G_y' probe is not as big as it seems to be from Figure 5.10.

The factor b in Eq[5.4] is of interest. Its value influences not only the 'frequency' of wiggles in the signal but also the position and the apparent width of the wiggled peak. With b being assigned to three different values, Figure 5.17a shows three plots at the big $T_{a'}$ which corresponds to the narrow width in Figure 5.14 while Figure 5.17b shows three plots at the small $T_{a'}$ which corresponds to the wide width in Figure 5.14. In Figure 5.17c, FT of Eq[5.4] at two different values of $T_{a'}$ are compared when b and c are constant.

In summary, although the behaviour of eddy currents in any practical situation could be much more complicated, the simulation of eddy currents using a simple expression has been carried out which successfully reassembled several key features of the experimental plots. From these simulations, it can be concluded that once there are

(a) Fourier transform of Eq[5.4] when Ta'=50, b=1.1 and c=5

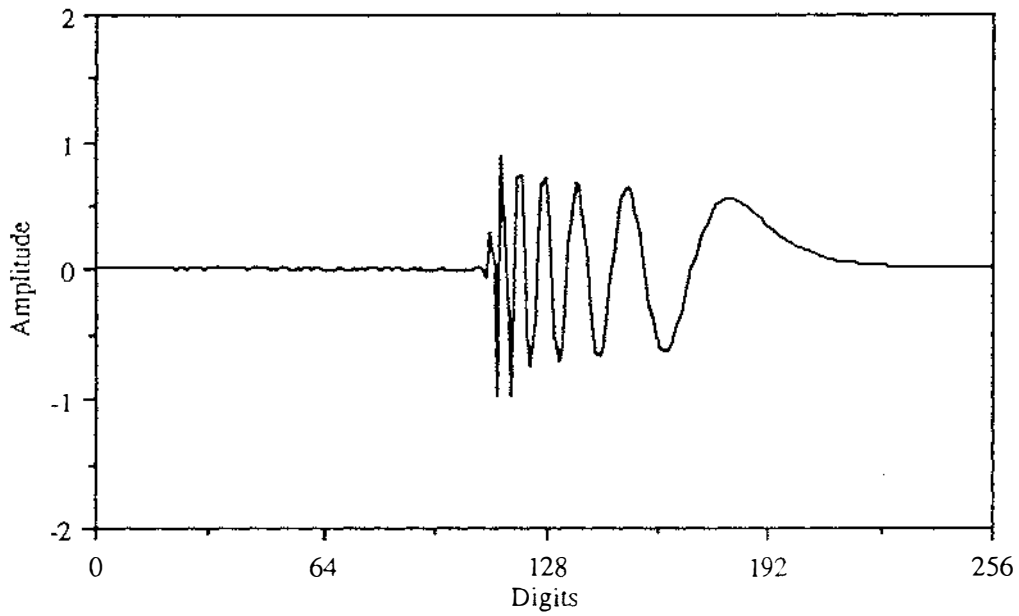

(b) The modulus of the simulation shown in (a)

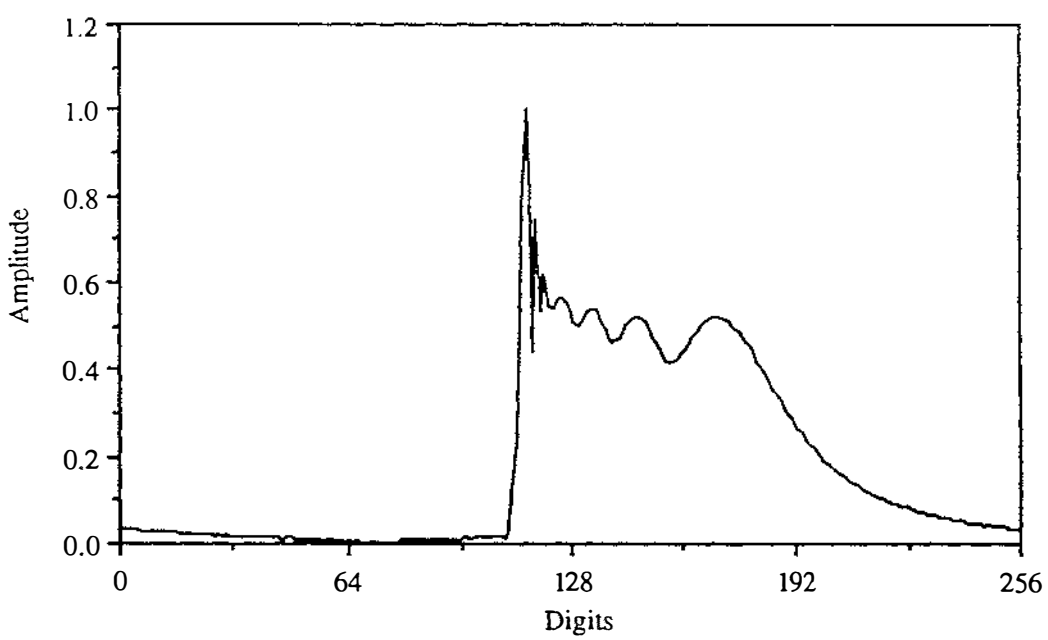

Figure 5.16 Simulation of the effect due to induced eddy currents

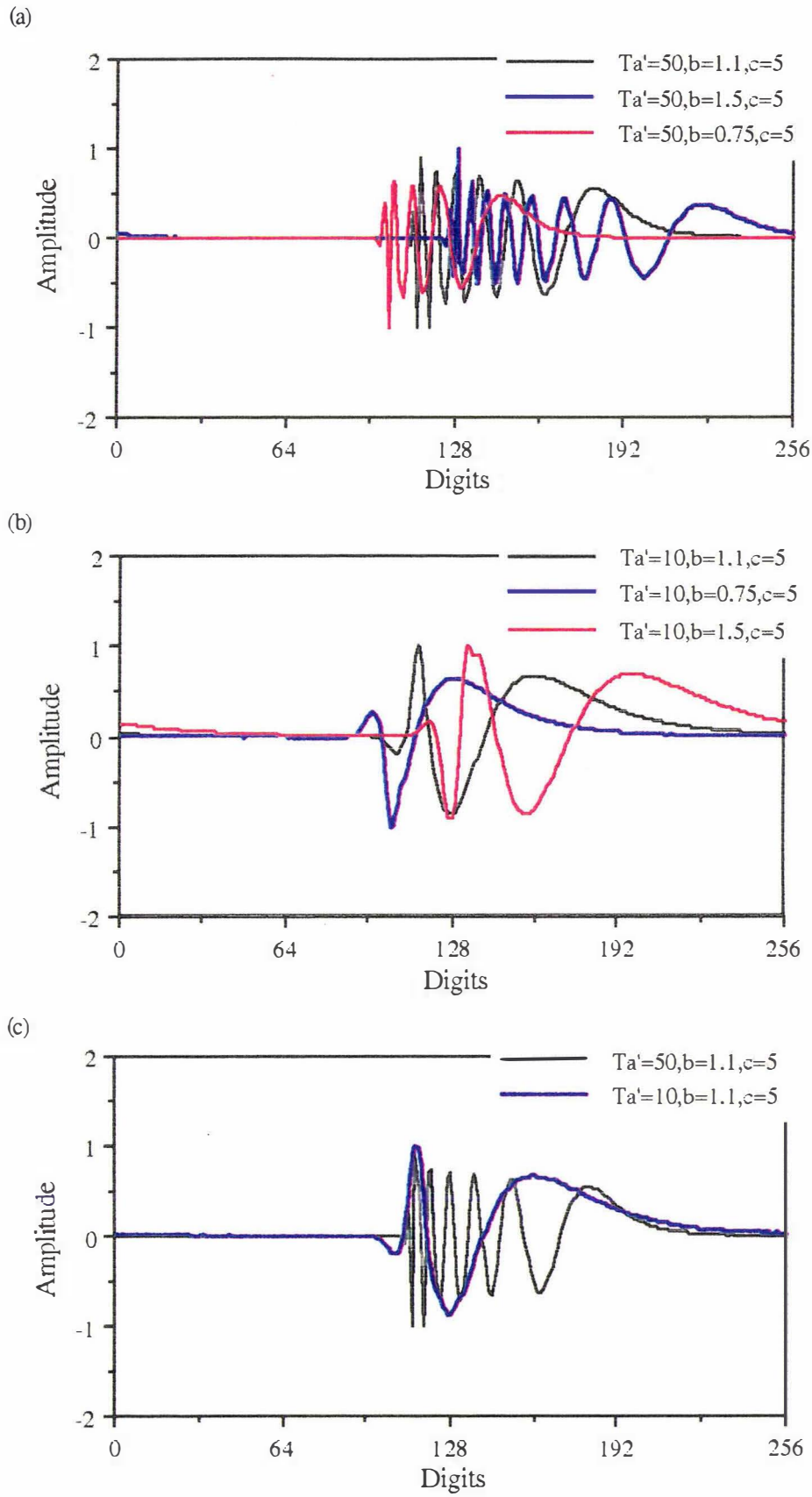

Figure 5.17 The influence of the factor b in Eq[5.4] during simulation

wiggles in the signal, the shift of the peak position and the broadening of the apparent width of the wiggled signal can no longer be simply interpreted as the effect of the B_0-like and G-like components of eddy currents respectively. Although a detailed interpretation of the influences due to eddy currents obviously requires further studies and is beyond the scope of this thesis, the conclusion of the simulation may be used as a guideline to understand the experimental results.

5.5 Static microscopic imaging experiments

In this section, some microscopic imaging results using static samples are given. These results serve as test images for the micro-imaging system.

5.5.1 Microslide phantom

A phantom with well defined dimensions is needed to test an imaging system and measure its spatial resolution. It was found that microslides (rectangular glass capillary tubes from the Camlab Ltd, Cambridge, England) are ideal phantoms for microscopic imaging because each has a precise width named the path length as shown in Figure 5.18. A phantom using two such microslides in a tube of water doped with 0.1% $CuSO_4$ was used as the imaging sample in the 2.1 mm rf coil of the standard imaging probe. A 360° PR method was used with an angle increment of 2°. The slice thickness was 200 μm. The band-width of the spectrometer was 10 kHz.

The obtained image is shown in Figure 5.19, which has a transverse pixel resolution of 14 μm with a S/N of 25.

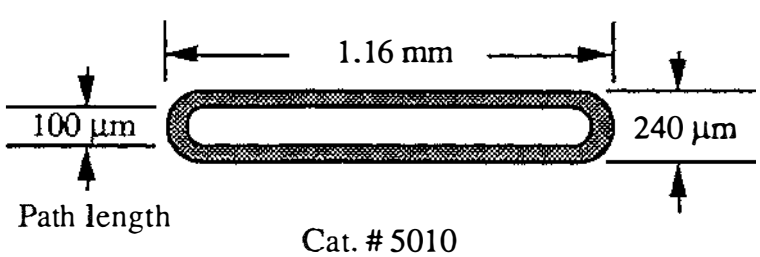

Figure 5.18 A microslide

5.5.2 Imaging using the new 'super-G_y' probe

To test the newly developed 'super-G_y' imaging probe, static imaging experiments were carried out using the same phantom as used in Ch 5.5.1. Considerable difficulties had been experienced in doing so. These difficulties related to the inconsistency of the signal phases as the relative magnitudes and signs of the G_z and G_x mapping gradients. Ideally there should be no phase shift associated with changing these mapping gradients, the phase of the signal being dependent only upon the detection phase of the spectrometer. However errors of up to 180° were observed as in the worst case of the oppositely signed G_x! Under these circumstances it was impossible to form an image because both G_x and G_z have to be employed simultaneously in a two-dimensional PR imaging experiment.

After some investigation it had found that by slightly adjusting the time delay between the 1 ms G_x and G_z pre-pulses and the 180° rf pulse all the phase differences could be eliminated and imaging experiments could be carried out successfully. One microscopic image of the static phantom obtained using this 'super-G_y' probe is shown in Figure 5.20.

The cause of such phase artifacts is probably the eddy currents induced in the surrounding metal by these gradient coils. By comparing the configurations and locations of the gradient coils in this new probe with those in the standard imaging probe, one should expect bigger eddies induced by the G_x and G_z coils of this new probe (because they are mounted on the metal surfaces of the probe's pc boards) and smaller eddies induced by the G_y coil (because it is mounted on a perspex block situated at the centre of the probe). This is indeed what it has been found! The extra phase shift due to the G_y gradient for this new probe is much smaller compared with that of the standard imaging probe because the G_y coil on the standard probe is mounted on the metal surfaces of the pc boards. Therefore the phase compensation for the PGSE gradient discussed in Ch 3.4 has not been needed in experiments using this new probe. Similarly, among the troublesome G_x and G_z coils, the phase difference of the positive and negative gradients of the G_z coil is smaller than that of the G_x because the G_z coil is further away from the metal pc boards (refer to Ch 4.2).

5.5.3 Imaging using the new plant-imaging probe

The testing of the plant-imaging probe has followed the same procedure as used for the 'super-G_y' probe. There are some signal phase differences between the two mapping gradients and between the oppositely signed imaging gradients, as expected from the previous experience with the 'super-G_y' probe. The problems were solved by a similar method to that discussed previously. A phantom which consists of one 1.3mm i.d. glass tube and two 200μm path-length microslides (#3520) was imaged successfully, as shown in Figure 5.21, where the 5.8 mm rf coil was used. The apparent coarseness of the image is due to the 6° PR method was employed in this experiment.

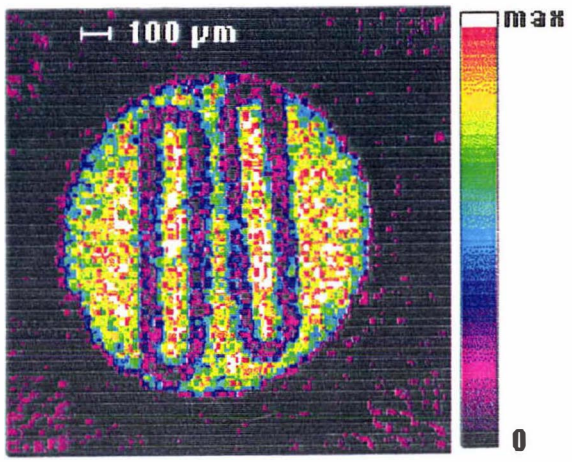

Figure 5.19 Static proton density image using the existing probe

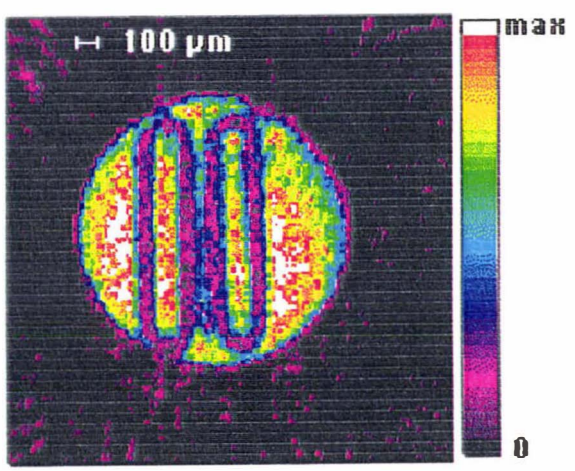

Figure 5.20 Static proton density image using the 'super-G_y' probe

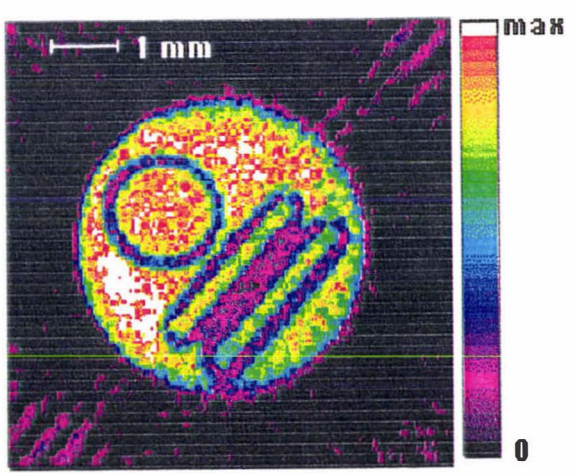

Figure 5.21 Static proton density image using the plant-imaging probe

5.6 H_2O and oil separation, T_1 contrast in imaging

The characteristic relaxation times, T_1 and T_2, of the sample can be used to impose a contrast on an image (refer to Ch 2.3), which offers a manner to identify various regions of a sample according to their T_1 or T_2. This form of identification is very simply made and can be useful when proton densities of these regions can not be clearly differentiated in a 'standard' imaging experiment.

For example, if one region of the sample has a T_1 of 0.06 second and other region has T_1 of 0.4 second, by using the inversion-recovery pulse sequence shown in Figure 5.22, one can get different images by varying the time τ. A τ value of 0.04 second (0.693×0.06) will give an image in which the "cross-over" nulls the signal from the region 1 leaving a signal only from the region 2. If τ equals 0.28 second then the image will contain a contribution only from the region 1. It is worth noting that the T_1 contrast pulse sequence shown in Figure 5.22 is almost identical with that shown in Figure 5.1 except that a 180° rf pulse precedes the experiment.

An imaging experiment was carried out, as part of a collaborative project with BHP Australia, using a phantom consisting of three glass tubes, one filled with doped water (T_1 of 60ms and T_2 of 30ms) and other two with ordinary kitchen oil (T_1 of 400ms and T_2 of 300ms). The experiment was performed using the standard imaging

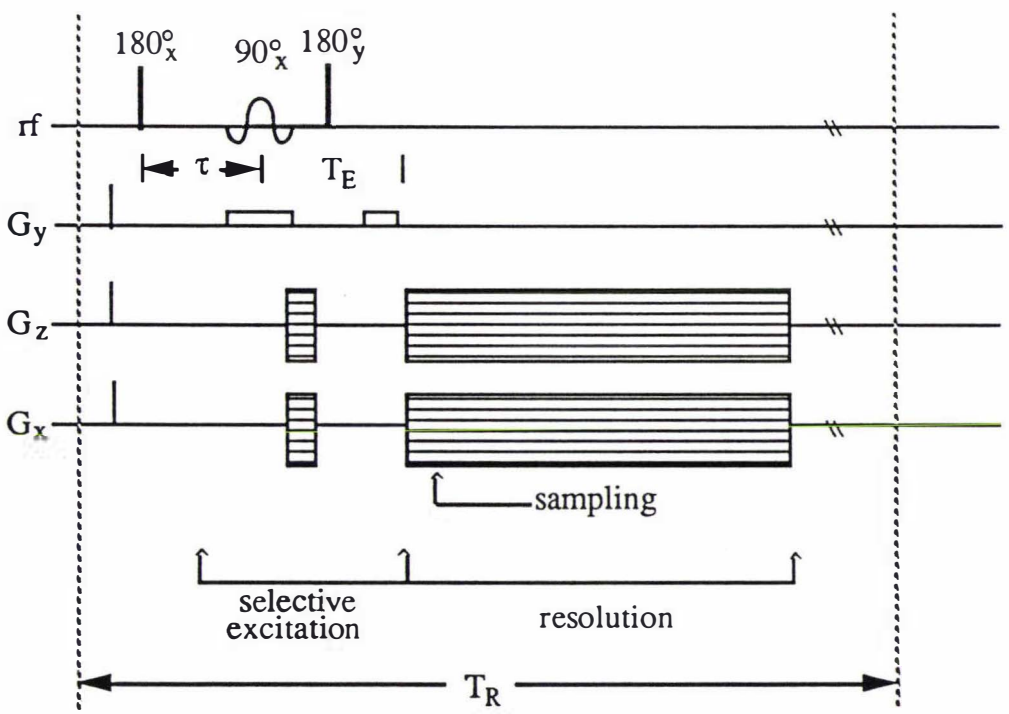

Figure 5.22 A pulse sequence used in T_1 contrast imaging

probe and 5.8 mm rf coil. Figure 5.23 shows the images obtained with (a) a τ of 0.04 s and (b) τ of 0.28 s. The water image exhibits very good suppression of the oil signal apart from the 'star tracks' caused by the zero-frequency glitch (a 180° PR method was employed in this experiment). The small 'tails' on the oil image are caused by the CH_3 and CH_2 groups in the oil having different chemical environments so that they resonate at two slightly different frequencies. During that experiment the resonant frequency of the spectrometer was set at the middle of these two frequencies therefore both groups were 'off-resonant' (with one over and other under) so causing the up and down tails. The superposition of the images in (a) and (b) is shown in Figure 5.23(c).

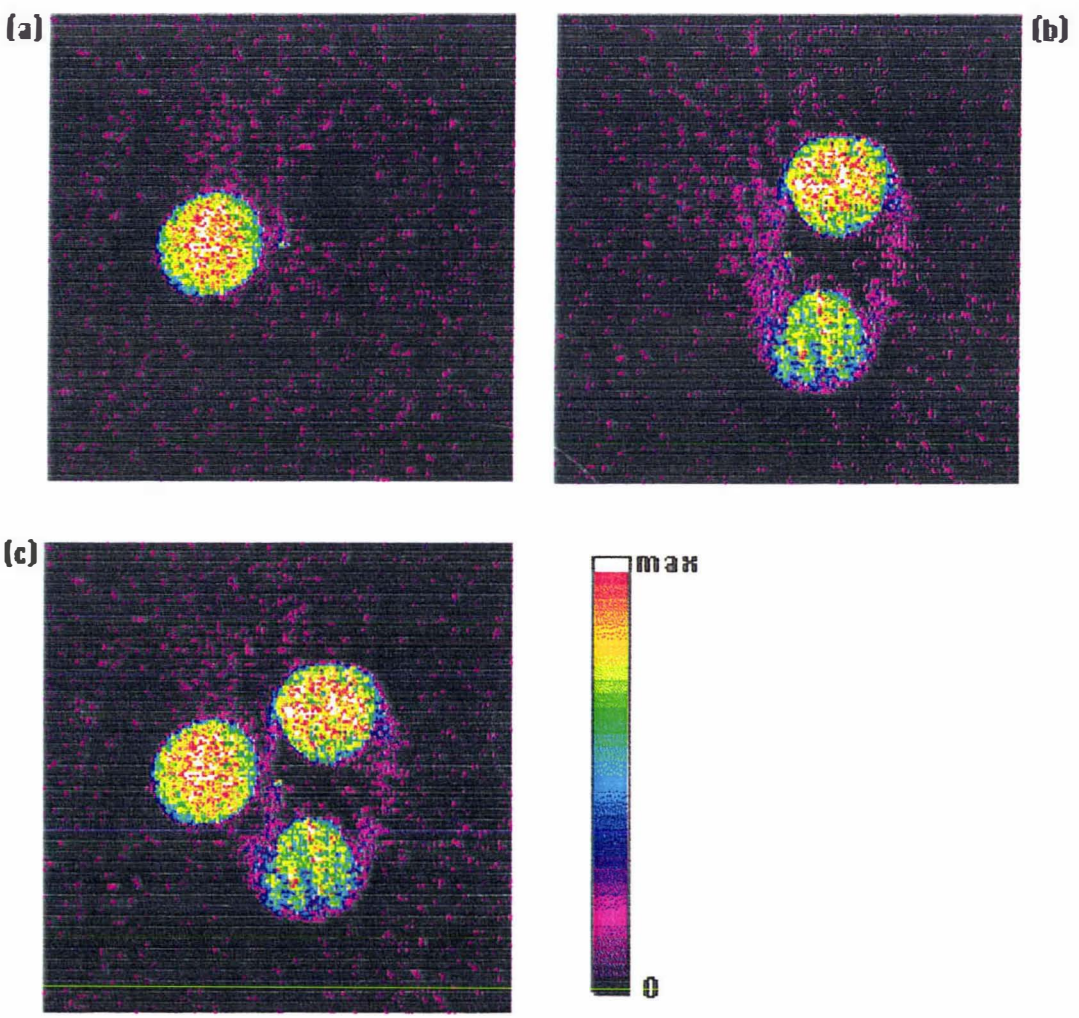

Figure 5.23 The images of T_1 contrast experiment: oil/water separation

5.7 Summary

This chapter has first discussed the practical considerations in designing static imaging experiments at the FX-60 micro-imaging system. The pulse sequence used in imaging experiments has also been discussed.

The next three sections in this chapter have been used to discuss three instrument-related issues in NMR microscopy, namely the attempt to improve spatial resolution by scaling down the receiver coil to 0.9 mm, the zero-frequency 'glitch' artifact and the effect of induced eddy current in imaging experiments. In the first issue, in order to improve spatial resolution, a 0.9 mm i.d. rf coil has been made and tested. The result wasn't much better than that from using the 2.1 mm i.d. rf coil. This has suggested that high sensitivity can not be achieved by simply scaling down the dimension of the receiver coil once the size of the coil has reached an optimum lower limit. In the second issue, the origin of the zero-frequency 'glitch' artifact has been discussed with some computer simulations. The means by which this artifact may be removed has been suggested. This approach has been tested in imaging experiments and the results are satisfactory. In the third issue, the effect of induced eddy current in our electromagnet has been measured for all gradient coils in three imaging probes. The results have been analysed and the reasons why the induced eddy current in an electromagnet produces fewer image artifacts than in a superconducting magnet have been suggested. Computer simulations of eddy induced effects have also been carried out based on a Bloch-like expression. The experimental waveforms have been reproduced successfully using that expression.

Some static phantoms have been imaged and the results are presented in this chapter. These images serve as tests of the imaging probes and the instrument. From these images it can be concluded that the design and manufacture of the two new imaging probes have been successful, and that microscopic resolution can be achieved in the electromagnet-based imaging system provided that care has been taken at every stage of the imaging procedure. Such high resolution is normally achieved using more expensive high-field superconducting magnets.

The use of T_1 contrast in imaging experiments has also been illustrated in this chapter. With a knowledge of T_1 relaxation times of the sample, the experimental results have shown that T_1 contrast can be incorporated into imaging experiments.

Chapter 6 Water Capillary Flow

A number of results for water capillary flow experiments are presented in this chapter. The first section discusses experimental aspects which are special to dynamic imaging. The next two sections demonstrate the capabilities and possible artifacts of both Dynamic NMR Microscopy and the 'one-shot' velocity microscopy. The results in this chapter serve as a test for the techniques developed in this thesis.

6.1 Designing experiments for dynamic imaging

In dynamic NMR micro-imaging, the slice excitation and spatial mapping in k space follow the same guide-lines appropriate to static imaging. These have been discussed previously in Ch 5.1. This section discusses those aspects of the method which are special to dynamic imaging.

6.1.1 Dynamic NMR Microscopy experimental design

A typical pulse sequence employed in Dynamic NMR Microscopy in our system is shown in Figure 6.1a, in which the filtered back-projection reconstruction method is employed. Compared with the pulse sequence used for static imaging (Figure 5.1), the selective excitation and spatial mapping segments are identical with those used for the static NMR micro-imaging, hence the choices of **k**-space mapping parameters follow the same guide-lines discussed previously. It should be noted that dynamic imaging requires all four quadrants to be sampled and both real and imaginary signals to be stored. In practice this means that both mapping gradients must be bipolar and both real and imaginary images have to be constructed simultaneously.

In the dynamic contrast period, a single dimension in **q** space is normally chosen so that the over-all imaging process is four dimensional. The direction of the **g** gradient determines the direction in which diffusion and flow are to be measured. The **g** gradient can either be produced by an independent power supply and/or gradient coil, or it can be combined with the corresponding k gradient but controlled separately. For example, to measure longitudinal flow, the g and G_y gradients can be combined. This

simplification may, however, lead to a smaller dynamic range for digital adjustment of k gradient if a large q gradient is required.

The choices of δ, Δ, and g, are dependent upon the magnitudes of velocity and diffusion to be measured in experiments. The velocity map is measured from the peak offset which ranges from -128 to +127 in a default digital scale. Some artifacts, digital rounding errors and the influence of the noise always exist in a velocity map and they range between -2 to +2 for stationary spins in a well-set experiment (refer to Ch 3.4). In order to obtain the maximum precision in the velocity measurement, it is therefore important for k_v values to be reasonably large. However the Nyquist sampling theorem requires that the entire P_s spectrum be situated below N/2 if the fold back effect is to be avoided. A velocity digit near $\pm N/2$ can also result in an incorrect FWHM value. Therefore it is important to select experimental parameters which will make k_{FWHM} sufficiently large (to avoid the signal truncation) while keeping k_v large but between $\pm N/2$.

While Δ has the same effect for both velocity and diffusion, the velocity phase shift is proportional to g and δ while the self-diffusion attenuation is proportional to g^2 and δ^2. Therefore an appropriate combination of these three parameters will always satisfy the above requirements for a particular experiment within the constraint of spin relaxation. The T_1 of the sample governs the longest Δ one can have for experiments. The T_2 of the sample needs to be longer or at least of order Δ otherwise the stimulated echo sequence has to be used. Figure 6.1b shows a dynamic imaging pulse in which the stimulated echo sequence is incorporated.

Other practical considerations special to Dynamic NMR Microscopy in our system relate to the two phase look-up tables in the TI-980A computer software. The stability of the signal and detection phases are of particular importance in dynamic imaging. There are two adjustable phase values in NMR spectrometers, the zero order (P0) and the first order (P1). P0 is the absolute signal phase while P1 is the frequency-dependent phase shift which relates to the time origin of sampling. By careful choice of sampling origin the need for P1 corrections in our system is avoided. However, the P0 phase in our system is very sensitive to different PGSE gradient levels and different mapping gradient directions, which is probably due to the imperfection of the gradient coil, the eddy current in the surrounding metals or the feed-back circuit of the lock circuit used in an electromagnet-based spectrometer. This P0 phase change of the signal can produce a false velocity 'base-line' in the final image. In our experiments the

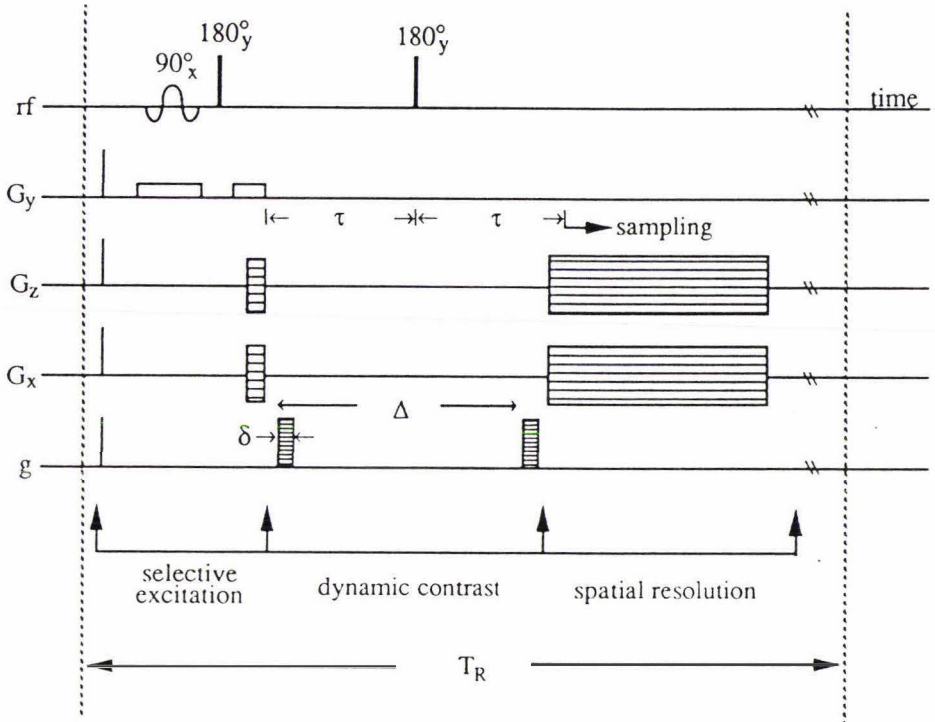

Figure 6.1a A pulse sequence for Dynamic NMR Microscopy experiments

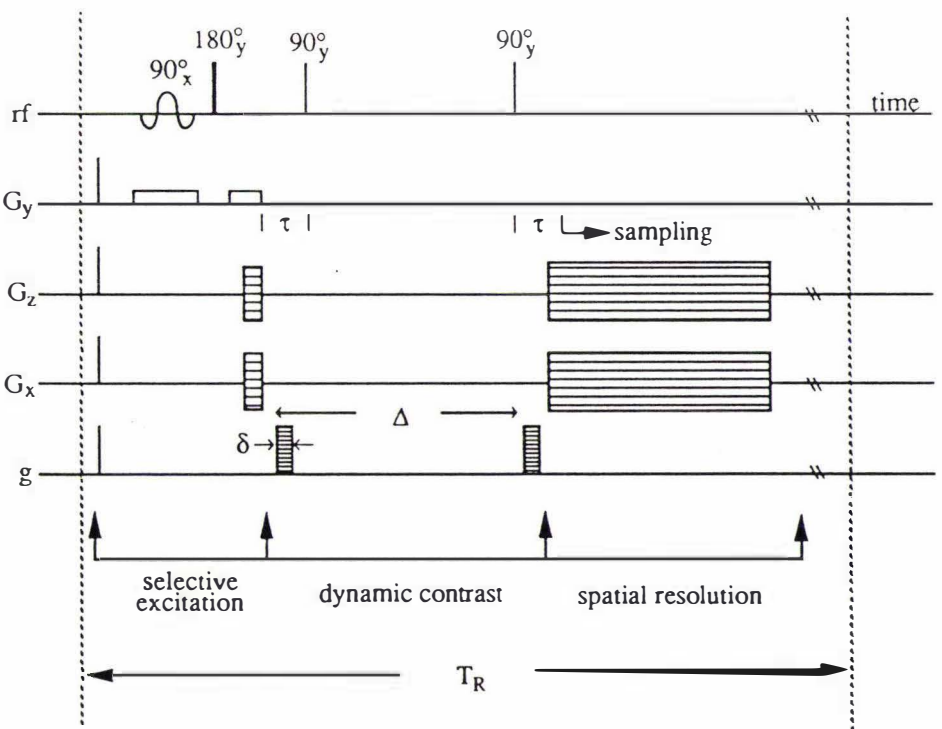

Figure 6.1b A stimulated-echo pulse sequence for Dynamic NMR Microscopy experiments

phases for all PGSE gradients are checked for each individual level before an imaging experiment starts and the results are stored in a table for automatic adjustment.

The other phase look-up table relates to the compensation of P0 phase differences due to orientation of the mapping gradients. In our system, due to the reasons which have been discussed previously in Ch 4.4, a phase-compensating table for the second, third and fourth quadrants is set up on the basis that the phase for the first quadrant is pre-set correctly. The four phase values in this table are adjusted to a compromise so that at the end of the four-quadrant image reconstruction the first real image (PGSE=0) is correctly in-phased and the first imaginary image is subject only to noise.

The initial Dynamic NMR Microscopy experiments[132] were carried out before the introduction of the Macintosh computers, the experiment being performed utilizing the Hitachi personal computer. At the moment there are two approaches to these experiments. The first (original) approach is to use one Hitachi computer to receive the 1-D projection profiles, reconstruct the data images and store the complete data set on a single 320 kbytes floppy disk. This approach limits the data image array size to 64×64 and the maximum number of q slices to 18. The second and newly developed approach is to incorporate both Hitachi and Macintosh computers during the data acquisition, letting the Hitachi to carry out the data image reconstruction and the Macintosh to handle the data image storage and analysis. Therefore the only limitation to the image array size and the number of q slices are the RAM size available in the Macintosh and the longest experimental time which can be tolerated. Experiments using 128×128 array sizes have been carried out successfully (a set of 18 data images occupies 1.125 Mbytes) and the results are presented later in Ch 7. Of course a more logical choice is to completely replace the Hitachi using a Macintosh, which is left for future work.

Laminar water flow through a circular tube, the classical Poiseuille velocity distribution, is an ideal candidate for dynamic imaging because its flow field consists of a wide range of different velocities. A constant water flow system can be established simply by using a small diameter capillary tube and two glass beakers containing water. The water can be doped with $CuSO_4$ to reduce the T_1 relaxation. The flow rate can be adjusted by the height difference Δh between the two water reservoirs. Provided that the volume flow rate is small and the diameters of the glass beakers are large, the influence of water level change during the hour-long experiment could be small. The existence of tiny air bubbles dissolved in the water is a problem because, during the experiment, these bubbles will gradually grow and stick to the wall of the capillary, resulting in a

decrease in the flow rate. To avoid this effect the water can be pre-treated in an ultrasonic bath for about twenty minutes to drive out the air bubbles. This has proved to be helpful but hasn't solved the problem completely, since the air dissolves again once the water is out of the ultrasonic oscillator.

To carry out the velocity-compensated Dynamic NMR Microscopy experiments, a pulse sequence with a double PGSE pulse train is used as shown in Figure 6.1c. In this pulse sequence, the last 180° rf pulse just before the application of the spatial mapping gradients is used to shift the start of the **k**-space sampling away from the falling edge of the strong PGSE pulse to avoid the eddy current problem.

6.1.2 'One-shot' velocity microscopy experimental design

The pulse sequence used in the 'one-shot' velocity microscopy is shown in Figure 6.2, in which the phase cycling table (Table 3.5) and the stimulated echo sequence were employed. The experimental design criteria for this 'one-shot' technique are similar to that used for Dynamic NMR Microscopy experiments. Gradient phase cycling requires that the PGSE gradient direction to be switched in a four-step sequence. Because the KEPCO power supply is a monopolar power supply, a physical switch of the output leads is required during the imaging experiment. A simple relay circuit (Figure 6.3) was wired which was controlled by a TTL output of the pulse programmer. A 50 ms settling time is given before the first action of the pulse sequence to allow the relay to be in good contact.

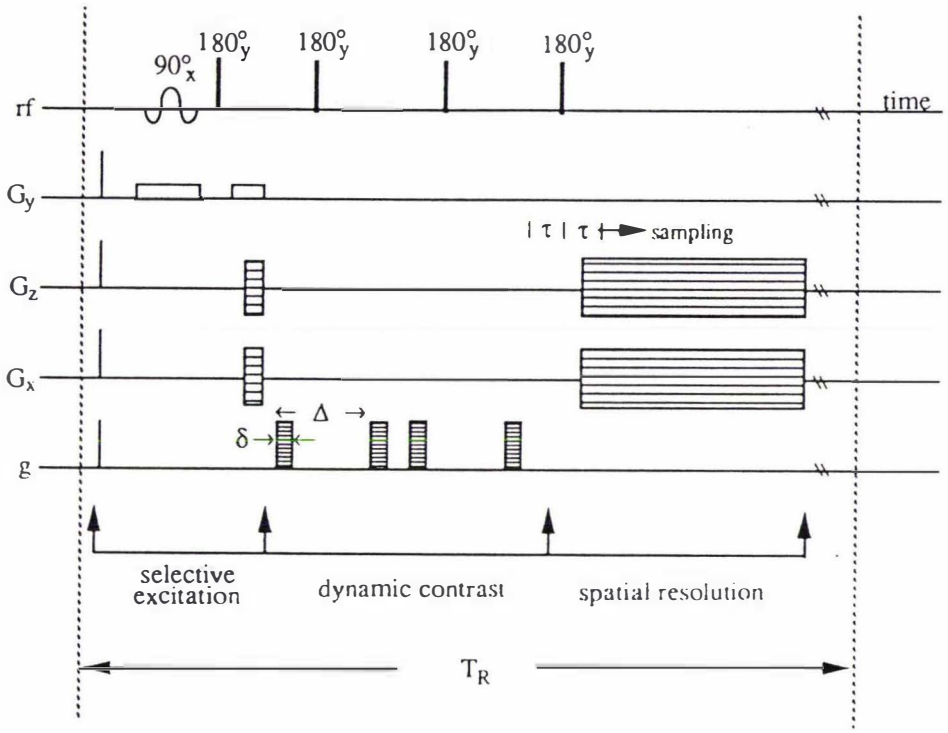

Figure 6.1c A pulse sequence for velocity-compensated Dynamic NMR Microscopy experiments

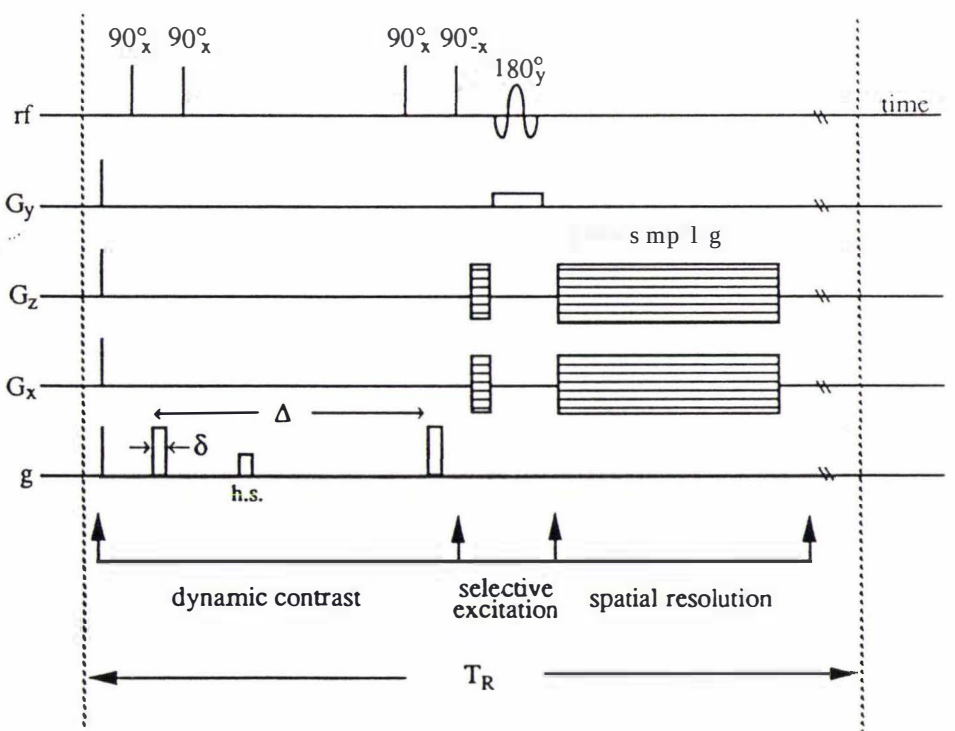

Figure 6.2 A stimulated-echo pulse sequence for the 'one-shot' velocity microscopy experiments

(a) The relay driven circuit

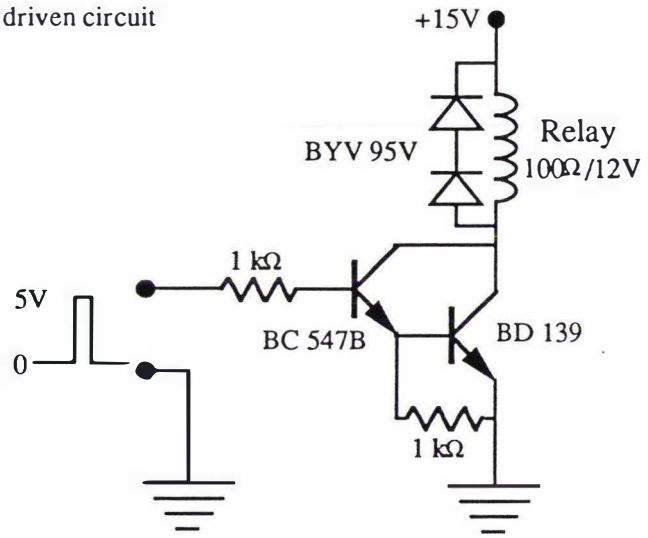

(b) The gradient switch circuit

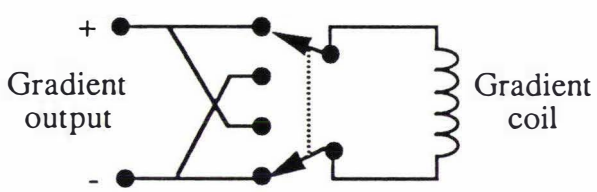

Figure 6.3 A relay circuit for the gradient switching

6.2 Capillary flow studied using Dynamic NMR Microscopy

The parabolical Poiseuille tube flow is ideal for testing the dynamic imaging technique, because it provides a wide range of velocities from a maximum at the centre to zero at the edge of the tube and its profile is well-described by Navier-Stokes equation (Eq[3.55]). In this section the capability of Dynamic NMR Microscopy is demonstrated through various experimental results for water capillary laminar flow. The precision of and artifacts associated with the measurements are also examined.

6.2.1 Poiseuille flow

The initial water Poiseuille flow experiment[132] using a 700 μm i.d. Teflon capillary tube produced a nice Poiseuille velocity profile, but with an velocity error about 20% and self-diffusion error over 200% (~6×10^{-9} m^2s^{-1}) for the water. After careful investigation and subsequent modifications both in hardware and software which have discussed in the previous chapters, both the velocity and self-diffusion maps can now be obtained accurately and precisely in the Dynamic NMR Microscopy experiments.

Figure 6.4 shows one set of the multiple q-slice data images acquired during a Poiseuille flow experiment with a maximum velocity about 6 mm s^{-1} established by a simple constant flow system. The experiment used the pulse sequence shown previously in Figure 6.1a, the direction of the PGSE gradient **g** being along the direction of flow (vertical y direction). The images were constructed with an array size of 64×64 at 6° steps from 0° to 360°. Some of the experimental parameters are summarized in the following table.

Table 6.1 Summary of experimental parameters in Poiseuille flow

Δ (ms)	δ (ms)	g (G/cm)	BW (kHz)	N_{acc}	T_R (sec)	Pixel resolution	
						Slice(mm)	Transverse(μm)
5	2	93.6	10	24	0.4	1	20

Successive real and imaginary images were obtained as q was increased by stepping the PGSE gradient in 18 intervals. There are three features on this set of data

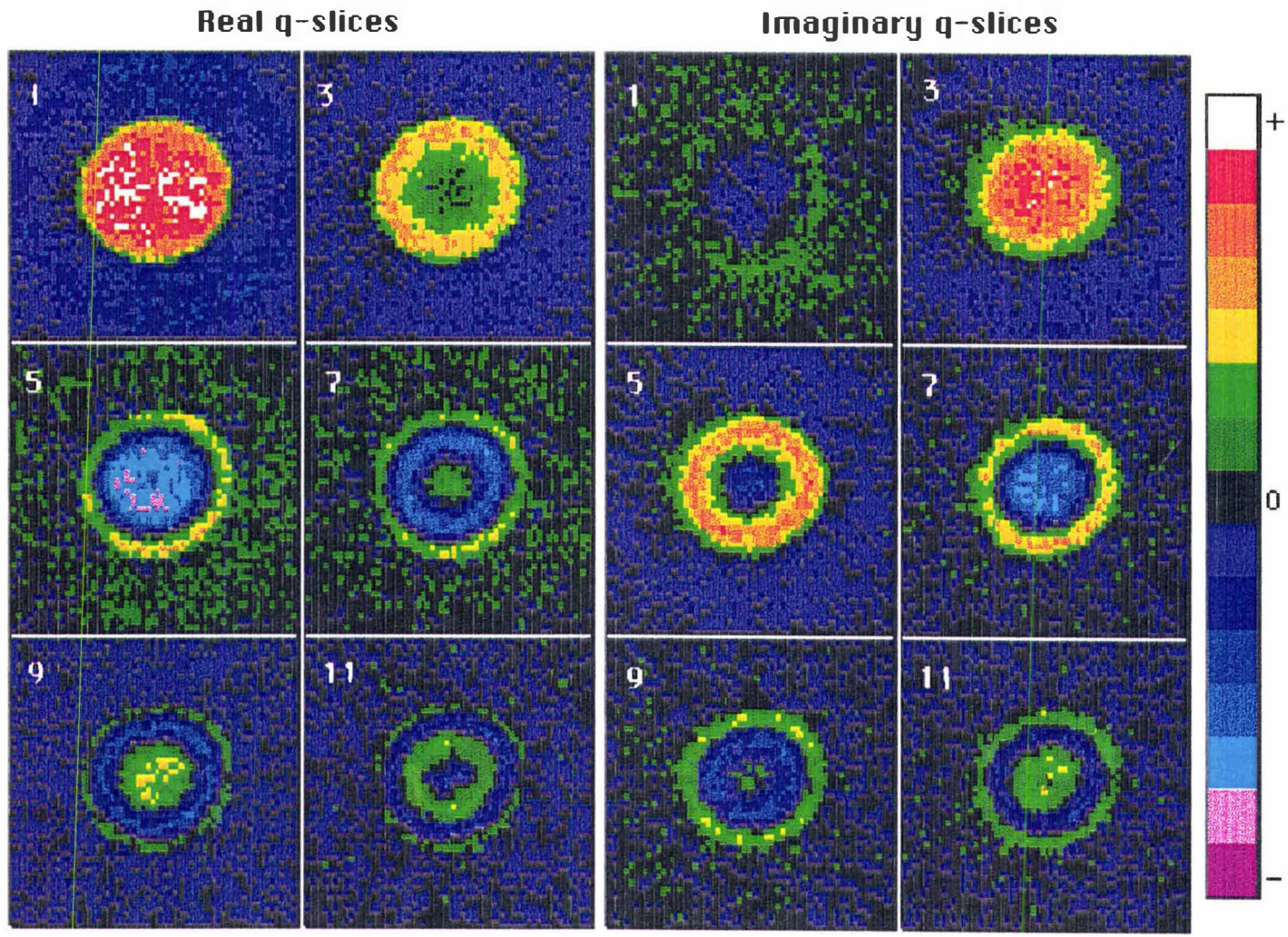

Figure 6.4 A typical set of q-slice data images for Poiseuille flow (q direction: axial)

images. First, the alternating and progressively-developing phase rings are typical for the centrally symmetric Poiseuille flow, representing an increase of the phase cycles as g is increased in magnitude (the second term in Eq[3.7]). A 90° phase difference is expected between each pair of corresponding real image and imaginary image. As predicted before in Eq[3.18], the first real image is exactly an ordinary static image, and the first imaginary is effective null. Second, the image intensity is attenuated as g is increased because of the diffusive motion (the first term in Eq[3.7]). Signals from the last real and imaginary images are effective zero, which satisfies the non-truncation requirement. Last, the circular symmetry of the image means there is no azimuthal dependence of the flow.

Velocity and self-diffusion at each pixel location are calculated from the Gaussian curve obtained by Fourier transforming the signals at this pixel along the applied q direction. A typical dynamic displacement profile, $P_S(Z,D)$, and linear regression plot obtained from this data set are shown in Figure 6.5. Maps of self-diffusion coefficient and velocity using both the FFT method and the Stejskal-Tanner method[50] are shown in Figure 6.6.

A series of capillary flow experiments were carried out at different flow rates using the above parameters and pulse sequence. Figure 6.7 compares stacked profile plots of velocity and self-diffusion maps for three different flow rates resulting from pressure heads of 0 mm, 30 mm and 60 mm respectively.

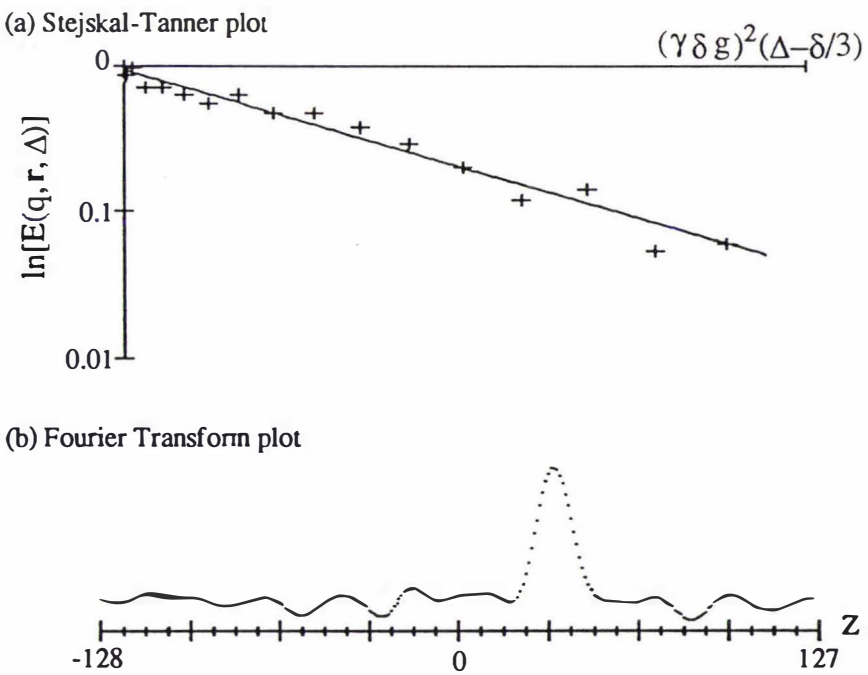

Figure 6.5 An example of a Stejskal-Tanner plot and its corresponding FFT plot

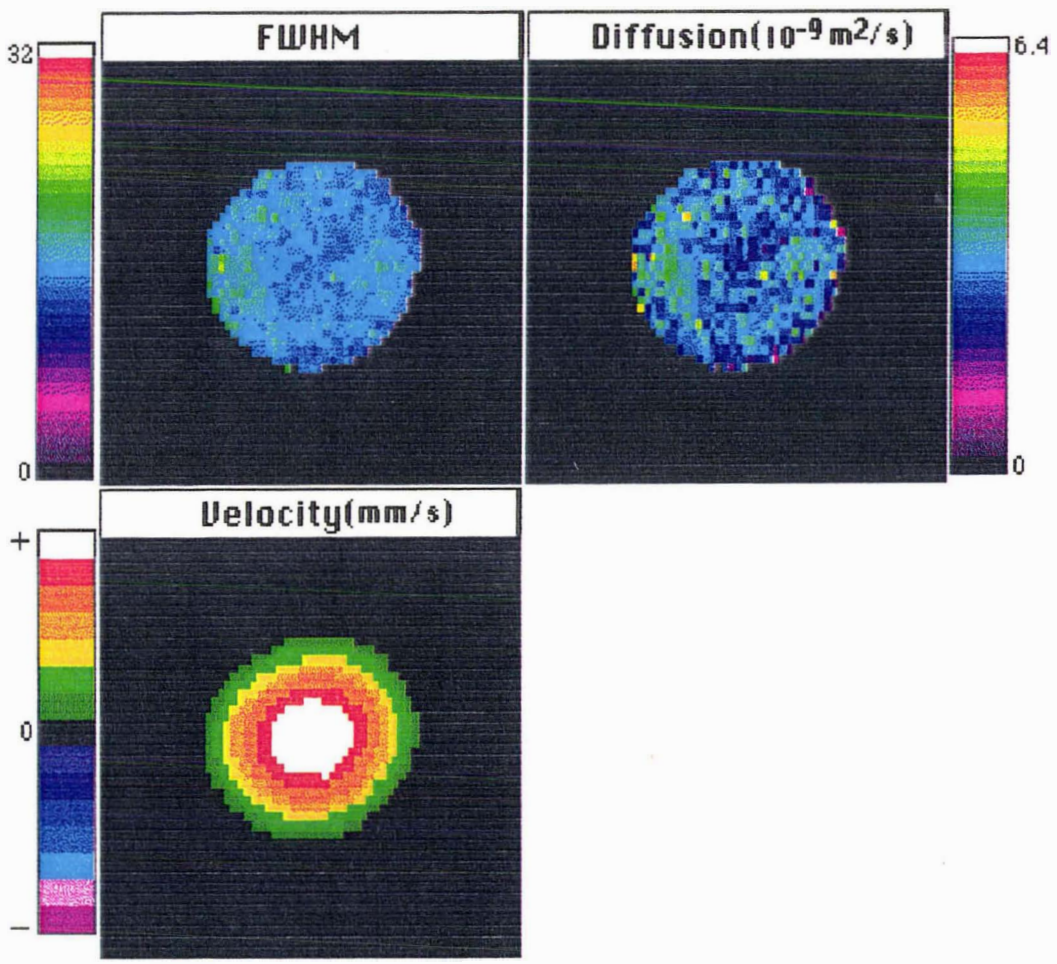

Figure 6.6 A typical set of velocity, FWHM and diffusion maps for Poiseuille flow

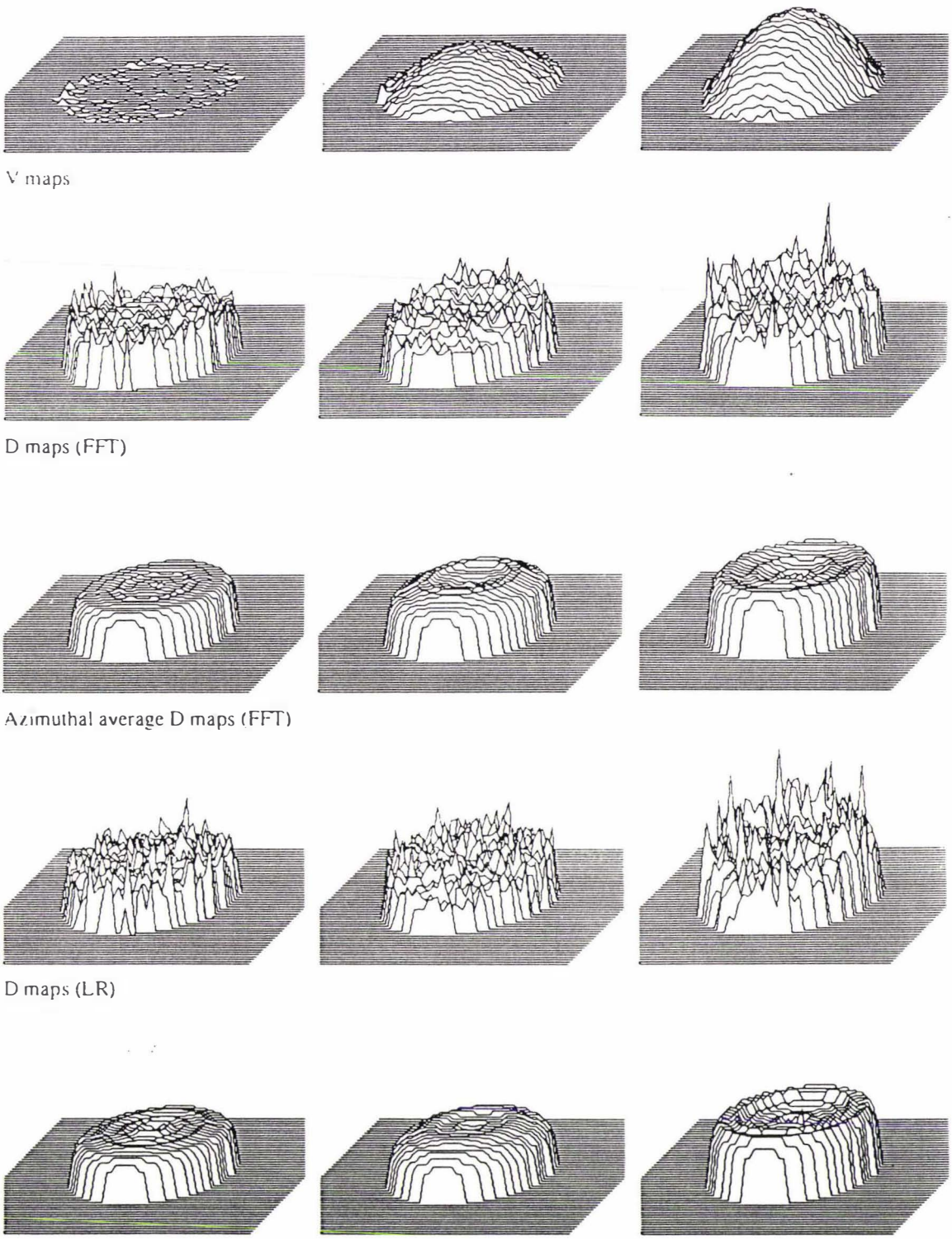

Figure 6.7 Stacked profile plots of velocity and diffusion maps for capillary flow experiments. (FFT refers to diffusion coefficients obtained from the FWHM values of the dynamic displacement profiles, and LR refers to diffusion values obtained by a linear regression fit to a Stejskal-Tanner plot.)

Precision and accuracy of the velocity measurement

The cross sectional plots through the centres of the velocity maps are given in Figure 6.8. The velocity profiles are well described by the quadratic dependence on radius predicted by Eq[3.55]. Table 6.2 gives a comparison of maximum velocities given by the theoretical calculation and by the velocity images. The agreement is excellent.

Table 6.2 Comparison of the theoretical calculation and the experimental results

Δh (mm)	Theoretical $V_{m\,a}$ (mm/s)	Experimental V_{max} (mm/s)	Error (%)
0	0±0	0.2±0.5	
30±4	3.4±0.7	3.5±0.5	+3
60±4	6.9±1.1	6.2±0.5	-10

In the above table, the experimental data are calculated using Eq[3.26], where N=256, n_D=17, g=0.936 T m^{-1}, $\gamma=2.675\times10^8$ $radT^{-1}s^{-1}$, $\delta=2\times10^{-3}$ s, $\Delta=5\times10^{-3}$ s; while the theoretical values are calculated using Eq[3.55], Eq[3.56] and Eq[3.57], where $\rho=0.996\times10^3$ kg m^{-3}, g=9.8 kg m^{-2}, l=3.21 m, $\eta=0.815\times10^{-3}$ (29°C), and $R=0.35\times10^{-3}$ m. The error in experimental values are estimates based on the discussion in Ch 3.4, while the error in theoretical flow rates arise mainly from the uncertainties of the water pressure head difference in the inlet and outlet reservoirs and the diameter of the Teflon capillary.

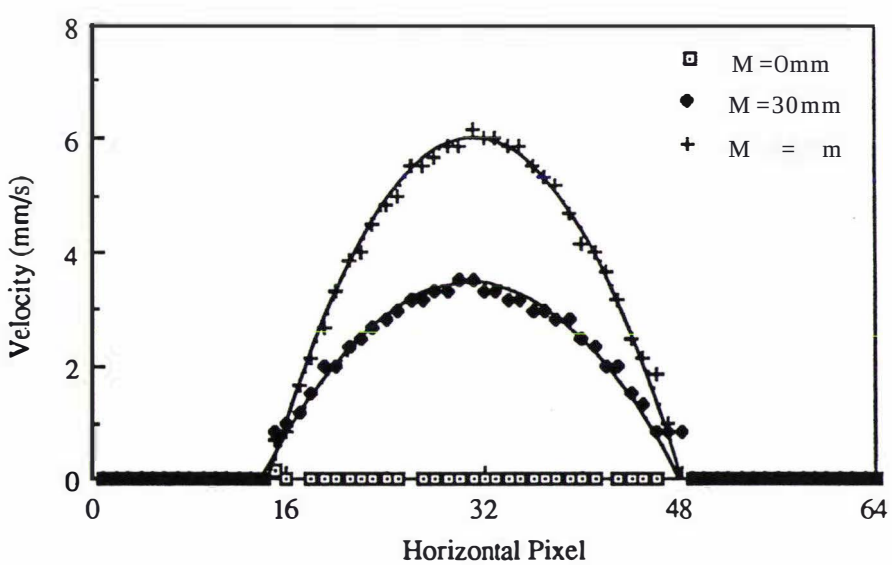

Figure 6.8 Cross sectional profiles through the centres of the velocity maps (the solid lines are theoretical Poiseuille curves)

It is worth noting that there are two additional error sources which haven't been included in the above error analysis, both of which will cause decreases in the experimental flow rate. The first source is the inevitable existence of tiny air bubbles on the wall of Teflon capillary, which will influence the flow rate for a given pressure head. The second source is the impact of water level change during the hour-long experiment. Given the diameter of the inlet and outlet reservoirs of 85 mm and Δh of 60 mm, the volume flow during a 3-hour-long experiment is about 15 ml, which causes a maximum of 5 mm water level change in the reservoirs for an initial 60 mm head difference, an 8 % drift! However, the actual impact of this level change could be less than, say, 8 %. This is because the q slices acquired under an incrementing PGSE gradient are unequally weighted in the subsequent analysis. The effect of diffusive motion causes image intensities in the later part of the q slices to be weak compared with these in the early part, so that any error occurring during the latter stage of the imaging experiment would have less influence on the subsequent analysis. It is obvious that the precision of the velocity measurement can be improved using a more stable constant flow system.

Precision and accuracy of the self-diffusion measurement

In the self-diffusion measurement, the zero flow rate data provides a useful reference and both the FWHM and linear regression analyses agree, giving correct values of 2.6×10^{-9} m^2s^{-1} for the water diffusion coefficient at 30 ^oC. The cross sectional profiles through the centres of the diffusion maps are shown in Figure 6.9.

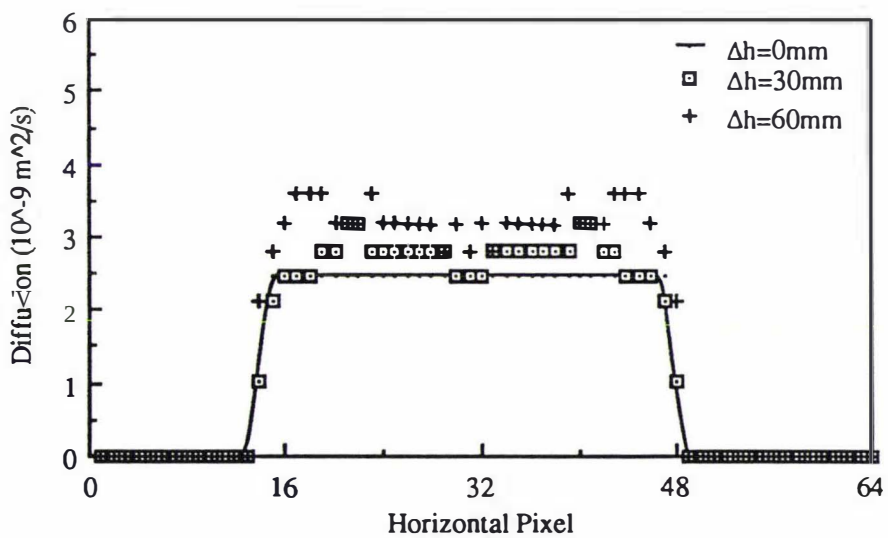

Figure 6.9 Cross sectional profiles through the centres of the self-diffusion maps

Analysis shows that velocity shear artifacts are indeed present at high flow rates, a point which is emphasized by azimuthally smoothing the data using ImageShow™. At a pressure head of 60 mm H_2O, the outer region at maximum radius exhibits a significant enhancement of the apparent diffusion coefficient. It is interesting to note that while the diffusion artifacts are obvious in the high flow experiment, the corresponding velocity maps are still quite accurate in the previous Figure 6.8.

The velocity shear in Poiseuille flow increases linearly to a maximum value of $2v_{max}/r_0$ at the edge of the capillary. Using the parameters of this experiment a maximum shear rate can be calculated as 30 s^{-1}. The transverse diffusion artifact associated with this shear, as given by Eq[3.38] and Eq[3.39], is of order 2%, a 1% effect on the line width which can be neglected. By contrast, Eq[3.37] predicts a combined (projection interpolation and apodization broadening) shear artifact in the line-width of 0.6×10^{-5} m $s^{-1/2}$. This compares with the value of $D^{1/2}$ for water of 5×10^{-5} m $s^{-1/2}$, 12 % effect. In 256-scale digital terms this additional broadening corresponds to around a digital value of 2 in comparison with the correct value of 14 for the FWHM arising from self-diffusion alone (2.6×10^{-9} m^2s^{-1} at 30°C [156]).

Unlike the velocity shear artifact, the shift in the apparent diffusion coefficient arising from flow in a non-uniform gradient is proportional to the velocity squared rather than the velocity gradient. In Poiseuille flow it therefore contributes most at the centre of the image. From Eq[3.51] and given the position of the 0.4 % gradient profile at ± 2.5 mm[132], the contribution to D_{eff} at the maximum flow rate of 6 mm s^{-1} may be estimated as ≤ 0.1 %. This effect is insignificant in the present context.

Both FFT and Stejskal-Tanner methods have been used to analyze the self-diffusion in the above experiments. Table 6.3 gives a comparison of averaged diffusions over the 95% of most frequent pixels in these diffusion images using both methods. They agree with each other.

Table 6.3 Averaged-diffusion values using FFT and Stejskal-Tanner methods

Δh (mm)	From FFT (10^{-9} m^2s^{-1})	From Stejskal-Tanner (10^{-9} m^2s^{-1})	% Error c.f. Standard	
			FFT	S-T
0	2.51	2.59	3	0.4
30	2.67	2.75	3	6
60	3.17	3.39	20	30

In the above table, the experimental data are calculated using Eq[3.28], where N=256, n_D=17, g=0.936 T m^{-1}, $\gamma=2.675\times10^8$ $radT^{-1}s^{-1}$, $\delta=2\times10^{-3}$ s, $\Delta=5\times10^{-3}$ s;

while the standard value is 2.6×10^{-9} m^2s^{-1} at 30°C calculated[156] from Mill's measurement.

The self-diffusion enhancement caused by the velocity shear prohibits an accurate measurement of self-diffusion in Dynamic NMR Microscopy. However, it will be shown that this enhancement can be removed by the velocity-compensated Dynamic NMR Microscopy, the results is presented in the next section.

The temperature dependency of the diffusion measurement

The accuracy of the diffusion measurement is also dependent upon a knowledge of the sample's temperature. In our system, there is no temperature control on the imaging probes. To simulate the real thermal surroundings, the temperature of the standard imaging probe has been measured using a dummy rf coil plastic form and a thermistor placed at the centre of the imaging probe. It was found that the probe temperature is around 28°C to 30°C when the spectrometer is idle. During a dummy imaging experiment with a maximum q gradient of 10 A current, Δ=5 ms, δ=2 ms and T_R=0.4 s, the pulsing of the gradients has warmed the probe over the equilibrium temperature the to 31.1°C! Continuous running has warmed the probe even higher. Therefore the real temperature of the probe with which the experiment is performed couldn't be determined very accurately in our current instrument.

To examine this temperature effect, a set of three water flow imaging experiments were carried out successively at the same pressure difference using a 2.9 mm i.d. glass tube (in order to minimize the velocity shear artifact). The maximum flow rate at the centre of the tube is about 6.6 mm s^{-1} and the velocity shear effect is expected to be small for this big diameter tube. The 95 % most frequent diffusion values averaged from three diffusion images have shown a successive increment from 2.50×10^{-9} m^2s^{-1} for the first image to 2.65×10^{-9} m^2s^{-1} for the second image and 2.85×10^{-9} m^2s^{-1} for the third image. This indicates that the probe temperature has risen from the initial 28.5°C to 31°C for the second and around 34°C for the third run.

Alternative imaging pulse sequence in Dynamic NMR Microscopy

In the application of the 'classical' dynamic imaging pulse sequence (Figure 6.1a), the artifact due to the slice selection gradient is quite obvious when the flow rate is high. Figure 6.10 shows some 1-D projection profiles acquired at different flow rates. It is clear that the phases of the spectrum have been distorted at high flow rates. In our imaging experiments, this phase distortion is compensated by adjusting the P0 phase of the spectrometer so that the base line of the 1-D spectrum is 'leveled', an

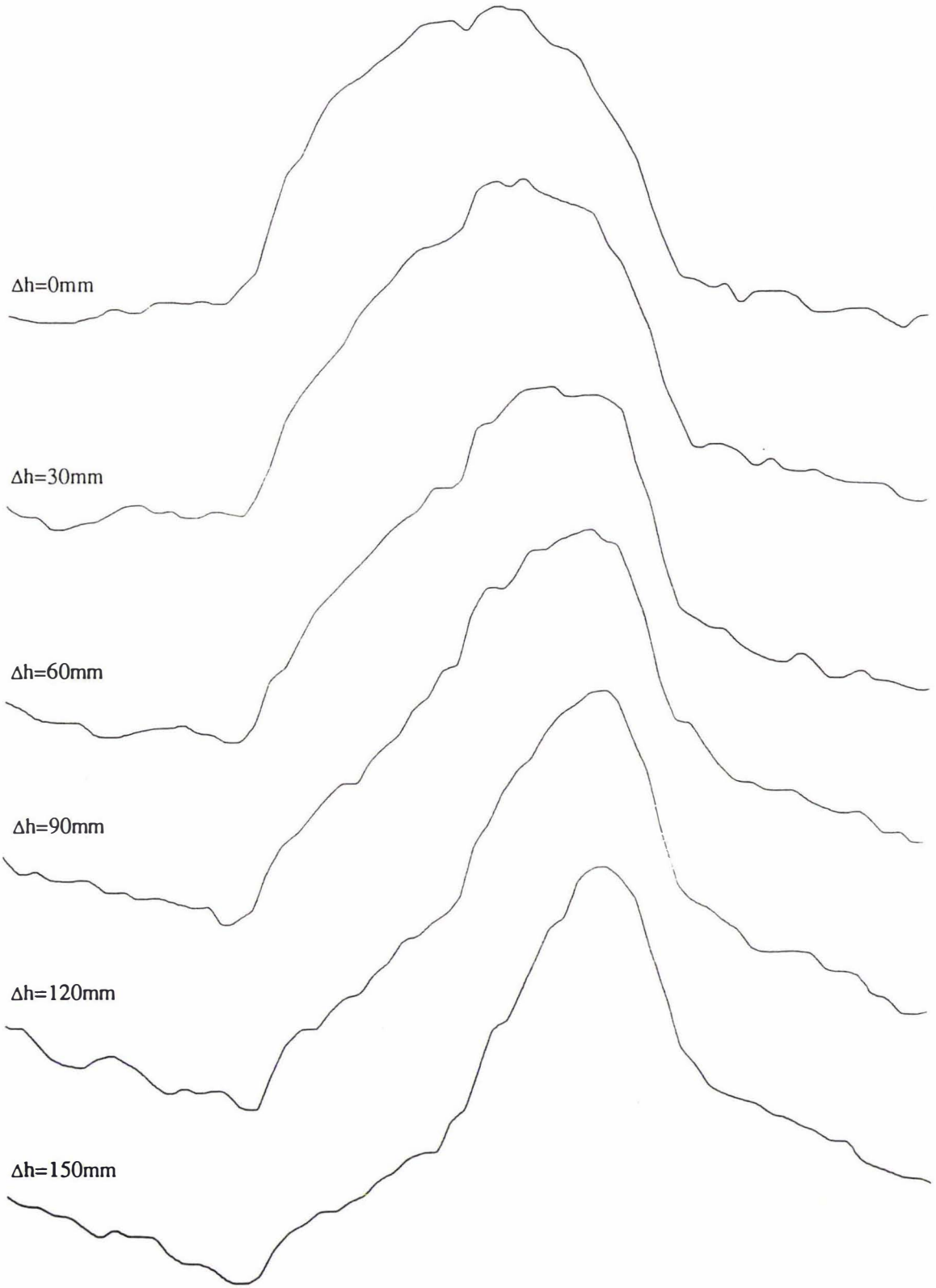

Figure 6.10 1-D projection profiles acquired using the pulse sequence shown in Figure 6.1a.

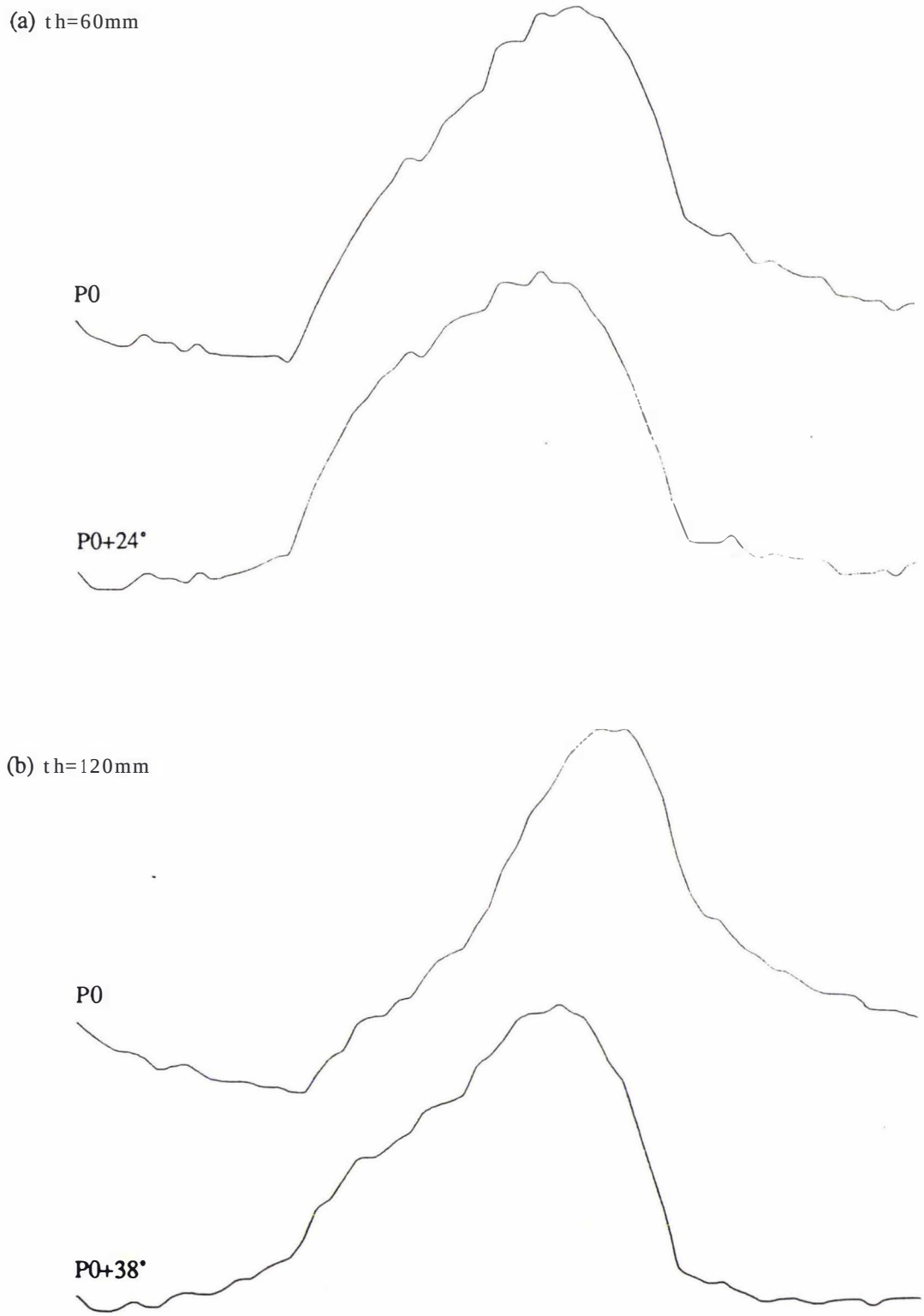

Figure 6.11 The effect of P0 phase compensation in flow imaging experiments.

example of such adjustment is given in Figure 6.11. It has found that the amount of this phase compensation is between 10° to 15° for every 3 mm/s velocity magnitude increment, which agrees with the prediction given by Eq[3.30].

In fact, the imaging pulse sequence used in the 'one-shot' velocity microscopy, Figure 6.2, can also be employed in Dynamic NMR Microscopy, provided the $90°_{-x}$ rf pulse is switched off and the PGSE level is updated during the multiple imaging experiment. This 'one-shot' pulse sequence (without the stimulated echo sequence) has been used in Dynamic NMR Microscopy for a series of different flow rates using the identical capillary sample. Figure 6.12 shows 1-D profiles for the same pressure differences as shown in Figure 6.10. There is no visible phase distortion when using this pulse sequence in Dynamic NMR Microscopy.

Using both pulse sequences, identical capillary sample and experimental parameters, imaging experiments were carried out at different flow rates. The velocity images obtained using both pulse sequences were almost identical. The cross sectional profiles through the centres of the velocity maps are given in Figure 6.13 (using the 'classical' pulse) and in Figure 6.14 (using the 'one-shot' pulse). Table 6.4 gives a comparison of maximum velocities obtained using both imaging pulse sequences.

Table 6.4 Comparison of the theoretical calculation and the experimental results

Δh (mm)	Theoretical V_{max} (mm/s)	Experimental $V_{max}(1)$ (mm/s)	Experimental $V_{max}(2)$ (mm/s)
0	0±0	0.1±0.5	0.02±0.5
30±4	3.4±0.7	2.8±0.5	2.8±0.5
60±4	6.9±1.1	6.0±0.5	6.2±0.5
90±4	10.3±1.3	8.8±0.5	8.8±0.5
120±4	13.7±1.7	11.7±0.5	12.0±0.5
150±4	17.1±2.1		15.2±0.5

In the above table, the experimental $V_{max}(1)$ refers to experiments using the 'classical' dynamic imaging pulse (Figure 6.1a) and the experimental $V_{max}(2)$ refers to experiments using the 'one-shot' imaging pulse sequence (Figure 6.2). The experimental values for Δh=0mm are the averaged values for the 95% most frequent values. The agreement is excellent, apart from an overall lower in the experimental values which is concluded to be caused by the water level drifting and the air bubble forming during the experiment.

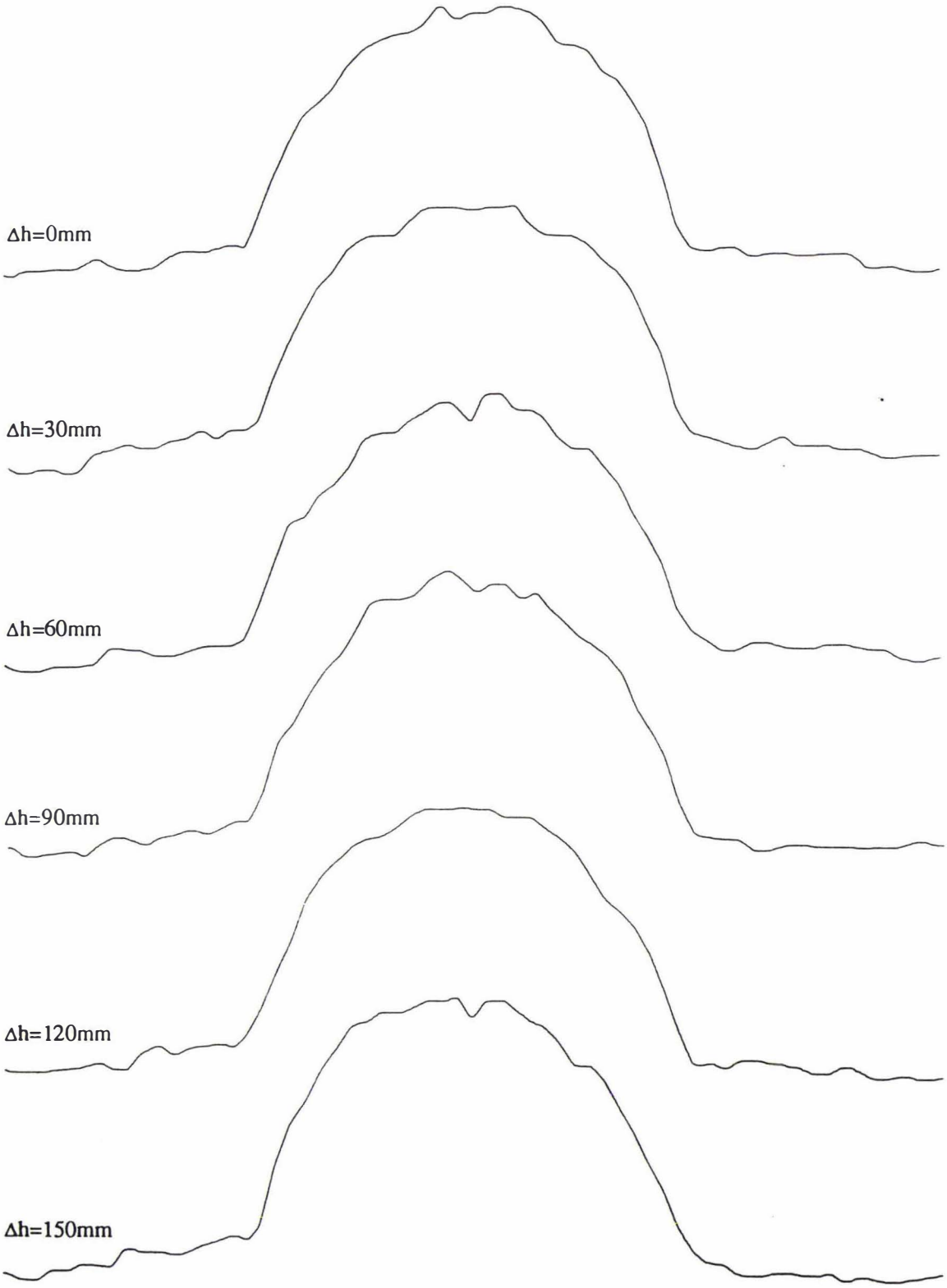

Figure 6.12 1-D projection profiles acquired using the pulse sequence shown in Figure 6.2.

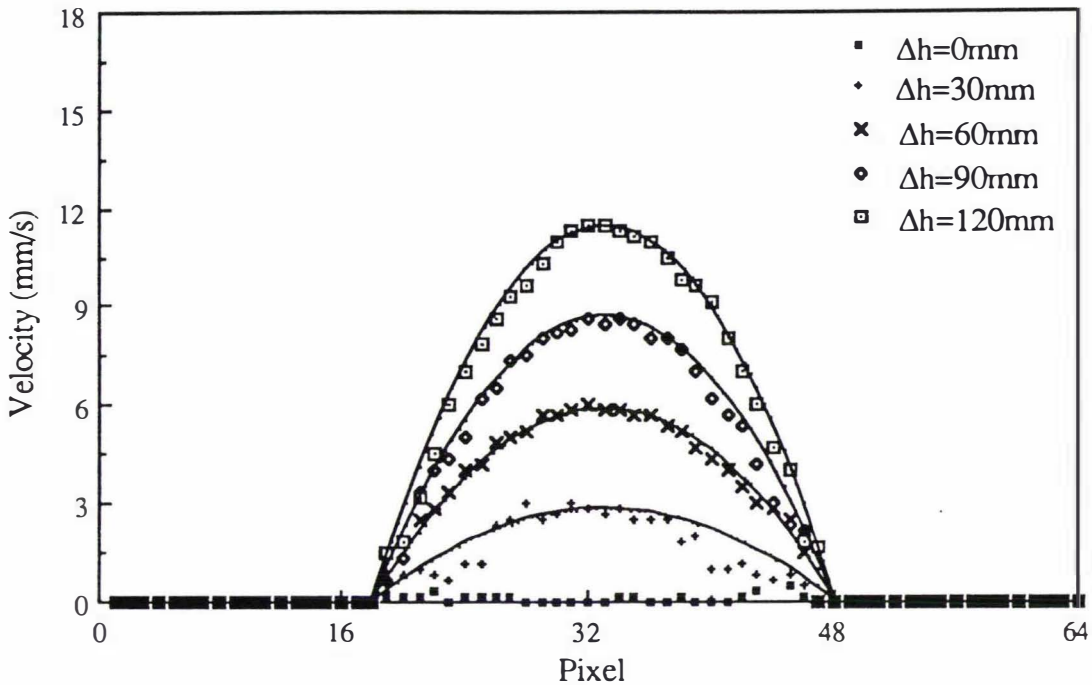

Figure 6.13 Velocity profiles of Poiseuille flows using the 'classical' dynamic imaging pulse

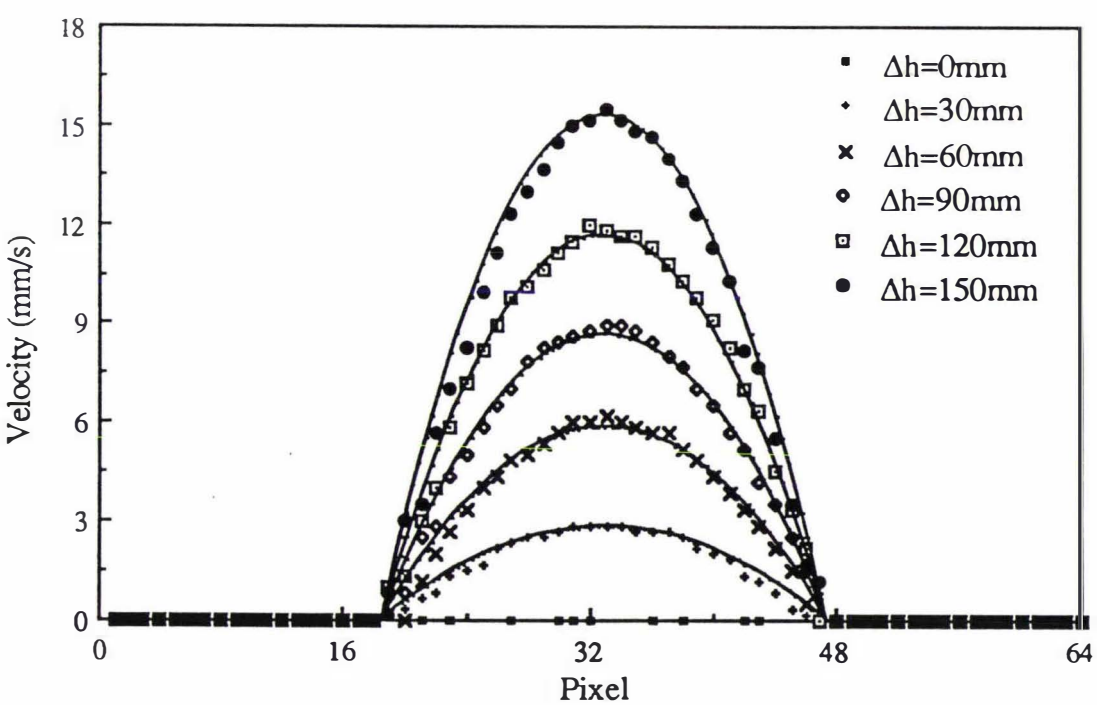

Figure 6.14 Velocity profiles of Poiseuille flows using the 'one-shot' dynamic imaging pulse

Measurement using the new 'super G_y' imaging probe

To test the new 'super-G_y' imaging probe, capillary flow imaging experiments were carried out using Dynamic NMR Microscopy and the 700 μm i.d. Teflon tube. The experimental parameters were very similar with those in Table 6.1 except the duration of the PGSE gradient was 0.4 ms. A much narrower SINC pulse was also employed (200 μm duration comparing with the previous 2 ms) due to the much powerful G_y gradient was used.

Figure 6.15 shows a cross sectional profile through the centre of the velocity image at a pressure head of 60 mm, which exhibits an excellent velocity profile for the classical Poiseuille flow. Several imaging experiments were carried out and some results are summarized in the following table using the calibration gradient value of 48.73 G cm^{-1} A^{-1} for the PGSE gradient.

Table 6.5 Summary of experimental results using the 'super-G_y' probe

Δh (mm)	Experimental V_{max} (mm/s)	D from FFT (10^{-9} m^2s^{-1})	D from Stejskal-Tanner (10^{-9} m^2s^{-1})
0	0.2±0.5	3.60	3.35
60±4	6.6±0.5	4.02	3.79

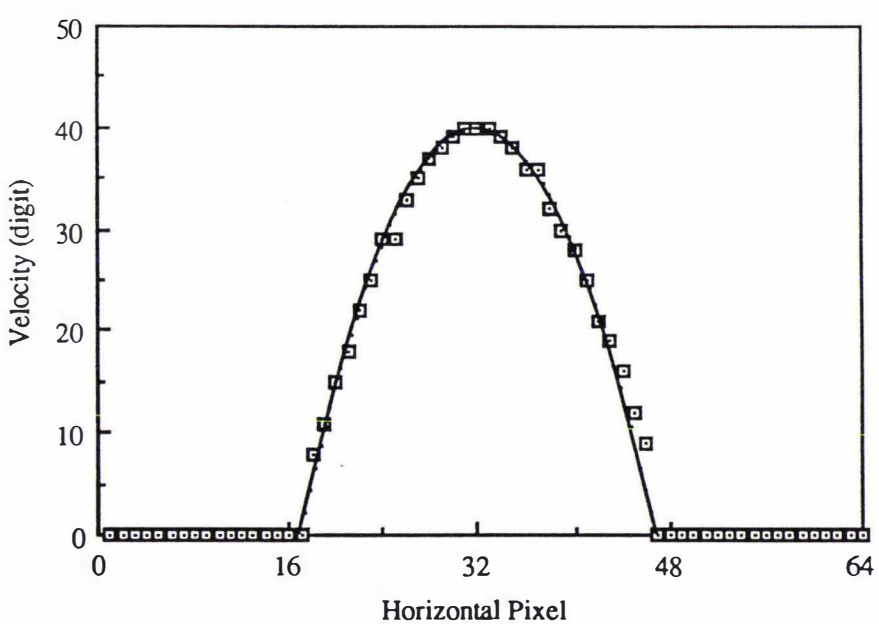

Figure 6.15 A cross sectional profile through the centre of the velocity map at Δh=60mm and using the 'super-G_y' imaging probe (the solid line is the theoretical Poiseuille profile)

By comparing these values with all the previous experimental measurements (Table 6.2 and 6.3), both velocity and diffusion were somewhat higher than expected. A repeated experiment confirmed the above results with a maximum velocity of 41 digit (corresponding to 6.6 mm/s) at Δh=60mm. This was strange since the previous instruments (both probe and capillary flow system) had been tested for various experiments many times. At a pressure head of 60 mm, the maximum velocity digit given by the imaging experiment had always been 35 to 37. This thus led to a conclusion that the original calibration value for the G_y gradient coil was inaccurate.

Considering the method by which the gradient strength was calibrated (Eq[4.11]), an error could be introduced by the assumption of the theoretical water self-diffusion value. This is because the temperature of the water sample was not determined accurately so that the theoretical diffusion value may have been incorrect. In fact, considering the high accuracy of velocity measurement, its result can be used as an alternative method to calibrate the gradient coil. Using the knowledge from the previous imaging experiments, the gradient strength for the G_y coil in this 'super-G_y' probe should be 51.6 G cm^{-1} A^{-1}, a 6 % error in the gradient magnitude. The imaging results summarised in Table 6.5 using this new g value are listed in the following table.

Table 6.6 Experimental results using 51.6 G $cm^{-1}A^{-1}$ for the 'super-G_y' probe

Δh (mm)	Experimental V_{ma} (mm/s)	D from FFT (10^{-9} m^2s^{-1})	D from Stejskal-Tanner (10^{-9} m^2s^{-1})
0	0.2±0.5	3.19	2.98
60±4	6.2±0.5	3.57	3.36

The results shown in this table are in much better agreement with the previous experimental results, with an exception that the diffusion is still a bit too high. This is probably caused by a higher sample temperature rise in this new imaging probe, an effect which is due to the close proximity of the powerful G_y coil and the sample space. A separate imaging experiment has confirmed this speculation, the results will be shown in Ch 6.2.4.

Measurement using the new imaging probe for plants

This new imaging probe has also been tested using Dynamic NMR Microscopy using water capillary flow sample. Velocity and diffusion images were obtained successfully, the results are similar with the previous ones.

6.2.2 Using the velocity-compensated Dynamic NMR Microscopy

In order to clarify the origin of the diffusion enhancement at the outer region, a velocity-compensated Dynamic NMR Microscopy experiment was carried out using the same 700 μm diameter capillary sample as used in Ch 6.2.1. The pulse sequence employed has shown previously in Figure 6.1c. Figure 6.16 shows a set of three experiments performed at increasing flow rates as in Figure 6.7. The velocity null is quite good at the lowest flow rate but is clearly imperfect at the highest. Despite this imperfection the suppression of velocity-induced phase shifts has significantly removed the diffusion artifact. All three experiments return correct diffusion FWHM and linear regression values right across the image, which implies that any artifact arising from shear at the edge of the capillary has been removed by this pulse sequence. Table 6.7 summaries some experimental data obtained in the three imaging experiments.

Table 6.7 Averaged-diffusion values using FFT and Stejskal-Tanner methods

Δh (mm)	Velocity (averaged) (digit)	D from FFT (10^{-9} m^2s^{-1})	D from Stejskal-Tanner (10^{-9} m^2s^{-1})
0	1.0	2.40	2.73
30	1.2	2.36	2.68
60	1.3	2.39	2.75

6.2.3 Opposite-signed flow

To demonstrate the ability of differentiating opposited signed velocities in the same flow field, a 500 μm i.d. plastic tube was passed through the 2 mm rf coil in both directions, thus producing a flow field with two identical but oppositely directed parts. The experimental parameters were similar with these in the previous Poiseuille flow experiments. The velocity image obtained using Dynamic NMR Microscopy is shown in Figure 6.17. It is clear from the symmetry of the two oppositely directed flows that Dynamic NMR Microscopy is capable of precise measurements of the signed velocity fields. The equivalent "velocity-compensated" maps are also shown in the same Figure.

There are two features which are worth noting in this experiments. First, there are two oppositely signed small 'residual' velocities left in Figure 6.17b. This is precisely the effect of the slice selection gradient on the velocity map. The reason why this effect is obvious in this bi-direction flow experiment but absent in the previous single-direction flow experiment is as the following. In the single-direction flow

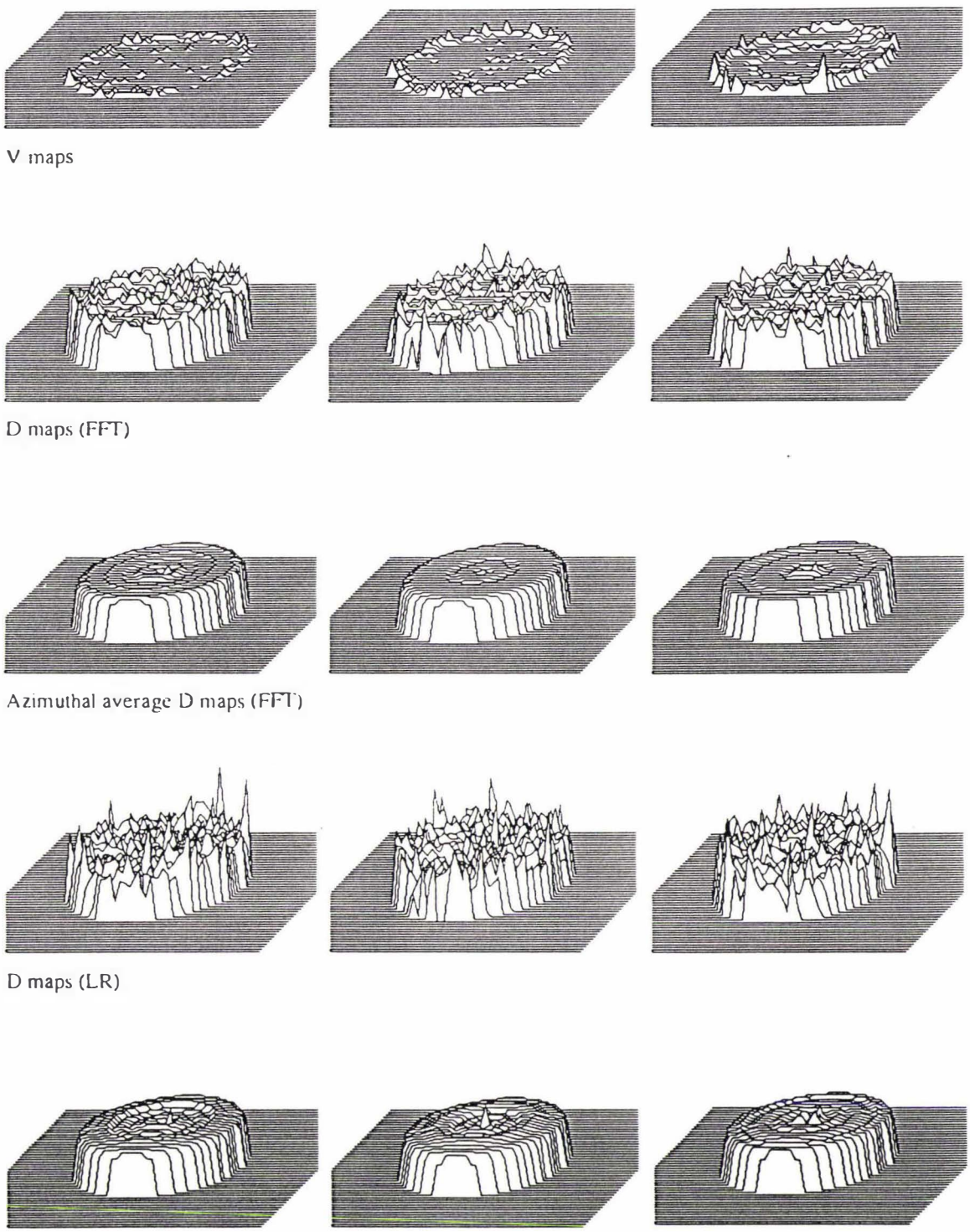

Figure 6.16 Stacked profile plots of velocity and diffusion maps for capillary flow experiments using the velocity-compensated Dynamic NMR Microscopy.

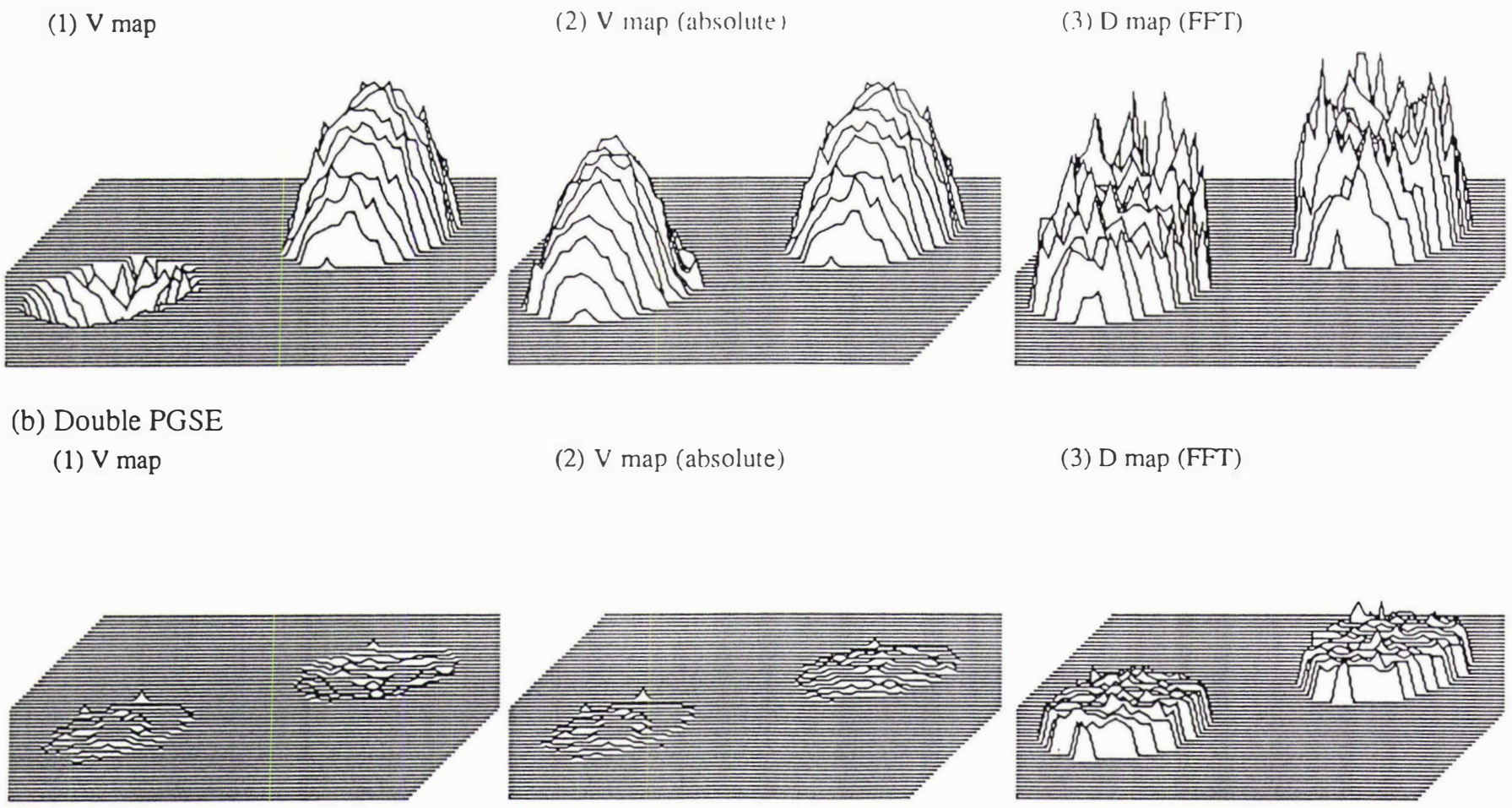

Figure 6.17 Stacked profile plots of velocity and diffusion maps for the opposite-signed capillary flow experiments using both single PGSE and double PGSE sequences.

experiment the phase of the spectrometer is set so that there is no apparent phase distortion for q equal to zero, which has actually compensated the phase shift due to the slice selection gradient (the procedure has been illustrated previously in Figure 6.11). But in the situation of there are oppositely signed velocities in the same velocity field, there is no way to compensate this slice-selection-induced phase distortion for both directions and the phase of the spectrometer has to be set for the average (zero) flow. This leads to the small velocity offset in each of the oppositely directed capillaries.

Second, the FWHM diffusion maps in Figure 6.17a are displayed for the 500 μm capillary for which the capillary edge shear will be 50% larger, as the shear effects increase as the capillary dimension diminishes. The velocity-compensated data yield correct water diffusion coefficients (using both FWHM and linear regression methods). By contrast the single PGSE apparent diffusion data is enhanced by approximately a factor of 2 for both methods. This enhancement cannot be explained by the enhanced shear rate alone. One is therefore led to postulate that part of the diffusion artifact is probably caused by some local transverse flow, as discussed previously in Ch 3.5.

This transverse motion can be introduced by two different sources, namely non-vertical sample tubes and the small bubbles adhering to the capillary wall. It is quite possible that the 500 μm plastic sample tube was not perfectly vertically placed inside the rf coil. Therefore some lateral spin migrations occurred which causes the spins to shift their positions to locations with different gradient field. The tiny air bubbles could also cause transverse velocity by disturbing the local flow patterns slightly. A 1 mm slice is sufficiently thick that the average velocity profile across the capillary will be correctly represented. A single pixel, which represents an average through the slice, will therefore have the correct mean velocity value but the velocity spread would be somewhat enhanced. Given a spin echo time scale of order 10 ms and a local velocity of order 10 mm s^{-1}, this spread would be effectively compensated by the double PGSE sequence provided that the region of disturbance has a size of order 100 μm or greater. If the bubbles were in fact smaller than this, and adsorbed on the wall, then the disturbance could still be expected to have this larger "coherence length" some hundreds of micrometers away from the wall in the central region of the capillary.

6.2.4 Using a 'one-projection' image reconstruction algorithm

A 'one-projection' image reconstruction algorithm was investigated which utilises the azimuthal symmetry in the capillary flow experiment. Provided that the centre of the image is at the centre of the projection, the filtered back-projection reconstruction method should be able to construct an image from only one projection. A Dynamic NMR Microscopy experiment was carried out at the usual manner as the g was stepped up to 10 A maximum current using the new 'super-G_y' imaging probe. The experimental parameters were identical with that used in the previous Ch 6.2.1, except that the repetition time, T_R, was 20 seconds and the signal was averaged 32 times for each projection. Therefore the total experimental time (18 pairs of data images) was still 3 hours.

Figure 6.18 shows the velocity and diffusion maps for this 'one-projection' Dynamic NMR Microscopy experiment for a pressure head of 60 mm. The parabolic velocity distribution and the flat diffusion map have demonstrated that this 'one-projection' reconstruction technique works well. A maximum velocity of 41 digit was obtained, again, in this flow experiment, which has re-confirmed our conclusion of incorrect g value in the calibration of the G_y gradient coil. In Ch 9, it will be found that this peculiar 'one-projection' reconstruction algorithm is the only practical choice in one of the polymer flow imaging experiments.

Another five identical experiments were carried out at a pressure head of 0 mm for this sample, with an intention to measure the diffusion coefficient accurately using

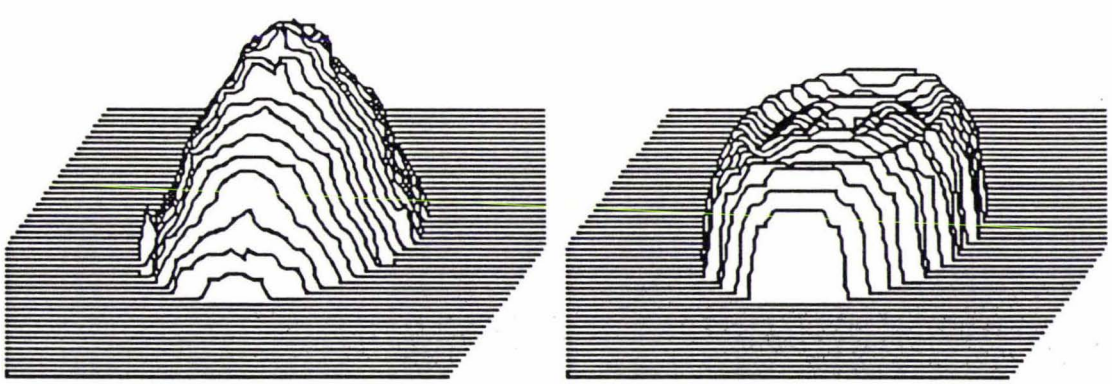

(a) Velocity map (b) Azimuthal-averaged FWHM map

Figure 6.18 V and FWHM maps from the 'one-projection' PR

this probe. Because a 20 second repetition time is long enough to dissipate most additional heat generated by the pulsing of the gradient current, this method should result in minimal temperature rise. The five diffusion maps were superposed and the final diffusion map is quite uniform, shown in Figure 6.19. An averaged diffusion coefficient of 2.63×10^{-9} m^2s^{-1} was obtained from this image, which is correct for a probe temperature of 30.5°C.

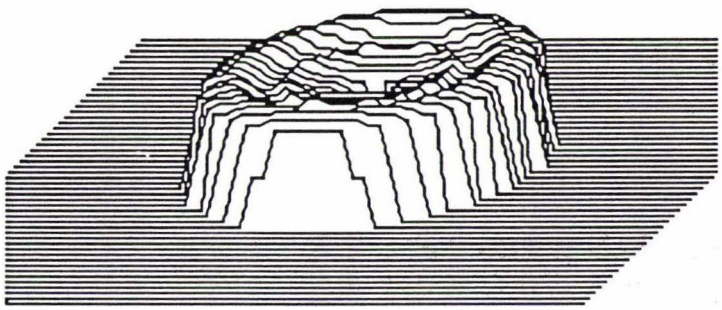

Figure 6.19 The averaged D map from D maps constructed using the 'one-projection' PR

6.3 Capillary flow studied using 'one-shot' velocity microscopy

The 'one-shot' velocity microscopy discussed in Ch 3.7 offers better time efficiency than the more comprehensive Dynamic NMR Microscopy. Once again the Poiseuille velocity distribution provides a good opportunity to test the technique and the results are presented in this section.

6.3.1 Poiseuille flow

A constant water laminar flow through 700 μm i.d. teflon tube was established using the identical sample system to that used in the previous multi-slice experiments. The pulse sequence has been shown previously in Figure 6.2, with the incorporation of the stimulated echo sequence. The direction of the PGSE gradient **g** was along the direction of flow. The images were constructed with an array size of 128×128 at 2° steps from 0° to 360°. Some of the experimental parameters are summarised in the following table.

Table 6.8 Summary of experimental parameters in 'one-shot' experiments

Δ (ms)	δ (ms)	g (G/cm)	BW (kHz)	N_{acc}	T_R (sec)	Pixel resolution	
						Slice(mm)	Transverse(μm)
80	0.2	9.36	10	32	0.4	1.5	12

It is worth noting that the long observation time Δ was not necessary for this capillary water flow experiment but was deliberately chosen to test the pulse sequence in anticipation of an *in vivo* plant experiment in which the flow rate were several orders of magnitudes smaller (in Ch 7).

Figure 6.20 shows the $\rho_{odd}(r)$ and $\rho_{even}(r)$ images obtained from four different flow rates, the respective sinusoidal and cosinoidal dependences of these images on the water velocity being apparent as v is increased. The corresponding final velocity images obtained using Eq[3.81] and Eq[3.82] are also shown in Figure 6.20. In the construction of the final velocity images, the signs of both $\rho_{odd}(r)$ and $\rho_{even}(r)$ images are used to interpret the phase shifts within the quadrants. Figure 6.21 shows cross-sectional profiles through the centres of the final velocity images. By comparing with the results in the precious section, it can be concluded that the velocity images obtained from this 'one-shot' velocity microscopy are almost as good as those from the more sophisticated Dynamic NMR Microscopy.

Table 6.9 gives a comparison of maximum velocities given by the theoretical calculation and by the 'one-shot' velocity images, the agreement is excellent.

Table 6.9 Comparison of the theoretical calculation and the experimental results

Δh (mm)	Theoretical V_{max} (mm/s)	Experimental V_{max} (mm/s)
0	0	0.1
30	3.4	3.0
60	6.8	6.4
90	10.2	10.0

6.3.2 Discussion of velocity image artifacts

Due to the two-step imaging procedure used in the current imaging system, i.e., obtaining ρ_{odd} and ρ_{even} separately, there is a quadrant mismatch artifact for this 'one-

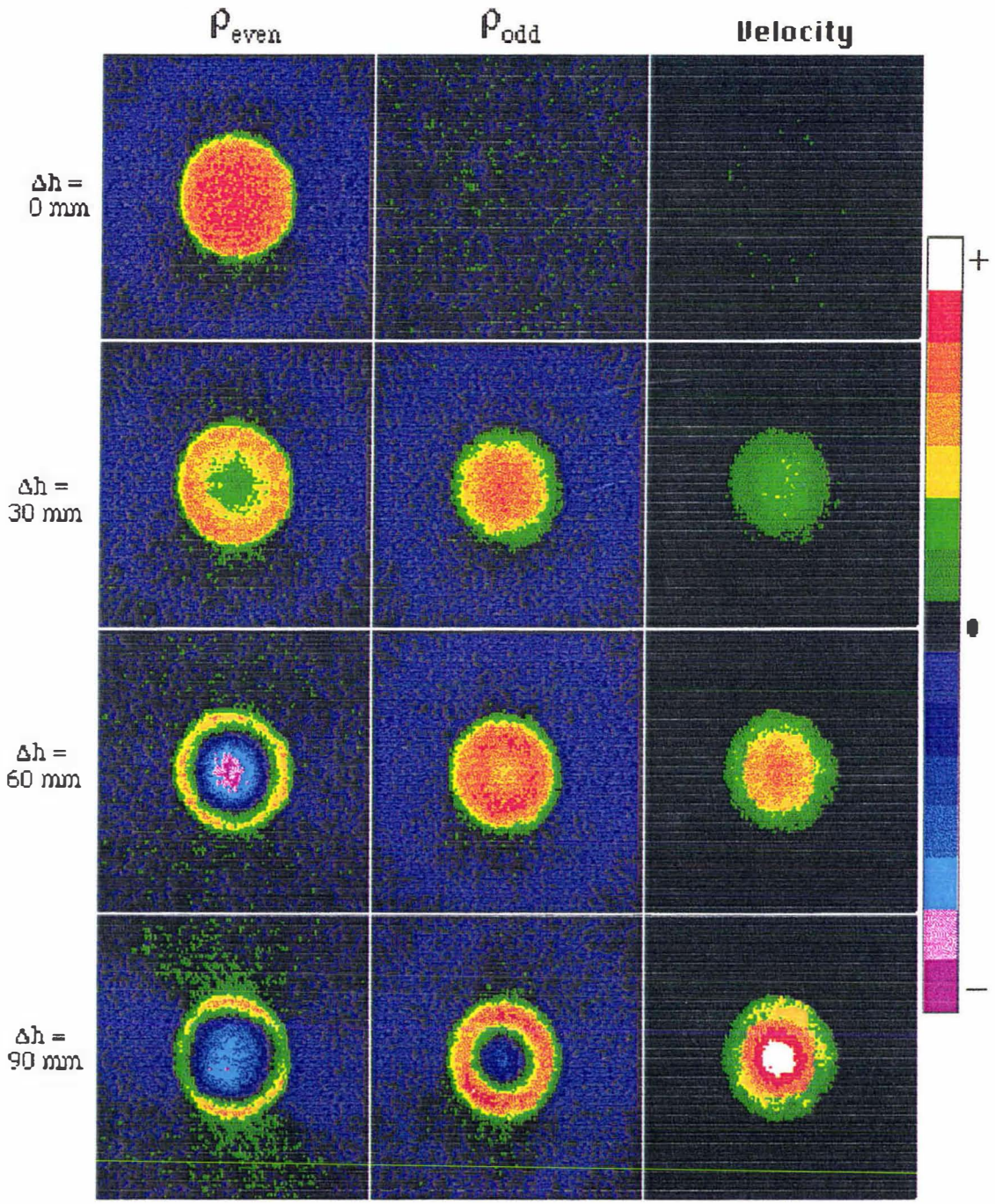

Figure 6.20 ρ_{even}, ρ_{odd} and velocity maps using the 'one-shot' velocity microscopy

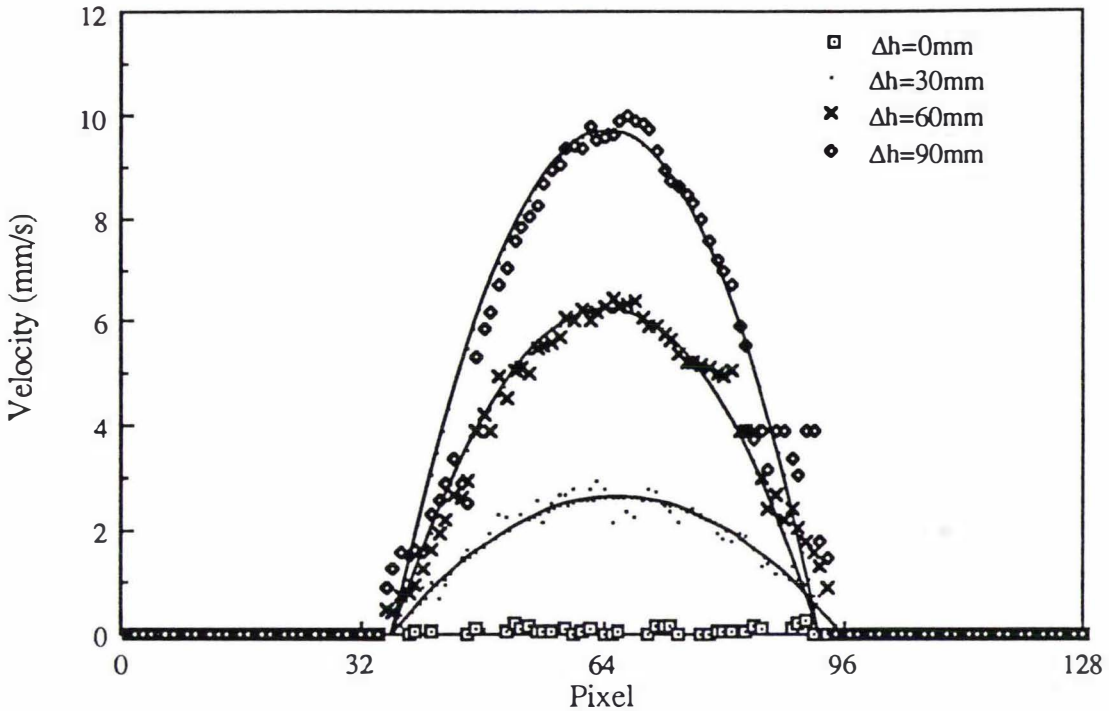

Figure 6.21 Velocity profiles of Poiseuille flows using the 'one-shot' technique

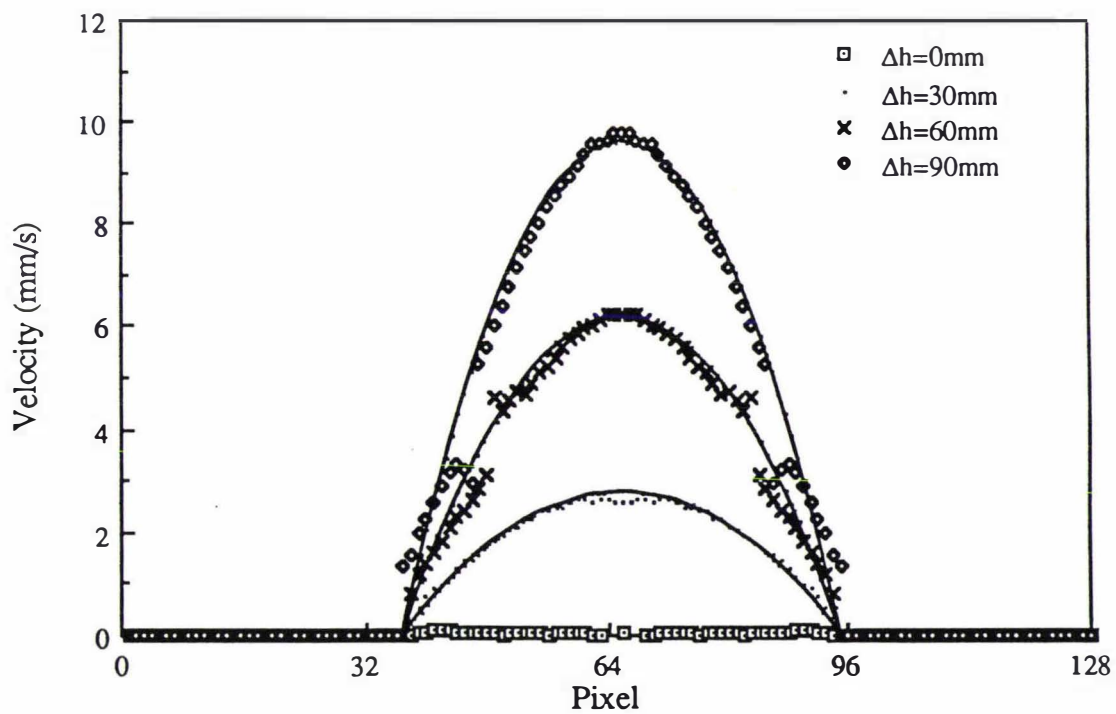

Figure 6.22 Azimuthal-averaged velocity profiles shown in Figure 6.21

shot' technique. This mismatch occurs if the respective sine and cosine images are not consistent and exhibits itself most intensely for phase shifts of around 90°, 180° and 270°. To clearly illustrate this problem, the azimuthal averaging routine in ImageShow™ has been used to azimuthally average the capillary flow images, utilising the fact that the velocity profile in a circular tube is axially symmetrical. Figure 6.22 gives the cross-sectional profiles through the centres of the azimuthal-averaged velocity images as shown in Figure 6.20.

It is interesting to note that while the velocity profile of a stationary sample is effectively zero and that at Δh=30mm is almost perfectly fitted, there are some 'gaps' in the velocity profiles at Δh=60mm and 90mm caused by the 'quadrant mismatch fold-back' of a few data points. These occur because the required pressure differences of a few centimetres of water are very difficult to maintain accurately, and furthermore, the flow rate is often slightly affected by some tiny air bubbles adhered on the wall of the Teflon capillary. Therefore the actual flow rates could have been slightly different during the separate experiments to obtain ρ_{odd} and ρ_{even} images.

Figure 6.23 shows the cross-sectional profiles through velocity images, also corresponding to Δh=60mm but using a different data set. Both profiles shown in Figure 6.23a and 6.23b were obtained using the same $\rho_{even}(\Delta h=0mm)$ and $\rho_{odd}(\Delta h=60mm)$ to calculate the apparent velocity values but with two different $\rho_{even}(\Delta h=60mm)$ to interpret the sign. The 'fold-back' effect which is obvious in Figure 6.23a disappears in Figure 6.23b. Clearly these quadrant mismatch artifacts would vanish if ρ_{odd} and ρ_{even} were obtained from a common set of acquisition (Table 3.6). This obvious improvement to the experiment could be achieved by an appropriate software modification.

While the accuracy of an experimental measurement can be improved by using a common data set procedure, the precision does vary across the velocity range due to the flatness of the sinusoidal dependence near the $\pm\frac{1}{2}\pi$ or $\pm\frac{3}{2}\pi$. The flat top of the velocity profile at Δh=30mm in Figure 6.22 is an example of such a problem. Adjustments of δ, Δ or g to displace the phase shift from these region can alleviate the problem.

In terms of other velocity artifacts as discussed for Dynamic NMR Microscopy, the 'time-of-flight' effect which is inevitable in Dynamic NMR Microscopy almost vanishes in this 'one-shot' technique because of a much smaller time delay between the selective excitation and the spatial mapping segments. In the measurement of flow with a direction normal to the imaging plane, the velocity artifact due to the slice selection

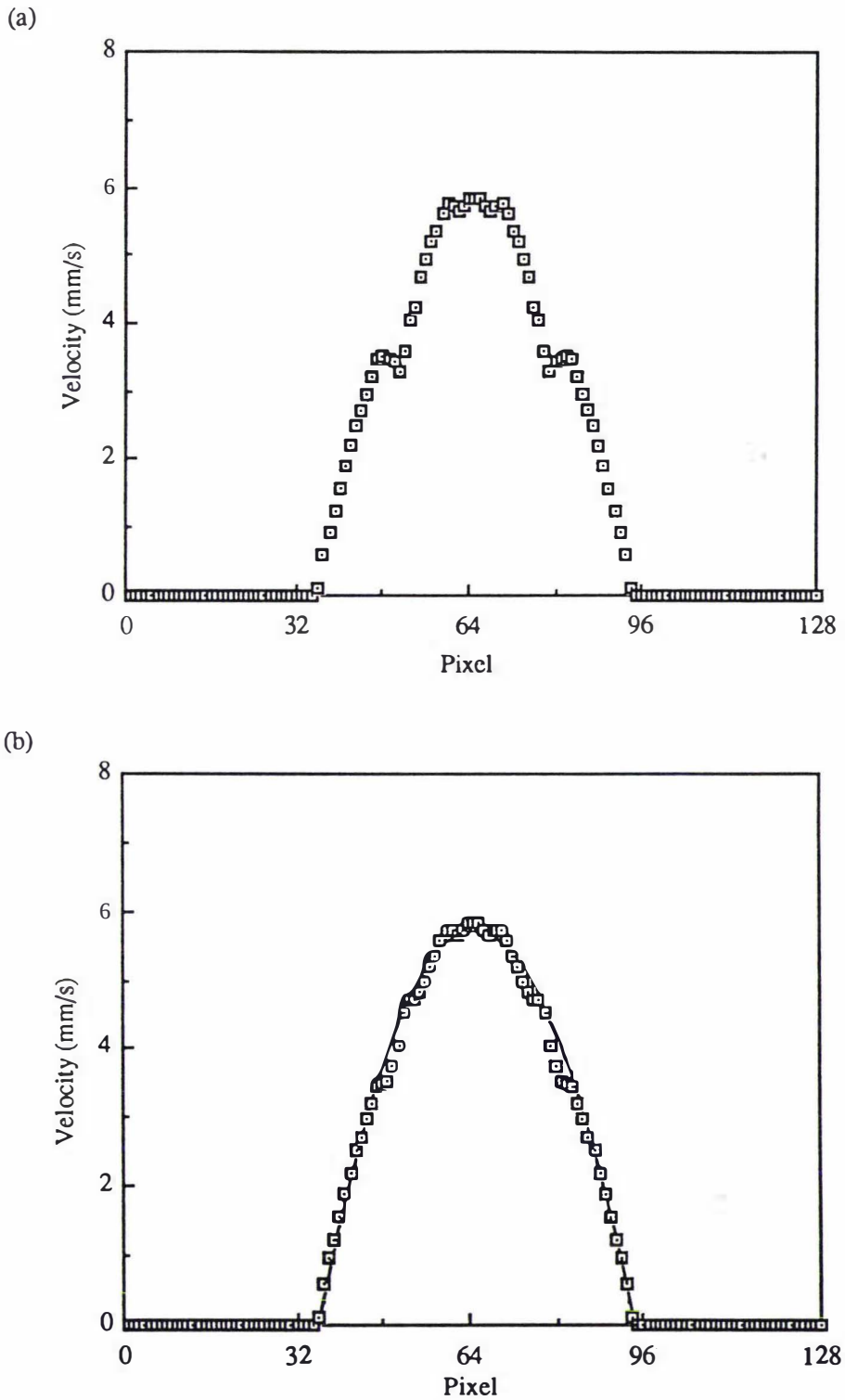

Figure 6.23 The 'fold-back' effect in the 'one-shot' velocity microscopy (the solid line is the theoretical Poiseuille fit)

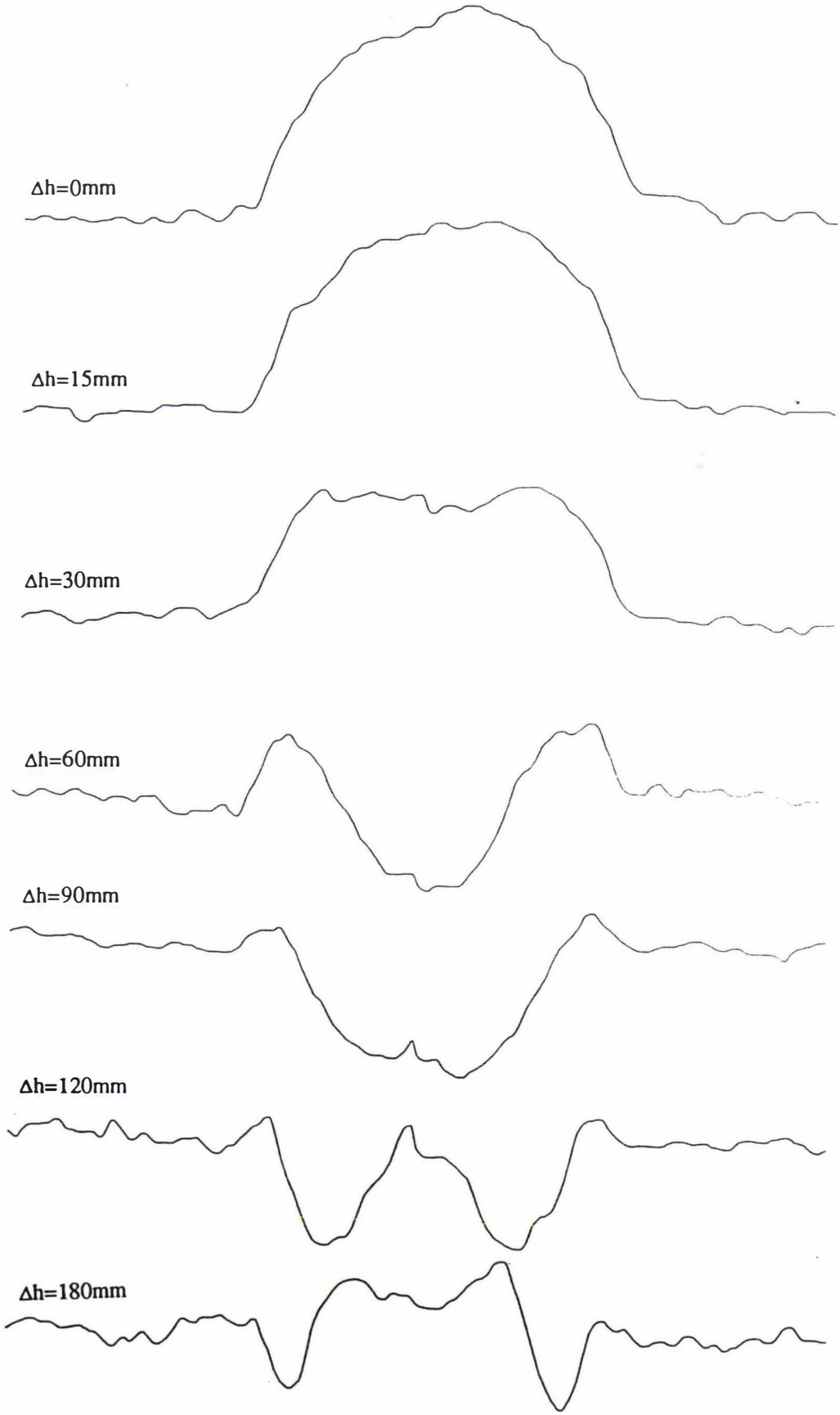

Figure 6.24a 1-D projection profiles of $\rho_{even}(r)$.

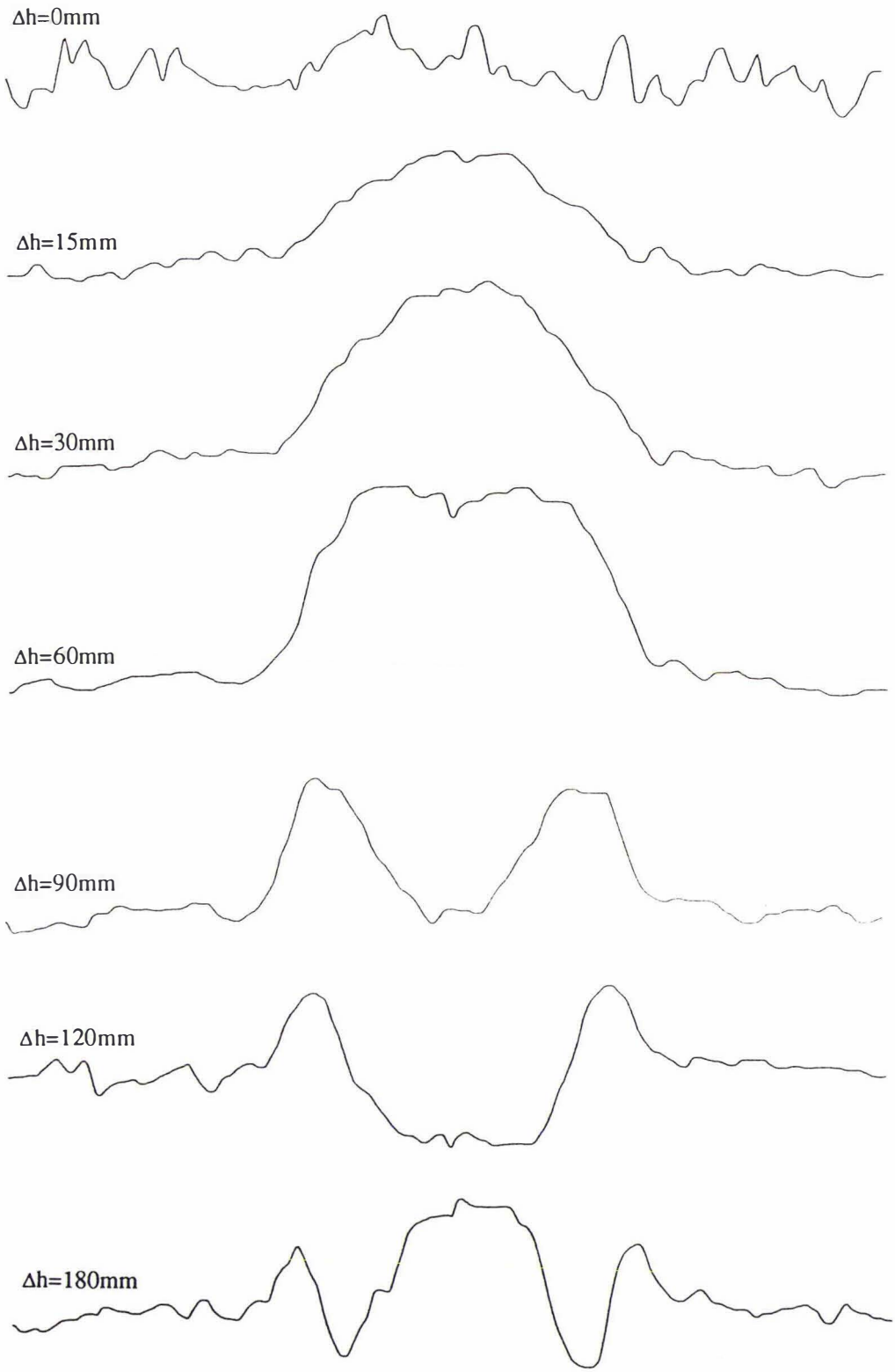

Figure 6.24b 1-D projection profiles of $\rho_{odd}(\mathbf{r})$.

gradient is also much smaller in this 'one-shot' technique because the 180° self-refocusing SINC pulse requires a more 'compact' gradient than the 90° slice selection sequence. While experiments with a maximum flow rate up to 10 mm/s (Δh=90mm) are presented in Figure 6.20, imaging experiments to a maximum flow rate of 20 mm/s were carried out using the 'one-shot' technique and the same experimental parameters, some 1-D projection profiles are shown in Figure 6.24 which were plotted using the same P0 phase setting. Comparing with the profiles in the last section, it is clear that the effect of the slice selection gradient was almost unnoticeable for these high flow rates.

6.4 Conclusion

Through water capillary flow results presented in this chapter, it has demonstrated that Dynamic NMR Microscopy is capable of simultaneous reconstruction of velocity and self-diffusion maps. Such measurements can be performed at a velocity resolution of a few tens of microns per second and at a spatial resolution of a few tens of microns. By comparing with the theoretical Poiseuille profile, it was shown that the velocity measurement can be made both accurate and precise, and able to differentiate opposite-signed velocity in the same field. Provided care has been taken during the experiment, the only potential artifact associated with the velocity map is the effect of the slice selection gradient if the velocity component in the measurement is normal to the slice plane. There is no simple method to remove this artifact completely but its effect can be minimized in the pulse sequence. The accurate measurement of self-diffusion by Dynamic NMR Microscopy, on the other hand, is much more difficult. It is demonstrated that the most serious diffusion artifact is associated with the velocity shear in the flow. However, by using an appropriate double-PGSE imaging pulse sequence, an accurate measurement of the self-diffusion can be achieved.

Comparing with the comprehensive Dynamic NMR Microscopy, the 'one-shot' velocity microscopy offers a time-efficiency in the measurement of velocity at a similar velocity sensitivity. This advantage is significant when working with biological samples *in vivo*. However, the precision of the velocity measurement using this 'one-shot' technique is largely dependent upon the signal-to-noise ratio of the images and is usually not as good as that of Dynamic NMR Microscopy. On the other hand, some velocity artifacts which are inevitable in Dynamic NMR Microscopy are no longer existed in the 'one-shot' technique. A much large flow rate can be easily measured using the 'one-shot' technique provided that the peculiar 'quadrant-mismatch' artifact is removed by an appropriate software modification.

Chapter 7 *In vivo* Botanical Studies

As discussed previously in Ch 4.3, imaging botanical samples *in vivo* at microscopic resolution is difficult. However, plants are ideal candidates for studying flow using an electromagnet-based spectrometer. This chapter presents applications of *in vivo* plant studies using both Dynamic NMR Microscopy and 'one-shot' velocity microscopy.

7.1 An application of 'one-shot' velocity microscopy, *Stachys sylvatica*

The time-efficient 'one-shot' velocity microscopy has been applied to a plant sample in order to measure the translocation of water in the xylem vessels of the vascular tissue *in vivo*. The experiment has demonstrated that a velocity as low as 45 $\mu m\ s^{-1}$ can be measured using this 'one-shot' technique.

7.1.1 Experimental arrangement

The flowering plant, *Stachys sylvatica L* (Hedge woundwort), has a 'square' stem and the specimen used in this experiment had a dimension of 3.1 mm by 2.7 mm at the imaging plane. The particular sample was obtained from the grounds of Massey University and left in an indoor water-soil container to allow roots to be formed at rhizome nodes until a full vigour of growth was restored (about four weeks). Because of the convenient shape of the plant, it was possible to use the standard imaging probe which suffers little from eddy current effect and for which the 'one-shot' method has proven successful. Before the experiment, soil surrounding the roots of the plant was carefully washed away, and directly following, the plant was passed through the 5.8 mm i.d. solenoidal rf coil. The roots were then placed in an 8 mm diameter glass tube which acted as a water reservoir in which soil-washed water was placed. Figure 7.1 shows the sample and the rf coil assembly. Attention was paid to ensure that the roots remained in water throughout the experiment. Measurements were taken at room temperature and under artificial illumination. It should be noted that the plant showed no sign of water stress after the experiment which lasted about 12 hours.

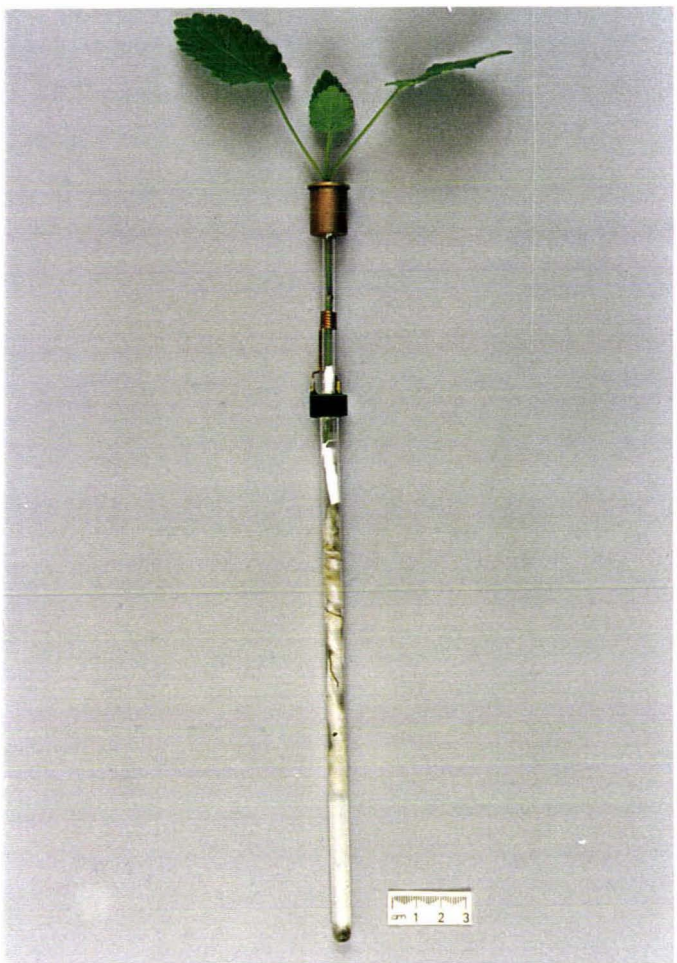

Figure 7.1 The sample assembly in the *Stachys sylvatica* experiment.

The pulse sequence was similar to that used in Ch 6.3 with PGSE gradient directed along the plant stem in anticipation of longitudinal flow in the vascular tissue. The combined effect of the three parameters g_m, Δ and δ is to achieve enough sensitivity to the delicate velocity but at the same time limiting the attenuating effect of the diffusive motion. The images were constructed with an array size of 128×128 in 2° steps from 0° to 360°, and the slice was selected at an intermodal region. Some of the experimental parameters are summarized in the following table.

Table 7.1 Summary of *Stachys sylvatica* experimental parameters

Δ (ms)	δ (ms)	g (G/cm)	BW (kHz)	N_{acc}	T_R (sec)	Pixel resolution	
						Slice(mm)	Transverse(μm)
160	0.7	23.4	10	128	0.8	2	75

7.1.2 Results and discussions

Figure 7.2 shows the $\rho_{even}(\mathbf{r})$, $\rho_{odd}(\mathbf{r})$ and velocity images obtained by this experiment, together with an optical micrograph of the cross section of the plant stem taken subsequently at the same slice location (Figure 7.3). It can be seen from the velocity image, that flow does occur in the vascular tissue region, in the direction from the roots to the top leaves, with a mean flow rate of about 45 μm s^{-1}. There are two noteworthy features of this *in vivo* plant experiment. First, the velocities occur right at the xylem area despite the fact that these areas are not the brightest features in the spin density image. Clearly therefore the velocity map does not arise from a residual signal artifact, which would be proportional to the total proton signal amplitude. Second the relatively low water proton signal can be noted in the vascular tissue despite the expectation that this region would contain the most free water. This effect may be caused by enhanced T_2 relaxation due to susceptibility variations in the vascular tissue.

From the optical micrograph it can be seen that there are about 30-50 vascular tubes in each vascular bundle area, with a mean internal diameter of each tube around 25-35 μm. Given a transverse pixel resolution in this experiment of 75 μm, it is clear that the signal contributing to each pixel is an average over several tubes and their surrounding tissues. One particularly nice feature of this 'one-shot' velocity imaging technique is the fact that only translocating water contributes to the velocity signal so that the values measured here should be a true representation of the actual fluid flow. Using the above experimental velocity values and the knowledge of vascular tube

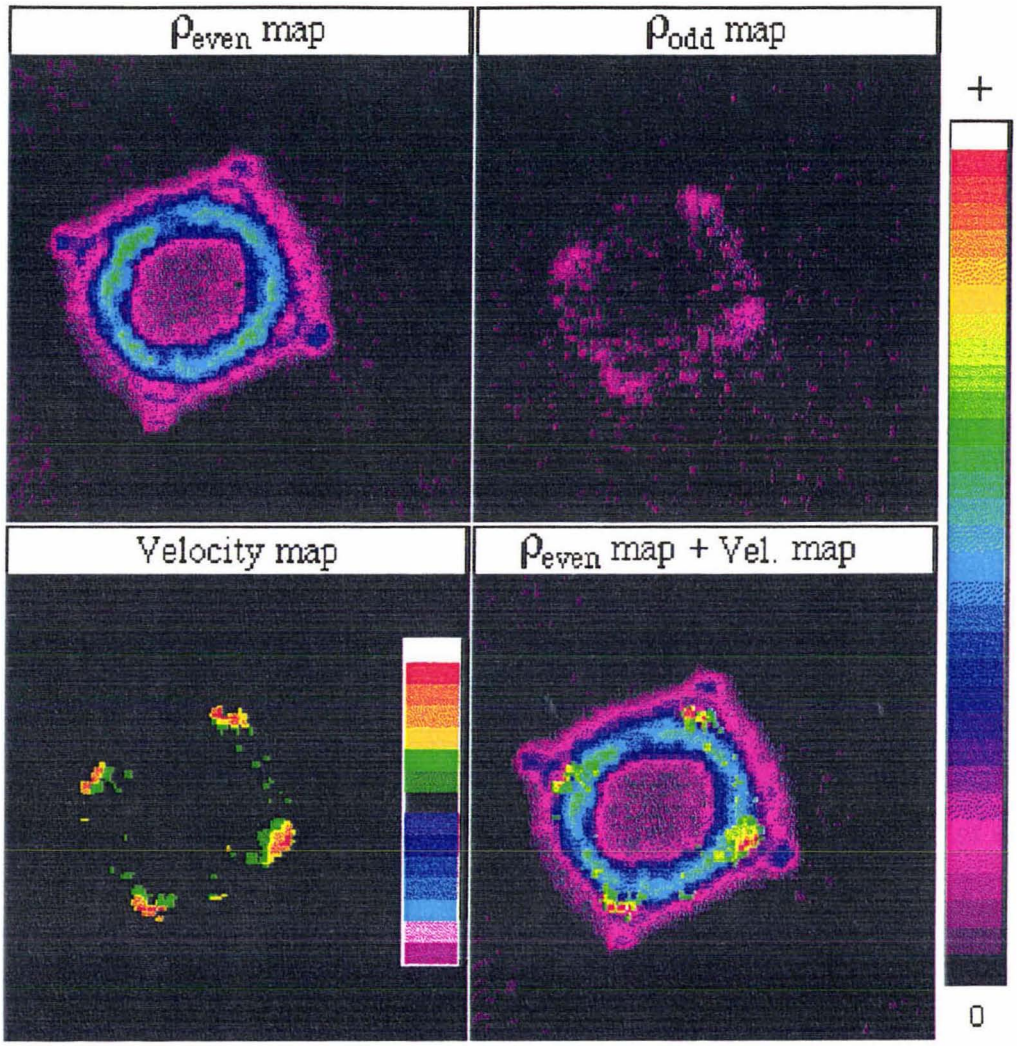

Figure 7.2 *In vivo* NMR images of the *Stachys* experiment.

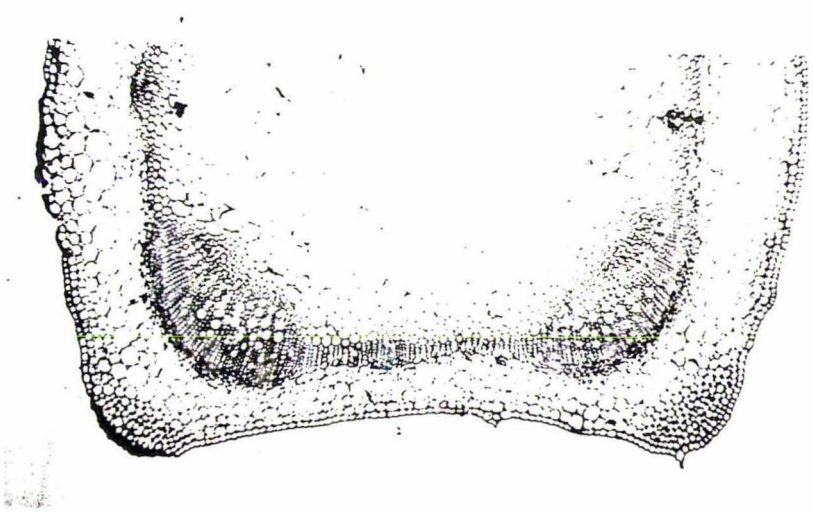

Figure 7.3 Optical micrograph of the stem of the *Stachys* sample.

geometry, the mass flow rate of the plant can be calculated as around 5.1×10^{-12} m^3s^{-1}, which gives a total volume flow over the experimental time about 0.22 cm^3. This corresponded closely with the actual water loss in the bottom tank, 0.3 cm^3.

7.2 Other botanical applications using 'one-shot' technique

A variety of plant samples were imaged using the 'one-shot' velocity microscopy in the standard imaging probe. These plants include *Stachys sylvatica* L., horsetail, moss, spring onion, snapdragon, clover, rock melon and runner bean. Apart from the successful *Stachys sylvatica* experiment described in Ch 7.1, no conclusive results could be drawn from the other plant flow experiments although quite a few experiments showed definite sign of vascular flow. The difficulty in imaging these plants is mainly caused by the damage to the sample in the preparation period and/or the sample-loading procedure. This difficulty often became greater when combined with delicate vascular flow and short tissue relaxation time. In this section, two of the *in vivo* imaging experiments are briefly described.

7.2.1 Horsetail: *Equisetum hyemale*

The horsetail, *Equisetum hyemale*, is classed as arthropsida. It has a unique anatomical structure[157]. Its long needle-shape stem makes it an ideal shape for imaging because it has only small and scaly leaves in a form of the sheath surrounding the lower part of each internode. *Equisetum* has very fine roots, formed at the nodes of the rhizome. There are six 'groups' of the carinal canals in each internode, and it is in these internode regions where the imaging experiments were performed.

The plants were grown openly in a concrete tank in the Department of Plant Biology, Massey University. Several samples were imaged using the 'one-shot' velocity microscopy method with parameter settings similar to those used in the *Stachys* experiment. The particular result presented here is for a very young rooted specimen attached to a piece of rhizome, the stem being about 1.8 mm in diameter and 50 cm long. The rooted stem was inserted through the 2 mm i.d. rf coil and the roots were then placed in a water reservoir situated underneath the probe. Attention was paid to ensure that the roots remained in water throughout the experiment.

The pulse sequence was similar to that used in the previous *Stachys* experiment. The PGSE pulse separation was 80 ms and pulse duration was 1.0 ms with a maximum gradient magnitude of 0.249 T m^{-1}. The spectrometer was operated at 10 kHz bandwidth with 0.8 s repetition time and 128 accumulation for each scan. The slice thickness was 2 mm and the slice was selected in an internode region.

The proton density and velocity maps are shown in Figure 7.4. An optical image was also taken after the *in vivo* imaging experiment at the imaging position (Figure 7.5). The pixel resolution of the images is 75 μm. The proton density map resembles the basic structures of the plant and is consistent with the optical image. The velocity map indicates there is upwards flow in the vicinity of the vascular tissue. An average velocity of (40±10) μm s^{-1} is obtained from these regions. The lower velocity in this experiment in comparison with that found for *Stachys* would seem to correspond with the smaller evaporative surface area of the *Equisetum* due to the nodal scale leaves. The resistance caused by the nodal discontinuity of the carinal canals would also reduce velocity of water flow. This result is also consistent with the early dye method which localised water flow to the carinal canals[158, 159].

7.2.2 Moss: *Dendroligotrichum dewdroides*

Moss is a type of fern, growing in damp native bush. It has interesting looking leaves but has neither an advanced root system nor a vascular bundle system. The water conducting tissue in moss is a central conducting strand of hydroids with thickened, non-lignified walls. It would be interesting to map the water transport route inside the moss stem. The particular samples used in the imaging experiment were taken from the floor of mountain forest near Erua and near Rangiwahia, Central North Island and kept in damp containers in the laboratory.

Much time has been spent trying to image water flow inside moss stem. The difficulty in this *in vivo* experiment was due to transport of water inside the moss occurring only when the leaves are surrounded by about 70 % humidity air. If the humidity of the air is too high, the plant stops taking water from the root whereas if the humidity is too low, the metabolism of the plant stops (These plants can survive without water for quite a long time). Flow had been seen during several imaging experiments but in each case with duration insufficient to enable image completion. Another difficulty associated with this moss flow imaging experiment is the lack of clearly defined region of vascular vessels. A proton map for one of the moss samples is

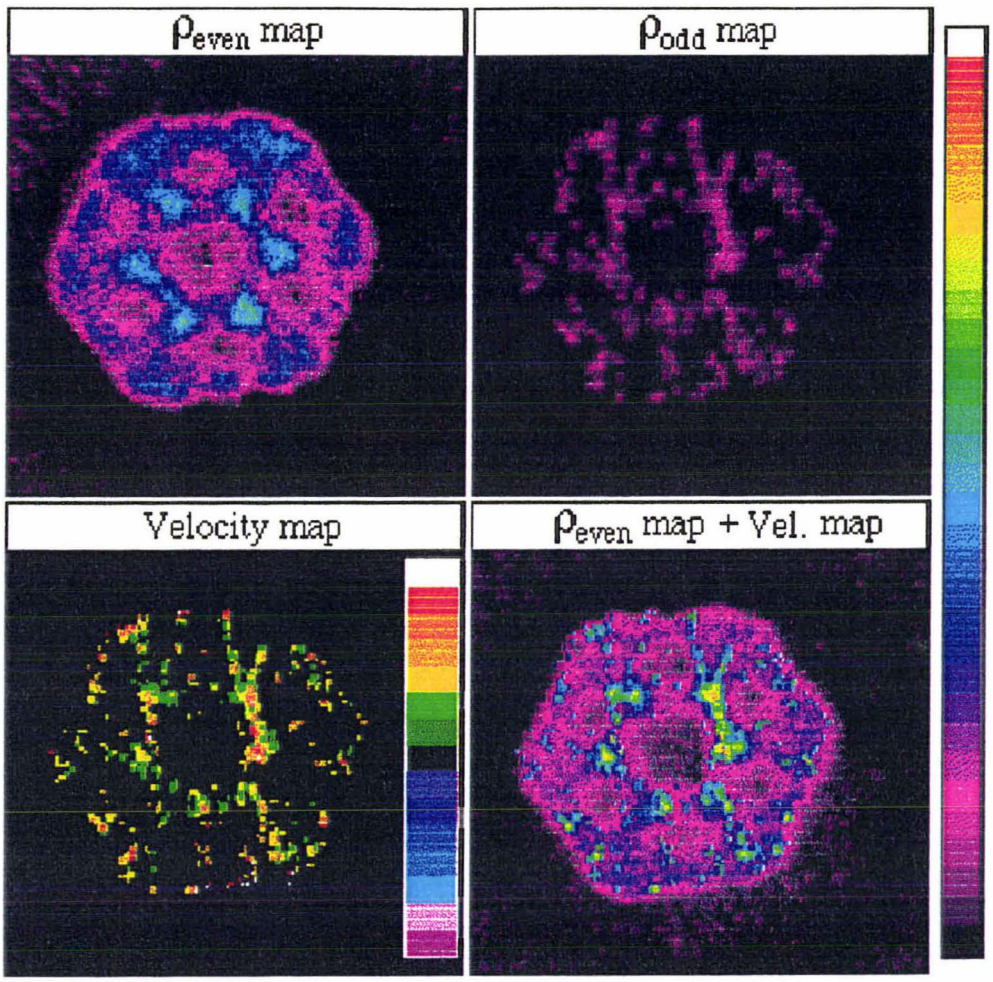

Figure 7.4 *In vivo* NMR images of the *Equisetum* experiment.

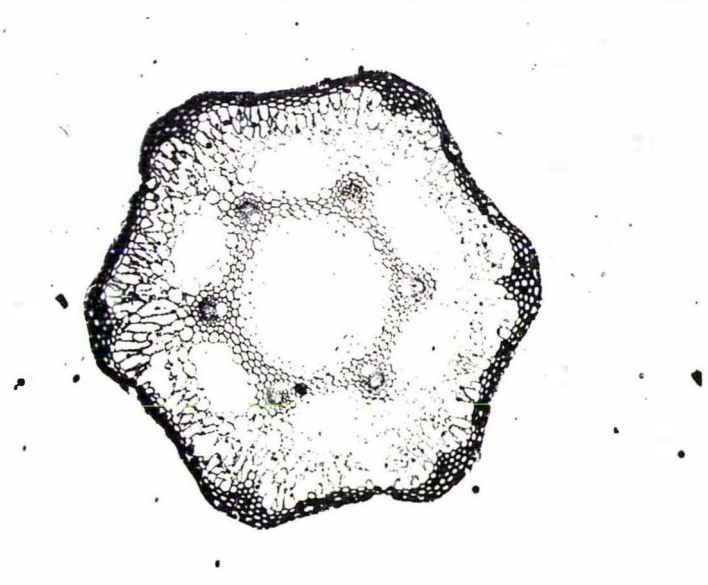

Figure 7.5 Optical micrograph of the stem of the *Equisetum* sample.

shown in Figure 7.6. These disadvantages were exacerbated by the relative short T_1 relaxation time of the moss sample.

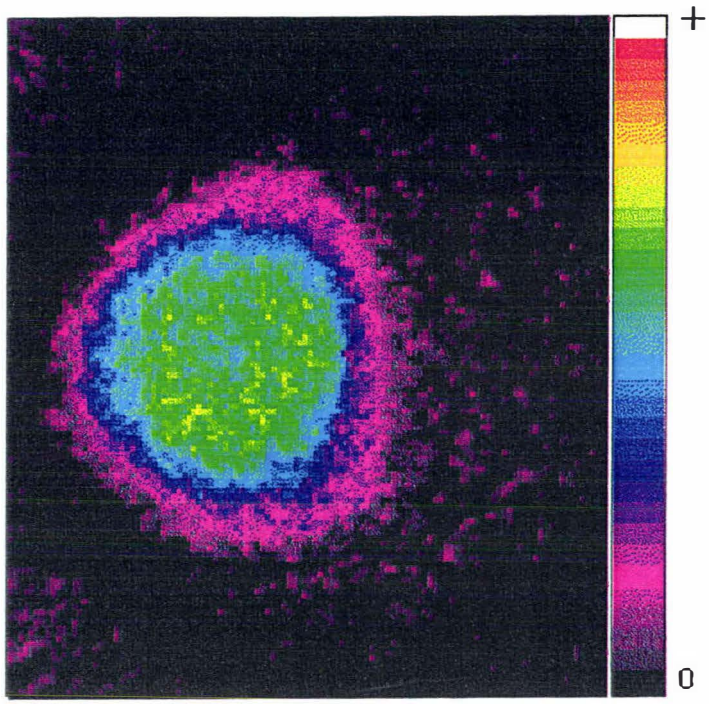

Figure 7.6 The proton map of a moss sample.

Figure 7.7 shows two 1-D images from one experiment in which the flow-sensitive image, $\rho_{odd}(\mathbf{r})$, clearly indicated flow (the inversion of the profile was due to the direction of the velocity encoding gradient). The lower trace arises from the moving water only, from which the water velocity may be determined as around 300 μm/s in the central conducting strand. The signal was averaged 160 times at 0.4 s repetition time with a slice thickness around 3 mm. The diameter of the stem was about 2 mm and the 6 mm i.d. rf coil was used. In this experiment the stem of the moss had been covered by a layer of Teflon tape to minimize water loss from the stem. The root of the plant was placed in a water tank and the leaves of the plant were surrounded by a plastic bag in which the humidity of the air was maintained by some damp paper tissue. The rather weak flow signal which was clear at the start of the experiment lasted only 30 minutes, insufficient time to complete the experiment.

Further work on this interesting plant would require a more efficient humidity and temperature control unit and some improvement of the signal-to-noise ratio of the imaging system.

(a) $\rho_{even}(r)$

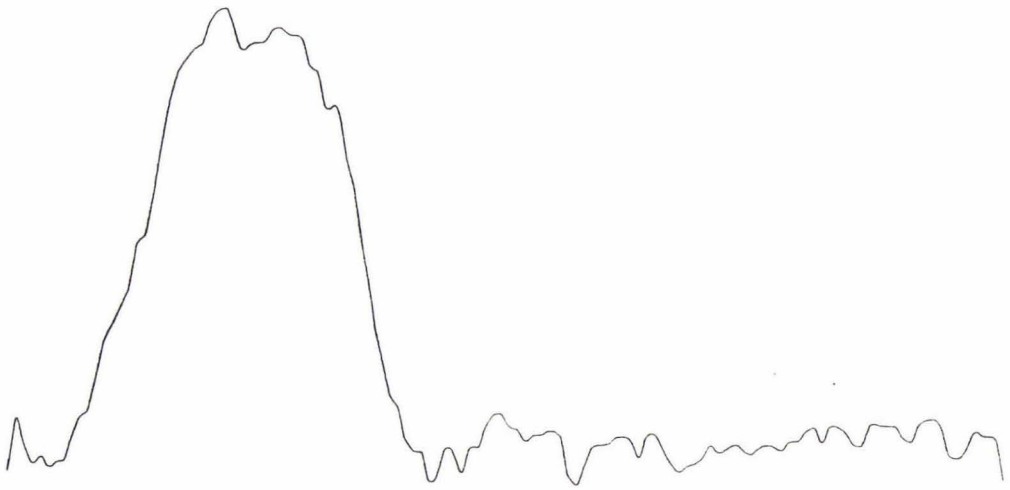

(b) $\rho_{odd}(r)$

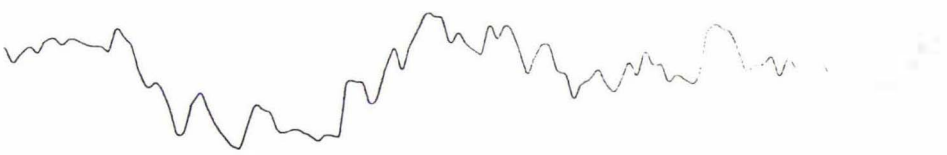

Figure 7.7 1-D images of the moss using the 'one-shot' technique.

7.3 Wheat grain velocity and diffusion imaging

Following the first successful *in vivo* experiment of imaging water transport inside a single wheat grain[123], a comprehensive study was carried out under a desire to correlate the water transport rate and the age of the grain. Although detailed physiological interpretations of the data are not clear, the results are consistent with the previous model.

7.3.1 Experimental preparation and arrangement

The wheat samples (cv *Otane*) were obtained from a greenhouse at the Fruit and Trees Division of DSIR in Palmerston North, and prepared following a procedure used previously[132]. An outline of sample preparation is given as follows (Figure 7.8). The wheat grain used for imaging was selected from the second to fourth spikelet from the top of the ear. Spikelets below and above the selected one were then carefully removed, and the rachis above the selected spikelet was cut off. The awns and the glumes of the selected grain were also removed but the palea and lemma of the grain were kept. There are two grains on each spikelet, one being used for imaging and its companion grain removed. This companion grain was weighted using a Mettler™ precision balance to obtain its fresh weight, and then placed in a constant temperature dryer controlled at 37°C. The companion grain was weighed again after several days to obtain the dry weight of the grain.

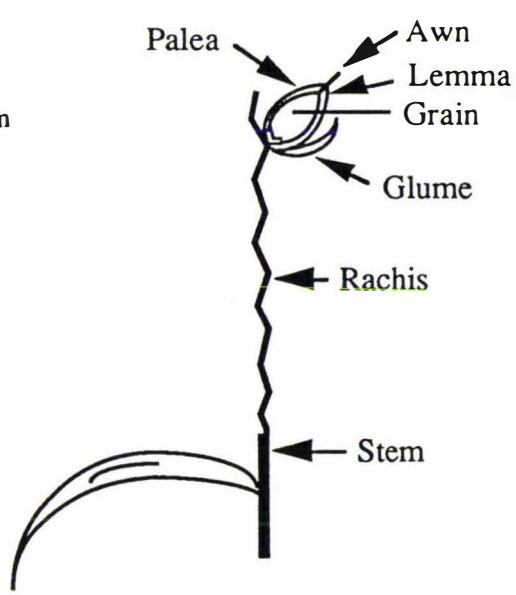

Figure 7.8

A schematic diagram of a wheat ear

A thin layer of moist cotton wool was then wrapped around the exposed rachis and a 'stop' mark taped to locate the imaging plane of the grain. Figure 7.9 shows schematically a prepared sample and the experimental arrangements. The electromagnet geometry is ideal for this application, allowing the pot containing the plant to be placed directly over the instrument. Three imaging experiments were carried out for each grain, two static imagings and one dynamic imaging. The total imaging time for each grain was about 10 hrs.

Dynamic NMR Microscopy experiments were carried out using the stimulated-echo pulse sequence (Figure 6.1b), since the T_1 and T_2 for the grain were measured as around 0.3 s and 34 ms respectively. The multi-q data images were acquired at 6° steps from 0° to 360° using a 64×64 digital array, the slice being selected at the middle of the grain. Some of the experimental parameters are summarised in the following table.

Table 7.2 Summary of experimental parameters for wheat flow imaging

Δ (ms)	δ (ms)	g (G/cm)	BW (kHz)	N_{acc}	T_R (sec)	Pixel resolution	
						Slice(mm)	Transverse(μm)
291	0.8	93.6	10	96	0.5	2	82

In order to compare the water density change during the time used for dynamic imaging, two NMR proton images were obtained at the same imaging plane using a standard static imaging pulse sequence before and after each dynamic imaging experiment. These static images were reconstructed in 2° steps from 0° to 180° using a 256×256 digital array. The signal was co-added 40 times for each projection angle with a slice thickness of 1 mm, while the transverse pixel dimension for the static image is 20 μm.

After the second static imaging experiment, each sample was removed from the rachis, sliced through the imaging position and photographed under an optical microscope. These colour optical slides were then digitized using a SONY CCD camera and converted into files which can be analyzed by ImageShow™.

7.3.2 Imaging Results

25 grains at different stages of growth were imaged, vascular flow being observed conclusively from 3 pots of wheat. The results are summarized in the

(a) A prepared wheat sample

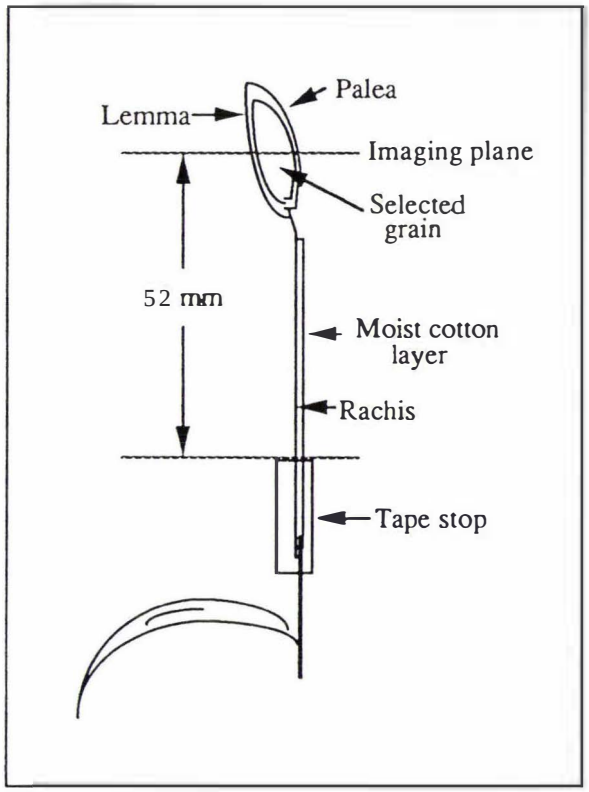

(b) Experimental arrangement

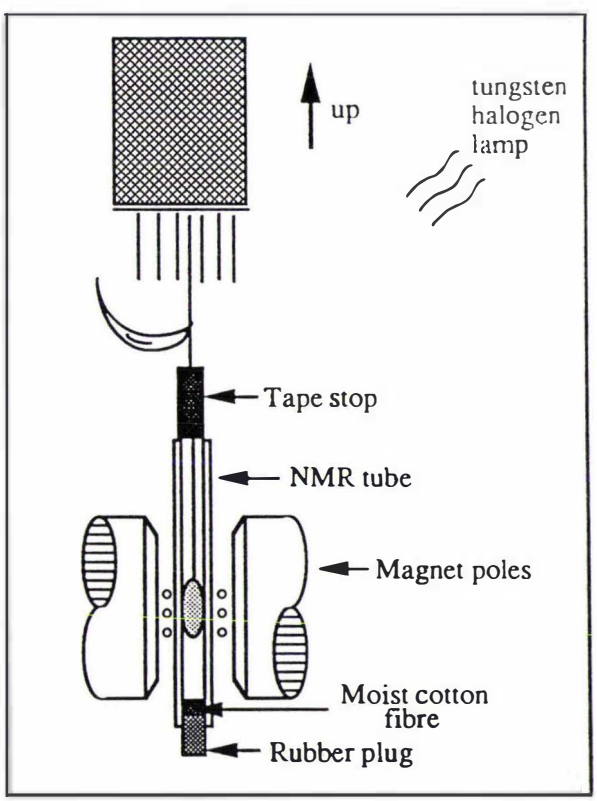

Figure 7.9 The sample arrangements for the wheat grain experiment.

following table, in which the question mark indicates those with some indication of vascular flow but for which the results were not conclusive.

Table 7.3 Summary of the wheat grain velocity imaging results

Date after Anthesis	Weight of Companion Grain fresh (mg)	dry (mg)	% water (w/w)	Indication of flow
...				
7	31	7	77.4	no
7	17	5	70.6	no
8	43	12	72.1	?
8	28	7	75.0	?
9	38	10	73.7	?
9	21	6	71.4	no
10	26	7	73.1	no
11	31	8	74.2	?
12	43	14	67.4	no
12	48	14	70.8	?
13	52	18	65.4	no
13*	40	13	67.5	yes
14	66	23	65.2	no
15	54	20	63.0	yes
15	54	22	59.3	no
16	58	24	58.6	no
17	34	13	61.8	yes
18	58	25	56.9	?
18	46	21	54.3	no
19	68	30	55.9	no
...				

A typical *in vivo* velocity image (the grain marked with *) is shown in Figure 7.10 together with the 'before-dynamic' and 'after-dynamic' NMR proton density maps and the digitized optical photo. It can be seen that a small outward velocity of approximately 60 $\mu m\ s^{-1}$ is apparent for water near the grain centre in the vicinity of the vascular tissue. Given the total image pixel area in the vicinity of the vascular tissue being of approximately 0.05 mm^2, this velocity corresponds to a volume flow rate of 12 $mm^3\ hr^{-1}$. The similarity of the proton images obtained before and after the Dynamic NMR Microscopy experiment suggests that no bulk relocation of water has occurred.

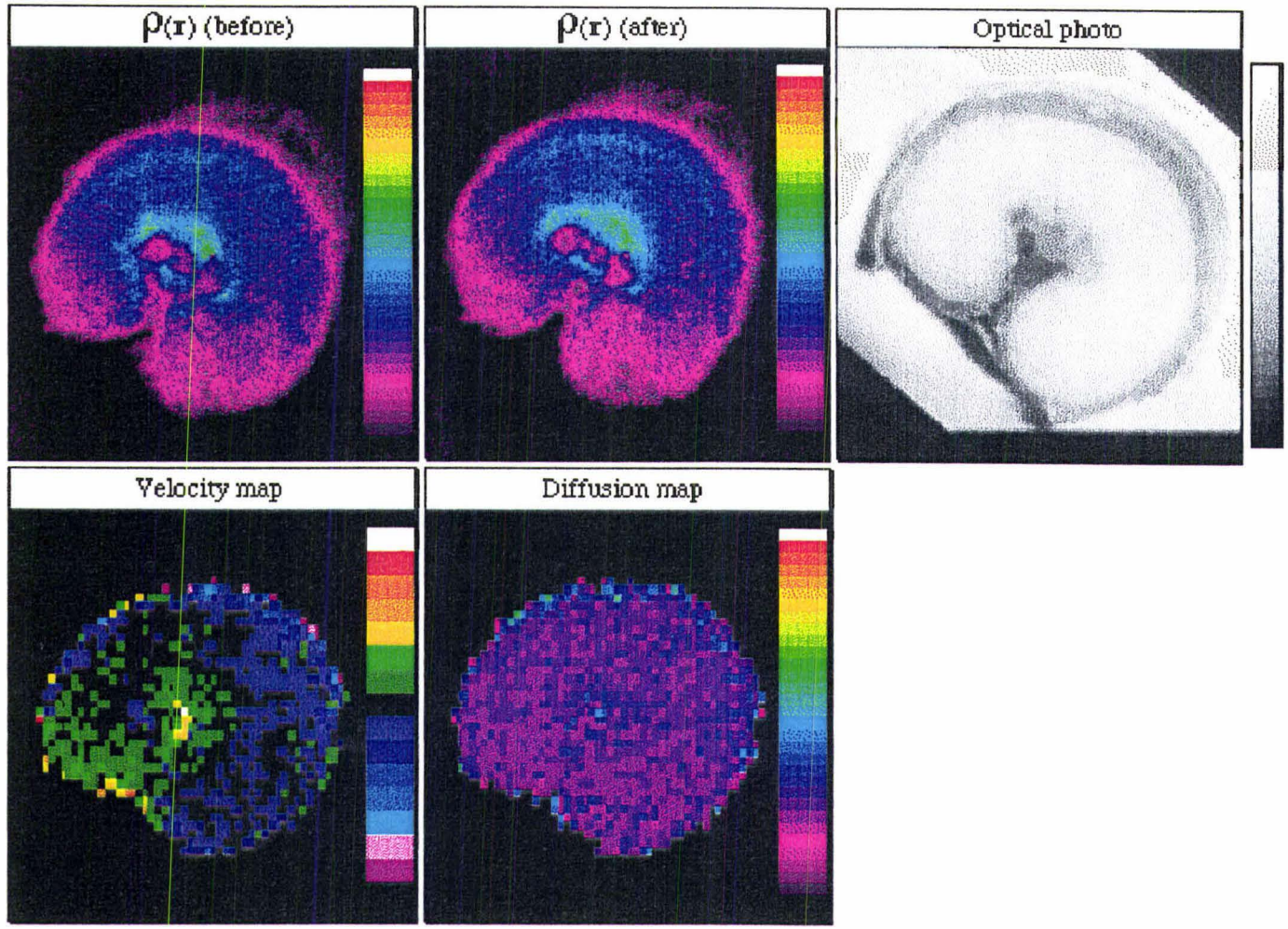

Figure 7.10 Maps of an *in vivo* wheat grain experiment.

7.3.3 Discussions

From the above results three conclusions can be drawn. First, the experimental data fits well the physiological model suggested in a previous study[123]. Second, because the true conducting area in the vascular tissue of a wheat grain is about 0.25×10^{-3} mm^2 (about 40 sieve tubes each grain, with an average internal radius of 1.4 μm for each sieve tube)[160, 161] which is much smaller than the image pixel area, the averaging of velocity over the image pixels must have occurred. Thus it suggests that the true velocity within the vascular tissue is higher than what has been measured from the imaging experiment. Finally, the flow rates in the early and later stages of the grain development are smaller than those around 13 to 17 days after anthesis. However, a precise correlation between the water transport rate and the age of the grain cannot be given definitively by the present study because the grain which shows no sign of flow could have been damaged (even partially) during the delicate and complicated pre-imaging preparation. A further study is required in which more grains with the same age are imaged.

One of the conundrums in NMR microscopy concerns the relationship between the true molecular density and the apparent density as indicated by the proton image amplitude. It is well known that the relative water proton image amplitude may be highly inconsistent with known water contents in different physical regions of the plant. It should be noted that some image contrast is always present in NMR imaging experiments because of the influence of spin relaxation between the time that the spins are excited and the time that the image signal acquisition begins. While this time delay can be reduced to some minimum value, of order a few ms, it is never in practice possible to entirely eliminate it and in consequence it is impossible to measure $\rho(\mathbf{r})$ directly. One commonly advanced explanation for strong relaxation contrast being present, is that physical boundaries between regions of differing susceptibility may strongly perturb the local magnetic field uniformity. It may be possible to extrapolate back to zero delay to obtain a corrected density image by obtaining images at different delay times. Here an alternative scheme is examined in which $\rho(\mathbf{r})$ is extracted from the inherently contrasted image by means of the self-diffusion map.

The relationship which is used for this scheme is calculated from a study of hydration and diffusion as a function of the relative humidity at which the endosperm tissue was equilibrated[162], shown in Figure 7.11. This relationship is used to map self-diffusion coefficient to a corresponding water density value. The resulting water density image is shown in Figure 7.12 and is somewhat different from the proton NMR

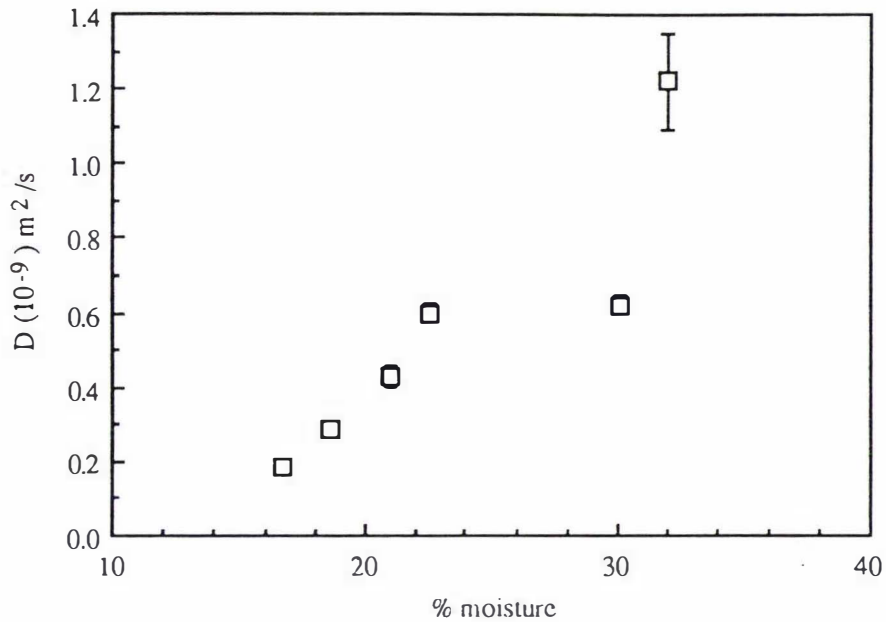

Figure 7.11 Wheat grain tissue diffusion coefficient vs moisture content (calculated from the data of Callaghan *et al* [162]).

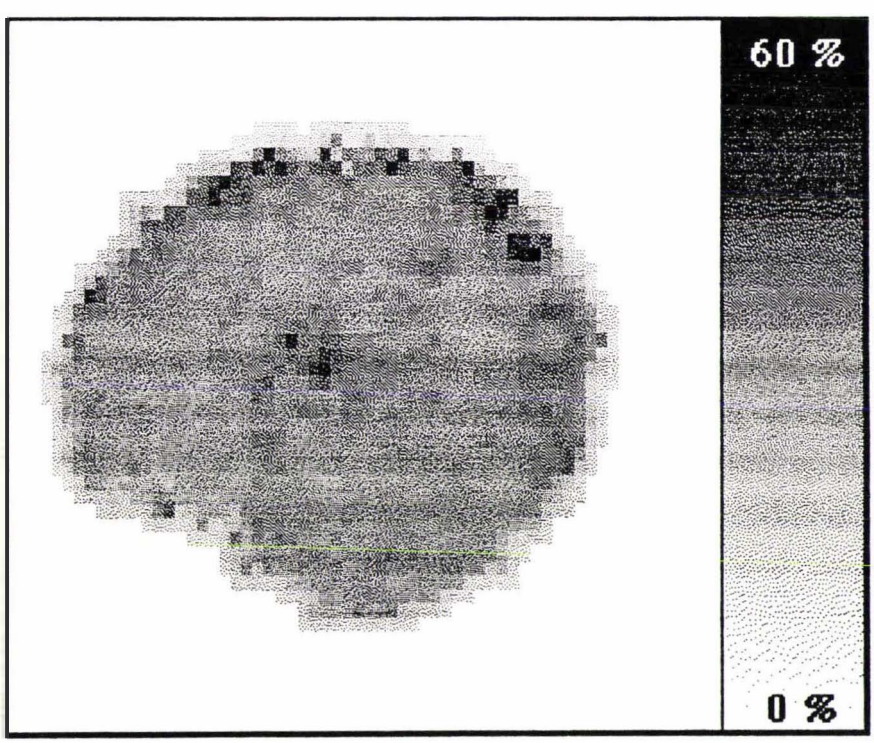

Figure 7.12 D-corrected proton map using the data in Figure 7.10 and 7.11.

image shown in Figure 7.10, suggesting that the water content is more uniform than the proton NMR image would indicate. One feature which does correspond however is the greater moisture content found in the central endosperm region of the grain. But the analysis may be complicated by a number of factors which are involved in the water-protein interactions[163]. It is clear that considerable care is needed in interpreting NMR microscopy images if they are to be used to provide a quantitative measure of local moisture content.

Of course one additional criticism of the indirect diffusion/moisture content approach concerns the difficulty in relating PGSE diffusion data for excised tissue with the diffusive behaviour of water in the *in vivo* grain. It should be noted however that our previous work on wheat grains has indicated that whereas the water flow is disrupted when the grain is detached from the stem, the diffusion map is not noticeably disturbed[123].

Clearly Dynamic NMR Microscopy provides a useful form of tomography in plant physiology, enabling a unique determination of water transport rates *in vivo*. Nonetheless there remains considerable difficulty in interpreting proton density maps in terms of true water concentration. Our data for water in wheat endosperm tissue suggests a discrepancy between the proton NMR image amplitude and the water concentration as indicated by the local self-diffusion coefficient.

7.4 Castor bean velocity and diffusion imaging

The transport of water and nutrients, for example sucrose, *via* vascular bundles, is of importance in both the growth and seed enlargement stages of plants. In the previous section, the transport of water within a single wheat grain was studied during the seed enlargement stage. The experiment described in this section dealt with a different physiological process, the transfer of oil reserve metabolites from the endosperm to the cotyledons and hypocotyl of the seedling during the initial growth stage in the castor bean, *Ricinus communis* L.

7.4.1 An introduction of the sample

The castor bean is an endospermic dicotyledon plant[164]. Figure 7.13 shows schematically the structure of a castor bean seedling. During the incubation stage, the growth of the seedling is concentrated in the hypocotyl. The curved narrow 'neck' of the hypocotyl is usually referred to as the 'hook'. Located at the endosperm end of the hook are the two initial 'leaves', the cotyledons whose absorptive surfaces are pressed against the inner surface of the endosperm. During the early growth of the seedling, the soluble nutrients, resulting from the breakdown of the oil reserve in the endosperm, are transported with water *via* the vascular bundles to the root end of the hook, where the maximum growth of the seedling occurs. Within the hypocotyl, there are eight vascular bundles each consisting of two different highly-specialized types of conducting tubes. These are the phloem sieve tubes and xylem vessels.

It is known that long-distance transportation of nutrients and water in plants is localized in the vascular tissue. A precise and quantitative picture of transport via the vascular tissue is, however, still unavailable because of the complexity of the plant tissues and the lack of accurate, sensitive and non-invasive measurement technique. It has been suggested[165] that in the castor bean seedling, the water which is initially taken in by the roots, could be circulated back to the endosperm after unloading the nutrients at the root end of the hook. In this model, the nutrients are transported *via* the phloem sieve tubes and the xylem vessels serve as the path for the back flow of water. It has also been suggested that the eight vascular bundles are associated with two cotyledons separately, i.e., four bundles are connected with each.

Water flow in the phloem sieve tubes is directed from the cotyledons to the roots and is caused by osmotic pressure differences over the semi-permeable membranes of the tubes. Water flow in the xylem vessels is directed from the roots to the cotyledons and is driven by a number of sources. These include transpiration, the volume increment of the growth process, the loading of certain nutrients in the root region due to the root pressure and the water flow to the phloem sieves tubes. The castor bean seedling offers a good system for studying the transport of nutrients in plants because during the first several days of its growth, a seedling is effectively a 'semi-closed system' and for which there is very little transpiration loss. If the growth rate and the dimensions of the conducting tissues are known, velocity mapping provides a means of studying such transport because the flow in xylem would be mainly driven by the supply to the phloem.

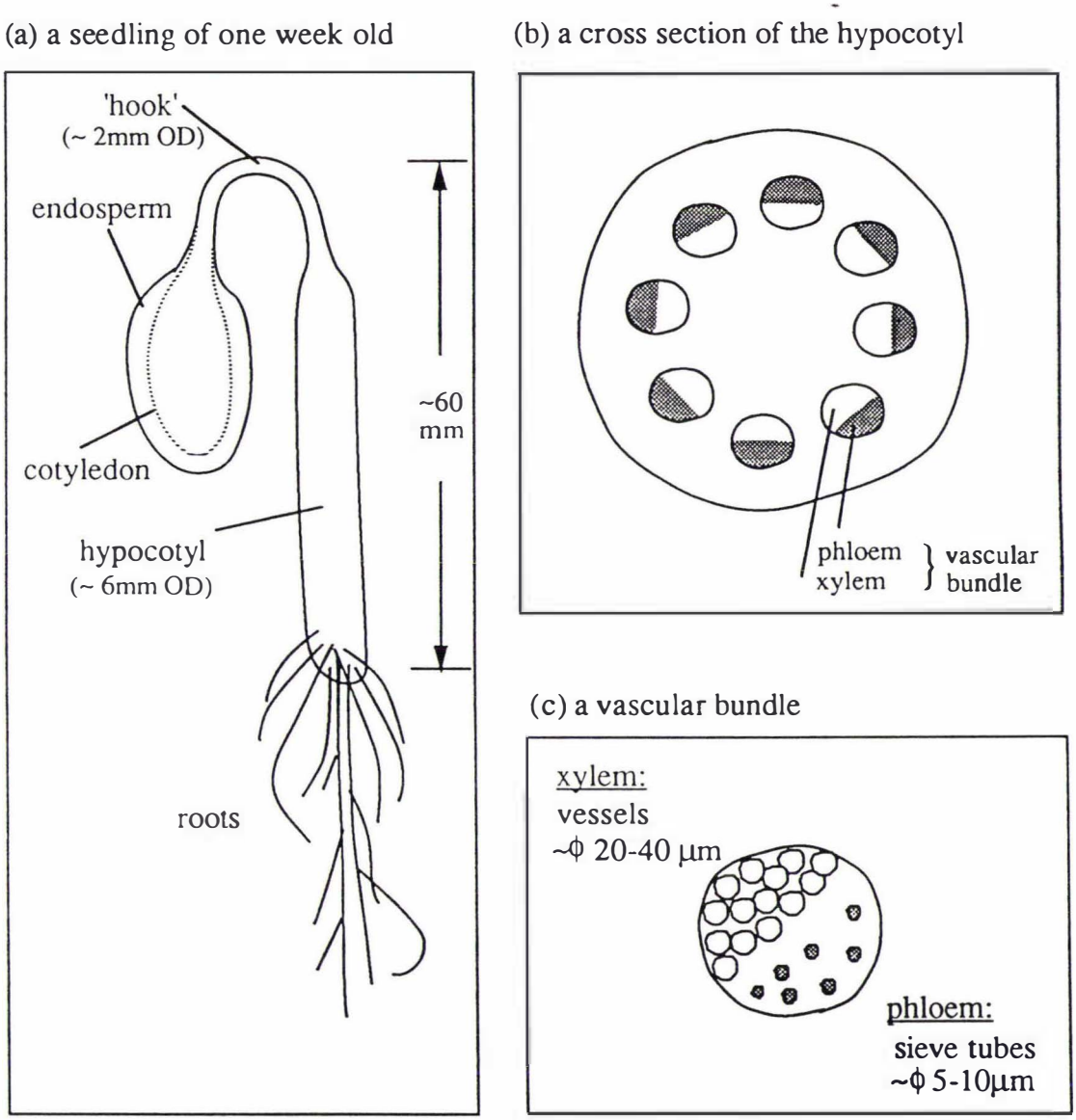

Figure 7.13 Schematic diagrams of a castor bean seedling.

7.4.2 Experimental arrangement

Imaging experiments were carried out using the newly developed plant-imaging probe. Several sealed containers were designed and manufactured to fit into the probe using either 0.5 mm thick plastic sheet or glass tubes. Each container has a water-filling tube, an overflow tube and a drainage tube so that the fluid inside these containers can be changed during an hour-long experiment. An air-bubbling tube can also be connected to the container which contains the roots of the sample. Figure 7.14 shows several different experimental arrangements appropriate to measuring flow in different parts of the castor bean and at different stages of development.

The castor bean seedlings were grown in the pure water solution under artificial illumination at 27°C constant temperature. The imaging experiment is performed using seedlings about a week old. For each sample, the rf receiver coil was wound directly at the position to be imaged. The numbers of turns on the rf coil varied between 6 and 10 depending upon the diameter. The inductance for each rf coil was therefore made roughly the same so that the rf tuning circuit did not have to be altered. After loading the sample, the probe was closed and the rf circuit tuned. Immediately after, the probe was positioned between the magnet pole pieces and the water and air tubes connected. The water in the containers was changed periodically and air bubbled into the root container constantly throughout the experiment.

20 seedlings were imaged, in which the initial 10 experiments were using the 'one-shot' velocity microscopy method, all subsequent experiments were using Dynamic NMR Microscopy. The failure to detect water vascular flow conclusively using the time-efficient 'one-shot' technique was due to the velocity in this 'semi-closed sample system' being very small. Measurement of velocities below 50 μm/s via the 'one-shot' method requires excellent stationary spin signal suppression. The proximity of the gradient coils to the magnet pole pieces in this purposely-built plant-imaging probe led to severe eddy current effects which caused gradient phase cycling to be ineffectual. By contrast Dynamic NMR Microscopy which doesn't rely on signal suppression is far less susceptible to these effects and gave considerable better results. All the results reported on here use a 128×128 image array size.

The pulse sequence used for these Dynamic NMR Microscopy experiments was similar to that used for the wheat grain imaging. The PGSE pulse separation, duration and maximum magnitude were 500 ms, 0.5 ms and 0.936 T m^{-1} respectively. The use of such a long stimulated-echo pulse separation made possible by the long T_1 of the

(a) imaging the 'hook'

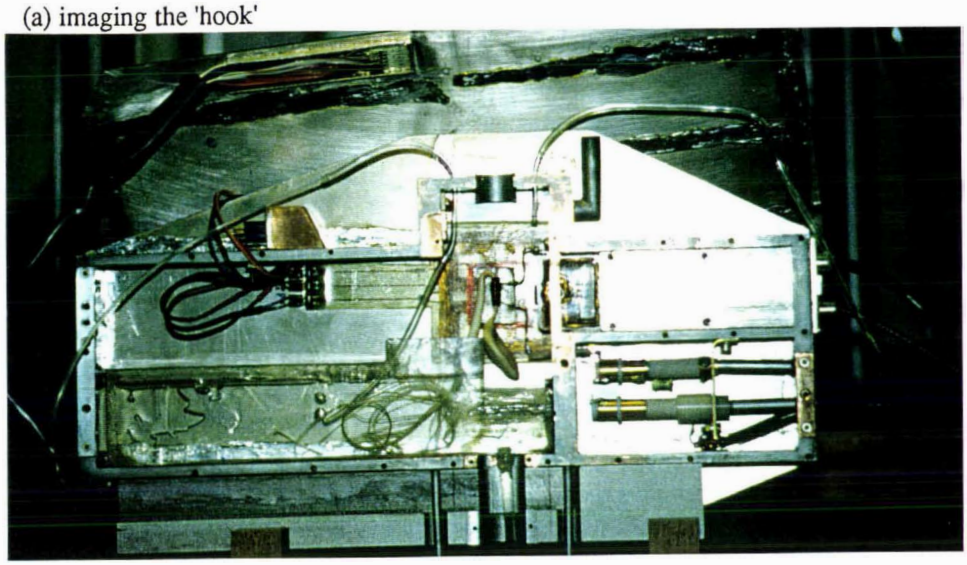

(b) imaging the 'stem'

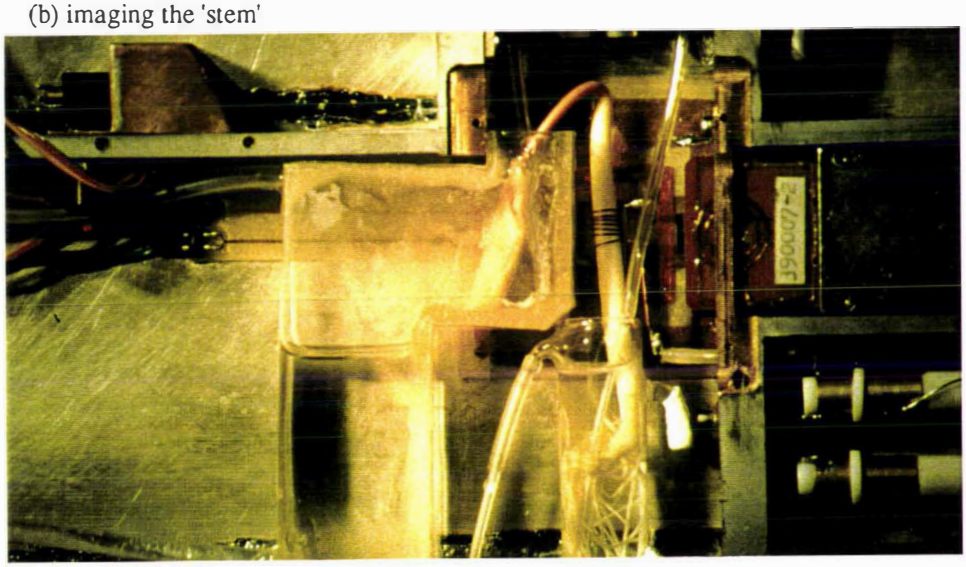

(c) imaging a mature seedling

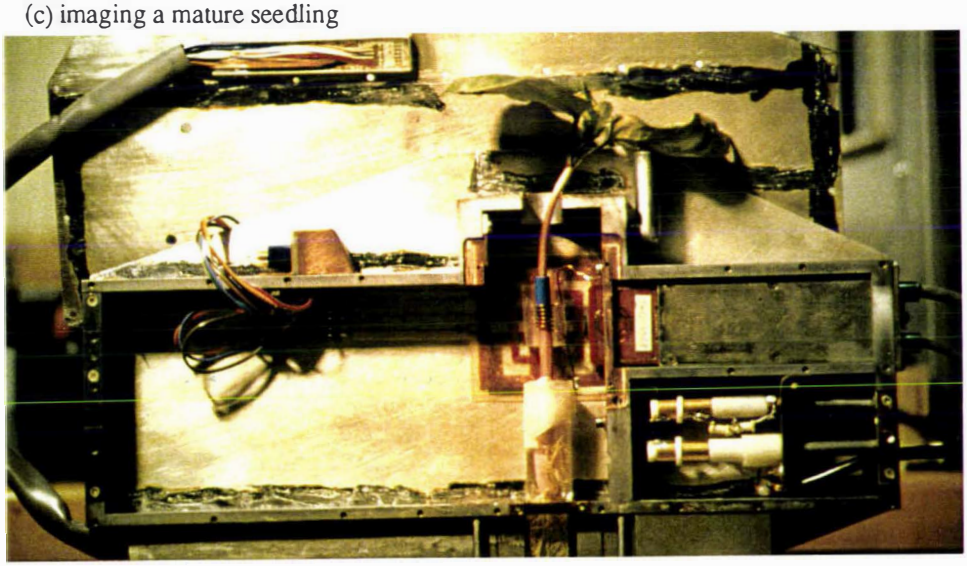

Figure 7.14 Photos showing experimental arrangements for the castor bean experiment.

sample resulting from the use of pure water during the incubation of the seedlings. It was discovered when proper nutrient solution was used, the T_1 of the sample reduced dramatically due to the presence of Mn^{2+} ions. The data images were acquired in 6° step from 0° to 360° with the signal averaged 40 times along each projection at a slice thickness of 2.5 mm, the band-width of the spectrometer being 10 kHz and the repetition time being 1.5 sec.

In order to identify the structure of the seedling and to correlate the velocity with the structure, a water density map was also obtained for each sample using normal (static) NMR imaging techniques in which the echo time (and hence relaxation contrast) was minimized. A pulse sequence similar to that shown in Ch 5.1 was employed in the static imaging in which image reconstruction was in 6° step from 0° to 360° using a 128×128 digital array. The signal was averaged 32 times for each projection angle with a slice thickness of 0.5 mm. The pixel dimension is about 60-70 μm for both static and dynamic images.

The design of this special imaging probe for plants has proved to be very successful. After the completion of both static and dynamic imaging experiments which lasted about 18 hours, all the seedlings were in excellent condition. In fact all the samples had grown about 1 cm during the experimental time. Optical photographs were taken from several seedlings after the imaging experiment at the imaging position using an optical microscope. Figure 7.15 shows an example.

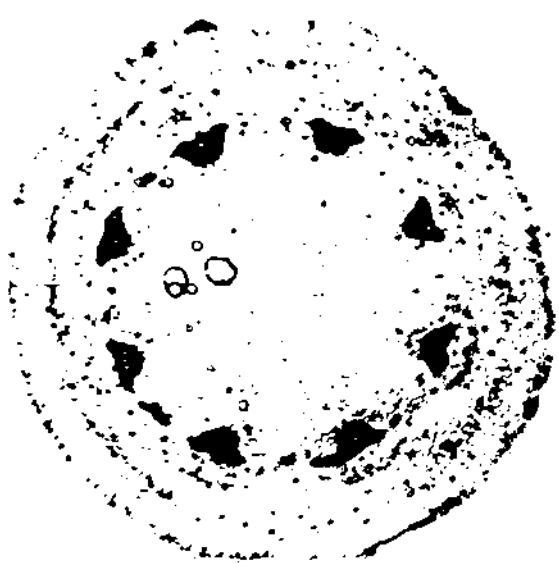

Figure 7.15 Optical photo of the stem of a castor bean sample (a mature bean)

7.4.3 Results and discussions

Figure 7.16a shows a set of images obtained at the lower part of the hypocotyl of seedling No 17. The velocity image clearly indicates water flow in the xylem area with a magnitude of between 6 to 12 $\mu m\ s^{-1}$. It should be noted that the contribution to this velocity which arises from seedling growth can be calculated, by the increment of the length of the seedling during the experimental period, as 1 to 2 $\mu m\ s^{-1}$.

To investigate the physiological relationship of the cotyledons to the vascular bundles, the endosperm end of the hook (seedling No 19) was carefully cut so that one piece of cotyledon was effectively separated. Figure 7.16b shows a set of images from this experiment in which it appears that water flows only in the uncut half-hypocotyl.

Another experiment used a more mature seeding (No. 20) which had been left in the incubation unit for about two or three weeks. The endosperm of this seeding had finished its role in the development stage of the plant. The cotyledons were still present but four new green leaves had developed. Figure 7.17 shows the results of this experiment, in which flow in the xylem vessels and in the phloem sieve tubes was measured simultaneously. These two flows were indeed in opposite directions, from the leaves in the phloem sieve tubes and to the leaves in the xylem vessels.

Imaging experiments at the hook region of the hypocotyl of the castor bean seedling were also carried out for several samples but the results were not conclusive. This was most likely due to the poorer signal-to-noise ratio due to the diameter of the hook being less than two millimetres.

In summary, this series of experiments on the castor bean has, for the first time, resulted in microscopic mapping of simultaneous flow in both the phloem sieve tubes and the xylem vessels of a plant. The velocity resolution of 6 $\mu m\ s^{-1}$ for this experiment is, to our knowledge, the lowest flow rate that has ever been measured in NMR imaging experiments. A more precise quantitative understanding of the transportation process in plants, however, awaits further work at improved signal-to-noise ratio.

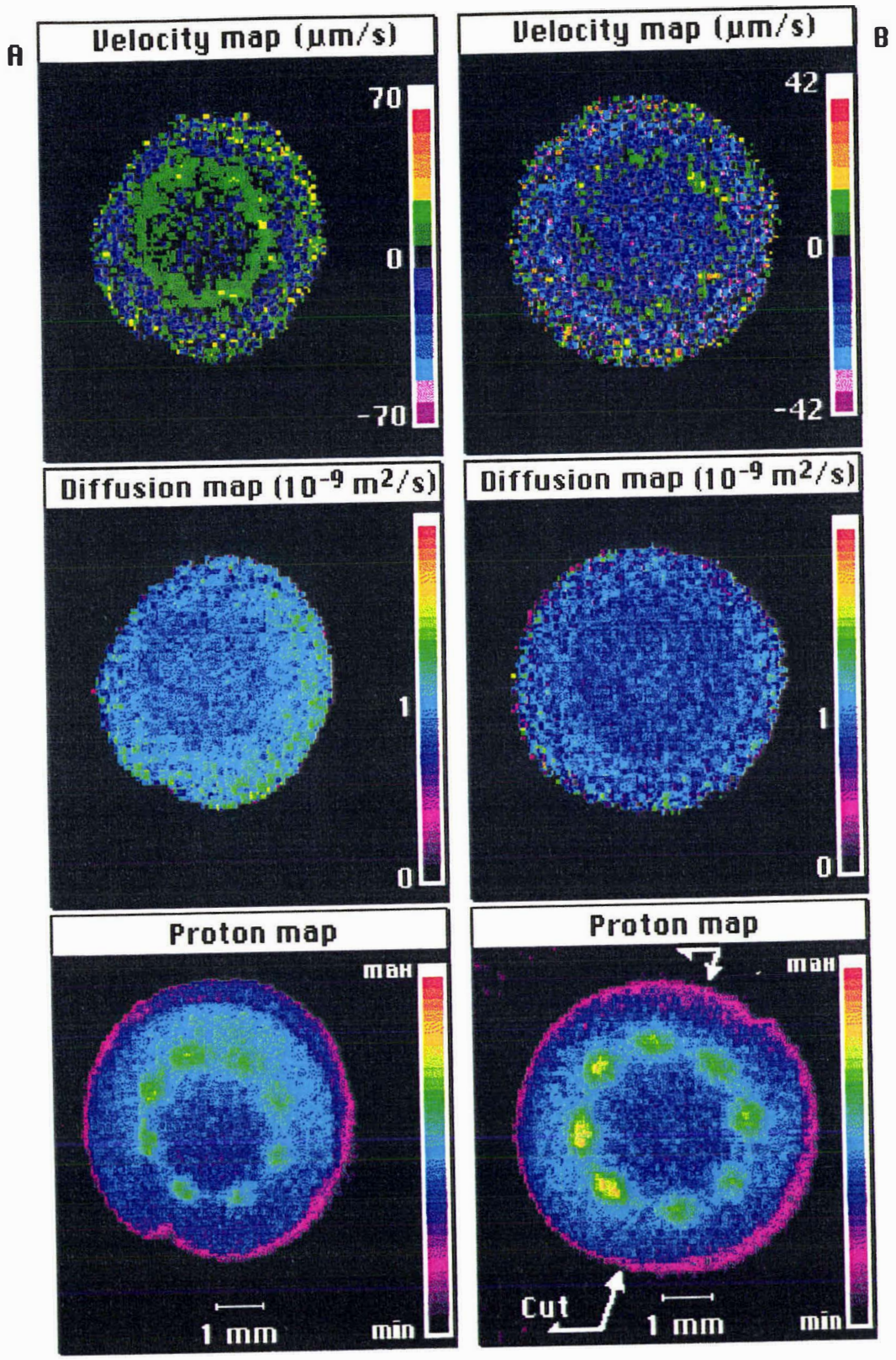

Figure 7.16 *In vivo* NMR images of the castor bean experiment (one-week old seedlings).

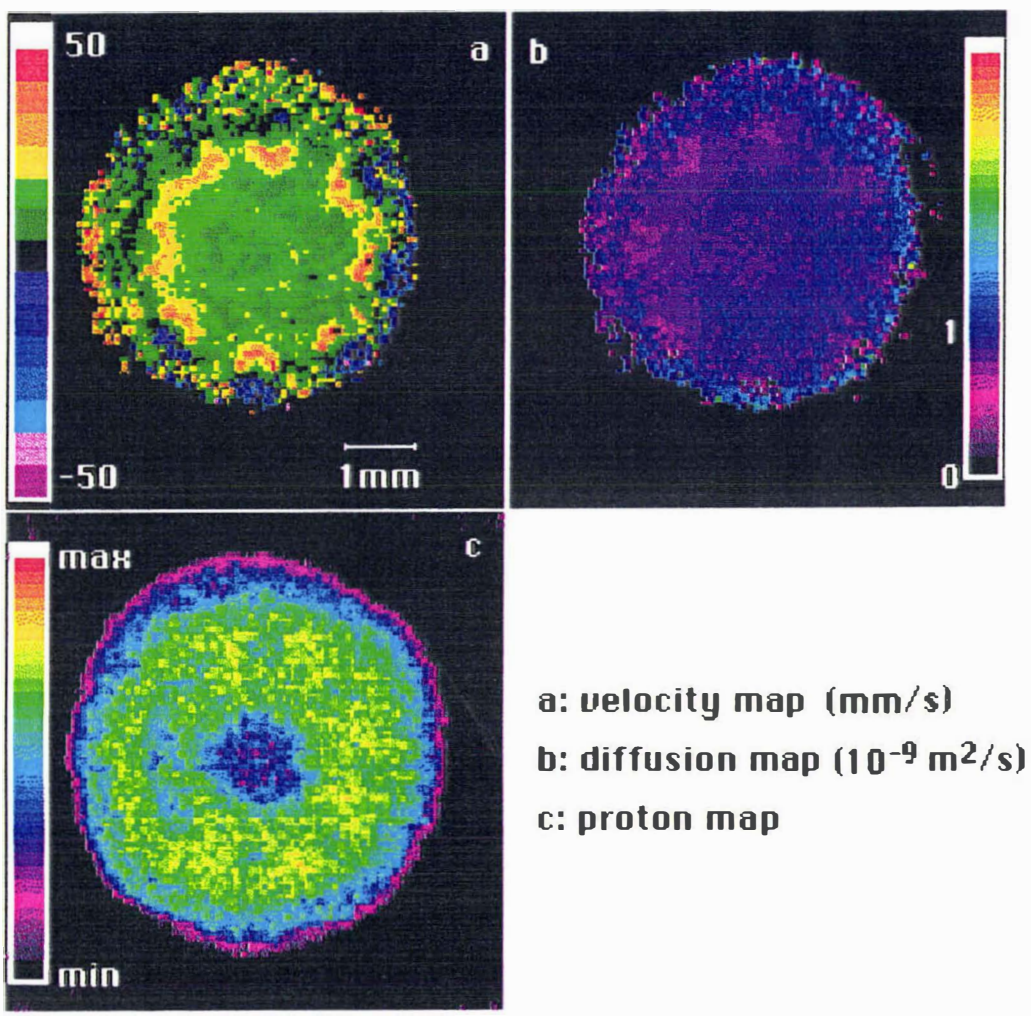

Figure 7.17 *In vivo* NMR images of the castor bean experiment (a mature seedling).

7.5 Conclusion

The experiments described in this chapter have demonstrated that both Dynamic NMR Microscopy and 'one-shot' velocity microscopy are powerful tools in the studies of botanical samples *in vivo*. The velocity measurement by Dynamic NMR Microscopy on the order of 10 μm/s in the castor bean experiment is the lowest flow rate which has ever been measured in a NMR imaging experiment. The time-efficient 'one-shot' method has also proved to be capable of detecting velocity as low as several tens microns per second in the *Stachys* experiment. These results are remarkable considering the somewhat insensitive 60 MHz spectrometer.

The difficulties associated with the measurement of velocity and self-diffusion using biological samples *in vivo* are also illustrated through various experiments presented in this chapter. This has suggested that a successful biological *in vivo* experiment may require major modifications in the imaging apparatus. In particular the castor bean experiment required the design and manufacture of a new plant-imaging probe.

When imaging heterogeneous-structured samples such as plants, each image pixel contains inevitably different portions of both stationary and moving spins. From the *in vivo* plant experiments described in this chapter, it can be concluded that there are two particularly nice features of the 'one-shot' velocity imaging technique. First, due to the fact that only moving water contributes to the velocity signal, the values measured in the 'one-shot' method should be a true representation of the actual fluid flow. In comparison, Dynamic NMR Microscopy collects signals from both stationary and moving spins and therefore can result in a velocity error. However, as shown in Ch 3.4, this method can give a true average when the average P_s overlap. The second nice feature of the 'one-shot' method is the magnitude of the velocity can be estimated (to some extent) during the on-line acquisition of $\rho_{odd}(\mathbf{r})$ signal. This feature hence provides an early indication if the vascular flow of the sample stops during the experiment. The velocity-sensitive sequence of the 'one-shot' method can also be used to produce 1-D velocity profile in short time. By contrast, the more comprehensive Dynamic NMR Microscopy requires much more time in which the flow rate of the sample needs to be stable. However, the 'one-shot' method requires excellent stationary signal suppression and hence is more sensitive to the presence of back-ground noise and induced eddy currents whereas Dynamic NMR Microscopy is far less susceptible to these effects and gives considerable more accurate and precise results.

Chapter 8 Fluid Dynamics: Water Flow through an Abrupt Stepped Tube

This chapter describes an experiment which was undertaken in order to measure velocity distributions of water flow at low Reynolds' number through cylindrical tubes exhibiting abrupt contraction and abrupt enlargement. The experiment was designed to quantitatively and accurately reveal the complex flows induced in these two configurations. The results from numerical simulations were also used to compare the measurements with the theoretical velocity distributions. These simulations were based on a numerical solution of the Navier-Stokes equation using the finite difference method.

8.1 An introduction to flow through abrupt stepped tubes

The tube configurations of interest are the 'abrupt contraction' (Figure 8.1a) and the 'abrupt enlargement' geometries (Figure 8.1b). While these two configurations appear identical, the velocity distributions depend upon the direction of flow (in fact these two arrangements were obtained by reversing the direction of flow). The experiments described here are performed with low Reynolds' numbers and therefore the flow is expected to be highly laminar. However, some eddies might be induced in the vicinity of the sharp corners. It is the velocity fields in the vicinity of the corners which are of particular interest in this experiment.

In describing fluid flow in circular cross-section tubes it is natural to use the cylindrical coordinates. The analysis can be further simplified by noting the azimuthal symmetry inherent in the geometry at low-Reynolds' number (the experiments described in Ch 6 have demonstrated this symmetry). By setting all azimuthal variations to zero the problem reduces to two dimensions. For an incompressible fluid with constant viscosity, the continuity equation and the Navier-Stokes equation expressed in cylindrical coordinates are therefore

(a) abrupt contraction

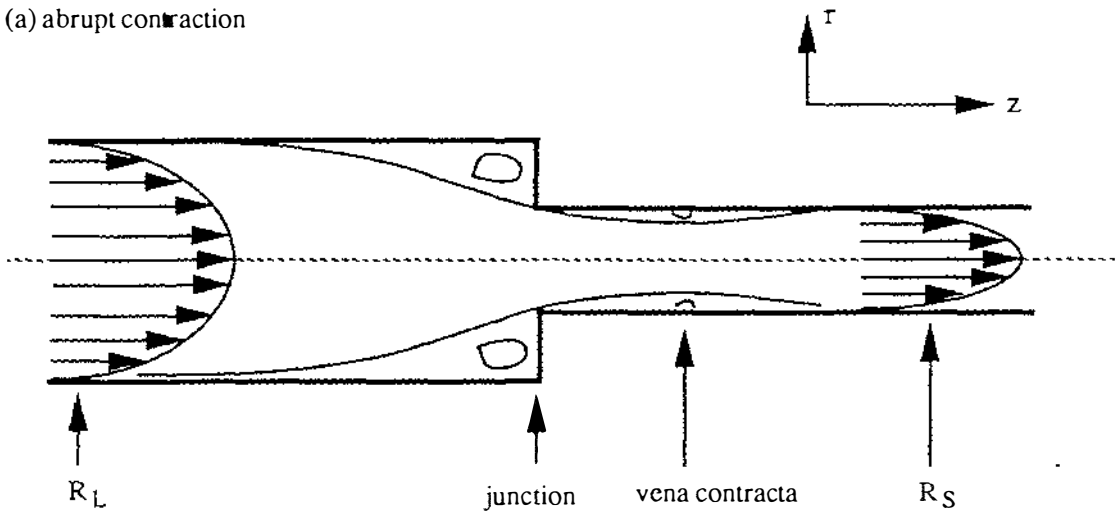

(b) abrupt enlargement

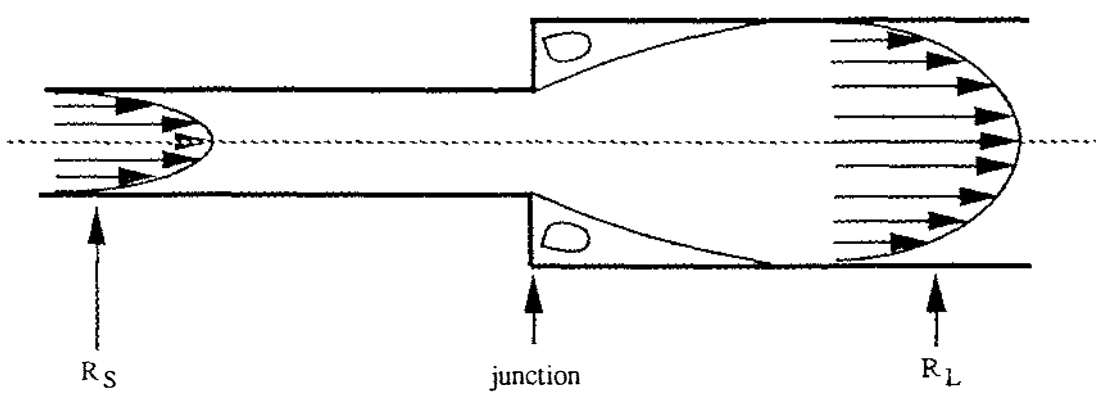

Figure 8.1 Abrupt stepped tubes

$$\frac{\partial v_r}{\partial r} + \frac{v_r}{r} + \frac{\partial v_z}{\partial z} = 0 \qquad [8.1]$$

$$\frac{\partial v_r}{\partial t} + v_r\frac{\partial v_r}{\partial r} + v_z\frac{\partial v_r}{\partial z} = -\frac{1}{\rho}\frac{\partial P}{\partial r} + \nu\{\frac{\partial}{\partial r}[\frac{1}{r\partial r}(rv_r)] + \frac{\partial^2 v_r}{\partial z^2}\} \qquad [8.2]$$

$$\frac{\partial v_z}{\partial t} + v_r\frac{\partial v_z}{\partial r} + v_z\frac{\partial v_z}{\partial z} = -\frac{1}{\rho}\frac{\partial P}{\partial z} + \nu[\frac{1}{r}\frac{\partial}{\partial r}(r\frac{\partial v_z}{\partial r}) + \frac{\partial^2 v_z}{\partial z^2}\} \qquad [8.3]$$

where ν and ρ are the kinetic viscosity and the density of the fluid respectively, their product, $\nu\rho$, is equal to the dynamic viscosity of the fluid, η. The radial and axial components of the velocity are v_r and v_z while P is the pressure.

For steady state flow far from the junction region, the radial velocity component and the rate of the velocity change longitudinally are zero. In this limit the above equations reduce to a single-dimensional relation, given by

$$\frac{\eta}{r}\frac{d}{dr}(r\frac{dv}{dr}) = \frac{dP}{dz} \qquad [8.4]$$

where dP/dz is the axial pressure gradient. This equation has been solved previously in Ch 3.5.6 and yields the classical Poiseuille velocity profile, namely,

$$v(r) = v_{max}(1 - \frac{r^2}{r_0^2}) \qquad [8.5]$$

where r_0 is the radius of the tube and v_{max} is the maximum velocity. For a tube in which the pressure head is provided by maintaining a height difference, Δh, between the inlet and outlet reservoirs, the maximum velocity is given by

$$v_{max} = (\rho g \Delta h) r_0^2/4\eta l \qquad [8.6]$$

in which the product $(\rho g \Delta h)$ represents the pressure decrement over the length l of the tube.

In order to describe flow in the junction region, however, it is necessary to solve Eq[8.1] to Eq[8.3] simultaneously. The total numbers of unknown variables can be reduced to two by utilizing the stream function, Ψ, and the vorticity function, Ω, defined respectively[166, 167] by

$$v_z = -\frac{1}{r}\frac{\partial \Psi}{\partial r} \qquad [8.7a]$$

$$v_r = \frac{1}{r}\frac{\partial \Psi}{\partial z} \qquad [8.7b]$$

and $$\Omega = \frac{\partial v_r}{\partial z} - \frac{\partial v_z}{\partial r} \qquad [8.8]$$

Thus Eq[8.1] to Eq[8.3] reduce to

$$\frac{\partial \Omega}{\partial t} + \frac{\partial (v_z \Omega)}{\partial z} + \frac{\partial (v_r \Omega)}{\partial r} = \nu\{\frac{\partial^2}{\partial r^2} + \frac{1}{r}\frac{\partial}{\partial r} - \frac{1}{r^2} + \frac{\partial^2}{\partial z^2}\}\Omega \qquad [8.9]$$

and $$[\frac{\partial^2}{\partial r^2} - \frac{1}{r}\frac{\partial}{\partial r} + \frac{\partial^2}{\partial z^2}]\Psi = \Omega r \qquad [8.10]$$

Eq[8.9] and Eq[8.10] describe the velocity distributions for the chosen geometry together with the appropriate boundary conditions and the conservation of the volume flow as

$$V_{in} R_{out}^2 = V_{in} R_{out}^2 \qquad [8.11]$$

where V_{in} and V_{out} are the maximum velocities for the large-diameter and small-diameter parts of the sample tube far from the junction region, and R_{in} and R_{out} are the radii for the large-diameter and small-diameter parts of the sample tube respectively.

8.2 An outline of the numerical simulation method

Because of the complex geometry in the junction region, analytical solutions are not possible and numerical methods must be used. There are several well established procedures for the numerical solution of the Navier-Stokes equation[168-170]. Numerical solutions of Eq[8.9] and Eq[8.10] were obtained using the finite difference approximation, by a visitor to the research group, Professor K.R. Jeffrey from the Physics Department of Guelph University, Canada. A brief description of the numerical method used is given here in a manner appropriate to our specific geometry and experimental conditions.

In accordance with the usual practice, it is useful to express the equations in non-dimensional form by introducing an appropriate length and velocity scale. Lengths are expressed in terms of the radius of the inlet tube, R_{in}, and velocities in terms of the maximum axial velocity at the inlet, V_{in}. The dimensionless forms of the stream function, vorticity and time are

$$\Phi = \frac{\Psi}{R_{in}^2 V_{in}} \qquad [8.12]$$

$$\omega = \frac{\Omega R_{in}}{V_{in}} \qquad [8.13]$$

and $$t = \frac{T V_{in}}{R_{in}} \qquad [8.14]$$

The non-dimensional forms of the Navier-Stokes equation (Eq[8.9] and Eq[8.10]) are therefore

$$\frac{\partial \omega}{\partial t} + \frac{\partial (v_z \omega)}{\partial z} + \frac{\partial (v_r \omega)}{\partial r} = \frac{1}{Re}\left[\frac{\partial^2}{\partial r^2} + \frac{1}{r}\frac{\partial}{\partial r} - \frac{1}{r^2} + \frac{\partial^2}{\partial z^2}\right]\omega \qquad [8.15]$$

and $$\left[\frac{\partial^2}{\partial r^2} - \frac{1}{r}\frac{\partial}{\partial r} + \frac{\partial^2}{\partial z^2}\right]\Phi = \omega r \qquad [8.16]$$

where Re is the Reynolds' number, given by

$$Re = \frac{V_{in} R_{in}}{\nu} \qquad [8.17]$$

Eq[8.15] and Eq[8.16] along with the non-dimensional forms of Eq[8.7] can be used to calculate the velocity distributions for the chosen geometries by applying appropriate boundary conditions and the conservation of the volume flow (Eq[8.11]). Considering our specific geometry and experimental conditions, a group of assumptions can be set as follows.

1. Fully developed Poiseuille flow is assumed far away from the junction region so that v_r, v_z, Φ and ω are all defined at the inlet and outlet.

2. The flow field along the axis must be investigated over lengths greater than twice the radius[171]. (At larger Reynolds' numbers the region investigated either side of the junction, especially down stream, must be larger).

3. The axial velocity v_z must be determined on the centre line where $r \rightarrow 0$.

4. On the centre line v_r and ω are zero while Φ is a constant.

5. On the walls of the tubes, v_r and v_z are equal to zero (no slip condition) and Φ is a constant which is set equal to zero. The vorticity must be calculated at each point along the wall.

6. On the walls Φ and $d\Phi/dr$ both equal zero and from these relationships first order or second order formulae[169] relating the vorticity on the boundary to the stream function in the near vicinity can be derived from Eq[8.16].

7. At the junction of the two tubes there are special problems at the corners. Moffatt[172] has shown that ω is singular at a sharp corner and there is a thorough discussion of this point in the book by Crochet et al.[173]; but again it is possible to express ω in terms of Φ.

The numerical simulation uses an iterative procedure to solve the coupled set of Eq[8.15] and Eq[8.16] for Φ and ω. The stream function is updated from the previous values of the vorticity using Eq[8.16] and then the vorticity is updated using Eq[8.15] and the velocities calculated from the previous values of the stream function. Relaxation techniques[174] are used to solve Eq[8.15] and Eq[8.16] because they are relatively simple to program and more importantly, because the overall solution is iterative, it is not necessary to carry the relaxation solutions of the individual equations to completion within each cycle.

In the simulations it was found convenient to use a square grid 0.05 mm on a side. The initial values of Φ and ω were normally set to values calculated for Poiseuille flow appropriate far from the junction region. For $Re < 100$, a stable solution can be obtained after 50-200 iterations. The details of the numerical simulation can be found in a paper submitted for publication[175].

8.3 Experimental arrangement

The stepped sample tube was made using two pieces of glass tube with internal diameters of 2.9 mm and 1.8 mm respectively, as shown in Figure 8.2. One end of the small-diameter tube was hand-polished to be smooth and flat, and then fitted tightly into the large-diameter tube to form an abrupt junction. This junction was also sealed using glue and teflon tape. The sample tube was placed vertically through the imaging probe. The vertical position of the abrupt junction inside the imaging probe can be adjusted by

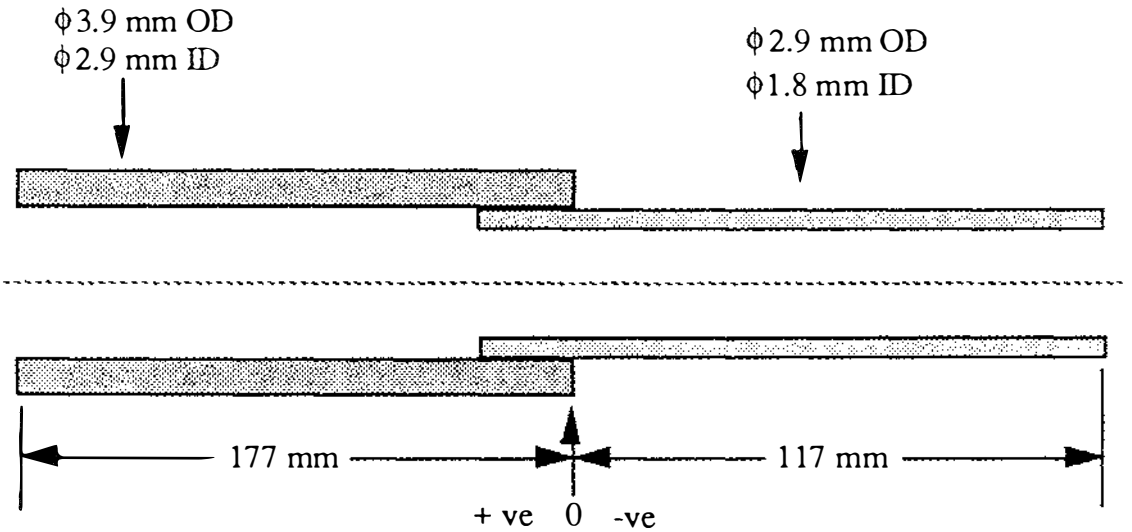

Figure 8.2 The stepped sample tube (not to scale)

rotating a screw. The junction has been labeled as the zero position and the large-diameter part as the positive direction and the small-diameter part as the negative direction.

Both ends of the sample tube were connected to two big glass beakers (5 l in volume and 21 cm in diameter) using plastic tubes. A 3.25 meter long small diameter plastic tube (0.9 mm i.d.) was also connected in series with the sample tube to deliberately increase the 'resistance' to the water sample. Constant water flow was established by adjusting the height difference of two water reservoirs to about 34 cm. Given the relatively small volume flow rate, the large-diameter beakers and the initially-high height difference, the percentage change of the water level during the hour-long experiment is insignificant. The water used was doped with 0.1% $CuSO_4$ to enhance T_1 relaxation.

A series of imaging experiments were performed at different positions of the sample tube at the ambient temperature of the probe which was around 30°C, each experiment taking about 3 hours to complete. Because the flow patterns explored in these experiments are essentially two dimensional (axial and radial), it was not necessary to collect data for the entire plane. It would have been sufficient to obtain data along a single direction perpendicular to the flow to obtain the axial and radial velocity profiles at a single position along the tube and such an experiment could be carried out in less than 10 minutes. However a mapping of the entire plane is helpful in the determination of the symmetry in the experimental flow pattern, an example will be given later in Ch 8.4.

Both the longitudinal and transverse flows were measured in separate experiments for the abrupt contraction and abrupt enlargement configurations. These two configurations were achieved by changing the direction of flow. The position of the water tanks relative to each other were changed to cause the flow to occur in the opposite direction while leave the sample tube untouched. Upon the Fourier transformation of the data, the direction sensitive velocity results are inverted to give a positive display. The images were constructed with an array size of 64×64 at 6° steps from 0° to 360°.

For the measurement of longitudinal flow, the q-gradient direction is the same as the slice selection gradient direction, so that a pulse sequence similar with that shown in Figure 6.1 was employed. In order to achieve about 6 mm/s maximum flow rate at the large-diameter part of the sample tube, the maximum flow rate at the small-diameter part of the sample tube is much higher. To minimize the velocity artifact of the slice selection gradient, the pulse sequence was optimized so that the phase shift induced by the slice selection gradient has reduced by a factor of four from the previous pulse sequence (reduced Δ_S from 4 ms to 2 ms, δ_S from 2 ms to 1 ms while kept G_S as 14 G/cm which corresponds to a slice thickness of 0.33 mm). The PGSE pulse separation, Δ, was 5 ms, the PGSE duration, δ, was 2.5 ms for the large-diameter tube and 1.0 to 1.768 ms for the small-diameter tube, the maximum q gradient was 0.936 T/m. The detection bandwidth was 10 kHz and the signal was co-added 24 times for the large-diameter part of the sample tube and 36 times for the small-diameter part.

For the measurement of transverse flow, however, the experiment becomes more complicated. Here the q-gradient direction is along one of the two mapping gradients. G_x was chosen in this experiment to apply both spatial mapping and the flow contrast. Due to the complex nature of the signal in dynamic imaging, four quadrant data acquisition is required which means that both mapping gradients have to be switched in directions during the imaging experiment. However, a switch of direction for the q gradient for different quadrants as the mapping gradient varies through is forbidden. It is obvious that separate controls are required for the transverse q-gradient pulses. One good solution would be to use an extra power supply which is gated separately to apply the q-gradient pulses. But this is not possible because of the limited numbers of TTL output gates available in our pulse programmer.

An alternative approach based on software modification is used in our experiments with a pulse sequence shown in Figure 8.3. During the imaging experiment, the signs of the two mapping gradients are stored in a table together with

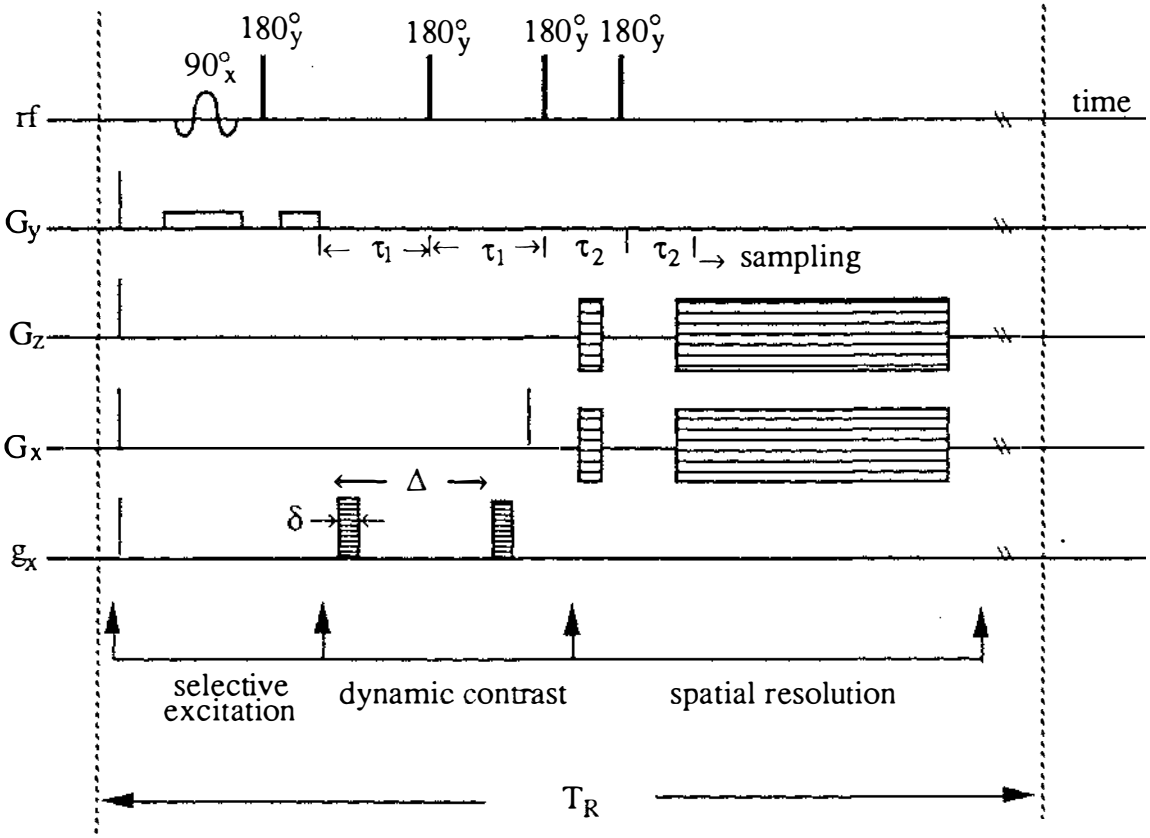

Figure 8.3 A pulse sequence for measuring transverse flow (x-direction)

the sequences of the gradient magnitudes. The modification to the TI-980A software includes the control of the ON/OFF state of the extra 180° rf pulse (the third $180°|_y$ pulse) in the pulse sequence. This pulse is switched in or out depending on the signs of the mapping gradients, the extra 180° pulse being ON when the mapping gradient is switched to the negative direction. This modification has the effect of maintaining a constant sign of motion-induced phase shift irrespective of the sign of the applied gradient. This pulse sequence has proved to work well. For the transverse flow experiments, the PGSE pulse separation was 13 ms, the PGSE duration was 9 ms and the maximum q gradient was 0.13 T/m. The detection band-width was 20 kHz and the slice thickness was 0.66 mm in order to gain better signal-to-noise ratio. In order to minimize the error due to the manual adjustment of the gradients, the maximum magnitudes of the mapping gradients remained unaltered during both the longitudinal and transverse imaging experiments .

8.4 'Air bubble' imaging

The initial experiments imaging the abrupt junction were carried out using the same water reservoirs as used in water capillary flow experiments. The two water reservoirs are about 600 ml in volume and 85 mm in diameter. While the velocity map in the regions far from the abrupt junction exhibits the usual Poiseuille distribution, the velocity and diffusion maps around the abrupt junction region turned out to be quite puzzling, a few velocity and diffusion images being shown in Figure 8.4.

The asymmetrical images are difficult to explain, one possibility being that the hand-polished junction was not symmetrical. This proved not the case because asymmetrical velocity and diffusion maps at the same position couldn't be repeated in separate experiments. After some investigation, it was found that the strange images coincided with the formation of tiny air bubbles under the influence of changing water pressure head. For a velocity of about 6 mm/s at the large-diameter tube, the total water level change during one imaging experiment was about 100 mm! This dramatic pressure drop (about 25%) together with the small flow rate caused some tiny air bubbles to form around the abrupt junction region from the dissolved air in water sample. If there is an air bubble in the selected thin slice, the image is distorted and asymmetrical.

It is interesting to note that these puzzling images have proven that the construction of velocity and diffusion images for an entire plane provides a useful tool to check the symmetry of the flow.

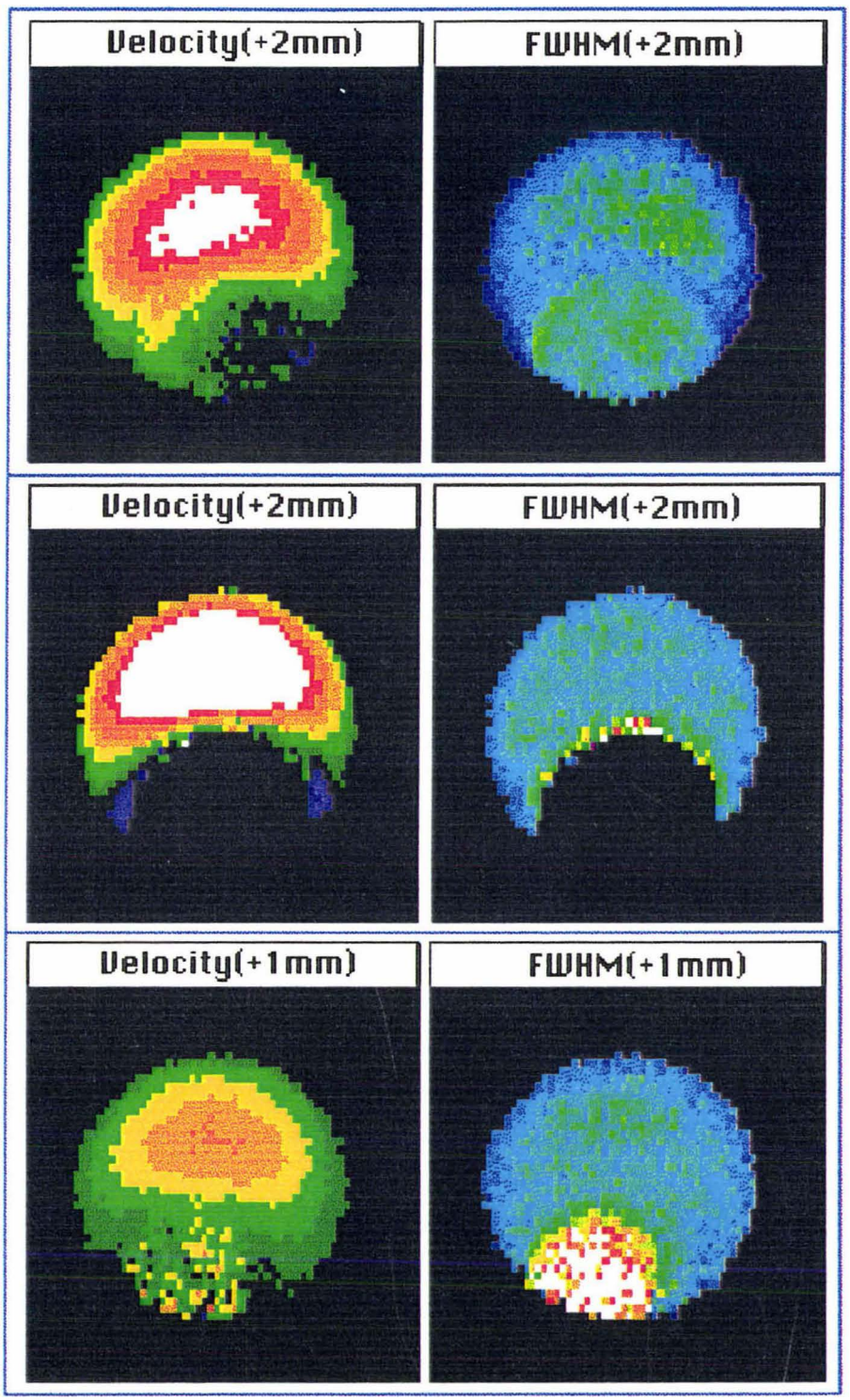

Figure 8.4 'Air bubble' imaging

8.5 Results of the flow through an abrupt contraction

At the positions of +9, +5, +4, +3 mm with the q gradient along the axial direction, the complex data images exhibit the same feature shown previously in Figure 6.4, with the centrally-symmetric alternating and progressively-narrowing phase rings. While velocity maps are of principal interest in this study, the diffusion maps also contain useful information and as it will be seen, are especially sensitive to transverse flow. Maps of the axial velocity and the diffusion coefficient from the four above positions are almost identical, one set of images being shown in Figure 8.5. The maximum velocity given by the velocity map is about 6.3 mm/s. The map exhibits a cylindrically-symmetric distribution which is consistent with the parabolic Poiseuille flow, while the averaged diffusion coefficient is about 2.5×10^{-9} m^2s^{-1}. The Reynolds' number for the flow is less than 15 and therefore the motion is expected to be highly laminar. This is proved by a separate imaging experiment at the +9 mm position with the q gradient along the radial direction, the velocity map is indeed zero.

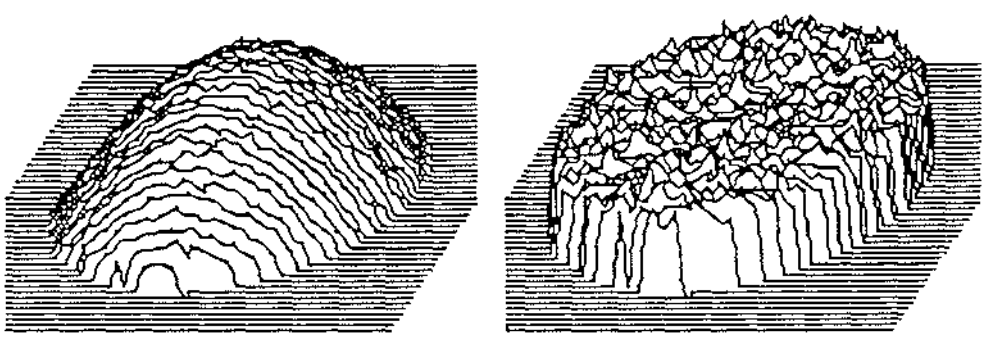

Velocity map FWHM map

Figure 8.5 Axial V and FWHM maps at +9mm above the abrupt contraction

The maps of the axial velocity and self-diffusion coefficient at -18 mm position are shown in Figure 8.6. The maximum velocity given by this velocity map is 17.0 mm/s which corresponds to a Reynold's number around 20. The velocity image exhibits an excellent Poiseuille distribution at this downstream position. The diffusion map shows a centrally-symmetric enhancement towards the wall of the small-diameter tube, which is caused by the high velocity shear at this region (refer to Ch 3.5).

Using the results in these separate imaging experiments and the knowledge of the sample tube geometry, these results can be tested for the conservation of the mass flow, Eq[8.11], and agree to within 4%. This error is most likely caused by the

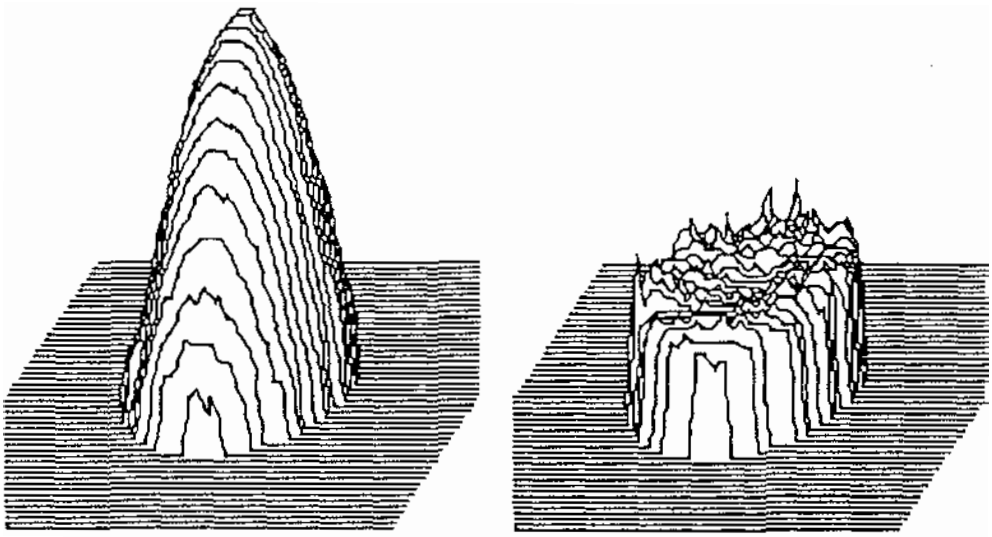

Velocity map FWHM map

Figure 8.6 Axial V and FWHM maps at -18mm below the abrupt contraction

diameter uncertainty in the small-diameter tube which is not a precision glass tube. It is in any case within the experimental uncertainty of the velocity measurement. The volume flow during one imaging experiment can be calculated as less than 250 ml, which causes a maximum of 4% water level change in the large-diameter reservoirs during one experiment. As discussed before in Ch 6.2, the actual impact of level change during the experiment would be less than the maximum 4%.

A series of imaging experiments were carried out at different positions of the sample tube between these extreme positions along both the axial and radial directions. Several interesting features of the flow are indeed present in the velocity and diffusion maps around the junction region. Figure 8.7 shows the velocity and diffusion maps near the junction region for the axial flow imaging experiment. The velocity image is no longer parabolic, a slight negative velocity ring around the high central velocities providing (inconclusive) evidence for a small eddy. The diffusion map can be separated into two maps with different scales using the knowledge of the diameter of the small tube. A cross-sectional profile through the diffusion map is shown in Figure 8.8. The diffusion for the outer region is quite uniform with an average value of 2.6×10^{-9} m^2s^{-1}. This is exactly equal to that of (stationary) free water suggesting that there is little movement at the corner. But the diffusion for the central region is enormous! This enhanced diffusion is caused by the additional phase incoherence due to the presences of both the high velocity shear and the local transverse flows.

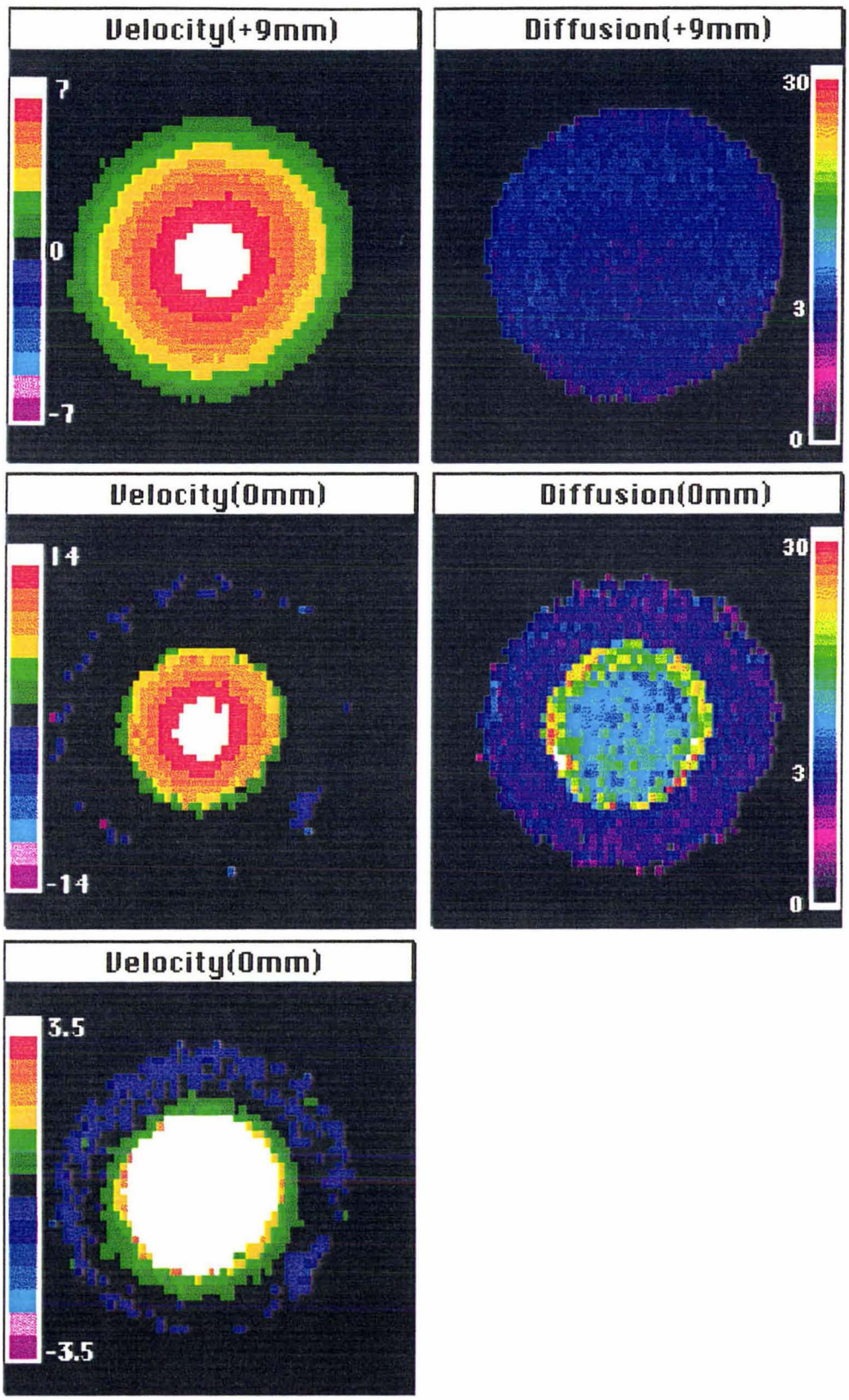

Figure 8.7 Axial velocity and diffusion maps at the abrupt contraction (Velocity: mm/s; Diffusion: 10^{-9} m^2/s)

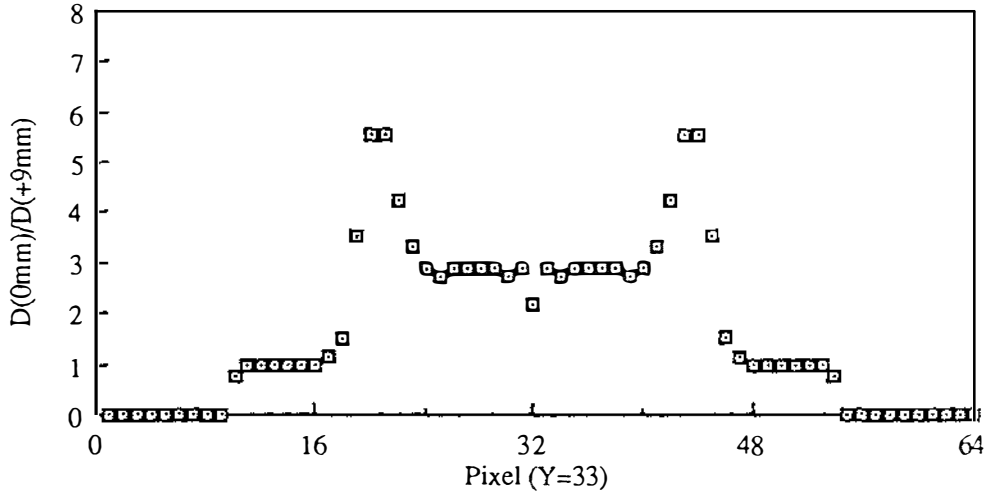

Figure 8.8 Enhanced diffusion coefficient at the abrupt junction (axial, azimuthal-averaged)

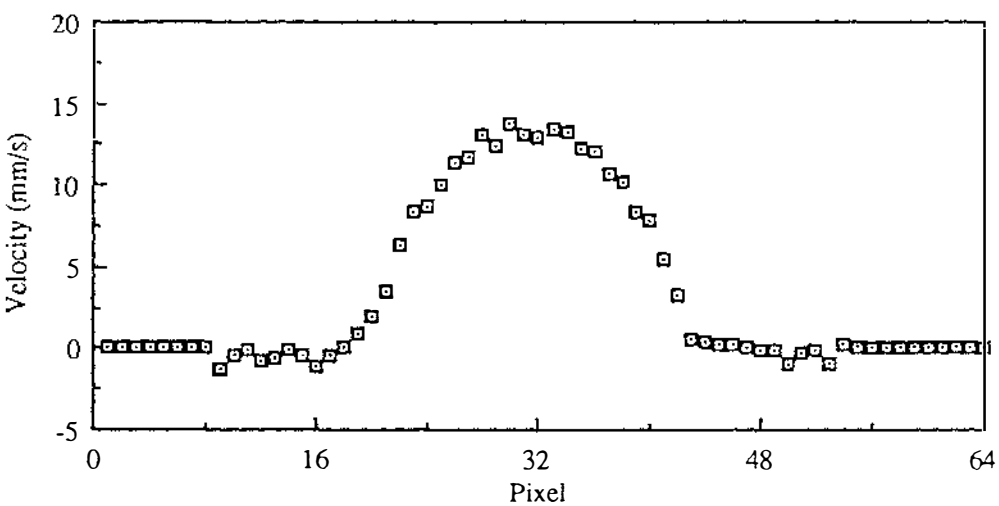

Figure 8.9 Axial velocity profile at the abrupt junction using PGSE gradient upto 1.22T/m

The velocity sensitivity was chosen so that the sampling of the maximum velocity satisfied the Nyquist theorem. Due to the large magnitude difference in the central stream velocity and the small eddies, the eddies with small digits will contain bigger error due to the presence of noise and the digitization. A more sensitive sequence was used during one experiment in which the maximum PGSE gradient was increased to 1.22 T/m so as to specially sense the small eddies. A cross sectional profile through the centre of the corresponding velocity map is shown in Figure 8.9, which gives a closer look at the eddies.

The multiple q-slice data images acquired at the 0 mm position are shown in Figure 8.10. It is interesting to note that the centrally-symmetric alternating and progressively-developing phase rings for the axial flow have changed, in the radial

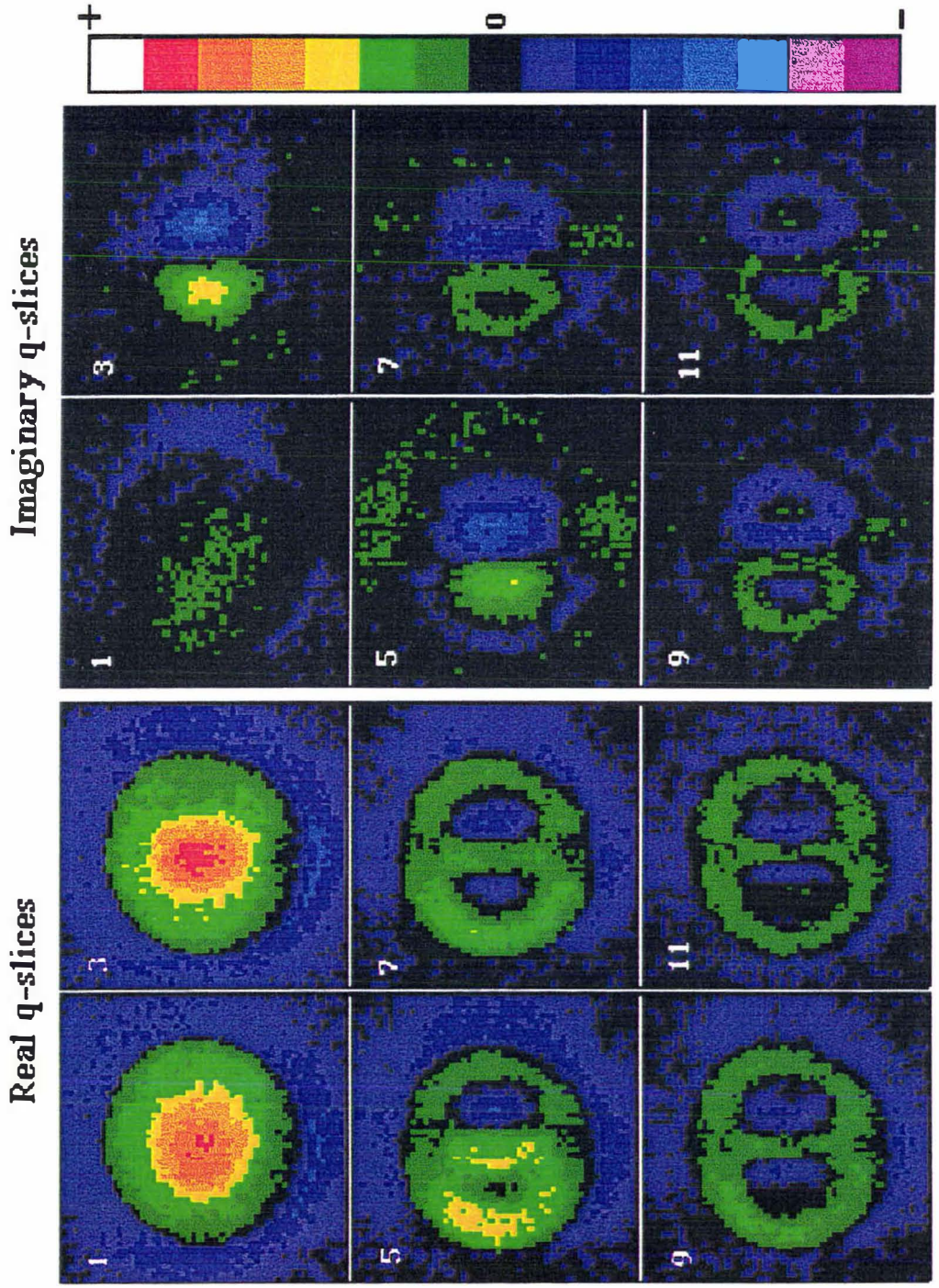

Figure 8.10 q-slices at the abrupt junction for radial flow

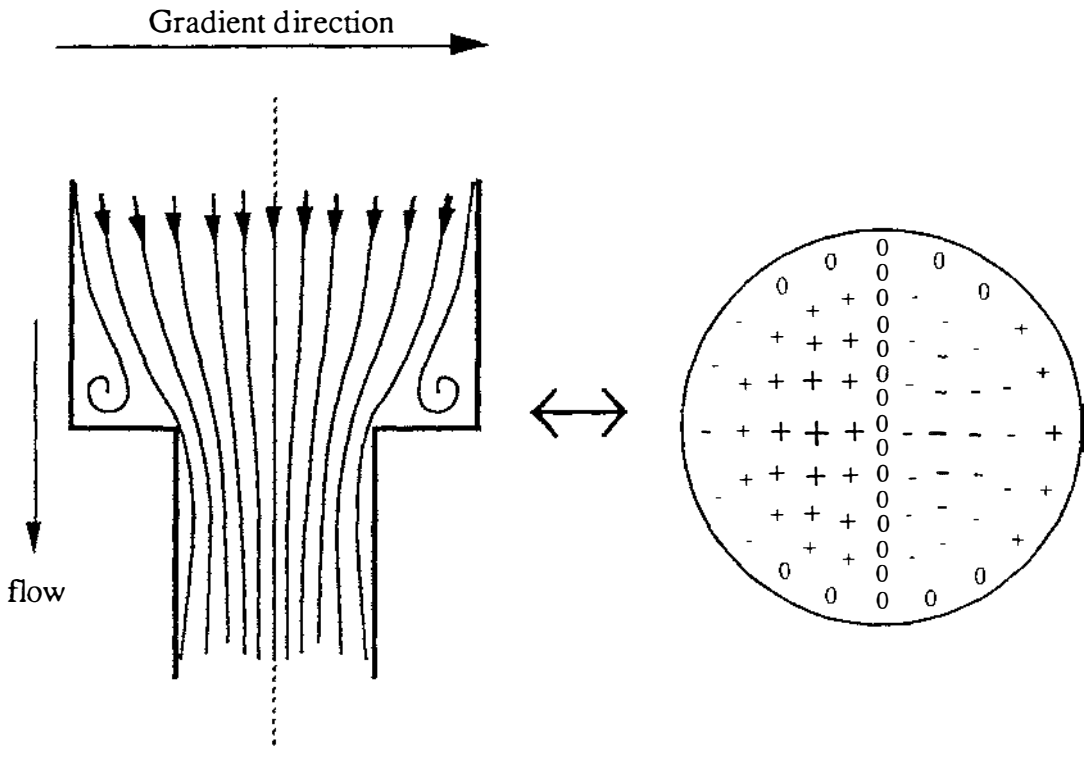

Figure 8.11 Encoding radial velocity using a 1-D linear gradient

flow, to a pair of phase rings with similar feature but a 90° phase difference in between. This is due to the manner we encode the velocity using a one dimensional linear gradient, shown schematically in Figure 8.11.

Maps of velocity and self-diffusion using the above data set are shown in Figure 8.12. In the velocity map, radial velocities are indeed present and are consistent with the prediction shown in Figure 8.11. Furthermore, the formation of an eddy at this junction region is obvious in the velocity map as represented by the small positive ring at the most outer position. In the diffusion map, the pattern of the non-uniformity in the image is consistent with the presence of the radial velocity and the manner in which we encode the velocity and diffusion.

Figure 8.13 shows the cross sectional profiles through the centres of the velocity maps at different positions, while Figure 8.14 compares the experimental profiles with the numerical solutions from the Navier-Stokes equation averaged over the slice thickness. The agreement is excellent.

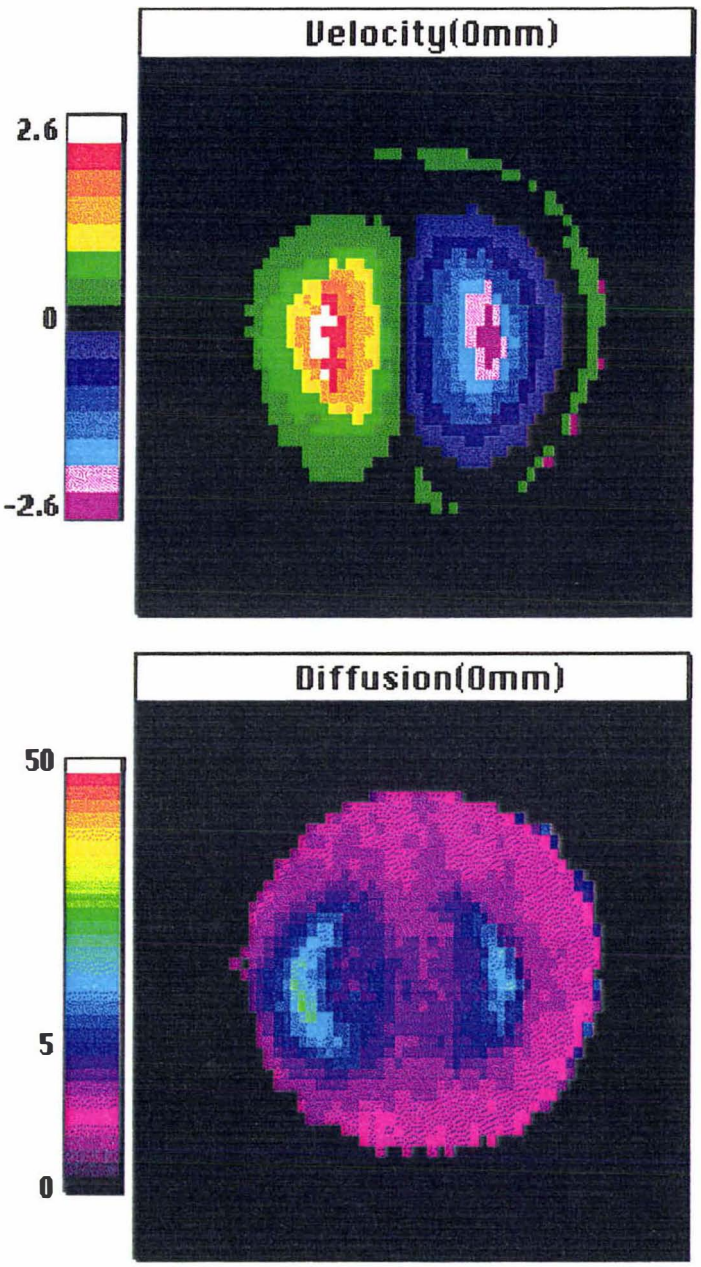

Figure 8.12 Radial velocity and self-diffusion maps at the abrupt contraction (Velocity: mm/s; Diffusion: 10^{-9} m^2/s)

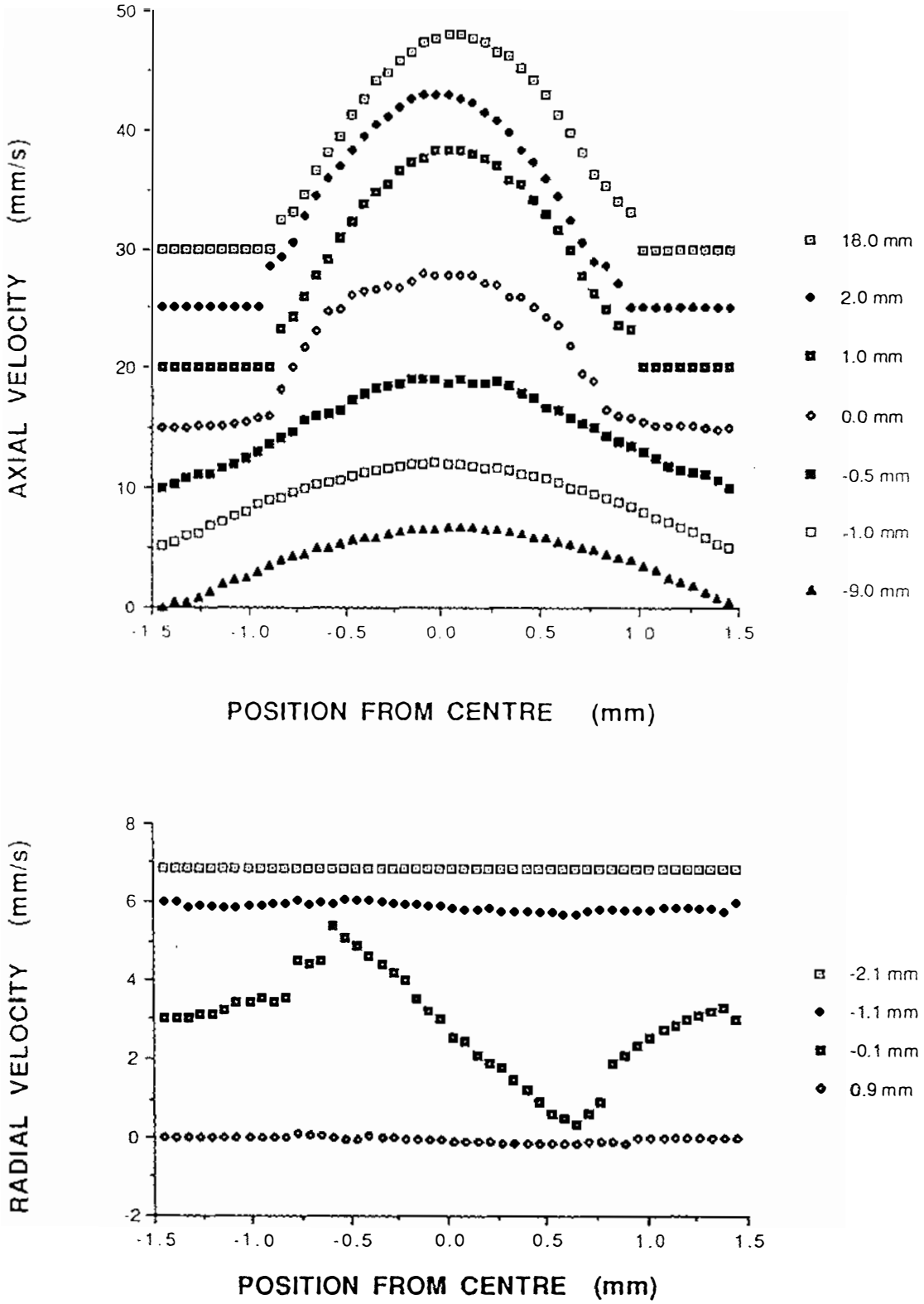

Figure 8.13 The axial and radial velocities for flow through an abrupt contraction. (The values are an average of the velocity within a slice perpendicular to the axis of the tube and the legend at at side of each graph indicates the centre of each slice.)

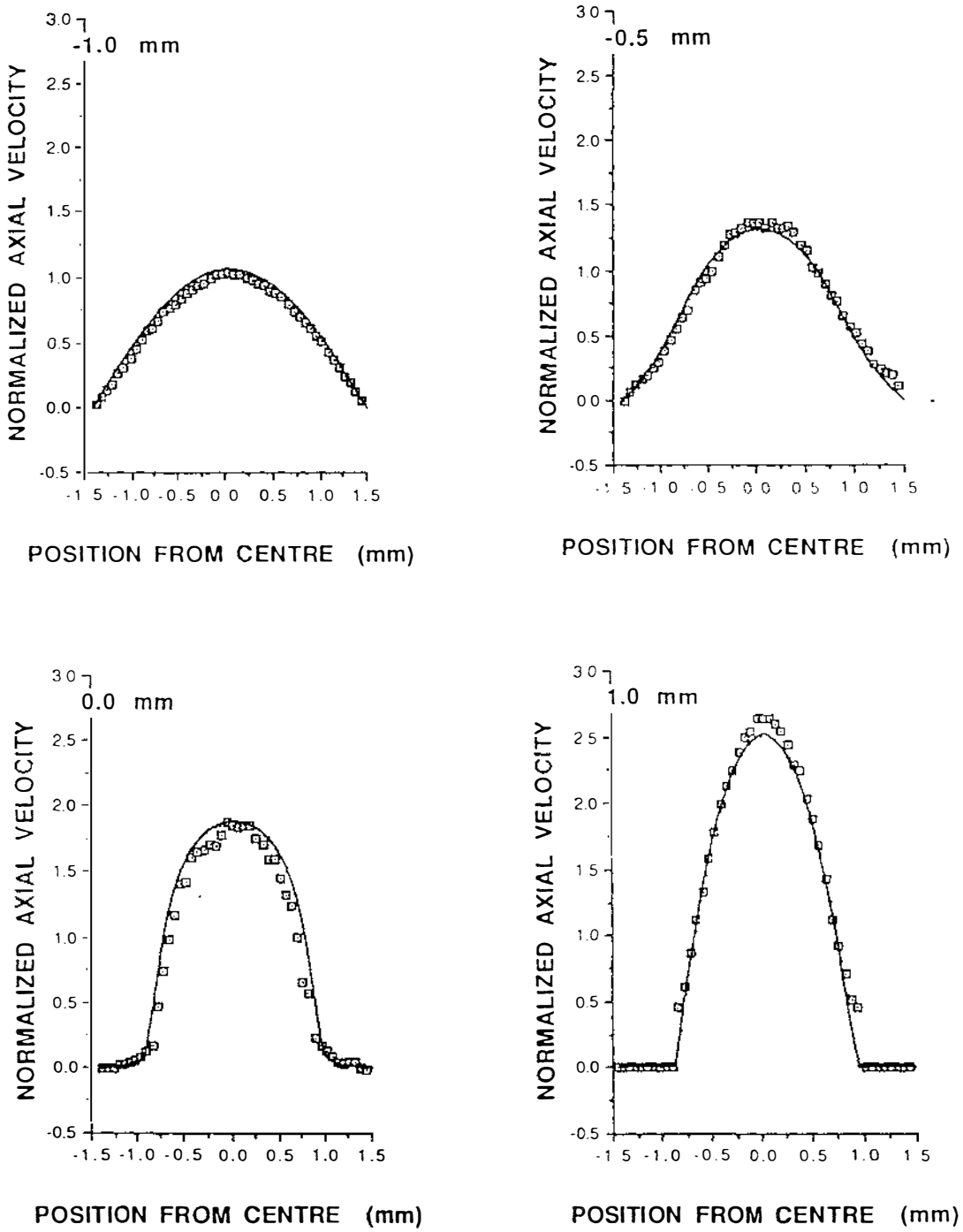

Figure 8.14a A comparison of the experimental and theoretical axial velocities for flow through an abrupt contraction. Data for four positions along the stepped tube are shown.

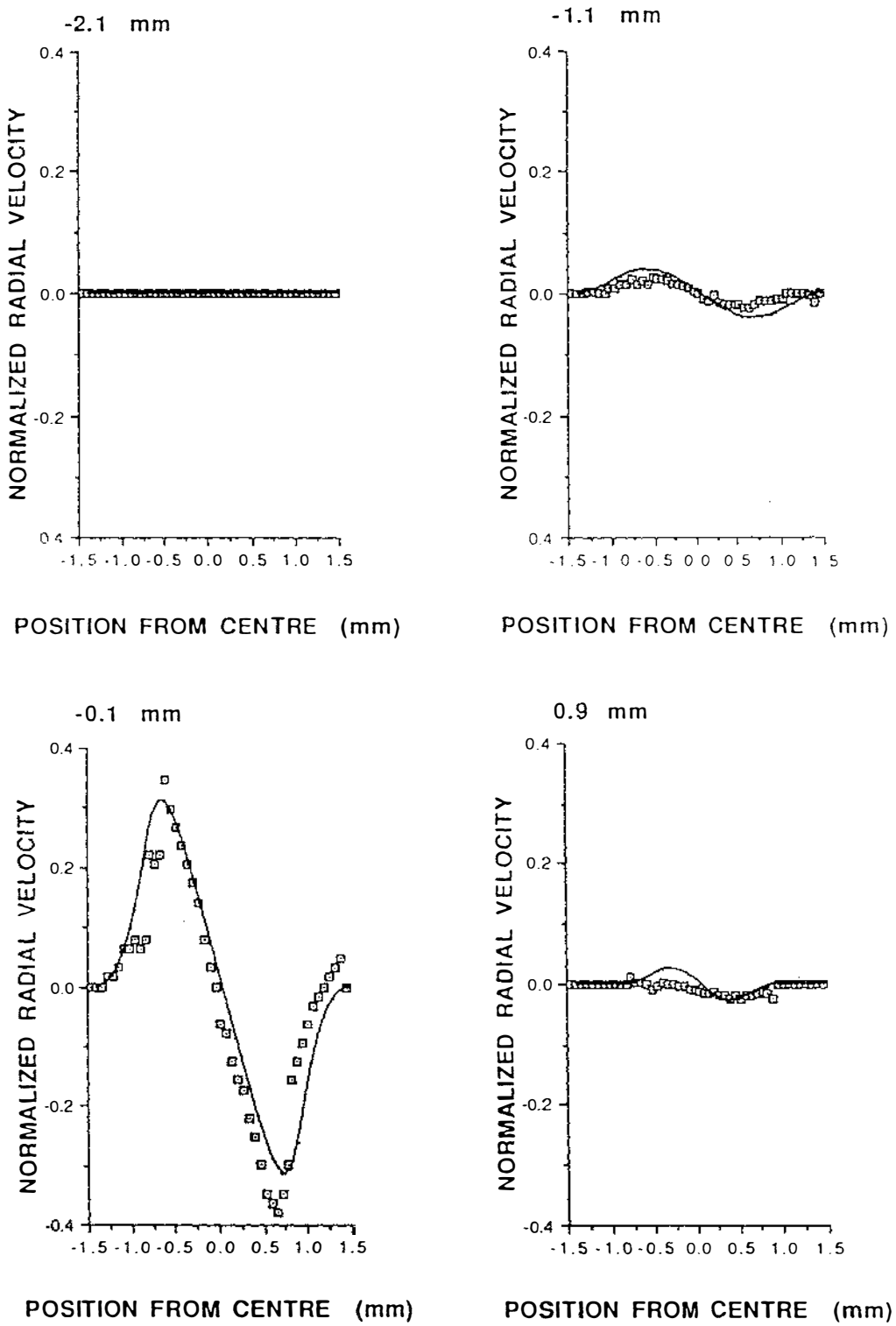

Figure 8.14b A comparison of the experimental and theoretical radial velocities for flow through an abrupt contraction. Data for four positions along the stepped tube are shown.

It is worth noting that for small velocities, the velocity resolution can be improved by using a bigger digital array during the Fourier analysis. Figure 8.15 compares the results using the identical data set but at two different digital array sizes, 256 and 1024. The improvement is obvious.

There are two points worth to mention here. First, the theoretical solution doesn't predict the formation of an eddy for this abrupt configuration under our experimental parameters (mainly due to the small Reynolds' number). Second, there is no clear evidence of the 'vena contracta' (minimum effective flow area)[176, 177], shown schematically in Figure 8.1, although some difficulties at -6 mm downstream position were experienced where the images were a bit noisy.

Experiments using the velocity-compensated Dynamic NMR Microscopy were also carried out at the junction region. Figure 8.16 shows the cross sectional profiles through the diffusion map at the junction position together with that using the single PGSE pulse sequence. The diffusion profile is made more uniform by using the double PGSE pulse.

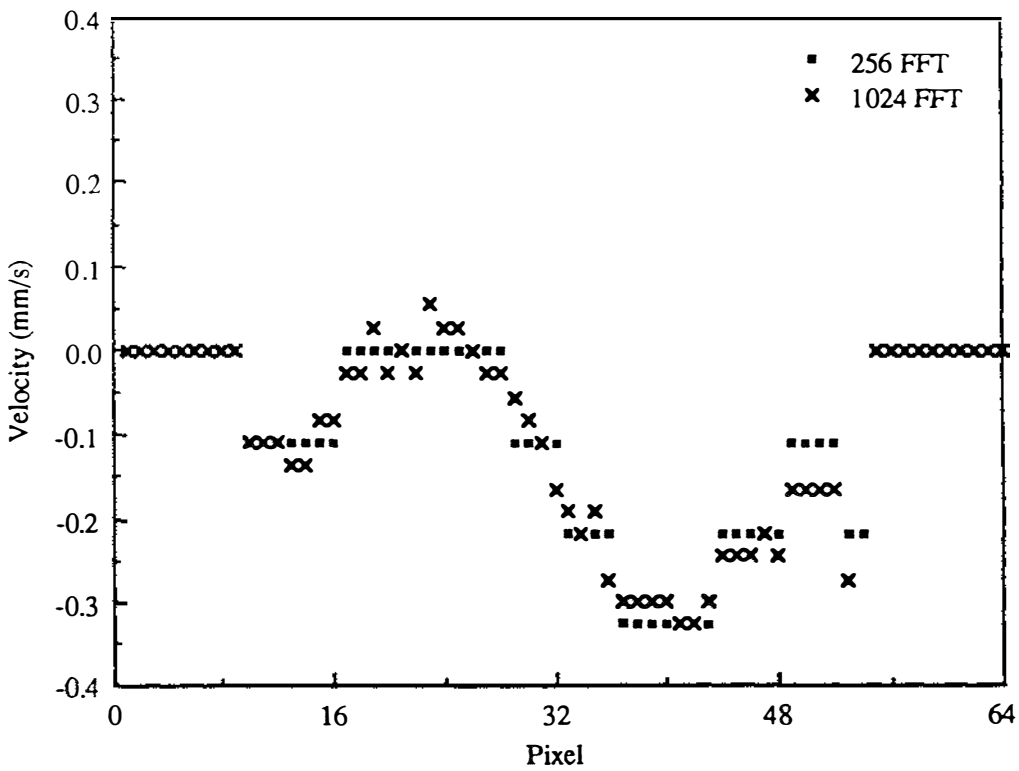

Figure 8.15 Comparison of 256 FFT and 1024 FFT in flow analysis (radial velocity at +1mm)

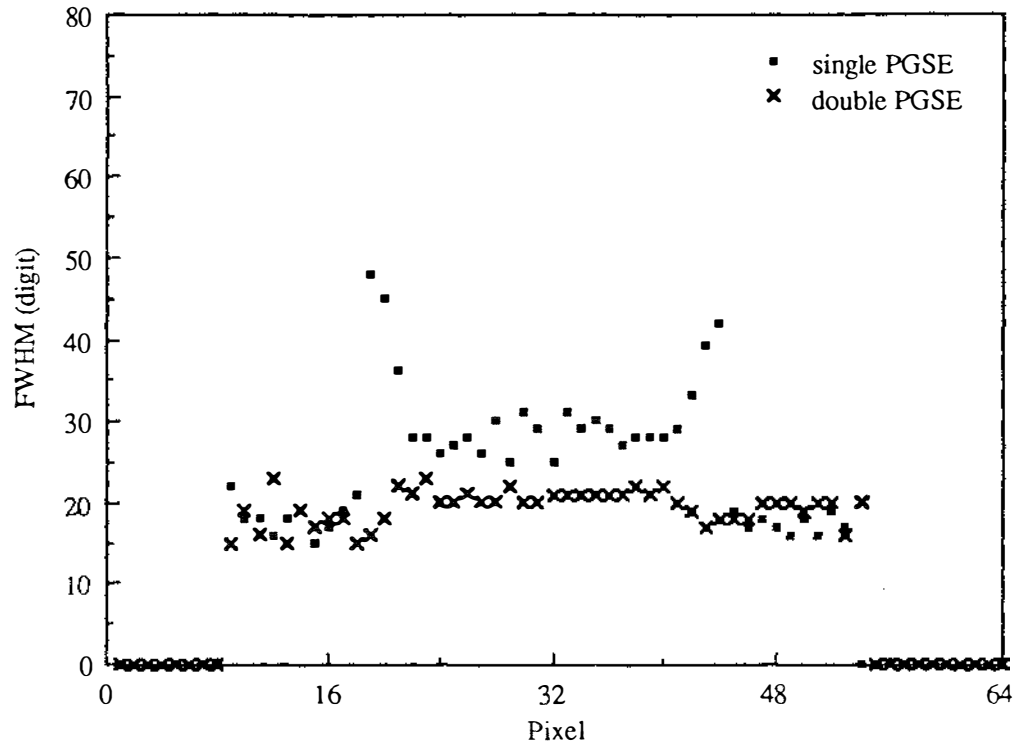

Figure 8.16 Radial FWHM profiles at the abrupt junction using both the single PGSE and double PGSE

8.6 Results of the flow through an abrupt enlargement

Imaging experiments were also carried out around an enlargement junction region along both the axial and radial directions. The velocity and diffusion maps at 0 mm position are shown in Figure 8.17. These images exhibit the same features as the contraction configuration. The evidence of the formation of an eddy is more clear in this configuration.

The cross sectional profiles through the velocity and diffusion maps are shown in Figure 8.18, while Figure 8.19 compares the experimental profiles with the numerical solutions from the Navier-Stokes equation. A small region of negative velocity at the 0 mm position shows the eddy and it does agree with the numerical simulation result. The experimental and theoretical plots are in excellent agreement specially in the radial velocity profiles (bearing in mind the fact that the radial velocities are a factor of 10 smaller than the axial velocities).

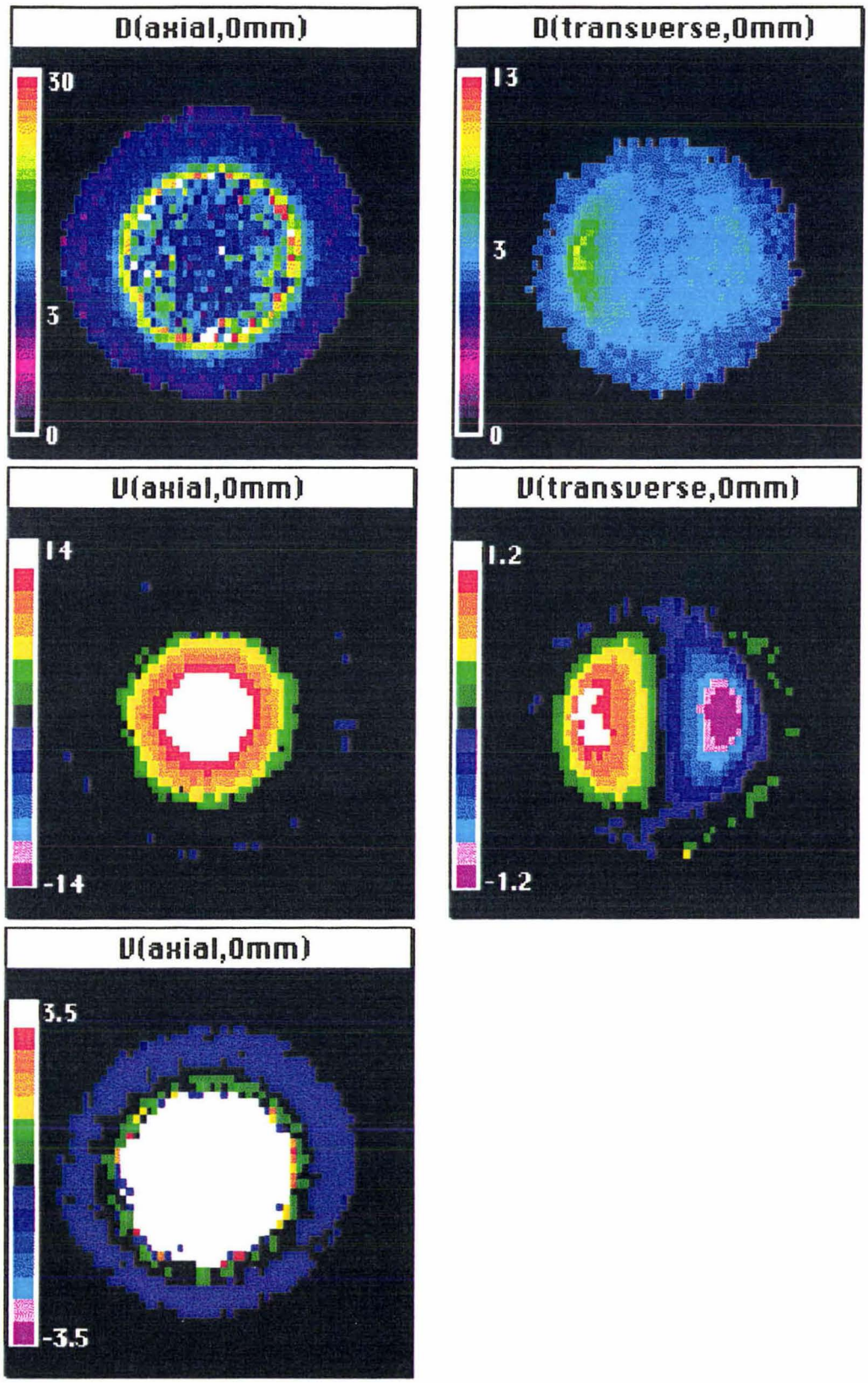

Figure 8.17 Velocity and diffusion maps at the abrupt enlargement (axial and radial)
(Velocity: mm/s; Diffusion: 10^{-9} m^2/s)

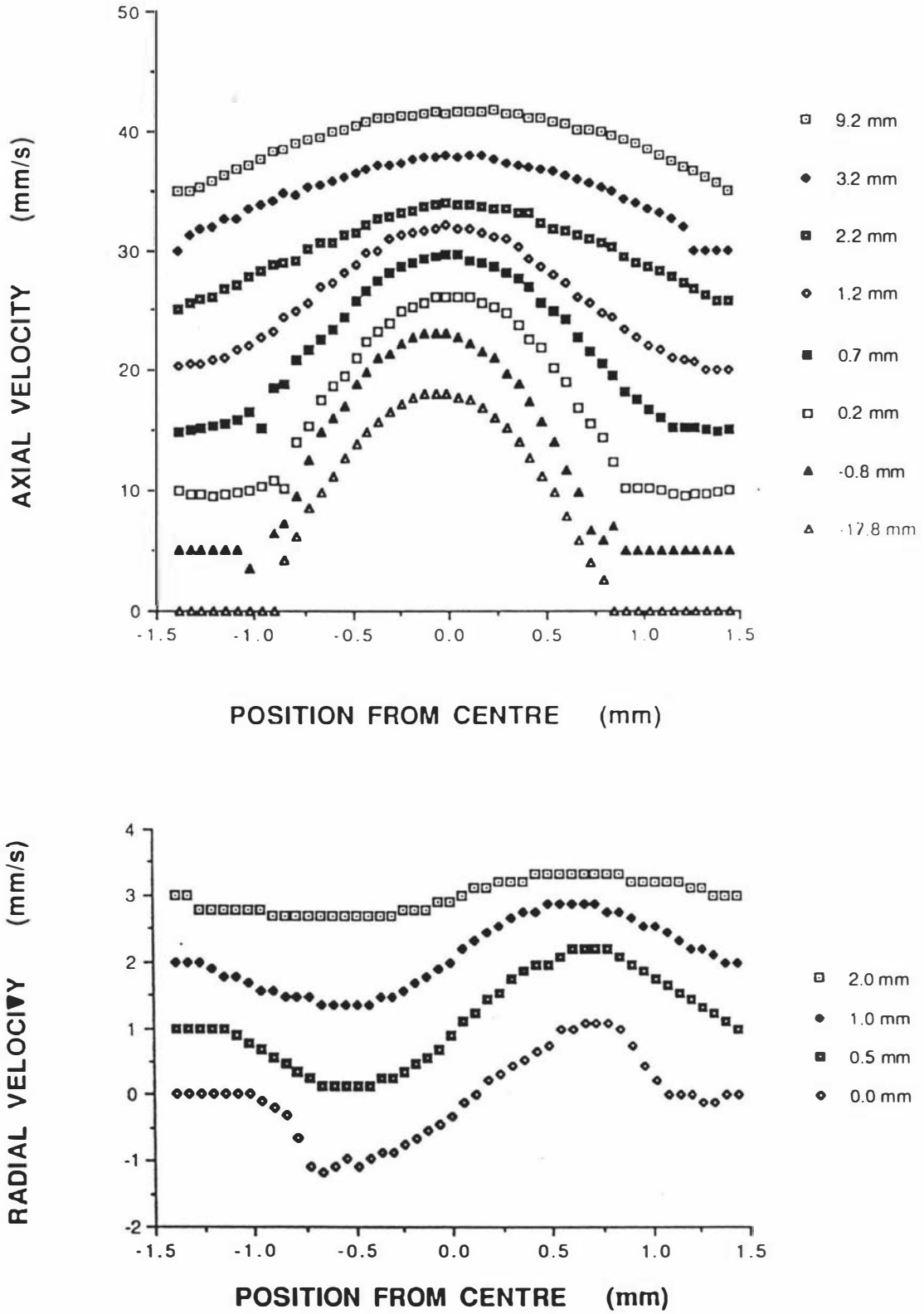

Figure 8.18 The axial and radial velocities for flow through an abrupt enlargement. (The values are an average of the velocity within a slice perpendicular to the axis of the tube and the legend at side of each graph indicates the centre of each slice.)

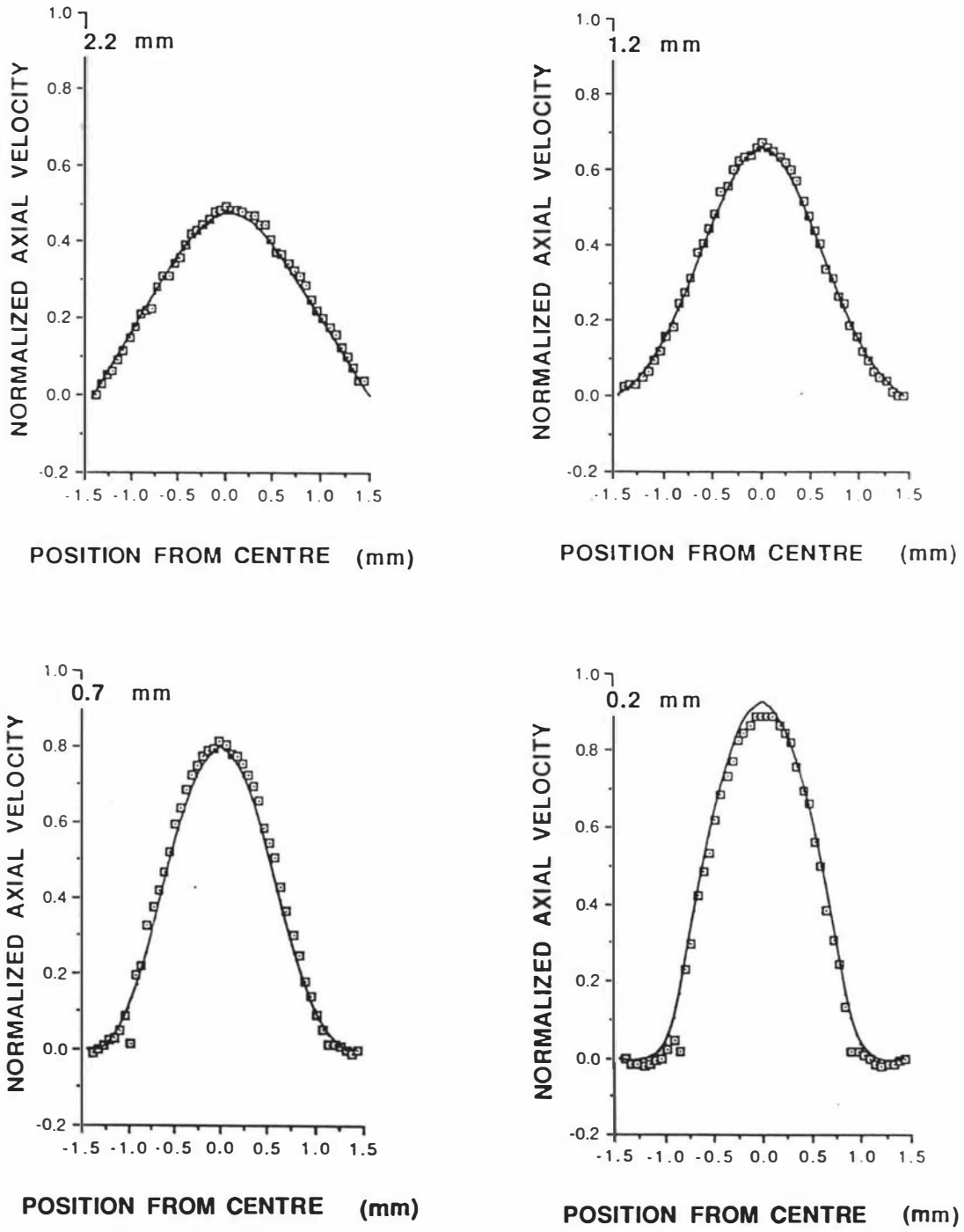

Figure 8.19a A comparison of the experimental and theoretical axial velocities for flow through an enlargement. Data for four positions along the stepped tube are shown.

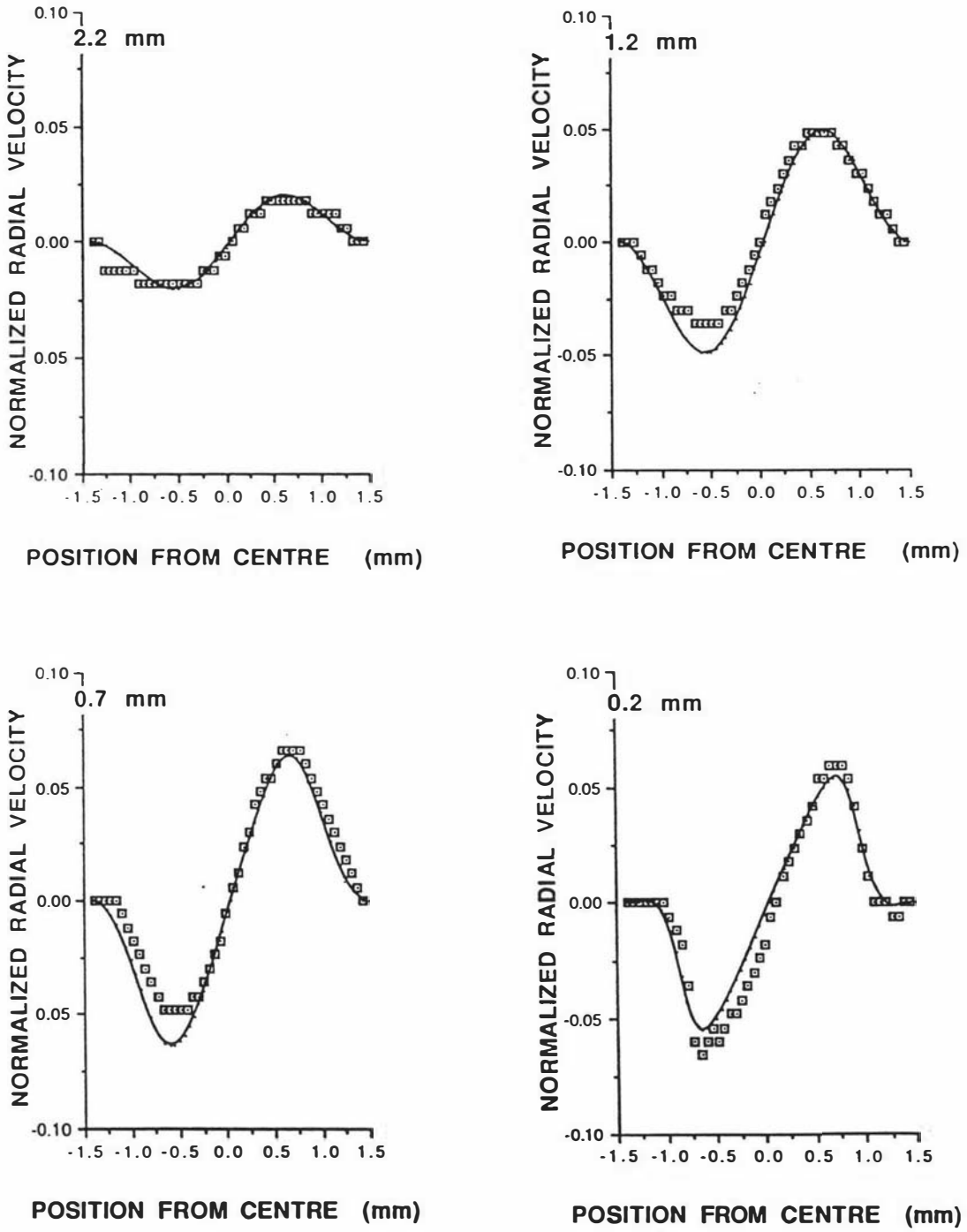

Figure 8.19b A comparison of the experimental and theoretical radial velocities for flow through an enlargement. Data for four positions along the stepped tube are shown.

8.7 Discussion and conclusion

The experiments described in this chapter have demonstrated that Dynamic NMR Microscopy can be used to obtain accurate measurement of the velocity vector field for non-trivial flow patterns. In particular, experiments were carried out successfully to measure the axial and radial components of the velocity in the junction region of an abrupt contraction and expansion in a tube. The induced eddies around the abrupt junction were observed for both configurations. To our knowledge, this is the first quantitative measurement at high resolution for such sample configurations. Numerical simulations were also performed to predict the theoretical velocity distributions. The experimental results are in excellent agreement with the theoretical prediction.

The digital image array used in this work was constrained to 64×64 by the computer memory size available at the time of measurement. A larger digital array size would improve the spatial resolution of the image. Further improvement can also be made by changing the q-contrast gradient to be two dimensional so that the axial and radial flows can be imaged at the same time, which would lead to better correlation in position between the axial and radial experiments.

It is expected that Dynamic NMR Microscopy will have many applications in both rheology studies and hydrodynamic engineering. For example, it is now recognized that the extensional viscosity is important in any discussion of non-Newtonian fluid behaviour[178, 179]. Measurements of the velocity for non-viscometric flows such as those occurring at abrupt contractions and expansions are excellent tests for models of extensional flow.

Chapter 9 Polymer Physics: Shear Thinning in a Non-Newtonian Fluid

In the previous studies of Newtonian fluid, namely water, the Navier-Stokes equations contained all of the basic physics and the experimental determinations of the velocity profile allow one to check the technique employed in the measurement by comparison with numerical methods of solutions of these equations for simple or complex geometries. In rheological studies of non-Newtonian fluids, however, the constitutive equations describing the relationship between the stress and strain must be validated by comparing theory with experiment. Measurements of velocity and self-diffusion profiles for even relatively simple geometries can provide excellent tests of any proposed constitutive equation.

The experiments described in this chapter[180] have used both Dynamic NMR Microscopy and the conventional PGSE diffusion measurement to study a non-Newtonian fluid, poly(ethylene oxide) (PEO). Velocity and self-diffusion profiles for water solutions of WSR301 PEO in laminar flow through a capillary were measured as a function of concentration and pressure gradient. Equilibrium self-diffusion coefficients were measured as a function of concentration for WSR301 PEO and as a function of molar mass for monodisperse PEO standards in D_2O. To investigate the relationship between the shear thinning of polymer macro-molecules and polymer Brownian motion, self-diffusions for WSR301 PEO in D_2O in the presence of the flow field were also measured. The results are interpreted using a simple adaptation of the entanglement/blob model.

9.1 An introduction to polymer and polymer flow

Polymers are long-chained (macro)-molecules which comprise a repetitive sequence of basic chemical subunits known as monomers. For example, poly(ethylene oxide) is a polymer whose monomeric unit is ethylene oxide. An essential parameter describing polymer molecules is the size of a polymer chain, because many properties of a polymer show a strong dependence upon its size. This size is given by the molar mass (M) with units of g mol^{-1}. A finite sized polymer sample consists of a large number of polymer molecules and each may have a different number of monomers hence different molecular weight. Therefore the quality of a polymer sample is

characterized by its polydispersity index, given by $\overline{M_w} / \overline{M_n}$ where $\overline{M_w}$ is the weight-averaged molar mass and $\overline{M_n}$ is the number-averaged molar mass. If this ratio is equal to one, the polymer sample is monodisperse while the amount by which it exceeds unity indicates the degree of polydispersity.

This thesis is not concerned with the stationary chain structure of polymer molecules nor the local motions or fluctuations of polymer molecules, but rather, the long range motions of *long, flexible, linear* polymer chains and their response to external influences. In polymer melts or polymer solutions in good solvents (a 'good' solvent is one in which the polymer chains repel each other), a polymer sample can be visualized as 'cooked spaghetti', where each flexible piece, called a random coil, is entangled with its neighbours (Figure 9.1). In the polymer literature the motions of random coils are often described by the tube model of Doi and Edwards[181-184] which is based on the reptation theory of de Gennes[185]. A detailed discussion[186-188] of the tube model and the reptation theory is beyond the scope of this thesis and only a very brief description is given here.

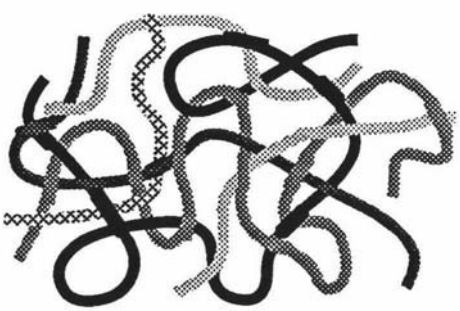

Figure 9.1

Entangled polymer chains

In Doi-Edwards theory, each random coil chain in the melt or semi-dilute solution is confined to a virtual 'tube'[189] formed by the envelope of all the obstacles which directly surround it (Figure 9.2a). The tube has a finite diameter which is determined by the averaged 'lattice' spacing and is small compared to the overall chain dimension when the chains are entangled. The random-coil chains can change their shape and move but they cannot intersect each other. For a chosen chain, the motion transverse to the tube is retarded by its entangled neighbours but the tangential motions of the long chain is unaffected. Thus the long chain moves by sliding along its own contour of the tube, via curvilinear diffusion. For any one chain at any time, the central part of the long chain is confined in the tube but the ends are free to explore new positions and generate new tube portions at random as they advance. It is easy to see

that, as the new end positions are located, the original tube loses its shape and position gradually until such a time that a complete new tube is formed (Figure 9.2b). The time taken to wipe out an original tube and to establish a new tube is called the tube renewal time, τ_d.

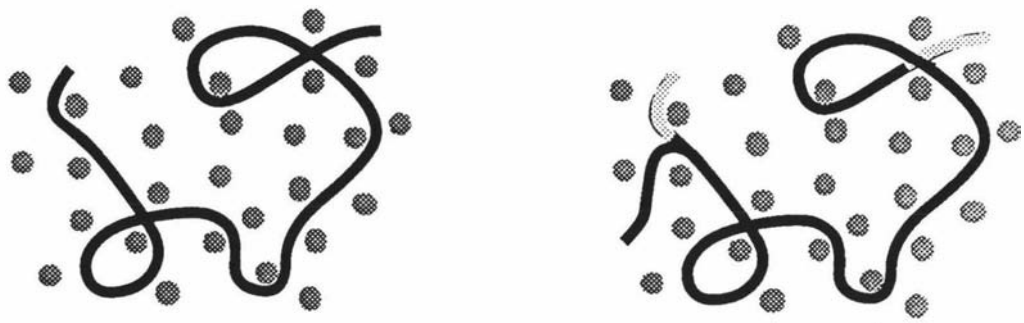

Figure 9.2 A virtual 'tube' formed by entangled polymer chains

High molar mass polymer melts and solutions exhibit unusual rheological properties. Among the non-linear viscoelastic properties of such complex liquids is the non-Newtonian dependence of the shear stress, σ_{xy}, on the shear rate, $\dot{\gamma}=\partial v_x/\partial y$. A number of constitutive equations have been developed to describe the relationship between the shear stress upon the shear rate[166]. One of the better known is that of the "power law" fluid[190]

$$\sigma_{xy} = K\dot{\gamma}^n \qquad [9.1]$$

where K and n are constants for a particular fluid. Whence the non-linear viscosity η may be written as

$$\eta(\dot{\gamma}) = K\dot{\gamma}^{n-1} \qquad [9.2]$$

The power law exponent, n, is unity for a Newtonian fluid and less than unity for a shear-thinning fluid[191] (Figure 9.3), which implies a decrease of the non-linear viscosity with increasing of the shear rate. Clearly the power law constitutive equation is phenomenological and suffers from a number of defects, including the divergence of the viscosity at zero shear in the case of shear thinning behaviour. Nonetheless it does provide quite a good empirical description in a number of experiments.

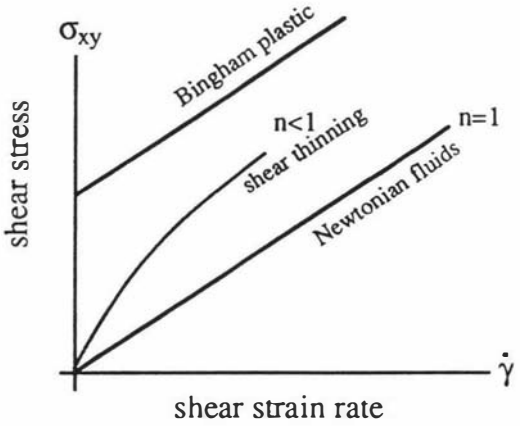

Figure 9.3

The relationship of shear rate vs shear stress

One of the challenges of polymer physics is to find a molecular basis for the constitutive equations. In the Doi-Edwards model the constitutive equation for entangled polymers is derived from the reptation theory and the onset of shear thinning is associated with a shear rate comparable with the slowest polymer relaxation process, the rate of tube disengagement, equal to τ_d^{-1}. $\eta(\dot{\gamma})$ is given by the product of the zero-shear viscosity, η_0, and the relaxation function $h(\dot{\gamma}\tau_d)$ shown in Figure 9.4.

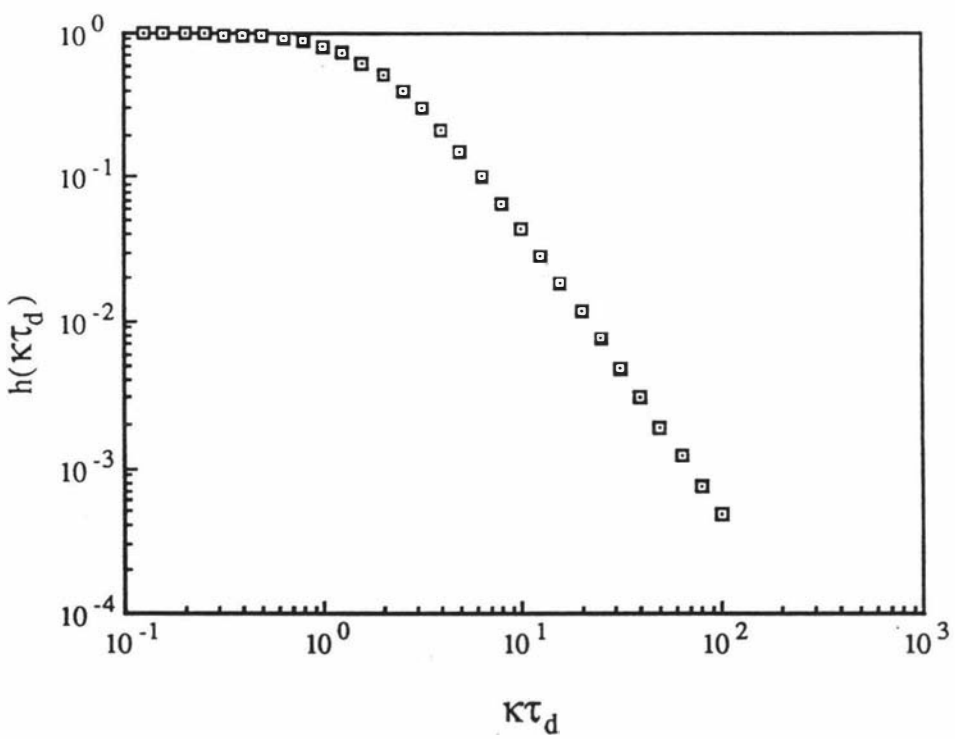

Figure 9.4 Doi-Edwards relaxation function

Clearly, since the viscosity decreases more rapidly than γ^{-1} for $\gamma\tau_d >> 1$, the shear stress must begin to decrease at some specific shear rate. This is the basis of the so-called "spurt effect"[192, 193] predicted for polymers in shear flow. Measurement of the shear-dependent viscosity provides a classical macroscopic test of the model. By contrast the microscopic tests of reptation theory usually involve a measurement of the molecular dynamics, and in particular the Brownian motion. In this regard centre-of-mass self-diffusion (D_s) data under zero shear conditions has provided a test[194, 195] of scaling laws based on the entanglement tube reptation model[184, 196]. For a semi-dilute solution ($c>c^*$, where c^* is a critical concentration at which polymer molecules in the solution overlap), the relevant scaling laws[184, 197] for molar mass (M) and polymer concentration (c) are

$$D_s \sim M^{-2} c^{(2-\nu)/(1-3\nu)} \qquad [9.3a]$$

$$\tau_d \sim M^3 c^{(3\nu-3)/(1-3\nu)} \qquad [9.3b]$$

$$\eta_0 \sim M^3 c^{3/(1-3\nu)} \qquad [9.3c]$$

where ν is the index relating the random coil end-to-end distance to the number of monomeric subunits (*ie* $R_0 \sim M^{\nu}$) and takes a value between 0.5 and 0.6 (good solvent) depending on the degree to which the polymer coil obeys Gaussian or excluded-volume statistics, an effect governed by solvent quality. It is worth noting that the same molar mass scaling laws apply for polymer melts provided that $M>M_c$ where M_c is the critical molar mass for the onset of entanglements[191].

To date, measurements of self-diffusion have been carried out only under zero-shear conditions. It would be interesting to monitor the Brownian motion under shear, and especially under shear rates sufficiently high to induce shear thinning effects. If shear thinning does arise from a breakdown in entanglement renewal as adjacent polymers separate, then the perturbation to the tube should cause a dramatic enhancement in D_s, as measured in the local frame of reference. Such measurements are made possible by Dynamic NMR Microscopy which offers several unique advantages over other techniques. For example, NMR measurement is not restricted to transparent liquids and requires no particulate dopant to enhance scattering, is sensitive to molecular length scales and can detect Brownian motion in the local frame of reference.

The experiments described here are designed to elucidate the molecular origins of rheological behaviour of high molar mass poly(ethylene oxide) molecules, by

measuring velocity and self-diffusion profiles for PEO in solution undergoing laminar flow through a 700 μm i.d. capillary. In comparison with a simple Couette flow device (Figure 9.5), a feature of the capillary flow experiment is the existence of a velocity shear which varies from zero at the centre of the flow to a maximum at the edge (Figure 9.6).

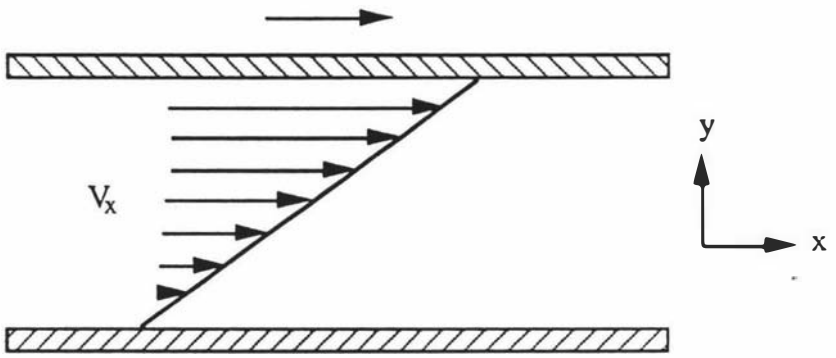

Figure 9.5 Velocity profile in simple Couette flow

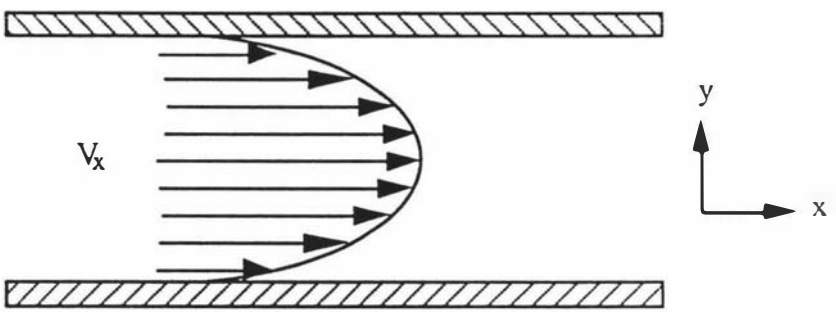

Figure 9.6 Velocity profile in Poiseuille flow

In the previous experiments using water samples, much attention was paid to the velocity measurement. In this polymer flow experiment, however, the precision and accuracy of the self-diffusion measurement are as important as those of velocity. Because of the finite transverse resolution employed (around 15 μm) there will be a velocity gradient within the imaging pixels which naturally leads to phase spreading effects in a manner akin to self-diffusion. Therefore the velocity-compensated Dynamic NMR Microscopy was also used to distinguish such a spread from that which arises from the Brownian motion, relying on the fact that the local molecular velocities are constant over the evolution time of the spin echo. Of course diffusion transverse to the

flow will upset the diffusion measurement but it is easy to show that such an effect will lead to insignificant perturbations to the apparent longitudinal diffusion coefficient provided that the shear rate is less than Δ^{-1}. The requirement restrictsγ to equal to or less than 100 in the measurement of diffusion. The tube renewal times of the polymer sample used are therefore required to be longer than a few milliseconds if shear thinning effects are to be examined via the self-diffusion coefficients. This requirement means that self-diffusion is measured over a time-scale, Δ, smaller than τ_d. At first sight it may appear that the observed motion will be dominated by internal modes of the polymer chain, rather than the desired centre of mass motion. In fact significant internal motion is only observed provided that the applied magnetic field gradient is sufficiently large that $2\pi q$ considerablely exceeds the inverse polymer dimensions, R_0^{-1}. For measurements using low q, centre of mass motion will strongly influence the spin echo decay even for $\Delta<\tau_d$. However where both $\Delta<\tau_d$ and $2\pi q<R_0^{-1}$, the echo attenuation will be weak and D_s difficult to measure.

9.2 Experimental details

Monodisperse poly(ethylene oxide) samples were obtained from Polymer Laboratories, Church Stretton, Shropshire, England; while polydisperse high molar mass poly(ethylene oxide), WSR301, was obtained from Union Carbide, New York. The following table summarizes the properties of these polymers.

Table 9.1: Poly(ethylene oxide) samples

	M_w	M_w/M_n
PEO standard	23 000	1.08
	56 300	1.05
	105 000	1.06
	253 000	1.07
	400 000	1.08
	750 000	1.13
	847 000	1.16
WSR 301	~ 3×10^6	~ 1.6

Equilibrium self-diffusion measurements were made for stationary samples of PEO dissolved in deuterium oxide using 4 mm-diameter sealed NMR tubes. These experiments were performed using a high-gradient PGSE probe developed in our

laboratory which could provide gradient amplitudes up to 17.7 T m^{-1}. The non-imaging PGSE experiments employed a pulse sequence shown previously in Figure 3.1, where the pulse durations (δ) and separation times (Δ) were in the ranges of 4.5 to 65 ms and 20 to 200 ms. Self-diffusion coefficients so obtained were time-scale independent and reflected the centre-of-mass Brownian motion.

The Dynamic NMR Microscopy experiments required large quantities of polymer solution. This restricted our work to the cheaper polydisperse WSR 301 poly(ethylene oxide). Because of this polydispersity, it is necessary to consider the averaging process appropriate to PGSE-NMR diffusion measurements. It may be shown that where an effective diffusion coefficient, D_{eff}, is calculated from the initial slope of a Stejskal-Tanner plot then D_{eff} is approximately related to the diffusion coefficient for the weight-averaged molar mass, $D(M_w)$, by[198, 199]

$$D_{eff} = D(M_w) \exp\{(\sigma^2/4)\alpha(\alpha-2)\} \qquad [9.4]$$

where $M_w/M_n = \exp(\sigma^2/2)$, σ is the standard deviation and α is the exponent which describes how D scales with M. The polydispersity of WSR301 was estimated using a gel permeation chromatography column calibrated using the PEO standards shown in Table 9.1 (the GPC measurements were carried out by Dr Rosie Wang who was a post-doctoral fellow at the department). These measurements suggest $M_w/M_n = 1.6$ while the peak mass value is close to 1×10^6 daltons. The nominal $\overline{M_w}$ of WSR301 is 4×10^6 daltons. This discrepancy is characteristic of the method dependence associated with molar mass measurement for a polydisperse polymer.

All equilibrium self-diffusion and Dynamic NMR Microscopy experiments were carried out at ambient temperature which was close to 30 °C. The arrangement for Dynamic NMR Microscopy experiment is shown schematically in Figure 9.7. A 120 cm^3 pressurized reservoir made of stainless-steel is connected to 0.7 mm i.d. HPLC tubing made of teflon and polymer solution is forced through the NMR imaging probe at a steady rate which is controlled by adjusting the applied pressure between 0 and 21 atmospheres. The flow experiments with WSR301 PEO/H_2O flow were carried out using the existing imaging probe and with PEO/D_2O flow were carried out using the new 'super G_y' imaging probe. The y direction is aligned with the capillary axis and the G_y coil was used for slice selection and to provide the PGSE gradient pulses.

Velocity and diffusion profiling experiments using WSR301 PEO/H_2O solutions were carried out with concentrations ranging from 0.5% to 4.5% w/v in

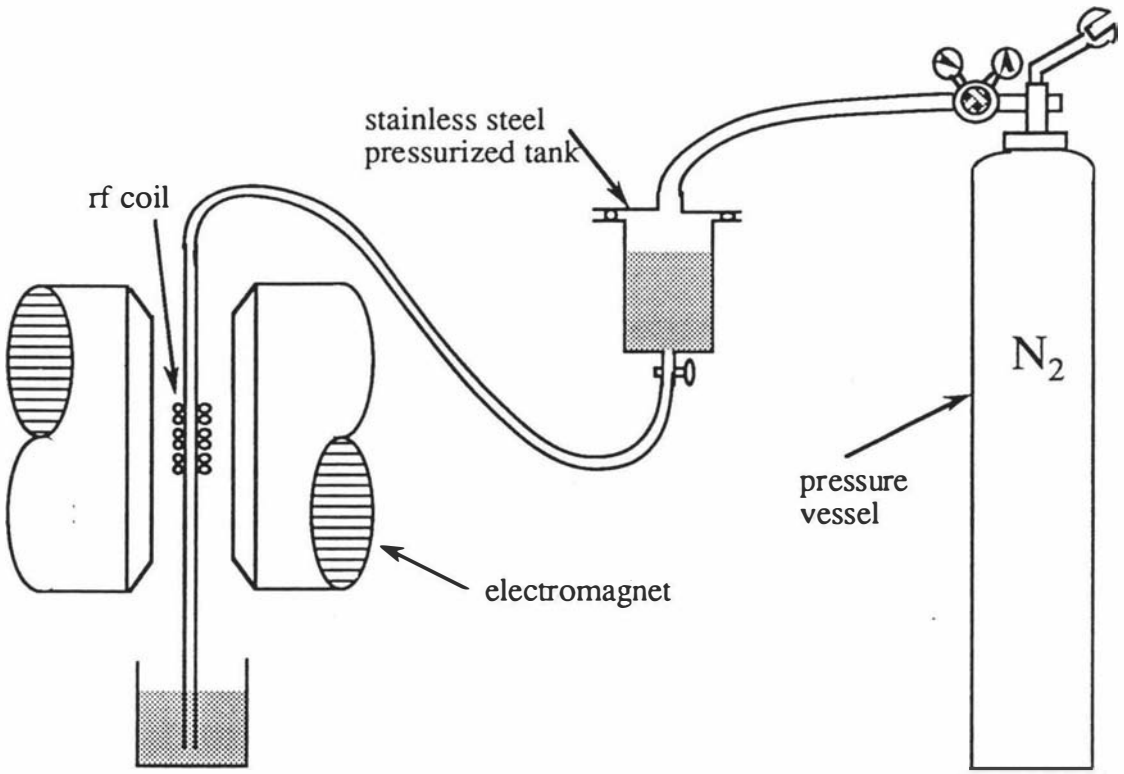

Figure 9.7 Schematic of the experimental arrangement for PEO capillary flow imaging

which 0.1 % $CuSO_4$ had been added in order to reduce the water proton T_1 relaxation time, so enhancing the available signal-to-noise ratio. This doping appeared to have no influence on the polymer solubility or upon the equilibrium polymer self-diffusion coefficients. Because the proton NMR signal is dominated by the solvent hydrogen nuclei in these measurements, the molecular self-diffusion coefficients so obtained correspond to the water molecules. The velocity maps should however reflect the combined flow of the polymer and solvent in the solution. The slice thickness in these experiments was 2 mm while the transverse pixel resolution is 15 μm. 18 successive real and imaginary q-space slices were obtained over a total measurement time of approximately 3 hours.

In order to obtain polymer self-diffusion coefficients the flow experiments were repeated using WSR301 PEO/D_2O solutions. For these experiments the much weaker proton NMR signal presented a special challenge in obtaining high spatial resolution. To circumvent this problem the advantage of the inherent azimuthal symmetry of the capillary tube was taken by reconstructing the complex q-slices from a single projection obtained from 4000 successive signal co-additions. This single-projection approach has been thoroughly tested in flow imaging experiments described in Ch 6.2. In 9 separate experiments employing the single-projection approach, 10 pairs of real and imaginary

q-slices were obtained and the diffusion coefficients for each pixel computed from the modulus images. The resulting diffusion maps for each experiment had poor signal-to-noise ratios so that the maps from the independent experiments were co-added. This addition process was checked by first co-adding the individual modulus images corresponding to the same gradient slices and recalculating the diffusion map.

At shear rates much higher than those employed in this work it is possible to break the polymer covalent bonds. As a test that the poly(ethylene oxide) molecules were undamaged in the present experiments the equilibrium self-diffusion measurements were repeated on a sample taken from the outflow reservoir and find polymer D_S values identical to those in fresh solutions.

9.3 Stationary self-diffusion measurement using PGSE

Figure 9.8 shows equilibrium self-diffusion data for different molar mass PEO standards in D_2O at 5.0% w/v concentration. It is clear that above 50 000 daltons the data are consistent with the usual $D_S \sim M^{-2}$ scaling characteristic of random coil polymers with concentrations above c*, the minimum concentration for the onset of entanglements. The concentration dependence of self-diffusion for WSR301 PEO in D_2O is shown in Figure 9.9. Despite the polydispersity of this material, the apparent scaling behaviour is remarkably close to $D_S \sim c^{-1.75}$, consistent with a random coil exponent, $\nu = 0.6$.

There is no intention in this thesis to argue the issue of whether such behaviour represents verification of the scaling hypotheses, but merely to emphasise three points. First it is clear that poly(ethylene oxide)/water exhibits self-diffusion behaviour similar to that observed using both Forced Rayleigh Scattering and PGSE NMR on a number of other polymer systems in the semi-dilute regime. Second it is likely that the transition from dilute to semi-dilute behaviour for WSR301 PEO in water is in the concentration range 0.5 to 1 % w/v and that this polymer is clearly entangled at the concentration of 4.5% w/v used in the diffusion mapping experiment later described. Finally, by comparing the equilibrium self-diffusion data in Figures 9.8 and 9.9 the PGSE-NMR effective molar mass for WSR301 may be estimated to be in the vicinity of 1.6×10^6 daltons. Use of Eq[9.4] yields $M_w = 3.2\times10^6$ daltons which is reasonably close to the nominal value quoted by the manufacturers.

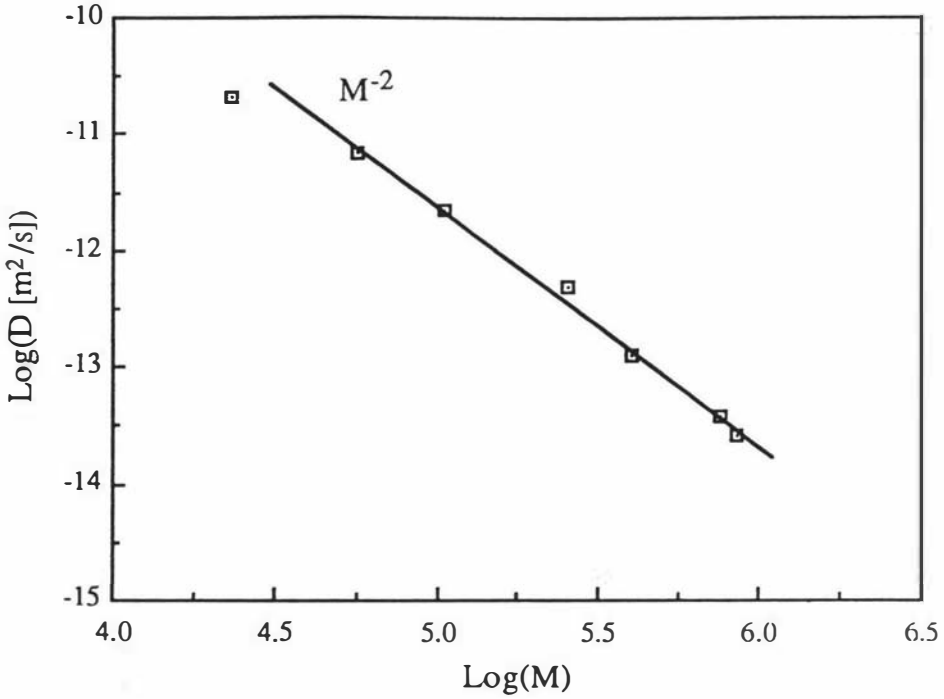

Figure 9.8 Double-logarithmic plot of polymer self-diffusion vs molar mass for PEO standards at 5.0% w/v concentration in D_2O at 30°C

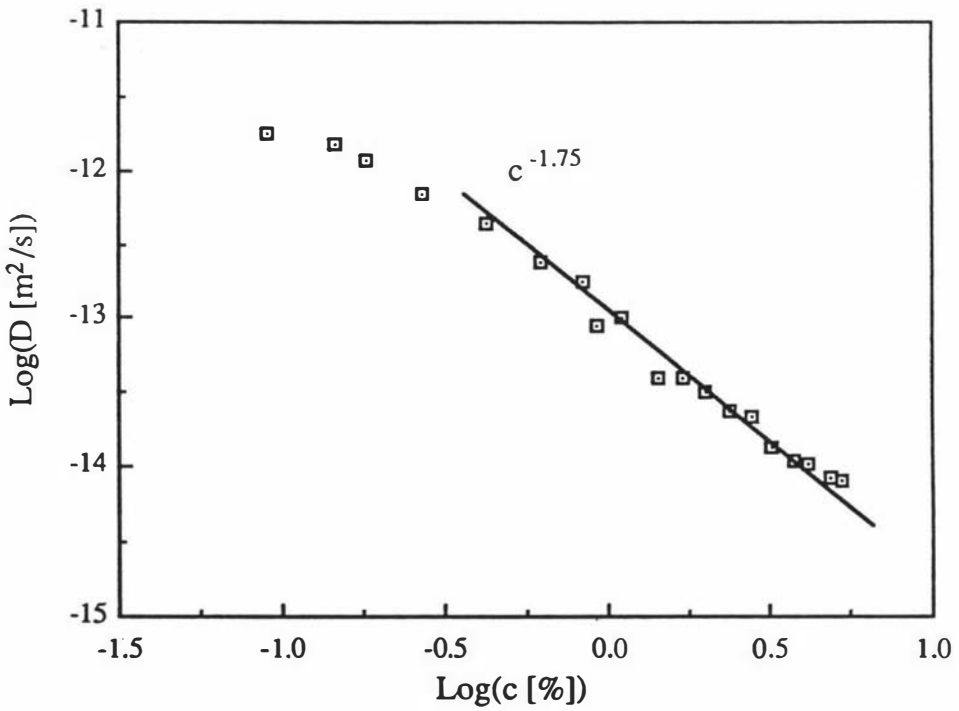

Figure 9.9 Double-logarithmic plot of polymer self-diffusion vs concentration (% w/v) for WSR301 PEO in D_2O at 30°C

Another estimation of the molar mass of WSR301 poly(ethylene oxide) may be obtained by estimating D_0, the self-diffusion coefficient in the zero concentration. Given the difficulty in obtaining self-diffusion coefficient at very low concentrations, it was found $D_0 \cong (2.5\pm0.5)\times10^{-12}$ m^2s^{-1}. By comparison with the data of Bortel and Kochanowski[200], the end-to-end length of the polymer, R_0, may be estimated as 1500±300 Å.

9.4 Experimental results in comparison with the power-law model

Velocity and diffusion maps for WSR301 PEO in water at 0.5% concentration flowing under a 3.9 kPa pressure head are shown in Figure 9.10 while a corresponding velocity and diffusion profile through a diametral chord is given in Figure 9.11. The central maximum velocity, v_{max}, is 6.5 mm s^{-1} while the maximum shear rate, apparent at the edge of the flow, is approximately 40 s^{-1}. It is apparent that the velocity profile closely resembles the Poiseuille flow characteristic of a Newtonian fluid while the water self-diffusion is uniform across the flow field. These results are qualitatively similar to those obtained in the water Poiseuille flow experiments which have been described previously in Chapter 6.

As the polymer concentration is increased above c* a transition in the shear dependence of the viscosity is observed. The progression is illustrated in Figure 9.12 where normalised velocity profiles are shown for various concentrations between 0.5% and 4.5 % w/v. Above 1% the Poiseuille behaviour is clearly perturbed. For convenience the data was fitted using a power law constitutive equation for which the solution to the Navier-Stokes equation is given by

$$v(r) = \left(\frac{\Delta P}{2K\Delta L}\right)^{1/n}\left(\frac{n}{n+1}\right)[R^{(n+1)/n} - r^{(n+1)/n}] \qquad [9.5]$$

where $\Delta P/\Delta L$ is the pressure gradient and R is the inside radius of the capillary.

The dependence of v_{max} on $\left(\frac{\Delta P}{2K\Delta L}\right)^{1/n}$ is tested in Figure 9.13. The data is clearly consistent with the power law behaviour but with an apparent exponent which decreases gradually with increasing concentration. For example an exponent of 0.4 is suggested for the highest concentration used (4.5% w/v) while at lower concentrations the apparent exponent is closer to 1, the index for Newtonian flow.

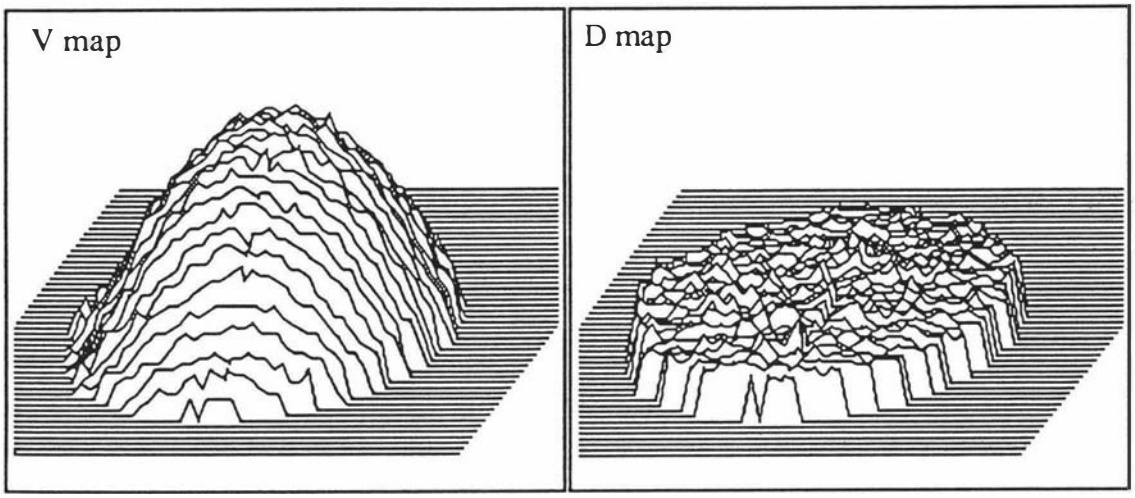

Figure 9.10 Velocity and self-diffusion maps for a 0.5% w/v WSR301 PEO/water in flow

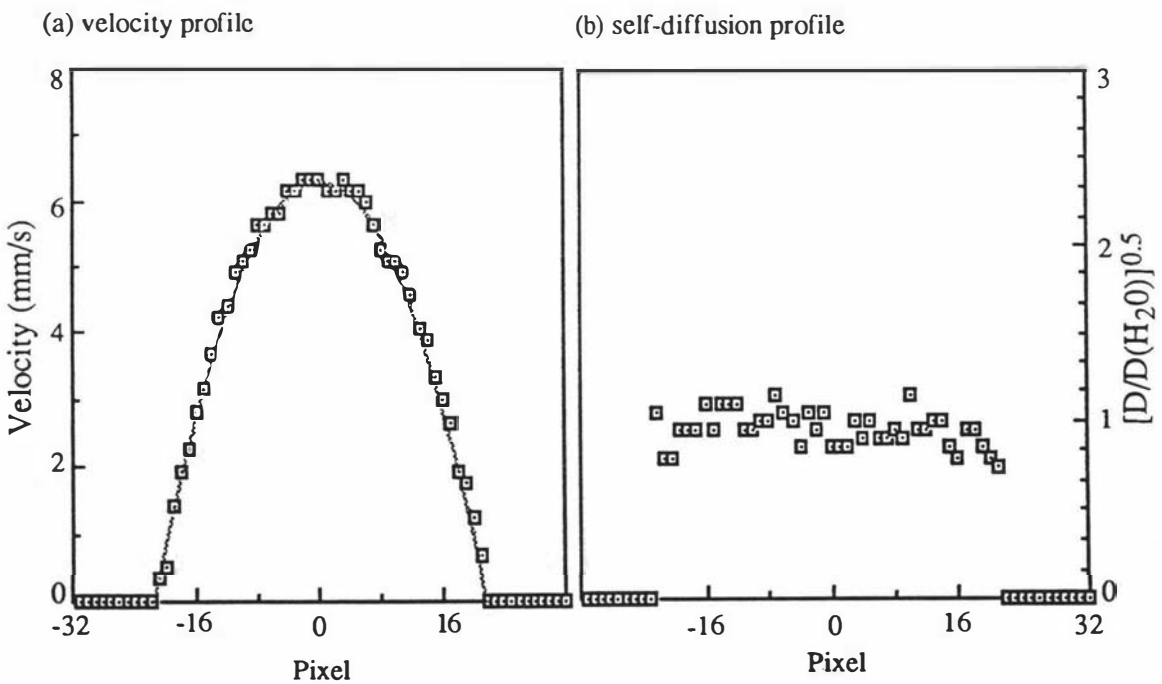

Figure 9.11 Profiles of the velocity and self-diffusion maps shown in Figure 9.10 (The solid line in velocity map corresponds to Poiseuille flow.)

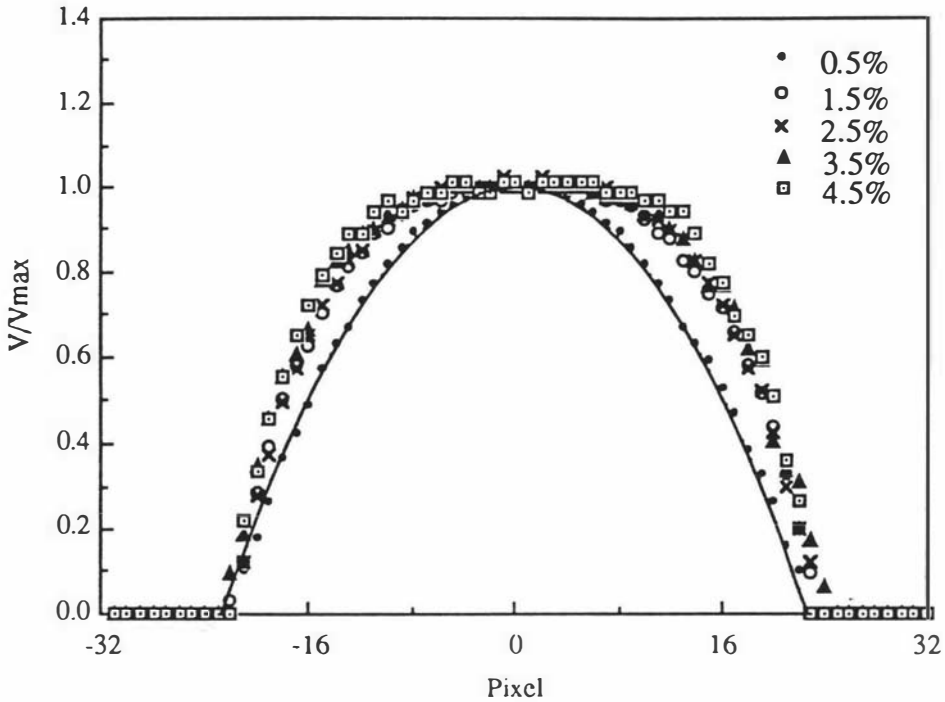

Figure 9.12 Normorlized velocity profiles for different concentration solutions of WSR301 PEO in water (The solid line is the Poiseuille profile.)

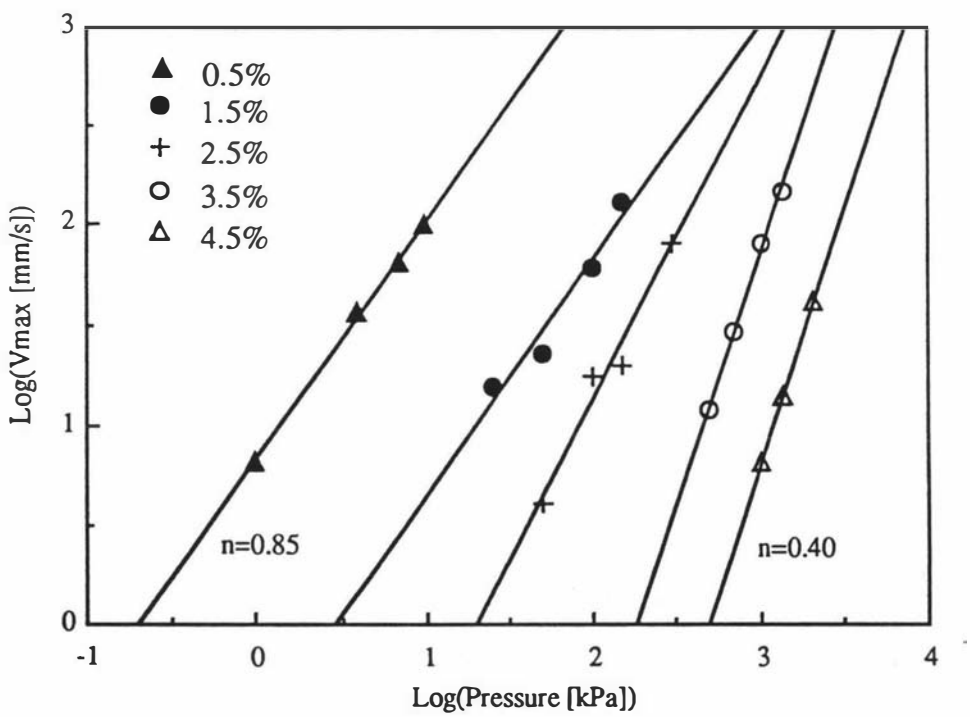

Figure 9.13 Double-logarithmic plot of Vmax vs the pressure for different concentrations of WSR301 PEO in water (The power law fittings are also given.)

The velocity and diffusion maps and corresponding profiles obtained at 4.5% w/v concentration and at a pressure head of 2100 kPa are shown in Figures 9.14 and 9.15. In this case v_{max} is 7.4 mm s^{-1} and the maximum shear rate at r=R is approximately 70 s^{-1}. Power law fits to the velocity profile exponents of 0.35, 0.40 and 0.45 are also shown. Again the 0.4 exponent works well. Conventional viscometric measurements were also carried out using Bohlin™ rheometer. The 0.4 exponent was found from the relationship of shear stress vs shear rate for the 4.5% w/v fluid. It is interesting that this same exponent has been found in laser Doppler anemometry experiments by Mackley[201] using polyethylene melts in capillary flow.

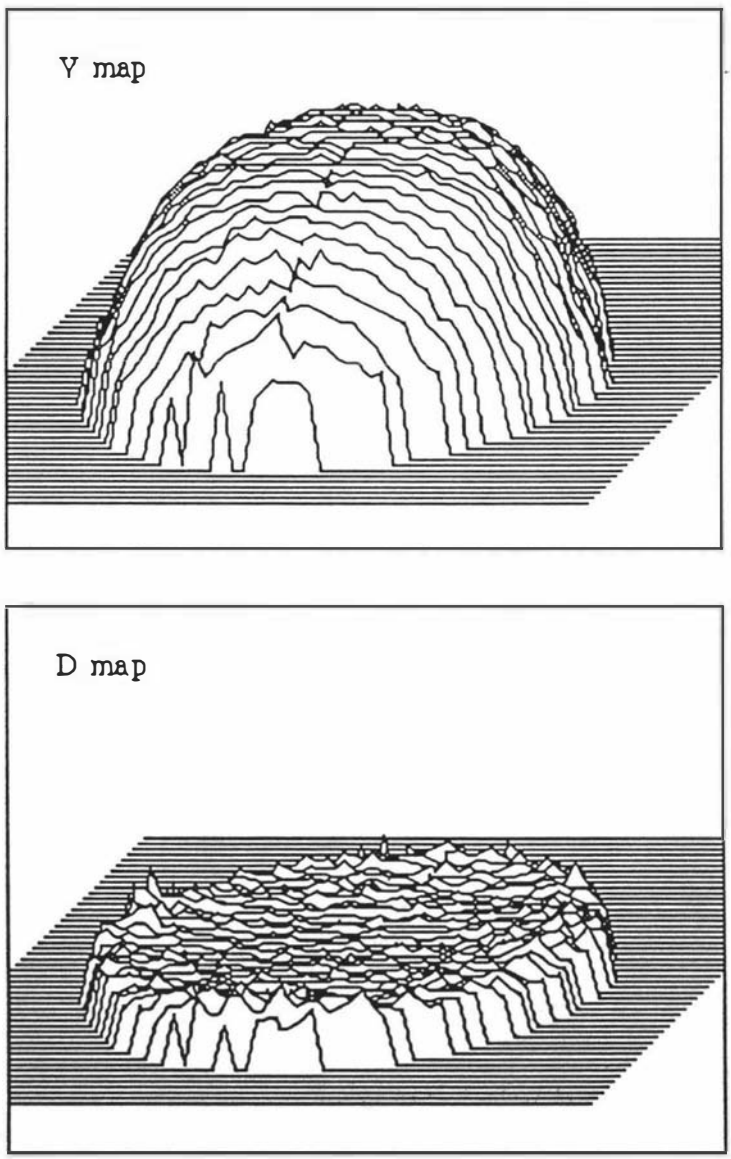

Figure 9.14 Stacked plots of V and D maps for a 4.5% w/v PEO/H_2O solution in flow (at 2100kPa pressure head)

(a) Velocity profile

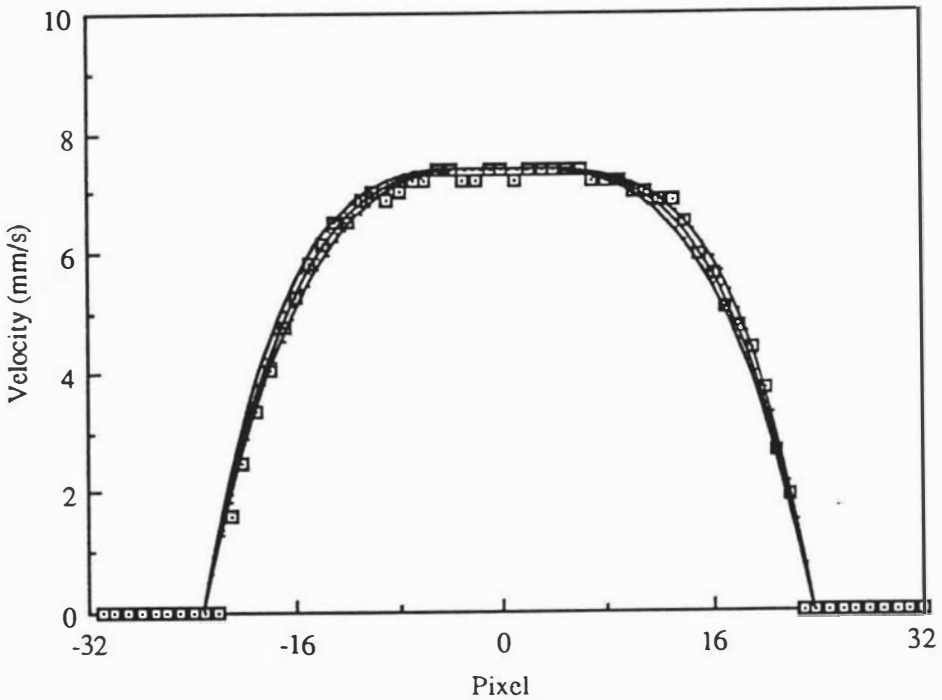

(b) Normalized diffusion profile

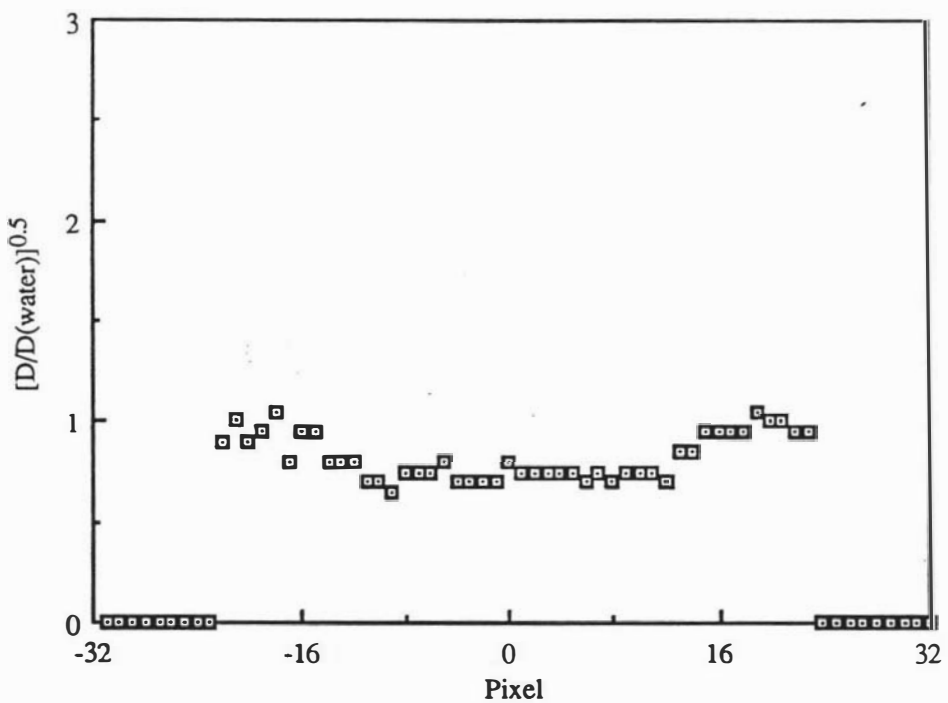

Figure 9.15 Profiles of the velocity and diffusion maps shown in Figure 9.14 for a 4.5% WSR301 PEO/H_2O solution in flow (The fits to the velocity profiles correspond to the power-law fluid with exponents 0.35, 0.4 and 0.45.)

There are two points which are worth noting here. First, for the flow of an entangled polymer, there have been some previous evidence[202] and a model due to de Gennes[203] which seem to indicate a slip boundary condition. However, the power law relationship given by Eq[9.5] assumes a boundary condition with zero velocity at the capillary wall. This zero-slip condition is in fact consistent with the data presented here. In Dynamic NMR Microscopy it is possible to locate the edge of the image with a resolution of one pixel. The velocity profiles of PEO/H_2O used in this work for all extrapolate to zero within this resolution. No evidence for slip has been found.

Second, in the above analysis, no particular significance is attached to the power law constitutive equation and other empirical models may describe the velocity profiles as well. In fact the central region of the measured velocity profile at 4.5% exhibits less shear than indicated by the power law fit. Such a feature is incorporated in the Bingham plastic description[190] in which the central region of such capillary flow is presumed to manifest plug-like behaviour.

To illustrate the simplistic nature of the power law model, velocity profiles of 4.5% PEO/H_2O solutions at two lower pressure heads, 1000 kPa and 1400 kPa, were also fitted using the power law relationship. The results are shown in Figure 9.16, where the maximum velocities were 1.1 mm/s and 2.3 mm/s respectively. Comparing with the best fit of n=0.40 for v_{max}=7.4mm/s, an exponent of 0.50 gives the best fit for v_{max}=1.1 mm/s and 0.45 gives the best fit for v_{max}=2.3mm/s. Therefore it is clear that the exponent, n, of the power law model is not constant at low shear rates but becomes constant as the shear rate increases (also refer to Figure 9.13).

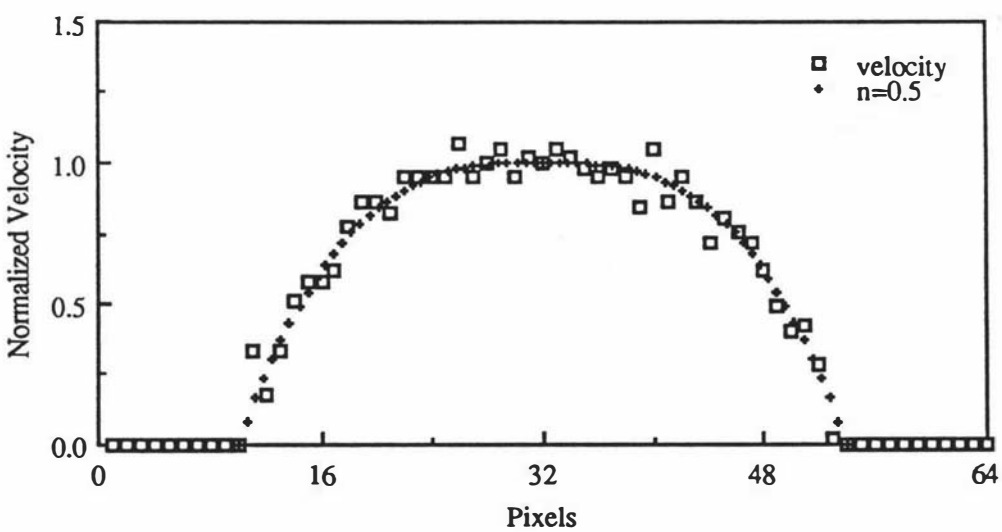

Figure 9.16a Velocity profile of 4.5% w/v PEO/H_2O solution at 1000kPa pressure head

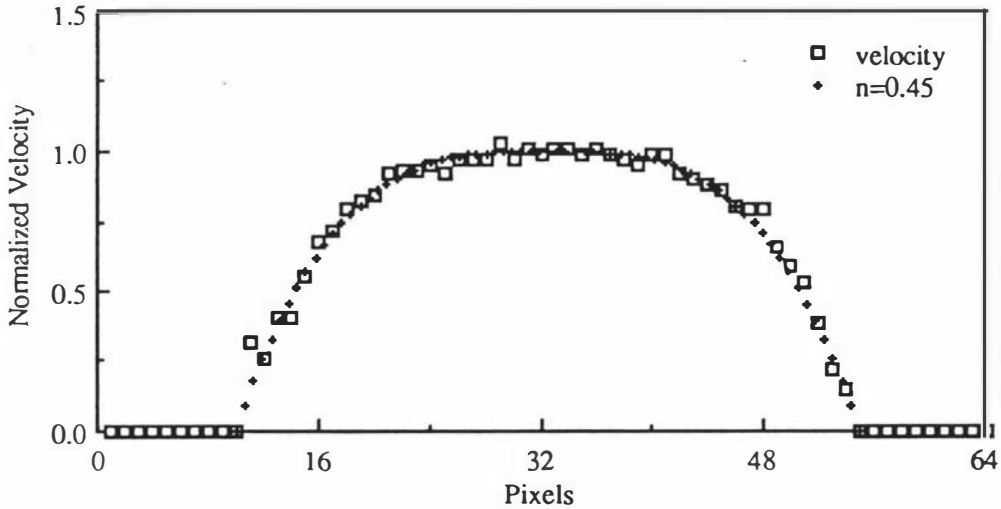

Figure 9.16b Velocity profile of 4.5% w/v PEO/H_2O solution at 1400kPa pressure head

The PEO/H_2O flow experiments were also performed in a separate imaging experiment where the viscous liquids were forced through a 2.9 mm i.d. glass tube. Figure 9.17a compares velocity profiles of 1.5% w/v WSR301 PEO/H_2O for two different diameter capillaries, 2.9 mm and 0.7 mm. The maximum velocities in both cases were equal to 2.5 mm/s. But in the larger diameter tube the velocity profile is closer to Poiseuille although both capillaries exhibit non-parabolic profiles. This indicates that the transition from Newtonian to non-Newtonian behaviour at this concentration requires at least the higher shear rates of the narrow capillary tube. Figure 9.17b compares the velocity profiles for these two different diameter capillaries at a higher concentration, 2.5% w/v WSR301 PEO/H_2O. Both velocity profiles are more consistent with a power law constitutive equation with a corresponding exponent of about 0.6. The maximum velocities in the two 2.5% cases were again similar, 2.2 mm/s for the 2.9 mm tube and 2.8 mm/s for the 0.7 mm tube. The same power law exponent is also shown in Figure 9.18 as the logarithm of maximum velocities against the logarithm of the pressure heads.

Clearly therefore high shear rates can be achieved by decreasing the diameter of the capillary or increasing the flow rate. The first approach is most favourable since increasing the flow rate will result in not only much larger volume flows but also the risk of exceeding the upper limit for velocity measurement. The required resolution can be retained as the capillary diameter decreases by reducing the diameter of the rf coil.

(a) 1.5%

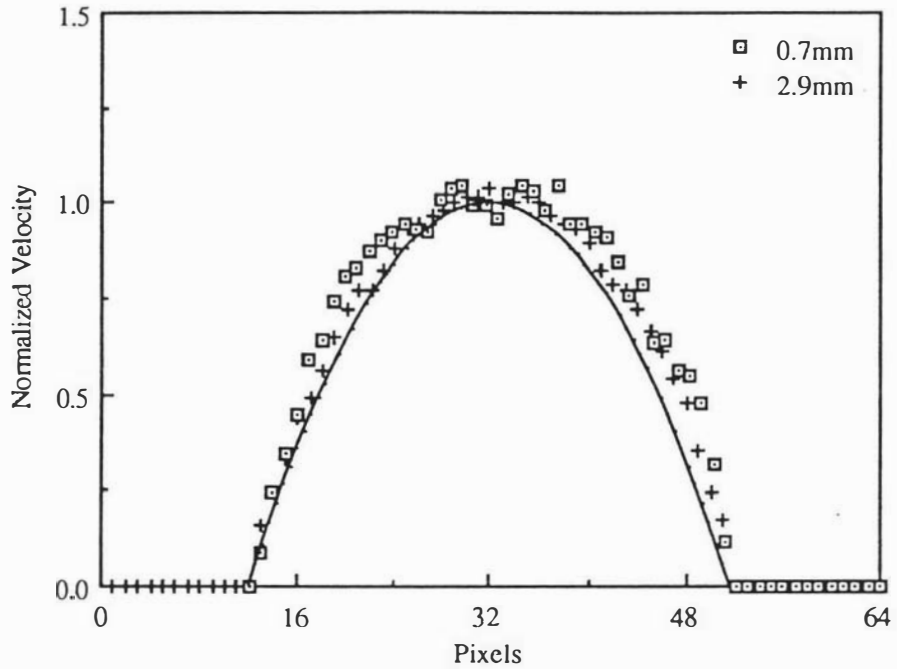

(b) 2.5%

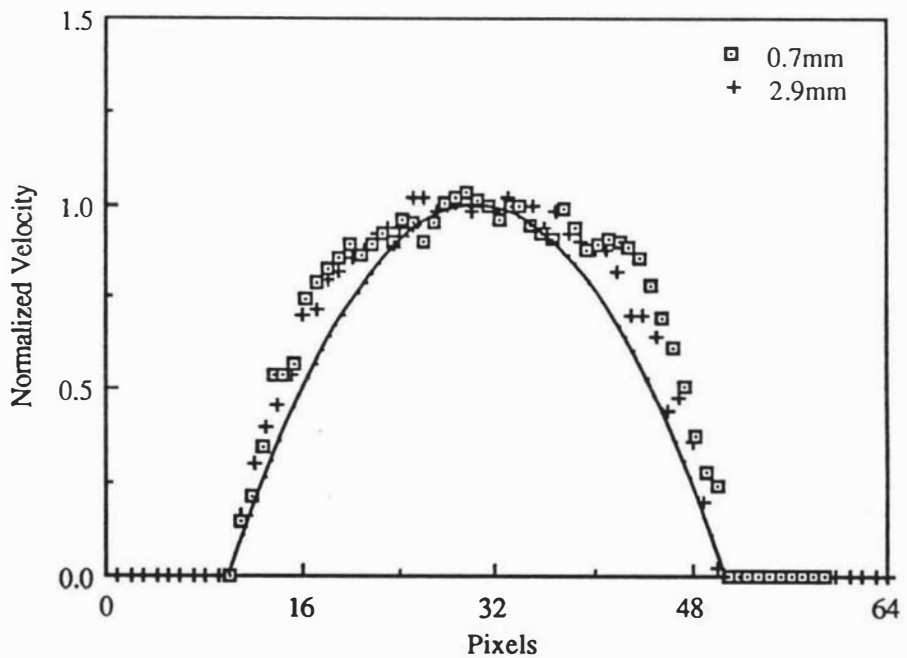

Figure 9.17 Comparisons of velocity profiles of 1.5% and 2.5% WSR301 PEO/H_2O solutions in flow through 0.7mm and 2.9mm tubes respectively

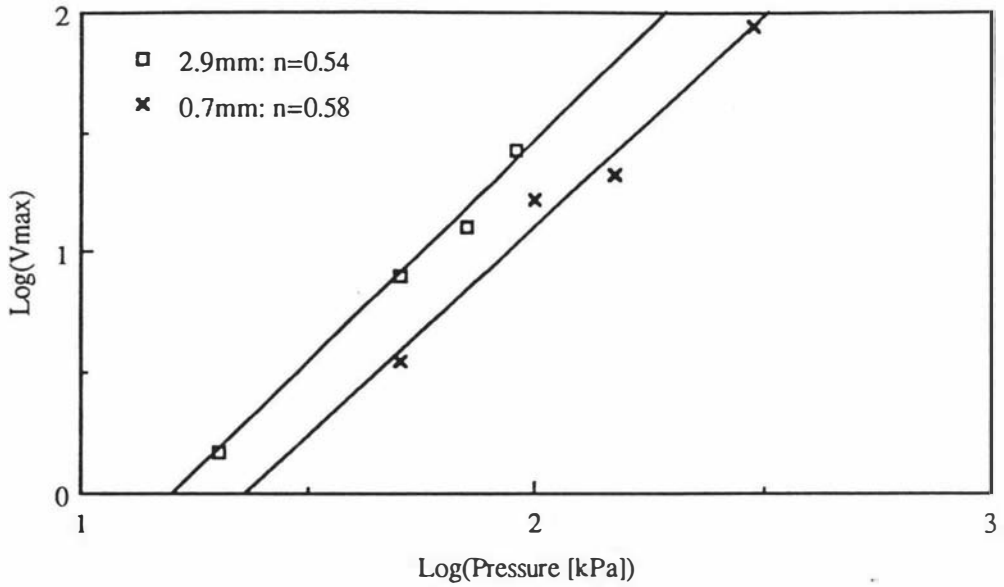

Figure 9.18 V_{max} vs Pressure for 2.5% w/v PEO/H_2O flow

At 4.5% w/v concentration, the existence of a critical radius in capillary flow is also consistent with the predictions of the Doi-Edwards model which is based on a microscopic description of the polymer dynamics. Fits to the velocity profiles using the Doi-Edwards theory have not been attempted because of the sensitivity of this model to molar mass and the high polydispersity of the polymer used in this work. It is clear however that the model can fit the data quite well. Nonetheless a further analysis will appeal to the tube/reptation model in seeking to explain the local molecular dynamics exhibited via the shear-dependence of the polymer self-diffusion coefficients, data which is more directly linked to the molecular depiction inherent in this theory.

9.5 Self-diffusion enhancement due to high shear

The self-diffusion coefficients of the water and polymer molecules must be determined in separate experiments because of their significant difference in magnitude (~10^{-9} m^2s^{-1} cf 10^{-14} m^2s^{-1}) and the need to suppress the signal from the solvent in the latter case. The (water) diffusion profile of 4.5% w/v PEO solution shown in Figure 9.15 does not exhibit the uniformity found for the 0.5% w/v PEO solution in capillary flow. In the 4.5% solution under flow, enhanced water diffusion is apparent in the region of high shear near the capillary walls. The polymer self-diffusion profiles are measured using the velocity-compensated Dynamic NMR Microscopy with

reconstruction from a single projection. Figures 9.19 compares polymer diffusion profiles for two adjacent chords in the vicinity of the capillary diameter. Figure 9.19a and 9.19b result from co-adding the diffusion maps from 9 independent experiments while Figure 9.19c and 9.19d are obtained by co-adding each of the 10 modulus images for corresponding g values and computing the diffusion map from the resulting set. These four maps are mutually self-consistent. Furthermore, in another experiment performed several months later using independently prepared polymer solution, precisely the same diffusive behaviour was observed.

In each case shown in Figure 9.19, the data exhibit a central region in which the self-diffusion coefficient is constant and less than or of order 10^{-13} m^2s^{-1}, but the diffusion coefficients rise sharply at a radius r≈0.5R, increasing in an approximately linear manner with radius until reaching a maximum value of around 5.5×10^{-13} m^2s^{-1}. The diffusion plateau in the capillary centre is in fact quite consistent with the equilibrium D_s value of 10^{-14} m^2s^{-1} for 4.5% w/v WSR301 PEO in water since the lower limit for diffusion measurement is approximately 10^{-13} m^2s^{-1} in the imaging experiment given the available signal-to-noise ratio. It should be noted that in the central region of the capillary the undisturbed tube renewal takes its longest value, τ_d. Because Δ is somewhat smaller than τ_d, this means that the centre of mass diffusion is difficult to observe in this region.

One possible explanation for diffusive enhancement as the shear rate increases, is the influence of self-diffusion transverse to the flow, since such motion in the presence of the velocity shear will cause a net phase shift in the double PGSE method. The previous analysis in Ch 3.5 has shown that this effect leads to apparent diffusion enhancement by $(1+\gamma^2\Delta^2D_\perp/D_{||})$. This factor could cause a doubling of the diffusion in the maximum shear region close to the walls (r>0.9R), assuming that $D_\perp/D_{||}$ is unity. However there is reason to believe that $D_\perp/D_{||}$ is less than unity because of likely deformation of the random coils. Further from the wall, the enhancement due to this transverse diffusion effect should be much smaller. It is most unlikely that this effect could cause the observed diffusive enhancement by nearly two orders of magnitude above the equilibrium D_s value.

The enhancement of polymer self-diffusion above a critical shear rate provides dramatic evidence for the molecular basis of shear thinning. This enhancement can be pictured as arising from the breakdown of polymer entanglements as the shear rate exceeds the rate of tube renewal, τ_d^{-1}. The data provides three related but separate quantitative tests[180] for any model. First, there is the value of the radius (and hence

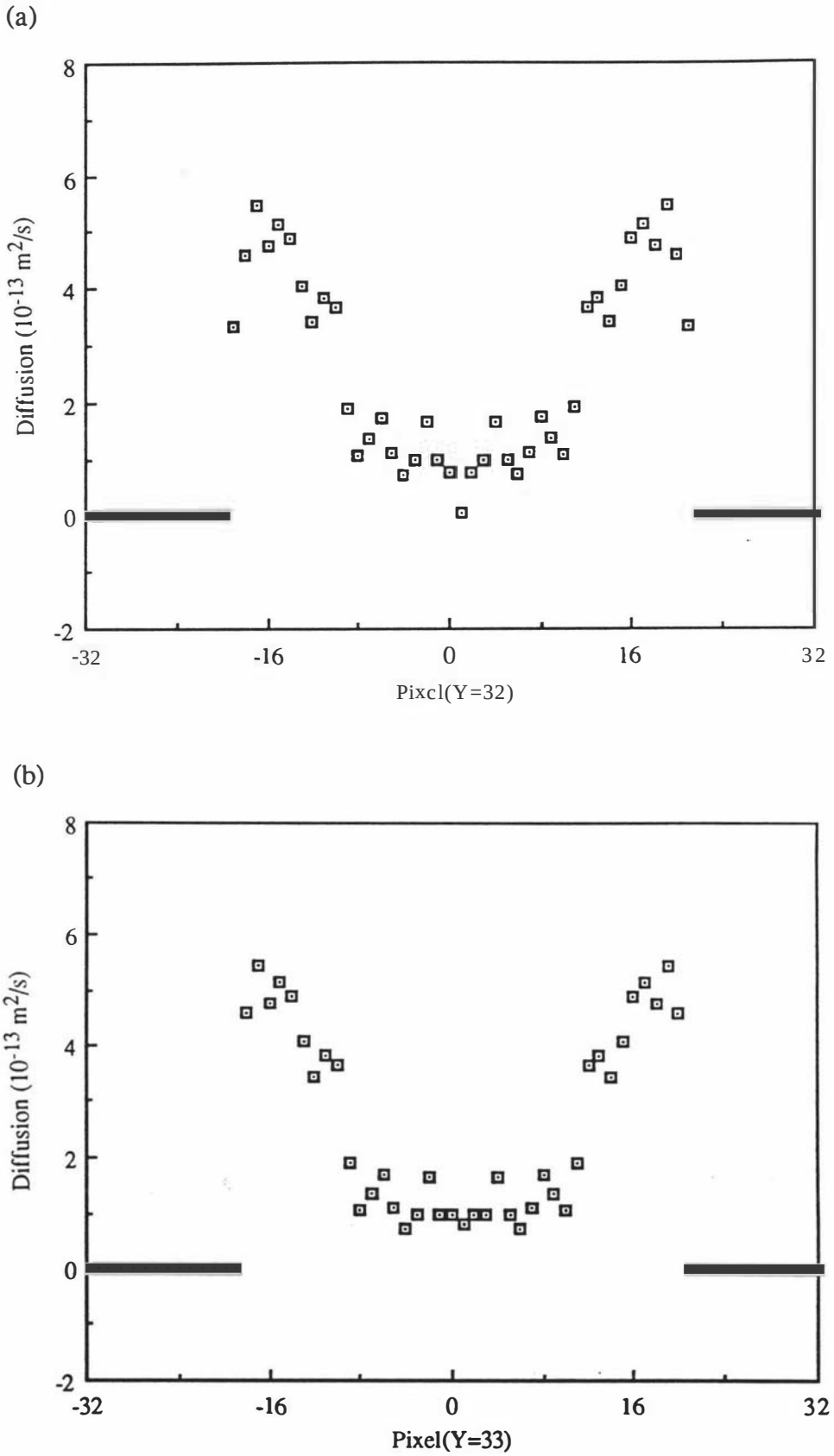

Figure 9.19 Polymer self-diffusion profiles for semidilute WSR301 PEO (4.5% w/v in D_2O) under flow through a 0.7mm capillary

(c)

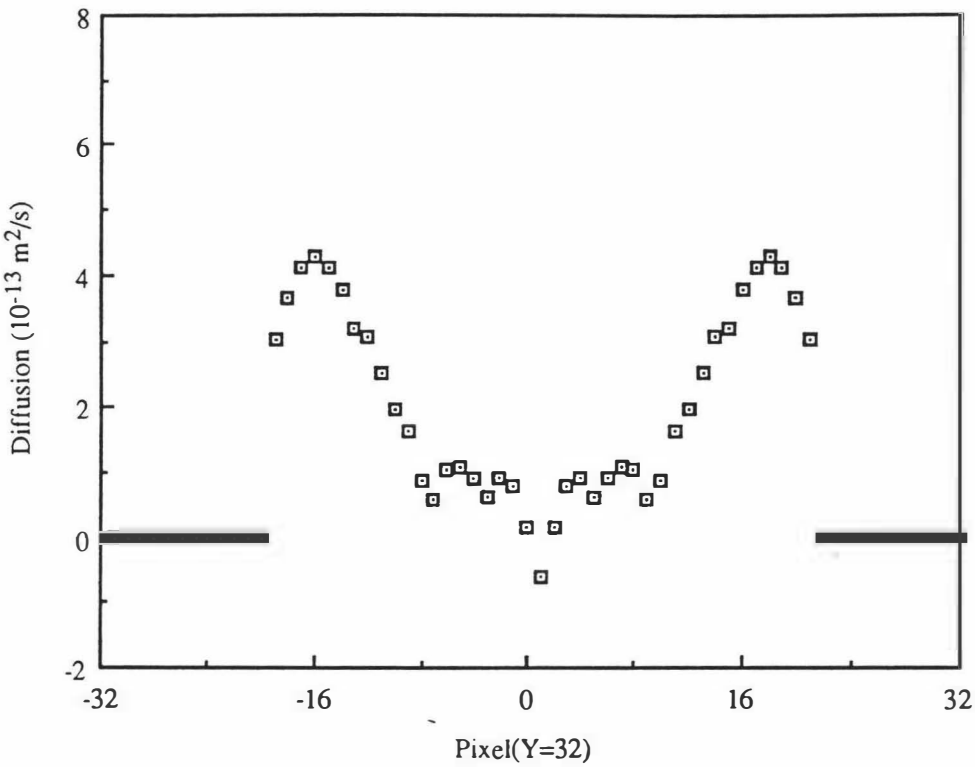

(d)

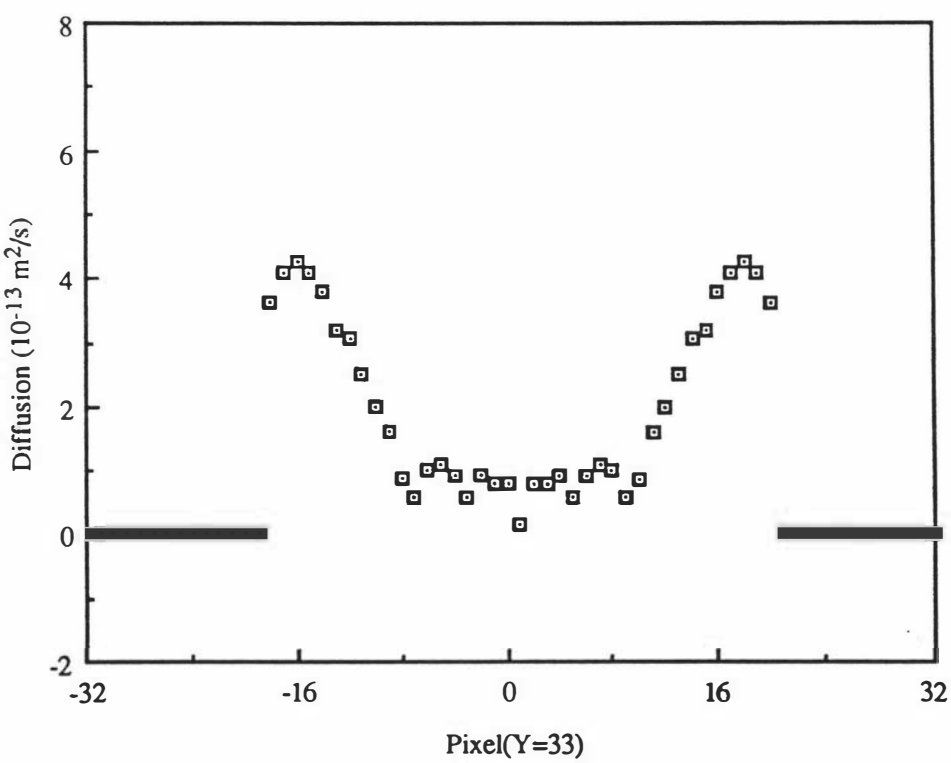

(Figure 9.19 continues)

shear rate) at which enhancement occurs. Second, beyond this critical radius the dependence of the local polymer self-diffusion coefficient upon local shear rate may be used to provide confirmation of the theory. Finally the existence of a plateau maximum value for the polymer self diffusion close to the capillary wall, along with the precise value of this maximum, provides yet another test.

By using the power law fit to the velocity profile, the shear rate which corresponds to the critical radius r_c can be calculated since

$$\frac{\partial v}{\partial r} = -\left(\frac{v_{max}}{R}\right)\left(\frac{n+1}{n}\right)\left(\frac{r}{R}\right)^{1/n}$$

$$= -\left(\frac{\Delta P r}{2K\Delta L}\right)^{1/n} \qquad [9.6]$$

whence for $r_c=0.5R$, $v_{max}=7.4$ mm s^{-1} and $R=350$ μm the critical shear rate is found to be $(0.08\ s)^{-1}$. By comparison the tube renewal time may be calculated from our knowledge of the equilibrium self diffusion coefficient since from the tube model

$$\tau_d = \frac{R_0^2}{3\pi^2 D_s} \qquad [9.7]$$

where R_0 is the rms end-to-end length of the polymer. Using a value of $R_0 \approx 1500 \pm 300$ Å for 1.6×10^6 daltons poly(ethylene oxide) in water, it is found $\tau_d \approx 0.08 \pm 0.03$ s. τ_d^{-1} is sufficiently close to the observed critical shear rate to suggest that the tube model may provide a useful approach in understanding the basis of shear thinning.

Our depiction[180] of the mechanism for diffusion enhancement is an adaptation of an proposal by Onuki[204] to explain coil stretch under simple shear for dilute polymer solutions. One normally associates coil stretch only with extensional flow. In Onuki's model the dilute coil forms a series of Rouse blobs of dimension ξ_R aligned along the direction of shear as shown in Figure 9.20a. While this extension is clearly unstable, the complete coil flips which occur from time to time are considered to be a rapid but occasional perturbation in the dilute solution model. Each blob is characterised by a Rouse relaxation rate, τ_R^{-1}, equal to the shear rate $\dot{\gamma}$. This identity leads to the relation

$$\frac{k_B T}{\xi_R^3 \eta_0} \approx \dot{\gamma} \qquad [9.8]$$

where η_0 is the solvent viscosity. The identity can also be obtained by equating the force required to unravel one blob, k_BT/ξ_R to the shear force acting on a neighbouring blob displaced in the flow by one blob diameter, $(6\pi\eta_0\xi_R)\dot{\gamma}\cdot\xi_R$. This equality forms the basis of the assumption that the polymer unravels into a sequence of aligned blobs.

The extension to semi-dilute solution is based on the depiction shown in Figure 9.20b. Suppose attention is focussed on one labelled chain. Because the tube is defined by surrounding chains which are in relative motion because of the shear, the tube topology is being continually redefined. For $\dot{\gamma}<\tau_d^{-1}$ the labelled chain reforms its tube more rapidly than the shear rate so that the topology is unperturbed in relation to equilibrium. For$\dot{\gamma}>\tau_d^{-1}$ only the ends of the chain will be able to form a tube whose primitive path has the conformation of a random coil. The size of this end region, ξ_c, will be determined by the relaxation time τ_c for "end tube" renewal with $\tau_c^{-1}=\dot{\gamma}$. Between the end sections of dimension ξ_c the chain will be extended in a linear sequence of blobs of dimension ξ_m, the concentration-dependent screening length. The end sections will consist of n_c such blobs arranged in the usual random path since only at the ends is the chain able to explore all possible conformations.

In essence therefore, while the total tube length remains unchanged and the total tube renewal time is identical to the equilibrium value of τ_d, the extension of the chain increases along the direction of shear. The tensile force associated with this loss of chain entropy will be counterbalanced by the drag on the end sections. This drag is however hard to estimate because of the difficulty in assigning an effective local viscosity. An alternative approach to calculating n_c (and hence ξ_c) is to calculate τ_c from reptation theory. The probability $\varphi(s,t)$ that a segment s of the primitive path of total length L remains at a time t is given by[184]

$$\varphi(s,t) = \sum_{p\ \mathrm{odd}} \frac{4}{p\pi} \sin\left(\frac{p\pi s}{L}\right) \exp(-p^2t/\tau_d) \qquad [9.9]$$

Integrating over a length L_c at the end of the chain gives an average probability

$$\varphi(t) = \sum_{p\ \mathrm{odd}} \frac{4L}{p^2\pi^2L_c} \left(1-\cos\left(\frac{p\pi L_c}{L}\right)\right)\exp(-p^2t/\tau_d) \qquad [9.10]$$

$\varphi(t)$ is dominated by components for which p is a multiple of L/L_c. Hence the longest relaxation time is of order $\tau_d(L_c/L)^2$.

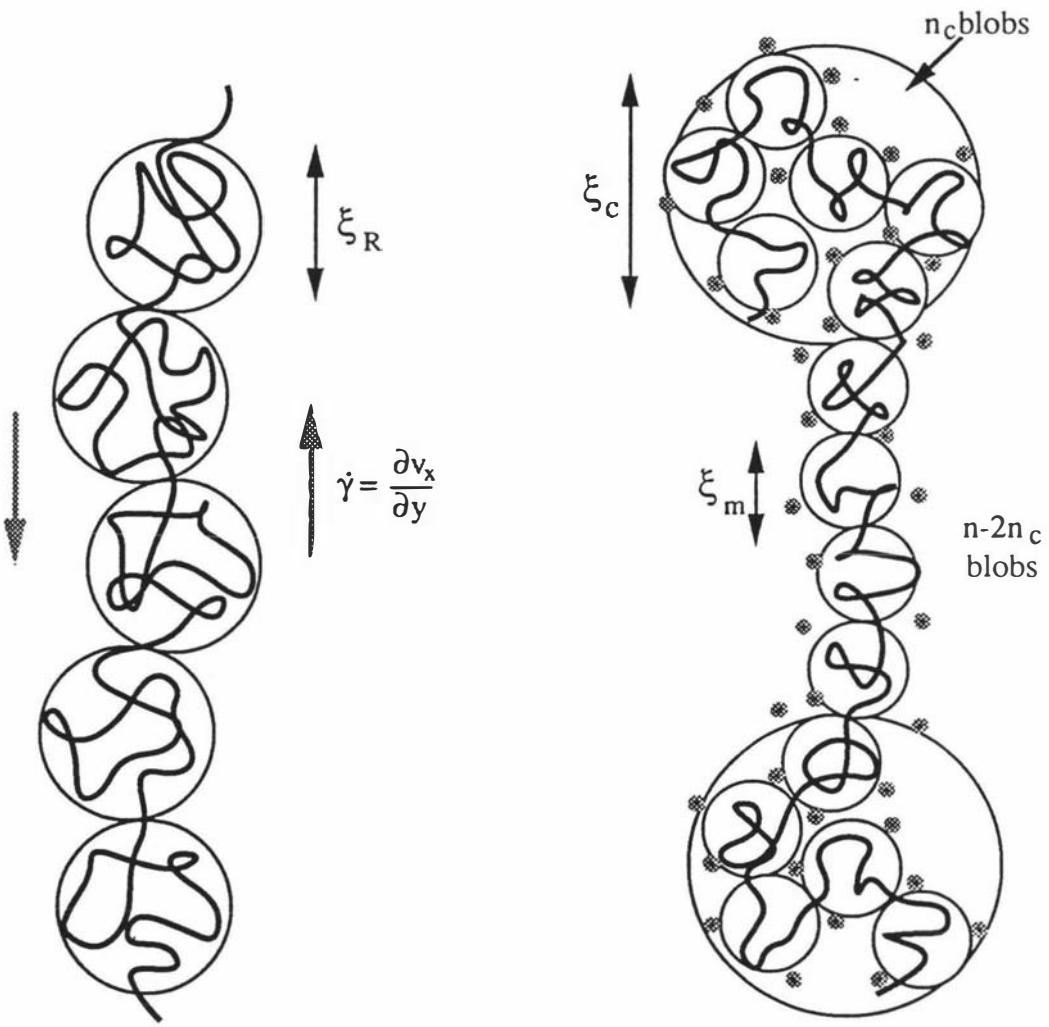

(a) The Onuki model

(b) Depiction of coil deformation under shear for semidilute conditions

Figure 9.20 Schematic model of polymer stretching under velocity shear

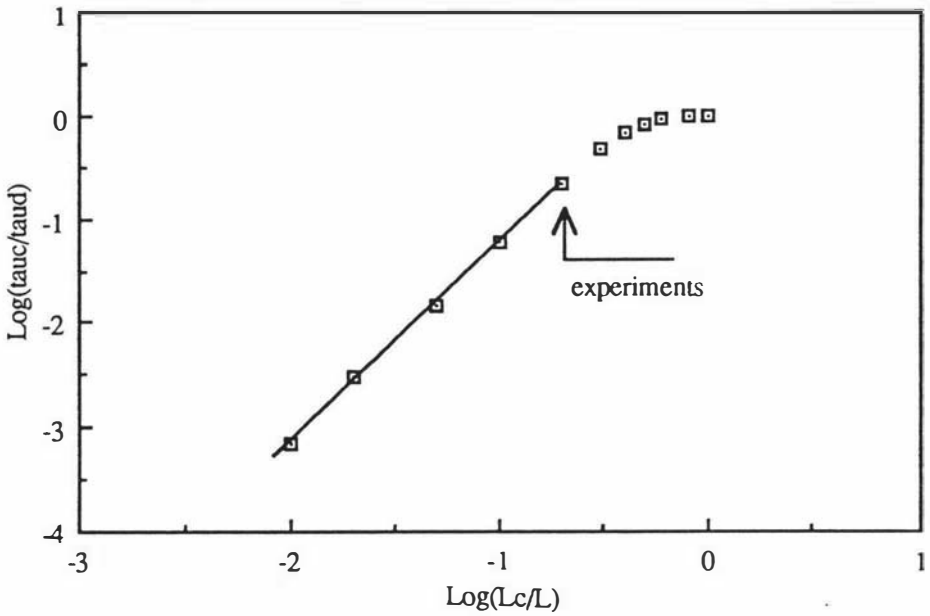

Figure 9.21 Relationship between the e^{-1} relaxation time, τ_c, and the length of the end tube, L_c, in the Doi-Edwards model

---

Numerical examination of Eq[9.10] shows that the e^{-1} relaxation time for $\varphi(t)$ depends quadratically on L_c/L only for $L_c<0.2L$ as shown in Figure 9.21. For larger values the dependence is weaker. In the experiments carried out here the shear rate ranges from below τ_d^{-1} to approximately $5\tau_d^{-1}$ at the edge of the capillary, a regime which contains only a small "quadratic" region as indicated in Figure 9.21. The average dependence of τ_c/τ_d on L_c/L is approximately linear over this region. In applying the"end tube" model both the linear approximation and a direct functional dependence of τ_c/τ_d on L_c/L obtained will be used by fitting a fourth order polynomial to the points shown in Figure 9.21. Thus a function f may be defined such that

$$\frac{L_c}{L} = f(\tau_c/\tau_d) \qquad [9.11]$$

In applying the condition$\gamma = \tau_c^{-1}$, it is helpful to make use of the equilibrium relationships for a "melt of n blobs", where each blob of size ξ_m is governed by the usual dilute solution statistics. Thus

$$\xi_m \approx bg^{\nu} \qquad [9.12]$$

$$\tau_d \approx \frac{3\pi\eta_0 n^3 \xi_m^3}{k_B T} \qquad [9.13]$$

where g is the number of statistical subunits of size b per blob. The total number of statistical subunits in the chain is given by N=ng. ξ_m and g are defined by the equilibrium concentration since $c \approx mg/\xi_m^3$ where m is the mass of one sub-unit. Since the concentration c* may be defined in a similar manner as that of mN/R_0^3, useful empirical estimates for n and ξ_m are given by[184]

$$n = \left(\frac{c}{c^*}\right)^{1/(3\nu-1)} \qquad [9.14]$$

$$\xi_m = R_0\left(\frac{c}{c^*}\right)^{-\nu/(3\nu-1)} \qquad [9.15]$$

Since $L=n\xi_m$ and $L_c=n_c\xi_m$, application of the linear dependence assumption, $\tau_c=\tau_d(L_c/L)$, to Eq[9.13] yields,

$$n_c = \left[\frac{k_BT}{3\pi\eta_0\dot{\gamma}\xi_m^3 n^2}\right] \qquad [9.16a]$$

Alternatively, using the exact functional dependence it is found

$$n_c = n\, f\left(\frac{k_BT}{3\pi\eta_0\dot{\gamma}\xi_m^3 n^3}\right) \qquad [9.16b]$$

The self-diffusion coefficient for Brownian motion along the direction of shear may thus be estimated as

$$D_{shear} \approx \frac{[2\xi_c+(n-2n_c)\xi_m]^2}{2\tau_d} \qquad [9.17]$$

This equation will break down when the shear rate is less than or of order τ_d^{-1} since it does not account for the amalgamation of the two "end tubes" when $n \approx n_c$. However it is clear that D_s approaches the equilibrium self-diffusion coefficient in this region so that we may directly assign this value when the shear rate is small. For large shears, such that $n_c \ll n$, the "end tubes" disappear and Eq[9.17] predicts a maximum self-diffusion rate

$$D_{max} = 3nD_s \qquad [9.18]$$

Therefore it may be speculated that the maximum diffusion rate apparent in the region near the capillary edge corresponds to polymer in which the shear rate is

sufficiently large that no "end tube" entanglements are present. Given an apparent c* of order 0.5 % w/v and an equilibrium D_s value of 1×10^{-14} m^2s^{-1}, D_{max} should be of order 5×10^{-13} m^2s^{-1}. This is remarkably close to the observed value.

The model used here[180] to explain the diffusive enhancement for r>0.5R is consistent with the notion that centre-of-mass diffusion can be effectively observed, despite the fact that $\Delta<\tau_d$. In this enhancement region the linear extension of the central section of the polymer implies that semi-local internal motion and centre-of-mass diffusion along the direction of flow are indistinguishable. Furthermore curvilinear reptation, which results in differing laboratory frame components of semi-local and centre-of-mass motion, occurs only at the polymer ends and then with a relaxation time, τ_c, which is shorter than the observation time Δ.

Eq[9.14] to Eq[9.17] enable the diffusion profile to be calculated directly from a knowledge of R_0 and c* alone, without the need for any additional adjustable parameters apart from the power law exponent, ν, which is assigned the value 0.6 for convenience. Of course our estimates of 1500 Å and 0.5 % w/v respectively are somewhat coarse given the polydispersity of WSR301 PEO. Nonetheless they serve in providing a reasonable test of the model. The theoretical curve based on these parameters and using the approximate linear dependence of end tube relaxation on L/L_c is shown in Figure 9.22a. The best fit to the data results using R_0=1400Å. Figure 9.22b shows the theoretical prediction when the end tube relaxation rate has the correct functional dependence on L/L_c. In this case the best fit results when R_0=1300Å. Both models reproduce several key features of the data. There is a sharp break in D_{shear} at a critical radius of about 1/2 the radius of the capillary. The dependence of D_{shear} on radius beyond the critical radius is approximately linear and at high shear rates near the edge of the capillary the theoretical values of D_{shear} rise less rapidly, approaching a plateau value of $3nD_s$. However it is clear that this plateau is not quite reached in the theoretical prediction so that this feature of the data cannot be explained using the simple model employed here.

The perturbation to polymer entanglement caused by the fluid shear will inevitably influence the Brownian motion of the solvent molecules, although this effect is bound to be quite minor in comparison with the polymer motion. The small enhancement of water diffusion apparent in Figure 9.15 is consistent with this effect. Finally it should be noted that it is also possible to probe very local molecular properties using NMR relaxation times. In the present instance it has been investigated whether there is evidence for local molecular ordering in the high shear region of the capillary.

(a) The linear approximation fit

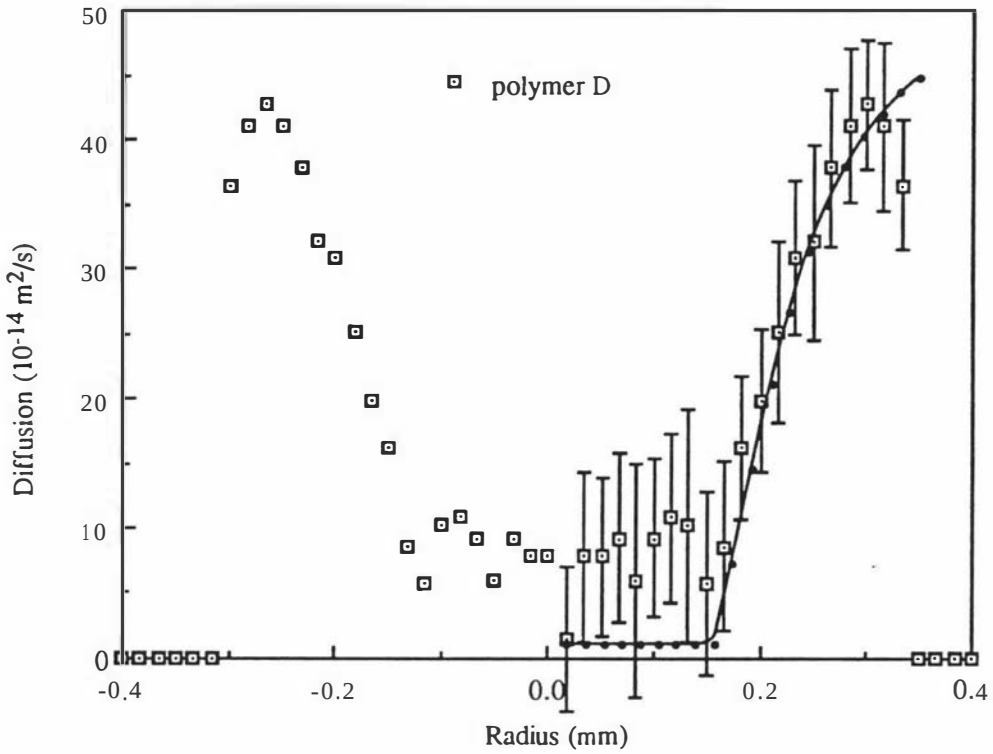

(b) The exact solution fit

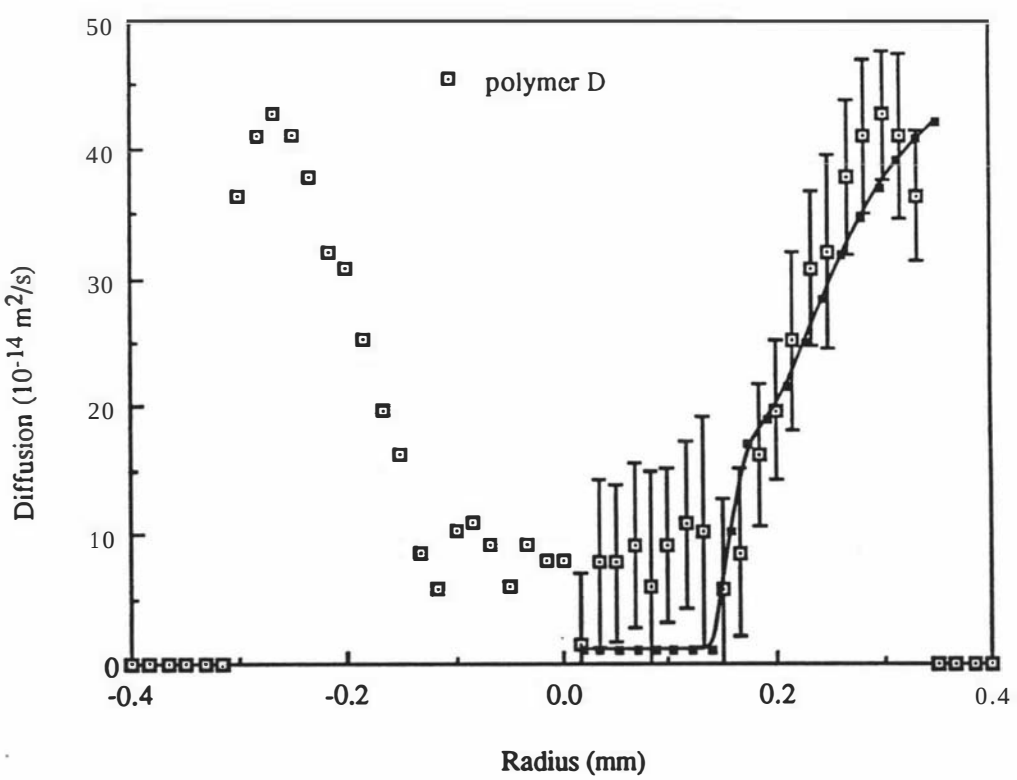

Figure 9.22 Experimental and theoretical polymer diffusion profiles for the 4.5% w/v WSR301 PEO/D_2O in flow

Any alignment will inevitably result in anisotropy of the proton-proton dipolar interaction in the CH_2 groups of the poly(ethylene oxide) segments. This would be manifested via enhanced transverse relaxation in a Hahn echo experiment although the dephasing caused by this local order would be refocussed in a solid echo. An examination has been carried out which compares Hahn and solid echo polymer images obtained for the 4.5% w/v WSR301 PEO/D_2O solution under the same flow conditions which produced diffusion enhancement. After compensating for the lower signal efficiency of the solid echo (approximately a factor of two), there is no evidence for shear-dependent relaxation effects so that the measurement suggests orientational disorder on a local scale. This is entirely consistent with the depiction of Figure 9.20b where alignment occurs only on a scale larger than a blob.

9.6 Conclusion

In the experiments described in this chapter, velocity profiles have been measured for water solutions of WSR301 PEO in laminar flow through a 700 μm i.d. capillary as a function of concentration and pressure gradient. A transition from Poiseuille flow to power law shear-thinning is apparent as the concentration is increased above c*. Equilibrium self-diffusion coefficients have been measured as a function of concentration for WSR301 PEO and as a function of molar mass for monodisperse PEO standards in D_2O and it is apparent that the data are consistent with the usual reptative scaling behaviour. A measurement of self-diffusion of PEO in the presence of the flow field indicates that shear thinning is associated with significant enhancement of the polymer Brownian motion along the axis of shear and these data are interpreted using a simple adaptation of the entanglement/blob model.

The analysis regarding to the PEO diffusion enhancement must necessarily be tempered by the fact that the polymer used in these capillary flow experiments is highly polydisperse, which is the reason of there is no evidence for the so-called 'spurt effect' in the experiments. Nonetheless several conclusions may be drawn. Dynamic NMR microscopy can become a powerful tool in studies of polymer dynamics, specially because it can provide precise velocity profiles to a spatial resolution of a few tens of microns, while at the same time making accessible measurements at the molecular level at various positions in the flow field. In particular it has been shown that it is possible to measure self-diffusion rates some 4 orders of magnitude slower than that of the free

water molecule in a flow field where the velocity spread in a single pixel greatly exceeds the spread due to Brownian motion.

In the present work clear evidence is seen for the breakdown of entanglements in semi-dilute solutions once the shear rate exceeds the equilibrium tube renewal rate, τ_d^{-1}. Application of some simple ideas from reptation theory and the blob model for semi-dilute polymer solutions has proven remarkably successful in explaining several qualitative features of the data. A more precise analysis awaits a repeat of these experiments using monodisperse polymer.

Chapter 10 Summary and Future Work

This thesis sets out to demonstrate that Dynamic NMR Microscopy can be used to obtain unique information about molecular dynamics of relevance to plant physiology, fluid dynamics and polymer physics, with a spatial resolution as fine as tens microns, with a velocity resolution down to several microns per second and with a self-diffusion sensitivity as low as several orders of magnitudes smaller than that of free water molecules.

By various modifications to and development of the existing imaging system, the water capillary flow experiments have shown that simultaneous measurement of velocity and self-diffusion can be made both accurately and precisely using Dynamic NMR Microscopy. Furthermore, the flow experiment in the junction region of an abrupt contraction and expansion in a tube demonstrated a measurement of the axial and radial components of a complex velocity field. Induced secondary flow, eddy, around the abrupt junction was observed. To our knowledge, this is the first quantitative measurement at microscopic resolution for such sample configurations. The velocity profiles were also compared with solutions of the Navier-Stokes equation obtained by finite difference numerical methods and the agreement is excellent.

Several *in vivo* botanical studies presented in this work have shown the potential applications of both Dynamic NMR Microscopy and the more time-efficient 'one-shot' velocity imaging method in plant physiology and other biological sciences. As indicated in these studies, conclusive results require great care in experimental planning, repeated experiments and the need for equipment purposefully-constructed to accommodate life-supporting systems. All these requirements are due to the delicacy of dynamic processes associated with the living botanical samples. The velocities of approximately 10 μm/s in the castor bean experiment and 45 μm/s in the *Stachys* experiment are to our knowledge the lowest flow rates that have ever been measured in NMR imaging experiments.

The polymer capillary flow experiments have shown that Dynamic NMR Microscopy can be used to investigate unusual rheological properties of high molar mass polymer solutions. In particular, a non-Newtonian fluid, poly(ethylene oxide), was studied. Velocity profiles for water solutions of WSR301 PEO in capillary flow were measured and fitted using the power law model. Self-diffusion profiles for monodisperse PEO standards in D_2O in the presence of the flow field were also measured. These were some four orders of magnitude slower than that of the free water

molecules in a flow field where the velocity spread in a single pixel greatly exceeds the spread due to Brownian motion. Clear evidence for the breakdown of molecular entanglements in semi-dilute solutions was observed once the shear rate exceeds the equilibrium tube renewal rate, τ_d^{-1}. The results were interpreted successfully using a simple adaptation of the entanglement/blob model.

From the experiments described in this thesis there is no doubt that Dynamic NMR Microscopy is a more sophisticated and comprehensive technique in comparison with the 'one-shot' velocity imaging method. However, there are some situations where the time-efficient 'one-shot' method could be a preferable choice provided that the sacrifice of the diffusion information is acceptable. In particular there are two nice features of the 'one-shot' velocity imaging method. First, due to the fact that only moving water contributes to the velocity signal, the values measured in 'one-shot' method should be a true representation of the average fluid flow in a single pixel despite the fact that both stationary and moving spins may present. In comparison, Dynamic NMR Microscopy collects signals from both stationary and moving spins within a single pixel therefore resulting in an 'averaged' velocity which may not precisely equal the true mean value. The second nice feature of the 'one-shot' method is that the magnitude of the velocity can be estimated (to some extent) during the on-line acquisition of $\rho_{odd}(\mathbf{r})$ signal. This feature therefore provides an early indication if the vascular flow of the sample stops during the experiment. The velocity-sensitive sequence of the 'one-shot' method can also be used to produce 1-D velocity profile in short time. By contrast, the more comprehensive Dynamic NMR Microscopy requires much more time in which the flow rate of the sample needs to be stable. However, the 'one-shot' method requires excellent stationary signal suppression and hence is more sensitive to the presence of back-ground noise, external interference and induced eddy currents whereas Dynamic NMR Microscopy is far less susceptible to these effects and gives considerable more accurate and precise results.

All the imaging experiments described in this work were carried out in a home-made imaging system based on a FX-60 spectrometer with a standard electromagnet. While the electromagnet geometry has some unique advantages over the vertical-bore superconducting magnets, its major drawback is the low sensitivity associated with the low polarizing field. This, together with the rather old 1974 spectrometer, has made imaging experiments non-trivial and time consuming. During the period of this work, there has been another unstated project which involved the design of an imaging system based on a 270 MHz spectrometer with a vertical wide-bore superconducting magnet. Most of the designs and some of the manufacture of the imaging additions have been done up to now. Due to the limitation of time and other non-technique reasons, this

project hasn't been completed and tested. The completion of this project and the arrival of a new 300 MHz commercial imaging instrument in the early 1992 will greatly improve the efficiency, precision, quality and ability of future imaging experiments.

Possible future experiments

Through the results presented in this thesis, it is clear that Dynamic NMR Microscopy is an accurate, sensitive and reliable technique which can be used to measure molecular motions in a totally non-invasive way. There are at least three different areas where Dynamic NMR Microscopy can be extremely useful, namely *in vivo* biological studies, rheological dynamics and polymer physics. There are several immediate future experiments which could be carried out using Dynamic NMR Microscopy.

The *in vivo* biological applications using Dynamic NMR Microscopy are obviously very challenging. For each of the *in vivo* imaging experiments described in this thesis, there remains further work which could be followed up. For example, the castor bean seedling offers an ideal sample system to study the xylem and the phloem flow in vascular tissues, further measurements should be made with an improved signal to noise ratio and resolution. Repeated wheat grain experiments could clarify the initial results regarding to the relationship between the vascular flow rate and the age of the grain. The *Stachys* experiment has shown some curious and unique features of the sample structure, further flow experiments together with the determination of $T_1(\mathbf{r})$ and $T_2(\mathbf{r})$ distributions will be very interesting in the understanding of susceptibility variations in the vascular tissue (the construction of true $T_1(\mathbf{r})$ and $T_2(\mathbf{r})$ maps are trivial with the modification to ImageShow™ software).

It should be noted that the choice of some plant samples in this work was determined by a desire to challenge the newly developed technique rather than by the biological or physiological significance of the samples, and that some experimental conditions and discussions in this work may reflect a physicist's 'conceptual' view of plants. With the confidence in Dynamic NMR Microscopy technique, the new high-field instrument and a bigger input from plant physiologists and botanists, experiments using biological- or physiological-significant samples at more careful experimental conditions will produce results which are more important in plant physiology and botany. For example, a systematic study of several different species of wheat grain could be not only very significant in plant physiology but also very important in economy.

Dynamic NMR Microscopy has proved to be a unique and powerful tool in the rheological studies. Further experiments imaging flows in non-circular tubes or other

abrupt configurations would be very interesting in rheological modelling, numerical simulation and hydrodynamic engineering. Although the current capillary flow device has the advantages of simplicity and stability, it requires a large amount of sample in circulation. A Couette geometry which consists of two concentric tubes with one stationary and the other in rotation also offers a wide range of velocity shear and can be used in Dynamic NMR Microscopy. Although this concentric tube device has the advantage of requiring very small amount of sample, it is relative complex to construct, demands high manufacturing precision and mechanical stability if high velocity shear is required and introduces some electrical and mechanical noise. A further disadvantage of this concentric tube device is that precious central space of the sample volume is wasted due to the presence of the central tube. Consequently, a bigger rf receiver coil has to be used which results in a lower detection sensitivity. However, the advantage of this device, namely the small-amount of sample, could become overwhelmingly important in many rheology experiments using expensive samples.

In studies of non-Newtonian fluids, Dynamic NMR Microscopy will be uniquely important due to its totally non-invasive detection and fine spatial resolution (down to 10 μm). Measurements of velocity profiles for non-viscometric flows such as those occurring at abrupt contractions and expansions are excellent tests for any proposed constitutive equation. The fine spatial resolution in images allows a very accurate measurement of the behaviour of non-Newtonian fluids at solid boundaries, since it is now recognized that the extensional viscosity is important in any discussion of non-Newtonian fluid behaviour.

In the PEO flow experiment described in this thesis, the so-called 'spurt effect' predicted for polymer in shear flow when the shear stress begins to decrease at some specific shear rate has not been observed due to the polydispersity of the sample. A repeat of these experiments using monodisperse polymer sample is expected in the near future which should provide a more precise 'picture' of the polymer dynamics.

The reptation theory and the tube model present a theoretical description for the dynamics of entangled polymer flows. The shear-dependent viscosity measurements performed by conventional rheometers provide a classical macroscopic test of the model. It has been shown in this thesis that the microscopic test of the model can be carried out by Dynamic NMR Microscopy to measure the shear-dependent Brownian motions. If the usual rotating cone-and-plate rheometer is constructed at the sample space in an imaging probe, these two types of shear-dependent measurements can in fact be performed simultaneously. The cone-and-plate device will have the same advantages of the previously discussed concentric tube device.

Possible methodological and experimental improvements

In terms of further improvements of the current methodology and instrument, filtered back-projection reconstruction, and possibly Fourier Imaging, are expected to be the main image reconstruction algorithms employed due to the high sensitivity. The fast imaging methods widely used in MRI such as Echo Planar Imaging will have little use in NMR microscopy due to the sensitivity loss. With the scaling up of Dynamic NMR Microscopy, however, these fast imaging methods could become the method of choice in q-space flow and diffusion imaging.

One difficulty associated with *in vivo* biological flow imaging is the instability of the sample, for example, the slow-down of the flow rate or even slow dying of the sample as shown in the moss (*Dendroligotrichum dewdroides*) experiment. One way to improve the chance of successful experiments is to change the order of angle increment in the PR algorithm. The standard algorithm uses a gradual angle increment such as 0, 2, 4, 6, 8, ... If the flow becomes slower or even stops during the process of imaging, the experiment will fail. A better angle increment sequence would be, for example, 0, 90, 180, 270; 44, 134, 224, 314; 22, 66, 112, 156, 202, 246, 292, 336; .... Therefore any slow-down of the flow rate will have an equal impact on the final image. This modification would be especially important in the 'one-shot' velocity microscopy. Such improvement can be done by the software modification.

In the present botanical studies, some improvement in sample preparations and more controlled experimental conditions may improve the results. For example, it has been pointed out, while this manuscript was being written, that the failure to measure vascular flow in some wheat grain experiments could be due to the effect of osmotic pressure change caused by numerous 'wounds' at the spikelet locations in the rachis. A better method to reduce the osmotic pressure change is to seal the 'leak' using wax. Such sample preparation should also lead to more accurate velocity measurement. It has also been pointed out that less attention has been paid to the effect of various soluble ions and nutrients in the root solution in some plant flow experiments (for example, the *Stachys* experiment). This is because various soluble ions in the root solution could effect the flow rate of sample. If one considers the effect of susceptibility variations in the vascular tissue in an imaging experiment, this consideration is more important.

Possible further applications

In many research areas such as chemistry or biological sciences, electrophoresis is a commonly used technique which separates ion-bonded molecules or particles on the basis of their drifts in an electrical field. The conventional method to visualise the separations is to dye the entire column to form the so-called 'finger prints'. However,

the mobility of some macro-molecules or particles, such as polymers or biological cells, could be several $\mu m\ s^{-1}\ cm\ V^{-1}$, which suggests another application of Dynamic NMR Microscopy, detecting the motions of molecules or particles in electrophoresis. The liquid or liquid-like media in electrophoresis permit the measurement of mobile particles at the direction of the electrical field lines. This is contrasted with other types of motions which are more difficult to measure, the oil/water flow in porous structures or liquid flow in chromatography. In these situations, although the long-range direction of molecular motions are along the pressure gradient lines, the local direction of molecular velocity could be in any arbitrary direction because the mobile molecules move between the gaps of closely packed solid obstacles. Furthermore, the solid obstacles in these situations are often small in comparison with the image slice thickness. Thus the signal averaging occurs within the image volume element.

With the arrival of the new high-field commercial imaging instrument, many experiments well-established in the NMR literature can be made possible or performed much more easily in our laboratory. For example, although Dynamic NMR Microscopy is theoretically a six-dimensional technique, only a four-dimensional approach has been used in this thesis. This is because any increase of q-dimensions will inevitably lead to excessively long experimental times. However there are some situations where one wishes to measure more than one q-dimension simultaneously or to measure velocity and self-diffusion at more than one slice position of a sample, such as the abrupt flow experiment or some biological applications. One possible solution to a more time-efficient Dynamic NMR Microscopy experiment is to incorporate Dynamic NMR Microscopy with multi-slicing techniques where the waiting time interval T_R can be used to obtain q-slices at other slice positions at no increase of experimental time.

The modern imaging instrument will also permit new applications of Dynamic NMR Microscopy. For example, chemical shift is an important parameter in many biological samples and has been used in the differentiation of biological tissues. It should be possible to image flows of chemically selected species by first chemically selecting a certain species and applying Dynamic NMR Microscopy subsequently. The same philosophy can also be applied to combine the relaxation time selection and Dynamic NMR Microscopy so to image part of the sample's flow field with specific relaxation times. A further natural extension of applications of Dynamic NMR Microscopy is to selectively map flows of other nuclei of interest such as ^{31}P which is of considerable biological importance.

References

1. Abragam, A.: "The Principles of Nuclear Magnetism", *Clarendon*, Oxford, (1960).

2. Slichter, C.P.: "Principles of magnetic resonance", *Harper and Row*, New York, (1963).

3. Shaw, D.: "Fourier Transform NMR Spectroscopy", *Elsevier*, Amsterdam, (1976).

4. Blum, K.: "Density Matrix Theory and Applications", *Plenum*, New York, (1981).

5. Ernst, R.R., Bodenhausen, G., and Wokaun, A.: "Principles of Nuclear Magnetic Resonance in One and Two Dimensions", *Clarendon*, Oxford, (1987).

6. Bloch, F., Hansen, W.W., and Packard, M.E.: "Nuclear induction", *Phys. Rev.*, **69**, 127 (1946).

7. Purcell, E.M., Torrey, H.C., and Pound, R.V.: "Resonance absorption by nuclear magnetic moments in a solid", *Phys. Rev.*, **69**, 37 (1946).

8. Bloch, F.: "Nuclear induction", *Phys. Rev.*, **70**, 460 (1946).

9. Hoult, D.I. and Richards, R.E.: "The Signal-to-Noise Ratio of the Nuclear Magnetic Resonance Experiment", *J. Magn. Reson.*, **24**, 71-85 (1976).

10. Hoult, D.I.: "The NMR Receiver: A Description and Analysis of Design", *Progress in NMR Spectroscopy*, **12**, 41-77 (1978).

11. Hahn, E.L.: "Spin echoes", *Phys. Rev.*, **80**, 580-594 (1950).

12. Hoult, D.I. and Richards, R.E.: "Critical factors in the design of sensitive high resolution nuclear magnetic resonance spectrometers", *Proc. R. Soc. Lond. A*, **344**, 311-340 (1975).

13. Garroway, A.N., Grannell, P.K., and Mansfield, P.: "Image formation by a selective irradiative process", *J. Phys. C: Solid State Phys*, **7**, L457-462 (1974).

14. Eccles, C.D. and Callaghan, P.T.: "Nuclear Magnetic Resonance Microscopy", *JEOL News*, **23A**(1), 10-15 (1987).

15. Balies, D.R. and Bryant, D.J.: "NMR Imaging", *Contemp. Phys.*, **25**(5), 441-475 (1984).

16. Brigham, E.O.: "The Fast Fourier Transform", *Prentice-Hall*, New Jersey, (1974).

17. Mansfield, P. and Grannell, P.K.: "NMR 'diffraction' in solids?", *J. Phys. C: Solid State Phys.*, **6**, L422 (1973).

18. Brooks, R.A. and Di Chiro, G.: "Principles of Computer Assisted Tomography (CAT) in Radiographic and Radioisotopic Imaging", *Phys. Med. Biol.*, **21**(5), 689-732 (1976).

19. Kumar, A., Welti, D., and Ernst, R.R.: "NMR Fourier Zeugmatogaphy", *J. Magn. Reson.*, **18**, 69-83 (1975).

20. Edelstein, W.A., Hutchinson, J.M.S., Johnson, G., and Redpath, T.W.: "Spin warp imaging and applications to human whole-body imaging", *Phys. Med. Biol.*, **25**, 751 (1980).

21. Johnson, G., Hutchinson, J.M.S., Redpath, T.W., and Eastwood, L.M.: "Improvements in performance time for simultaneous three-dimensional NMR imaging", *J. Magn. Reson.*, **54**, 374-384 (1983).

22. Lauterbur, P.C.: "Imaging formation by induced local interactions: examples employing nuclear magnetic resonance", *Nature*, **242**, 190-191 (1973).

23. Kamei, H. and Katayama, Y.: "Microscopic NMR Imaging", in "IEEE/ Eight Annual Conference of the Engineering in Medicine and Biology Society", Fort Worth, Texas, (1986).

24. Aguayo, J.B., Blackband, S.J., Schoeniger, J., Mattingly, M., and Hinterman, M.: "Nuclear magnetic resonance imaging in a single cell", *Nature*, **322**(10), 190-191 (1986).

25. Eccles, C.D. and Callaghan, P.T.: "High-Resolution Imaging. The NMR Microscope", *J. Magn. Reson.*, **68**, 393-398 (1986).

26. Johnson, G.A., Thompson, M.B., Gewalt, S.L., and Hayes, C.E.: "Nuclear Magnetic Resonance Imaging at Microscopic Resolution", *J. Magn. Reson.*, **68**, 129-137 (1986).

27. Callaghan, P.T. and Eccles, C.D.: "Sensitivity and Resolution in NMR Imaging", *J. Magn. Reson.*, **71**, 426-445 (1987).

28. Haase, A., Frahm, J., Matthaei, D., Hänicke, W., and Merbolt, K.-D.: "FLASH Imaging: Rapid NMR Imaging Using Low Flip-Angle Pulses", *J. Magn. Reson.*, **67**, 258-266 (1986).

29. Gyngell, M.L.: "The Application of Steady-State Free Precession in Rapid 2DFT NMR Imaging: FAST and CE-FAST Sequences", *Magn. Reson. Imaging*, **6**, 415-419 (1988).

30. Mansfield, P.: "Multi-planar image formation using NMR spin echoes", *J. Phys. C: Solid State Phys.*, **10**, L55-L58 (1977).

31. Mansfield, P. and Pykett, I.L.: "Biological and Medical Imaging by NMR", *J. Magn. Reson.*, **29**, 355-373 (1978).

32. Ernst, R.R.: "Methodology of magnetic resonance imaging", *Quarterly Rev. Biophys.*, **19**(3/4), 183-220 (1987).

33. Mansfield, P. and Morris, P.G.: "NMR Imaging in Biomedicine", *Academic Press*, New York, (1982).

34. Maudsley, A.A., Hilal, S.K., Perman, W.H., and Simon, H.E.: "Spatially Resolved High Resolution Spectroscopy by "Four-Dimensional" NMR", *J. Magn. Reson.*, **51**, 147 (1983).

35. Martin, J.F. and Wade, C.G.: "Chemical-Shift Encoding in NMR Images", *J. Magn. Reson.*, **61**, 153-157 (1985).

36. Haase, A. and Frahm, J.: "Multiple Chemical-Shift-Selective NMR Imaging Using Stimulated Echoes", *J. Magn. Reson.*, **64**, 94-102 (1985).

37. Pope, J.M. and Sarafis, V.: ed. "Chemistry in Australia", Vol. **57**, *Royal Australian Chemical Institute*, Melboume, 221 (1990).

38. Callaghan, P.T.: "Principles of Nuclear Magnetic Resonance Microscopy", *Oxford University Press*, Oxford, (1991).

39. Posse, S. and Aue, W.P.: "Susceptibility Artifacts in Spin-Echo and Gradient-Echo Imaging", *J. Magn. Reson.*, **88**, 473-492 (1990).

40. Suryan, G.: "Nuclear resonance in flowing liquids", *Proc. Indian Acad. Sci. [Sect. A]*, **33**, 107-111 (1951).

41. Carr, H.Y. and Purcell, E.M.: "Effects of Diffusion on Free Precession in Nuclear Magnetic Resonance Experiments", *Phys. Rev.*, **94**(3), 630-638 (1954).

42. Packer, K.J.: "The study of slow coherent molecular motion by pulsed nuclear magnetic resonance", *Mole. Phys.*, **17**(4), 355-368 (1969).

43. Jones, D.W. and Child, T.F.: "NMR in Flowing System", *Adv. in Magn. Reson.*, 123-148 (1976).

44. Singer, J.R.: "NMR diffusion and flow measurements and an introduction to spin phase graphing", *J. Phys. E: Sci. Instrum.*, **11**, 281-291 (1978).

45. Singer, J.R.: "Blood flow rates by nuclear magnetic resonance measurements", *Science*, **130**, 1652 (1959).

46. Arnold, D.W. and Burkhart, L.E.: "Spin-Echo NMR Response from a Flowing Sample", *J. Appl. Phys.*, **36**, 870-871 (1965).

47. Karczmar, G.S., Twieg, D.B., Lawry, T.J., Matson, G.B., and Weiner, M.W.: "Detection of Motion Using B_1 Gradients", *Magn. Reson. Med.*, **7**, 111-116 (1988).

48. Bourgeois, D. and Decorps, M.: "A B_1 Gradient Method for the Detection of Slow Coherent Motion", *J. Magn. Reson.*, **91**, 128-135 (1991).

49. Hahn, E.L.: "Detection of Sea-Water Motion by Nuclear Precession", *J. Geophys. Res.*, **65**(2), 776-777 (1960).

50. Stejskal, E.O. and Tanner, J.E.: "Spin Diffusion Measurements: Spin Echoes in the Presence of a Time-Dependent Field Gradient", *J. Chem. Phys.*, **42**(1), 288-292 (1965).

51. Walton, J.H. and Conradi, M.S.: "Flow Velocity Measurement with ac Gradients", *Magn. Reson. Med.*, **4**, 274-281 (1987).

52. Klammler, F. and Kimmich, R.: "An NMR method for volumn-selective determination of velocities by frequency encoding", *J. Phys. E: Sci. Instrum.*, **22**, 74-78 (1989).

53. Stejskal, E.O.: "Use of Spin Echoes in a Pulsed Magnetic-Field Gradient to Study Anisotropic Restricted Diffusion and Flow", *J. Chem. Phys.*, **43**(10), 3597-3603 (1965).

54. Moran, P.R. and Moran, R.A.: "Imaging True Motion Velocity and Higher Order Motion Quantities by Phase Gradient Modulation Techniques in NMR Scanners", in "Technology of NMR", P.D. Esser and Johnson, R.E., Editor. *New York Soc. Nucl. Med.*, New York, p. 149 (1984).

55. Young, I.R., Bydder, G.M., and Payne, J.A.: "Flow Measurement by the Development of Phase Differences during Slice Formation in MR Imaging", *Med. Reson. Med.*, 3, 175-179 (1986).

56. Cho, Z.H., Oh, C.H., Kim, Y.S., Mun, C.W., Nalcioglu, O., Lee, S.J., and Chung, M.K.: "A new nuclear magnetic resonance imaging technique for unambiguous unidirectional measurement of flow velocity", *J. Appl. Phys.*, **60**(4), 1256-1262 (1986).

57. Cho, Z.H., Oh, C.H., Mun, C.W., and Kim, Y.S.: "Some results of High-Flow-Velocity NMR Imaging Using Selection Gradient", *Magn. Reson. Med.*, **3**, 857-862 (1986).

58. Kim, Y.S., Mun, C.W., Jung, K.J., and Cho, Z.H.: "Further Improvement of High-Speed NMR Flow-Velocity Measurement Using a Differential Phase-Encoding Technique", *Magn. Reson. Med.*, **4**, 289-296 (1987).

59. Singer, J.R.: "Blood Flow Measurements by NMR of the Intact Body", *IEEE Trans. Med. Imaging*, **NS-27**(3), 1245-1249 (1980).

60. Battocletti, J.H., Halbach, R.E., Salles-Cunha, S.X., and Sances, A., Jr: "The NMR blood flowmeter-theory and history", *Med. Phys.*, **8**(4), 435-443 (1981).

61. Crooks, L.E.: "Recent developments in nuclear magnetic resonance imaging and flow measurements", *IEEE Trans. Nucl. Sci.*, **NS-31**(4), 1006-1009 (1984).

62. Bradley, W.G., Jr, Waluch, V., Lai, K.S., Fernandez, E.J., and Spalter, C.: "The Appearance of Rapidly Flowing Blood on Magnetic Resonance Images", *Am. J. Roentgeno.*, **143**, 1167-1174 (1984).

63. van Dijk, P.: "Direct Cardiac NMR Imaging of Heart Wall and Blood Flow Velocity", *J. Comput. Assist. Tomogr.*, **8**(3), 429-436 (1984).

64. Axel, L.: "Blood Flow Effects in Magnetic Resonance Imaging", *Am. J. Roentgeno.*, **143**, 1157-1166 (1984).

65. O'Donnell, M.: "NMR blood flow imaging using multiecho, phase contrast sequences", *Med. Phys.*, **12**(1), 59-64 (1985).

66. Nayler, G.L., Firmin, D.N., and Longmore, D.B.: "Blood Flow Imaging by Cine Magnetic Resonance", *J. Comput. Assist. Tomogr.*, **10**(5), 715-722 (1986).

67. Swain, I.D. and Grant, L.J.: "Methods of measuring skin blood flow", *Phys. Med. Biol.*, **34**(2), 151-175 (1989).

68. Garroway, A.N.: "Velocity measurements in flowing fluids by NMR", *J. Phys. D: Appl. Phys.*, **7**, L159-L163 (1974).

69. Singer, J.R. and Crooks, L.E.: "Nuclear Magnetic Resonance Blood flow Measurements in the Human Brain", *Science*, **221**, 654-656 (1983).

70. Kose, K., Satoh, K., Inouye, T., and Yasuoka, H.: "NMR flow Imaging", *J. Phys. Soc. Japan*, **54**(1), 81 (1985).

71. Axel, L., Shimakawa, A., and MacFall, J.: "A Time-of-Flight Method of Measuring Flow Velocity by Magnetic Resonance Imaging", *Magn. Reson. Imaging*, **4**, 199-205 (1986).

72. Merboldt, K.-D., Hänicke, W., and Frahm, J.: "Flow NMR Imaging Using Stimulated Echoes", *J. Magn. Reson.*, **67**, 336-341 (1986).

73. Wehrli, F.W., Shimakawa, A., Gullberg, G.T., and MacFall, J.: "Time-of-Flight MR Flow Imaging: Selective Saturation Recovery with Gradient Refocusing", *Radiology*, **160**, 781-785 (1986).

74. Saloner, D., Moran, P.R., and Tsui, B.M.W.: "Velocity imaging by rapid cycle tagging", *Med. Phys.*, **14**(2), 167-171 (1987).

75. Foo, T.K.F.: "Non-Subtractive MR Angiography using Stimulated Echoes", in "Abstracts of 8th Annual Meeting, SMRM", Amsterdam, Netherlands, (1989).

76. Patz, S. and Hawkes, R.C.: "The Application of Steady-State Free Precession to the Study of Very Slow Fluid Flow", *Magn. Reson. Med.*, **3**, 140-145 (1986).

77. Tyszka, M., Hawkes, R.C., and Hall, L.D.: "Steady State Free Precession Moving Reference Frame Sensitivity", in "Abstracts of 8th Annual Meeting, SMRM", Amsterdam, Netherlands, (1989).

78. Waluch, V. and Bradley, W.G.: "NMR Even Echo Rephasing in Slow Laminar Flow", *J. Comput. Assist. Tomogr.*, **8**(4), 594-598 (1984).

79. Feinberg, D.A., Crooks, L.E., Sheldon, P., Hoenninger, J., III, Watts, J., and Arakawa, M.: "Magnetic Resonance Imaging the Velocity Vector Components of Fluid Flow", *Magn. Reson. Med.*, **2**, 555-566 (1985).

80. Frahm, J., Merboldt, K.-D., Hänicke, W., and Haase, A.: "Flow Suppression in Rapid FLASH NMR Images", *Magn. Reson. Med.*, **4**, 372-377 (1987).

81. Redpath, T.W. and Jones, R.A.: "FADE-A New Fast Imaging Sequence", *Magn. Reson. Med.*, **6**, 224 (1988).

82. Lee, J.N., Riederer, S.J., and Pelc, N.J.: "Flwo-Compensated Limited Flip Angle MR Angiography", *Magn. Reson. Med.*, **12**, 1-13 (1989).

83. Nishimura, D.G., Macovski, A.M., and Pauly, J.M.: "Magnetic Resonance Angiography", *IEEE Trans. Med. Imaging*, **MI-5**(3), 140-151 (1986).

84. Moran, P.R.: "A Flow Velocity Zeugmatographic Interlace For NMR Imaging in Humans", *Magn. Reson. Imaging*, **1**, 197-203 (1982).

85. Bourgeois, D. and Decorps, M.: "Quantitative imaging of slow coherent motion by simulated echoes with suppression of stationary water signal", *J. Magn. Reson.*, **94**(1), 20-33 (1991).

86. Lucas, P.G.J., Penman, D.A., Tyler, A., and Vavasour, E.: "Measurement of fluid flow profiles using pulsed NMR", *J. Phys. E: Sci. Instrum.*, **10**, 1150-1152 (1977).

87. Bourgeois, D. and Decorps, M.: "A New Method for Detection of Ultra Slow Coherent Motion Using B_0 Gradients", in "Abstracts of 8th Annual Meeting, SMRM", Amsterdam, Netherlands, (1989).

88. Caprihan, A., Davis, J.G., Altobelli, S.A., and Fukushima, E.: "A New Method for Flow Velocity Measurement: Frequency Encoded NMR", *Magn. Reson. Med.*, **3**, 352-362 (1986).

89. Hennig, J., Mueri, M., Friedburg, H., and Brunner, P.: "MR Imaging of Flow Using the Steady State Selective Saturation Method", *J. Comput. Assist. Tomogr.*, **11**(5), 872-877 (1987).

90. Merboldt, K.-D., Hänicke, W., and Frahm, J.: "Rapid Fourier flow Imaging Using FLASH Sequences", *Magn. Reson . Med. Bio.*, **1**(2), 137-146 (1988).

91. Firmin, D.N., Klipstein, R.H., Hounsfield, G.L., Paley, M.P., and Longmore, D.B.: "Echo-Planar High-Resolution Flow Velocity Mapping", *Magn. Reson. Med.*, **12**, 316-327 (1989).

92. Norris, D.G., Haase, A., Henrich, D., and Leibfritz, D.: "Projective Flow Imaging with Snapshot-FLASH", in "Abstracts of 8th Annual Meeting, SMRM", Amsterdam, Netherlands, (1989).

93. Kose, K.: "One-Shot Velocity Mapping Using Multiple Spin-Echo EPI and Its Application to Turbulent Flow", *J. Magn. Reson.*, **92**, 631-635 (1991).

94. Dumoulin, C.L., Souza, S.P., Walker, M.F., and Wagle, W.: "Three-Dimensional Phase Contrast Angiography", *Magn. Reson. Med.*, **9**, 139-149 (1989).

95. Callaghan, P.T., Eccles, C.D., and Xia, Y.: "NMR microscopy of dynamic displacements: k-space and q-space imaging", *J. Phys. E: Sci. Instrum.*, **21**, 820 (1988).

96. Bryant, D.J., Payne, J.A., Firmin, D.N., and Longmore, D.B.: "Measurement of Flow with NMR Imaging Using a Gradient Phase and Phase Difference Technique", *J. Comput. Assist. Tomogr.*, **8**(4), 588-593 (1984).

97. Redpath, T.W., Norris, D.G., Jones, R.A., and Hutchison, J.M.S.: "A new method of NMR flow imaging", *Phys. Med. Biol.*, **29**(7), 891-898 (1984).

98. Callaghan, P.T.: "Pulsed field gradient nuclear magnetic resonance as a probe of liquid state molecular organization", *Austr. J. Phys.*, **37**, 359-387 (1984).

99. Stilbs, P.: "Fourier Transform Pulsed-Gradient Spin-Echo Studies of Molecular Diffusion", *Prog. NMR Spectros.*, **19**, 1-45 (1987).

100. Kärger, J., Pfeifer, H., and Heink, W.: ed. "Principles and Application of Self-Diffusion Measurements by Nuclear Magnetic Resonance", "Adv. Magn. Reson.", ed. J.S. Waugh. Vol. **12**, *Academic Press*, San Diego, 1-89 (1988).

101. Le Bihan, D., Turner, R., and MacFall, J.R.: "Effect of Intravoxel Incoherent Motions (IVIM) in Steady-State Free Precession (SSFP) Imaging: Application to Molecular Diffusion Imaging", *Magn. Reson. Med.*, **10**, 324-337 (1989).

102. Neeman, M., Freyer, J.P., and Sillerud, L.O.: "Pulsed-Gradient Spin-Echo Diffusion Studies in NMR Imaging. Effects of the Imaging Gradients on the Determination of Diffusion Coefficients", *J. Mag. Reson.*, **90**, 303-312 (1990).

103. Merboldt, K.-D., Hänicke, W., and Frahm, J.: "Self-Diffusion NMR Imaging Using Stimulated Echoes", *J. Magn. Reson.*, **64**, 479-486 (1985).

104. Ahn, C.B., Lee, S.Y., Nalcioglu, O., and Cho, Z.H.: "An improved nuclear magnetic resonance diffusion coefficient imaging method using an optimized pulse sequence", *Med. Phys.*, **13**(6), 789-793 (1986).

105. Turner, R.: "Single-Shot Diffusion Imaging at 2.0 Tesla", *J. Magn. Reson.*, **86**, 445-452 (1990).

106. Meyer, R.A. and Brown, T.R.: "Diffusion Measurements by Microscopic NMR Imaging", *J. Magn. Reson.*, **76**, 393-399 (1988).

107. Merboldt, K.-D., Bruhn, H., Frahm, J., Gyngell, M.L., Hänicke, W., and Deimling, M.: "MRI of "Diffusion" in the Human Brain: New Results Using a Modified CE-FAST Sequence", *Magn. Reson. Med.*, **9**, 423-429 (1989).

108. Taylor, D.G. and Bushell, M.C.: "The spatial mapping of translational diffusion coefficients by the NMR imaging technique", *Phys. Med. Biol.*, 30(4), 345-349 (1985).

109. Eccles, C.D., Callaghan, P.T., and Jenner, C.F.: "Measurement of the Self-Diffusion Coefficient of Water as a Function of Position in Wheat Grain using Nuclear Magnetic Resonance Imaging", *Biophys. J.*, **53**, 77-81 (1988).

110. Merboldt, K.-D., Hänicke, W., Gyngell, M.L., Frahm, J., and Bruhn, H.: "Rapid NMR Imaging of Molecular Self-Diffusion Using a Modified CE-FAST Sequence", *J. Magn. Reson.*, **82**, 115-121 (1989).

111. Weisenberger, L.A. and Koenig, J.L.: "NMR Imaging of Solvent Diffusion in Polymers", *Appl. Spec.*, **43**(7), 1117-1126 (1989).

112. Le Bihan, D., Breton, E., Lallemand, D., Aubin, M.-L., Vignaud, J., and Laval-Jeantet, M.: "Separation of Diffusion and Prefusion in Intravoxel Incoherent Motion MR Imaging", *Radiology*, **168**, 497-505 (1988).

113. Callaghan, P.T. and Xia, Y.: "Velocity and Diffusion Imaging in Dynamic NMR Microscopy", *J. Magn. Reson.*, **91**, 326-352 (1991).

114. Tanner, J.E. and Stejskal, E.O.: "Restricted Self-Diffusion of Protons in Colloidal Systems by the Pulsed-Gradient, Spin-Echo Method", *J. Chem. Phys.*, **49**(4), 1768-1777 (1968).

115. Merboldt, K.-D., Hänicke, W., and Frahm, J.: "NMR Imaging of Restricted Diffusion", *Ber. Bunsenges. Phys. Chem.*, **91**, 1124-1126 (1987).

116. D'Orazio, F., Bhattacharja, S., Halperin, W.P., and Gerhardt, R.: "Enhanced Self-Diffusion of Water in Restricted Geometry", *Phys. Rev. Lett.*, **63**(1), 43-46 (1989).

117. Kärger, J., Pfeifer, H., and Rudtsch, S.: "The Influence of Internal Magnetic Field Gradients on NMR Self-Diffusion Measurements of Molecules Adsorbed on Microporous Crystallites", *J. Magn. Reson.*, **85**, 381-387 (1989).

118. Callaghan, P.T.: "Susceptibility-Limited Resolution in Nuclear Magnetic Resonance Microscopy", *J. Magn. Reson.*, **87**, 304-318 (1990).

119. Axel, L. and Morton, D.: "MR Flow Imaging by Velocity-Compensated/Uncompensated Difference Images", *J. Comput. Assist. Tomogr.*, **11**(1), 31-34 (1987).

120. Moran, P.R., Saloner, D., and Tsui, B.M.W.: "NMR Velocity-Selective Excitation Composites for the Flow and Motion Imaging and Suppression of Static Tissue Signal", *IEEE Trans. Med. Imaging*, **MI-6**(2), 141-147 (1987).

121. Xiang, Q.S. and Nalcloglu, O.: "Differential Flow Imaging by NMR", *Magn. Reson. Med.*, **12**, 14-24 (1989).

122. Hayward, R.J., Packer, K.J., and Tomlinson, D.J.: "Pulsed field-gradient spin echo N.M.R. studies of flow in fluids", *Molec. Phys.*, **23**(6), 1083-1102 (1972).

123. Jenner, C.F., Xia, Y., Eccles, C.D., and Callaghan, P.T.: "Circulation of water within wheat grain revealed by nuclear magnetic resonance micro-imaging", *Nature*, **336**, 399 (1988).

124. Meiboom, S. and Gill, D.: "Modified spin-echo method for measuring nuclear relaxation times", *Rev. Sci. Instr.*, **29**, 688 (1958).

125. McCall, D.W., Douglass, D.C., and Anderson, E.W.: "Self-Diffusion Studies by Means of Nuclear Magnetic Resonance Spin-Echo Techniques", *Ber. Bunseges. Phys. Chem.*, **67**, 336-340 (1963).

126. Torrey, H.C.: "Bloch Equations with Diffusion Terms", *Phys. Rev.*, **104**(3), 563 (1956).

127. Wang, M.C. and Uhlenbeck, G.E.: "On the Theory of the Brownian Motion II", *Rev. Mod. Phys.*, **17**, 323-342 (1945).

128. Egelstaff, P.A.: "An introduction to the liquid state", *Academic Press*, London and New York, (1967).

129. Ernst, R.R.: "Magnetic Resonance with Stochastic Excitation", *J. Magn. Reson.*, 3, 10-27 (1970).

130. Kärger, J. and Heink, W.: "The Propagator Representation of Molecular Transport in Microporous Crystallites", *J. Magn. Reson.*, **51**, 1-7 (1983).

131. Callaghan, P.T.: "PGSE-MASSEY, a Sequence for Overcoming Phase Instability in Very-High-Gradient Spin-Echo NMR", *J. Magn. Reson.*, **88**, 493-500 (1990).

132. Xia, Y.: "Static and Dynamic Imaging using Magnetic Field Gradients", [MSc thesis], *Massey University, New Zealand* (1988).

133. Xia, Y. and Callaghan, P.T.: "Measurement of Diffusion and Flow at Microscopic Resolution by NMR Imaging", in "Heat and Mass Transfer '89", *University of Canterbury*, Christchurch, New Zealand, (1989).

134. Cebeci, T. and Bradshaw, P.: "Physical and Computational Aspects of Convective Heat Transfer", *Springer-Verlag*, New York, (1984).

135. While, F.M.: "Heat Transfer", *Addison-Wesley*, Massachusetts, (1984).

136. JEOL: "JEOL FX-60 Software", *JEOL Ltd.*, Japan, (1974).

137. Eccles, C.D.: "Microscopic NMR Imaging", [PhD thesis], *Massey University, New Zealand* (1987).

138. Anderson, W.A.: "Electrical Current Shims for Correcting Magnetic Fields", *Rev. Sci. Instrum.*, **32**(3), 241-250 (1961).

139. Tanner, J.E.: "Pulsed Field Gradients for NMR Spin-Echo Diffusion Measurements", *Rev. Sci. Instrum.*, **36**(8), 1086-1087 (1965).

140. Apple Computer Inc.: "Inside Macintosh", *Addison-Welsley Publishing Company Inc.*, (1985).

141. Hilbert, C. and Clarke, J.: "DC SQUIDs as Radio-Frequency Amplifiers", *J. Low Temp. Phys.*, **61**, 263-280 (1985).

142. AMPTEK Inc.: "Charge Sensitive Preamplifier", *AMPTEK Inc., Bedford, MA 01730 USA* (1990).

143. Kirschman, R.K.: Ed. "Low-Temperature Electronics", *IEEE Press* (1986).

144. Mansfield, P. and Chapman, B.: "Active magnetic screening of coils for static and time-dependent magnetic field generation in NMR imaging", *J. Phys. E: Sci. Instrum.*, **19**, 540-545 (1986).

145. Mansfield, P. and Chapman, B.: "Active Magnetic Screening of Gradient Coils in NMR Imaging", *J. Magn. Reson.*, **66**, 573-576 (1986).

146. Mansfield, P. and Chapman, B.: "Multishield Active Magnetic Screening of Coil Structures in NMR", *J. Magn. Reson.*, **72**, 211-223 (1987).

147. Turner, R., Chapman, B., Howseman, A.M., Ordidge, R.J., Coxon, R., Glover, P., and Mansfield, P.: "Snap-Shot Magnetic Resonance Imaging at 0.1 T Using Double-Screened Gradients", *J. Magn. Reson.*, **80**, 248-258 (1988).

148. Bowtell, R. and Mansfield, P.: "Screened coil designs for NMR imaging in magnets with transverse field geometry", *Meas. Sci. Technol.*, **1**, 431-439 (1990).

149. Jacobsohn, B.A. and Wangsness, R.K.: "Shapes of Nuclear Induction Signals", *Phys. Rev.*, **73**, 942-946 (1948).

150. Duczmal, T., Kubiak, J., Buckmaster, H.A., and Milligan, P.: "The Determination of Absolute and Relative B Gradients Using Rapid-Scan NMR. A Computational Modeling Evaluation", *J. Magn. Reson.*, **77**, 471-482 (1988).

151. LaPage, J., Bernalite, A., and Lindholm, D.A.: "Analysis of Resistivity Measurements by the Eddy Current Decay Method", *Rev. Sci. Instrum.*, **39**(7), 1019-1026 (1968).

152. van Vaals, J.J. and Bergman, A.H.: "Optimization of Eddy-Current Compensation", *J. Magn. Reson.*, **90**, 52-70 (1990).

153. Jehenson, P., Westphal, M., and Schuff, N.: "Analytical Method for the Compensation of Eddy-Current Effects Induced by Pulsed Magnetic Field Gradients in NMR Systems", *J. Magn. Reson.*, **90**, 264-278 (1990).

154. Crozier, S.: "High-field Nuclear Magnetic Resonance Microspectroscopy and Adjunct Pulsed Field Gradient Techniques", [PhD Thesis], *University of Queensland*, Australia (1991).

155. Siebold, H.: "Design optimization of main, gradient and rf field coils for MR imaging", *IEEE Trans. Magn.*, **26**(2), 841-846 (1990).

156. Mills, R.: "Self-Diffusion in Normal and Heavy Water in the Range 1-45°", *J. Phys. Chem.*, 77(5), 685-688 (1973).

157. Ogura, Y.: "Comparative Anatomy of Vegetative Organs of the Pteridophytes", *Gebruder Borntraeger*, Berlin, (1972).

158. Meyer, F.J.: "Das Leitungssystem von *Equisetum arvense*", *Jb. wiss. Bot.*, **59**, 263-286 (1920).

159. Bierhorst, D.W.: "Morphology of vascular plants", *McMillan*, New York, (1971).

160. Lingle, S.E. and Chevalier, P.: "Development of the Vascular Tissue of the Wheat and Barley Caryopsis as Related to the Rate and Duration of Grain Filling", *Crop Science*, **25**, 123-128 (1985).

161. O'Brien, T.P., M.E., S., Lee, J.W., and Smart, M.G.: "The Vascular System of the Wheat Spikelet", *Aust. J. Plant Physiol.*, **12**, 487-511 (1985).

162. Callaghan, P.T., Jolley, K.W., and Lelievre, J.: "Diffusion of Water in the Endosperm Tissue of Wheat Grains as Studied by Pulsed Field Gradient Nuclear Magnetic Resonance.", *Biophys. J.*, **28**, 133-141 (1979).

163. Back, P.J., Coy, A., Xia, Y., Callaghan, P.T., Diamante, L.M., and S.L., U.: "Some biological applications of motional contrast in n.m.r. microscopy", *Int. J. Biol. Macromol.*, **13**, 181-189 (1991).

164. Priestley, J.H., Scott, L.I., and Harrison, E.: "An introduction to Botany", *Longmans, Green & Co Ltd*, London, (1964).

165. Köckenberger, W., Xia, Y., Jeffrey, K.R., and Callaghan, P.T.: *Planta*, to be submitted (1992).

166. Bird, R.B., Stewart, W.E., and Lightfoot, E.N.: "Transport phenomena", *Wiley*, New York, (1960).

167. Tritton, D.J.: "Physical Fluid Dynamics", *Van Nostrand Reinhold*, New York, (1977).

168. Roache, P.J.: "Computational Fluid Dynamics", *Hermosa Publishers, Albuquerque*, New Mexico, (1972).

169. Peyret, R. and Taylor, T.D.: "Computational Methods for Fluid Flow", *Springer-Verlag*, New York, (1983).

170. Fletcher, C.A.J.: "Computational Techniques for Fluid Dynamics", *Springer-Verlag*, Berlin, (1988).

171. Tanner, R.I.: "Engineering Rheology", *Clarendon Press*, Oxford, (1985).

172. Moffat, H.K.: "Viscous and Resistive Eddies Near a Sharp Corner", *J. Fluid Mech.*, **18**, 1 (1964).

173. Crochet, M.J., Davies, A.R., and Walters, K.: "Numerical Simulation of Non-Newtonian Flow", *Elsevier Science Publishers*, Amsterdam, (1984).

174. Press, W.H., Flannery, B.P., Teukolsky, S.A., and Vetterling, W.T.: "Numerical Recipes", *Cambridge University Press*, Cambridge, (1989).

175. Xia, Y., Jeffrey, K.R., and Callaghan, P.T.: "Imaging Velocity Profiles: Flow Through an Abrupt Contraction and Expansion", *AIChE J*, in press (1992).

176. Peerless, S.J.: "Basic Fluid Mechanics", *Pergamon Press*, Oxford, (1967).

177. Massey, B.S.: "Mechanics of Fluids", *Van Nostrand Reinhold (UK) Co. Ltd.*, Berkshire, England, (1983).

178. White, S.A. and Baird, D.G.: "Flow visualization and birefringence studies on planar entry flow behavior of polymer melts", *J. Non-Newtonian Fluid Mech.*, **29**, 245 (1988).

179. Barnes, H.A., Hutton, J.F., and Walters, K.: "An Introduction to Rheology", *Elsevier*, Amsterdam, (1989).

180. Xia, Y. and Callaghan, P.T.: "Study of Shear Thinning in High Polymer Solution Using Dynamic NMR Microscopy", *Macromole.*, **24**(17), 4777-4786 (1991).

181. Doi, M. and Edwards, S.F.: "Dynamics of Concentrated Polymer Systems", *J. Chem. Soc., Faraday Trans. 2*, **74**, 1789-1801 (1978).

182. Doi, M. and Edwards, S.F.: "Dynamics of Concentrated Polymer Systems. Part 2 - Molecular Motion under Flow", *J. Chem. Soc., Faraday Trans. II*, **74**, 1802-1817 (1978).

183. Doi, M. and Edwards, S.F.: "Dynamics of Concentrated Polymer Systems. Part 3 - The Constitutive Equation", *J. Chem. Soc., Faraday Trans. II*, **74**, 1818-1832 (1978).

184. Doi, M. and Edwards, S.F.: "The Theory of Polymer Dynamics", *Oxford University Press*, Oxford, (1987).

185. De Gennes, P.G.: "Reptation of a Polymer Chain in the Presence of Fixed Obstacles", *J. Chem. Phys.*, **55**(2), 572-579 (1971).

186. Graessley, W.W.: "Entangled Linear, Branched and Network Polymer Systems - Molecular Theories", *Advances in Polymer Science*, **47**, 67-117 (1982).

187. De Gennes, P.G. and Léger, L.: "Dynamics of Entangled Polymer Chains", *Ann. Rev. Phys. Chem.*, **33**, 49-61 (1982).

188. Léger, L. and Viovy, J.L.: "Entangled polymers", *Contemp. Phys.*, **29**(6), 579-595 (1988).

189. Edwards, S.F.: "The statistical mechanics of polymerized material", *Proc. Phys. Soc. Lon.*, **92** (Pt 1), 9-16 (1967).

190. Skelland, A.H.P.: "Non-Newtonian Flow and Heat Transfer", *John Wiley and Sons*, New York, (1967).

191. Ferry, J.D.: "Viscoelastic Properties of Polymers", *John Wiley and Sons*, New York, (1980).

192. Vinogradov, G.V.: "Critical regimes of deformation of liquid polymeric systems", *Rheol. Acta*, **12**, 273-289 (1973).

193. McLeish, T.C.B. and Ball, R.C.: "A Molecular Approach to the Spurt Effect in Polymer Melt Flow", *J. Polym. Sci.: Part B: Polym. Phys.*, **24**, 1735-1745 (1986).

194. Léger, L., Hervet, H., and Rondelez, F.: "Reptation in Entangled Polymer Solutions by Forced Rayleigh Light Scattering", *Macromole.*, **14**, 1732-1738 (1981).

195. Tirrell, M.: "Polymer Self-Diffusion in Entangled Systems", *Rubber Chemistry and Technology*, **57**, 523-556 (1984).

196. De Gennes, P.G.: "Scaling Concepts in Polymer Physics", *Cornell University Press*, Ithaca, (1979).

197. De Gennes, P.G.: "Dynamics of entangled polymer solutions. I The Rouse model. II Inclusion of hydrodynamic interactions.", *Macromole.*, **9**, 587-598 (1976).

198. Callaghan, P.T. and Pinder, D.N.: "Influence of polydispersity on self-diffusion measurements", **18**, 373 (1985).

199. Callaghan, P.T. and Lelievre, J.: "Polysaccharide and Solvent Self-Diffusion: The Influence of Polymer Size and Shape", *Anal. Chem. Acta*, **189**, 145 (1986).

200. Bortel, E. and Kochanowski, A.: "Molecular Properties of High Molecular Weight Poly(ethylene oxide)s in Aqueous Solutions. Determination of Molecular Weights and Related Parameters", *Makromol. Chem., Rapid Commun.*, **1**, 205-210 (1980).

201. Mackley, M.R. and Moore, I.P.T.: "Experimental Velocity Distribution Measurements of High Density Polyethylene Flowing Into and Within a Slit", *J. Non-Newtonian Fluid Mech.*, **21**, 337-358 (1986).

202. Burton, R.H., Folkes, M.J., Narh, K.A., and Keller, A.: "Spatial variation in viscosity in sheared polymer melts", *J. Mater. Sci. (GB)*, **18**, 315-320 (1983).

203. De Gennes, P.G.: "Viscometric flows of tangled polymers", *Compt. Rend. Acad. Sci. Paris B.*, **288** (14), 219-220 (1979).

204. Onuki, A.: "Conjectures on Elongation of a Polymer in Shear Flow", *J. Phys. Soc. (Japan)*, **54**, 3656-3659 (1985).

Publications

1. Y. Xia and P.T. Callaghan, "The Measurement of Diffusion and Flow in Polymer Solutions using Dynamic NMR Microscopy", *Makromol. Chem., Macromol. Symp.*, **34**, 277 (1990).

2. P.T. Callaghan and Y. Xia, "Velocity and Diffusion Imaging in Dynamic NMR Microscopy", *J. Magn. Reson.*, **91**, 326 (1991).

3. P.J. Back, A. Coy, L.M. Diamante, S.L. Umbach, Y. Xia and P.T. Callaghan, "Some biophysical applications of motional contrast in NMR microscopy", *Int. J. Biol. Macromol.*, **13**, 181 (1991).

4. Y. Xia and P.T. Callaghan, "Study of Shear Thinning in High Polymer Solution Using Dynamic NMR Microscopy", *Macromolecules*, **24** (17), 4777-4786 (1991).

5. Yang Xia and Paul T. Callaghan, ""One-Shot" Velocity Microscopy: NMR Imaging of Motion Using a Single Phase-encoding Step", *Magn. Reson. Med.*, **23**, 138-153 (1992).

6. Y. Xia, K.R. Jeffrey and P.T. Callaghan, "Purpose-designed Probe for Dynamic NMR Microscopy in an Electromagnet", *Magn. Reson. Imaging*, in press (1992).

7. Yang Xia, Kenneth R. Jeffrey and Paul T. Callaghan, "Imaging Velocity Profiles: Flow Through an Abrupt Contraction and Expansion", *AIChE J.*, in press (1992).

8. Y. Xia, V. Sarafis, E.O. Campbell, P.T. Callaghan, "Non Invasive Imaging of Water Flow in Plants by NMR Microscopy", *Protoplasma*, to be submitted (1992).

9. W. Köckenberger, Y. Xia, K.R. Jeffrey, and P.T. Callaghan: *Planta*, to be submitted (1992).